HEATSTORE

Final report on tools and workflows for simulating subsurface dynamics of different types of High Temperature Underground Thermal Energy Storage

Prepared by: Thomas Driesner (ed); ETH - Eidgenössische Technische Hochschule Zürich

Benno Drijver, Peter Oerlemans, Hetty Mathijssen; IF Technology

Mariëlle Koenen, Stefan Carpentier, Maartje Struijk, Jan Diederik van Wees, Jasper Griffioen; TNO

Stijn Beernink, Martin Bloemendal, Niels Hartog; KWR Watercycle Research Institute

Julian Mindel, Daniel Birdsell, Benoit Lamy-Chappuis, Thomas Driesner; ETH - Eidgenössische Technische Hochschule Zürich

Luca Guglielmetti, Ovie Etureya, Andrea Moscariello; Université de Genève

Peter Alt-Epping, Christoph Wanner, Larryn W. Diamond, Daniela van den Heuvel; University of Berne

Florentin Ladner, Geo-Energie Suisse AG

Rubén Vidal, Maarten Saaltink & Sebastia Olivella; UPC - Universitat Politecnica de Catalunya

Sigrún Tómasdóttir, Gunnar Gunnarsson, Edda Sif Aradóttir, Thomas Ratouis; Reykjavik Energy

Charlotte Rey, Patrick Egermann; Storengy

Charles Maragna; BRGM

Christoph M. König, Torsten Seidel, Timo König; delta h Ingenieurgesellschaft

Geoffroy Gauthier, PlanEnergi

Carsten Møller Nielsen, GEUS

Fátima Viveiros, Catarina Silva, Pedro Freire, José Virgílio Cruz, Vittorio Zanon; IVAR University of the Azores

Checked by: Thomas Driesner, ETH, WP2 leader

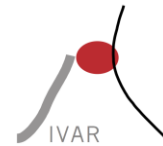Approved by: Holger Cremer, HEATSTORE coordinator

Summary

This report documents the achievements in simulating subsurface dynamics of different types of High Temperature Underground Thermal Energy Storage (HT-UTES) in Work Package 2 of the HEATSTORE project. For each case study, the site-specific conceptual model(s), selection of modelling tool(s), numerical approach(es) and workflow(s) is provided and results as well as, partly, validation approaches are discussed. This report is complemented by HEATSTORE deliverable D2.2 on the details of academic simulation codes that were used for some of the case studies (Tómasdóttir, S. & Gunnarsson, G. (ed) 2021: HEATSTORE – Final report on UTES-type/site-specific simulators based on academic/research codes. GEOTHERMICA – ERA NET Cofund Geothermal. 58 pp.) and D5.3 (Diaz-Maurin, F. & Saaltink, M.W. (eds.) 2021: Model validation for subsurface dynamics, GEOTHERMICA – ERA NET Cofund Geothermal. 110 pp.) that provides a comprehensive report of HEATSTORE's model validation activities.

Modelling was performed on

- Five sites with a High Temperature - Aquifer Thermal Energy Storage concept (HT-ATES), at Agriport A7 and Kopper Cress, Netherlands; Geneva and Berne, Switzerland; and Reykjavik, Iceland. High temperature water sources differ and range from conventional hydrothermal deep geothermal through heated groundwater used in a geothermal power plant to waste heat from waste incinerators. A broad variety of tools and pre-processing workflows to arrive at conceptual models is presented and reflects the different degrees of prior knowledge and maturity of the project. Process simulation focused on heat transfer and flow with geochemical and geomechanical modelling adding important factes for some of the project.
- An advanced example of borehole thermal energy storage (BTES, French pilot project).
- Warm water storage in old undergorund coal mine working (MTES, German project).

The report includes four sections on other modelling activities - one report on deep subsurface reconaissance assessment for UTES in Denmark and one on operating UTES examples in Denmark, followed by two reports on transferring the capabilities of advanced academic simulation tools used in HEATSTORE to other geothermal applications, i.e., constraining the nature of a high-enthalpy reservoir on the Azores and scenario modelling for superhigh-temperature resource development and utilization in Iceland.

www.heatstore.eu

About HEATSTORE

High Temperature Underground Thermal Energy Storage

The heating and cooling sector is vitally important for the transition to a low-carbon and sustainable energy system. Heating and cooling is responsible for half of all consumed final energy in Europe. The vast majority – 85% - of the demand is fulfilled by fossil fuels, most notably natural gas. Low carbon heat sources (e.g. geothermal, biomass, solar and waste-heat) need to be deployed and heat storage plays a pivotal role in this development. Storage provides the flexibility to manage the variations in supply and demand of heat at different scales, but especially the seasonal dips and peaks in heat demand. Underground Thermal Energy Storage (UTES) technologies need to be further developed and need to become an integral component in the future energy system infrastructure to meet variations in both the availability and demand of energy.

The main objectives of the HEATSTORE project are to lower the cost, reduce risks, improve the performance of high temperature (~25°C to ~90°C) underground thermal energy storage (HT-UTES) technologies and to optimize heat network demand side management (DSM). This is primarily achieved by 6 new demonstration pilots and 8 case studies of existing systems with distinct configurations of heat sources, heat storage and heat utilization. This will advance the commercial viability of HT-UTES technologies and, through an optimized balance between supply, transport, storage and demand, enable that geothermal energy production can reach its maximum deployment potential in the European energy transition.

Furthermore, HEATSTORE also learns from existing UTES facilities and geothermal pilot sites from which the design, operating and monitoring information will be made available to the project by consortium partners.

HEATSTORE is one of nine projects under the GEOTHERMICA – ERA NET Cofund and has the objective of accelerating the uptake of geothermal energy by 1) advancing and integrating different types of underground thermal energy storage (UTES) in the energy system, 2) providing a means to maximize geothermal heat production and optimize the business case of geothermal heat production doublets, 3) addressing technical, economic, environmental, regulatory and policy aspects that are necessary to support efficient and cost-effective deployment of UTES technologies in Europe. The three-year project will stimulate a fast-track market uptake in Europe, promoting development from demonstration phase to commercial deployment within 2 to 5 years, and provide an outlook for utilization potential towards 2030 and 2050.

The 23 contributing partners from 9 countries in HEATSTORE have complementary expertise and roles. The consortium is composed of a mix of scientific research institutes and private companies. The industrial participation is considered a very strong and relevant advantage which is instrumental for success. The combination of leading European research institutes together with small, medium and large industrial enterprises, will ensure that the tested technologies can be brought to market and valorised by the relevant stakeholders.

Document Change Record

This section shows the historical versions, with a short description of the updates.

Version	Short description of change
2019.06.12	First version, Thomas Driesner
2019.06.20	All items (Sections, Figure, sections) formatted coherently using Word's cross-referencing etc.; added comments for final editing requests. Thomas Driesner
2019.06.27	Final editing of M9 intermediate version according to inputs of contributors
2021.06.30	Unedited raw compilation of M35 version, based on contributors input
2021.10.29	Pre-final M35 version
2021.11.08	Final M35 version
2021.11.17	Added Danish chapter from M9 version upon request from GEUS
2021.11.18	Revised final version

Table of Content

1 Introduction

Modelling subsurface dynamics of high temperature underground thermal energy storage (HT-UTES) provides key inputs for (pre-)feasibility studies, environmental impact assessment, system design and optimization, and sustainable operation. As numerical modelling is comparatively cheap and efficient, establishing a set of reliable modelling tools and workflows for different types of HT-UTES is a key activity in HEATSTORE. For example, geologic risk (uncertainty about formation properties and resulting operation conditions to be encountered at depth) is an important barrier for positive investment decisions that could be assessed by simulating different scenarios already in the pre-drilling phase.

The dynamics in geothermal underground processes are governed by coupled Thermo-Hydro-Mechanical-Chemical (THMC) processes, of which typically only subsets are relevant for a given geothermal technology. Currently, a variety of simulation tools from hydrogeology/porous media are used to assess design, control and efficiency of HT-UTES systems. For example, geothermal flow (TH) or reactive geothermal flow (THC) in porous media can routinely be modelled with a variety of well-established codes, most of them available to the HEATSTORE consortium, but most have not yet been validated or benchmarked for HT-UTES application.

Standardized and comprehensive modelling workflows for project development from (pre-)feasibility studies to implementation and operation have generally remained the exception rather than the rule across a wide spectrum of geothermal technologies. Providing a set of tested and benchmarked tools and workflows for demonstrating their advantages and increasing the credibility of modelling as an efficient and reliable key method in geothermal project development is the key objective of this work package and links or feeds directly to work packages 1, 3, 4, and 5.

This report relates to Task 2.1 ("Modelling toolsets and workflows for optimal and efficient HT-UTES of different types"), which is an umbrella task that encompasses all activities on modelling the subsurface dynamics at the HEATSTORE sites. The report reflects the initial selection tools, methods and anticipated workflows of the Work Package 2 partners at month 9 into the project. A particular emphasis has been put onto how existing geologic information and system specifications have been conceptualized to translate them into adequate numerical models, including the selection of physical and chemical processes to be included, which varies between the different HEATSTORE sites. Most groups put a strong emphasis on scenario development to cover the range of geologic uncertainty and utilization options.

During the course of the project, WP2 will closely interact with WP3 ("Heating System integration and optimisation of design and operation") and WP5 ("Monitoring and validation to assess system performance and workflow") in order to achieve the most reliable and valuable modelling approaches to HT-UTES. An updated version of this report is due Month 35 and will include actual results, validation approaches and recommendations.

Sections 0 (Azores Study) and 5.4 (Superhigh Temperature Resource in Iceland) show the initial approaches of HEATSTORE to demonstrate how advanced academic codes that are introduced into HT-UTES modelling in Tasks 2.1 and 2.2 ("Integrating advanced academic simulation codes into diverse geothermal project development workflows") can be applied to other geothermal application beyond HT-UTES. We decided to include these sections here to show the full picture of modelling approaches.

2 High Temperature Aquifer Thermal Energy Storage (HT-ATES)

2.1 Dutch pilot site Agriport A7 at Wieringermeer

Benno Drijver[1], Mariëlle Koenen[2], Stefan Carpentier[2], Peter Oerlemans[1]

[1]IF Technology, [2]TNO

2.1.1 Introduction

Agriport A7 is a large horticultural area, that is being developed in the Wieringermeer polder in the north-western part of the Netherlands. Historically, the horticultural sector uses large quantities of natural gas for heating greenhouses and production of electricity and CO_2 (CO_2 is used to stimulate the growth of the crops). The ambition of the horticultural sector is to become more sustainable and less dependent on fossil fuels. One of the ways to reach this goal is to use deep geothermal energy systems for heating. Currently, three deep geothermal doublets at 1900-2400 m depth are in operation for heating of the greenhouses, that are operated by the energy company ECW (Energy Combination Wieringermeer). The geothermal heat is provided to a (district) heating network, that transports the heat to the customers (Figure 2.1.1).
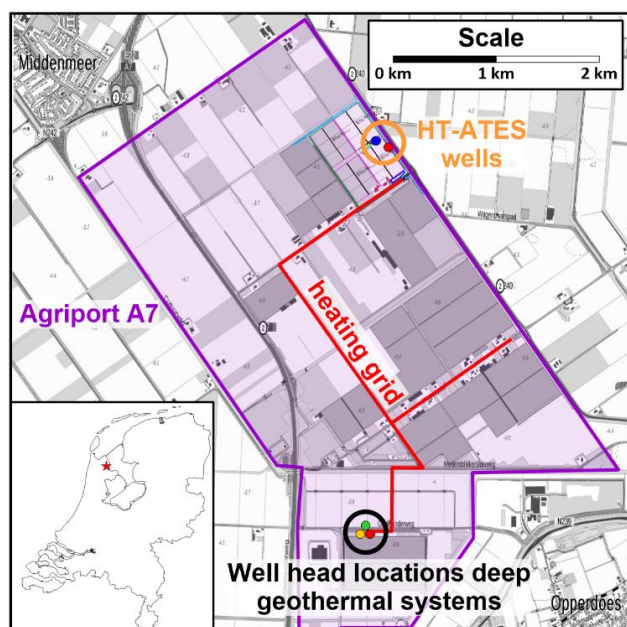
Figure 2.1.1 Project location, locations of the HT-ATES wells, the heating grid and (surface) locations of the deep geothermal doublets.

The geothermal systems can provide approximately 60% of the current heat demand in the winter months. The remaining part of the heat is provided by biomass. In the summer months, the heat demand is small and there is significant overcapacity. ECW wants to use this overcapacity to store the heat in a shallower aquifer by HT-ATES. In the winter period the stored heat will be recovered and used for heating. This would allow ECW to provide more sustainable heat to the customers. Figure 2.1.2 shows the heat supply to the customers in a future scenario including a HT-ATES system.

Agriport A7 is under development: new greenhouses are being built and will be built in the coming decades, which means that the heating grid and its transport capacity will need to grow. At the same time, the geothermal heat production capacity is increasing, because of the realisation of new geothermal wells. The investment costs for a heating grid strongly depend on the piping diameter. As a consequence, creating extra heat transport capacity is expensive. The largest heat transport capacity is required in the winter period. In the summer period the heat transport capacity of the heating grid is much larger than the heat demand requires. The HT-ATES system was placed at the other end of the heating grid. In this way, the overcapacity in the heat transport capacity of the heating grid is used to transport heat to the other end of the heating grid in the summer period and stored by a HT-ATES system. In the winter period, the heat that is recovered from the HT-ATES is provided directly to the customer. This helps to reduce the requirements to

the capacity of the heating grid, especially when HT-ATES would be implemented on a much larger scale. In this way, HT-ATES helps to use the heat transport capacity of the heating grid more efficiently.
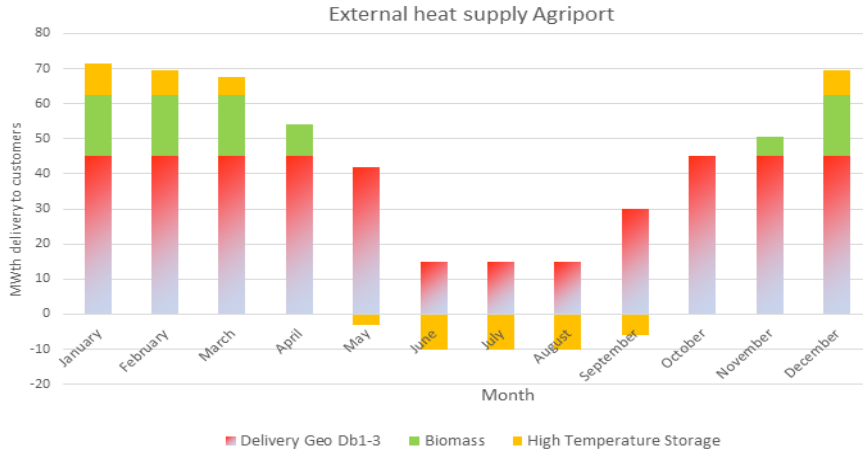
Figure 2.1.2 Future heat supply scenario for Agriport A7. Geo Db1-3 represent the three geothermal doublet systems.

Figure 2.1.3 shows a scheme of the HT-ATES system and its connection to the heating network and the customers. The heat from the deep geothermal systems is stored in the HT-ATES at ~83 °C (2 °C temperature loss in the heat exchanger). The intended storage volume is 440,000 m³ per year, assuming a flow rate of 150 m³/h and injection of heat at full capacity during ~2900 hours (~4 months). In the winter period, hot water is extracted from the hot well. At the start of the extraction phase, the temperature of the recovered water will be close to the injection temperature. During the winter season, the temperature of the extracted water will gradually decrease. When the extraction temperature drops below the minimum required extraction temperature (also referred to as the cut-off temperature, in this case 55 °C), the operation of the HT-ATES is stopped.
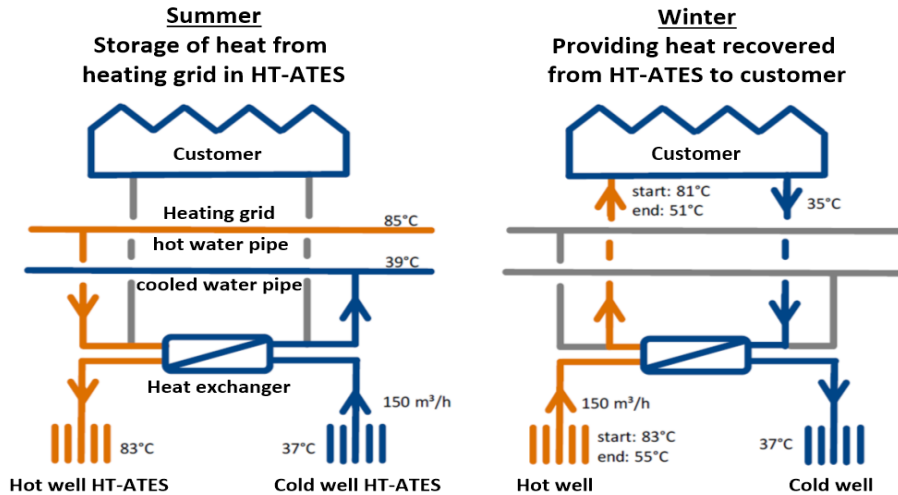
Figure 2.1.3 Schematic overview of the HT-ATES system in heat storage mode (summer) and heat recovery mode (winter) including temperatures and flow rates.

2.1.1.1 Subsurface conditions at the ECW Demonstration site

Figure 2.1.4 shows schematic cross section with the geology and the well trajectories of the first deep geothermal doublet and the HT-ATES wells. The deep geothermal reservoir wells produce and inject water in the Slochteren Formation (Permian age) and the HT-ATES wells use the Maassluis Formation (early Pleistocene age).
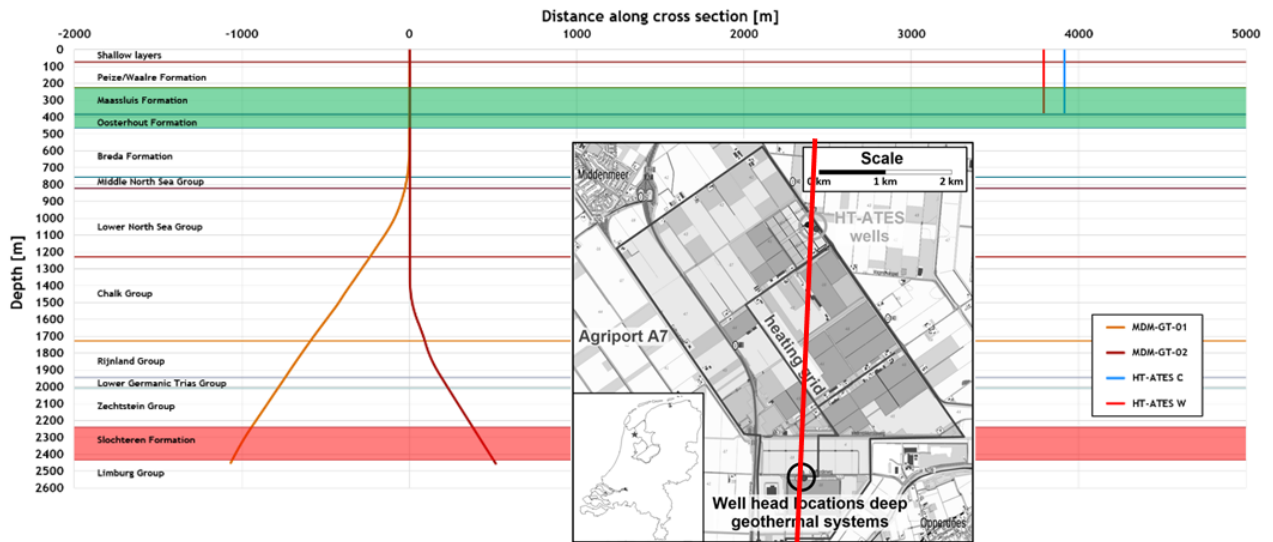
Figure 2.1.4 Schematic cross section of the geology and the well trajectories of the first deep geothermal doublet (MDM-GT-01 and MDM-GT-02) and the HT-ATES wells (HT-ATES C and HT-ATES W).

In the surrounding area, the information on the intended storage aquifer was limited. Therefore, the uncertainty about the exact aquifer properties and conditions was relatively large. Following one of the key recommendations from the early stage results of the HEATSTORE project (Bakema and Drijver, 2018; Drijver et al., 2019; Kallesøe and Vangkilde-Pedersen, 2020), a test drilling was performed in 2019, to investigate the Maassluis and Oosterhout formations (both of marine origin) as possible target formations for HT-ATES. In the test drilling two potential storage aquifers were found, both consisting of unconsolidated sand: one between 360 and 383 m depth (aquifer 4, part of the Maassluis Formation) and another between 424 and 463 m depth (aquifer 5, part of the Oosterhout Formation). After careful consideration of the test drilling results, aquifer 4 was selected as storage aquifer (Drijver et al. 2020).
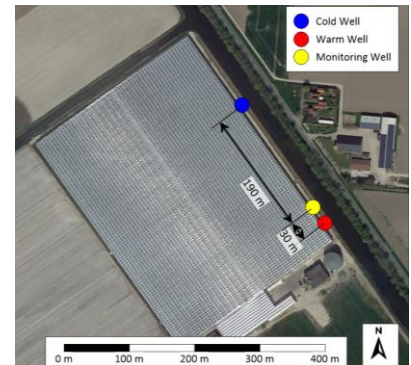
Figure 2.1.5 Locations of the HT-ATES wells and the monitoring well (= test drilling).

During spring of 2020 the HT-ATES wells were drilled. The hydrogeology at both well locations proved to be very similar to the conditions at the location of the test drilling. The locations of the HT-ATES wells and the test drilling (that will be used as a monitoring well in the operational phase) are shown in Figure 2.1.5. Figure 2.1.6 shows a

schematic cross section over the HT-ATES wells and the monitoring well.

2.1.1.2 Research questions

The model simulations are intended to predict the effects of HT-ATES on the subsurface and to support the design of the system and its monitoring plan. The focus of these simulations is on the development of the heat plume, the dissipation of heat to the confining layers, the recovery efficiency and prevention of clogging caused by scaling.

In order to construct a detailed and functional design for the HT-ATES, certain research questions have to be addressed. These research questions apply to the following topics:

- Seismic reprocessing for subsurface characterization
- Thermal effects of the HT-ATES system on the subsurface
- Geochemical effects of the HT-ATES system on the subsurface

Seismic reprocessing for subsurface characterization

Test drillings often encounter different geological layering and hydrogeological characteristics than predicted by hydrogeological models. Especially at the depth interval relevant for HT-ATES systems, the existing hydrogeological models are based on a limited number of drillings. The main research question is whether additional data can be obtained from reprocessing of existing seismic data with the focus on this depth interval, and whether a fast and therefore cost-effective workflow can be developed to gain insight in the subsurface where data is sparse. Such a methodology could reduce the necessity of very expensive test drillings, support the site selection of a test drilling for HT-ATES systems and/or give information on the lateral continuity of geological layers in the area of interest.

Figure 2.1.6 Schematic cross section across the ECW HT-ATES wells and the monitoring well and the hydrogeological conditions as derived from the test drilling.

Research questions:

- Can existing seismic lines, applied to investigate the deep subsurface, be used to obtain more information on the relatively shallow subsurface?
- Can we develop a workflow for fast-track reprocessing of existing seismic data?

Thermal effects of HT-ATES

The main goal of HT-ATES is temporary storage of heat in the subsurface and recovery of (part of) the stored heat when heat demand is large. Due to several processes in the subsurface, part of the stored heat is lost. These heat losses reduce the amount of heat that can be recovered, causing a reduction of the recovery efficiency, and lead to thermal effects in the immediate vicinity of the HT-ATES system.

Research questions:

- What is the expected recovery efficiency: what part of the stored heat can be recovered at a useful temperature level?
- What is the thermal impact of HT-ATES system at ECW on the subsurface (in and around the storage aquifer, and around the hot well casings)
- What is the optimal design for the doublet system, based on thermal interference between hot/cold well?
- At what distance from the monitoring well, should the HT-ATES wells be placed?
- Based on the modelling results: what recommendations can be made for the monitoring plan?

Geochemical effects of HT-ATES related to water treatment

One of the key aspect for HT-ATES systems is the prevention of clogging caused by the precipitation of minerals. In the period 1976-1988 six experimental HT-ATES systems were initiated in different countries (USA, Switzerland, Denmark, Sweden, France), partly in the framework of the ECES (Energy Conservation

through Energy Storage) research projects from the International Energy Agency (IEA). The idea was to use the projects for thermal energy supply after the experimental phase, but due to serious operational problems this did not occur. One of the main problems encountered (Sanner, 1999; Snijders, 2000) was clogging due precipitation of minerals (clogging of wells, heat exchanger, piping, etc.). In the following years, water treatment methods have been developed to solve these problems. Different water treatment options are described in paragraph 2.3 of HEATSTORE D2.1 (Nielsen and Vangkilde-Pedersen, 2019). The experiences with water treatment in full scale HT-ATES projects in The Netherlands are described by Drijver (2011).

At the ECW project, water treatment by addition of CO_2 was selected. This method has not been used in full scale HT-ATES projects yet, but has been tested successfully in experiments. CO_2 treatment for HT-ATES was developed at the University of Stuttgart and tested with good success in Switzerland at SPEOS-Dorigny (Sanner (ed.), 1999 ; Koch and Ruck, 1992). The method was further developed within IEA-ECES Annex 6 (Koch and Ruck, 1993, reference in Sanner (ed.), 1999) and tested in Canada (Adsett et al., 1997). In water treatment systems using membranes (e.g. Reverse Osmosis systems), CO_2-treatment has also been used for scaling prevention. It has been used successfully in pilot projects for the production of drinking water from brackish groundwater in The Netherlands (Hartog, 2018, personal communication) and has also been proposed for scaling prevention in deep geothermal projects (GPC/KWR, 2015).

Research questions related to water treatment and its geochemical effects are:

- What is the required dosage and how does this dosage develop in subsequent years of operation?
- What are the uncertainties and how to deal with those uncertainties?
- What are the associated requirements for monitoring in the operational phase?

2.1.2 Subsurface characterization by seismic reprocessing

2.1.2.1 Reprocessing approach

The existing seismic line SL7608, which is located in the area of Middenmeer, was reprocessed conventionally and by Active Controlled Source Interferometry (ACSI, Figure 2.1.8) using the workflow shown in Figure 2.1.9. This workflow works with GLOBE Claritas seismic processing software to do the relatively conventional pre-processing and Prestack Time Migration. Subsequently, proprietary Matlab algorithms developed by TNO perform image enhancements like denoising and bandwidth extension. The shallow seismic reprocessing workflow results are analysed in OpendTect software where aquifer boundaries are semi-automatically tracked with pattern-recognition algorithms and outputted in grid files. The reprocessed data was then compared to the pre-drilling prior foreseen aquifer interfaces, the post-drilling posterior observed markers and the most recent regional hydrogeological model REGIS II.

Cross-correlation of signals recorded at **A** and **B**

turns **multiple reflections** into (pseudo) **primary reflections**
turns **receivers** into **virtual sources**
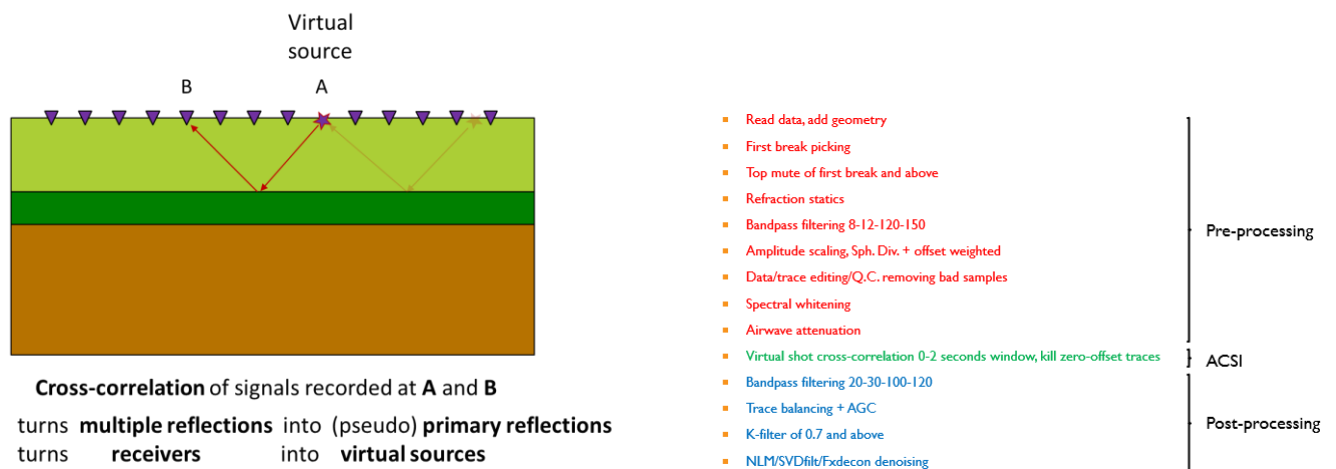
Figure 2.1.7 Seismic reflection interferometry (ACSI).

Figure 2.1.10 Modelling workflow.

2.1.2.2 Results and discussion

The results on the reprocesses seismic stacks can be found in Boullenger et al. (2020). The interpreted ACSI results are shown in Figure 2.1.12 and Figure 2.1.11. The reprocessing of the seismic line was a geophysical and technical success; with this workflow it is possible to obtain data from existing seismic lines that were originally applied to the deeper subsurface. Yet, Time/depth conversion proved challenging as the seismic velocities used have large uncertainties, and the workflow requires more development regarding especially velocities/time-depth conversion and interpretation methodology. A solution at hand is to put more effort in the careful construction and smoothing of the interval velocity model after migration in the reprocessing, which will provide more stable velocities. A more advanced approach is to use Full Waveform Inversion solutions for automatic extraction of the velocities from reprocessed shot gathers. A recently developed algorithm developed at TU Delft and pioneered at TNO is Joint Migration Inversion (JMI), which gives accurate velocity models suitable for depth conversion.

The exercise for the HT-ATES site in Middenmeer did not provide much more insight to what was available from the hydrogeological model REGIS II. Shallow reflections were retrieved in the reprocessed data where none were in the original processed data, and also some new ones that were not present in REGIS II (Figure 2.1.11). Time/depth conversion proved challenging as the seismic velocities used have large uncertainties, still the well-tie with the test drilling showed to be relatively good.

Figure 2.1.12 The interpreted ACSI results.
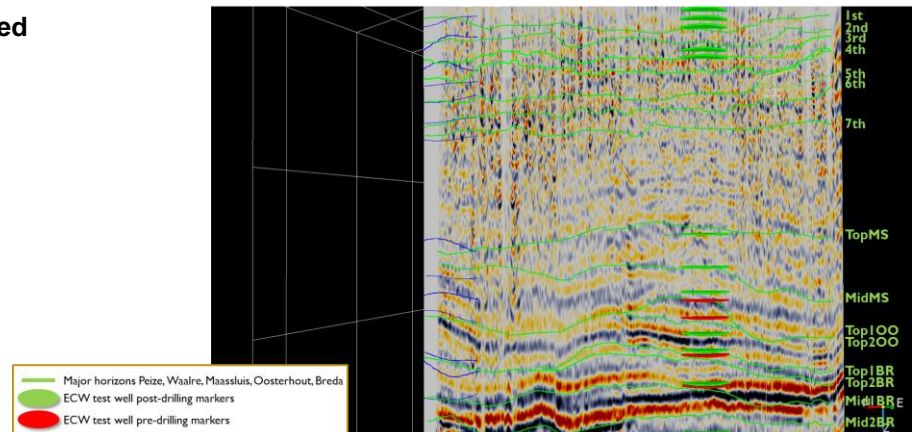
Figure 2.1.11 The interpreted ACSI results plotted on the REGIS II model.
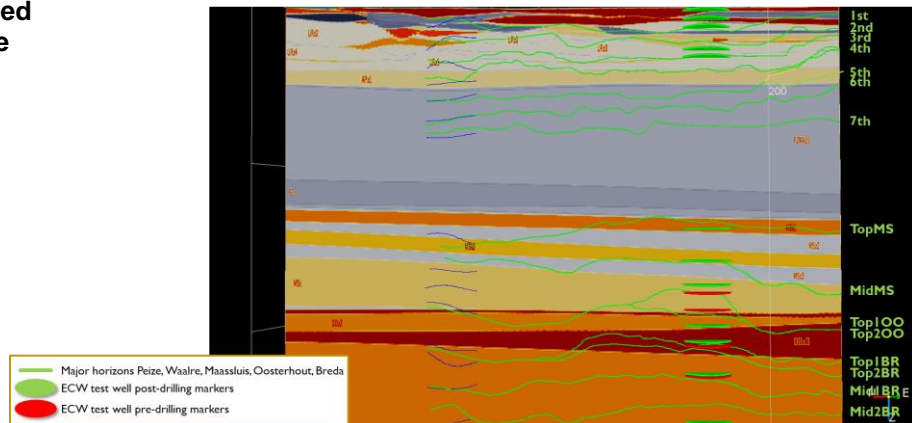
Most interpreted horizons in the reprocessed data match the revised well lithography from the drill test, and are already present in the most recent updated REGIS II model. It is not certain on which data the pre-drilling markers were based, probably an earlier version of REGIS-II. Some interpreted horizons in the reprocessed data are more accurately predicting the revised/right well markers than the most current REGIS II, especially in the deeper Breda formation. However, some interpreted horizons in the reprocessed data are less accurate than REGIS II, especially in the Oosterhout formation. In the shallower part, Maassluis and above, the reprocessed data, REGIS-II and post-drilling markers agree quite well. The most value in the reprocessed data is that it identified some doubled interfaces, perhaps clay lenses, on top of the Oosterhout and Breda formations.

Overall, the results of the reprocessed data support the initial idea that there is good lateral continuity of the layers in the Middenmeer area. The drillings of the warm and cold wells further confirm this. Therefore, the geological model developed for the thermal simulations, based on the test drilling and assuming lateral continuity, did not need to be adapted. Further, these insights on the (hydro)geological conditions in the area of Middenmeer will be useful for the design of potential additional HT-ATES systems in the future.

In general, this workflow could be highly beneficial in areas of sparse well-coverage for which seismic data is available. The workflow will be applied in the Dutch research programme WarmingUP (www.warmingup.info) to screen the subsurface suitability of the Leeuwarden area in the north of the Netherlands for HT-ATES. In Leeuwarden, hardly any well data is available. A geothermal test well will be drilled in June 2021 and shallow subsurface analyses will be performed in the well for the purpose of a potential, future HT-ATES system. Seismic reprocessing of existing seismic lines will be integrated with the well data (well-tie) in order to screen the shallow subsurface for suitable heat storage locations and evaluate the lateral heterogeneity/continuity of the layers. In case of a positive outcome, the results will be used for site selection of a HT-ATES test drilling.

2.1.3 Model simulations of thermal effects

HT-ATES systems are used to store heated water in aquifers that typically have a lower natural temperature. The injection of hot water induces heat transport processes, which in turn cause heating of the subsurface. In successful HT-ATES settings, the majority of the stored heat can be recovered. Still, over the lifetime of a HT-ATES system, a net amount of heat will be lost to the surrounding subsurface material, as a result of unavoidable heat losses. Within HEATSTORE, numerical heat transport models were set up to simulate the subsurface heat transport processes occurring around HT-ATES systems, providing insights in both the thermal recovery efficiencies of the HT-ATES system and its thermal impact on the subsurface.

For the HT-ATES system at ECW in the Netherlands specifically, the Heat and Solute Transport 3D (HST3D) software of IF Technology was used to address the following research questions:

- What distance between the hot and cold HT-ATES wells is optimal for the thermal recovery efficiency?
- What are the thermal effects of the stored heat on its surroundings?
- What are the thermal effects of the hot well casings on its surroundings, for various types of backfilling material? And what is the impact of these heat losses on the thermal recovery efficiency?
- What do the modelling results imply for the monitoring activities of the HT-ATES system?

The general modelling approach using the HST3D software is provided first, followed by the descriptions of the three thermal model scenarios that were set up to address the research questions, and their results.

2.1.3.1 Modelling approach: Heat and Solute Transport 3D software

Heat and Solute 3D Software

The Heat and Solute Transport 3D (HST3D) software is capable of simulating heat and solute transport in water-saturated groundwater systems (Kipp, 1987). The model numerically solves the fluid, heat and solute transport by the following equations. The flow equation of the model is formed by the conservation of total fluid mass and Darcy's Law for fluid flow in porous media. The conservation of enthalpy for fluid and porous medium is used for the heat transport equation. For the solute transport, the conservation of mass of a solute species, which may decay or adsorb to the porous medium, is applied. The model includes dependency of fluid viscosity on temperature and solute concentration, as well as the dependency of fluid density on pressure, temperature and solute concentration. These latter temperature-dependent properties are specifically important in HT-ATES systems, as temperature ranges are larger compared to regular (low temperature) ATES systems, resulting in significant variation in fluid viscosity and density, which in turn affects the flow field around HT-ATES wells.

HST3D workflow

In HST3D, a 3D grid was constructed with highest grid density around the wells. Subsequently, the hydrogeological and thermal properties were assigned to the grid nodes, including boundary conditions, so that the modelled domain represents the subsurface domain of interest. Vertical wells were added in the model and several time-periods were defined to allow for various flow rates over the course of the simulation. HT-ATES specific functionalities like the application of a cut-off temperature during recovery of the stored heat from the hot well was added. When the input for a HST3D scenario was defined, the model was run to simulate the subsurface heat transport processes that occur within the model domain, given the well operations. During the simulation, an iterative process was applied to steadily increase the timesteps of each iteration, provided that the physical equations were solved successfully. This process optimizes the simulation time, without causing numerical inaccuracies. After the simulation has finished, subsurface temperature distribution (X,Y,Z), well temperatures and pressures, and thermal recovery efficiencies of the wells can be extracted from the output files and visualized. The model results were investigated to address the research questions posed.

Three different HST3D models were set up to address the three research questions related to heat transport. Each of these models is discussed below and the results and interpretations from these models are described as well.

2.1.3.2 Scenarios, results and discussion

Choice of well locations

During the design phase, the following question was posed: *"What distance between the hot and cold HT-ATES wells is optimal for the thermal recovery efficiency?"*. This question was addressed by running several HST3D scenarios with different well distances.

Placing the wells far apart would cause relatively high heat losses to the surroundings. When the distance between the wells is reduced, part of the heat losses from the hot well can be captured by the "cold" well. However, placing the wells too close to each other would cause interference between the hot and cold well, adversely affecting the thermal performance of the system. The optimal well distance should be small enough to prevent large-scale heat losses to the surroundings, while keeping the well interference within an acceptable range. Although the well distance was varied for the different scenarios, the subsurface properties and the pumping scheme applied to the scenarios remained constant. It has to be noted, that the actual operation of the HT-ATES system in practice (stored and recovered volumes and temperatures per cycle) are uncertain to some extent. In finding the optimal well distance, the thermal recovery efficiency, as well as the production temperatures at the hot/cold wells, have been the primary assessment parameters.

Model setup

Spatial discretization: The horizontal extent of the model is 4 x 4 km, made up by 93 and 73 nodes in X and Y directions respectively. In the vertical direction, the model domain extend from 1 – 600 mbgs, with 40 nodes. The grid density is highest near the well screens. With this spatial discretization, simulation results were not affected by the boundary conditions.

Subsurface input parameters: The subsurface parameters provided to the model were based on the test drilling results. The subsurface structure is visualized in Figure 2.1.6. The hydrogeological and thermal properties assigned to the HST3D models are shown in Table 2.1.1.

Table 2.1.1 Hydrogeological and thermal properties assigned to the models. Hydraulic conductivity values apply to the natural groundwater temperature in the storage aquifer at ECW (15,5 °C).

Zone number	Name of geological zone	Depth of bottom	Depth of top	Hydraulic conductivity			Porosity	Storativity	Vertical compressibility	Heat capacity of solid	Bulk thermal conductivity coefficient
				x	y	z					
		[m]	[m]	[m/d]	[m/d]	[m/d]	[-]	[-]	[-]	[MJ/(m³ °C)]	[W/(m °C)]
1	Clay-surface	-4	-1	0.1	0.1	0.01	0.35	4.49E-04	1.51E-08	2	2
2	Aquifer1	-17	-4	15	15	3.75	0.35	7.32E-04	5.59E-09	2	2.4
3	Clay1	-33	-17	0.1	0.1	0.01	0.35	4.72E-04	2.85E-09	2	2
4	Aquifer2-A	-47	-33	10	10	2.5	0.35	3.00E-04	2.03E-09	2	2.4
5	Clay-local	-53	-47	0.1	0.1	0.01	0.35	1.11E-04	1.73E-09	2	2
6	Aquifer2-B	-67	-53	10	10	1	0.35	2.31E-04	1.53E-09	2	2.4
7	Clay-2	-74	-67	0.01	0.01	0.001	0.35	1.04E-04	1.37E-09	2	2
8	Aquifer 3	-229	-74	40	40	10	0.35	1.54E-03	8.59E-10	2	2.4
9	Clay-3	-360	-229	0.01	0.01	0.001	0.35	8.74E-04	5.26E-10	2	2
10	Aquifer-Stora(	-383	-360	12.7	12.7	3.175	0.35	1.36E-04	4.47E-10	2	2.4
11	Clay-4	-425	-383	0.01	0.01	0.001	0.35	2.38E-04	4.24E-10	2	2
12	Aquifer 5	-460	-425	6.5	6.5	1.625	0.35	1.90E-04	3.99E-10	2	2.4
13	Clay base	-600	-460	0.01	0.01	0.001	0.35	7.01E-04	3.56E-10	2	2

Boundary conditions: Constant temperature and pressure boundaries were applied to the outer faces of the model. A horizontal pressure gradient was added to the model to account for the hydraulic gradient in aquifer 3 (resulting in groundwater flow in northwestern direction). The initial temperature is 15,5°C throughout the model, in line with the measured natural groundwater temperature in the storage aquifer.

Pumping scheme of HT-ATES wells: For the HT-ATES system at ECW, the pumping scheme as shown in Figure 2.1.13 was applied. From year 4 onwards, the pumping scheme remains the same for each year. In year 1-3, the pumping scheme deviates slightly from year 4, because of operational considerations during start-up of the system. The models were simulated for 10 years of HT-ATES operation. Injection temperatures are 85 °C at the hot well and 30 °C at the cold well. During heat recovery from the HT-ATES system, a cut-off temperature of 55 °C was applied to the hot well, meaning that extraction from the hot well stops for the rest of the season, when a production temperature of 55 °C is reached at the hot well.
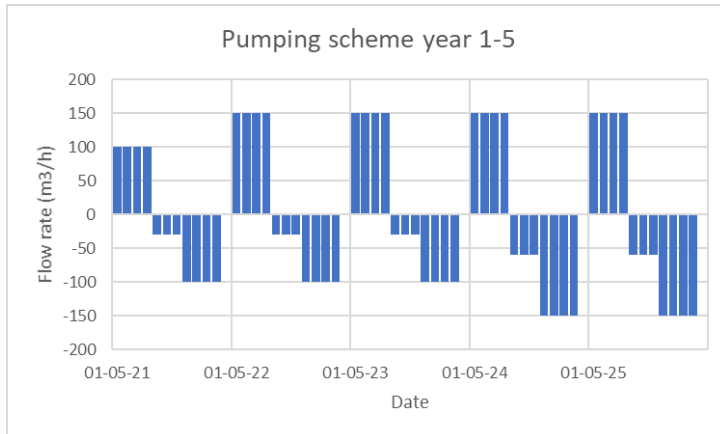
Figure 2.1.13 Pumping scheme applied in the first five years of the simulations. Positive flow rates represents heat storage, while negative flowrates represent recovery of the stored heat.

In Table 2.1.2, the flow rates applied to the wells are shown for each phase of each year. To account for some uncertainty in the pumping scheme, two extra simulations were performed, in which flow rates are decreased (red) or increased (yellow) by a factor 0.75. The aim is to find the optimal well distance, which offers satisfactory results for the basic pumping scheme, but also for the scenarios where the flow rates would be multiplied or divided by a factor 0.75.

Table 2.1.2. Various pumping schemes applied during the simulations. The base case pumping scheme is shown without color mark. The two additional pumping schemes differ slightly from the base case, as shown in red (minimum flow rates) and yellow (maximum flow rates).

Phase → Jaar	Phase 1: Charge (4 mnth) m³/h	Phase 2: Discharge (3 mnth) m³/h	Phase 3 Discharge (4 mnth) m³/h	Phase 4 Rest
1	75/100/133	30	100	0
2	113/150/200	30	100	0
3	113/150/200	30	100	0
4 - 10	113/150/200	45/60/80	113/150/200	0

Well distance scenarios

Using the model input as described above, several scenarios were constructed, each with different well distances. For low temperature ATES systems, well distances corresponding to approximately 2 – 3 times the thermal radius are typically applied (e.g. Sommer et al., 2013). For these simulations, the well distance was varied between 1.5 – 2.5 times the thermal radius, slightly smaller than typical for low temperature ATES systems, because some thermal interference can have a positive effect (when part of the heat losses from the hot well can be captured by the cold well). According to the base case pumping scheme, 440.000 m³ of hot water is injected in the hot well each year, assuming a flow rate of 150 m³/h during 4 months. Given the

aquifer dimensions, the thermal radius corresponding to this storage volume is about 100 m. Therefore, the well distances were varied between 150 and 250 m.

Results and discussion

Figure 2.1.14 shows the thermal recovery efficiencies corresponding to a well distance of 220 m. Both the base case pumping scheme (orange) and the other schemes show satisfactory results, compared to scenarios in which other well distances were applied (not shown). Note that from the fourth year onwards, more water (hence more heat) is produced from the hot well (see Figure 2.1.15), compared to earlier years. This results in higher thermal recovery efficiencies. Also, the scenario with large storage volume (charging 4 months with 200 m³/h) offers high recovery efficiencies, which is in accordance with earlier findings that larger heat storage systems generally show higher recovery efficiencies.
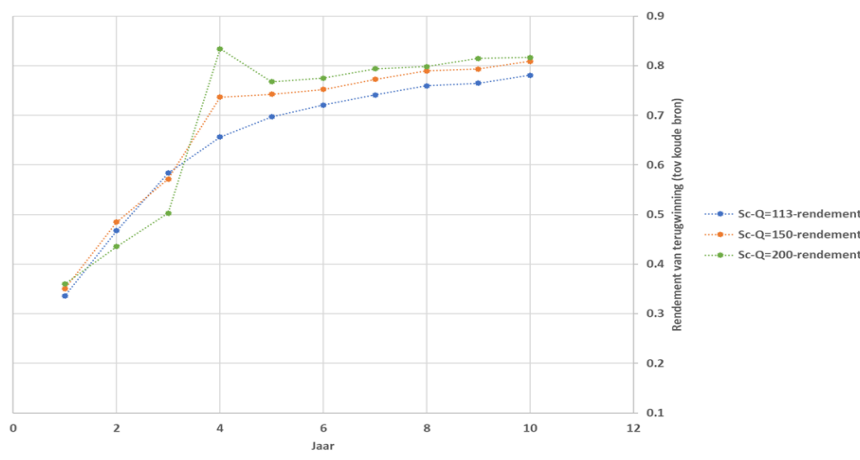
Figure 2.1.14 Thermal recovery efficiencies (vertical axis) for the first 10 years (horizontal axis) of HT-ATES operation, for a well distance of 220 m. The three lines represent the efficiencies that correspond to the three different pumping schemes, with orange as the base case scheme.

Thermal interference

Although the thermal recovery efficiencies seem satisfactory for a well distance of 220 m, it is still to be checked whether thermal interference between the hot and cold well remains within an acceptable range. To this end, the production temperatures of the hot and the cold wells were plotted, as shown in Figure 2.1.16 for the scenarios with well distance of 220 m.

The figure shows that the production temperature at the hot well decreases during the recovery of heat from the hot well (red lines), until the cut-off temperature of 55 °C is reached. Then the system is shut down and temperatures only show a small decrease until the system switches to heat storage mode again. For the scenario with a high flow rate and large storage volume (right hand side of Figure 2.1.16), the cut-off temperature is not even reached in the second and third years, when the heat demand is relatively low compared to later years.
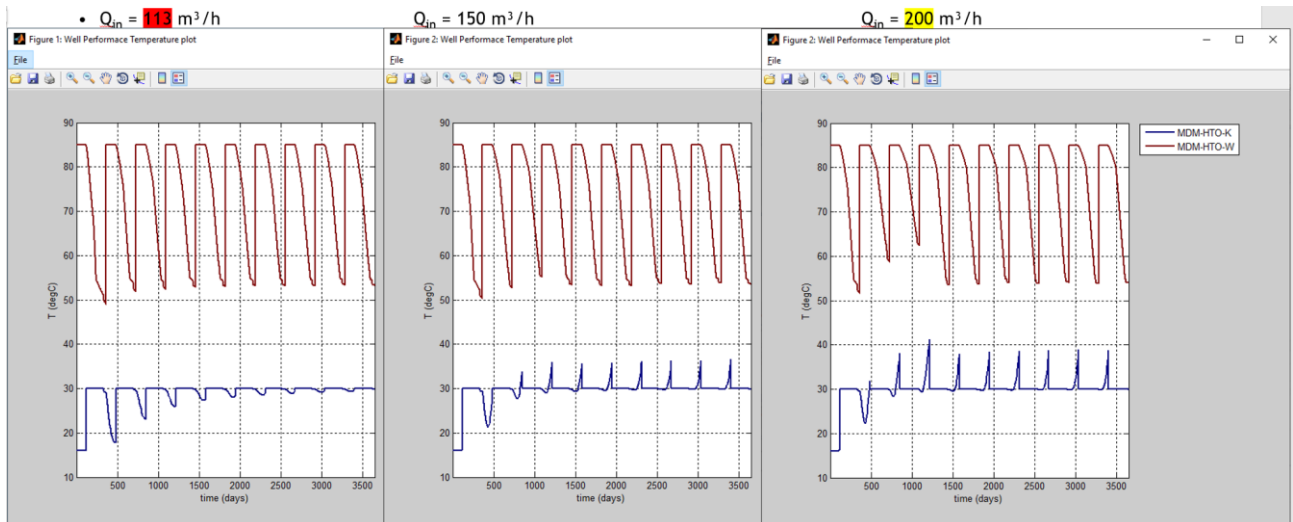
Figure 2.1.16 Calculated temperatures in the hot (red) and cold (blue) well of the HT-ATES system. The graph in the middle shows the well temperatures resulting from the base case pumping scheme, and the left/right graphs show the results for the lower/higher flow rates.

Looking at the production temperatures at the cold well, it becomes clear that scenarios with larger heat storage volumes (i.e. pumping schemes applying higher flow rates) show higher production temperatures in the cold well at the end of the heat storage period. This is because the heat injected at the hot well reaches the cold well. This could be interpreted as a reason to consider a larger well distance. However, the low production temperatures at the cold well in the scenario with low flow rates (left hand side of Figure 2.1.16) show that the production temperature remains relatively low during the first years. Placing the wells further apart would lead to a further decrease of the production temperature at the cold well. Importantly, following the guidelines for the prevention of sand production at the wells (which is dependent of the hydraulic conductivity hence also on the extraction temperature), the maximum flow rate of the HT-ATES system is typically limited by the minimum temperature at the cold HT-ATES well, because of the relatively high viscosity of colder water. Therefore, the temperature at the cold well should remain high enough to facilitate a sufficient flow rate for the HT-ATES system during charging of heat.

For the well distance of 220 m, the production temperatures at the cold well are sufficient to allow for a satisfactory flow rate during heat storage, for both the base case pumping schemes and the minimum/maximum flow rate scenarios. Scenarios with a smaller well distance showed considerable thermal interference between the wells for the maximum flow rate scenario, while larger well distances would further decrease the production temperature at the cold well, thereby limiting the flow rate during heat storage too significantly.

Conclusions

Based on the results and the considerations described above, it was concluded that for a well distance of 220 m both the thermal recovery efficiencies and the thermal interference between the hot and cold wells were satisfactory for the ECW case, for both the base case pumping scheme and the scenarios with decreased and increased storage and recovery volumes. This well distance corresponds to approximately 2.2 times the thermal radius of the hot well. The well distance of 220 m was chosen as the optimal well distance and this conclusion was subsequently used as input for the choice of the well locations.

2.1.4 Thermal impact in and around the storage aquifer

2.1.4.1 Introduction

In the Netherlands, a Water permit is required for the construction and operation of a HT-ATES system. The permit application is supported by a report in which the hydrological, geomechanical and thermal effects of

the HT-ATES system are described. Below, the thermal effects as calculated during the permitting procedure are described, as a means to address the following research question:

"What are the thermal effects of the stored heat on its surroundings?"

This question was addressed by running one HST3D scenario, in which HT-ATES is operated for 30 years, followed by a period of 100 years without HT-ATES activity. The model details and the simulation results are described below.

2.1.4.2 Model Setup

A model was constructed to simulate the thermal effects of the stored heat on its surroundings. The spatial discretization and the hydrogeological properties assigned to the model are the same as for the well-distance simulations (see Table 2.1.1).

Pumping scheme. The pumping scheme applied to the model is shown in Figure 2.1.17. From year 4 to year 30, the flow rates remain constant for each year. In year 1-3, the pumping scheme deviates slightly from year 4-30, because of operational considerations during start-up of the system. Injection temperatures are 90 °C at the hot well (somewhat higher than the expected value: worst case approach) and 30 °C at the cold well. During discharging of the HT-ATES system, a cut-off temperature of 55 °C was applied to the hot well. Note that flow rates during discharging of heat are relatively high as to make sure that the cut-off temperature is reached at the hot well and all usable heat is recovered each year.
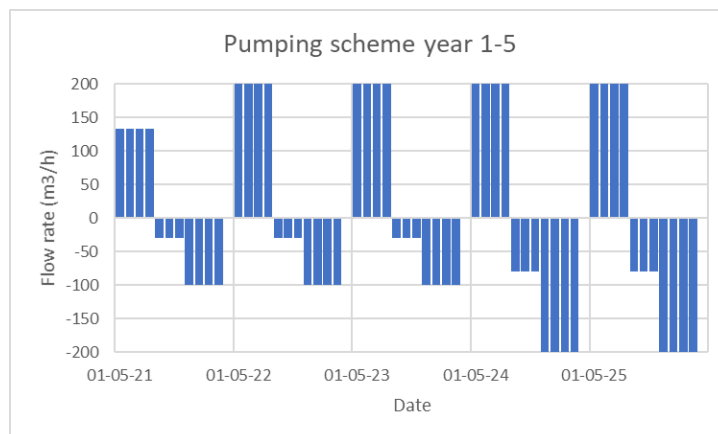
Figure 2.1.17 Pumping scheme applied in the first five years of the simulation. Positive flow rates represent charging, while negative flowrates represent discharging of the hot well.

The stored heat volumes and the injection temperatures at the hot well represent a worst-case scenario, to make sure that the actual thermal effects of the HT-ATES system will remain within the margins that are allowed by the permit.

The model is run for 130 years: The HT-ATES system is operated for 30 years, followed by a period of 100 years without activity to investigate the thermal impact of the HT-ATES system after shutdown on the long term.

2.1.4.3 Results and discussion

Using the input parameters as described above, the thermal impact of the HT-ATES system on the subsurface was calculated. The results are shown in Figure 2.1.18 to Figure 2.1.20.
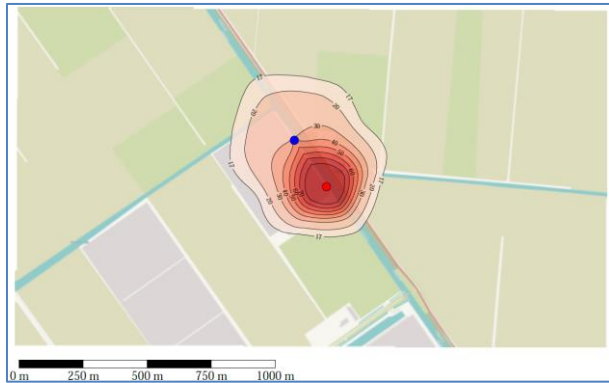
Figure 2.1.18 Top view of the temperature distribution (ºC) at the top of the storage aquifer, after 30 years of operation (end of summer, i.e. after heat storage and before recovery of heat). Map is oriented northward.
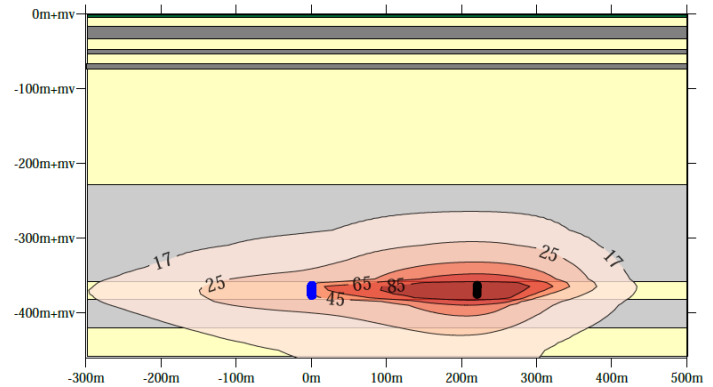
Figure 2.1.19 Cross section along the well screens, showing the temperature distribution (ºC) in the subsurface directly after the 30th storage cycle (before heat recovery). Sand layers are shown in yellow and clay layers in grey. The hot and cold well screens are shown in black and blue respectively.
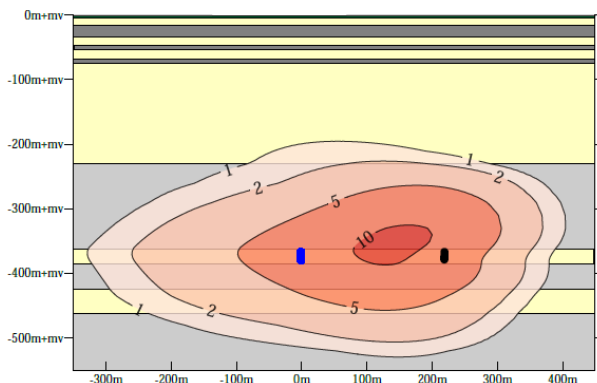
Figure 2.1.20 (left). Cross section along the well screens, showing the increase in temperature (ºC) with respect to the natural groundwater temperature, 100 years after shutdown of the HT-ATES system. Sand layers are shown in yellow and clay layers in grey. The hot and cold well screens are shown in black and blue respectively.

In the figures, the area of thermal impact, i.e. where temperature has increased 1 °C or more compared to natural conditions, are shown. The thermal impact area of the HT-ATES system after 30 years of operation extends up to 300 m from the wells, in the storage aquifer (see Figure 2.1.18). Based on the simulation results, density driven flow has a limited effect on the thermal recovery efficiency, allowing for a high thermal recovery efficiency hence limited thermal impacts. When storage volumes are smaller, recovery efficiencies may decline but the thermal impact areas will be smaller too. The thick clay layer overlying the storage aquifer plays a major role in limiting the thermal effects of the heat storage on shallower aquifers. Assuming that the HT-ATES system is shut down after 30 years of operation, the heat transport processes continue to spread the residual heat over the surrounding ground volume. However, a hundred years after shutdown, a maximal temperature increase of 2 °C is experienced in the aquifer at 200 mbgs, and only locally (see Figure 2.1.20). The natural groundwater flow, in northwestward direction (i.e. towards the left hand side of Figure 2.1.19 and Figure 2.1.20) causes the temperature effects to extend further downstream, than upstream.

2.1.4.4 Conclusions

Given the hydrogeological parameters that were derived from the test drilling results, combined with the expected pumping scheme, the thermal effects of the stored heat on the surroundings were calculated. These simulations were performed within the permitting procedure context. The dimensions of the aquifer combined with the large storage volumes allow for relatively high thermal recovery rates, which in turn limits the heat losses to the surroundings. Additionally, the thick clay layer overlying the heat storage aquifer plays a major role in limiting the thermal effects to shallower layers. Altogether, the simulation results supported that the thermal effects were acceptable, i.e. no other subsurface interests will be violated.

2.1.5 Heat losses from the well casings

2.1.5.1 Introduction

The simulations described in section 2.1.3 are focussed on the heat transport processes that occur in the storage aquifer. An aspect that was not included is heat exchange through the well casing during transport in the depth range between the surface and the storage aquifer. During the storage of heat into the hot well of the HT-ATES system, groundwater with a temperature of up to 85 ºC is flowing through the well casing. However, the area surrounding the well casing initially has a much lower temperature. Because of the temperature difference some heat will be lost by heat conduction through the well casing to the surrounding subsurface. As a consequence, the direct vicinity of the well will heat up to some extent. During the design phase a number of simulations were performed to investigate the role of different types of backfilling material on these heat losses. Backfilling material has to be installed at the HT-ATES wells, filling the space between the well casings and the borehole wall. During the design phase, it was discussed whether a backfilling material with better insulating properties (lower thermal conductivity) would effectively decrease the heat losses from the well casings, and whether this more expensive material would be technically preferential over standard backfilling materials. Additionally, the loss of heat from the well casings will have a certain impact the thermal recovery efficiency. Anticipating the heat losses from the hot well casings, but lacking quantitative insights in the impact of these processes, the following research question was posed:

"What are the thermal effects of the hot well casings on its surroundings, for various types of backfilling material? And what is the impact of these heat losses on the thermal recovery efficiency?"

In order to answer these questions, a HST3D model was set up to simulate the heat losses from the casings to the subsurface surroundings.

2.1.5.2 Model setup

Spatial discretization. The model extends 2 km in the horizontal dimensions (X, Y). Near the well, the X,Y grid density is high with a distance between the nodes of 3 to 50 cm within 1.5 m distance of the wells. Farther from the well, the distance between the nodes is increased gradually. The vertical extent of the model is 360 m, from surface to the top of the storage aquifer at 360 mbgs. The vertical distance between the nodes ranges from 3 to 15 m.

In the grid, the casing is represented by a square vertical column of 32 x 32 cm. The backfilling material is situated around the casing, with a thickness of 15 cm in X and Y directions. Using these sizes, the outer surface areas of the well casing and backfilling material are the same as the outer areas of the circular well casing and borehole respectively. This choice was made because the heat transported from the well casing to the subsurface depends on the heat flux, which is in turn sensitive to contact area. This discretization is expected to be the best approach to accurately simulate heat losses by conduction from the well, taking into account the actual design of the well.

Subsurface input parameters. Around the borehole, the subsurface is divided in various horizontal layers, corresponding to the geological formations, with hydrogeological and thermal properties as depicted in Table 2.1.1. The backfilling material is situated between the well casing and the borehole wall. For these simulations, three types of backfilling material, each with a different thermal conductivity coefficient, were applied to the model: sand, clay and spherelite-concrete (spherelite for short). The hydrogeological and thermal properties of the backfilling material depend on the type of backfilling material used, as shown in Table 2.1.3

Table 2.1.3. Hydrogeological and thermal properties of the three backfilling materials used.

Gravelpack Material	Hydraulic conductivity [m/d]			Porosity [-]	Heat capacity of solid [MJ/(m³ ºC)]	Bulk thermal conductivity coefficient [W/(m ºC)]
	x	y	z			
Sand	100	100	100	0.35	2	2.4
Clay	0.1	0.1	0.01	0.35	2	1.8
Spherelite	0.1	0.1	0.01	0.35	2	0.44

Initial conditions. A hydraulic head (pressure) gradient of 0.2 m/km was superimposed on the hydrostatic pressure field to form the initial pressure field. The gradient represents the regional hydraulic gradient as is applicable to the third aquifer. The direction of the flow is NNW, but in this scenario the groundwater flow direction was set from the hot well to the cold well (i.e. close to NNW), in order to be able to show the temperature effects in the vertical plane through the hot and cold well.

Initial temperatures are 13 °C for the complete subsurface domain of the model, except for the boreholes of the hot and cold well, where initial temperatures are set to 85 °C and 30 °C respectively. Solute concentrations were not included hence not simulated in the model.

Boundary conditions. The temperatures applied to the hot well casing are dependent of the time of the year, as shown in Table 2.1.4. The temperature applied to the cold well casing is 30 ºC all year round. These conditions applied to the well casings are assumed to be worst-case, since in practice it is expected that the time-averaged temperatures of the well casings are lower. The initial pressure boundary condition was fixed during the complete simulation. Constant temperature boundary conditions were applied to the sides and bottom of the model.

Table 2.1.4. Temperatures applied to the hot well casing depend on the time of year.

Month	Season	Operational condition	Temperature applied to hot well casing (°C)	Notes
1 - 4	Summer	Heat storage	85	Estimated temperature of the hot well casing during heat storage
5 - 11	Autumn, winter	Heat recovery	67	Average water temperature during heat recovery (based on other simulations)
12	Spring	No flow	55	Cut-off temperature

Temporal discretization. Each cycle (year) exists of three periods, as shown in Table 2.1.4. These periods are used to change the temperatures of the well casings. The other boundary conditions remain the same during the complete simulation. The simulation was run for 20 years.

2.1.5.3 Results and discussion

Thermal effects of the well casing

The calculated temperature distribution in the shallower subsurface after 20 years of HT-ATES operation, is shown in Figure 2.1.21, for the three scenarios using different backfilling materials.
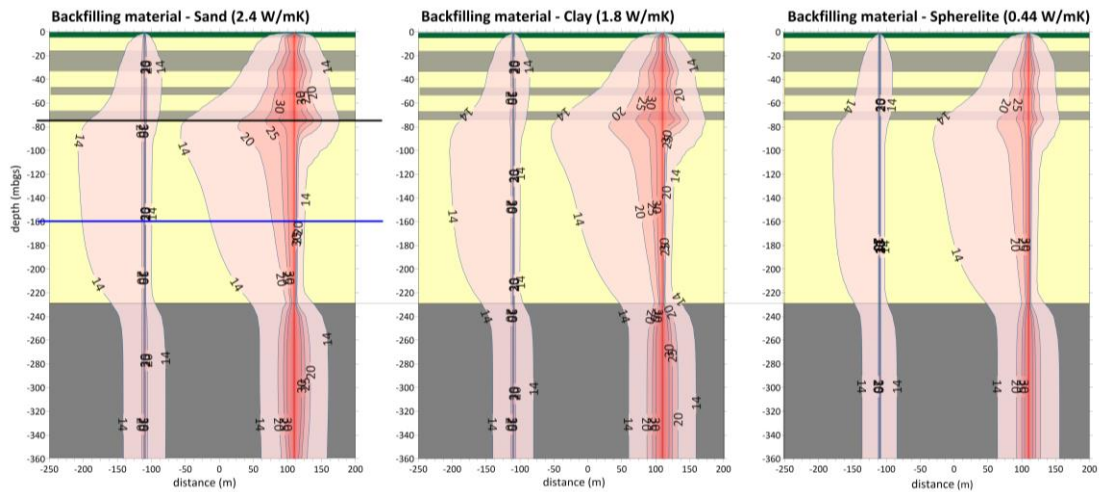
Figure 2.1.21 Subsurface temperatures around the well casings after 20 years of heat storage, for a scenario with different backfilling materials: sand (left), clay (middle) and insulating spherelite (right). For the sand scenario, the two horizontal lines indicate the depths for which topviews of temperature distributions are shown in Figure 2.1.22.

Figure 2.1.22 presents two topviews of the temperature distribution at the middle (left) and top (right) of the 3rd aquifer after 20 years of heat storage, for the scenario with sand as backfilling material.

Figure 2.1.22 Top view of the temperature distribution at the middle (left hand side) and top (right hand side) of the 3rd aquifer, after 20 years of heat storage with sand as backfilling material.

In the thick clay layer (230 – 360 mbgs) located directly above the heat storage, no groundwater flow occurs and in this layer, after 20 years of heat storage, the 25 °C isotherm is located at a distance of about 15, 14 and 10 m for the sand, clay and spherelite backfilling materials respectively (see Figure 2.1.21). So heating from the well casings does not have a large-scale impact on the surroundings in thick clay layers.

The third aquifer, located at a depth of 76 – 230 mbgs, contains coarse sands which facilitates a relatively high horizontal groundwater flow velocity of about 10 m/y from the hot to the cold well. Because of this, the thermal effects of the well casings are larger in downstream direction. The 25 °C isotherm is located at a maximum horizontal distance of 16, 13 and 8 m from the well casings for sand, clay and spherelite backfilling materials respectively. Figure 2.1.21 and Figure 2.1.22 both show that the thermal impact is highest downstream of the hot well, at the top of the aquifer. This is explained by a combination of vertical and horizontal flow within the aquifer. Groundwater in the aquifer is heated near the hot well casing, and starts flowing upward by buoyancy flow (e.g. Van Lopik et al., 2015). The figures show that this process mainly occurs near the hot well, where temperature differences between the well casing and natural groundwater are largest. Heated water accumulates towards the top of the aquifer near the hot well (see Figure 2.1.22). Around the cold well, this effect is much smaller. The regional groundwater flow causes (heated) water to be transported towards the cold well continuously.

The simulations indicate that heating of the 3rd aquifer can be observed in the monitoring well (located 30 m downstream of the hot well), after 5 years already (not shown), but only after 20 years will temperatures exceed 25 °C, and only at the top of the third aquifer. Since the model represents a worst-case scenario, it is assumed that the thermal impact of heating from the well casing will be smaller in reality.

Altogether, the scenarios show that the application of spherelite effectively limits the temperatures in the direct vicinity of the well casings, compared to the sand and clay scenarios. However, the thermally affected zones (i.e. +1 °C compared to natural temperatures) seem to be of comparable sizes. Also, although the properties of the backfilling material may be significantly different, the volumes of backfilling material are relatively small compared to the subsurface volumes around it, meaning that the backfilling material can only control heat losses to a limited extent.

Design considerations

The buoyancy flow along the hot well casing in the third aquifer causes upward heat transport. This vertical flow is helped when coarse sand with high hydraulic conductivity is used as backfilling material. Therefore, in the design of the HT-ATES wells, the backfilling material in the third aquifer consists of sand alternated with clay plugs to reduce upward flow through the backfilling material to some extent.

Impact of heat losses through the well casings on thermal recovery efficiency

Spherelite is a non-standard material in backfilling ATES wells, and significantly more expensive compared to clay and sand. Although the thermal effects on the subsurface are smaller using spherelite, the difference with the scenarios with sand/clay as backfilling materials was not sufficiently distinctive to choose for spherelite. Therefore, as an additional criterium, the impact of the backfilling material on the thermal recovery efficiency of the HT-ATES system was estimated. This was done by estimating the conductive heat flux occurring through the backfilling material, based on the thermal conductivity of the backfilling material and the temperature at the end of the 20th heat storage cycle. The steepest thermal gradient was used to obtain a worst-case estimate. The loss of thermal recovery efficiency was calculated as the percentual heat loss relative to the yearly amount of heat stored in the HT-ATES system.

The calculations showed that at the hot well 2.5, 2.3 and 1.6 % of the stored heat was lost through the well casings, for the sand, clay and spherelite backfilling materials respectively. The use of spherelite would only reduce thermal recovery efficiency with 0.9%point compared to sand and 0.7%point compared to clay, for the worst-case scenarios. From a practical point of view, using spherelite-concrete plugs instead of clay plugs posed some risks both for the sealing capacity, as spherelite it is less ductile compared to clay. Based on the modelling results and given the practical considerations, the use of the non-standard and more expensive spherelite backfilling material would offer only limited advantages over sand/clay and hence it was decided not to use this material. Instead, a combination of clay and sand was used as backfilling material for the HT-ATES wells.

2.1.5.4 Conclusions

The simulations showed that the thermal effects of the hot well casings on the surrounding subsurface are predominantly controlled by the hydrogeological and thermal properties in the subsurface layers outside the borehole wall. The use of different types of backfilling material has a limited effect on the thermal impact in the area surrounding the HT-ATES wells. The calculations show that 2.5, 2.3 and 1.6 % of the stored heat is

lost through the well casings of the hot well, for sand, clay and spherelite backfilling materials respectively. Spherelite backfilling material has a relatively low thermal conductivity (0.44 W/(m K)) compared to the standard backfilling materials clay and sand (1.8-2.4 W/(m K)) and shows a smaller thermal impact on the subsurface, although the differences were mainly observed in the direct vicinity of the hot well. Although heat losses are smaller when spherelite is used, the advantage of the use of spherelite-concrete is too small to justify the application of this relatively expensive material. The differences between clay and sand backfilling materials were insignificant.

The model simulations show that the heating around the casing of the hot well results in upward flow in the third aquifer that is driven by the reduced density of the heated water. In the design of the HT-ATES wells, the backfilling material in the third aquifer consists of sand alternated with clay plugs to reduce upward flow through the backfilling material to some extent.

2.1.6 Model simulations of geochemical effects related to water treatment

Geochemical and reactive transport simulations are applied to predict the geochemical effect of increased temperature, and its impact on the performance of the system. The geochemical simulations have been used to define a water treatment procedure to prevent scale formation and related operational problems. The results of the simulations are used to design a proper monitoring plan.

2.1.6.1 Modelling approach

The geochemical simulations are applied to assess the scaling potential of carbonates in the HT-ATES system as a result of the temperature increase and the related decrease in solubility of carbonates. The groundwater in the Netherlands is generally slightly oversaturated with carbonate minerals like calcite and dolomite, and heating of the groundwater can induce precipitation and cause clogging of the system. Water treatment is applied to prevent clogging related to precipitation of carbonates. For the design of the water treatment system it is important to know how much CO_2 has to be added, how this CO_2 dosing will develop over the years and what the consequences are for the gas pressure in the groundwater. Model simulations have been performed to get a better insight into these issues. Two types of models have been used, which are described in the following paragraphs.

2.1.6.2 Scenario 1 (PHREEQC)

Setup of the calculations

PHREEQC, a program that has been specifically developed for performing geochemical calculations, has been used to investigate the required CO_2-dosage in subsequent cycles. In these calculations, the groundwater composition that was found in the test well was used as a starting point. Step by step, the changes that the groundwater experiences are simulated, like addition of CO_2, changes in temperature and precipitation or dissolution of calcite.

According to Sanner, ed. (1999) "The greatest problem in HT-UTES is the precipitation of carbonates, especially of the different species of calcium carbonate". According to Knoche et al. (2003), scaling problems in heat exchangers of HT-ATES plants largely consist of calcite precipitation. In the PHREEQC calculations, the saturation index of calcite (the most common type of calcium carbonate) was therefore used as an indicator for potential scaling. In each step, e.g. after a change of the temperature, the model calculates the calcite saturation index (SI_{cc}). When SI_{cc} is higher than the initial value for the aquifer, it is assumed that precipitation of calcite occurs until SI_{cc} reaches the initial value. When SI_{cc} is below the initial value, the groundwater is assumed to be aggressive: calcite can dissolve from the storage aquifer until SI_{cc} reaches the initial value. In this way, the model can simulate dissolution or precipitation of calcite and/or calculate the saturation index when calcite dissolution and precipitation are switched off. In the last case the SI_{cc} value reflects the tendency for dissolution or precipitation of carbonates. The same method was used for the geochemical (scaling) simulations that were used to find the settings for the dosage of HCl in Zwammerdam and no clogging issues were reported for that system (Drijver, 2011).

In an HT-ATES system, the groundwater experiences a number of changes, which are included in the geochemical calculations. As a starting point, the initial groundwater composition has to be to specified, including the associated pressure and temperature. Based on this information PHREEQC calculates the initial SI_{cc}. The first change that the groundwater experiences when the HT-ATES is taken into operation is a

pressure drop because of pumping the water to the surface: the pressure drops from reservoir pressure to the pressure in the surface installations. In the surface installations, CO_2 is added to the groundwater and the groundwater is heated to 85 °C. The heated groundwater is pumped back via the hot well into the aquifer, so that the pressure increases again. In the aquifer, the groundwater interacts with the sediment and calcite precipitation or dissolution may take place. The stored hot water is extracted again in the winter season (pressure drop due to pumping to the surface) and cooled in the surface installations (the heat is extracted and used in the greenhouses). Then, the pressure increases again because the groundwater is returned to the aquifer via the cold well. Finally, the cooled water interacts with the sediment in the aquifer and calcite may precipitate or dissolve. This completes the first cycle and the groundwater is back in the aquifer in the vicinity of the "cold well". Subsequently, the same cycle is repeated every year: pumping up from the "cold well", CO_2 dosing, heating, injection in the hot well, bringing the groundwater into equilibrium with the calcite that is present in the aquifer, pumping up from the hot well, cooling, injection in the cold well and again: bringing the groundwater into equilibrium with the calcite that is present in the aquifer.

The above steps have been included in the geochemical calculations. The PHREEQC calculations are therefore also performed in a number of steps as listed below. It has to be noted, that these calculations have been performed during the design phase. Therefore the temperatures used in the calculations slightly differ from the temperatures used in the previous sections.

1) Initial situation

Specifying the initial composition of the groundwater at the pressure and temperature of the storage aquifer and calculating the associated calcite saturation index.

2) Extraction from the cold well and CO_2 dosing

The pressure is decreased from the reservoir pressure to the pressure in the surface installations and CO_2 is added. The amount of CO_2 that is added is such that the saturation index after heating to 85 °C is equal to the initial saturation index as calculated in step 1.

3) Heating to 85 ° C

Increasing the temperature to 85 °C (at the pressure in the surface installations).

4) Injection into the hot well and equilibrate with calcite

Increase of the pressure to the pressure in the storage aquifer and equilibrate with calcite until the calcite saturation index is equal to the initial saturation index that was calculated in step 1.

5) Extraction from the hot well and decrease in temperature

The pressure is decreased from the reservoir pressure to the pressure in the surface installations and the groundwater is cooled to 30 °C (expected average injection temperature in the cold well).

6) Injection into the cold well and equilibrate with calcite

Increase of the pressure to the pressure in the storage aquifer and equilibrate with calcite until the calcite saturation index is equal to the value that was found for the initial situation.

7) Repeat steps 1 to 6

Steps 1 to 6 are repeated for each storage and recovery cycle. For each subsequent cycle the required CO2 dosage is calculated. The calculations have been performed for the first 5 cycles (5 years).

Results

In Table 2.1.5 the CO_2-dosage that was found for subsequent cycles is shown. Table 2.1.5 shows that the CO2-dosage (and the associated partial pressure of CO2) increases significantly in subsequent cycles. This is caused by the dissolution of calcite in the vicinity of the cold well in each cycle. As a result, the amount of calcite that is dissolved in the groundwater becomes higher in each subsequent cycle. When more calcite is dissolved, a higher CO2 dosage is required to prevent oversaturation. And a higher CO2-dosage leads to an increase in the dissolution of calcite after cooling. In the long run, this would lead to very high dosages.

Table 2.1.5 Overview of the results of the PHREEQC calculations

Year	Description	Temperature [°C]	Pressure [bar]	CO₂-dosage [mmol/l]	SI$_{cc}$	partial pressure CO₂ [bar]
0	Initial situation	15.5	37	-	0.48	0.01
1	Extraction and CO₂-dosage	15,5	5	1,49		
	Heating	85	5	-	0.48	0.17
	Injection in hot well	85	37	-	0.48	
	Equilibration with calcite	85	37	-	0.48	
	Extraction and cooling	30	5	-		
	Injection in cold well	30	37	-		
	Equilibration with calcite	30	37	-	0.48	
2-5	Same steps as in year 1			Year 2: 2.68 Year 3: 5.95 Year 4: 15.92 Year 5: 51.70		Year 2: 0.33 Year 3: 0.73 Year 4: 1.95 Year 5: 6.31

For the HT-ATES system of Zwammerdam similar calculations were performed and the same increase in dosage was predicted. In practice, however, less acid needed to be dosed than follows from the above calculation method and the dosage did not increase over time either. Possible explanations are:

- In practice, dissolution of carbonates is less than in the model calculations. This may be because carbonates do not occur everywhere in the aquifer and/or the dissolution process does not proceed quickly enough to reach the equilibrium situation.
- As a result of a water imbalance (when the amount of water that is pumped from the cold well to the warm well differs from the amount of water that is pumped the other way around), part of the extracted water will have the initial groundwater composition (and thus a much lower calcite content).
- As a result of processes at the edge of the bubble (diffusion, dispersion and density-driven groundwater flow) and mixing of water from different depths in the well, the increase in the calcite content is reduced.
- Changes in the concentrations of natural inhibitors for carbonate precipitation may lower the required dosage. Here the mobilisation of organic carbon is relevant, and possibly also other ions like magnesium and phosphates.
- Reactions may occur in which acid is formed (in that case acid is already added in the subsurface):
  Methanogenesis $\quad 2\ CH_2O + H_2O \quad \rightarrow \quad CH_4 + CO_2 + H_2O \quad \rightarrow \quad CH_4 + H^+ + HCO_3^-$
  Sulphate reduction $\quad 2\ CH_2O + SO_4^{2-} + Fe^{2+} \rightarrow \quad FeS + 2\ H_2O + 2\ CO_2 \rightarrow \quad FeS + 2\ H^+ + 2\ HCO_3^-$

The above points show, that there is still significant uncertainty. Although the modeling results suggest an exponential increase in the required dosage, data from practice suggest otherwise. There is still a lack of knowledge on what will actually occur. Therefore, it is important to carefully monitor the evolution of the groundwater composition during the operational phase. If it turns out that the required dosage increases too quickly, than a fallback scenario is needed. In this case the fallback option is to remove part of the CO₂ by degassing during heat recovery in the winter season (after cooling). This option is also mentioned in Sanner ed. (1999) and reduced the degree of calcite undersaturation in the groundwater before it is returned to the

aquifer by injection through the cold well. This strongly limits the amount of calcite that dissolves around the cold well and thus limits the increase in the required dosage. An additional advantage is that this degassing also limits the increase in gas pressure due to the addition of CO_2 (and possible methanogenesis).

2.1.6.3 Scenario 2 (ToughREACT)

Reactive transport simulations were performed with the TOUGHREACT software version 3.32 (Xu et al., 2017) to simulate coupled THC (Thermal-Hydro-Chemical) processes during loading and unloading of the HT-ATES. A 3D subsurface model was built in TOUGHREACT based on the subsurface characteristics of the HT-ATES site to simulate the injection of hot water with simultaneous production of cold water, the flow and heat evolution, and corresponding water-rock interactions. The water-rock interactions allow the assessment of near-well porosity and permeability changes and corresponding effect on the flow properties of the rock. In addition, the model allows prediction of the changes in water composition with time, which will be used to predict scaling within the near-well zone and the prevention of scaling by water treatment. TOUGHREACT is a numerical simulator for non-isothermal multiphase fluid flow and geochemical transport (Xu and Pruess, 2001). The simulator introduces reactive chemistry into the TOUGH2 simulator on multiphase and multicomponent fluid flow in porous and fractured media (Pruess et al., 2012). Mass and energy balances are solved implicitly using Newton-Raphson iterations. The reactive transport is simulated by an (iterative or non-iterative) operator-splitting approach. For the purpose of these simulations the ECO2N equation of state and the thermoddem database (Blanc et al., 2012) were used. ECO2N is a fluid property module describing thermodynamics and thermophysical properties of H_2O-NaCl-CO_2 mixtures (Pruess, 2005). Mineral dissolution and precipitation reactions are implemented as kinetic processes, using the rate expression given by Lasaga et al. (1994) and Xu et al. (2017). Upon mineral reactions, the volumetric portion of the rock minerals and hence the porosity changes. Porosity changes are calculated by the software after each time step using mineral specific molar volumes. The permeability alterations, as a result of porosity changes, are described by the Verma and Pruess (1988) relation:

$$\frac{k}{k_i} = \left(\frac{\phi - \phi_c}{\phi_i - \phi_c}\right)^n$$

Where k is the permeability, k_i the initial permeability, ϕ the porosity, ϕ_i the initial porosity, ϕ_c the critical porosity below which the permeability goes to zero, and n is a power law exponent. This relation considers the pore morphology of a material, which consists of pore throats and pore bodies. The permeability can decrease significantly if pore throats get clogged, leaving a relatively high porosity in place but the pores are disconnected.

Model setup

The 3D reactive transport model in TOUGHREACT is based on the geological and geochemical characteristics resulting from the test drilling. At the time, the final design of the HT-ATES system was not yet prepared. Hence, the model shows some deviations from the system which was built for operation. The model consists of 10 layers, the upper and lower layers represent the over- and underburden with thicknesses of respectively 80 and 45 m. The 8 aquifer layers in between are each 2.25 m thick so 18 m in total. The mesh is 600 x 545 m in horizontal direction, with the 'hot well' (injector during heat storage and producer during heat recovery) and 'cold well' (producer during heat storage and injector during heat recovery) 195 m apart. The 10 cells adjacent to the wells are each 5 x 5 meter. Further away, the sizes of the cells increase to 10 and 20 m with outer cells being 100 x 20 m to create sufficient volume for pressure dissipation. The initial aquifer porosity, horizontal and vertical permeability used in the model are 0.35, $1.26 \cdot 10^{-11}$ m^2 and $3.16 \cdot 10^{-12}$ m^2, respectively. In the simulations, only the first loading phase (4 months at 150 m^3/h) was simulated, as the validation of the model by monitoring data will be done based on geochemical data obtained during that phase. After model validation, subsequent phases will be simulated. Both the validation and the simulations of the subsequent phases will be reported in deliverable D5.3.

For the initial groundwater composition, an average composition of the measured baseline water samples was used. The rock mineralogy is represented by a simplified mineral composition (Table 2.1.6) based on an average rock mineralogy as measured by XRD (Dijkstra et al., 2020). Considering the relatively short time scale and the slow mineral kinetics of silicates, only calcite and dolomite were allowed to dissolve and precipitate. The kinetic parameters are shown in Table 2.1.7.

Table 2.1.6 Simplified mineralogy used in the simulations based on XRD analyses of sample material from the Middenmeer site.

Mineral	Rock volume fraction
Quartz	0.889
K-feldspar	0.071
Calcite	0.018
Dolomite	0.002
Pyrite	0.001
Smectite	0.014
Kaolinite	0.005

One of the key uncertainties regarding the geochemical reactivity is the saturation level at which mineral precipitation takes place. The PHREEQC calculations demonstrated an initial calcite saturation index (SI) of 0.48. In the current simulations the initial pH is assumed to be slightly lower (7.2), considering that some degassing of the samples might have taken place during sampling. The corresponding initial SI for calcite and dolomite was calculated by TOUGHREACT to be 0.3 and 0.9 respectively. It is common for calcite and dolomite to be supersatured in the (relatively) shallow subsurface. With higher temperatures, the supersaturation will go down. Yet, the exact relation between supersaturation and temperature is unknown, and other conditions, such as the presence of inhibitors, also play a role (Griffioen, 2020). Two different relationships have been evaluated. In addition, other processes might occur at increased temperature, such as mobilisation of organic matter. Yet, these processes are out of scope for this project.

It should be noted that the reactivity of dolomite under these conditions is yet unclear. Scenarios were run with and without the reactivity of dolomite included. Monitoring data might give insight in the processes occurring and can be used for model validation and scenario selection.

Table 2.1.7. Parameters describing the kinetics of mineral reactions at 25°C: dissolution rate constant (k25 in mol/m2s), activation energy (Ea in kJ/mol), and reaction order parameter (n). Parameters are taken from Palandri and Kharaka (2004). Mineral surface area (Ams) are in cm2/g.

	Acid mechanism			Neutral mechanism		Base/carbonate mechanism			
Mineral	k_{25}	E_a	n	k_{25}	E_a	k_{25}	E_a	n	A_{ms}
Calcite	5.01E-01	14.4	1.0	1.55E-06	23.5	-	-	-	9.8
Dolomite	6.46E-04	36.1	1.0	2.95E-08	52.2	7.76E-06	34.8	1.0	9.8

First, batch simulations were run to initialize the water composition for the base case scenario (without the addition of CO_2) and for the water treatment scenario (with the addition of CO_2), and to evaluate the impact heating on the chemical conditions.

Next, reactive transport simulations were run. A base case model was run to evaluate the effect of carbonate scale on the flow properties. A second model was run to assess the spatial impact of water treatment by CO_2, using the results from the batch simulations on the required CO_2 dosing.

Results batch simulations

The following conditions were simulated:

- The initial geochemical conditions
- Conditions after heating to 83°C, representing conditions in the pipeline after the heat exchanger
- Conditions after heating to 83°C including calcite and dolomite reactions, representing conditions in the near well zone.

These conditions were performed for the base case scenario and for the scenario with CO_2, hence six batch simulations in total (Table 2.1.8). In the simulations with mineral reactions included, the SI values were set at 0. These simulations were run to show the tendency of the mineral reactions.

Table 2.1.8. Batch simulation scenarios

Scenario	T (°C)	With/without CO_2	With/without reactions	Representation of
1	19.6	no water treatment	no mineral reactions	Initial groundwater composition
2	83	no water treatment	no mineral reactions	Conditions after heat exchanger
3	83	no water treatment	mineral reactions	Conditions in near well zone
4	19.6	With CO_2 added	no mineral reactions	Conditions prior to heat exchanger
5	83	With CO_2 added	no mineral reactions	Conditions after heat exchanger
6	83	With CO_2 added	mineral reactions	Conditions in near well zone

The predicted values for the saturation index and the pH for the various scenarios are shown in Figure 2.1.23.

Heating of the water from the initial temperature to 83°C in the heat exchanger increases the SI of calcite and dolomite from 0.3 and 0.9 to 0.9 and 2.5 respectively. The pH goes down from 7.2 to 7.0. If calcite and dolomite reactions are included (to SI values of 0) minor calcite dissolves and dolomite precipitates. The corresponding pH is 6.1. Even though SI values of both calcite and dolomite are positive, if both minerals are allowed to react dolomite precipitation 'forces' calcite to dissolve.

The addition of 1.49 mmol CO_2 per liter water at the initial temperature decreases the SI of calcite and dolomite from 0.28 and 0.9 to   -0.18 and -0.1 respectively and a pH of 6.7. After heating the SI values are 0.5 and 1.7 respectively and the pH is 6.6. If calcite and dolomite reactions are allowed, minor calcite dissolves and dolomite precipitates. Slightly more calcite dissolves than in the base case scenario, and slightly less dolomite precipitates. The corresponding pH is 6.0.

Hence, the addition of 1.49 mmol CO_2 per liter water decreases the SI after heating from 0.9 and 2.5 to 0.5 and 1.7 for calcite and dolomite respectively. Yet, they remain well above the initial values of 0.3 and 0.9, whereas the PHREEQC calculations predicted that 1.49 mmol of CO_2 was required to keep the SI of calcite at the initial value of 0.48 after heating.
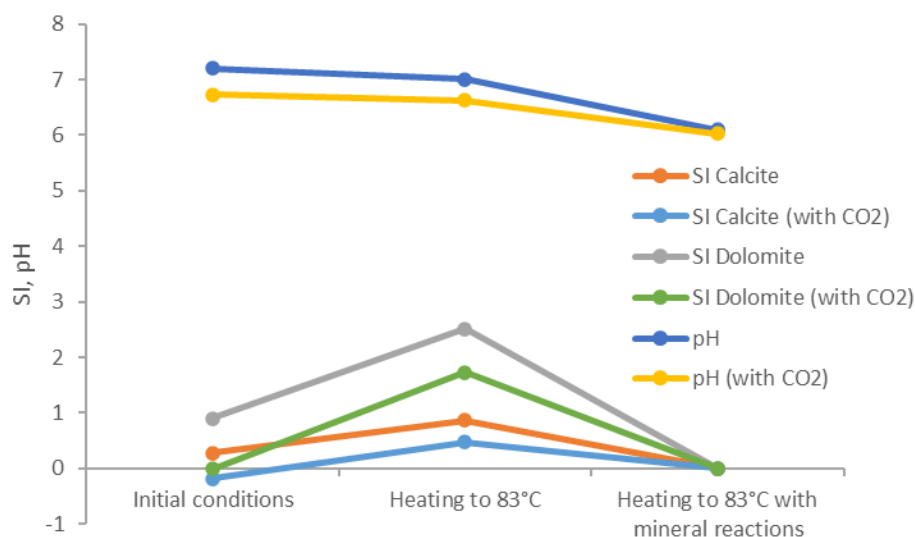

Figure 2.1.23 Batch reaction results.

Results reactive transport simulations

Eight different scenarios were simulated (Table 2.1.9). Scenarios were run with and without water treatment (CO_2 added to the injection water). Scenarios were run in which both calcite and dolomite were allowed to dissolve or precipitate and in which only calcite precipitation from the water was allowed (representative for the conditions modelled with PHREEQC, see above). The sensitivity of the results to the relation of carbonate supersaturation with temperature was tested: the SI of calcite goes from 0.3 (initial supersaturation) to 0 at a temperature of 80°C, and the SI of dolomite from 0.9 (initial supersaturation) to 0 at a temperature of 150°C; at 80°C the groundwater goes to equilibrium with calcite and at 150°C with dolomite. In another scenario both for calcite and dolomite the SI goes from the initial value to zero between 80°C and 150°C, which effectively means that the SI remains at the initial supersaturation level at all temperature conditions in the model. It should be noted that these temperature dependencies are arbitrary, based on the general trend that supersaturation of carbonate minerals goes down with increasing temperature, and dolomite precipitation is not as common in low temperature regimes as calcite. Scenario 8 is most similar to the PHREEQC simulation.

Table 2.1.9. Reactive transport simulation scenarios.

Scenario	With/without CO2	Mineral reactions	SI calcite 0.3 to 0[*]	SI dolomite 0.9 to 0[*]
1	no water treatment	Calcite and dolomite	19 to 80°C	19 to 150°C
2	no water treatment	Calcite and dolomite	80 to 150°C	80 to 150°C
3	with CO_2 added	Calcite and dolomite	19 to 80°C	19 to 150°C
4	with CO_2 added	Calcite and dolomite	80 to 150°C	80 to 150°C
5	no water treatment	Calcite precipitation only	19 to 80°C	-
6	no water treatment	Calcite precipitation only	80 to 150°C	-
7	with CO_2 added	Calcite precipitation only	19 to 80°C	-
8	with CO_2 added	Calcite precipitation only	80 to 150°C	-

The model results show that in the reservoir around the hot well calcite starts to dissolve and dolomite starts to precipitate. The net result is a porosity decrease. The amount of calcite dissolution and dolomite precipitation is greatly affected by the relation of supersaturation with temperature, whereas there is only minor impact of the addition of CO_2.

In the scenarios in which only calcite precipitation is allowed, calcite indeed precipitates around the hot well. The porosity decreases correspondingly. Compared to the scenarios with calcite and dolomite (e.g. comparing scenario 1 and 5), the porosity decrease is smaller. Again, the amount of precipitation is affected by the relation of supersaturation with temperature. Yet, in contrast to the simulations with calcite and dolomite, in these simulations the effect of water treatment is clear. Calcite precipitation is limited by the addition of CO_2. Simulation 8 is most similar to the scenario simulated with PHREEQC, and the results show only minor calcite precipitation and porosity decrease, implying that PHREEQC and TOUGHREACT results are highly comparable (bearing in mind that the initial conditions were slightly different).
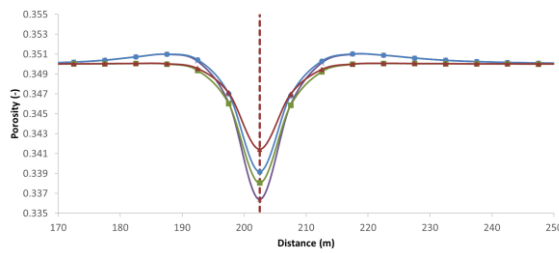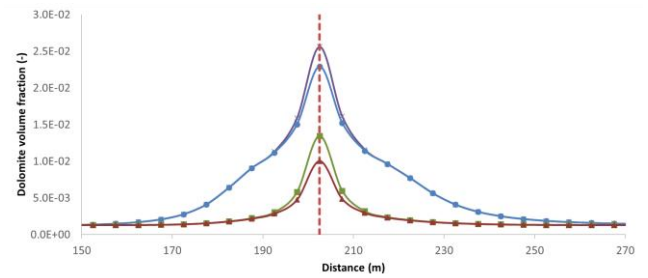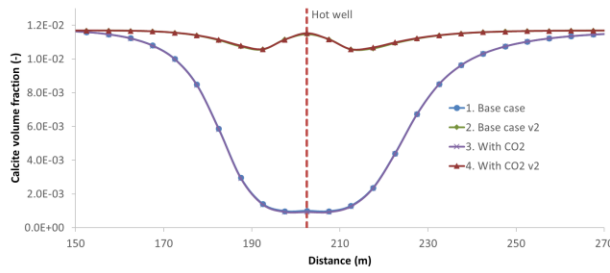
Figure 2.1.24 Simulated calcite and dolomite fraction and corresponding porosity around the hot well after 4 months of loading at 150 m³/h for scenarios 1 - 4.
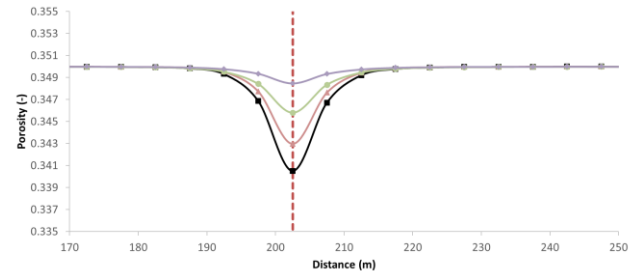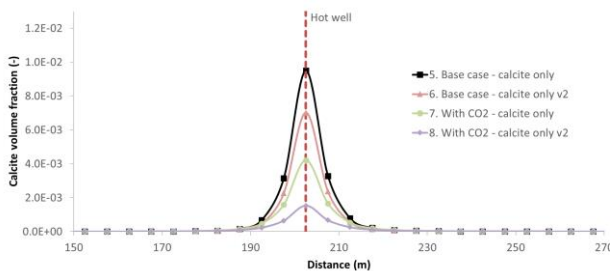

Figure 2.1.25 Simulated calcite fraction and corresponding porosity around the hot well after 4 months of loading at 150 m³/h for scenarios 5 - 8.

2.1.7 Conclusions and recommendations

2.1.7.1 Model simulations of thermal effects

Well distance

Based on the modelling results, it was concluded that for a well distance of 220 m (i.e. 2.2 times the thermal radius of the hot well), both the thermal recovery efficiencies and the thermal interference between the hot and cold wells were optimal for the ECW case, for both the base case pumping scheme and the scenarios with decreased and increased storage and recovery volumes. These results were used in the design phase for the choice of the well locations.

Effects of heat storage on surrounding subsurface

Given the hydrogeological parameters that were derived from the test drilling results, combined with the expected pumping scheme, the thermal effects of the stored heat on the surroundings were calculated. These simulations were performed within the permitting procedure context and therefore reflected a worst-case scenario. The dimensions of the aquifer combined with the large storage volumes contribute to a high thermal recovery efficiency, meaning that the thermal impact on the surroundings is relatively limited too. Additionally, the thick clay layer overlying the heat storage aquifer plays a major role in limiting the thermal effects to shallower layers. Altogether, the simulation results supported the conclusion that the thermal effects were acceptable, i.e. no other subsurface interests will be violated.

Heat losses by the hot well casing

The simulations showed that the thermal effects of the hot well casings on the surrounding subsurface are predominantly controlled by the hydrogeological and thermal properties in the subsurface layers outside the borehole wall. The use of different types of backfilling material has a limited effect on the thermal impact in the area surrounding the HT-ATES wells. The calculations show that 2.5, 2.3 and 1.6 % of the stored heat is lost through the well casings of the hot well, for sand, clay and spherelite backfilling materials respectively. Spherelite backfilling material has a relatively low thermal conductivity (0.44 W/(m K)) compared to the standard backfilling materials clay and sand (1.8 and 2.4 W/(m K)) and shows a smaller thermal impact on the subsurface, although the differences were mainly observed in the direct vicinity of the hot well. Although heat losses are smaller when spherelite is used, the advantage of the use of spherelite-concrete is too small to justify the application of this relatively expensive material. The differences between clay and sand backfilling materials were insignificant.

The model simulations show that the heating around the casing of the hot well induces upward density-driven flow in the coarse-grained third aquifer. In the design of the HT-ATES wells, the backfilling material in the third aquifer consists of sand alternated with clay plugs to reduce upward flow through the backfilling material to some extent. Also, piezometers at the top of the third aquifer were included in the design to monitor possible increase in salinity as a result of the upward transport of water within the aquifer.

What do these results mean for the design and monitoring program of the HT-ATES of ECW?

2.1.7.2 Model simulations of geochemical effects related to water treatment

What do these results mean for the design and monitoring program of the HT-ATES of ECW?

PHREEQC results

Model simulations have been performed in PHREEQC to calculate the CO_2-dosage that is required to keep the calcite saturation index after heating at or below the value that was found for the initial situation. The simulations show that dosing of CO_2 works, but also causes dissolution of carbonates in the aquifer. As a consequence, the concentration of carbonates in the treated groundwater increases in each subsequent cycle and causes an increase in the required dosage of CO_2. According to the simulation results, the required dosage would increase exponentially in subsequent cycles, which would lead to an unacceptable situation after a number of years. However, results from the Zwammerdam HT-ATES project do not show an increase in the required dosage of hydrochloric acid (which was used for water treatment in that project). There are different possible explanations for these contradictory results. Probably, the complexity of all the processes that occur is not sufficiently reflected in the PHREEQC model.

Given the contradictory results, the complexity of all the different geochemical processes and the relevance for the operation of the HT-ATES plant, it is important to carefully monitor the evolution of the groundwater composition during the operational phase. In case the required dosage increases too much, the option of removing part of the dissolved CO_2 before returning the cooled water through the cold well is used as a fallback scenario. This option is also mentioned in Sanner ed. (1999) and reduces the degree of calcite undersaturation in the groundwater before it is returned to the aquifer by injection through the cold well. This strongly limits the amount of calcite that dissolves around the cold well and thus limits the increase in the required dosage. An additional advantage is that this degassing also limits the increase in gas pressure due to the addition of CO_2 (and possible methanogenesis).

TOUGHREACT results

The reactive transport simulations predict carbonate reactions to occur around the hot well during loading, resulting in a net porosity decrease. In the scenario with addition of CO_2, the porosity decrease is very small. It is concluded that the TOUGHREACT simulations suggest that the required CO_2-dosage is slightly higher than follows from the PHREEQC calculations. This is attributed to small differences in the model input and/or differences in the way the geochemical calculations are performed. During the first loading phase the porosity, and therefore the permeability decrease is limited, which will not have a negative impact on the operations. Yet, with each next cycle, the reactions will continue and the porosity and permeability decrease as well. This might lead to clogging of the pore space and corresponding injection problems during loading and production problems during unloading in case the dosage of CO_2 is too low.

2.1.7.3 Recommendations for HT-ATES design and monitoring program

Based on the modelling results, the following choices for the design and monitoring activities are recommended, for the ECW HT-ATES system.

Thermal effects

Design

- The distance between the hot and cold well was designed at 220 m.
- The distance between the hot well and the monitoring well was designed at 30 m, downstream of the hot well.
- Optic fibre DTS cables were installed over the full depth of the hot well, cold well and monitoring well, allowing for high frequency temperature measurements along the full depth of the boreholes. The data can be used to validate models and to obtain insights in the subsurface heat transport processes.
- Flow rates and injection/production temperatures at the wells are registered continuously, to enable reconstruction of the real pumping scheme and calculation of the thermal effects and the recovery efficiency of the HT-ATES system.
- Both clay and sand (hence not spherelite-concrete) was chosen as backfilling material in the wells.
- Additional piezometers were installed at the top of the 3rd aquifer, to investigate whether upward flow along the heated well casing causes upward transport of deeper saline groundwater.

Monitoring

- Temperature measurements at various depths along the wells, to track thermal impact of HT-ATES on the subsurface and to register variation in temperatures along the well screens.
- Registrations of flow rates and injection/production temperatures, that will enable reconstruction of the pumping scheme and calculation of the thermal effects and the thermal recovery efficiencies (model validation).
- Measurements of the salinity at the top of the third aquifer, to monitor possible upward transport of deeper, more saline water as a result of density driven (upward) flow along the hot well casing.

Geochemical effects

Design

The model results and the experiences in practice clearly show that heating of groundwater that is saturated with carbonates leads to oversaturation which can lead to precipitation of carbonates. If scaling will actually occur depends on a number of conditions, but at high temperatures the risk of scaling has to be taken into account. Therefore, a water treatment system using CO_2 was incorporated in the design of the ECW HT-ATES project. Given the PHREEQC modelling results, the possibility of degassing in case of the carbonate concentrations in the treated groundwater continue to increase has to be taken into account. This degassing option is not installed in the ECW HT-ATES plant, but can be added later when required.

Monitoring

Geochemical processes are highly complex and many uncertainties exist. The various scenarios that were modelled give different predictions on the severity of the reaction on the porosity decrease. Hence the question if and how fast porosity and permeability decrease might lead to operational issues cannot easily be answered. Comparison of the monitoring data with the model results will provide more insights in the geochemical processes that will occur. Frequent monitoring during the various operational phases is therefore essential.

Since the HEATSTORE project is ending in the second half of 2021, only one period of heat storage will take place within the project period. As a consequence, no results from the recovery of heat will become available during the HEATSTORE project. For the HEATSTORE project, it is recommended to monitor the calcium, magnesium and bicarbonate concentration and the pH in the monitoring well. These results will give indications whether calcite precipitates or dissolves, and whether dolomite precipitates. It will allow the selection of the model that fits best with the actual processes taking place, and define a relationship between supersaturation of calcite and dolomite with temperature. It will not be possible to evaluate in detail the

processes of inhibition, but the relationships will be a pragmatic approach to define the amount and rate of carbonate reactions.

The validation of the reactive transport model will be based on the water composition at the monitoring well. To distinguish between the four different scenarios that were run with water treatment (scenarios 3, 4, 7 and 8 in Table 2.1.9), the pH and the calcium and magnesium concentrations are relevant (Figure 2.1.26). These parameters will be measured from water samples taken from the monitoring well during the loading phase.
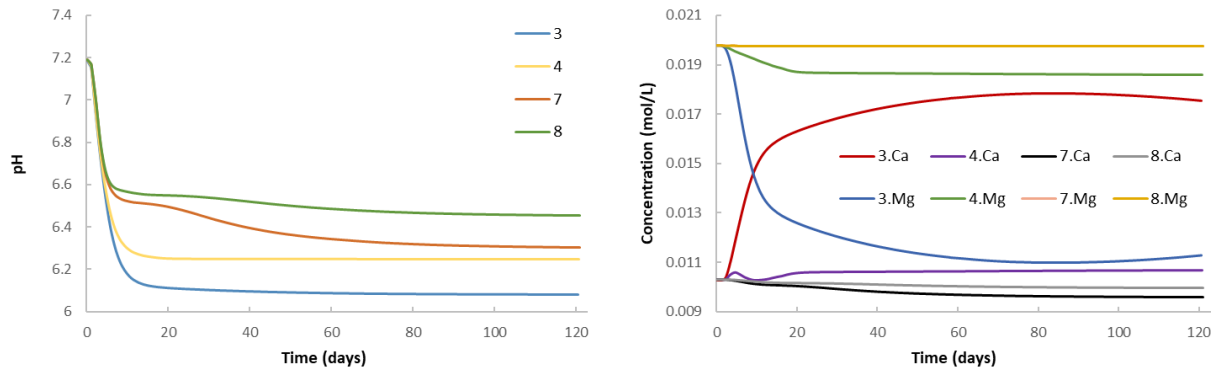

Figure 2.1.26. The predicted pH values and calcium and magnesium concentrations with time at the location of the monitoring well for the four scenarios with water treatment. Note that the magnesium concentrations for scenario 7 and 8 are equal and they remain stable since dolomite reactions are excluded from these simulations.

The monitoring program for the longer term should also include sampling and analysis of the groundwater that is retrieved from the hot well during the winter season (heat recovery mode) and from the cold well during the summer season (heat storage mode). Careful analysis of the observed changes in the groundwater composition will provide more insight in the development of the required dosage on the long run and the necessity of degassing as a fallback scenario.

2.1.8   References

Adsett, J., Cruickshanks, F., Thottan, J.A. and Burris, D. (1997). Groundwater Treatment for Aquifer Thermal Energy Storage. Proceedings MEGASTOCK '97, 7th International Conference on Thermal Energy Storage, June 18-21 1997, Sapporo, Japan, pp. 703-708.

Bakema, G. and Drijver, B. (2018). State of the art HT-ATES in The Netherlands - Evaluation of thermal performance and design considerations for future projects. Draft report Heatstore work package 1. IF Technology, Arnhem, The Netherlands.

Blanc, Ph., Lassin, A., Piantone, P., Azaroual, M., Jacquement, N., Fabbri, A., Gaucher, E.C., 2012. Thermoddem: A geochemical database focused on low temperature water/rock interactions and waste materials. Applied Geochemistry 27, 2107-2116.

Boullenger, B. et al. 2020: Seismic reprocessing for shallow structure of aquifers, GEOTHERMICA – ERA NET Cofund Geothermal. This presentations represents HEATSTORE project milestone number MS1.3.

Dijkstra H., de Boer C., Griffioen J. and Koenen M. (2020). Workflow to evaluate the risk of mineral scaling in a HT-ATES system and application to a potential site in Middenmeer, The Netherlands. TNO report 2020 R10437.

Drijver, B.C. (2011). High Temperature Aquifer Thermal Energy Storage (HT-ATES): Water treatment in practice. First National Congress on Geothermal Energy, Utrecht, The Netherlands.

Drijver, B., Bakema, G. and Oerlemans, P. (2019). State of the art of HT-ATES in The Netherlands. European Geothermal Congress 2019, Den Haag, The Netherlands.

Drijver, B., Oerlemans, P. and W. Bos (2020). Full-scale HT-ATES tests demonstrate that current guidelines considerably overestimate sand production risks in deeper unconsolidated aquifers. 1st Geoscience & Engineering in Energy Transition Conference, 16–18 November 2020, Strasbourg, France.

GPC IP, KWR, Ministry of Economic Affairs and Productschap Tuinbouw (2015). Report assessment of injectivity problems in geothermal greenhouse heating wells.

Griffioen J. (2020). A literature review on the precipitation of Ca, Ca-Mg and Fe carbonates and its inhibition under HT-ATES conditions. TNO report R11204.

Kallesøe, A. J. and Vangkilde-Pedersen, T. (2020). HEATSTORE – Underground Thermal Energy Storage (UTES) - State of the Art, Example Cases and Lessons Learned. Proceedings World Geothermal Congress 2020, Iceland.

Kipp, K.L. (1987). HST3D: a computer code for simulation of heat and solute transport in three-dimensional ground-water flow systems. US Geol Surv Water Resour Invest Rep 86-4095.

Knoche, G., Koch, M. J.W. Metzger (2003). Scaling-tests on Groundwater for use in high-temperature-ATES in respect to calcite precipitates in heat exchangers. Proceedings Futurestock 2003, Warsaw, Poland.

Koch, M. and Ruck, W. (1992). Injection of CO2 for the Inhibition of Scaling in ATES Systems. Paper Presented at the 1992 Intersociety Energy Conversion Engineering Conference, San Diego, California August 3-4, 1992.

Lasaga, A.C., Soler, J.M., Ganor, J., Burch, T.E. and Nagy, K.L., 1994. Chemical weathering rate laws and global geochemical cycles. Geochimica et Cosmochimica Acta 58 (10), 2361-2386.

Lopik, J. van, Hartog, N., Zaadnoordijk, W.J., Cirkel, D.G. and A. Raoof (2015). Salinization in a stratified aquifer induced by heat transfer from well casings. Advances in Water Resources 86 (2015) 32–45.

Nielsen, J.E. and Vangkilde-Pedersen, T. (eds.) (2019). Underground Thermal Energy Storage (UTES) – general specifications and design. HEATSTORE project report, GEOTHERMICA – ERA NET Cofund Geothermal. 58 pp.

Palandri, J.L. and Kharaka, Y.K. (2004). A compilation of rate parameters of water-mineral interaction kinetics for application to geochemical modelling. U.S. Geological Survey Open file report 2004-1068.

Pruess K. (2005). ECO2N: A TOUGH2 fluid property module for mixtures of water, NaCl, and CO2. LBNL-57952.

Pruess K., Oldenburg C. and Moridis G. (2012). TOUGH2 user's guide, version 2. LBNL-43134.

Sanner, B. (ed.) (1999). High Temperature Underground Thermal Energy Storage, State-of-the-art and Prospects. Giessener Geologische Schriften, 67, 158 p., 1999.

Snijders, A.L. (2000). Lessons from 100 ATES projects - The developments of aquifer storage in the Netherlands. Proceedings TERRASTOCK 2000, Stuttgart, Germany.

Sommer, W., J. Valstar, P. van Gaans, T. Grotenhuis, and H. Rijnaarts (2013). The impact of aquifer heterogeneity on the performance of aquifer thermal energy storage, Water Resour. Res., 49, 8128–8138, doi: 10.1002/2013WR013677.

Verma, A. and Pruess, K., 1988. Thermohydrological conditions and silica redistribution near high-level nuclear wastes emplaced in saturated geological formations. Journal of Geophysical Research 93 (B2), 1159-1173.

Xu T. and Pruess K. (2001). Modeling multiphase non-isothermal fluid flow and reactive geochemical transport in variably saturated fractured rocks: 1. Methodology. America Journal of Science 301, 16-33.

Xu T. Sonnenthal E., Spycher N. and Zheng L. (2017). TOUGHREACT V3.32 Reference manual: A parallel simulation program for non-isothermal multiphase geochemical reactive transport. LBNL-Draft.

2.2 Dutch pilot site Koppert Cress: analysis of HT-ATES field performance and the impact of storage conditions

Authors: Stijn Beernink MSc, Martin Bloemendal PhD, Niels Hartog PhD

KWR Water Research Institute

2.2.1 Introduction

2.2.1.1 UTES concept and specifications

To overcome the temporal discrepancy between energy demand and availability, Underground Thermal Energy Storage (UTES) techniques can be used. A commonly used method to store both heat and cold in aquifers in the subsurface is Low Temperature Aquifer Thermal Energy Storage, LT-ATES (Bloemendal et al., 2015). LT-ATES systems have been operating in the Netherlands since the early 1990s. They are applied for buildings of any type, but larger office and utility buildings dominate their use (Graaf et al., 2016). An Aquifer Thermal Energy Storage (ATES) system generally consists of one or more pairs of tube wells that simultaneously pump groundwater to extract or store thermal energy in the subsurface, thereby changing the groundwater and subsurface temperature (Figure 2.2.1).The size of these systems varies mostly from 10,000 to 5,000,000 m^3 storage volume per year, depending on type and size of associated building (Bloemendal & Hartog, 2018).
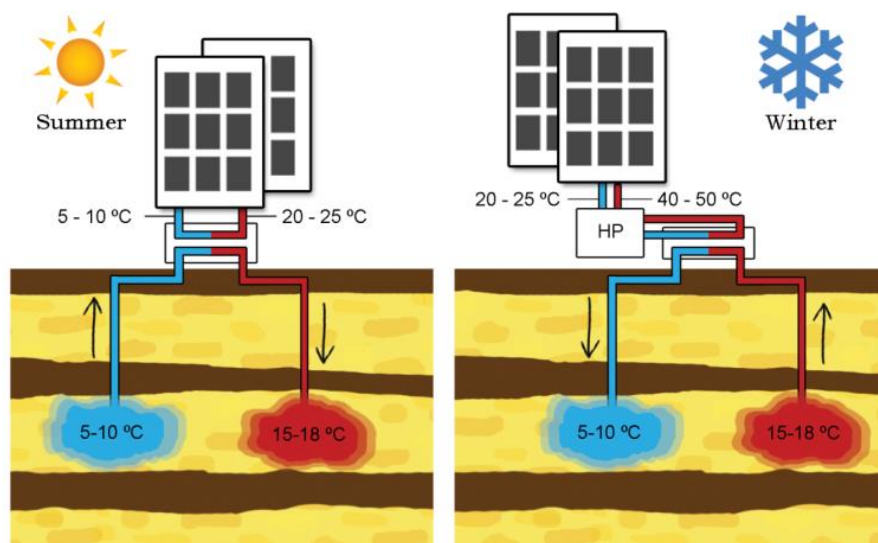

Figure 2.2.1 ATES-doublet working principle. Left: summer (extraction of cold, injection of heat). Right: winter (extraction of heat, injection of cold). Building heating is done in combination with a Heat Pump (HP).

ATES systems usually operate at low temperatures (max 25°C due to Dutch legislation). However, often heat is available at higher temperatures, e.g. geothermal heat, Combined Heat and Power (CHP) or waste heat. Storing this heat in periods of excess (summer) allows to utilize this high quality heat during winter time (Figure 2.2.2). The same concept of ATES can be used to store and recover this heat in a high temperature (HT-)ATES system (> 25 °C), Figure 2.2.3. The main advantages of HT-ATES are that 1) high temperature heat can be used directly for heating (e.g. buildings, utility, greenhouses) and is therefore useful for more applications and 2) more energy can be stored per volume groundwater (and therefore also per m^2 of available subsurface space (Drijver et al., 2012).
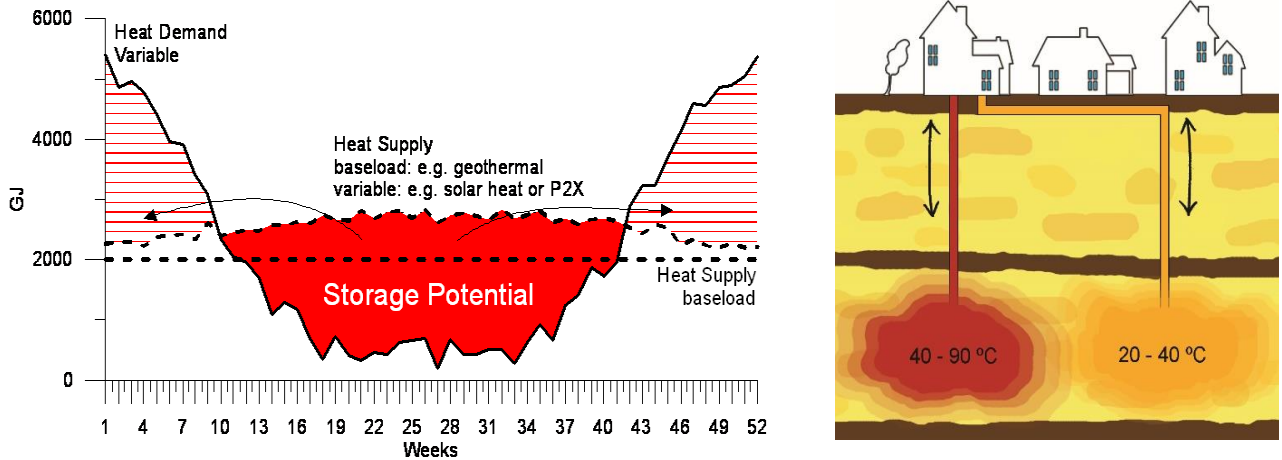
Figure 2.2.3 Basic working principle of HT-ATES. Left: storage potential of high quality heat with baseload heat supply. Right: concept of a combined HT-ATES doublet, with storage of heat at the hot well (40-90°C) and the cooler well with lower temperature (20-40 °C) for storage of the remaining heat in the return flow.

2.2.1.2 Performance of (HT-)ATES systems

The performance of the ATES system is defined by how much of the stored energy can be recovered after storage. Bloemendal and Hartog (2018) describe the impact of storage conditions on the recovery efficiency of low temperature ATES systems (Figure 2.2.4) and provide a generic overview of the most important processes affecting low temperature ATES systems. For HT-ATES, at temperatures generally ranging from 25-90°C, the physical characteristics (as well as the chemical composition) of the groundwater can be affected considerably. Due to the density decrease of heated water, density-driven (buoyancy) flow can therefore become an important factor when storing at high temperatures which can negatively affect the recovery efficiency (Schout et al., 2013; van Lopik et al., 2016).

HT-ATES systems have been used in the past in the Netherlands (1980s), but most of these systems failed due to technical difficulties. Currently a few operational/pilot HT-ATES systems exist worldwide (Holstenkamp et al., 2017; Schout et al., 2013). One of the operational pilot HT-ATES systems in the Netherlands is that of Koppert Cress in Monster, the Netherlands. This pilot is used in the HEATSTORE project as a case study and contributes to research in WP2, WP4 and WP5. For the research in work package 2 that is described here, the storage conditions of Koppert Cress are used as a reference. The further validation/calibration of the site specific numerical model will be initiated and performed in WP5 of the HEATSTORE project.
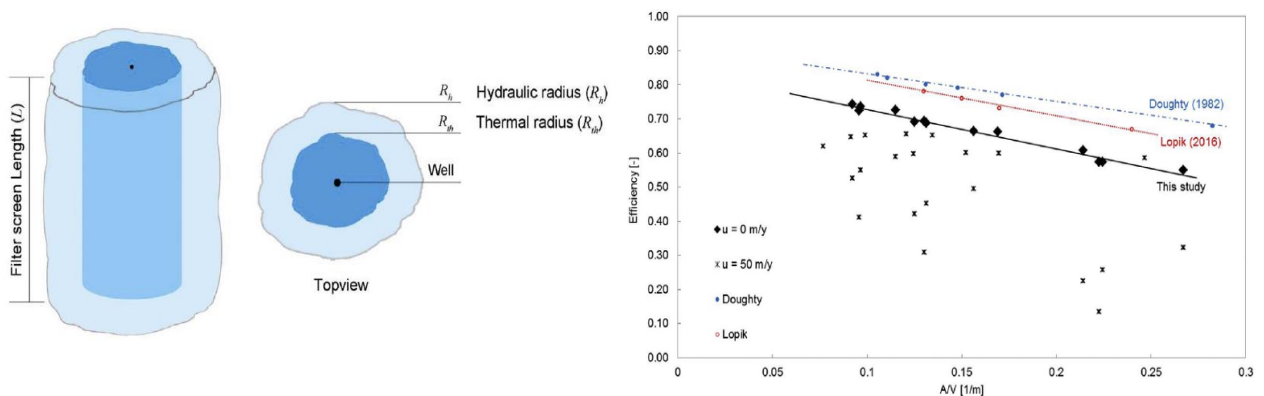

Figure 2.2.4 Left: concept of resulting subsurface thermal and hydrological storage cylinder for an ATES system assuming homogenous aquifer properties. Right: Simulated relationship between A/V and efficiency (η) for low temperature ATES. Source: (Bloemendal & Hartog, 2018).

2.2.1.3 Goal and approach

Globally, HT-ATES systems have a large potential to temporarily, from diurnally to seasonally, store large amounts of heat. However, until now limited experience with HT-ATES systems is available. In this study we therefore analyse the performance and operational characteristics of the currently operational Koppert Cress ATES system, which has a pilot license to store heat at temperatures >25 °C. By doing so, we try to increase our understanding of the application and optimization of HT-ATES systems in practice.

Subsequently, we investigate how the Koppert Cress system would perform under changing storage conditions. To do this, we use the measured operational data and geohydrological properties of the Koppert Cress case study and use this to make a generic model that is subsequently compared to a set of generic simulations of the performance of a HT-ATES well under varying storage conditions. By doing so we try to get insights in the performance of the Koppert Cress system when the future operational strategy changes. Moreover, we try to distil generic insights from the gathered simulation data to support the development of generic guidelines for future HT-ATES designs.

In section 2.2.2, the methods for analysis of the case study is provided alongside with background information on HT-ATES and the Koppert Cress case study. Also, the numerical model is explained and the simulation scenarios are explained. In section 2.2.3, the results of the analysis of the Koppert Cress system is shown. Subsequently, the generic analysis of HT-ATES recovery efficiency under varying storage conditions is given. Finally, in section 0 results are discussed and the main conclusions are drawn.

2.2.2 Methods

2.2.2.1 Case study: the Koppert Cress ATES system

Koppert-Cress is a horticulture company situated in the western part of the Netherlands. To provide sustainable heating and cooling, an ATES system was installed with 4 warm and 4 cold wells (Figure 2.2.5). This ATES system is operational since 2012. As part of a Dutch research project the normal ATES was converted to a HT-ATES pilot (Bloemendal et al., 2020; Bloemendal et al., 2019). To obtain insights in the effect of higher storage temperature on the performance, heat spreading and water quality changes associated to the ATES, the site is intensively being monitored.

The greenhouses of Koppert Cress have a large heat demand in winter, compared to their cooling demand in summer. Therefore, excess heat, harvested from (around) their greenhouses is stored in the warm wells in summer to be used in winter. This comprises of multiple 'passive' heat sources from e.g. solar panels, aquathermal heat generation and waste-heat from a CHP plant. After the start of the transition from LT-ATES to HT-ATES in 2015, these heat sources were gradually added to the heating and cooling system (Bloemendal et al., 2020).

In the Westland region where Koppert Cress is situated, multiple geothermal projects are currently initiated. Possibly, Koppert Cress will be able to obtain heat from one of these geothermal wells in the near future. This will have a big impact on the total amount and temperature of yearly stored heat; effectively resulting in an increase of storage volume and the injection temperature in the warm wells.
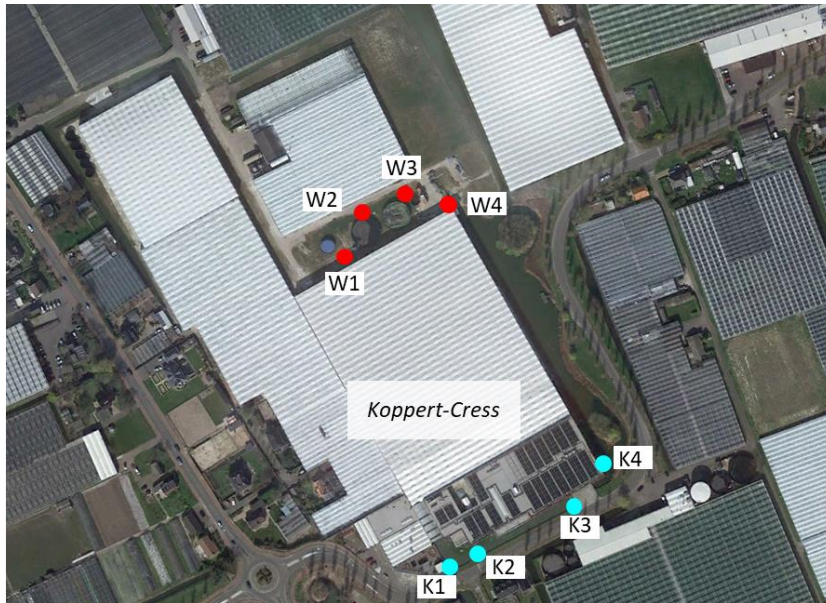
Figure 2.2.5 Overview of Koppert-Cress site with the warm and cold well locations. The individual warm and cold wells are placed apart 40 to 50m. The distance between the cold and warm wells is ~250m.

Hydrogeological characterization

The first aquifer in the subsurface at the Koppert Cress location is not available for the ATES system because this aquifer is reserved for application fresh water storage and recovery, a technology many greenhouse also use for their fresh water supply. The deeper formations Oosterhout and Maassluis are less frequently used compared to the shallow aquifer, resulting in limited and uncertain data on their characteristics. The ATES system utilizes 2 aquifers of 20m thickness with screens up to ±170m depth (Figure 2.2.6). This means that, in total, 16 well screens are used for the ATES system, divided over 8 wells and 2 aquifers. The horizontal (K_h) and vertical (K_v) hydraulic conductivity of both aquifers are estimated to be K_h=35 and K_v=7 m/d. The regional model Regis was used to determine this.
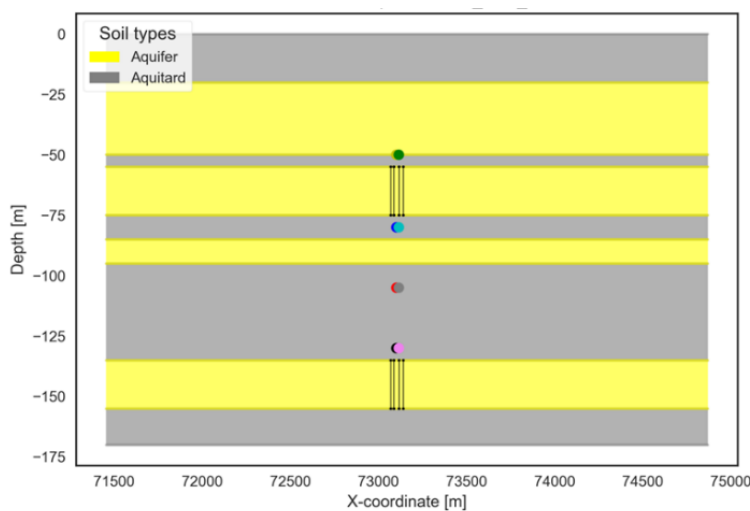

Figure 2.2.6 Conceptual representation of the hydrogeology and one well of the Koppert Cress case study site, two black striped rectangles represent well screen location. Right: Vertical temperature measurements (DTS) at 4m and 18m of the warm HT-ATES well.

Groundwater flow

The regional groundwater flow direction is West, towards the sea. However, at the pilot site (Figure 6) the groundwater flow direction is east due to a large groundwater extraction in Delft. This extraction is being stopped over the course of a period of about 10 years[1]. As a result, over time, the groundwater flow direction in the Westland area will be West everywhere. However, in both situations the head gradients in the Westland area are limited resulting in relatively small groundwater flow velocities, usually <1 m/y. It is therefore expected that these relatively low groundwater flow velocities does not have a significant influence on the performance of the ATES systems in this area (Bloemendal & Hartog, 2018).
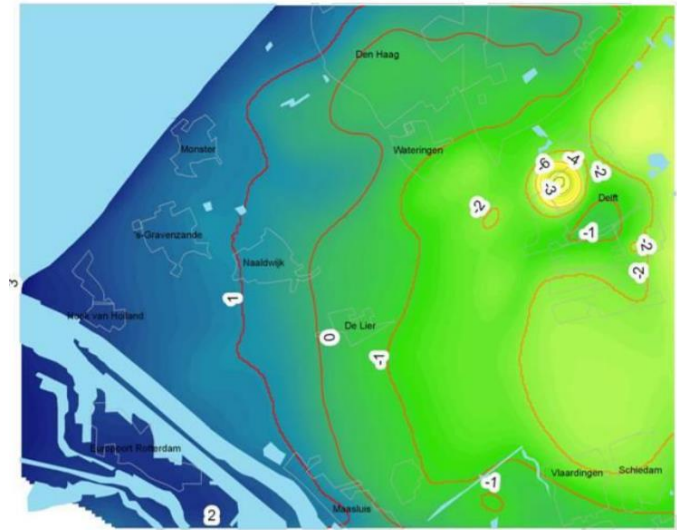
Figure 2.2.7 Groundwater heads in the combined 2nd/3rd aquifer. (Sanchez et al., 2012)

Available operational data

To monitor the Koppert Cress ATES system, several operational and environmental aspects are being measured. Regarding the operational data of the wells of the KC system, data is available from 2012 – 2020. Both 5-min and hourly data is available of the temperature and flows (in/out) of all 8 wells. An example of the available data is given in Figure 2.2.8. Here, the heating loads to and from, the average temperature of the warm well and the thermal radius of the warm wells (R_{th}) based on this during the last 3 years is shown.

Figure 2.2.8. Example of the available data for the Koppert Cress pilot site. Daily heat to and from the warm ATES wells, well temperature and size of the thermal radius in the 2.5 year period from august 2017 to March 2020 is shown.

---

[1] https://www.delft.nl/milieu/bodem/grondwateronttrekking-delft-noord

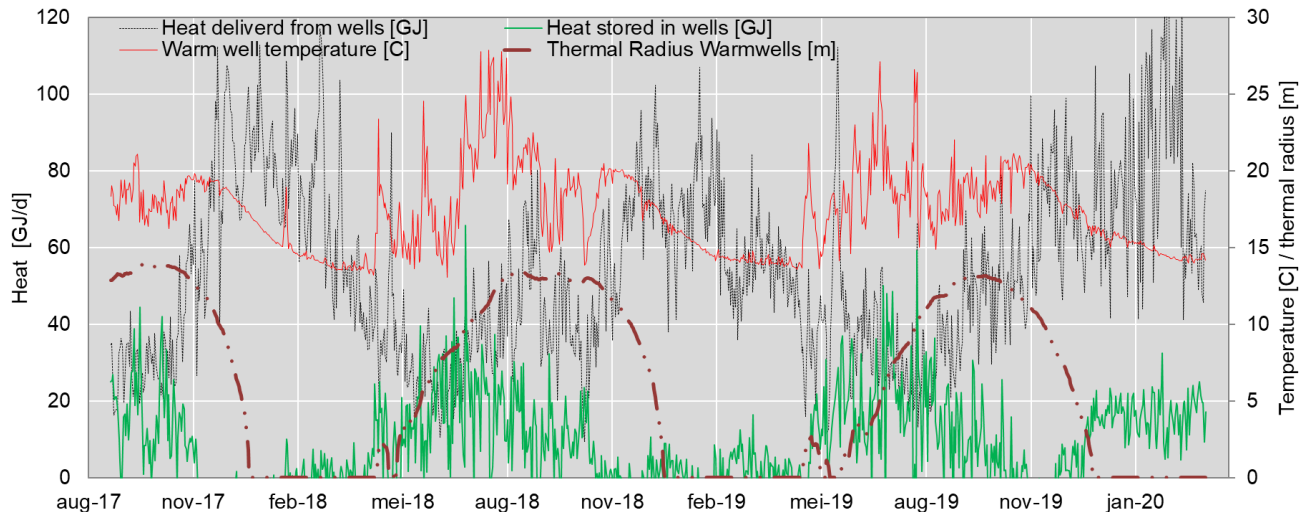Next to the operational data of the ATES system, the temperature distribution in the subsurface around warm well 1 of the KC ATES system is being monitored using Distributed Temperature Sensing (DTS) (Figure 2.2.9). This allows to closely monitor the temperature profile and heat distribution around the warm well. An analysis of the monitored data, and validation of the numerical model based on the DTS measurements is done in work package 5 of the HEATSTORE project.
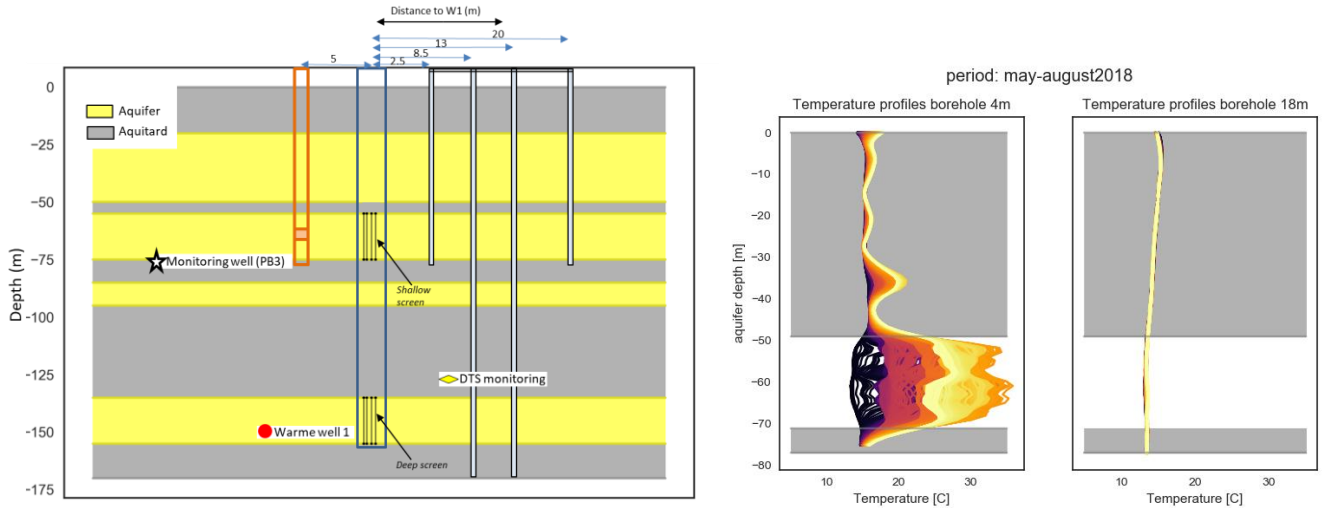

Figure 2.2.9 Left: subsurface layering and monitoring infrastructure around warm well 1 from the Koppert-Cress ATES system. Right: An example of the measured temperature of the groundwater with the DTS cables at 4 and 18m distance from warm well 1.

2.2.2.2 Numerical simulation of HT-ATES

In this chapter we explain which processes are relevant for HT-ATES and a brief explanation of the model setup is given. A more detailed explanation is given in the specific modelling report (D2.2) of the HEATSTORE project (Tomasdottir & Gunnarsson, 2019).

Processes relevant for simulation of HT-ATES

Previous studies have shown that the thermal recovery efficiency of LT-ATES systems are negatively affected by thermal energy losses from the stored volume by mostly conduction (Bloemendal & Hartog, 2018). While for high temperature (e.g. >40 °C) ATES systems, the negative impact of the buoyancy of the stored hot water on thermal recovery efficiency typically needs to be considered (van Lopik et al., 2016), for low temperature ATES systems buoyancy flow does not play an important role (Buscheck et al., 1983).

Mechanical dispersion and heat conduction spread the heat over the boundary of the cold and warm water bodies around the (HT-)ATES wells. As a consequence of the seasonal operation schedule, diffusion losses are negligible (Bloemendal & Hartog, 2018). Both other processes are described by the effective thermal dispersion (D_{eff}) which illustrates the relative contribution of both processes to the losses, following:

$$D_{eff} = \frac{\kappa_{Taq}}{nc_w} + \alpha\frac{v}{n},$$

where, the first term represents the conduction, which depends on the volumetric heat capacity (c_w) of water and the thermal conductivity (k_{Taq}) and porosity (n) of the aquifer material which are considered to remain constant at about 0.15 [m2 /d] in a sandy aquifer with porosity of e.g. 0.3. The rate at which conduction occurs can be determined by the increasing standard deviation: $\sigma = 2D_T t$, with DT, the effective thermal dispersion (the left hand term of Eq. (3) and t the storage time). For half a year storage period the rate at which heat moves through conduction is about 7 m. The second term of Eq. (3) represents the mechanical

dispersion, which depends on the dispersivity (α) of the subsurface, porosity and the flow velocity of the water (v), which is the sum of the force convection due to the infiltration and extraction of the well, as well as the ambient groundwater flow (u). For ATES wells that fully penetrate an aquifer confined by aquitards, the dispersion to cap and bottom of the thermal cylinder (Fig. 3) is negligible due to the lack of flow (Doughty et al., 1982). With regularly applied values of 0.5–5 for the dispersivity (Langevin, 2008), the dispersion is in the same order of magnitude as the conduction at flow velocities of 0.01–0.1 m/d. Bloemendal and Hartog (2018) thus showed that, for ATES system with a seasonal operating strategy, conduction losses are the main processes leading to energy losses for low temperature (<25°C) ATES systems.

The effect of temperature on density and viscosity

Both the density and viscosity of the water are functions of salinity, temperature and pressure. However, for the depth range of interest, the dependency of pressure is negligible (Lopik et al., 2016; Sharqawy et al., 2012). Salinity values are assumed homogeneous in this study[2], therefore only the temperature dependency is of interest. The density and viscosity of water with increasing water temperature is given in Figure 2.2.10.
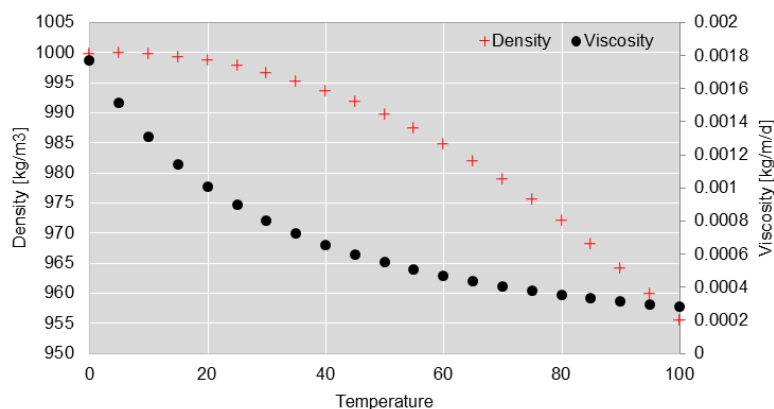

Figure 2.2.10 Water density (Eq. 2) and viscosity (Eq. 4) as a function of temperature.

Simulation software: SEAWAT

The simulations done for this study are done using SEAWAT (Langevin et al., 2008). SEAWAT is a model that couples the finite-difference code MODFLOW (Harbaugh et al., 2000) and MT3DMS (Zheng & Wang, 1999) that is flow and transport (Hecht-Mendez et al., 2010; Langevin et al., 2010) and adds viscosity and density effects coupled to temperature. SEAWATv4 uses the governing equations for groundwater flow and solute transport as well as the equations of state for fluid density and viscosity. Van Lopik et al. (2016) calibrated an axisymmetric model of a high temperature (80 °C) ATES system against monitoring data, in which buoyancy flow was a dominating process. The model set-up and parameter values in this study follow their work.

Implementation of density and viscosity

Normally, a linear relationship is used to calculate the changing density in the SEAWAT model (Langevin et al., 2008; Lopik et al., 2015; Thorne et al., 2006). However, for HT-ATES this leads to a relatively large difference with the actual non-linear relationship shown in Figure 2.2.10. To use this non-linear relationship, we altered the original SEAWAT executable and implemented the following relationship:

$$\rho(T) = 1000 - \frac{(T-4)^2}{207}$$

This is explained in more detail in the WP2.2 report (Tomasdottir & Gunnarsson, 2021). The temperature also affects fluid viscosity (μ [kg/m/d]), to which the hydraulic conductivity is proportional (Fetter, 2001). The relation between viscosity and temperature may be approximated following Voss (1984);

---

[2] The salinity gradient strongly depends on local hydrogeological conditions and the material and geologic history of the aquifer. Aquifers near the coast to the extent that they have sufficient continuous recharge, have a relatively sharp interface between fresh and saline water. Aquifers with zero or little recharge tend to have a smooth, up to an almost constant vertical density gradient (Robinson et al., 2006).

$$\mu(T) = 2.394 \cdot 10^{-5} \cdot 10^{\frac{248.8}{T+133.2}}$$

Axisymmetric model setup

The simulations done for this study are performed with an axisymmetric model setup. This means that one injection/extraction well is simulated which is located in the outer left boundary of the modelling grid (Figure 2.2.11). An axisymmetric modelling setup is used because these kind of modelling grids need a relatively small amount of computing power compared to a 3D modelling setup, while the results are equal (Langevin, 2008; Louwyck et al., 2014). This enables us to use a detailed grid discretization near the wells, resulting in highly accurate modelling results for these single storage/injection wells. However, processes that need to be addressed with a 3D model like interaction between wells and the influence of ambient groundwater flow cannot be taken into account.
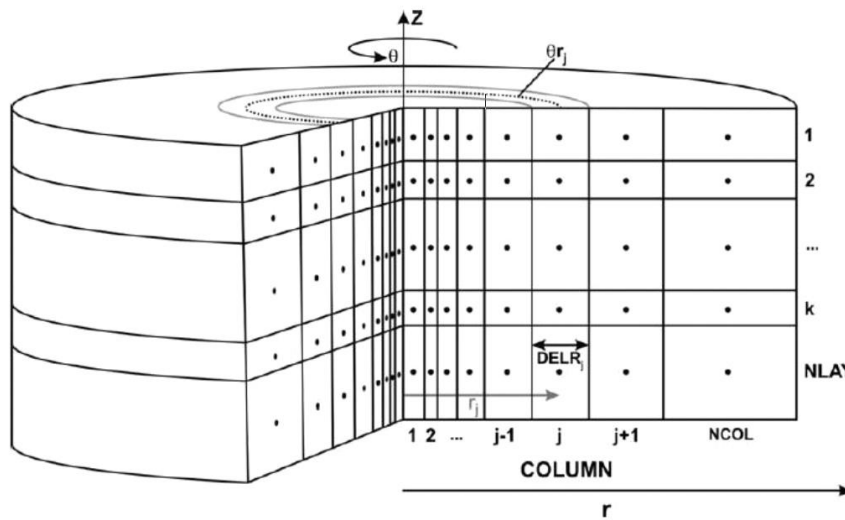

Figure 2.2.11 Axisymmetric representation of a 3D MODFLOW grid (Langevin, 2008).

Discretization

The grid applied within the axisymmetric SEAWAT grid is a vertical section of one row, with distance along the columns and depth along the layers. The well screen is situated in different layers in the first column. A doublet is represented by 3 rows, where the two outer rows model the warm and cold well, while the middle row was set to inactive to prevent interaction between the outer rows. Horizontal cell size Δx is 1m close to the well. From 100m to 2500m Δx increases logarithmically (in 40 steps) until a maximum cell size of 100m is reached. This results in a total of approximately 40,000 cells.

The Courant number is the ratio transport distance during one time step over the cell size (Courant et al., 1967) and should be smaller than 1 for accurate calculation. The applied time step has a large influence of this (e.g. day or month). In general, the Courant number should be smaller than 1 at several meters away from the well and onwards, where buoyancy flow, conduction, dispersion matter. For the used SEAWAT model, the courant number is set at maximum 0.8 in the advection package.

Model layers

Vertical cell size Δz is 0.5m for the entire model to allow for sufficient detail and insight in the vertical buoyancy flow component. Vertical cell size is sufficiently small to account for the vertical movement (buoyancy) that is calculated based on the density and viscosity differences. Further reduction of Δz to 0.25 or 0.1 did not lead to significant differences while this does significantly increase total calculation time.

The model can be thought of to consist of an aquifer that is confined by 20m thick aquitards at its top and bottom. No recharge was applied. Constant head, temperature and salinity boundaries were applied at outer boundary. The top of the upper confining layer has a constant temperature. The aquifer thickness varies over the simulated scenarios. The wells screens of the doublets are always fully penetrating the aquifer thickness.

The flow from the injection screen entering different model layers is calculated proportionally to the transmissivity of each model layer. The extraction temperature as calculated by SEAWAT for every cell representing the well screen, and weighted compared to the extracted flow for each cell (weighted average).

Parameter values and aquifer properties

The basic setup of parameter values follows van Lopik et al. (2016) adapted to axisymmetric flow according to Langevin (2008). These values are given in Table 2.2.1. Aquifer properties were taken as homogeneous; the effect of heterogeneity on the recovery efficiency of LT-ATES systems has been studied by Caljé (2010), Sommer et al. (2013), Possemiers et al. (2015) and Xynogalou (2015), who concluded that only in specific conditions heterogeneity may have a considerable effect. The hydraulic conductivity has negligible effects on thermal losses due to conduction for LT-ATES systems (Bloemendal & Hartog, 2018), but the vertical hydraulic conductivity affects the buoyancy flow. For aquitards, the hydraulic conductivity was set to 0.005 m/d both are common values for the Netherlands. The other thermal and numerical parameters follow literature values and are given in Table 2.1.1.

Table 2.2.2
MODFLOW simulation parameters (Caljé, 2010; Hecht-Mendez et al., 2010; Langevin et al., 2008)

Parameter	Value	Package
Solid heat capacity[*]	710 kJ/kg °C	RCT
Water reference density	1,000 kg/m^3	RCT
Solid density[*]	2,640 kg/m^3	RCT
Water thermal conductivity	0.58 W/m/°C	RCT
Solid thermal conductivity	2 W/m/°C	RCT
Thermal distribution coefficient[#]	$1.7 \cdot 10^{-4}$ m^3/kg	RCT
Thermal retardation[+]	2.21	RCT
Porosity	0.3	BTN
Specific storage aquifer	$6 \cdot 10^{-4}$ /m	LPF
Longitudinal dispersion	0.5 m	DSP
Transversal dispersion	0.05 m	DSP
Vertical dispersion	0.005 m	DSP
Effective molecular diffusion heat[#]	0.15 m^2/day	DSP
Effective molecular diffusion salt	$8.64 \cdot 10^{-6}$ m^2/day	DSP

Model input data and simulation period for generic analysis

The total input volume is divided over the year following a sine function (Figure 2.2.13). This results in 5 months of injection, 1 month of storage, 5 months of extraction and again 1 month of storage. The injection temperature at the well is set constant, according to the defined injection temperature. the extraction temperature is calculated based on the weighted average of the extracted volume at the well screen during one time step (monthly time step). In total, 72 time steps of 1 month are being ran for each simulation (total 6 years). Because the simulation starts in winter, the first 3 months of extraction are with the ambient groundwater temperature. The last year recovery efficiency is thus calculated based after the fifth complete years of injection and extraction (Figure 2.2.12).
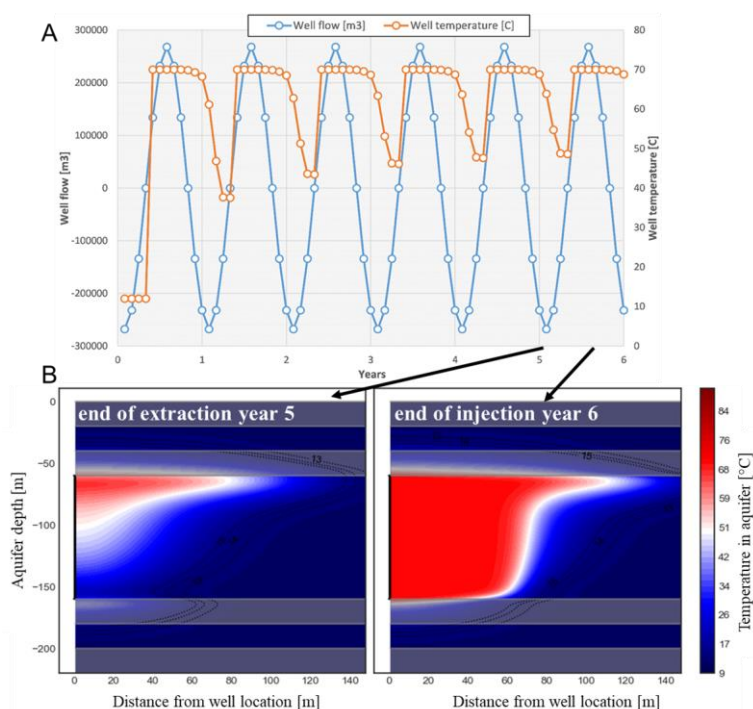

Figure 2.2.12 Example overview of model input and output for a 70 °C simulation scenario in a storage aquifer of 100m thickness. A. figure of the monthly well flow and well temperature, B. side view of the stored thermal volume in the axisymmetric model.

Varied storage parameters for generic analysis

The field properties of the Koppert Cress ATES system are used to perform an analysis of HT-ATES performance. However, it is expected that the storage conditions of the KC ATES system will change in the near future or can deviate from the estimated values.

Regarding operational aspects, the addition of geothermal heat to the Koppert Cress system will result in higher storage volumes and higher storage temperatures. Regarding hydrogeological conditions, the current ATES of Koppert Cress is located in two 20m thick aquifers. Thus, in total 40m of well screen is used. However, if Koppert Cress in the near future wants to store more heat at even higher temperatures (e.g. >70 °C), the current aquifers might be less suitable / not available because of permitting requirements. Therefore, other (deeper) aquifers can potentially be interesting as well. Also, the hydraulic conductivity of these deeper aquifers will probably differ from the currently estimated hydraulic conductivity, which for both storage aquifers was estimated at K_h=35 and K_v=7 m/d. Moreover, the estimated hydraulic conductivity is highly uncertain because of the lacking information on these aquifers in the Netherlands. Therefore, the storage condition parameters are varied and their parameter value range is given in Table 2.2.3 and schematized in Figure 2.2.14. The parameter ranges were chosen based on the Koppert Cress characteristics and commonly found storage conditions in the Netherlands (Bloemendal & Hartog, 2018). Altogether, the sensitivity analysis resulted in more than 300 unique model results.

Table 2.2.3 Varied storage conditions used as input for the sensitivity analysis.

Storage condition parameter	Lowest value	Highest value
Aquifer thickness	20	100
Horizontal hydraulic conductivity	1	35
Vertical hydraulic conductivity	0.125	10
Storage volume (m³/year)	100,000	1,000,000
Storage temperature	15	90

From the two hydraulic conductivity values an average geometric hydraulic conductivity can be calculated:

$$K_{avg} = \sqrt{K_h * K_v}$$

Please note, the addressed hydraulic conductivities in this study are the initial hydraulic conductivity at ambient groundwater temperature. When the storage temperature increases, the hydraulic conductivity of the aquifer also increases (due to decreasing viscosity and density of the ground water). This is taken into account automatically in the numerical model.
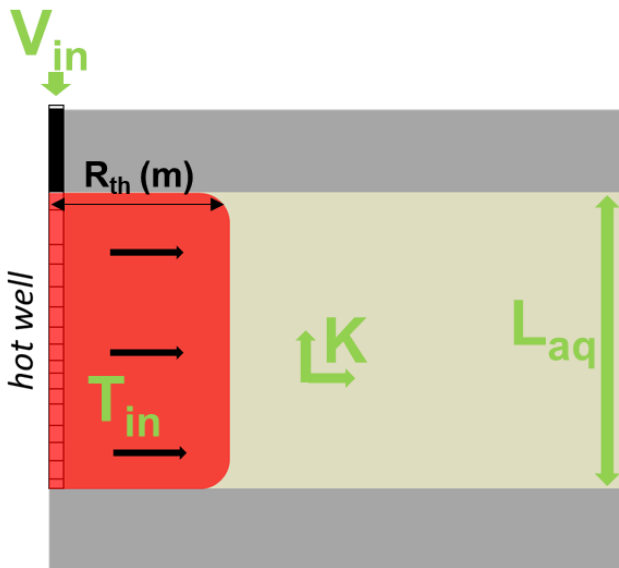

Figure 2.2.14 Schematic overview of the varied storage conditions for the modelling exercise. Tin= storage temperature, Vin= storage volume, K= horizontal and vertical hydraulic conductivity, Laq=aquifer thickness.

2.2.2.3 Assessment framework

The recovery efficiency (η) is used to analyse the performance of a (HT-)ATES system and defines the fraction of energy that is lost to the subsurface. The thermal energy stored in an (HT-)ATES system is defined as the temperature difference between the infiltrated water and the surrounding ambient groundwater, for either heating or cooling purposes. As in other ATES studies (Bloemendal & Hartog, 2018) the recovery efficiency (η_{th}) of an ATES well is defined as the portion of recovered energy (E_{out})that was initially injected E_{in}.) For this ratio between extracted and infiltrated thermal energy (E_{out}/E_{in}), the total infiltrated and extracted thermal energy is calculated as the cumulated product of the extracted/injected volume with the temperature difference of the injected/extracted infiltration and extraction temperatures ($\Delta T = T_{inj/extr} - T_{amb}$) for a given time horizon (which is usually one or multiple storage cycles), as described by (adapted from Bloemendal and Hartog (2018) :

$$\eta_{th} = \frac{E_{out}}{E_{in}} = \frac{(T_{extraction} - T_{ambient}) \cdot V_{extraction} \cdot \rho \cdot c_w}{(T_{injection} - T_{ambient}) \cdot V_{injection} \cdot \rho \cdot c_w}$$

with, V being the extracted/injected volume during each time step. To allow unambiguous comparison of the results, the generic simulations in this study are carried out with equal yearly storage and extraction volumes ($V_{in} = V_{out}$).

2.2.3 Results

In the first part of the results section we analyse the ATES case study site: Koppert Cress (KC). In this part we investigate the operational characteristics of the ATES system and we determine the performance of the storage system. In the second section we use the KC results as a starting point and generalize the operating conditions to determine the performance under more generalized conditions. Finally, in the third section we compare the generalized KC scenario with the results of the generic sensitivity analysis we try to provide insight in the impact of varying storage conditions on HT-ATES performance in general.

2.2.3.1 Case study: Koppert Cress ATES system operational data analysis

Temperature of ATES wells

Figure 2.2.15 and Figure 2.2.18 show the well temperature of the warm and cold wells respectively. These plots include both the raw hourly data as well as the daily weighted average temperatures. The weighted temperature is calculated according to:

$$T_{day} = T_{ambient} + \frac{\sum_{n=24}(T_{hourly} - T_{ambient}) \cdot V_{hourly}}{\sum_{n=24}(V_{hourly})}$$

An ambient temperature of 12.5°C was estimated based on the extraction temperatures measured at the start of available monitoring data. However, the system was already operating a couple of months when the monitoring dataset started, so there is an uncertainty in the exact value for ambient temperature.

The diurnal variation in the use of the wells causes the warm well to be charged during the day and discharged during the night, as a result the daily average temperatures shows a less spiky pattern (Figure 2.2.15). Also the heat which is stored seasonally is stored at a lower temperature, due to this operation strategy. Another cause of the strong variations in the raw data is the way heat is collected from the environment, i.e. partly with solar heat collectors, which provide high temperatures during short moments in time when radiation is high.

Warm wells

The start of the transition from normal ATES to HT-ATES is indicated in Figure 2.2.15 and also reflected in the temperature levels. In 2015 and 2016 the maximum infiltration temperature is 30°C, while from 2017 onwards also groundwater temperatures of >30°C are registered, due to the addition of the solar collectors to the system. The relative mild increase of the injection temperatures is a result of the environmental sources of heat (from the green house, surface water, solar collectors) which are charged into the warm well. The temperature data of sub-ambient temperature is caused by the diurnal variation and sometimes very low flow rates. The last years this happens more frequently and is associated with the strong imbalance at which the system is operating: over the course of the years the cold well has grown and starts interacting with the warm wells from 2017 onwards.
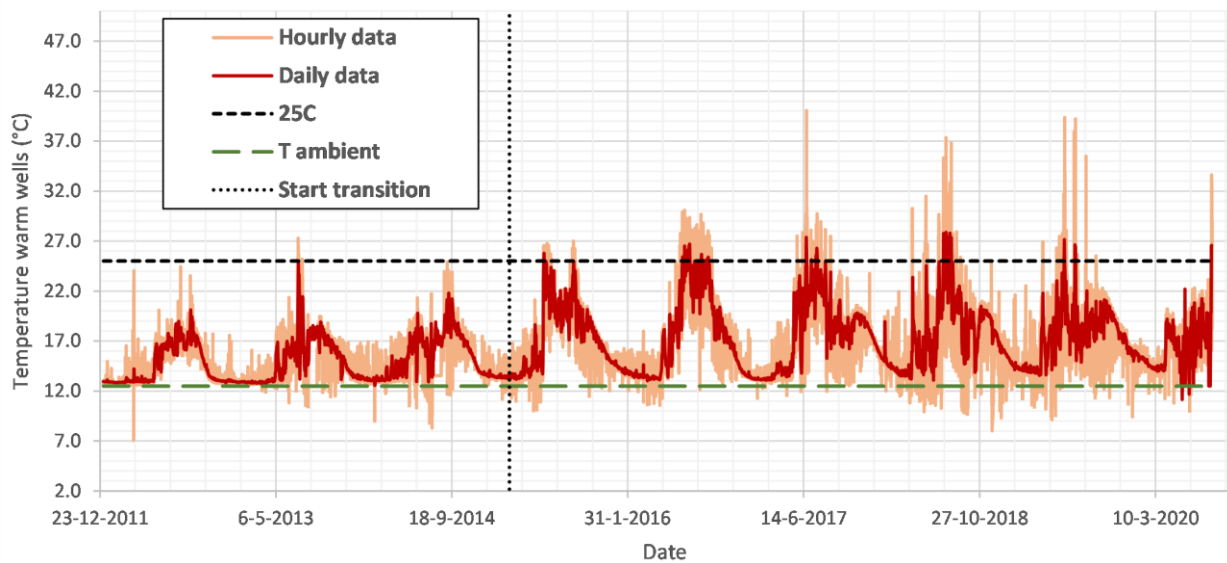
Figure 2.2.15 Warm well temperature of the 4 warm ATES wells of Koppert-Cress (2012-sept 2020). Transition to higher storage temperature from 2015 onwards.

The maximum injection temperature

To illustrate the warm well temperature responses, the injection and extraction data of the well are analysed during a series of the warmest days in the hot summer of 2018. Figure 2.2.16 shows the daily injection and extraction temperature and volume of the warm wells. This shows that the daily average injection temperature is >30°C during some of the days, while at the same time, the extraction temperature during the night are <25°C in almost all cases, and always <30°C. The strong variation in injection temperature is caused by the way of heat collection, depending on the weather conditions.
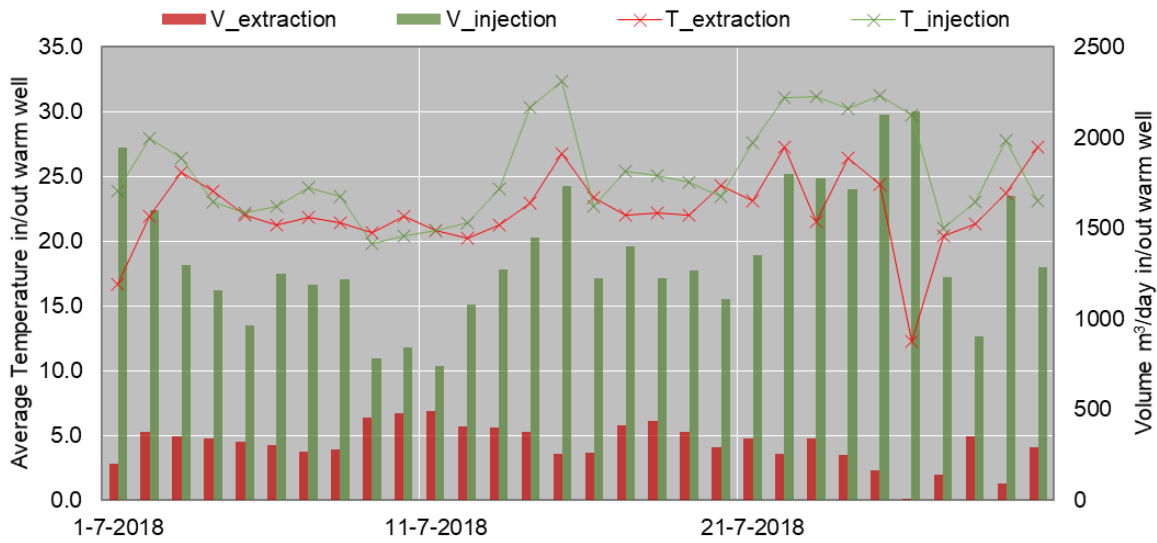
Figure 2.2.16 Daily total injection and extraction volume and daily average injection and extraction temperature for the warm wells.

Figure 2.2.17 shows the raw 5 min data for temperature and well flowrates. It shows that when warm wells inject heat (negative flow from cold well) during the day, warm water with high temperature is injected, >40°C. But when subsequently water is extracted during the following night, the extraction temperature from the warm well is mostly <30°C. Figure 2.2.15 and Figure 2.2.16 show that the daily average extraction temperature exceeds 25°C incidentally. Figure 2.2.17 now also shows that during early mornings the extraction temperature exceeds 30°C incidentally.

Figure 2.2.17 Discharge of cold wells and temperature warm wells from 24-7-2018 to 28-7-2018

Cold wells

The cold well temperature is affected less by the transition to a HT-ATES. From early 2017 the cold well temperature decreases, which is caused by the installation of a second heat pump. Despite the strong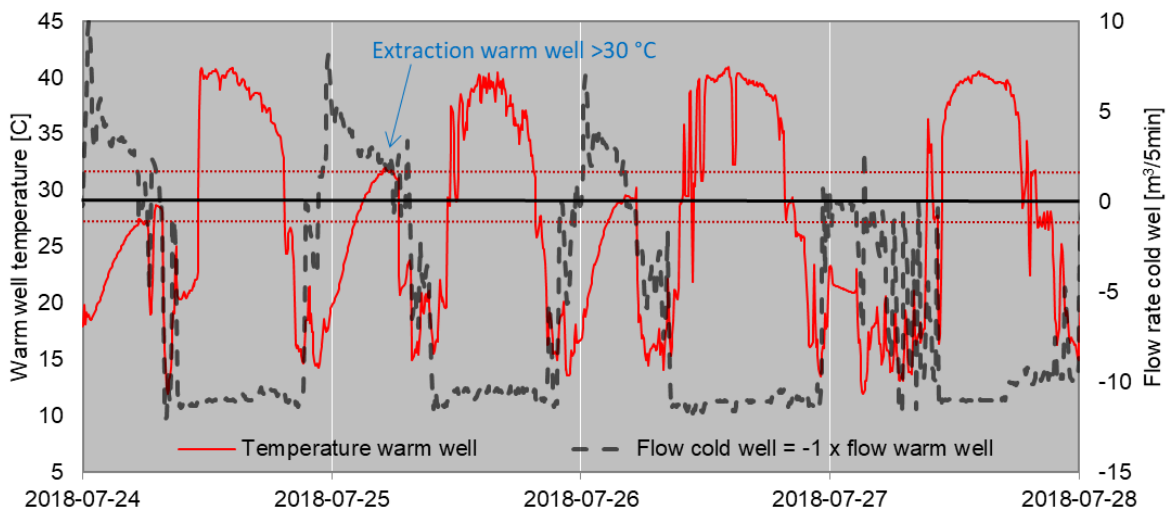 imbalance towards a large surplus in the cold well, still relatively high temperatures are monitored incidentally. This is during low flow rates, and caused by heating of the water in the pipes in the plant room, these are no longer visible in the weighted average daily temperatures.
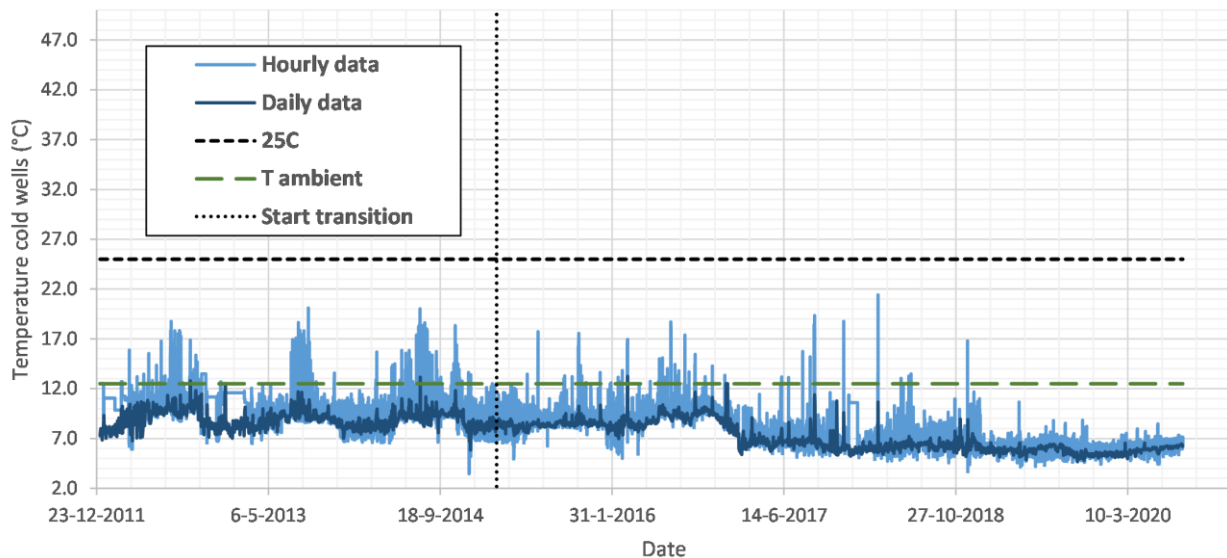

Figure 2.2.18 Well temperature of the 4 cold ATES wells of Koppert-Cress (2012-sept 2020). Transition to higher storage temperature from 2015 onwards.

General view on well temperatures

From 2015 onwards higher temperatures are stored in the warm wells, gradually increasing over time, as operation is optimized and more heat sources are added to the system. However, the daily average warm well temperature is only incidentally >25°C, due to the strong diurnal variations in mode of operation and outside air dependent heat production from the heat sources to be stored in the warm well. Due to thermal retardation and strong dispersion effect in the close vicinity of the well screen (Bloemendal & Hartog, 2018), strong peaks in the injection temperature are flattened out and not visible in extraction temperature, both after short and long storage cycles.

Storage volumes and energy balance

The ATES wells of Koppert-Cress have a capacity of 40 m³/hr each, so 160 m³/hr in total. During the day the wells can change flow direction multiple times, as a result the total measured injection volume in a well during the charging season has a net and gross storage volume which may differ. When these short cycle charging and extraction occurs more often, the difference between net and gross storage volume may differ considerably. The net volume in a well is calculated according to

$$V_{net} = V_{in\_gross} + V_{extr\_gross}$$

Extractions have negative and injections have positive values. Figure 2.2.19 shows the difference between the net hourly and net daily volumes, indicating the diurnal pumping cycle executed by Koppert-Cress. In July 2018 there is a net storage in the warm well, also heat is extracted during the night. Figure 2.2.20 shows the daily injection and extraction rates as well as the net daily rate, indicating that in general Koppert-cress is extracting more from the warm well than the cold well and the net volume in the warm well is considerably

smaller than the gross volume injected in the warm well. This affects the size of the warm zone around the well.
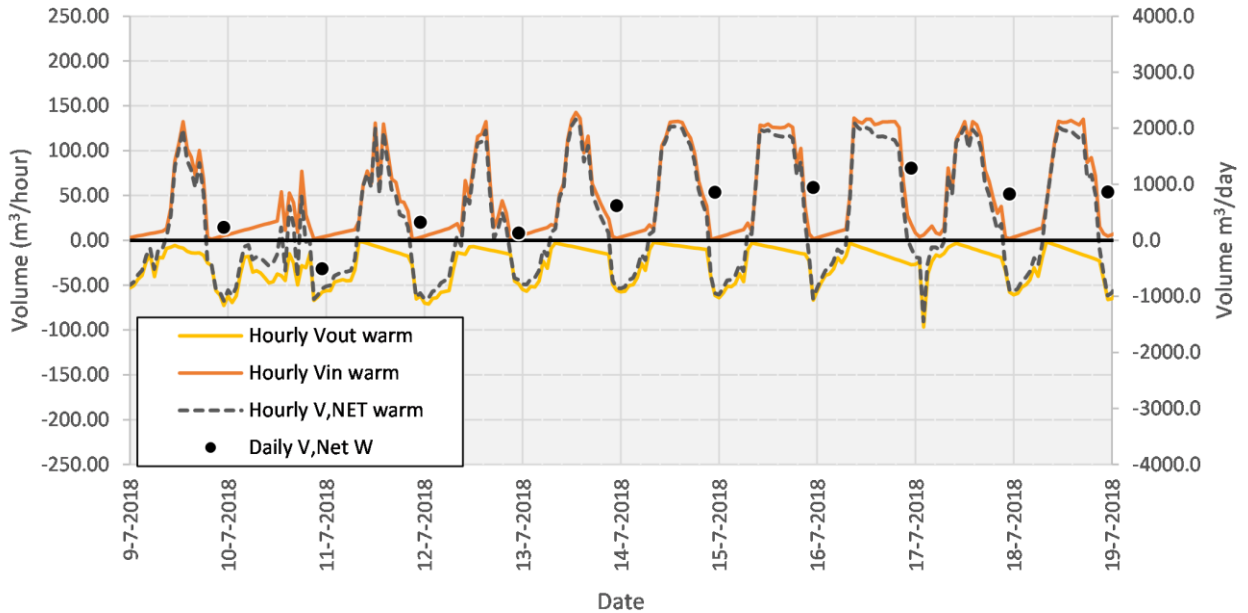
Figure 2.2.19 Net hourly flow rates of the warm well and resulting net daily volumes during the summer of 2018.
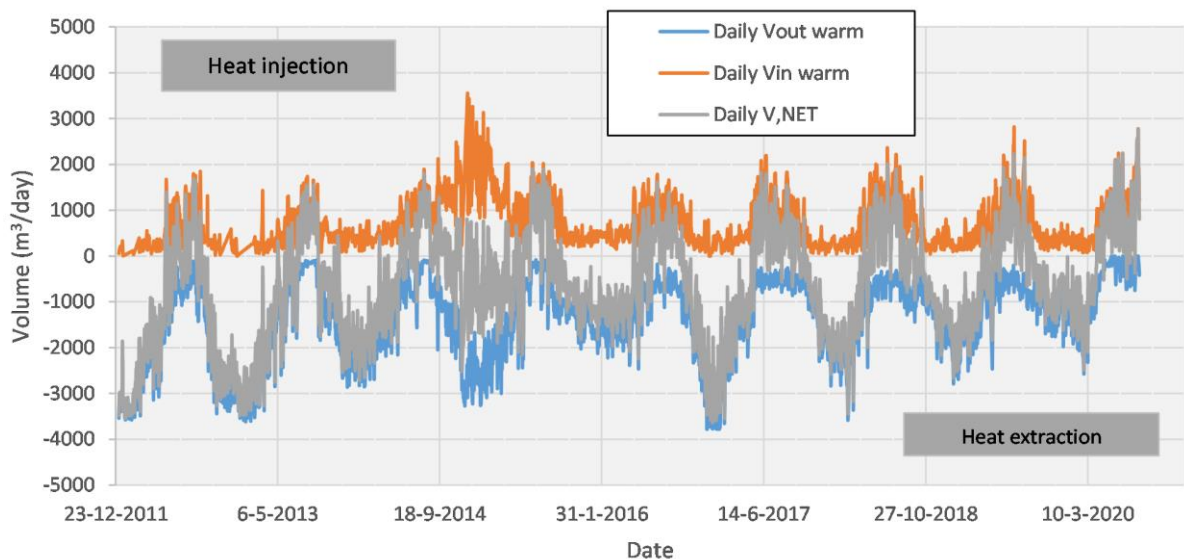
Figure 2.2.20 Daily gross injection and extraction in/from warm well and net total flows during monitoring period.

The diurnal storage cycles are typical for how the ATES system of Koppert-Cress is operated during spring and fall. On top of the diurnal cycles, also a seasonal cycle is visible. To assess performance of the seasonal storage, the net storage volume provides insights on the volume of heat that is stored seasonally. This is the volume that needs to be analysed to assess the seasonal losses.

Using the gross flow data the volume balance ratio (r_V) is identified according to Beernink et al. (2019):

$$r_V = \frac{V_{in\_gross} + V_{extr\_gross}}{V_{in\_gross} - V_{extr\_gross}}$$

Extractions have negative and injections have positive values. Similarly this is done for the energy balance ratio (r_E), by taking into account the extraction and injection temperatures:

$$r_E = c_w \cdot \frac{\Delta T_{in} \cdot V_{in\_gross} + \Delta T_{extr} \cdot V_{extr\_gross}}{\Delta T_{in} \cdot V_{in\_gross} - \Delta T_{extr} \cdot V_{extr\_gross}} = \frac{E_{in\_gross} + E_{extr\_gross}}{E_{in\_gross} - E_{extr\_gross}}$$

Figure 2.2.21 shows that since both ratios are cumulative in time, their values are less subject to change as time proceeds. The following insights follow from this figure:

- The volume ratio is negative, meaning that the warm well is depleted each winter, and the cold well grows every year because cold groundwater is left behind at the end of each summer.
- In the winter of 14/15 there was not much heating demand, resulting in the temporarily peak in the volume and energy balance ratios.
- The imbalance in energy ratio is smaller than for the volume ratio, this is cause by the fact that the temperature difference is larger during injection of the warm well, compensating a bit for the imbalanced flows. The temperature difference between de injection and extraction varies between 0-4°C, on average the difference is about 1°C.
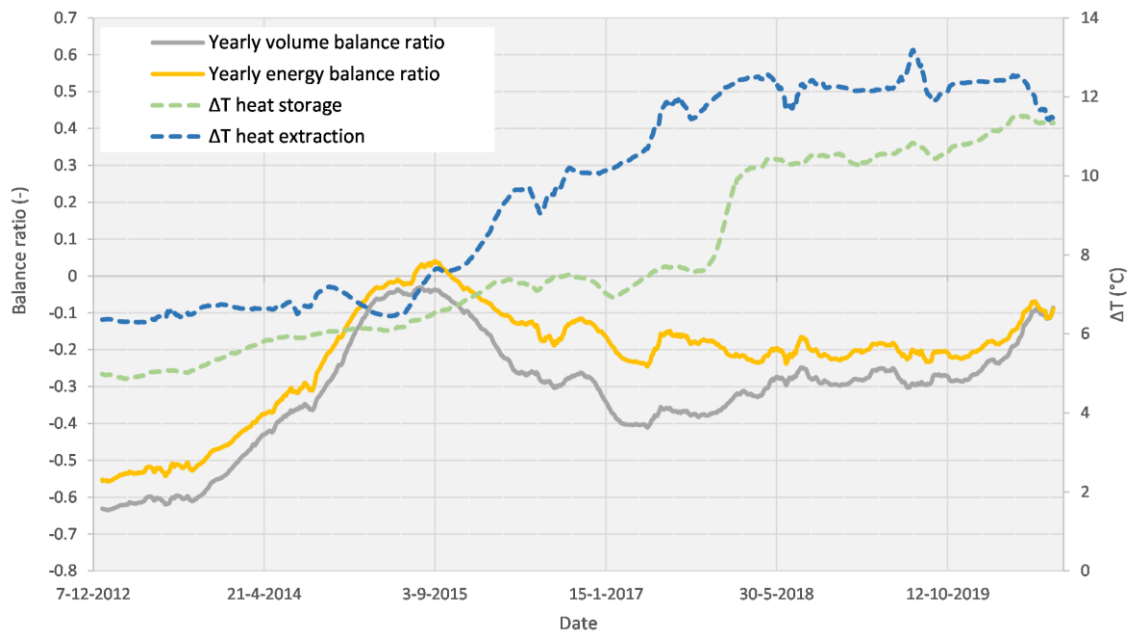

Figure 2.2.21 The yearly averaged volume and energy balance ratio of Koppert-cress warm wells and the yearly averaged ΔT (Twarm - Tcold) during heat storage and heat extraction.

The large energy/volume imbalance was also investigated with a simulation of a 3D model using the monitored data of the injected and extracted volumes and temperatures to identify the heat distribution in the subsurface. To do this, a relatively course model (5x5m grid) was used to simulate the temperature distribution in the upper and lower storage aquifer (Figure 2.2.22). As would be expected from the actual pumped data, these results show the large surplus of cold groundwater around the cold wells, due to the imbalance discussed previously.
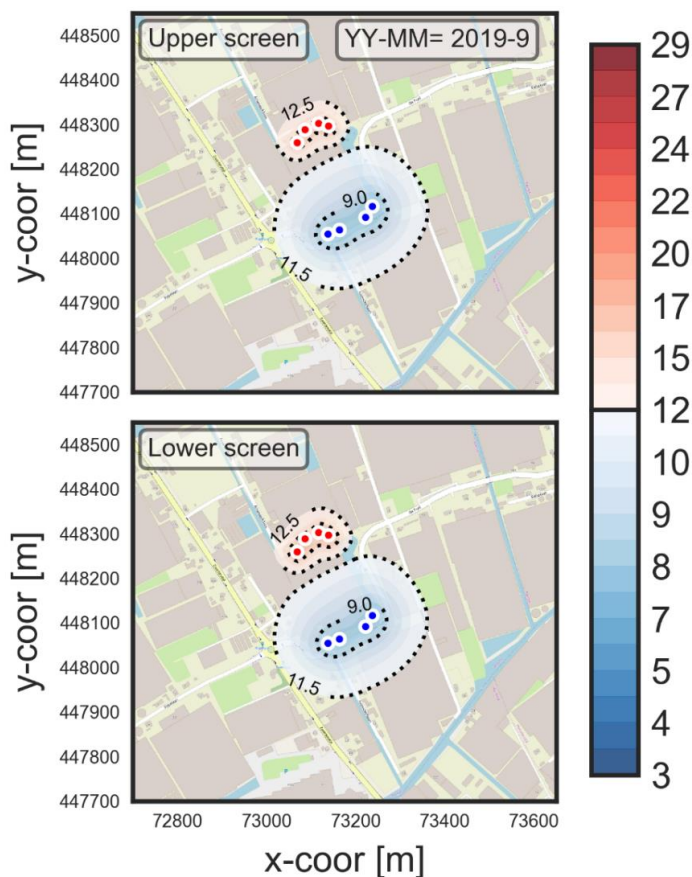
Figure 2.2.22 Temperature distribution in the top and deep aquifer at the end of the simulation period of the monitoring data: 2012-2019. Here, the temperature distribution is given at the end of summer; the thermal radius of the warm wells is at their maximal size. A course SEAWAT model (5x5m grid) was used to get an insight in the temperature distribution.

Warm and cold well recovery efficiencies

Following the energy balance ratio and the net storage volumes the total amount of warm/cold groundwater in the warm/cold wells is plotted in Figure 2.2.23, together with the temporal recovery efficiencies.

The following insights follow from this figure:

- The warm well is depleted each winter, and the cold well grows every year.
- Despite the nett abstraction of the warm well, still around 3% of the heat remains in the subsurface, as the maximum recovery efficiency of the warm well is 97% at the end of winter. These are losses that could be due to conduction into the confining layers..
- The cold well recovery efficiency is structurally low due to the volume imbalance, as 60% of the cold groundwater is left behind in the aquifer.
- As all heat is extracted from the warm well, the thermal impact caused by the heat storage is expected to be small. Over the course of 5 years 1.1 TJ of heat stays behind in the warm wells, while at the same time almost 23TJ of cooling capacity remains in the cold wells. As a result, most impact on groundwater temperature is expected at/around the cold wells.
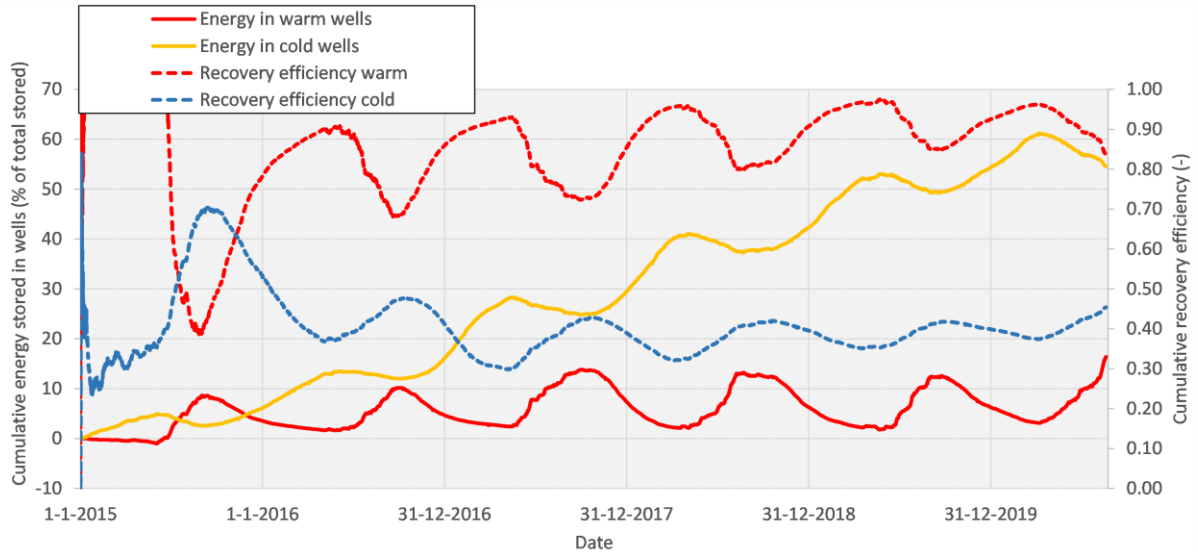
Figure 2.2.23 Fraction of total stored net volume in each well during 2015 till Sept 2020 and the warm and cold well recovery efficiency.

Diurnal storage cycle efficiency

As about 25-30% of the heat extracted from the warm wells is stored on a diurnal cycle, it is also of interest to assess the short cycle recovery efficiency. During these short cycles the difference in injection and extraction volumes may differ a lot, i.e. in summer, large amount of heat are stored, while at night small amounts are extracted and vice versa in winter. During short cycle storage heat may be lost to the aquifer, this is likely to be larger when the warm well is not charged much at the end of winter (net Volume is low), and the opposite in summer. As a result, the short cycle recovery efficiency may vary strongly during the year. The short cycle recovery efficiency is calculated according to:

$$\eta_{shor-cycle} = \frac{(\frac{E_{extr}^{day}}{E_{in}^{day}})}{(\frac{V_{out}^{day}}{V_{in}^{day}})}$$

Figure 2.2.24 shows the short cycle recovery efficiency together with the temperature of the warm wells of Koppert-Cress. This shows the positive effect of charging period during each summer on the efficiency after summer, resulting in efficiencies of 120% and higher. However, as the warm well temperature drops, also the short cycle recovery efficiency drops sometimes as low as 40%. The ratio in the short cycle injection and extraction volumes affect these numbers also. When analysing the days at which same injection and extraction volumes only with different net storage volumes, the differences are less strong: around 100% for large net storage volumes and 70% for depleted warm well.

Figure 2.2.24 Short cycle daily recovery efficiency of the warm wells over the years. When the well temperature is relatively high, the short cycle daily recovery efficiency is also high, and vice versa.
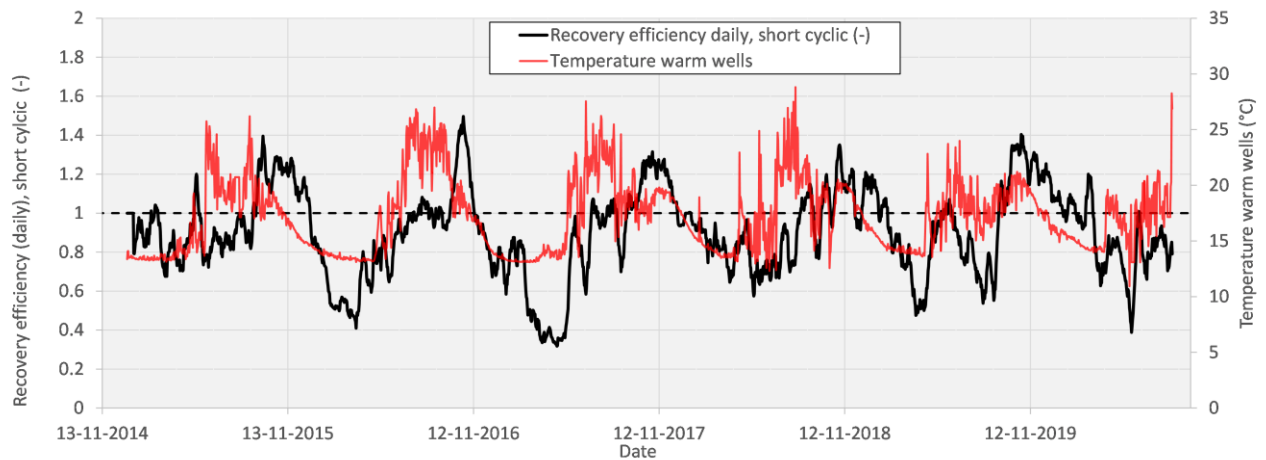
Discussion and Conclusion

From 2015 onwards, the transition from regular LT-ATES to HT-ATES started. Temperatures >30°C are injected irregularly. The increase in storage temperature results in a larger ΔT between the wells, reaching a yearly average ΔT of 12°C, which is twice as high compared to the Dutch ATES system average (Willemsen, 2016).

The imbalanced use of the warm and cold wells has a dominating influence on the recovery efficiencies of the warm and cold wells. Due to the larger amount of groundwater extracted than injected from/in the warm wells, almost all heat is recovered each year. The overall recovery efficiency is therefore almost 100%. Contradictory to this, much cooling capacity is left behind in the cold wells, resulting in poor cold well efficiency.

The short-cyclic use of the wells cause about 25-30% of the heat to be stored in the aquifer only for a short amount of time, as a result of this short storage time losses are small and recovery efficiencies relatively high. Especially when the warm well is reasonably charged, short-cyclic recovery efficiencies are high.

The analysis of the behaviour of the ATES wells of Koppert-Cress shows that insufficient heat is stored in the warm well to meet the heating demand, resulting in an imbalance and a depleted warm well at the end of winter. Due to improvements to the system, more heat has been stored during the last years of operation, but this should be further increased to optimize performance of the system.

The expected future addition of a geothermal heat source can provide in the required amount of extra heat. It is expected that this will subsequently lead to a more balanced system with higher and less variable storage temperatures in the warm wells. To evaluate the effect of this or other future changes, it is important to assess application of HT-ATES under various temperature levels, aquifer thickness and storage volume.

2.2.3.2 Koppert Cress: impact of operating conditions on performance

The analysis in the previous chapter showed us that the Koppert Cress case study is an imbalanced system with storage in two aquifers divided over 4 warm and 4 cold wells operated with a complex dynamic operation. Furthermore, the injected temperature is only incidentally above 30 °C and on average only 19 °C. To analyse how the operational performance is impacted by the specific KC operating conditions compared to more generally assessed operating strategies (1 aquifer, volume balance) we set up three extra scenarios.

To do this, the daily operational data is used as input for the axisymmetric model setup. By doing this we simplify the actual well placement to by representing the 4 warm wells and 4 cold wells as a single storage volume in one well. The simulations are done using the geohydrological conditions and properties for the KC case study as presented in chapter 2.2.2.1. For each well type (warm and cold) a separate axisymmetric model row is used, combined into one model. With these simulations, we go in three steps from a system

using the real operational data and the real hydrogeology of the KC system to a generalized scenario with only one storage aquifer operating with a volume balance (Figure 2.2.25).

Scenario 1 uses the daily operation data with two axisymmetric models using the geohydrology of Koppert Cress. This represents the actual performance of the Koppert Cress system. Subsequently (scenario 2), the same geohydrological model is used to explore what the recovery efficiency would be for the system if the extracted and injected flows were operating at volume balance. Finally (scenario 3), the two aquifers (both 20m thickness) are combined into one 40m thick aquifer. To do this the upper aquifer is expanded.
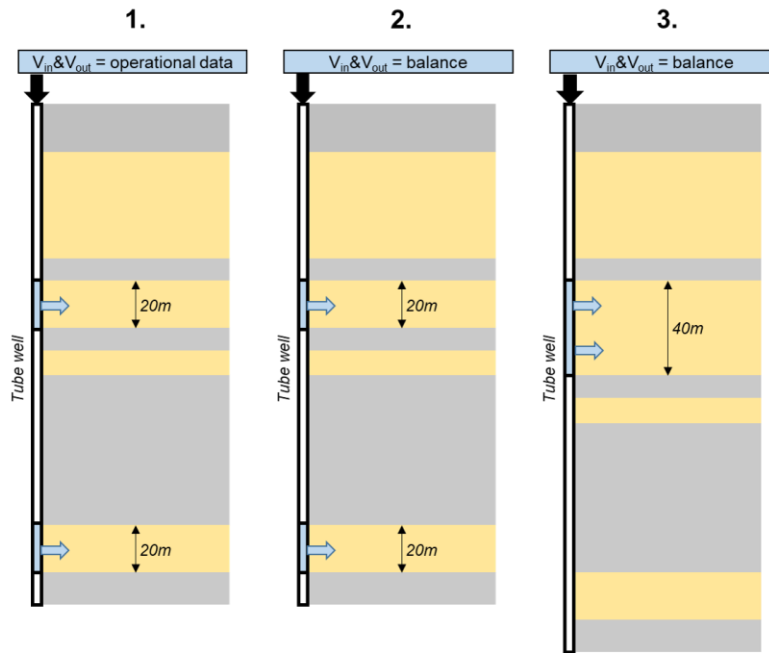
Figure 2.2.25 Schematic overview of the side view and input data of the three axisymmetric models used for the modelling study.

Model input

The difference between the daily monitored flow data of the KC ATES system and the volume balance input is shown in Figure 2.2.26. For the operational data, the volume stored in the cold wells is much larger than the volume stored in the warm wells. Also, the behaviour of the volume data is irregular between consecutive days, and, is variable between the years. The latter being influenced by the climate, the heat/cooling demand and the changes in the heating and cooling system of KC. In contrary, the same net amount of volume is stored with the volume balance method with a normal sine function. The largest amounts of volume are stored in the warm wells in the middle of summer and oppositely most volume is stored in the cold wells in the middle of winter. This timing overall seem to match the measured operational data adequately.

The used temperature input for the generic models is calculated using the operational data of KC as the weighted average well temperature of the daily volume and temperature. This results in an average storage temperature of 19 °C for the warm well and 7.5 °C for the cold well. The combined volume and temperature input for the three scenarios is given in Table 2.2.4.
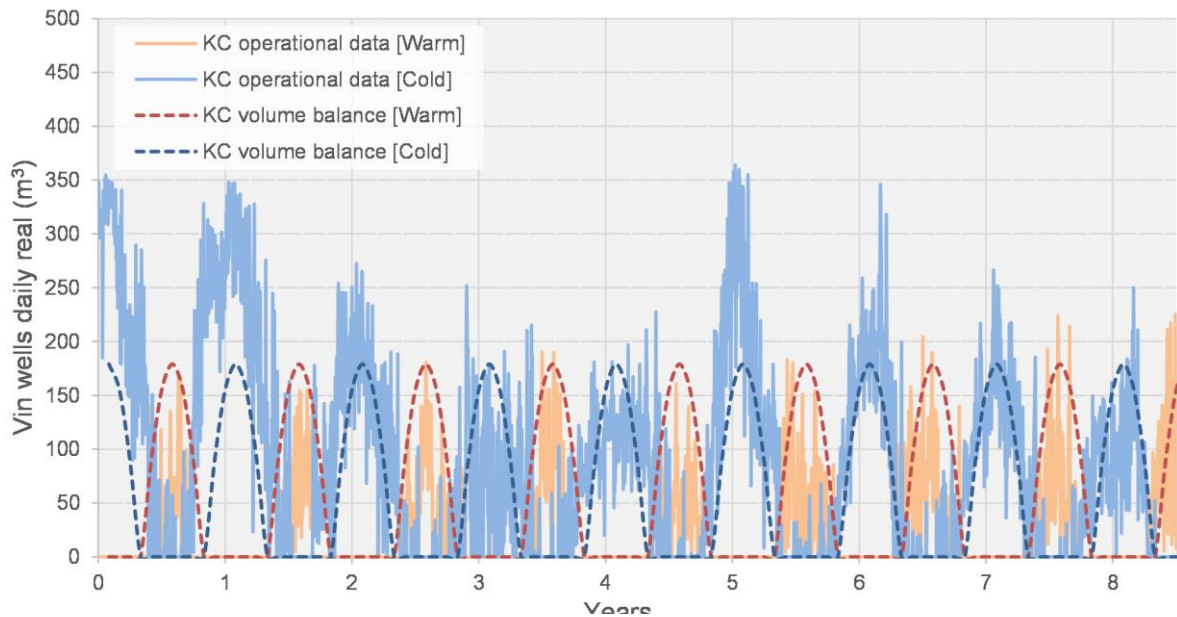
Figure 2.2.26 Difference between the volume distribution input of the actual KC system (daily, variable and imbalanced) and the volume input for the simplified scenarios with Vin=Vout.

Table 2.2.5 Modelled scenarios to assess the difference between the actual operating strategy of the KC system(scenario 1) and the generalized scenarios (2 and 3).

	Scenario	T$_{inj}$ warm wells °C	T$_{inj}$ cold wells °C	V$_{in}$ warm wells (m^3/year)	V$_{in}$ cold wells (m^3/year)
1	KC: operational data (2012-2020)	Variable (average ~19)	Variable (average ~7.5)	80,000	320,000
2	KC balance, 2 aquifers	19	7.5	200,000	200,000
3	KC balance, 1 storage aquifer	19	7.5	200,000	200,000

Results

The simulated well temperature of the warm and cold well for the three scenarios is given in Table 2.2.6. The first scenario, that was run with the operational data and has storage in both aquifers, show more extreme temperature variations compared to the second and the third scenario. This is mainly the case because of the volume imbalance and the irregular storage temperature observed in the operational data. Due to the volume imbalance, the warm well is 'empty' for the last months of winter each year. Because of this, the warm well temperature decreases to the ambient groundwater temperature (12.5 °C). For the cold well, the opposite is true; the volume inside the cold wells continues to grow over the years, the effect of extraction from these wells is therefore not visible in the cold well temperature.

For scenario 2 and 3, the storage volume is equal to the extraction volume (balance). Scenario 2 stores volume in both aquifers, while in scenario 3 all volume is stored in a combined aquifer of 40m thickness. There is only a small difference in simulated well temperature of the warm and cold wells of scenario 2 and 3. The warm and cold well temperature of scenario 2 drop slightly more towards the ambient groundwater temperature during extraction, indicating that this scenario experiences slightly more energy losses during storage.
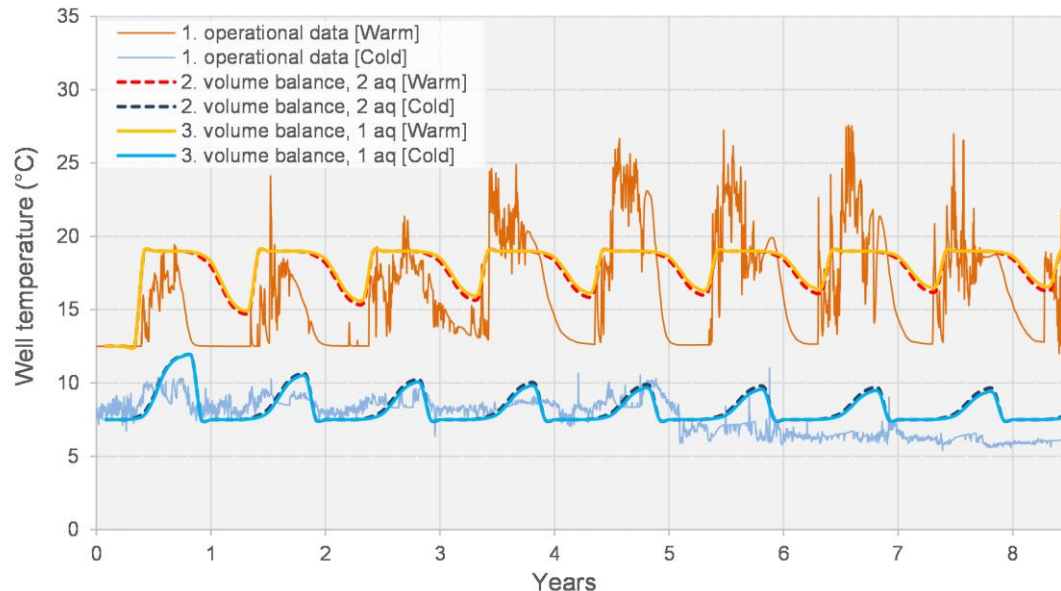
Figure 2.2.27 Differences between the model results of the warm and cold well temperatures of scenario 1. operational data, 2. the balance scenario with two aquifers and 3. the volume balance scenario with the single storage aquifer.

Due to the volume imbalance in scenario 1, the average recovery efficiency of the warm well is much higher compared to the cold well, 0.85 compared to 0.27 (Table 2.2.7). In the last year, this difference is much smaller, which is the case because the specific cooling demand is relatively high in this year compared to previous years. Because the extraction from the wells is not influenced by any yearly variations for the second and the third scenario, it is hard to compare the calculated last year recovery efficiency of scenario 1 to scenario 2 and 3.

Table 2.2.7 Model results: recovery efficiency of the three scenarios for the Koppert Cress system

	Scenario	Volume balance?	Average warm well recovery efficiency (-)	Average cold well recovery efficiency (-)	Last year warm well recovery efficiency (-)	Last year cold well recovery efficiency
1	KC: operational data (2012-2020)	NO	0.85	0.27	0.88	0.69
2	KC balance, 2 aquifers	YES	0.75	0.76	0.80	0.80
3	KC balance, 1 storage aquifer	YES	0.79	0.80	0.84	0.84

Figure 2.2.28 The recovery efficiency of the three different model scenarios. For the warm and cold wells both the overall recovery efficiency and the last year recovery efficiency is given.

For scenario 2 and 3, the recovery efficiency of the warm and cold wells is equal. Because the injected and extracted volumes are equal, the energy that is lost during storage is proportionally the same, also reflecting the lack of influence by buoyancy flow at the hot well at operational storage temperatures. Scenario 3 has a 4% higher recovery efficiency compared to scenario 2. Combining the storage volume into one 40m thick aquifer is in this case thus more efficient.

2.2.3.3 Generic analysis KC: impact of varying storage conditions on performance

In this section we compare the recovery efficiency of the Koppert Cress simulation (scenario 3) discussed in the previous section with the results of the generic sensitivity analysis. By doing so, we try to explore how the possible addition of a geothermal heat source in the future will impact the performance of the KC HT-ATES system. As explained in section 0, various storage conditions are varied with a value range based on the Koppert Cress conditions and more generally observed ATES conditions in the Netherlands. An analysis on the impact of varying storage conditions on performance is done here using the last year recovery efficiency of the warm well of HT-ATES systems operating in volume balance.

Impact of varying storage temperature

The Koppert Cress system (storage at 19 °C) has a slightly lower recovery efficiency compared to the other two low temperature scenarios (15 and 30 °C, Figure 2.2.29). This is the case because the storage volume is smaller than the presented generic simulations (400,000 compared to 500,000 m³/year). This indicates that larger storage volumes result in a higher recovery efficiency.

Regarding higher storage temperatures, the recovery efficiency decreases significantly at relatively high temperatures (>50 °C), Figure 2.2.29. For the Koppert Cress system, storage at 90 °C results in a recovery efficiency of 0.55 in the last year of simulation, which is 30% lower compared to storage at low temperature. Because the recovery efficiency for storage <30 °C does not vary, a temperature increase up to 30 °C does not yet lead to energy losses due to buoyancy flow during storage for these storage conditions.
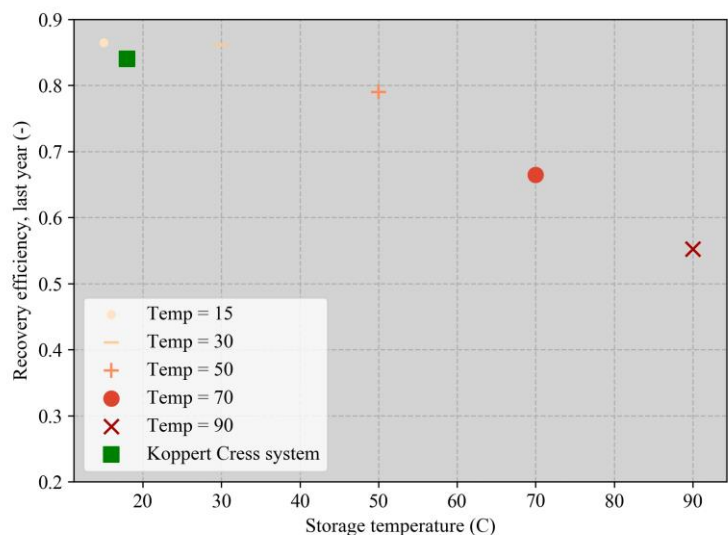
Figure 2.2.29 The effect of increasing the storage temperature for the Koppert Cress system. Difference between the presented recovery efficiency: the KC system yearly stores 400,000 m3, the generic results yearly store 500,000 m3.

Impact of varying storage volume

The recovery efficiency increases with increasing storage volume from 100,000 to 1,000,000 m³ per year for the different storage temperatures (Figure 2.2.30). The KC results (400,000 m³) are in line with the other recovery efficiency results at low storage temperature. At storage temperature above 50 °C the increase in recovery efficiency with increasing storage volume is much larger compared to the low storage temperature scenarios with increasing storage volumes. By comparison, for T_{inj}=30°C the recovery efficiency increases 5% when increasing the storage volume from 100,000 to 1,000,000 m³. For the 90 °C scenarios, the recovery efficiency increases more than 30% for the same volume increase.
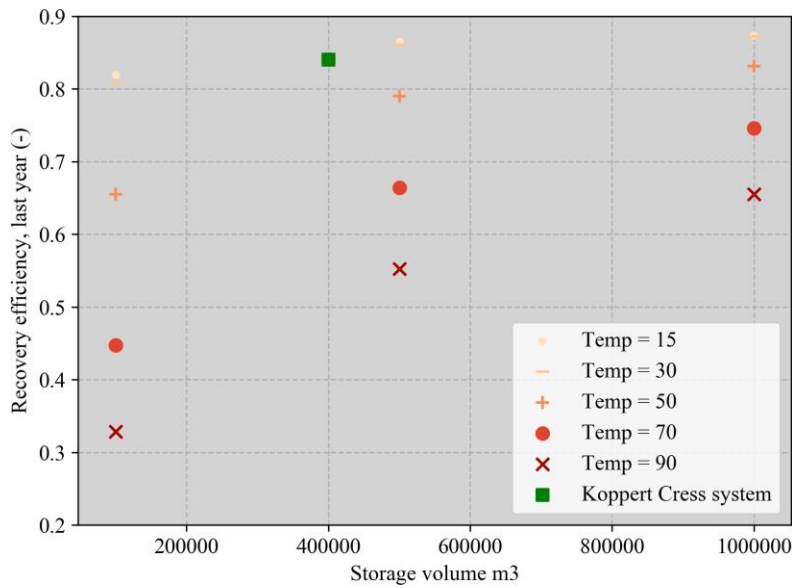
Figure 2.2.31 Varying storage volume (100,000-1,000,000 m3) and storage temperature (15-90 °C) for te 40m thick Koppert Cress aquifer (Kh=35, Kv=7).

Impact of changing aquifer thickness

The aquifer thickness has a strong impact on the recovery efficiency under varying storage temperatures (Figure 2.2.32). For the low temperature scenarios we observe that the recovery efficiency increases with larger aquifer thickness. Between L_{aq}=20m and L_{aq}=80m the recovery efficiency increases from 0.83 to 0.88. Oppositely, for high storage temperature (>50 °C), the recovery efficiency decreases at larger aquifer thickness. At T_{inj}=90 °C the recovery efficiency decreases from 0.72 at L_{aq}=20m to 0.34 at L_{aq}=80m, a difference of almost 50%.
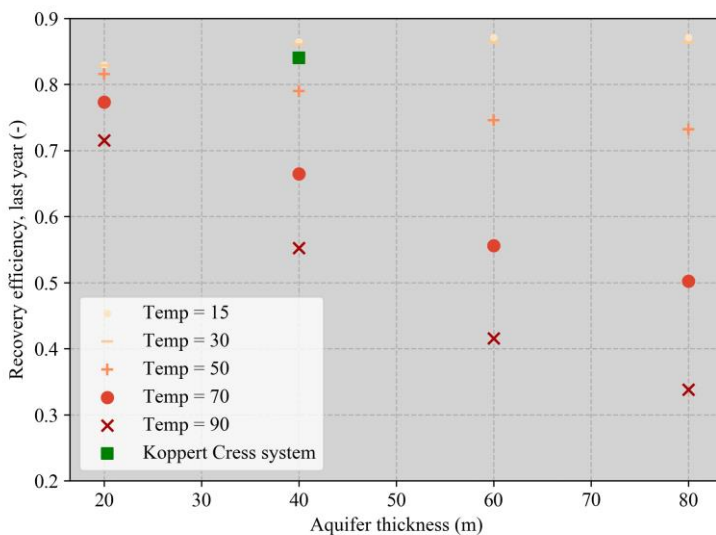
Figure 2.2.32 Varying aquifer thickness (20 - 80 m) compared to the 40m thick Koppert Cress aquifer. Vin=500,000 m3 for the generic results, 400,000 m3 for the Koppert Cress case. Equal hydraulic conductivity (Kh=35, Kv=7) is used for all scenarios. A small difference can be observed between the generic low temperature results and the Koppert Cress recovery efficiency because of the storage volume difference.

Storage volume geometry

The results of the numerical simulations indicated that both the storage volume and the aquifer thickness strongly impact the recovery efficiency of HT-ATES. Since it was shown for LT-ATES systems that the Area/Volume ratio of the thermal volume determines the losses due to conduction (Bloemendal & Hartog, 2018), we evaluated this for the modelled HT-ATES scenarios. The A/V is calculated as following:

$$\frac{A}{V} = \frac{2}{L} + \frac{2}{R_{th}}$$

With R_{th}:

$$R_{th} = \sqrt{\frac{c_w V_{in}}{c_{aq} \pi L}}$$

For a given storage volume, the A/V ratio is optimal for a L/R_{th} ratio of 2.

The relationship between the observed recovery efficiency of this study and of the study of Bloemendal and Hartog (2018) shows that the low temperature scenarios here are also linearly correlated to the A/V ratio (Figure 2.2.33). In comparison to Bloemendal and Hartog (2018) the recovery efficiency calculated in this study are relatively high. This can be explained because A) a different value for thermal conductivity is used and B) because the study of Bloemendal and Hartog (2018) calculated the overall recovery efficiency, not the recovery efficiency in the last year.
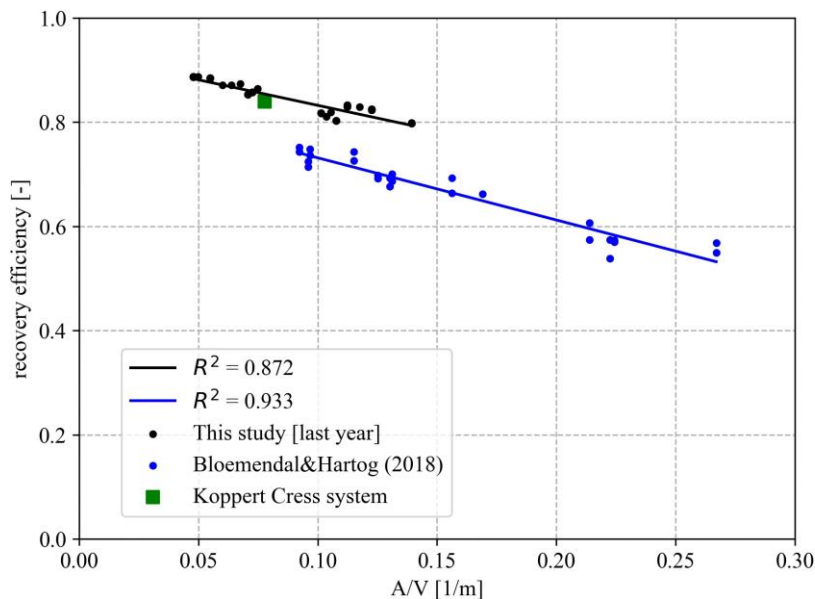
Figure 2.2.33 The correlation between the recovery efficiency and the A/V ratio. Results of this study (15 °C) are compared to the results of Bloemendal and Hartog (2018), a similar relationship is observed.

This insight can help us to understand the results in the previous sections. The relationship with A/V is able to explain why the recovery efficiency at low storage temperature increases with larger storage volumes (Figure 2.2.31) and larger aquifer thickness (Figure 2.2.32). Based on the Koppert Cress conditions (L_{aq}=40m and V_{in}=400,000) and increase in storage volume or aquifer thickness will lead to lower A/V ratio and thus the recovery efficiency increases due to relatively decrease in conduction losses. y

We observed that recovery efficiencies decrease at storage temperatures >50 °C. The A/V ratio does not provide a correlation for the recovery efficiency at higher storage temperatures (Figure 2.2.34). Most HT-ATES recovery efficiencies are significantly lower compared to the found A/V relationship, however, for some

high temperature scenarios, the recovery efficiency is situated closely to the linear A/V relationship. This shows us that, even at higher storage temperature, conduction losses can be dominant.
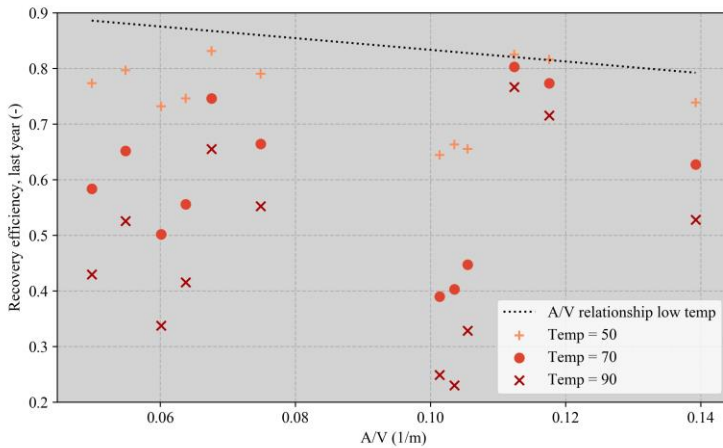
Figure 2.2.34 The recovery efficiency for all storage geometry scenarios in relationship to the A/V ratio under varying storage temperature (50 - 90 °C). These scenarios all have equal hydraulic conductivity Kh=35, Kv=7 m/d).

From Figure 2.2.34 we can conclude that the A/V ratio is not able to predict the performance of ATES systems at high storage temperature when buoyancy impact is significant. However, from the previous sections we did found that the recovery efficiency of the high temperature scenarios is impacted by the storage volume and the aquifer thickness; the recovery efficiency increased for decreasing aquifer thickness and increasing storage volume. This corresponds to increasingly flatter storage volumes. The ratio of aquifer thickness (L_{aq}, m) divided by the thermal radius (R_{th},m); L/R_{th} can be used to combine the aquifer thickness and the storage volume into one parameter that described the shape of the thermal volume. Small L/R_{th} (<2) corresponds to relatively flat thermal storage volumes, while large L/Rth >2 correspond to relatively thin thermal storage volumes.

In Figure 2.2.35, the same results are presented that where shown in Figure 2.2.34. The recovery efficiency for a given storage temperature is strongly correlated to the L/Rth ratio; the recovery efficiency increases for decreasing L/Rth ratio. The decrease in L/Rth from 2 - 0.2 can have a huge impact on the recovery efficiency. As example, the recovery efficiency for storage at 90 °C would increase from 0.25 to >0.75 when the L/R_{th} is decreased from 2 – 0.2. From this we can conclude that the ratio L/R_{th} is thus important in determining the amount of buoyancy flow losses that will occur for a given storage scenario.

Figure 2.2.35 Recovery efficiency of high storage temperature scenarios with varying L/Rth. Storage volumes with a small L/Rth have a relatively flat storage geometry, and oppositely, large L/Rth corresponds to a relatively thin storage geometry.

2.2.4 Discussion and conclusions

2.2.4.1 Transition from LT-ATES to HT-ATES for Koppert Cress case study

When the Koppert Cress pilot was initiated, it was expected that over the years enough additional heat sources would be available to sea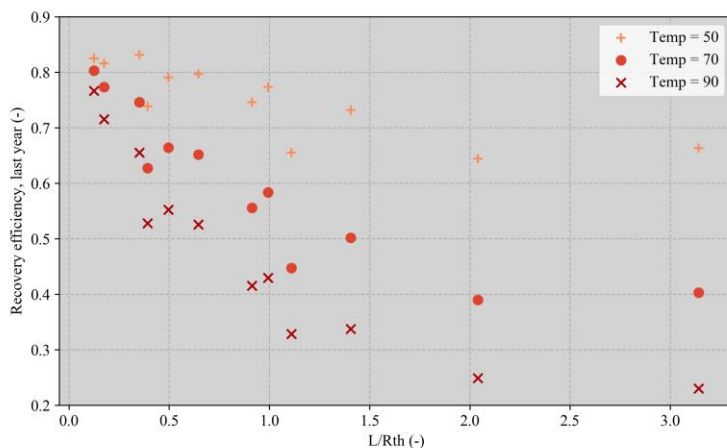sonally store large amounts of heat, resulting in storage of heat at temperatures between 30-40 °C. However, analysis of the system showed that the yearly heat demand of the greenhouses of Koppert Cress exceeds the amount of heat stored in the wells. Also the temperature of the available heat is limited because it is harvested from environmental sources. This results in an imbalanced ATES system that only stores heat at temperatures >25 °C during the hottest days of the years. A considerable part (25-20%) of the stored heat is retrieved within a day or week.

In spite of these conditions, with respect to energetic performance and greenhouses gas emissions savings the Koppert Cress (HT-)ATES system is highly successful, according to Bloemendal et al. (2020). By allowing storage temperatures >25°C, Koppert Cress was able to use their heating and cooling system more efficiently. More sources of heat were included over the years, which resulted in more heat storage in the warm wells. The increase in ΔT between the cold and warm wells led to a strong increase in yearly produced heat. Overall, the transition from LT-ATES to HT-ATES resulted in a decrease of 30-70% of GHG emission (depending on the electricity source). While the GHG emission decreased significantly, the costs of operating the ATES system decreased with 10%.

2.2.4.2 Impact of varying hydraulic conductivity on HT-ATES performance

Until now, the initial hydrogeological properties that were estimated for the Koppert Cress storage aquifers (K_h=35, K_v=7 m/d) were used consistently for all analyses. However, as already indicated, the actual hydraulic conductivity of aquifers are in most cases uncertain. Because it is relatively difficult to estimate/measure the horizontal hydraulic conductivity of aquifers, adequate data is lacking for most aquifers in the Netherlands (and worldwide). Moreover, the vertical hydraulic conductivity is even more uncertain, and is often calculated from the horizontal hydraulic conductivity using an anisotropy factor ranging between 2-10 (Bloemendal & Hartog, 2018; Xynogalou, 2015).

For low temperature scenarios, where conduction losses are dominant, hydraulic conductivity has no impact on the recovery efficiency (Figure 2.2.36). For storage temperatures >50 °C however, a large decrease of the recovery efficiency can be observed for decreasing average hydraulic conductivity ($\sqrt{K_h * K_v}$). Similar to the results in section 2.2.3.3, the losses due to buoyancy flow are also impacted by the storage volume and the storage temperature. For the scenarios with a relatively small storage volume (100,000 m³) in Figure 2.2.37, the decrease in hydraulic conductivity from 15 to 2 m/d leads to a major increase of recovery
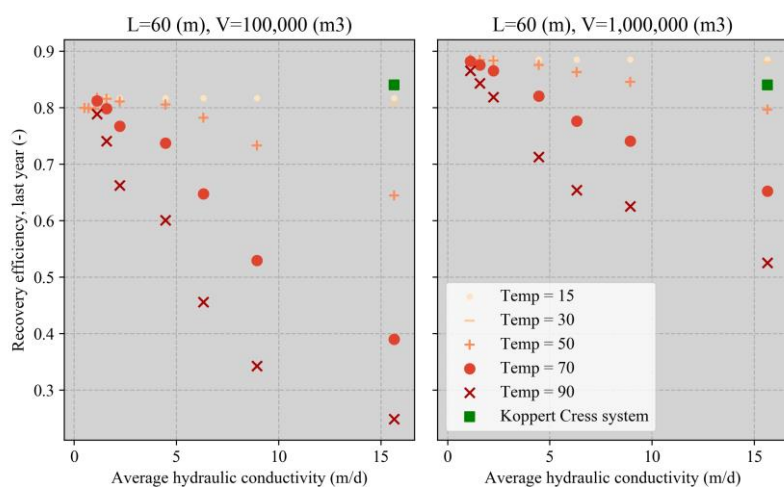
Figure 2.2.36 Impact of average hydraulic conductivity (√ (K_h*K_v)) on the recovery efficiency for Laq=60m. Left: Vin=100,000 m3, Right: Vin=1,000,000 m3. The Koppert Cress system is slightly different from the low temperature scenarios shown here (Laq=40m, Vin=400,000 m3).

efficiency from 0.8 to 0.25. For the larger storage volume, the same effect is observed, but the difference in recovery efficiency is smaller 0.85 to 0.52. We can thus conclude that a combination of the storage temperature and the hydraulic conductivity determines the magnitude of the losses due to buoyancy flow.

The combined impact of all storage conditions on the recovery efficiency of the high storage temperature scenarios is provided in Figure 2.2.38. For a given storage volume geometry (L/R$_{th}$), the combination of both the storage temperature and the hydraulic conductivity determine the recovery efficiency. Lowest recovery efficiency values are thus observed for storage at 90 °C with relatively high hydraulic conductivity values at relatively large L/R$_{th}$ (recovery efficiency ~0.25). However, with relatively low hydraulic conductivity or small L/R$_{th}$ ratio, the recovery efficiency can significantly increase for this scenario to values up to 0.8. At small L/R$_{th}$ or low hydraulic conductivity, conduction losses are dominant, even for relatively high storage temperatures.
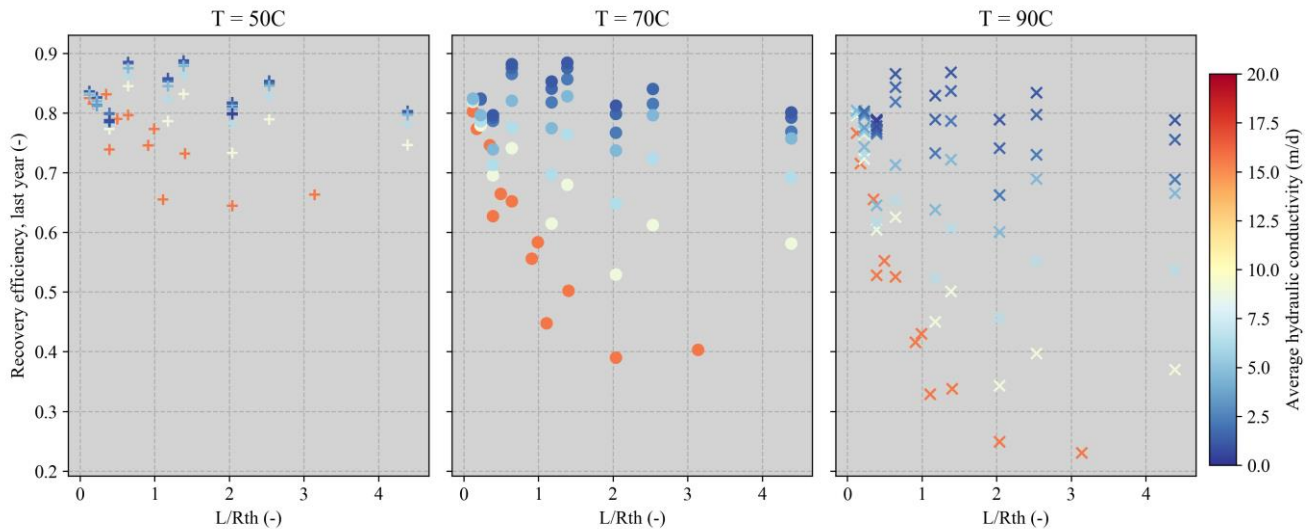
Figure 2.2.38 Recovery efficiency for varying storage geometries (L/Rth) and varying average initial hydraulic conductivity ($\sqrt{(K\_h*K\_v)}$) for storage at 50, 70 and 90 ° C.

The results show that insight in the horizontal and vertical hydraulic conductivity is important to accurately predict if buoyancy flow losses will have a considerable impact on the recovery efficiency of HT-ATES systems. Hydraulic conductivity also determines the maximum well flow rate; and with that also the amount of volume that can be injected/extracted per meter screen length per year. For higher horizontal hydraulic conductivity, the maximal amount of flow (m^3/s) per meter screen length increases while the pressure gradient/pumping energy decrease. Also, for higher hydraulic conductivity, less problems related to well clogging due to suspended particles is expected. Hence, for HT-ATES systems, large hydraulic conductivity can be preferential regarding costs and clogging risks, but may also have a strong negative impact regarding the recovery efficiency of HT-ATES wells.

2.2.4.3 Impact of heterogeneity of hydrogeological properties on performance

Currently, subsurface properties (e.g. the hydraulic conductivity, thermal conductivity, porosity) were assumed homogeneous for each layer type (aquifer or aquitard) in the numerical model. We know that in practice aquifers are not homogeneous and can vary both vertical and horizontal, where stronger heterogeneities are usually present in vertical direction. The effect of heterogeneity has been studied for LT-ATES systems (Caljé, 2010; Sommer et al., 2013) and was found to be only of minor impact on the recovery efficiency of these systems. For HT-ATES systems, however, the impact of heterogeneities might be more important considering the insights from this study. It is found that the shape of the thermal volume L/R$_{th}$ determines the impact of buoyancy flow on the recovery efficiency at higher storage temperatures. So, when an aquifer is subdivided in multiple thin aquifers due to vertical heterogeneity in hydraulic conductivity, this could have a positive impact on the recovery efficiency because this would reduce buoyancy flow. It is therefore recommended that future research addresses the impact of (vertical) heterogeneity on HT-ATES performance.

2.2.4.4 Expected performance of the Koppert Cress HT-ATES system at increased storage temperature and volume balance

The dynamic operational characteristic of the Koppert Cress HT-ATES system has a strong contrast with the generic analysis of varying storage conditions which is often used in performance analysis studies (Collignon et al., 2020; Jeon et al., 2015; Schout et al., 2013). The analysis of operational data of Koppert Cress in this research showed that the HT-ATES is not only used for seasonal heat storage, but is also used frequently used as a night/day buffer. This results in highly efficient short cycle storage of heat. The generic modelling approach does not take this short cycle behaviour into account. This shows us that pumped volumes and recovery efficiencies are reasonably expected to be higher than is computed/expected based on the generic seasonal modelling approach. Also, the effect of the volume imbalance is shown to have a positive effect on the modelled recovery efficiency of the warm well. On the other hand, a long-term imbalanced system will also lead to negative interaction between the two well types of the HT-ATES system. Future improvements on the HT-ATES of Koppert Cress could focus on optimal HT-ATES pumping strategy (short cycle? Imbalanced?) and further improve heat harvesting and injection temperature.

2.2.4.5 Generic conclusions

From the generic analysis we showed that the combined effect of the assessed wide range of storage conditions have a strong impact on the expected recovery efficiency of a HT-ATES system. For low temperature ATES scenarios (<30 °C), buoyancy flow is not important and conduction is the main cause of heat loss. Conduction losses can be limited by minimizing the A/V ratio of the storage volume.

At higher storage temperatures, buoyancy flow may have a significant impact on the recovery efficiency, additional to the conduction losses. Low hydraulic conductivity values will prevent buoyancy flow to occur, even at relatively high storage temperatures (e.g. 90 °C). Also, the storage geometry (L/R_{th}) determines the actual impact of buoyancy flow on the recovery efficiency of the stored thermal volume. Meaning that, even if heat is stored at high temperatures in an aquifer with high hydraulic conductivity (circumstances leading to large buoyancy flow), a relatively flat storage geometry (small L/R_{th}) will prevent buoyancy flow losses to dominate.

2.2.5 Work Package Interfaces

The monitored data of the Koppert Cress HT-ATES system will also be used in WP5 of the HEATSTORE project to calibrate and validate the developed HT-ATES models. Both the measured injection/extraction temperatures and the measured groundwater temperatures with the DTS cables will be used to do this.

2.2.6 Potential issues related to IP

We don't expect any issues regarding IP.

2.2.7 References

Beernink, S., Hartog, N., Bloemendal, M., & Meer, M. v. d. (2019). *ATES systems performance in practice: analysis of operational data from ATES systems in the province of Utrecht, The Netherlands*. Paper presented at the European Geothermal Congress, The Hague, Netherlands.

Bloemendal, M., Beernink, S., Bel, N., Hockin, A. E., & Schout, G. (2020). *Transitie open bodemenergiesysteem Koppert-Cress naar verhoogde opslagtemperatuur. Evaluatie van energiebesparingen en grondwatereffecten*. Retrieved from Nieuwegein: https://library.kwrwater.nl/publication/61755396/

Bloemendal, M., Beernink, S., Hartog, N., & Van Meurs, B. (2019). *Transforming ATES to HT-ATES. Insights from dutch pilot project*. Paper presented at the European Geothermal Congress EGC, Den Haag.

Bloemendal, M., & Hartog, N. (2018). Analysis of the impact of storage conditions on the thermal recovery efficiency of low-temperature ATES systems. *Geothermics, 17*, 306-319. doi:10.1016/j.geothermics.2017.10.009

Bloemendal, M., Olsthoorn, T., & van de Ven, F. (2015). Combining climatic and geo-hydrological preconditions as a method to determine world potential for aquifer thermal energy storage. *Science of the Total Environment, 538* ((2015)), 621-633.

Buscheck, T. A., Doughty, C., & Tsang, C. F. (1983). Prediction and analysis of a field experiment on a multilayered aquifer thermal energy storage system with strong buoyancy flow. *Water Resources Research, 19*(5), 1307-1315. doi:10.1029/WR019i005p01307

Caljé, R. (2010). *Future use of aquifer thermal energy storage inbelow the historic centre of Amsterdam.* (Msc), Delft University of Technology, Delft.

Collignon, M., Klemetsdal, Ø. S., Møyner, O., Alcanié, M., Rinaldi, A. P., Nilsen, H., & Lupi, M. (2020). Evaluating thermal losses and storage capacity in high-temperature aquifer thermal energy storage (HT-ATES) systems with well operating limits: insights from a study-case in the Greater Geneva Basin, Switzerland. *Geothermics, 85*, 101773. doi:https://doi.org/10.1016/j.geothermics.2019.101773

Courant, R., Friedrichs, K., & Lewy, H. (1967). On the partial difference equations of mathematical physics *IBM Journal of Research and Development, 11*(2), 215–234. doi:https://dx.doi.org/10.1147%2Frd.112.0215

Doughty, C., Hellström, G., & Fu Tsang, C. (1982). A Dimensionless parameter Approach to the Thermal Behavior of an Aquifer Thermal Energy Storage System. *Water Resources Research, 18*(3), 571-578.

Drijver, B., Aarssen, B., & De Zwart, B. (2012). *High-temperature aquifer thermal energy storage (HT-ATES): sustainable and multi-usable*. Paper presented at the Innostock 2012.

Fetter, C. W. (2001). *Applied Hydrogeology* (4th ed.). Upper Saddle River, NJ, USA.

Graaf, A. d., Heijer, R., & Postma, S. (2016). *Evaluatie Wijzigingsbesluit bodemenergiesystemen*. Retrieved from Cothen:

Harbaugh, A. W., Banta, E. R., Hill, M. C., & McDonald, M. G. (2000). Modflow-2000, the u.S. Geological survey modular ground-water model—user guide to modularization concepts and the ground-water flow process Virginia: US Geological Survey.

Hecht-Mendez, J., Molina-Giraldo, N., Blum, P., & Bayer, P. (2010). Evaluating MT3DMS for Heat Transport Simulation of Closed Geothermal Systems. *Ground water, 48*(5), 741-756.

Holstenkamp, L., Meisel, M., Neidig, P., Opel, O., Steffahn, J., Strodel, N., . . . Növig, T. (2017). *Interdisciplinary review of medium-deep Aquifer Thermal Energy Storage in North Germany*. Paper presented at the 11th International Renewable Energy Storage Conference, IRES, Dusseldorf, Germany.

Jeon, J.-S., Lee, S.-R., Pasquinelli, L., & Fabricius, I. L. (2015). Sensitivity analysis of recovery efficiency in high-temperature aquifer thermal energy storage with single well. *Energy, 90*, 1349-1359. doi:https://doi.org/10.1016/j.energy.2015.06.079

Langevin, C. D. (2008). Modeling Axisymmetric Flow and Transport. *Ground water, 46*(4), 579-590. doi:10.1111/j.1745-6584.2008.00445.x

Langevin, C. D., Dausman, A. M., & Sukop, M. C. (2010). Solute and heat transport model of the Henry and hilleke laboratory experiment. *Ground water, 48*(5), 757-770. doi:10.1111/j.1745-6584.2009.00596.x

Langevin, C. D., Thorne, D. T., Dausman, A. M., Sukop, M. C., & Guo, W. (2008). *SEAWAT Version 4: A computer program for simulation of multi-Species Solute and heat transport*. Retrieved from Reston, Virginia:

Lopik, J. H., Hartog, N., Zaadnoordijk, W. J., Cirkel, D. G., & Raoof, A. (2015). Salinization in a stratified aquifer induced by heat transfer from well casings. *Advances in Water Resources, 86*, 32-45. doi:10.1016/j.advwatres.2015.09.025

Lopik, J. H. v., Hartog, N., & Zaadnoordijk, W. J. (2016). The use of salinity contrast for density difference compensation to improve the thermal recovery efficiency in high-temperature aquifer thermal energy storage systems. *Hydrogeology Journal*. doi:10.1007/s10040-016-1366-2

Louwyck, A., Vandenbohede, A., Bakker, M., & Lebbe, L. (2014). MODFLOW procedure to simulate axisymmetric flow in radially heterogeneous and layered aquifer systems. *Hydrogeology Journal, 22*(5), 1217-1226. doi:10.1007/s10040-014-1150-0

Possemiers, M., Huysmans, M., & Batelaan, O. (2015). Application of multiple-point geostatistics to simulate the effect of small-scale aquifer heterogeneity on the efficiency of aquifer thermal energy storage. *Hydrogeology Journal, 23*(5), 971-981.

Sanchez, M. F., Klein, J., Essink, G. O., Raat, K., & Paalman, M. (2012). *Effecten van brijninjectie op de grondwaterkwaliteit en functies in het Westland* Retrieved from Delft / Nieuwegein:

Schout, G., Drijver, B., Gutierrez-Neri, M., & Schotting, R. (2013). Analysis of recovery efficiency in high-temperature aquifer thermal energy storage: a Rayleigh-based method. *Hydrogeology Journal, 22*(1), 281-291. doi:10.1007/s10040-013-1050-8

Sharqawy, M. H., Lienhard, J. H., & Zubair, S. M. (2012). Thermophysical properties of seawater: a review of existing correlations and data. *Desalination and Water Treatment, 16*(1-3), 354-380. doi:10.5004/dwt.2010.1079

Sommer, W., Valstar, J., van Gaans, P., Grotenhuis, T., & Rijnaarts, H. (2013). The impact of aquifer heterogeneity on the performance of aquifer thermal energy storage. *Water Resources Research, 49*(12), 8128-8138. doi:10.1002/2013wr013677

Thorne, D. T., Langevin, C. D., & Sukop, M. C. (2006). Addition of simultaneous heat and solute transport and variable fluid viscosity to SEAWAT. *Computers & Geosciences, 32*, 1758-1768. doi:10.1016/j.cageo.2006.04.005

Tomasdottir, S., & Gunnarsson, G. (2019). *HEATSTORE – Interim report on UTES-type/site-specific simulators based on academic/research codes*. Retrieved from

van Lopik, J. H., Hartog, N., & Zaadnoordijk, W. J. (2016). The use of salinity contrast for density difference compensation to improve the thermal recovery efficiency in high-temperature aquifer thermal energy storage systems. *Hydrogeology Journal, 24*(5), 1255-1271. doi:10.1007/s10040-016-1366-2

Voss, C. I. (1984). *A finite-element simulation model for saturatedunsaturated, fluid-density-dependent groundwater flow with energy transport or chemicallyreactive single-species solute transport*. Retrieved from Reston, Va:

Willemsen, N. (2016). *Rapportage bodemenergiesystemen in Nederland*. Retrieved from Arnhem:

Xynogalou, M. (2015). *Determination of optimal separation well distance for Single Borehole ATES systems in the Netherlands, implementing an axisymmetric numerical model.* (MSc), Delft University of Technology, Delft.

Zheng, C., & Wang, P. P. (1999). *MT3DMS: A Modular Three-Dimensional Multispecies Transport Model for Simulation of Advection, Dispersion, and Chemical Reactions of Contaminants in Groundwater Systems; Documentation and User's Guide*.

2.3 Swiss pilot site Geneva

Julian Mindel[1], Daniel Birdsell[1], Luca Guglielmetti[2], Ovie Etureya[2], Andrea Moscariello[2], Thomas Driesner[1],

[1]Eidgenössische Technische Hochschule Zürich, [2]Université de Genève

The Geneva HEATSTORE project is linked to the staged Geothermie2020 strategy of the Canton of Geneva and assesses the geologic feasibility, potential, performance, sustainability, and energy system integration of high-temperature aquifer energy storage (HT-ATES) in the Western Geneva Basin (Figure 2.3.1). The target area is arguably the geologically most challenging of all HEATSTORE pilot sites with significant topography at its boundaries, major thrust and strike-slip faults off-setting and intersecting the potential storage aquifers and high building density at the surface. The aquifers themselves are slightly to moderately inclined due to the large-scale deformation in the Alpine foreland.

The geologic complexity adds additional tasks to the modelling activities; namely - as the project is currently in the exploration phase - the challenge to assess which parts of the aquifers possess the best potential to act as reliable and efficient storage volumes. This may in turn influence the exploration strategies.
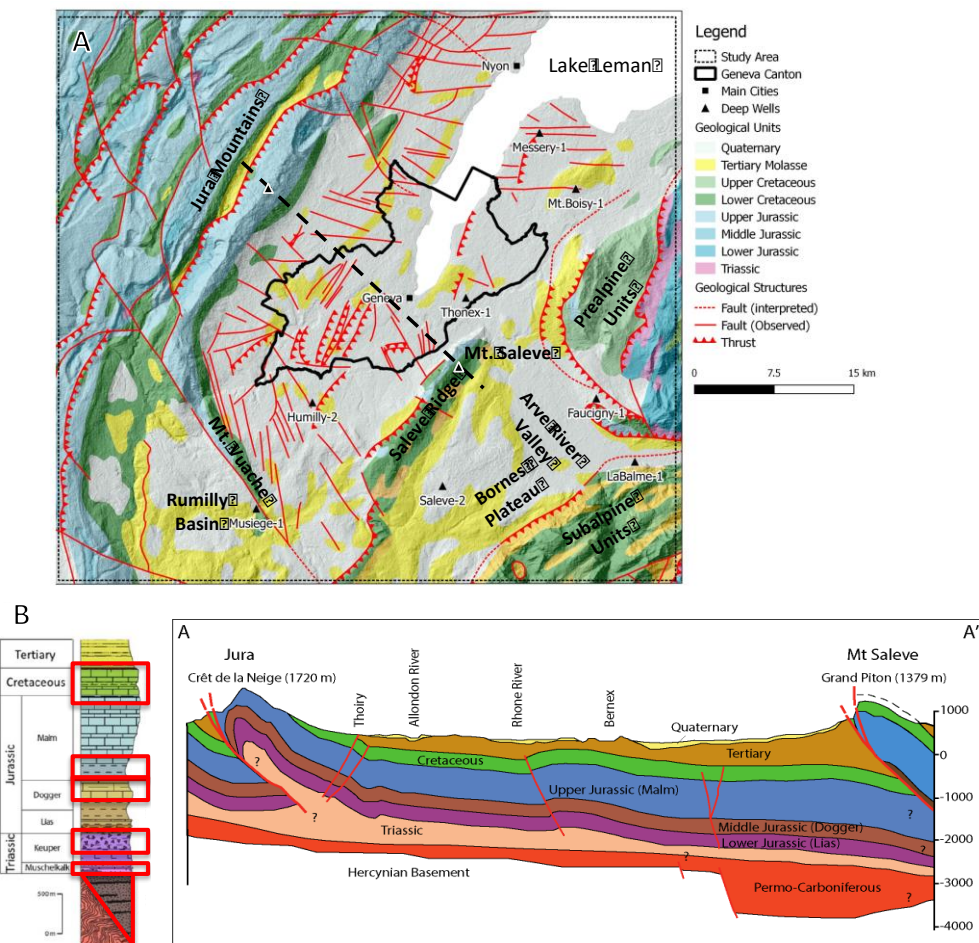

Figure 2.3.1 A. Geological maps of the study area with indication of the location of the main deep well. B. Geological cross-section and stratigraphic section showing the main geothermal targets

2.3.1 UTES concept and specifications, scope and aims of the study

The Geneva pilot aims at assessing the feasibility of seasonal storage of up to 50 GWh/a waste heat from the Cheneviers incinerator (Canton of Geneva), using a high temperature aquifer thermal energy storage concept. Several target aquifers exist at different depths and are being explored and characterized phase to better constrain options for HT-ATES. The modelling inputs of HEATSTORE WP2 therefore also aim at providing improved guidance for optimal site selection in a complex geologic situation.

This geologic complexity makes the Western Geneva basin potentially "difficult" for HT-ATES, due to significant topography at the boundaries potentially imposing artesian hydraulic conditions, due to strike-slip and thrust faults leading to compartmentalization of aquifers and providing potential leak-off structures, due to inclination of aquifers raising the question of the role of buoyancy in storage, and due to variable sedimentary facies within the aquifers leading to heterogeneity. Modelling therefore starts with addressing the question of how these complexities can potentially affect possible storage by simulating generic scenarios of geologic situations to be encountered in the Geneva underground.

The *Geothermie 2020* program carried out by the Services Industriels de Genève (SIG) and by the Canton of Geneva geological service (GESDEC) and public authorities aims at developing geothermal energy across the Canton. The development strategy aims at collecting new data to characterise the subsurface and assess its geothermal potential covering the largest variety of application from local heating and cooling, district heating, thermal storage and, in the future, power production if the geological conditions in the subsurface will be proven favourable.

The program started in 2012 and since then, geological and geophysical data have been collected and combined to locate drilling targets. The goal was to drill into the Mesozoic units in different tectonic settings and at increasing depth. During the project time two wells, GEO-01 and GEO-02 were drilled, aiming at characterizing the upper part of the Mesozoic sequence, composed by the Lower Cretaceous and the Upper Jurassic (Malm) units. Such geological units are considered as important geothermal targets according to the geophysical, geological and petrophysical data available and they include two horizons which are potentially very favourable for geothermal development. The Top Lower Cretaceous is known to be represented by an erosional and karstified surface which, despite being discontinuous, shows porosity and permeability conditions that can be favourable for fluid circulation. The Malm is locally composed by a patch reef complex, rather heterogeneous in geometry and irregular in spatial distribution, but with potentially favourable petrophysical conditions. Both GEO-01 and GEO-02 aim at tapping the two main geothermal targets in different structural settings.

The current HT-ATES concept planned for the Canton of Geneva is based on the waste heat discharged into the environment by the Les Cheneviers incineration plant. The total amount of heat discharged by the incineration plant reaches 50 GWh/y and the temperature ranges between 80 and 120°C. Such heat could be stored in the subsurface during low heat demand seasons and delivered in winter though the district heating network. The assessment of site-specific geological layers to be utilized in the design of such a storage system is based on data gathered from exploration wells in the area (see section 2.3.3.1), and thus at least three main development strategies have been identified:

- **Geologic complexity**: The study area is characterized by strong heterogeneities in terms of reservoir petrophysical parameters as demonstrated by hydrocarbon and geothermal exploration wells drilled in the past. Such variations are mainly dominated by stratigraphic, sedimentological and diagenetic processes as well as by presence of fault corridors, which have been identified according to 2D reflection seismic data. The role of such faults zones in the study area is still uncertain as they may either act as preferential flow paths for groundwater or act as impermeable barriers causing compartmentalization of the potential HT-ATES reservoirs.

- **Environmental impact**: The main potential environmental impacts associated to production and injection operations that can affect the Geneva area are surface deformation and seismicity. The HT-ATES system will perform under an operational strategy based on seasonal load/unload cycles of the aquifer, which can theoretically cause ground uplift during loading and subsidence during unloading. Seismicity in geothermal projects is an impact usually associated to injection in deep reservoirs. Considering the seasonal storage/production operations planned, and although there are no records of

seismicity associated to ATES projects, it is an element of impact that has to be considered, modelled, and monitored.

- **Operational risk**: The main operational risks are associated to chemical processes of mineral dissolution and precipitation that can occur in the reservoir, and corrosion and scaling in the wells and in the gathering systems (i.e. pipes, heat exchangers). Such risks can strongly affect the life-time performances of the HT-ATES system and therefore have to be quantified to identify the best mitigation strategy.

These three challenges are to be tackled by establishing a workflow that includes a flexible reservoir modelling approach and corresponding application tools. Such a combination will help predict reservoir performance and support SIG in designing the HT-ATES systems according to the heat availability and demand fluctuations over the life-time of the project.

Two basic conceptual approaches will be combined into the modelling workflow to help identify the optimal operational conditions, mitigate the environmental impacts, and minimise the operational risks:

- Thermo-Hydro (**TH**) modelling will focus on the dynamic thermal flow scenarios to optimise the storage and production operations according to thermal power inputs in terms of heat source and demand, and to the available 3D geological and petrophysical static model

- Thermo-Hydro-Mechanical (**THM**) modelling will aim at evaluating the effects of the HT-ATES Systems on ground deformation seismicity. Efforts will focus in a first instance in predicting the effect of the 6-8 months production tests at GEO-01 and will be validated by the monitoring techniques which will be applied (i.e. GPS levelling, INSar, Micro earthquake monitoring network are in definition). Once the operational scenarios will be defined, THM modelling will be also used to predict longer-term the effects.

The (thermo-hydro-chemical) **THC** modelling suggested in the Month 9 version of this report was eventually restricted to PHREEQC calculations to interpret comprehnsive laboratory and field results, which will not be repeated here. They are available in appendix 7 of the Swiss national HEATSTORE project report (Guglielmetti et al., 2021).

2.3.2 Subsurface Conditions

Since the density of suitable drilling sites is low on the Geneva territory, the choice of geological sites is strongly influenced by surface boundary conditions such as proximity to the waste water network, suitability of nearby crops, and SIG's future plans to increase the district heating network coverage. Drilling targets have nevertheless been defined according the available geological and geophysical data, which consists mainly of 2D reflection seismic data. This allowed the identification of the Mesozoic units as the most favourable targets for geothermal development. With these targets in mind, it is important to have a broader view of the surrounding geology to be able to construct geometrically relevant simulation models.

2.3.2.1 Regional Geology

The Greater Geneva Basin (GGB) covers the westernmost part of the Alpine Molasse basin, including the Canton of Geneva the surrounding French territory. It covers an area of about 2000 km^2 extending from the town of Nyon to the NE, down to the Vuache Mountains to the SW and it's limited by the Jura Haute-Chaine to the NW and by the subalpine nappes towards SE (see Figure 2.3.1). It is comprised of a 3000 meter thick sedimentary cover of Tertiary and Mesozoic age, principally composed of carbonates and marls overlying a crystalline basement often presenting tectonic depressions filled with Permo-Carboniferous clastic sediments (Signer & Gorin, 1995).

The tectonic evolution of the GGB is associated with the alpine compressional phase that caused the decoupling of the sedimentary succession from the basement by a detachment surface occurring on the Triassic evaporites (Guellec, et al., 1990; Sommaruga, 1999; Affolter & Gratier, 2004; Arn, et al., 2005). Inherited basement reliefs and normal faults bounding Permo-Carboniferous troughs might have played a role in the nucleation of the Mesozoic north-westward thrusts observed in the SE sector of the Geneva Basin and Bornes Plateau (Gorin, et al., 1993; Signer & Gorin, 1995).

In response to the alpine compression, the Mesozoic and Cenozoic sedimentary cover of the GGB underwent some shortening while locally coupled to a rotational motion. This shortening was absorbed through the formation of the fold and thrust structures of the Jura arc mountains during the late Miocene and

Early Pliocene (Meyer, 2000; Homberg, et al., 2002; Affolter & Gratier, 2004) and by the coeval formation of accommodation of strike-slip faults. The most relevant surface evidence of such structures is the NW-SE Vuache fault (Charollais, et al., 2007), which cross-cuts the entire basin and bounds the western side of the study area.

A series of smaller-scale NW-SE striking left-lateral wrench faults affect the south-western part of the Geneva area. Unlike the Vuache fault, no obvious connections between these structures and the Jura Mountains can be drawn across the study area (Rousillon, 2018) (Brentini, 2018) as suggested in previous interpretations (Signer & Gorin, 1995) (Paolacci, 2012). Towards the northeast of the basin, the structural configuration is dominated by E-W striking faults. NW-SE and E-W strike slip faults occur as series of sub-vertical individual faults often affecting most of the Mesozoic sequence, down to the Triassic decollement surface, with associated smaller-scale sets of conjugates. Throughout the Cenozoic interval, the most important faults often present themselves in a flower structure. This shallow subsurface expression is consistent with fault geometries observed in Tertiary Molasse outcrops (Charollais, et al., 2007) (Angelillo, 1987).

Based on stratigraphic record of two previous wells (Humilly-2 and Thonex-01) and the outcrops surrounding the Geneva Basin in the Jura Mountains, Vuache Mountains and Saleve Ridge, the nature of the Mesozoic–Cenozoic sequence can be summarized as presented in Table 2.3.1. Where relevant, all depth measurements presented are considered true vertical depth (TVD) below ground level (b.g.l.) unless otherwise explicitly stated.

Table 2.3.1 Summary of the Mesozoic–Cenozoic sequence at the Geneva Basin

Era	Period	Epoch	Lithology
Mesozoic	Trias	Late	Locally exposed in the Jura Mountains, its thickness is variable ranging between 1000 and 1300 meters in the Jura, to less than 500 meters underneath the Molasse Basin. It is usually divided into three intervals according to the German classification: - *Buntsandstein* mainly composed of continental sandstones at the base; - *Muschelkalk* showing marly limestones, evaporites and dolomites in the middle; - *Keuper* comprising a lower thin interval called Lettenkohle made of lignite and dolomite, and a thick upper interval of evaporites (gypsum and halite) at the top. (Brentini, 2018).
	Jurassic	Lias	Argillaceous and marly shales alternating with well-bedded, argillaceous and sandy limestones. This unit is located at a depth between 2500 and 3000 meters. A total thickness of 442 meters was observed in the Humilly-2 well and decreases towards the South East (Brentini, 2018).
		Dogger	Composed of oolithic and marly limestones alternating with abundant marly strata, broadly crops out in the Jura Mountains and attains 230 meters in thickness in the Humilly-2 well. (Brentini, 2018)
		Malm	Competent, often massive, shallow-marine platform carbonate deposits. Locally the Malm interval could be highly fractured and karstified. Biothermal reefs facies are developed mainly during the Kimmeridgian-Thitonian interval and make this horizon a potentially interesting geothermal target where hot waters can circulate. The Purbeckian formation represents the last Jurassic stage and is more argillaceous than the underlying units observed in the Salève mountain. It is composed by shallow-water limestones and was drilled in the Humilly-2 and Thônex-01 wells where thicknesses of 1009 meters and at least 711 meters were observed, respectively.

Cenozoic	Cretaceous	Lower	Fine grained/bioclastic and fine quartz-rich bioturbated limestones alternating with organic-rich marls accumulated with a shallow and warm water environment. The top of the Lower Cretaceous is characterized by an erosive and highly karstified sequence boundary surface. Lower Cretaceous limestones are the only ones preserved in the study region, and crop out in the Jura, Vuache, and Saleve mountains. They were reached by the all the wells in the study area.
	Tertiary	Oligocene	In the GGB area the Lower Freshwater Molasse (LFM) is observed in outcrops and borehole record. This unit can reach ca 1500 meters in thickness in the SE part of the Canton of Geneva (Brentini, 2018). Approximately 427m of Tertiary sediments were drilled in GEO-01 well,1300 meters are recorded in the Thonex-01 well, and only 370m in the Humilly-2 well. The transition between Tertiary and Early Cretaceous is marked by a karstified erosional surface on top of which lie the deposits of the Eocene "Sidérolithique" and the overlaying "Gonpholite" units (Charollais, et al., 2007), forming an important seismic marker and potential geothermal target. These two units are rather discontinuous in lateral extent and show a thickness that ranges between 0 and 40 meters.
	Quaternary		Comprised of heterogeneous glacial and fluvio-glacial and glacio-lacustrine sequences. Considerable lateral changes in thickness are observed, locally reaching more than 200 meters in correspondence with erosional morphological depressions genetically linked to the Wurm and Riss glaciation (Moscariello, et al., 2018).

2.3.2.2 Local geothermal and groundwater conditions

The thermal state across the Western Alpine Molasse Basin (WAMB, see Figure 2.3.2) from Aix-les-Bains to Yverdon-les-Bains is characterized by normal geothermal gradient conditions (25-35˚C/kilometre). Some areas show enhanced thermal regime, such as in Aix-les-Bains and Yverdon-les-Bains, mainly associated with artesian upward fluid circulation through fault corridors within Jurassic and Lower Cretaceous aquifers, and within the basal Permo-Carboniferous to Lower Triassic sediments.

The geothermal conditions across the WAMB have been constrained by a UniGe study based on geostatistical modelling of temperature data records retrieved by a number of hydrocarbon exploration wells drilled earlier than 1990s across the whole area (Chelle-Michou, et al., 2017).

A hydrogeological model has not yet been defined for the Geneva site. Data from the GEO-01 well shows that a considerable groundwater flow characterizes the northern part of the studied area, which is also proximal to the natural recharge zone located in the Jura Mountains. At the GEO-01 well, the flowrate measured at wellhead after drilling operations was approximately 50 l/s at a temperature of 34˚C and a pressure of 12 bars[3]. Tracer tests are ongoing and preliminary results show that groundwater flow in the study area is approximately 20 meters/year.

An important additional observation is that data from the Thonex-01 well seems to indicate that such artesian conditions do not prevail across the basin. In 1993, Thonex-01 intersected the same formations as the GEO-01 well, and water inflows at 70 ˚C and 88 ˚C were observed at approximately 2050 meters and 2530 meters, respectively. Pumping tests carried out in 1993 revealed that the maximal flow-rate attainable is about 3 litres/second. The Thonex-01 well currently discharges a natural artesian flow of 0.3 litres/second. Geochemical investigations carried out in 2010 by the University of Neuchatel estimated the age of the sampled water to approximately 10.000-15.000 years, based on carbon isotopes. Assuming that the recharge area for the Thonex-01 waters is the Jura Mountains and a negligible contribution comes from the southern reliefs, the regional groundwater flow is about 1.6 meters/year.

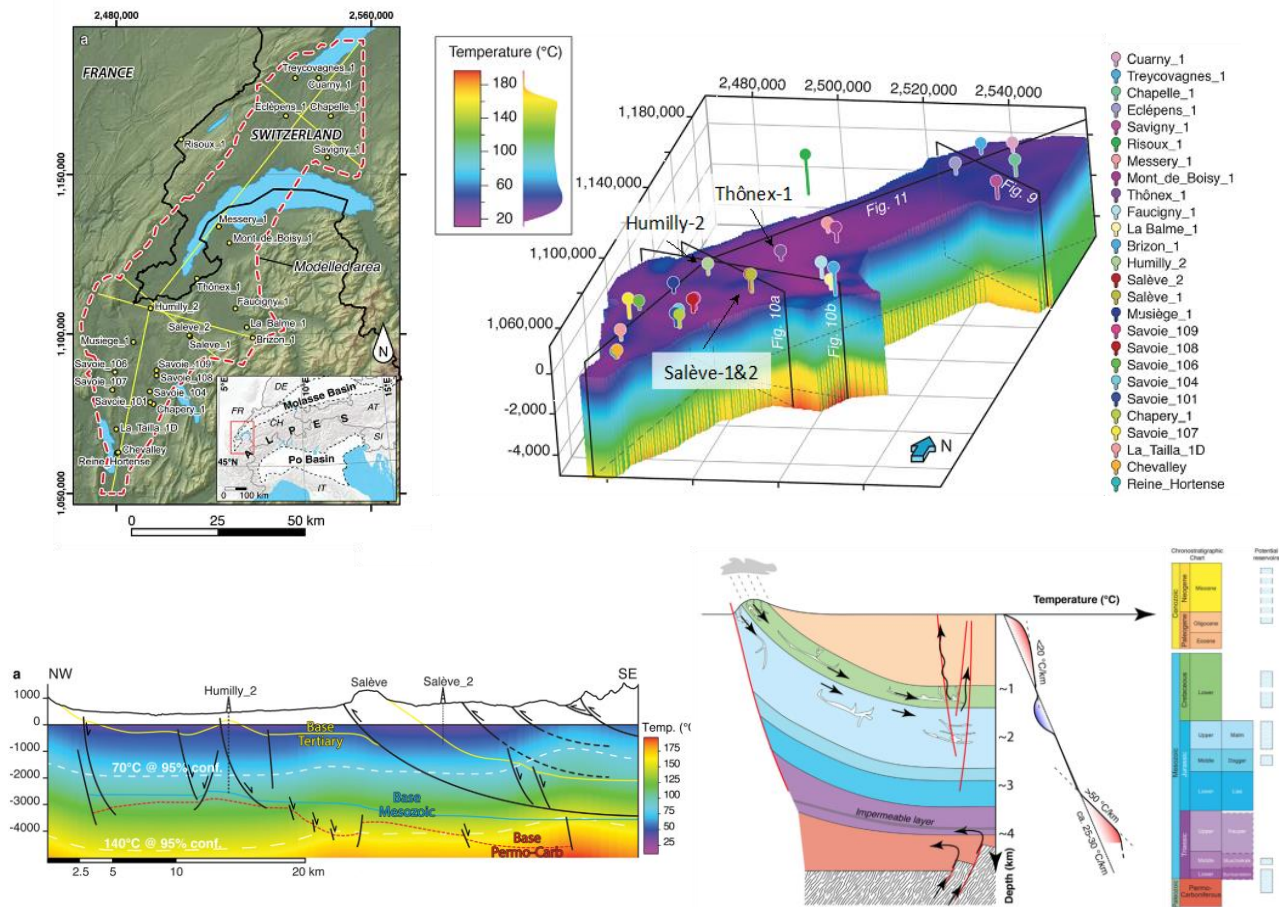
[3] Personal communication from SIG

Figure 2.3.2 Top left: location of the WAMB and the hydrocarbon wells across the area. Top right: 3D thermal model of the WAMB. Bottom left: 2D section across the WAMB. Bottom right: Illustration the circulation model in the WAMB. (modified from (Chelle-Michou, et al., 2017)).

Since December 2018 a water and gas sampling campaign has been carried out on shallow cold water springs and in the GEO-01 and Thonex-01 well to further assess the transition time, origin of the fluid, depth of circulation, water-rock interactions, mixing processes, of groundwater in the Mesozoic Units. A detailed summary is available from Guglielmetti et al. (2021).

2.3.2.3 Well operation and history

Four wells in the Geneva area have been drilled (GEO-01, GEO-02, Thonex-01, Humilly-2) and provide information about groundwater flow within the Mesozoic units. GEO-01 has been drilled between 2017 and 2018 by SIG as the first exploration well in the framework of the Geothermie 2020 program. The position of this well was selected according to interpretation of existing 2D seismic data that allowed to identify the strike slip system, to be hydro-geologically close to the groundwater infiltration area (Jura Mountains), and to be located at the surface on a field of public domain, easily accessible from the main roads, close by wastewater pipeline and near potential final users. Thonex-01 was drilled for geothermal purposes to tap a fault zone in the Jurassic units identified on 2D seismic lines, and eventually feed a hospital located in the proximities of the well. Finally, Humilly-2 is a hydrocarbon exploration well drilled with the goal to tap potential reservoirs in the Tertiary Molasse and lower Mesozoic units.

GEO-series Wells

The geothermal exploration research wells GEO-01 and GEO-02 were dedicated to the HEATSTORE project and are part of a larger prospective set of wells. Figure 2.3.3 depicts an illustration of the geologic setting in the Geneva area, the conceptual placement of exploration wells GEO-01 to GEO-04, and the main structural target features at each well location.

GEO-01 and GEO-02 wells targeted the Upper Mesozoic units (Lower Cretaceous and Upper Jurassic Carbonate formations) but different structural settings: while GEO-01 was drilled into a sub-vertical east-west trending strike-slip fault zone, GEO-02 aimed to evaluate the performance of the same Mesozoic units at greater depth and in a different structural framework, defined by a sequence of low-angle trust and back-trust faults. The two well locations are approximately 6 kilometres apart from each other, and their purpose is the acquisition of geological, geophysical, geochemical, hydrogeological, and petrophysical data. The main intent for drilling two wells in a reservoir characterization perspective is to constrain the geothermal groundwater dynamic conditions and improve the understanding of the lithological, structural, and petrophysical heterogeneities in HT-ATES-viable reservoir units in the Geneva underground. The conceptual geological setting of the study sites at the GEO-01 and GEO-02 wells is a stratigraphic sequence of subparallel horizons gently dipping towards the southeast. These horizons are locally cut by fault zones that are thought to potentially enhance the flow conditions, hence the permeability, in the reservoirs located in the Mesozoic units.

Legend:
- Cenozoic Unit: Quaternary and Tertiary Molasse
- Lower Cretaceous Carbonates
- Upper Jurassic (Malm) Carbonates
- Middle Jurassic (Dogger) Carbonates
- Lower Jurassic (Lias) Carbonates
- Trias Evaporites and Carbonates
- Permo-Carbniferous sediments
- Crystalline Basement
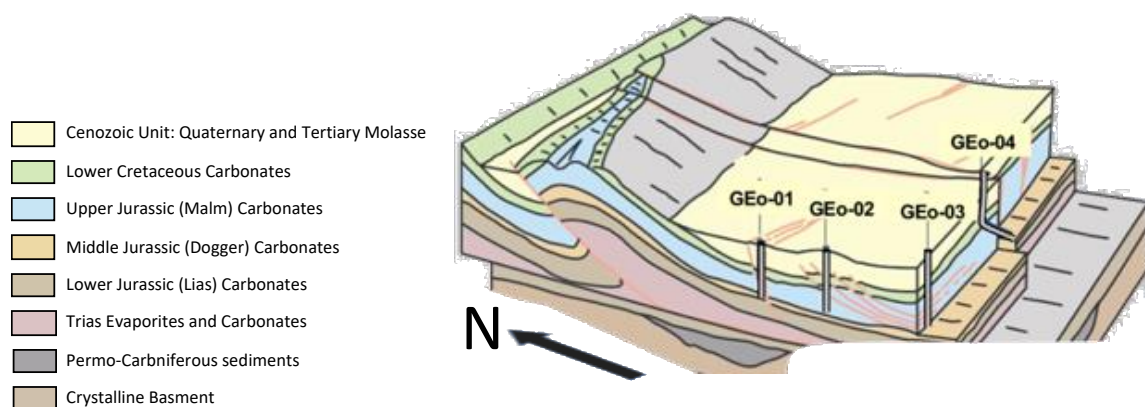
GEO-01 (744m b.g.l.): Strike-slip fault system, E-W oriented
GEO-02 (1100m b.g.l.): Thust and back-thust structures
GEO-03 (1500m b.g.l.): Same as GEO-02 but deeper
GEO-04 (1500m b.g.l.): Directional well in a Strike-slip fault

Figure 2.3.3 Illustration of the local Geology, locations and targets of the planned GEO-series wells (modified from (Nawtratil del Bono, et al., 2019)

GEO-01 well is 744 m deep and drilled into the Cenozoic Units down to 407 MD (Measured Depth) to then enter the Mesozoic carbonates of the Lower Cretaceous unit down to 648 m MD and eventually penetrated the Upper Jurassic carbonates until bottom hole. Artesian fluid flow condition characterizes this well, with a flow rate of 55l/s, 32.4℃ wellhead temperature and 8bars wellhead pressure, representing a very encouraging geothermal resource suitable for heat production and direct uses. Geothermal fluids rise towards the surface along a strike-slip fault structure cutting through the Lower Cretaceous and Upper Jurassic carbonates, being the former responsible of more than 70% of the total mass discharged (Guglielmetti et al., 2020). The natural recharge of the system here is from the Jura Mountain chains and circulation at depth is related to the hydraulic gradient. The faults encountered in the Lower Cretaceous are most likely open faults, laterally confining and vertically promoting localized fluid circulation.

GEO-02 well is 1456 m deep and drilled the same units as GEO-01 reaching the top of the Lower Cretaceous at 769.9m MD. Artesian fluid flow condition characterizes this well, with low flow rate of 0.3-0.6l/s, 18˚C even if the measured bottom hole temperature observed at the end of the drilling operations was

about 55˚C and about 12 bars stabilized wellhead pressure and 8bars. As per GEo-01 the natural recharge of the system is expected to be dominated by meteoric waters infiltrating in the Jura Mountain chains and circulation at depth is related to the hydraulic gradient. The fractures encountered in the Lower Cretaceous and Upper Jurassic are most likely mineralized and tight, preventing large fluid flow in this region. The locations of GEO-01 and GEO-02 were selected according to the optimal compromise between expected subsurface conditions, drill site accessibility, and proximity to potential final users. With particular focus on thermal energy storage, the data collected during prospection phase, drilling operations, and production tests were used to assess whether the regions where GEO-01 and GEO-02 wells were to be drilled are suitable for HT-ATES projects coupling subsurface characterization, surface implementation, and energy systems optimisation.

GEO-01 Well

Well GEO-01 is located approximately 4 km away from the Cheneviers incineration plant and 3 km from the existing district heating network. A 6-month production test program is currently running until April 2019. The well has tapped a flower structure strike-slip fault zone in the Mesozoic units, which has revealed to host groundwater flow at 34 ˚C. Artesian flow conditions at the well-head were observed (50 l/s 12 bars pressure), which could be categorized as a success in terms of potential direct use. The artesian conditions, however, do represent a challenge for aquifer heat storage in the Mesozoic units. Nevertheless, data collected along the complete well section are currently being analysed by the University of Geneva to identify potential heat storage targets and locations in the Molasse sequence. This data is also being used to provide more detailed insights about the regional fault architecture, which can also be of particular interest for HEATSTORE. Such faults can act either as preferential flow channels or permeability barriers potentially affecting the compartmentalization of the reservoir. Details of the GEO-01 stratigraphy (see Table 2.3.2) were used to construct the initial geological model of the area which will then be used for reservoir modelling.

Table 2.3.2 GEO-01 stratigraphic summary

Depth (true vertical depth)	Formation
0-27	**Quaternary:** clastic deposits mostly include limestone and Alpine metamorphic lithology
27-404	**Tertiary Molasse:** The upper part (27-112 meters) is mainly composed by alternations of light brown and greenish clays and marls including gypsum deposits while the lower part (112-335 meters) consist of fine-grained siliciclastic sandstone with carbonate cement. The sandstone composition is mostly made of quartz and subordinately feldspars and black mica. The base of this formation is characterized by abundant coal fragments. The bottom of the Molasse (335-404 meters.) is composed by continental lacustrine limestone alternating with well cemented marls levels.
404-427	**"Urgonian"** unit Autochthonous.
427-512	**Grand Essert Formation / Pierre Jaune de Neuchatel + Marnes d'Hauterives (Hauterivian):** composed by a fine-grained limestone, locally showing fractures filled with calcite, glauconite and pyrite, alternating with marls containing 20-30 % of quartz
512-532	**Vuache Formation (Valenginian):** mostly composed by a bioclastic mudstone-grainstone limestone
532-555	**Chambotte Formation (Valenginian-Barriasian):** light coloured bioclastic and oolithic limestone
555-600	**Vions Formation (Berriasian):** mainly bioclastic fine-grained limestone
600-614	Fault zone within the **Pierre-Chatel Formation (Berriasian):** yellowish bio-detrital limestone alternated.
614-648	**Goldberg Formation (Purbekian Autoctonous – Lower Berriasian):** green marls and brownish fine-grained limestone
648-744.6	**Vouglans Tidalites Formation (Portlandian Autoctonous - Tithonian):** bioclastic limestone with local transitions to oolitic white-reddish limestones

Thonex-01 Well

The Thonex-01 geothermal well was drilled by SIG in 1993 in the Geneva outskirts, as an exploration well to assess tapping a potential geothermal reservoir in the Jurassic fractured limestone at approximately 2500 meters in depth. The aim was to eventually produce hot water to provide it to the local district-heating network. This well represents the only deep borehole located on the Geneva Canton and intercepts both Base Tertiary and Top Upper Malm horizons, which are now potential targets for the geothermal development promoted by SIG and public authorities, in the framework of the Geothermie 2020 program. To attain reasonable flow rate the well was designed to reach deep aquifers in the Jurassic limestone, which were observed to have a porosity of about 8% that can increase up to 25% in case of enhanced fracture conditions due to karstification processes observed in the Humilly-2 well (Geologie-Geophysique, 1979).

Thonex-01 was drilled with a deviated geometry starting from 696 meters (see Figure 2.3.4) having a N35E azimuth and a final 25˚dip, reaching a TVD of 2530 meters (2690 meters MD[4]). The well is cased down to 1790 meters MD. Two main water inflows were observed at approximately 2000 meters depth and at bottom hole. Despite the favourable bottom-hole temperature (88˚C), the well productivity was too low (0.3 l/s) to begin commercial operations.

Prior to drilling 2D reflection seismic campaigns were carried out by CGG in 1980s, and allowed to identification of the base of the Tertiary Molasse sediments and some structural features (Negron, 1987) (Gorin, 1989). Additional high-resolution seismic data were collected in 1992 by the University of Geneva focusing on the detection of brittle structures. This campaign revealed a vertical throw of about 20 millisecond two-way-time (twt), which corresponds to about 30-40 meters. Two additional seismic lines were collected in 2010 to further improve the identification of the faults.
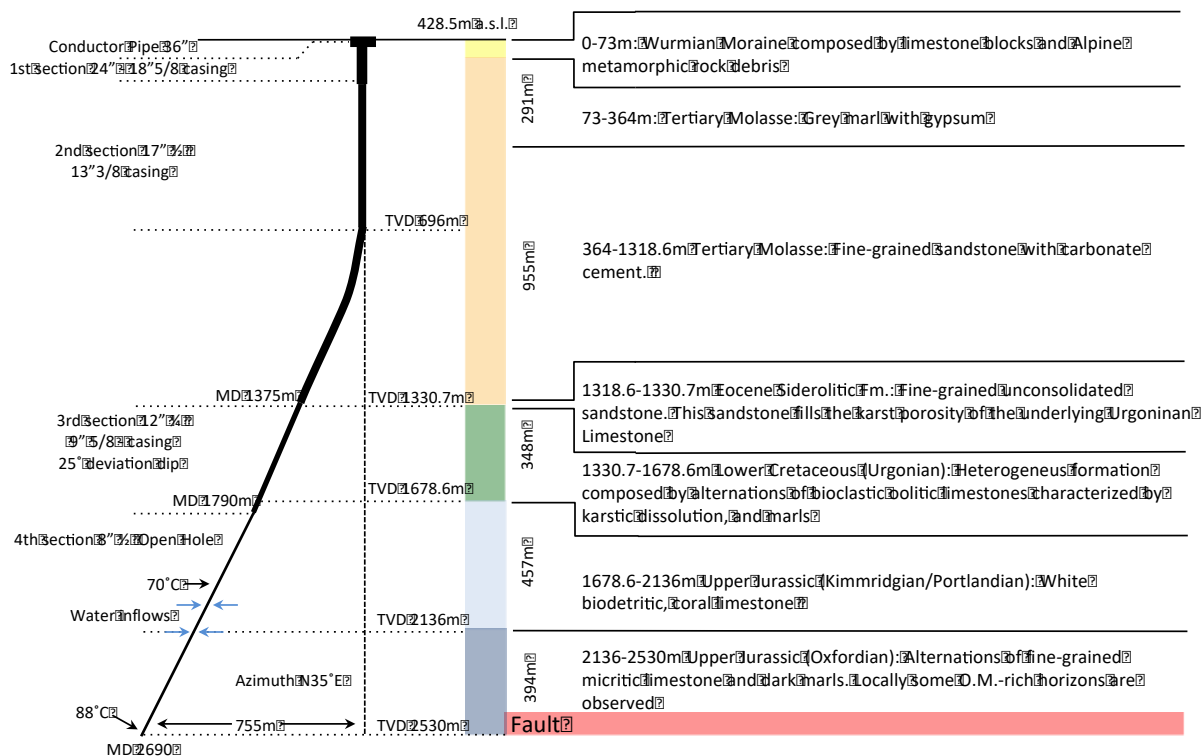

Figure 2.3.4 Thonex-01 well schematic stratigraphy, geometry and completion characteristics (modified from (Jenny, et al., 1995)

---

[4] In contrast to true vertical depth (TVD), measured depth (MD) is the distance from the well head, measured along the well path

In 2008 some maintenance operations were carried out to evaluate the feasibility to reach potential deeper targets. Therefore, the following downhole operations were carried out:

- Acoustic calliper, which revealed some deformation of the well section at different depths, and some damages in the casing. Finally, the section of the well was so reduced below 1120 meters that deeper investigation proved impossible.
- Video inspection was carried out to determine the main cause of the obstructions. The video inspection revealed large amount of scaling across the whole section of the well, which was completely clogged at 1100 meters in depth.
- Geochemical analysis of scaling material revealed a composition being mainly Fe, S and Ca minerals, which are typical for such type of low flow rate geothermal wells.
- Coil tubing well cleaning was finally operated to remove the obstructions across the complete accessible section of the well. These operations resulted in a cleaning of the well down to 1810m in depth.
- Temperature logs were made every 250 meters MD. A temperature of 67˚C was recorded at 1800 meters MD.

The Thonex-01 stratigraphic study was used to construct the initial geological model of the area which was used both for the vertical seismic profile (VSP) feasibility study and the following interpretation of the VSP results. A summary of the encountered formations is presented in Table 2.3.3. The structural analysis based on bore hole logging tool (Geologie-Geophysique & Geoproduction Consultant, 1994) data carried out on the Mesozoic section between 1940-2100 and 2400-2610 meters, highlight the occurrence of both open and closed fractures. The open fractures are generally oriented N65W which corresponds to the direction of the regional tectonic constraints. For these fractures, aperture ranges between 0.03 and 0.3 millimetres. On the other hand, closed fractures are oriented N15W with a general dip of 45 degrees. A high density of fractures is observed at the base of the well (2455.9-2529.7 meters) which has been interpreted as a fault zone.

Table 2.3.3: Thonex-01 stratigraphic summary

Depth (TVD)	Formation
0-73	**Quaternary:** clastic deposits mostly include limestone
73-1318.1	**Tertiary Molasse:** The upper part (73-364 m) is mainly composed by grey marls including gypsum deposits while the lower part (364-1318.6 m TVD b.g.l.) consist of fine-grained siliciclastic sandstone with carbonate cement.
1318.1-1330.7	**Siderolitic**
1330.7-1425.1	**Vallorbe Formation (Fm)** ("Urgonian" unit Autoctonous – Barremian)
1425.1 -1546.9	**Grand Essert Fm / Pierre Jeune de Neuchatel + Marnes d'Hauterives** (Hauterivian) composed by a fine-grained limestone, locally showing fractures filled with calcite, glauconite and pyrite, alternated with marls with 20-30% of quartz content;
1546.9 – 1582.7	**Vuache Fm** (Valenginian): mostly composed by a bioclastic mudstone-grainstone limestone;
1582.7 – 1599.2	**Chambotte Fm** (Valenginian-Barriasian): light coloured bioclastic and oolithic limestone;
1599.2 – 1615.6	**Vions Fm** (Berriasian): mainly fine-grained limestone.
1615.6 – 1654.8	**Pierre-Chatel Fm** (Berriasian): yellowish bio-detrital limestone
1654.8 – 1678.6	**Goldberg Fm** (Purbekian Autoctonous – Lower Berriasian): green marls and brownish fine-grained limestone.
1678.6 - 1822	**Vouglans Tidalites Fm**. (Portlandian Autoctonous - Tithonian): bioclastic limestone with local transitions to oolitic white-reddish limestones .
1822 – 1958.6	**Landaize-Etiolets Fm** (Upper Kimmeridgian): grainstone and wackestone of reef environment.
1958.6 – 2038.6	**Tabalcon Limestone Fm** (Middle Kimmeridgian): fine-grained bio-detrital limestone.
2038.6 – 2136	**Micritic limestone**
2136 - 2389.6	**Cephalopodes and Pseudolithographic Limestone Fm** (Lower Kimmeridgian - Upper Oxfordian): micritic marly light brown limestone alternated with thick marls interval.
2389.6 - 2530	**"Calcaires Lités"** (Upper Oxfordian): marly limestones.

Humilly-2 well

Humilly-2 (HU-2) is an oil and gas exploration well drilled by Société Nationale des Pétroles d'Aquitaine (SNPA) between October 1968 and January 1969. The borehole is located at the centre of the Geneva Basin sensu stricto (s.s.), in the French department of Haute-Savoie, approximately 2.5 kilometres south of the Swiss-French border. It was drilled on top of a small N-S trending anticline structure, originally considered as a hydrocarbon trap. The well total depth (TD) reaches the Carboniferous at 3051 meters MD (or 3047.3 meters TVD). The well borehole diameter starts with 0.63 meters and decreases to 0.216 meters at the bottom. The trajectory was intended to be vertical, however there is a slight deviation towards the west in the deeper half of well section.

The Thonex-01 geothermal well is the closest deep well to HU-2 in the Geneva Basin. The primary target of the well were potential hydrocarbon reservoirs in the Tertiary (Molasse) and Mesozoic units, as well as (in particular) the Triassic units. Although only few hydrocarbon indications were detected, fresh water aquifers were recognised in the upper stratigraphic layers such as the Oligocene USM (i.e. Lower Freshwater Molasse), Eocene sandstones, Lower Cretaceous, and Upper Jurassic units. Since no commercial hydrocarbon volume was available, the well was plugged and abandoned.

The Humilly-2 well can be considered as a reference well because it is located at the centre of the basin, and it penetrates the complete Cenozoic and Mesozoic sedimentary sequence. A variety of well-logging tools were used and several cores were retrieved. Moreover, it provides seismic velocity data used to calibrate seismic models (i.e. interval velocities, check shots). Data from the HU-2 well has been used for calibrating the correlation with other wells considered in this study. Finally, it also provides key petrophysical parameters to perform dynamic modelling.

2.3.3 Modelling approach

For the subsurface modelling a workflow has been defined as follows:

1. Pre-processing: geological and petrophysical parameters retrieved from the available hydrogeological information, geophysical surveys and GEO-01 well data, were used to produce a representatitve simplified 1x1x1 km^3 subsurface model resembling the GEO-01 site. This model allowed performing a sensitivity study of the physical processes and geologic factors influencing a potential ATES system. For this study, variations of operational schemes were not considered.

2. Real geological surfaces (units' interfaces, faults and fracture distribution) may be added to the 3D model to reproduce the more realistic subsurface geometries. However, most simulations reported here have been performed on simplified geometries.

3. Integration of energy system constraints to run predictive models over the life-time of the ATES system. Such scenarios were defined by SIG and UniGe according to the SIG's district heating systems development plan. A version of the models developed for point 1 were used as representation of a subsurface storage, and connected to system modelling to assess compatibility with surface constraints and to optimise the storage potential as a fraction of the waste heat supply and real heat demand. System integration simulations are reported in HEATSTORE's deliverable D3.3 (Allaerts et al., 2021).

2.3.3.1 Computational approach and software

For a detailed review of the computational approaches and software the readers are referred to HEATSTORE's deliverable D2.2 (Tómasdóttir. & Gunnarsson, 2021). Here, we mainly summarize some essential, mostly non-technical steps, in how we approached the model development.

Our aim is to simulate underground fluid flow, heat transport, geomechanics, and chemical reactions to estimate the efficiency, feasibility, and safety of using the Geneva subsurface as an HT-ATES site. For conceptual, mathematical, and computational convenience, we divided our simulation efforts into TH = Thermal-Hydrological and THM = Thermal-Hydrological-Mechanical.

TH simulations focused on (a) assessing thermo-hydrological challenges to heat storage in the complex subsurface of the Geneva Basin and (b) on quantifying overall thermal efficiency plausible-yet-simplified realizations of the underground heterogeneity (i.e. formation layers, faults and fractures) as well as pre-existing hydrological conditions (e.g. ground water flow). TH simulations will also acted as a screening process to determine scenarios to be further simulated by THM models, which in turn focused primarily on

locating and quantifying mechanical-related safety issues (e.g. ground surface deformation and subsurface stresses and strains).

TH Conceptual Model

The TH conceptual model assumes Darcy flow of the fluids and neglects rock structural-mechanic (M) and fluid/rock chemical processes (C), and thus focuses on providing a first basic understanding of plausible fluid flow (H) and heat transfer (T) conditions. It allows modelling of injection of a buoyant compressible percolating fluid that is able to exchange heat with its surroundings via advection and conduction processes. It is, however, not aimed at representing effects such as the thermal expansion of the rock surrounding the fluid, fracture mechanical/chemical sealing/opening, and chemical permeability alteration. To further reduce complexity and aid computational effort, the model also assumes that only one single phase fluid (i.e. water) occupies the totality of the void space available in the rock (i.e. pore space). This results in an averaged rock-fluid bulk material which is the essence of porous media assumptions and also allows for further simplifications such as the assumption of an averaged flow velocity (i.e. Darcy velocity) existing over an arbitrary portion of the domain, the instantaneous thermal equilibrium between fluid and rock, and the subdivision of the heat transport mechanisms (i.e. advective heat transport is performed by the fluid, while conductive heat transport is performed mainly by the rock material, depending on porosity) .

To use an accurate equation of state for water and thus capture any buoyancy effects as well as transient pressure effects (i.e. particularly present during changes in operation modes) as accurately as possible in such a fluid-saturated medium, we also allow fluid density, enthalpy, and heat capacity to be functions of pressure and temperature. This renders the resulting set of partial differential equations (PDEs) with non-linear characteristics.

Considering, for the time being, that the material properties of the porous rock to be isotropic, locally uniform (e.g. to a minimum discrete level of a computational cell), and constant, the governing equations that represent our assumptions are dictated by classic (Bear, 1972) conservation laws of mass (1), momentum (2) (a.k.a. Darcy's Law), and energy (3) + (4), and may thus be expressed by:

$$\frac{\partial(\rho_f \phi)}{\partial t} + \nabla \cdot \left(\rho_f \mathbf{v}\right) + q_{\rho,f} = 0 \tag{1}$$

$$\mathbf{v} = -\frac{k}{\mu}\left(\nabla p - \rho_f \mathbf{g}\right) \tag{2}$$

$$\frac{\partial(\phi \rho_f h_f)}{\partial t} + \nabla \cdot \left(\rho_f h_f \mathbf{v}\right) = 0 \tag{3}$$

$$C_{p,t}\frac{\partial T}{\partial t} - \nabla \cdot (\lambda_t \nabla T) + q_H = 0 \tag{4}$$

where ρ_f is the fluid density, ϕ is the porosity, $\mathbf{v}$ is the Darcy velocity vector, $q_{\rho,f}$ represents fluid mass sources and sinks, p is the fluid pressure, $\boldsymbol{g}$ is gravitational acceleration, k is the permeability, and μ is the fluid viscosity. Equations (3) and (4) conform the law of conservation of energy, by assuming that heat is transported via advection only by the fluid (3), and by conduction via a combination of the rock and the fluid (4). We purposely neglect kinetic, potential, and viscous dissipation effects, h_f is the specific enthalpy of the fluid, $C_{p,t}$ is the non-specific bulk heat capacity, T is the bulk temperature, λ_t is the bulk thermal conductivity, and q_H represents heat sources and sinks. It is important to note that we also opt at this stage to ignore effects of salinity transport, and that such a feature could be added in the near future if expectations of its effect on the system becomes of greater concern.

A numerical discretization approach (e.g. Finite Elements, Finite Volumes) is used on equations (1) to (4), to create a solution algorithm that will provide the necessary discrete solution for our simulations. The conceptual model is aimed at addressing particular scenarios of interest linked to local geological and hydrological conditions. These scenarios include modelling the influence of groundwater flow and geologic heterogeneity (i.e. presence of fractures and faults, reef structures, etc.) on the storage and recovery capabilities of the system.

THM Conceptual Model

A porous media is expected to expand when hot fluid is injected into it. There are two mechanisms that cause this expansion: (1) thermal expansion, and (2) gradients in pore pressure, which act like a body force. These deformations can affect fluid flow by altering the porosity and permeability of the porous media as it deforms. Furthermore, the motion of the solid matrix means that fluid velocity must be considered as a velocity relative to the solid rock. The deformations can also alter the heat transfer by "advecting" the heat with solid grain motion. Finally, the thermal and hydrological systems are also coupled through the equation of state and the fluid motion, which advects heat. The most notable aspect of the mechanical expansion in the context of HT-ATES may be the potential for the ground surface to deform. While ground surface deformation has been studied in other contexts, it has received very little attention in the context of HT-ATES, and it could lead to regulatory and/or geotechnical challenges.

The THM model allows for the simulation of surface deformation and subsurface stresses and strains. Preliminary modelling efforts may focus either on 2D models with several geologic layers and radial coordinates or 3D models with simplified geology. Simulations that abstract some of the site-specific details can offer insights into scenarios that would cause unacceptable levels of surface deformation and/or stress changes. Three-dimensional models with more complex geology and well spacing will be used later in the project. We use a thermo-poro-elastic formulation (Cheng, 2016). Fluid flow is governed by the continuity equation of fluid mass and uses Darcy's equation for fluid flux as shown in equations (1) and (2), but a term accounting for the solid skeleton velocity (i.e. $\mathbf{v}_s$) must be added to capture the mechanical coupling:

$$\frac{\partial(\rho_f\phi)}{\partial t} + \rho_f\phi \cdot \mathbf{v}_s + \nabla \cdot (\rho_f\mathbf{v}) + q_{\rho,f} = 0 \tag{5}$$

Likewise, the heat equation must also add a solid velocity term:

$$\frac{\partial \mathrm{K}}{\partial t} + \mathrm{K}\nabla \cdot \mathbf{v}_s - \nabla \cdot \left(\lambda\nabla T + h_f\rho_f\frac{k}{\mu}(\nabla p - \rho g)\right) + q_H = 0 \tag{6}$$

where $\mathrm{K} = (1-\phi)\rho_r c_r T + \phi\rho_f\epsilon_f$ is the heat energy density, ρ_r is rock density, ϵ_f is the internal energy of the liquid, and c_r is the specific heat capacity of rock. The geomechanics equations are governed by the force equilibrium equations, assume linear elasticity with isotropic materials, and incorporate pore-pressure and thermal stresses into the stress:

$$\frac{\partial \sigma_{ij}}{\partial x_j} = -\mathrm{F}_j \tag{9}$$

$$\sigma_{ij} = \lambda\epsilon\delta_{ij} + 2G\epsilon_{ij} - \alpha P\delta_{ij} - \alpha_d T\delta_{ij} \tag{10}$$

where index notation is used and σ_{ij} represent the components of the stress tensor, ϵ_{ij} represent the components of the strain tensor, ϵ is the volumetric strain, F is a body force, λ and G are Lamé parameters, α is the Biot coefficient, and α_d is the drained thermoelastic effective stress coefficient. The governing equations are coupled through several variables including porosity (which can be altered by mechanical and thermal strains), permeability, effective stress, advective heat flux, solid velocity, and the equation of state.

The assumptions in these governing equations seem to be justified for HT-ATES systems, and they can be re-evaluated after preliminary results. As in the TH model, we assume viscous dissipation has a negligible contribution to the heat equation since large temperature differences are injected and extracted, an assumption which has precedent (Bear & Corapcioglu, 1981). Single-phase, single-component fluid flow is assumed, which neglects the possibility of dissolved salts to alter the fluid density. This is an acceptable assumption since the THM results are focused primarily on mechanical effects, and fluid flow is of secondary interest. Plastic deformations are not accounted for because we assume that plastic (i.e. large) deformations would occur only under unacceptable UTES operating conditions. If plastic deformations are shown to be important, they can be incorporated into simulations later in the project.

2.3.4 Modelling Results

2.3.4.1 TH sensitivity study

Simplified Model

Based on the detailed gelogical study carried out by the University of Geneva (UniGe) and Services Industriels de Genève (SIG) (c.f. Figure 2.3.3), a cube-shaped $1\ km^3$ geological model was constructed by UniGe using the original analysis of a collection of subsurface datasets. The latter included 2-D seismic reflection data, petrophysical data, and well reports from the recently drilled GEO-01 well. The analysis was coupled to the interpretation of data available from the GEOMOL 3D Project (Bayerisches Landesamt für Umwelt, n.d.) (Swiss Federal Office of Topography, n.d.) , where a 3D geological model of the Geneva area can be extracted. All horizons were initially considered as horizontal surfaces, simplifying structures in preparation for simulation work, however a dip angle of 15º was introduced in the simulation scenarios to include its possible effects on the thermal efficiency.

While keeping the supplied material properties in mind, we have further simplified the model geometry to the basic necessary elements for an ATES, consisting of a single permeable aquifer rock layer confined between two layers with lower permeability and porosity (see Figure 2.3.5). This characteristic and idealized configuration tends to prevent heat and fluid loss, as well as heat contamination to the surroundings (Dincer & Rosen, 2011), and its simplification was assumed sufficient for a first design iteration given the relatively large amount of simulations needed. As part of one of the possible variants, we have also introduced a model containing a 15° dip angle (see Figure 2.3.5c).
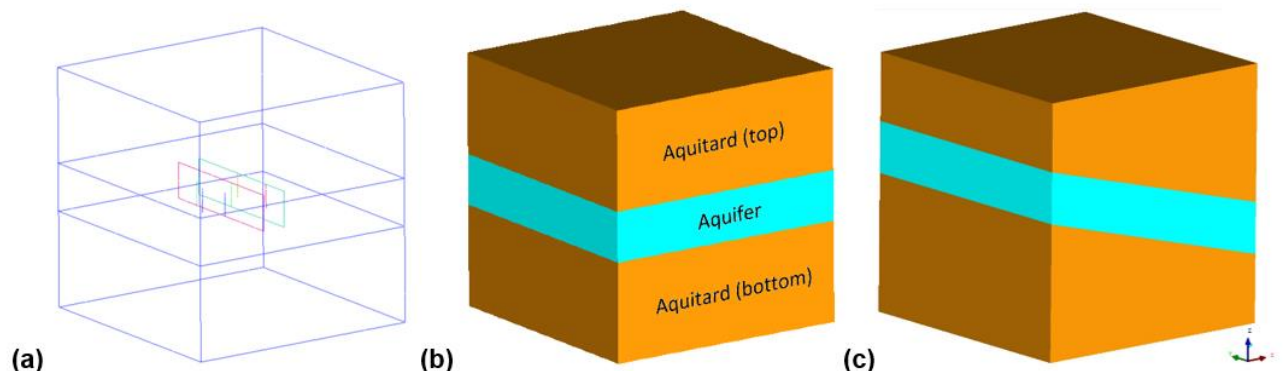

Figure 2.3.5 Geometrical/Geological model representing the basic elements of an ATES, depicting (a) possible well and fracture locations, (b) a flat version of the model, and (c) a version of the model possessing an aquifer with a 15º angle of dip.

Analysis of 2D reflection seismic data has revealed a considerable presence of fault corridors in the studied area, and since their role is still uncertain (Rousillon, 2018) they could be acting as groundwater channels, or have become impermeable obstacles and compartmentalized target aquifers. Basing ourselves on an initial groundwater measurement carried out at the well GEO-01 of 20 [m/yr] and measured values of permeability, we have chosen to take a moderately conservative approach in our groundwater velocity value assumptions (i.e. 2 [m/yr]).

The main activity of the TH studies comprised a sensitivity study of the impact of different geologic and physical effects on HT-ATES exergy efficiency in variants of the idealized geometry mentioned above. The study was published as a contribution to the World Geothermal Congress 2020+1 and the main points are summarized in this section.

The following factors affecting efficiency that were addressed:

- Buoyancy: How does aquifer permeability, aquifer thickness, and dip affect efficiency?
- Groundwater flow: How significant is the heat-signature drift?

- Fractures: Will faults, fractures, and other features redirect groundwater flow and/or cause significant energy leaks?
- Aquifer thickness: How much heat is lost to the confining aquitards, and what are the effects on efficiency and environmental impact? How important are screen lengths?
- Well pattern: Are there significant advantages to using a particular pattern?
- Combined: Considering equal amounts of injected and produced volumes, what are the combined effects of all these parameters on the discharged temperature?

Based on these topics, we developed a matrix of geologically-based simulation scenarios. We narrowed the scope of the resulting combinatorial problem by performing an analysis making simplifying assumptions, using key design factors, and fundamental operational constraints and insight provided by our project partners (de Oliveira, et al., 2017). Each scenario consists in turn of a group of simulation cases (i.e. sub-scenarios), that collectively allow addressing at least one of the fundamental questions. The parameters that may vary within each case include the following:

- Aquifer permeability k and thickness L, and dip.
- Groundwater flow (vgw).
- Number of auxiliary wells and screen length (L/2).
- Presence of fractures in two locations: with respect to groundwater flow, upwind and downwind of the storing injector well.

For clarity and reducing the number of simulations to a manageable volume, the following variations were not included:

- Volumes, rates, water temperature and/or amount of energy injected.
- Charge, discharge, and storage periods as well as the number of cycles.
- Solid thermal material properties (i.e. specific heat capacity and thermal conductivity)
- Aquifer depth.

Material and groundwater flow parameters obtained from the geological interpretations and measurements were provided by UniGe and SIG to be used in the simplified model for the simulations. A summary of the values used, including permeability and thickness values related for key variants is presented in Table 2.

Due to the geologic setting, it is likely that aquifers within the studied area are fractured and offset. The surrounding topography, major thrust and strike-slip faults, and the fact that throughout the the Cenozoic interval the most important faults often present themselves in a flower structure (Charollais, et al., 2007) (Angelillo, 1987), make a fracture/faulted setting very likely. Furthermore, the planned a prospective GEO-02 well is scheduled to reach 1100 [m] in depth, drilling into a reef complex associated to a sequence of thrust faults. Although smaller-scale fractures and cracks may improve the permeability of the aquifer formations, the evident presence of larger ones increases the need to consider fractures and faults explicitly in our simulation models.

As shown in Table 2.3.4, smaller scale fractures and cracks are taken into accound via an "effective" matrix porosity and permeability in the aquifer region. In terms of scenario variants, the modelled option F0 denotes a model without any other explicit fractures. Using the ground water flow direction as a reference, a single fracture is located 50 [m] in front or Upwind of GW_1 (i.e. the main charging well) for variant FU , while an identical fracture set 50 [m] behind or Downwind of GW_1 for variant FD. These last two cases implement a single fracture as a zone of specific assumed width and properties (also shown in Table 2.3.4) and therefore while porosity is high, it is not equal to 1, which would be the case for a perfectly void fracture.

Table 2.3.4 Summary rock material parameters

Parameter	Units	Aquitard (top)	Aquifer	Aquitard (bottom)
Density (ρ_r)	[kg/m³]	2450	2450	2680
Permeability (k) (original matrix)	[m²]	10^{-17}	10^{-15}	10^{-17}
Permeability K13 (k) (fractured, effective)	[m²]	10^{-17}	10^{-13}	10^{-17}
Permeability 5K13 (k) (fractured, effective)	[m²]	10^{-17}	$5 \cdot 10^{-13}$	10^{-17}
Permeability K12 (k) (fractured, effective)	[m²]	10^{-17}	10^{-12}	10^{-17}
Porosity (ϕ) (matrix, effective)	[-]	0.01	0.2	0.01
Permeability (k) (fracture, effective)	[m²]	N/A	10^{-11}	N/A
Porosity (ϕ) (fracture, effective)	[-]	N/A	0.5	N/A
Fracture thickness	[m]	N/A	0.1	N/A
Specific Heat Capacity ($c_{p,r}$)	[J/(Kg·K)]	860.2	832.9	849.9
Thermal Conductivity λ_r (λ_r)	[W/(m·K)]	2.275	2.806	2.692
Thickness L200 (L)	[m]	400	200	400
Thickness L300 (L)	[m]	350	300	350
Thickness L400 (L)	[m]	200	400	400
Groundwater velocity (v_{gw}) (assumed)	[m/yr]	N/A	2	N/A

Operational design

The HT-ATES system will be integrated into Geneva's district heating network through the Les Cheneviers incineration plant, and thus some reasonably accurate input can be obtained to run predictive models over its projected lifetime. Thermal power output from the waste incineration plant, demand, and temporal load/unload cycles over a one year time frame were provided by UniGe and SIG based on SIG's district heating systems development plan (Services Industriels de Genève, 2019). With this information we obtained the necessary parameters for all the simulation configurations needed.

Table 2.3.5: Summary of basic input parameters.

Total Energy to Inject (E_{GWh}) (per year cycle)	50 [GWh]
Temperature of injection (T_i)	90 [℃]
Period of injection/charge (t_c)	120 [days]
Period of production/discharge (t_d)	120 [days]
Period of storage (2) ($t_{s,1}$, $t_{s,2}$)	60 [days], 65.25 [days]
Volume injected (V_i)	622080 [m³]
HT-ATES life time	15 [yr]

The basic operational yearly cycle strategy consists of a period of continuous charge for 120 [days], followed by storage for 60 [days], discharge for 120 [days], and further storage for 65.25 [days]. A basic average volumetric flow rate q_V can be determined by first calculating the total volume of water V_i at T_i necessary to deliver E_{GWh}, and dividing it by the charge time period,

$$V_i = \frac{E_{GWh}}{\rho_f c_{p,f} \Delta T} \qquad q_V = \frac{V_i}{t_c} \left[\frac{\text{m}^3}{\text{s}}\right] \tag{7}$$

Where $c_{p,f}$ and ρ_f are the isobaric specific heat and density of the fluid. The temperature change ΔT in this case is the difference between T_i and the original water temperature before it was heated at the waste incinerator plant (ΔT is assumed 70 [°C]). It is useful then to estimate the hydraulic r_w and thermal r_{th} radii of an ideal cylinder of aquifer rock (Bloemendal & Hartog, 2018), given by

$$\pi r_w^2 L \phi = V_i \rightarrow r_w = \sqrt{\frac{V_i}{\pi L \phi}} \qquad r_{th} = \sqrt{V_i \frac{c_{p,f}\rho_f}{\pi L \left(c_{p,f}\rho_f \phi + c_{p,r}\rho_r (1 - \phi)\right)}} \tag{8}$$

Given the porosity ϕ, specific heat capacity $c_{p,r}$ and density ρ_r provided for the aquifer rock, equations shown in (2) can be plotted together as a function of the aquifer thickness L.
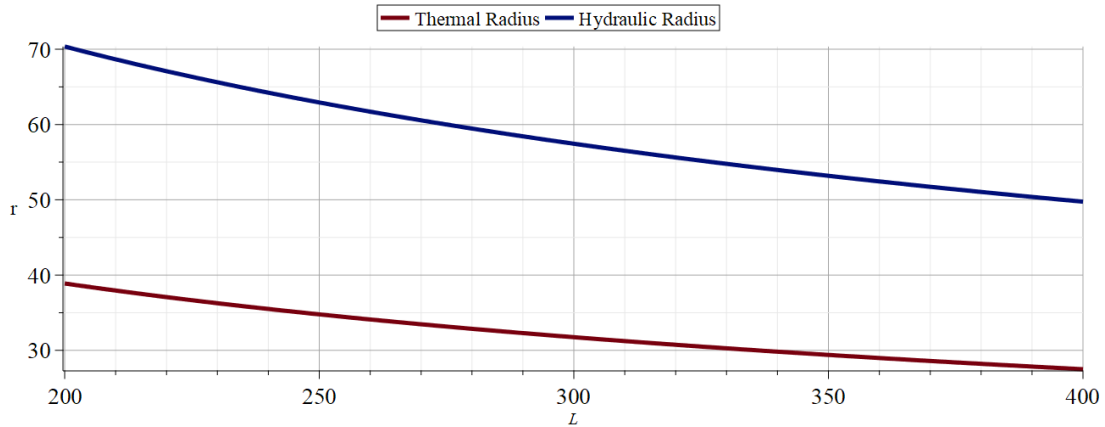
Figure 2.3.6 Hydraulic (red) and thermal (blue) radii as a function of aquifer thickness (L)

Based on Figure 2.3.6, to prevent the thermal front from reaching the auxiliary wells (Ganguly & Mohan Kumar, 2015), and assuming the possibility of a single, a doublet, and a 5-spot well strategy, a basic table of essential simulation input parameters was developed and is presented in Table 2.3.6. Recommendations for well spacing in the literature vary between a single thermal radius r_{th} and three thermal radii, and consequently an intermediate value was chosen.

Table 2.3.6: Summary well-strategy-based simulation configuration parameters.

Scenario variant code	Radial distance from centre well [m]	Main well flow rate [m³/s] inj/prod	Aux. well flow rate [m³/s] inj/prod
single	N/A	0.06/-0.06	N/A
doublet	141	0.06/-0.06	0.06/-0.06
5spot	141	0.06/-0.06	0.015/-0.015

A basic well design and the corresponding well names to be used in each scenario variant corresponding to well strategy, can be observed in Figure 2.3.7. The 'single' case assumes that an auxiliary well exists to

satisfy environmental re-injection requirements, but it is sufficiently far from the main well so that its effects can be neglected. For any particular simulation, all wells involved are fully vertical and have the same screen length, which is vertically centered on the aquifer layer. The screen length was designed as one half of the aquifer thickness.
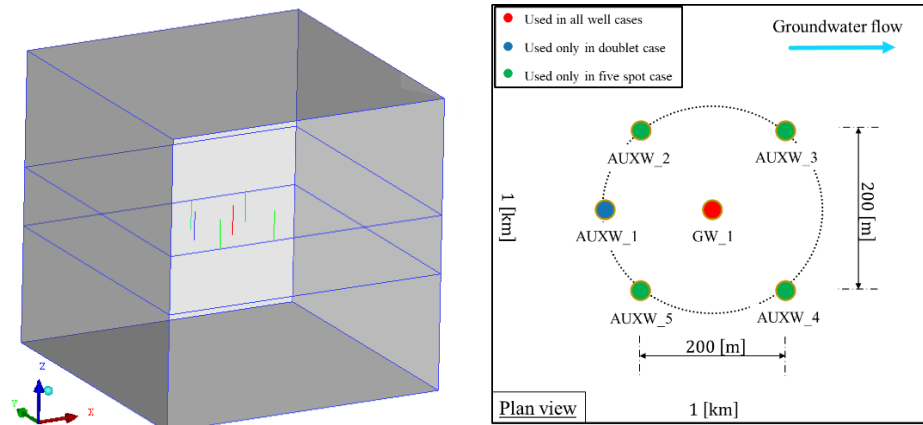

Figure 2.3.8 Well pattern (a) 3D design, and (b) plan view of their locations and names.

Essential Conditions

To achieve the intial groundwater flow conditions we must solve a steady state problem based on equations (1) and (4). To achieve this we define a reference surface condition of temperature and pressure at depth 0 [m] . Values for lateral hydrostatic boundary conditions are obtained, and an extra pressure based on the groundwater hydraulic head is added only to one of the boundaries (i.e the inlet) where the negative normal matches the groundwater flow direction. The boundary conditions are then fixed throughout the transient part of the simulation. A summary of the applied conditions is provided in Table 2.3.7.

Table 2.3.7: Summary of essential conditions applied during initialization and transient simulation. Unless specified, boundary locations not mentioned are assumed to be set to the *Natural* condiction for a particular variable.

Variable	Type (location)	Value or function	Applied During	Comment
Pressure	Dirichlet (top boundary)	101325 [Pa]	Initialization	All other boundaries set to *natural* conditions (no-flow)
Pressure	Dirichlet (inlet and outlet boundaries)	Hydrostatic	Initialization and Simulation	In the YGW case, it includes groundwater pressure at the inlet boundary.
Temperature	Dirichlet (top boundary)	10 ºC	Initialization and transient simulation	Constant surface temperature condition.
Temperature	Neumann (bottom boundary)	Heatflux 0.064 [W/m²]	Initialization and transient simulation	Heat flux is converted to a temperature gradient via the fluid and rock thermal conductivity values adjacent to the boundary.
Enthalpy and Fluid Density	Inflow/Outflow (inlet and outlet boundaries)	Functions of *p* and *T*, depending on flow direction and upwind values	Transient simulation	Allows entry and exit of mass and enthalpy on boundaries of the domain without the need to set a *Dirichlet* condition for outflux.

Results and Discussion

We obtained results for 324 simulations produced by the combinations of simulation variants. To assess the effects of the varying parameters on the cyclic efficiency using this relatively large volume of data, we applied an exergetic analysis for the HT-ATES expected life time. This type of analysis is favorable with respect to an energetic basis, since it accounts for the temperature at which water is produced from the aquifer (Dincer & Rosen, 2011). For reference, the energy efficiency η_{En} of an ATES system is given by

$$\eta_{En} = \frac{\int_{t_d} \left\{ \int_{\Omega_{GW\_1}} q_{h,out} d\Omega \right\} dt}{\int_{t_c} \left\{ \int_{\Omega_{GW\_1}} q_{h,in} d\Omega \right\} dt} \tag{9}$$

where Ω_{GW_1} is the volume immediately surrounding the well, $q_{h,in}$ and $q_{h,out}$ are the only enthalpic sources and sinks present within Ω_{GW_1} during charging and discharging, respectively, t_c is the charging time, and t_d is the discharge time. Exergy is a measure of the theoretical maximum amount of work that could be extracted from the flow, and is comparable to Carnot's efficiency of a reversible heat engine. Exergy efficiency η_{Ex} may be calculated in a similar fashion to η_{En},

$$\eta_{Ex} = \frac{\int_{t_d} \left\{ \int_{\Omega_{GW\_1}} q_{h,out} \left(1 - \frac{T_{ref}}{T}\right) d\Omega \right\} dt}{\int_{t_c} \left\{ \int_{\Omega_{GW\_1}} q_{h,in} \left(1 - \frac{T_{ref}}{T_i}\right) d\Omega \right\} dt} \tag{10}$$

where T is the temperature measured at the well, T_i is the injection temperature, T_{ref} is a reference temperature (i.e. both in Kelvin in this case), such as the original environmental temperature of the aquifer before its use as an ATES, or a threshold temperature below which the exergy input and output is assumed not useful to produce work. Exergy efficiency tends to be lower than energy efficiency in ATES systems, given that as T approaches T_{ref} the exergy contribution approaches zero. If $T < T_{ref}$ at any point in time, the amount of exergy for that period is negative. As a result, the amount of energy input, stored, and discharged from the ATES will only be *useful*, or of good enough *quality*, as long as the temperature of the flow can be maintained above T_{ref}. Over subsequent cycles and theoretically depending on the discharge time and overall length of each cycle, the exergy lost to the aquifer surroundings results in an increase of the temperature near the well at the end of each cycle, thus increasing η_{En} and η_{Ex} over time as shown in Figure 2.3.9.
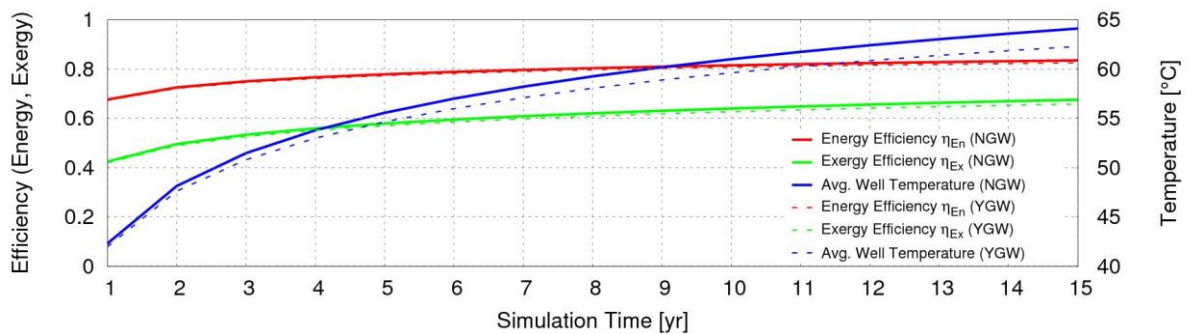

Figure 2.3.9 Energy and Exergy efficiency variation with time for the expected ATES lifetime comparing a case with and without groundwater flow: 'L400_K13_5spot_NGW_F0_FLAT', and 'L400_K13_5spot_YGW_F0_FLAT'. The right-hand axis depicts temperature measurement at well GW_1 for the end of each cycle.

Given our observation that efficiencies increase monotonically over time, we found it practical to use the values for the last cycle as a measure of performance for our analyses. A summary exergy efficiency values at the end of life of the ATES for each of 324 simulations is presented in Figure 2.3.10, using a reference temperature T_{ref} of 50 [°C] or 323.15 [K].
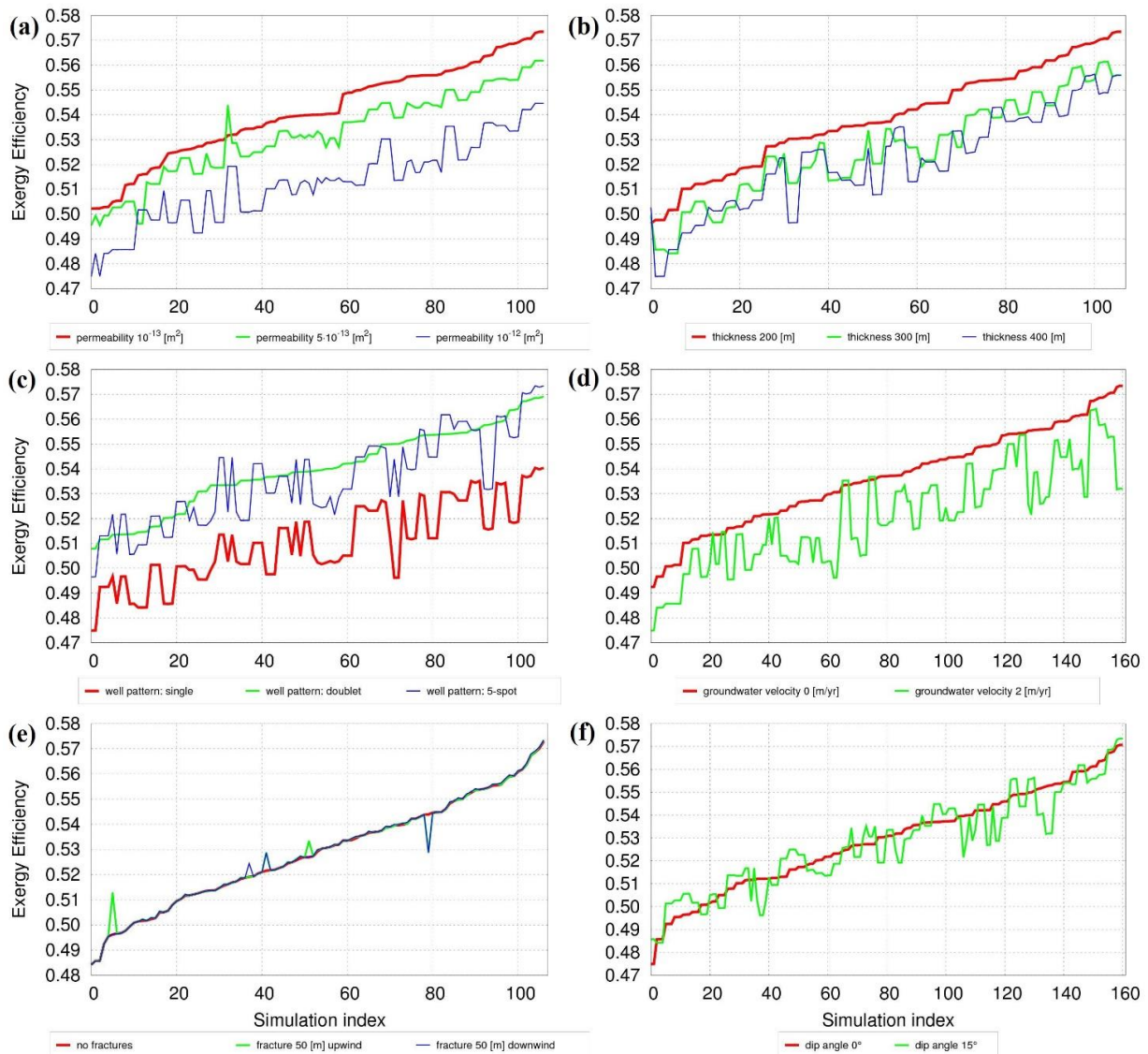
Figure 2.3.10 Exergy efficiency measured at the end of the ATES lifetime. Each graph represents a particular horizontal ordering of the same set of results, sorted in increasing exergy efficiency. The simulation index is an arbitrary number guide pointing to a subset of otherwise identical simulations that only differ by one particular parameter: (a) aquifer permeability, (b) aquifer thickness, (c) well pattern, (d) groundwater velocity, (e) fracture configuration, and (f) aquifer dip angle.

Aquifer Permeability and Thickness

Results shown in Figure 2.3.10 (a) display a significant performance increase with decreasing permeability, where improvements range between 2% to 4%. This can be attributed to the fact that if we assume equal screen length (*L/2*), flow velocities to be similar due to equal injection rates, and that injection pressures are not a mechanical issue, then the lower permeability allows for a better containment of energy during the storage periods. Higher permeabilities allow the heat signature to be more mobile and particularly subjected to drift due to buoyancy and groundwater effects. Buoyancy effects can be observed in further detail through Figure 2.3.11 (a), (d), and (g), where three simulations differ only with respect to aquifer permeability.

For the thicknesses considered in this study, Figure 2.3.10 (b) shows a consistent increase of exergy efficiency with decreasing thickness, where improvements can range from 0.5% to 3%. If we once more consider uniform injection rates across simulations and a screen length of *L/2*, a thicker aquifer decreases

the injection flow rate per meter of screen length and thus the necessary injection pressure. Nevertheless, it also decreases the thermal radius r_{th} and thus shifts the location of the heat loss from a vertical one into the confining layers to a lateral one into the aquifer surroundings (see Figure 2.3.11 (a), (b), and (c)). More heat may thus be lost due to both conduction and convection within the aquifer, as can be noticed in Figure 2.3.11 (i).

The case of permeability and thickness highlights a main issue with ATES systems in which the optimal condition for flow where less injection pressure is needed for the same injection rate, conflicts with the optimal conditions for energy containment.
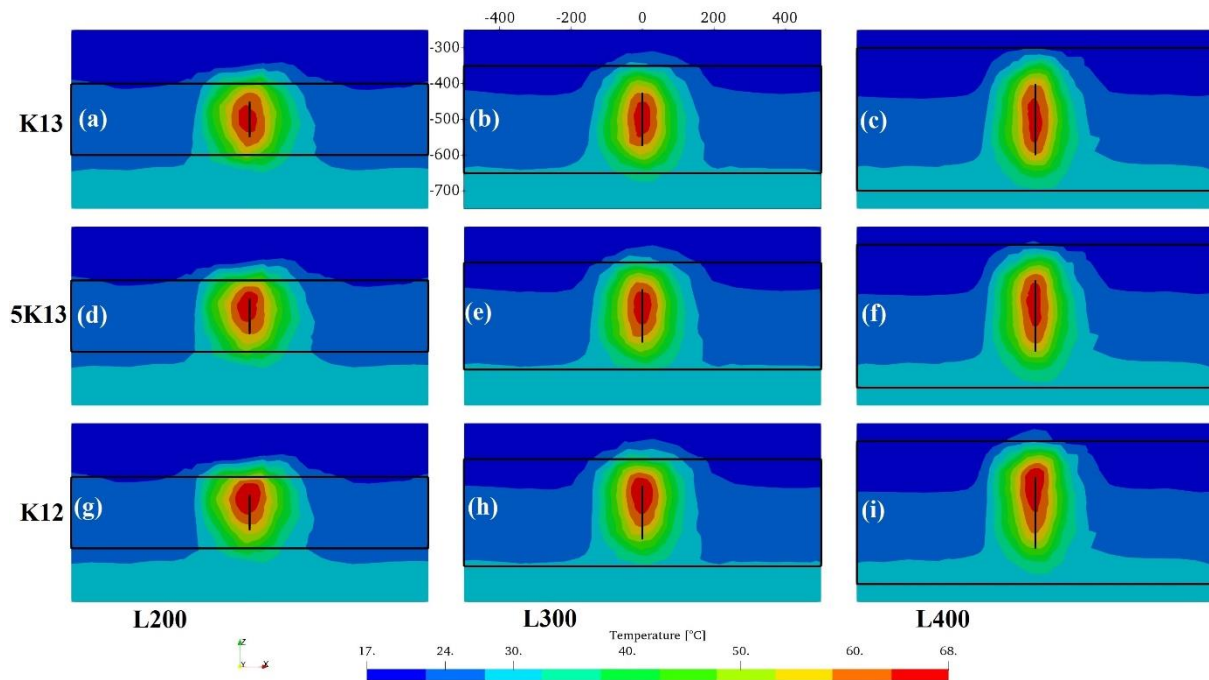
Figure 2.3.11 Temperature plots through the middle x-z plane (i.e. vertical) of the domain for 9 simulations with no inclination (FLAT), no groundwater flow (NGW), equal well pattern (single), and no fractures (F0), at the end of year 15 depicting the effects of permeability and thickness on ATES performance. Row-wise, K13 (a,b,c), 5K13 (d,e,f), and K12(g,h,i) permeabilities have been applied to the top, middle and bottom rows respectively, while column-wise, L200 (a,d,g), L300 (b,e,h), and L400 (c,f,i) have been applied to the left, middle and right columns of simulations, respectively. The vertical domain has been trimmed up to between -250 and -750 [m].

Well Pattern and Groundwater flow (single, doublet, 5spot, NGW, YGW)

Our results show that presence and proximity of auxiliary wells is essential to the performance of an ATES system. Figure 2.3.10(c) shows that the single well pattern, which also models the case for which auxiliary wells are markedly far away to provide pressure support, is consistently outperformed by the doublet and 5-spot patterns. In turn, the 5-spot pattern outperforms the doublet somewhat marginally in only some of the cases. From a cost-effectiveness point of view, the doublet pattern appears to be superior. Snapshots of the simulation results using each pattern can be observed in the columns of Figure 2.3.12.

As shown in Figure 2.3.10(d) performance of the ATES is affected negatively in general, and by up to 4% in some cases due to introduction of groundwater flow at 2 [m/yr]. This is mainly caused by the heat signature tending to drift away from the wells due to advective transport by the groundwater current, as can be observed comparing the two rows of simulations in Figure 2.3.12.

Fracture Configuration and Aquifer Dip Angle (F0, FU, FD, FLAT, INCL)

Fracture configurations chosen for this study show negligible effects on efficiency, as evidenced by the frequently overlapping curves in Figure 2.3.10 (e), even though the fractures are within 50 [m] of the GW_1
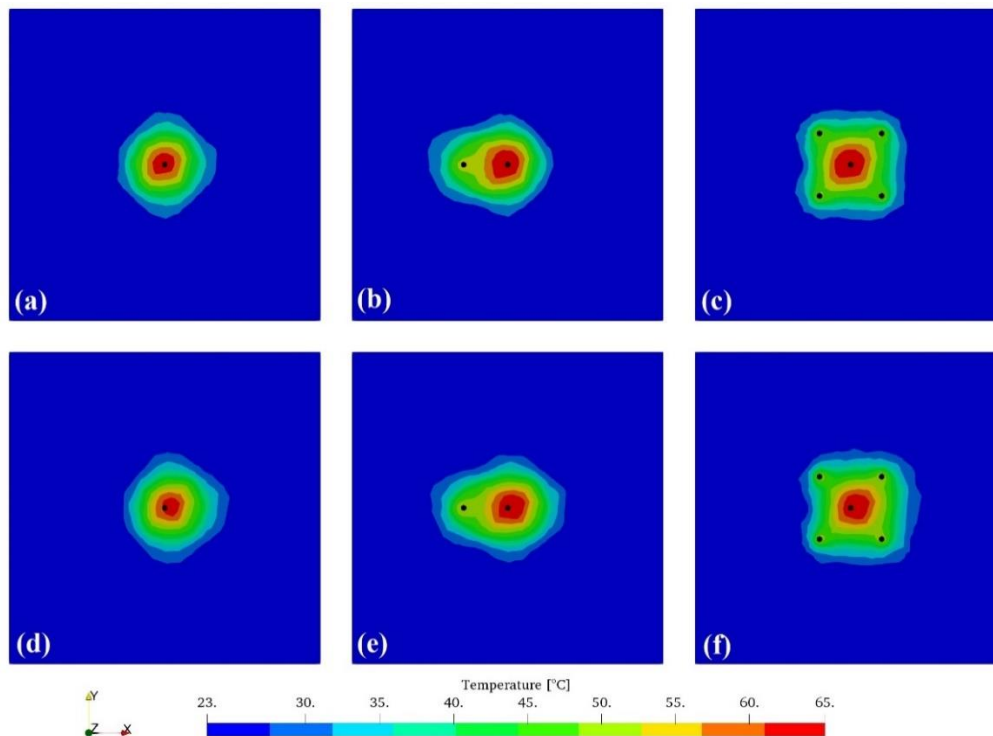
Figure 2.3.12 Well pattern and groundwater effects on the temperature signature at the end of the ATES lifetime in a full-domain middle x-y planar cross section for 6 simulations with no inclination (FLAT), no fractures (F0), equal permeability (K12), and equal thickness (L200). Row-wise, NGW (a,b,c), and YGW (d,e,f), groundwater conditions have been applied to the top, and bottom rows respectively, while column-wise, single (a,d), doublet (b,e), and 5spot (c,f) have been applied to the left, middle and right columns of simulations, respectively.

and auxiliary wells. Our initial assessment points towards the fracture permeability and thickness being considered low and the fractures not being close enough to GW_1 or any of the auxiliary wells. This result warrants further study of fracture configurations to be tested, most likely in a separate form due to the practically limitless number of realizations possible.

Some sensitivity to aquifer dip angle does appear to exist, as can be observed in Figure 2.3.10 (f). Nevertheless, a clear effect cannot be established without a further, and more detailed study. Sensitivity might be higher for aquifers that are thinner than 200 [m], which is the lowest value used in this study.

Conclusions

We have carried out a numerical study of various HT-ATES system realizations based on parameters of aquifer permeability, aquifer thickness, well pattern, groundwater conditions, dip angle, and fracture configurations. By simplifying an originally complex geological situation, we obtained a series of scenarios aimed at a fundamental understanding of how ATES systems respond to their settings and surroundings, and how to best design them. Considering the geology, material properties, fluid properties, and industry-based operational conditions we have also investigated the plausibility storing hot water and recovering it at the maximum temperature possible via an exergetic analysis of a large number of simulations.

Our study further confirms some observations that have already been made in the literature, particularly with respect to groundwater drift and buoyancy effects present in high permeability aquifers. We have also observed that when active, auxiliary wells help mitigate pressure-peak related effects, improve the thermal front sweep, and also provide some measure of shielding against the drift due to the flow of groundwater.

In particular, we observed that although a permeability design sweet-spot could be numerically found for a particular geologic/geometric configuration, the design process is rather driven by the geo-availability in the

prospective site, thus highlighting the importance of a thorough and continued (hydro-)geological study. In a similar light, lower aquifer thicknesses seem to be a favorable configuration, although to inject an equal amount of energy through a water volume rate at the same temperature, higher injection pressures are required which may impose mechanical limitations. Furthermore, particularly in terms of simulations when flow-rate values are equivalent, permeabilities do impose a numerical limitation since resulting injection and production pressure values can be unrealistically high and low, respectively. Further work should be carried out in expanding this study, particularly to better contextualize the geological configurations with particular emphasis on fractures and faults, analyze the effects of aquifer depth, and assess the influence of surface temperature conditions.
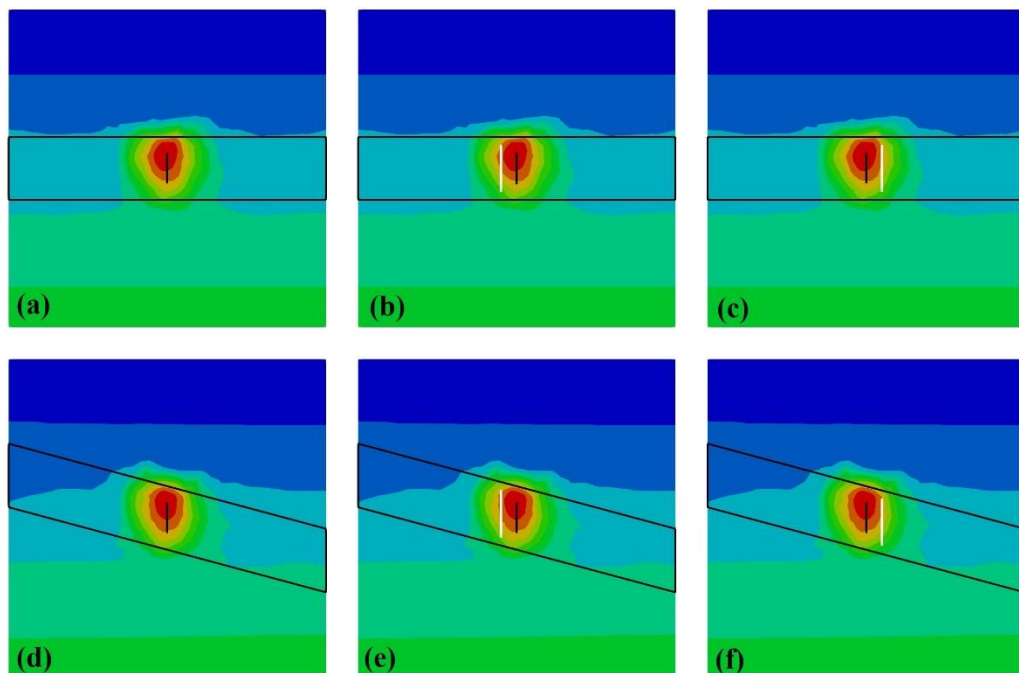
Figure 2.3.13 Fracture configuration and aquifer dip angle effects on the temperature signature at the end of the ATES lifetime in a full-domain middle x-z planar (i.e. vertical) cross section for 6 simulations with equal permeability (K12), equal thickness (L200), equal well pattern (single), and no groundwater flow (NGW). Row-wise, FLAT (a,b,c), and INCL (d,e,f), diap angle conditions have been applied to the top, and bottom rows respectively, while column-wise, F0 (a,d), FU (b,e), and FD (c,f) fracture configurations have been applied to the left, middle and right columns of simulations, respectively. Well GW_1 and aquifer perimeter are demarcated by black lines, while fractures are shown as white lines.

2.3.4.2 THM Modelling

THM and HM modelling were carried out by ETHZ with the goal to predict the potential ground deformation effects associated with repeated seasonal cycles on injection and extraction. A porous medium is expected to expand when hot fluid is injected into it. There are two mechanisms that cause this expansion: (1) thermal expansion, and (2) gradients in pore pressure, which act like a body force. These deformations can affect fluid flow by altering the porosity and permeability of the porous media as it deforms. Furthermore, the motion of the solid matrix means that fluid velocity must be considered as a velocity relative to the solid rock. The deformations can also alter the heat transfer by "advecting" the heat with solid grain motion. Finally, the thermal and hydrological systems are also coupled through the equation of state and the fluid motion, which advects heat. The most notable aspect of the mechanical expansion in the context of HT-ATES may be the potential for the ground surface to deform. While ground surface deformation has been studied in other contexts, it has received very little attention in the context of HT- ATES, and it could lead to regulatory and/or geotechnical challenges.

In early work (e.g. Birdsell and Saar 2020), we established that an auxiliary well is important to balance pore pressure within the reservoir, which reduces HM deformation and allows for higher flow rates. This is consistent with the design of many LT-ATES systems and with results from the hydro-thermal modelling within HEATSTORE. Therefore, all our predictive models used an injection-extraction doublet pair.

We explored two aspects of ground deformation at the Geneva wells using HM and THM models. First, we modelled ground deformation during the pumping test at GEO-01 and compare to measurements from Work Package 5. Secondly, we performed predictive simulations of the potential ground deformation resulting from HT-ATES to explore the question: what ground deformation could we expect if GEO-01 or GEO-02 were used as one well in an HT-ATES doublet? For the pumping test, we restricted our simulations to HM because changes in temperature were not expected to be significant. For the predictive modelling of deformation during HT-ATES operations, we performed both HM and THM simulations. In all cases, we added as much realism from the Geneva-area geology and energy systems as possible, while balancing complexity with enough simplicity to efficiently run and interpret the models.

Subsidence during the GEO-01 pumping test

There are two goals for the hydro-mechanical (HM) modelling of the GEO-01 pumping test. Firstly, the HM modelling is used to understand potential for ground subsidence during the pumping test. This includes investigating the sensitivity of hydrologic and mechanical parameters on ground subsidence. Secondly, by comparing modelled deformation to GPS deformation data, we are able to infer a lower bound on the static, field-scale Young's modulus of the GEO-01 site.

Figure 2.3.14 shows the predicted ground subsidence versus time for several permeability scenarios. For all permeabilities, the magnitude of the subsidence increases as the pumping test progresses. Smaller permeabilities result in a greater predicted subsidence. For example after 60 days, the predicted subsidence is <0.1 cm for a permeability of 6×10^{-13} m^2, whereas subsidence is >1.3 cm for permeability of 10^{-13} m^2. For the range of permeability observed at GEo-01 (i.e., 10^{-14}-10^{-13} m^2), the subsidence is relatively insensitive to the permeability.
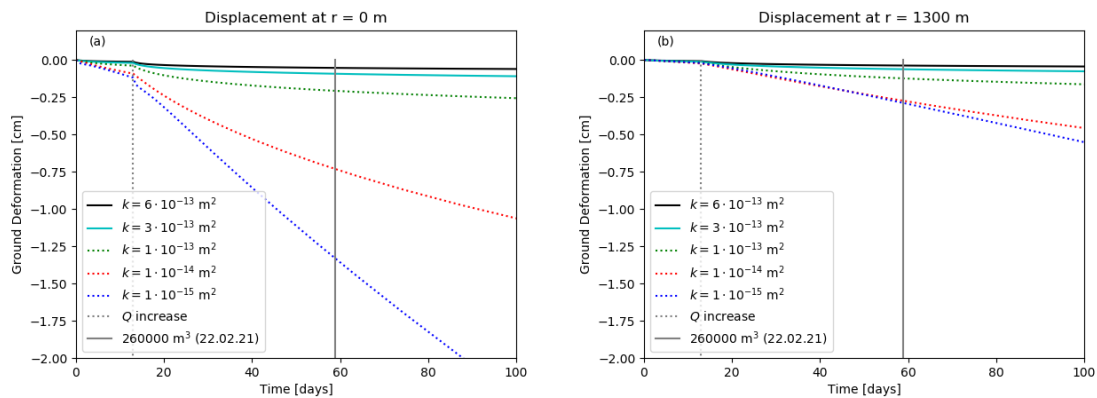
Figure 2.3.14 - The effect of permeability on subsidence at the locations of GPS monitoring stations: (a) at the well and (b) 1300 m away from the well. Black and teal solid curves represent the range of permeability from the GEO-01 pumping test, while dotted lines represent hypothetical, lower-permeability scenarios.

Figure 2.3.15 shows subsidence from two sources: (a) GPS monitoring near GEO-01 from Nicolas Houlié Geologie GmbH and SIG and (b) the HM numerical model. There is not a clear trend of subsidence (or uplift) in the GPS data. The ground deformation was both positive (upwards) and negative (downwards), depending on the time and the GPS station. For the most part, the magnitude of deformation was less than the size of the error bars, so we cannot interpret any significant deformation from the GPS data. In contrast, the numerical model shows a clear trend of subsidence that increases with increasing time. A sensitivity analysis was performed on the Young's modulus, and smaller Young's modulus corresponds to a larger magnitude of subsidence. This makes intuitive sense because Young's modulus is a measure of the strength of the rock, and a weaker rock will deform more under the same pressure change.

Since the modelled ground deformation is sensitive to the employed Young's modulus, it is important to have a good estimate of the Young's modulus. There are two aspects of estimating Young's modulus that need to be considered. First, the Young's modulus needs to represent the quasi-static physics of poroelasticity, rather than the dynamic physics of seismic waves. Second, the Young's modulus needs to reflect the field-scale rock deformation. At this scale, it is computationally difficult to account for mechanical heterogeneity, and it is useful to upscale mechanical properties that account for the stronger (in-tact rock) and weaker (fractures, faults, and joints) portions of the subsurface. While some effort has been made to upscale mechanical properties (Khajeh, Chalaturnyk, & Bosivert, 2012), there are still not well-established ways of upscaling to our knowledge.

We use two ways to estimate the field-scale Young's modulus for the predictive simulations in Sec. 2. The first estimate comes from seismic data, which gives the dynamic Young's modulus (Koumrouyan, 2019). However, the dynamic modulus must be converted to a static Young's modulus according to a heuristic correlation, which introduces some uncertainty (Eissa & Kazi, 1988). This seismic-based approach gives a static modulus ~35 GPa.

In the second approach, we propose to put a lower bound on the static, field-scale Young's modulus through comparison to GPS deformation data at GEO-01. The GPS data in Figure 2.3.15 shows that no ground deformation has occurred, within the confidence of the error bars. In the numerical model, the Young's modulus must be less than ~35 GPa to result in deformation that is larger than the error bars on the GPS data. Therefore, we infer that the Young's modulus could possibly be one to two orders of magnitude larger than the estimate from seismic data and must be ≥35 GPa. Smaller error bars from the experimental GPS data and/or a longer duration of the pumping test could facilitate a tighter estimate on the Young's modulus.
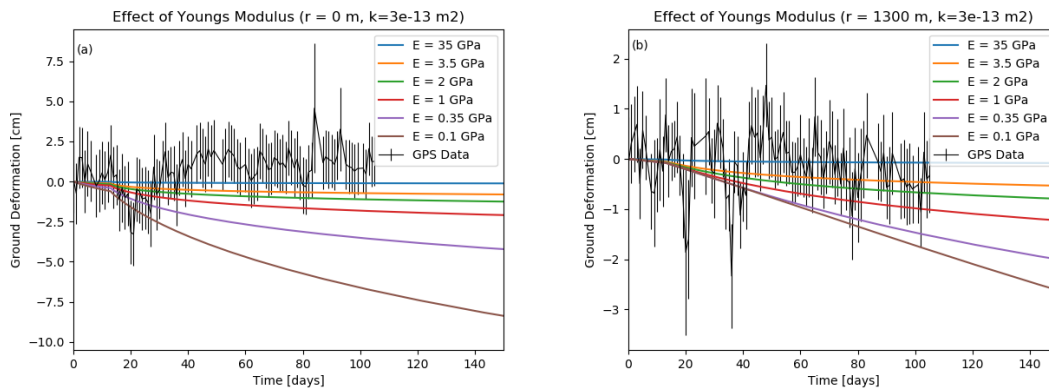
Figure 2.3.15 - Ground deformation versus time (a) at the well, representing the first GPS station, and (b) 1300 m from the well, representing the second GPS station. Black lines represent GPS data with error bars, and colorful lines represent HM model results for a sensitivity analysis on Young's modulus.

HM predictive simulations

In this section, we set up predictive HM models to answer the question: what poroelastic ground deformation could we expect if GEO-01 or GEO-02 were used as one well in an HT-ATES doublet? We consider several scenarios that vary parameters such as: targeted reservoir, reservoir permeability, and Young's modulus.

Four scenarios are simulated, which are summarized in Table 2.3.8. The GEo-01 scenario uses the permeability from the GEo-01 pumping test. GEo-02 Scenario 1 investigates targeting the LC-UJ and uses a permeability that agrees with values observed from a pumping test at GEo-02 and also within the range observed at the Thônex well. GEO-02 Scenarios 2 and 3 target the Siderolithic. Due to the uncertainty in the permeability of the Siderolithic at GEo-02, the GEo-02 Scenarios 2 and 3 use reservoir permeabilities that match GEo-02 Scenario 1 and the GEo-01 scenario, respectively. To investigate the uncertainty of the Young's modulus, each scenario is run with three values to cover the full range of uncertainty identified: 35 GPa, 2 GPa, and 0.35 GPa. The non-reservoir formations are assigned permeability of m² for all simulations.

Table 2.3.8 - Predictive Simulation Scenarios and Results

Well and Scenario	Targeted Reservoir and Depth [m]	Reservoir Permeability [m²]	Reservoir Thickness [m]	Flow Rate [kg/s]	Young modulus [GPa]	Years simulated	Maximum ground deformation [cm]
GEO-01	LC-UJ (400 – 750)	$3*10^{-13}$	350	60	35	15	<0.01
					2	1	0.10
					0.35	15	0.49
GEO-02 Scen. 1	LC-UJ (750-1450)	$7*10^{-16}$	700	3.9	35	15	0.015
					2	1	0.053
					0.35	1	0.055
GEO-02 Scen. 2	Siderolitic (600-750)	$7*10^{-16}$	150	0.7	35	1	<0.01
					2	1	0.015
					0.35	1	0.016
GEO-02 Scen. 3	Siderolitic (600-750)	$3*10^{-13}$	150	60	35	1	<0.01
					2	1	0.097
					0.35	1	0.40

Figure 2.3.16 shows change in pressure and ground surface deformation for GE0-02 Scenario 1 with GPa. The pressure in the aquifer is shown at the end of each operational stage in Year 1. While the changes in pressure are large at the end of the Injection and Drawdown stages, the pressure dissipates to near the baseline in the resting stages (i.e., Falloff and Buildup). The pressure in later years do not change substantially from the first cycle and are therefore not plotted.

The ground surface rises near the well that injects and falls near the well that produces fluid. Furthermore, the ground surface deformation reaches its largest magnitude at the end of the first year Injection stage.
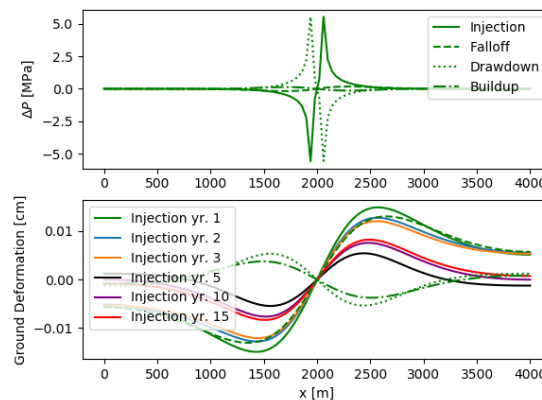
Figure 2.3.16 - Results for GEO-02 Scenario 1 with GPa. (Top) Difference in aquifer pressure from the initial condition versus x along the line seen in Figure   1.1 .4(c) at the end of each stage in Year 1. (Bottom) Ground deformation versus xalong the line seen in Figure   1.1 .4(b) at the end of each stage in Year 1 (green) and at the end of the Injection stage in later years.

In Figure 2.3.17 we present the pressure and ground deformation at the end of the first year of injection for each scenario. Analysing only the first year is justified because the pressure does not change substantially from year to year, and the magnitude of ground surface deformation tends to be largest in the first year. Additionally, this approach saves computational cost so that the full 15-year lifetime is only run for GEO-01 and GEO-02 Scenario 1 (see Table 2.3.8)

The largest change in pressure is reached in GEO-02 Scenario 1, followed by GEO-02 Scenario 2. This makes sense because these are the scenarios where the flow rate is limited by the hydraulic fracturing constraint. The GEO-01 scenario and GEO-02 Scenario 3 both employ a large permeability, and therefore pore pressure gradients are not large. Additionally, the pressure profile does not change substantially between the scenarios with Young's modulus equal to 35 and 2 GPa. This suggests that the pressure profile may approach a steady state by the end of each injection stage, because the Young's modulus affects the storage of fluid.

The ground surface deformation is sensitive to the Young's modulus but is relatively small even when the lower-bound Young's modulus is used. For the large Young's modulus (35 GPa), the maximum magnitude of ground surface deformation is <0.02 cm (for GEo-02 Scen. 1, Table 2.3.8). For the smallest Young's modulus (0.35 GPa), the maximum magnitude of ground surface deformation is <0.5 cm (for GEO-01, see Table 2.3.8)
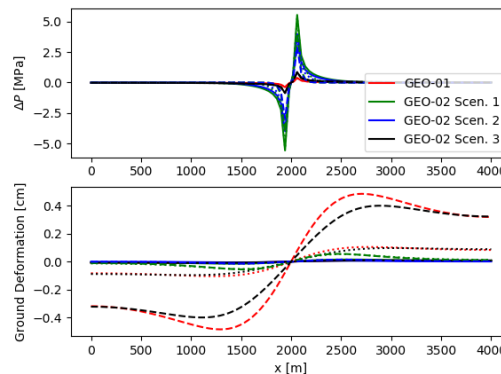
Figure 2.3.17 - Top) Difference in aquifer pressure from the initial condition versus spatial coordinate x along a line that intersects the two wells and (Bottom) ground surface deformation versus x at the end of Year 1 injection for each scenario. Solid lines use Young's modulus equals 35 GPa, dotted lines use 2 GPa, and dashed lines use 0.35 GPa. The cold/production well and hot/injection well are located at x = 1925 m, and x = 2075 m, respectively.

THM predictive simulations

In this section we present 3D THM simulations with the goals of understanding (a) if poroelastic or thermoelastic deformation will be larger and (b) if reservoir geometry will play a significant role in the amount of deformation.

Figure 2.3.18 shows the base-case pore pressure, temperature, and displacement response on the vertical, centre plane that intersects the two wells. The pore pressure is elevated at the injection well and decreased at the production well and has reaches a steady state before the end of the simulation. The thermal plume extends away from the injection well and is pulled preferentially towards the production well. The horizontal displacement in the x direction is laterally away from the injection well and towards the production well. The vertical displacement is upward above the reservoir and downward below the reservoir.
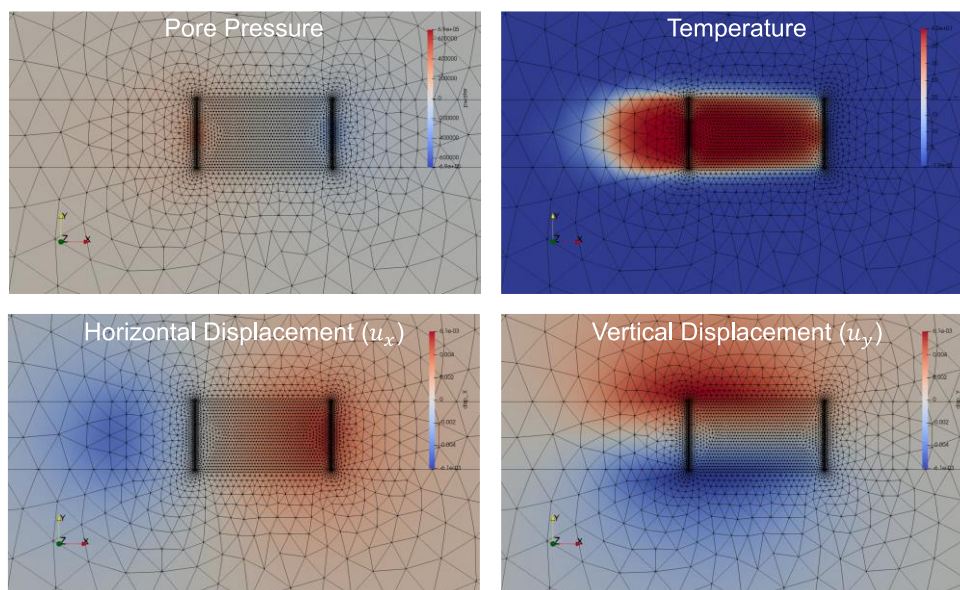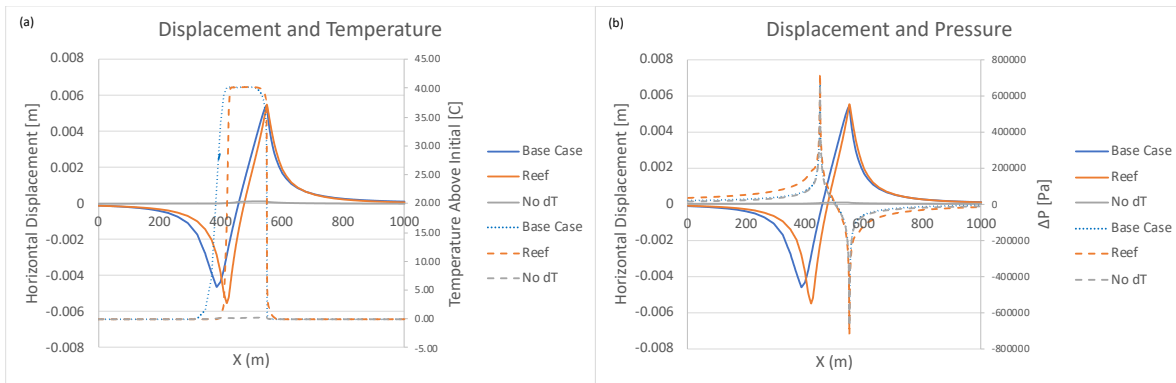

Figure 2.3.18 - Horizontal displacement, temperature, and pressure in the middle of the aquifer for three scenarios. The injection and production wells are located in the highly discretized regions on the left and right, respectively

The horizontal displacement within the reservoir is analysed in Figure 2.3.19 for all three scenarios. In the first and second scenarios (the base case and the reef scenarios, respectively), the horizontal displacement reaches a maximum magnitude of approximately 0.5 cm, while in the third scenario (i.e., the one with no) the maximum magnitude of displacement is <0.01 cm. In the first and second scenarios, the region between the wells and somewhat past the injection well are heated to 35°C. The end of this elevated-temperature region corresponds closely with the location of the maximum magnitude of deformation. The pore pressure response is almost identical for the first and third scenarios, while the second scenario has more gradual pressure falloff due to the lower permeability outside of the reef. It appears that the thermoelastic deformation is more influential than the poroelastic deformation, for the scenarios considered.

Figure 2.3.19 - Horizontal displacement, temperature, and pressure in the middle of the aquifer for three scenarios. The solid lines show the displacement response, and the dashed lines show the (a) temperature and (b) pressure response.

The vertical displacement at the top of the reservoir (not the ground surface) is shown in Figure 2.3.20. The first scenario has the largest amount of uplift (0.60 cm), followed closely by the second scenario (0.57 cm), with scenario three displaying much less vertical deformation (<0.01 cm). In fact, the third scenario shows a small degree of downward deformation near the production well, which is not observed in the first and second scenarios. This suggests that the thermoelastic effect is causing upward deformation at the top of the reservoir, while the poroelastic effect is causing upward deformation at the injection well and downward deformation at the production well.
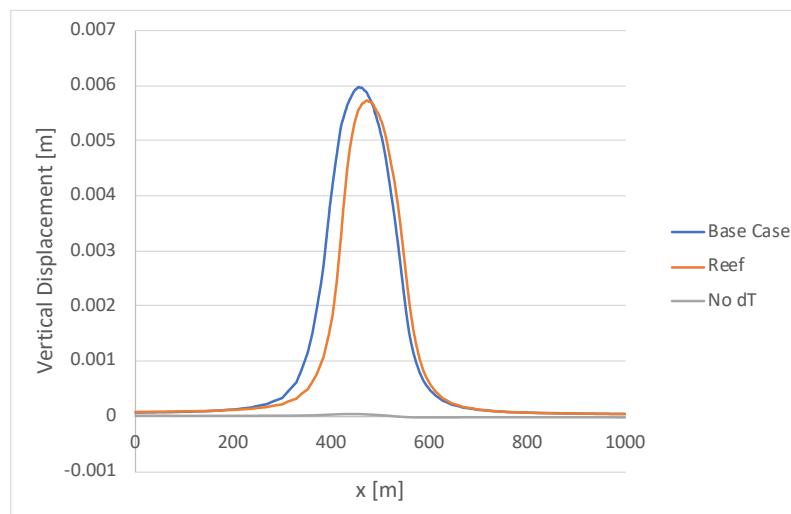

Figure 2.3.20 - Vertical displacement versus x along the top of the reservoir

Thermo-Hydraulic-Mechanical and Hydro-Mechanical conclusions

THM and HM simulations were performed to explore potential for ground surface deformation: (a) during the pumping test at GEo-01 and (b) in a predictive mode for HT-ATES operations at GEo-01 and GEo-02.

The THM results indicate that both pore pressure and temperature changes can lead to deformation. However, it is too early to draw definitive conclusions from the THM work because only a small parameter space was explored. It was not possible to explore a large parameter space due to numerical convergence problems. Therefore, future work could focus on improving 3D THM numerical simulators and applying them to understand HT-ATES.

In most HM simulations, the deformation remains small, suggesting that poroelastic deformation is manageable. For the GEo-01 pumping test, the GPS data shows no significant deformation. Modelling suggests that, given no deformation has occurred thus far, it is unlikely that large deformation will occur for the full duration of the pumping test. In the predictive HT-ATES simulations, the two scenarios with largest deformation both utilize the lower-bound value for the field-scale Young's modulus. One scenario targets a relatively shallow reservoir (GEo-01) and the other targets a relatively shallow and relatively thin reservoir (GEo-02 Scenario 3). All other scenarios resulted in ≤0.10 cm of ground surface deformation. It seems that poroelastic deformation can be managed by choosing operating pressures and flow rates based on the target reservoir in conjunction with monitoring. For example, flow rate may need to be curtailed if: (a) reservoir permeability, thickness, or depth are not sufficient, especially if the pressures would approach the hydraulic fracturing threshold or (b) observed deformation becomes large.

2.3.5 References

Allaerts K., De Oliveira F., Hollmuller P., Guglielmetti L., Quiquerez L., Maragna C., Rey C., Gauthier G., Kleinlugtenbelt R., Octaviano R., and Clarijs M. (2021): *UTES and its integration in the heating system - Defining optimal design and operational strategies for the demonstration cases*, GEOTHERMICA –ERA NET Cofund Geothermal. 100p+ appendices.

Altwegg, P. et al., 2013. *Inventaire géothermique et structural du canton de Neuchâtel : IGS-NE. Final Report ,* s.l.: s.n.

Bayerisches Landesamt für Umwelt, n.d. *GeoMol: Assessing subsurface potentials of the Alpine Foreland Basins for sustainable planning and use of natural resources.* [Online]
Available at: http://www.geomol.eu/home/index_html

Bear, J., 1972. *Dynamics of Fluids in Porous Media.* New York: Dover Publications.

Bear, J. & Corapcioglu, M. Y., 1981. A mathematical model for consolidation in a thermoelastic aquifer due to hot water injection or pumping.. *Water Resources Research,* 17(3), pp. 723-736.

Bernier, P. (. .. ,. 9. (.-2. 8. p., 1984. *Les formations carbonatées du Kimméridgien et du Portlandien dans le Jura méridional. Stratigraphie, micropaléontologie, sédimentologie,* Lyon: Documents des laboratoires de geologie.

Birdsell, D.T., and Saar, M. O. (2020) Modeling Ground Surface Deformation at the Swiss HEATSTORE Underground Thermal Energy Storage Sites. Proceedings World Geothermal Congress 2020+, paper 22046.

Brentini, M., 2018. *Impact d'une donnée géologique hétérogène dans la gestion des géo-ressources: analyse intégrée et valorisation de la stratigraphie à travers le bassin genevois (Suisse, France). PhD Thesis..* Geneva: University of Geneva.

Cacace, M. & Jacquey, A. B., 2017. Flexible parallel implicit modelling of coupled thermal–hydraulic–mechanical processes in fractured rocks.. *Solid Earth,* 8(5), pp. 921-941.

Charollais, J. et al., 2007. La Molasse du basin franco-genevois et son substratum. *Arch.Sci.,* Issue 60, pp. 59-174.

Chelle-Michou, C. et al., 2017. Geothermal state of the deep Western Alpine Molasse Basin, France-Switzerland. *Geothermics,* Volume 67, pp. 48-65.

Cheng, A. H., 2016. *Poroelasticity.* Oxford, Mississippi, USA: Springer.

Donzeau, M., Wernli, R., Charollais, J. & Montjuvent, G., 1997. *Carte géoogique de la France (1/50'000), feuille Saint-Julien-en-Genevois (653)..* Orléans: BRGM.

Donzeau, M., Wernli, R., Charollais, J. & Montjuvent, G., 1997. *Notice explicative, Carte géol. France (1/50'000), feuille Saint-Julien-en-Genevois (653).* Orléans: BRGM .

Gaston, D. R. et al., 2015. Physics-based multiscale coupling for full core nuclear reactor simulation.. *Annals of Nuclear Energy,* Volume 84, pp. 45-54.

Geologie-Geophysique, 1979. *Energie geothermique dans le Canton de Geneve. Etude complementaire.,* s.l.: Service cantonal de Geologie, Departement de l'Interieur et de l'Agricoulture. Unpublished Report..

Gorin, G., 1989. *Interprétation géologique de la champagne sismique GG87 dans le Canton de Genève.,* s.l.: Département de l'Intérieur et de l'Agriculture, service cantonal de géologie, Genève. Unpublished Report.

Guglielmetti, L., Eichinger, F., and Moscariello, A. (2021) Geochemical Characterization of Geothermal Waters Circulation in Carbonate Geothermal Reservoirs of the Geneva Basin (GB). Proceedings World Geothermal Congress 2020+, paper 14092.

Homewood, P., Allen, P. A. & Williams, G. D., 1986. Dynamics of the Molasse Basin of Western Switzerland. *Spec. Publs. Int. Ass. Sediment,* Volume 8, pp. 199-217.

Homewood, P., Rigassi, D. & Weidmann, M., 1989. Le bassin molassique Suisse. In: Dynamique et méthodes d'étude des bassins sédimentaires Ed. Technip. pp. 299-314.

Hydrogeo Environnement, 2017. *Evaluation des calcaires du Crétacé des forages du LEP : caractérisation de la ressource et préparation au contrôle lithostratigraphique des futurs forages GEothermie 2020.,* s.l.: s.n.

Ingeneurs Résonance, 2017. *Stockage de chaleur dans le Malm du bassin genevois. ÉTUDE DU COMPORTEMENT THERMO-HYDRAULIQUE D'UN SYSTÈME HT-ATES EN AQUIFÈRE PROFOND.,* s.l.: Rapport technique TR-6001.031/NL.

Meyer, M., 2000. *Le complexe récifal kimméridgien-tithonien du Jura méridional interne (France), évolution multifactorielle, stratigraphie et tectonique.* Geneva: University of Geneva.

Moscariello, A., Clerc, N., Pierdona, L. & Haller, A. D., 2018. *Exploring the interface between shallow and deep geothermal systems: new insights from the Mesozoic-Cenozoic transition..* Bern, 16th Swiss Geoscience Meeting .

Muralt, R., 1999. *Processus hydrogéologiques et hydrochimiques dans lescirculations profondes des calcaires du Malm de l'arc jurassien (zones deDelémont, Yverdon-les-Bains, Moiry, Genève et Aix-les-Bains). ,* s.l.: CommissionGéotechnique Suisse.

Nawtratil del Bono, C., Martin, F., Meyer, M., 2019. *GEothermie 2020: Avancée du programme et premiers succès. Presentation, Journée Romande de Geothermie 2019*

Negron, J., 1987. *Rapport d'interpretation sur l'etude de sismique a reflexion Geothermie de Geneve 1987. Mission 140, 36, 52. Compagnie Generale de Geophysique.,* s.l.: Unpublished report.

Paluszny, A., Matthaei, S. K. & Hohmeyer, M., 2007. Hybrid finite element–finite volume discretization of complex geologic structures and a new simulation workflow demonstrated on fractured rocks. *Geofluids,* p. 186–208.

Paolacci, S., 2012. *Seismic facies and structural configuration of the Western Alpine Basin and its substratum (France and Switzerland). PhD Thesis.* s.l.:University of Geneva, unpublished.

Poulet, T. & Veveakis, M., 2016. A viscoplastic approach for pore collapse in saturated soft rocks using redback: an open-source parallel simulator for rock mechanics with dissipative feedbacks.. *Computers and Geotechnics,* Volume 74, pp. 211-221..

Rigassi, D., 1957. Le Tertiaire de la Région Genevoise et Savoisienne.. *Bull. Ver. Schweiz. Petroleum-Geol.u.-Ing. ,* Volume 24/66, pp. 19-34.

Rousillon, E., 2018. *Characterisation and rock typing of deep geothermal reservoirs in the Greater Geneva Basin (Switzerland & France). Doctoral Thesis. no Sc. 5196.* Geneva: University of Geneva.

Schegg, R., 1993. Thermal Maturity and History of the Sediments in the North Alpine Foreland Basin (Switzerland, France). , Université de Genève, Volume 15. 194 Pages. *Publications du Département de Géologie et Paléontologie, Université de Genève,* Volume 15, p. 194.

Signer, C. & Gorin, G., 1995. New geological obserbations between the Jura and the Alps in the Geneva area, as derived from reflection seismic data. 88/2, p. 235-265. *Eclogae geol. Helv.,* Volume 88/2, pp. 235-265.

Signorelli, S., Andenmatten Berthoud, N. & Kohl, T., 2004. *Geothermischer Ressourcenatlas der Schweiz. Erarbeitung und Bewertung des geothermischen Potentials der Schweiz. ,* s.l.: Bundesamts für Energie BFE.

Tómasdóttir, S. & Gunnarsson, G. (ed) 2021: HEATSTORE – Final report on UTES-type/site-specific simulators based on academic/research codes. GEOTHERMICA – ERA NET Cofund Geothermal. 58 pp.

Vuataz., D. F. & Giroud, N., 2010. *Caractéristiques géochimiques du fluide profond du forage géothermique Thônex-1, Genève,* Neuchâtel: Rapport CREGE12-10/01.

Xia, Y. et al., 2017. Design, modelling, and evaluation of a doublet heat extraction model in enhanced geothermal systems.. *Renewable energy,* Volume 105, pp. 232-247.

2.4 Swiss pilot site Bern Forsthaus

Peter Alt-Epping[1], Larryn W. Diamond[1], Daniela van den Heuvel[1], Christoph Wanner[1], Daniel Birdsell[2], Rubén Vidal[3], Maarten W. Saaltink[3] and Sebastià Olivella[3],

[1]*Uni Bern,* [2]*Eidgenössische Technische Hochschule Zürich,* [3]*Universitat Politècnica de Catalunya*

2.4.1 Conceptualization

2.4.1.1 Location & UTES concept and specifications, scope and aims of the studyTES concept and specifications, scope and aims of the study

The Forsthaus Heat Storage project is run by Geo-Energie Suisse AG (GES) on behalf of Energie Wasser Bern (ewb). It is supported by the Swiss Federal Office of Energy and is part of the Swiss contribution to the European Geothermica-HEATSTORE project.

The Forsthaus project is located in the northern part of the city of Bern (Switzerland) next to ewb's power production site "Energiezentrale Forsthaus" (Figure 2.4.1) .
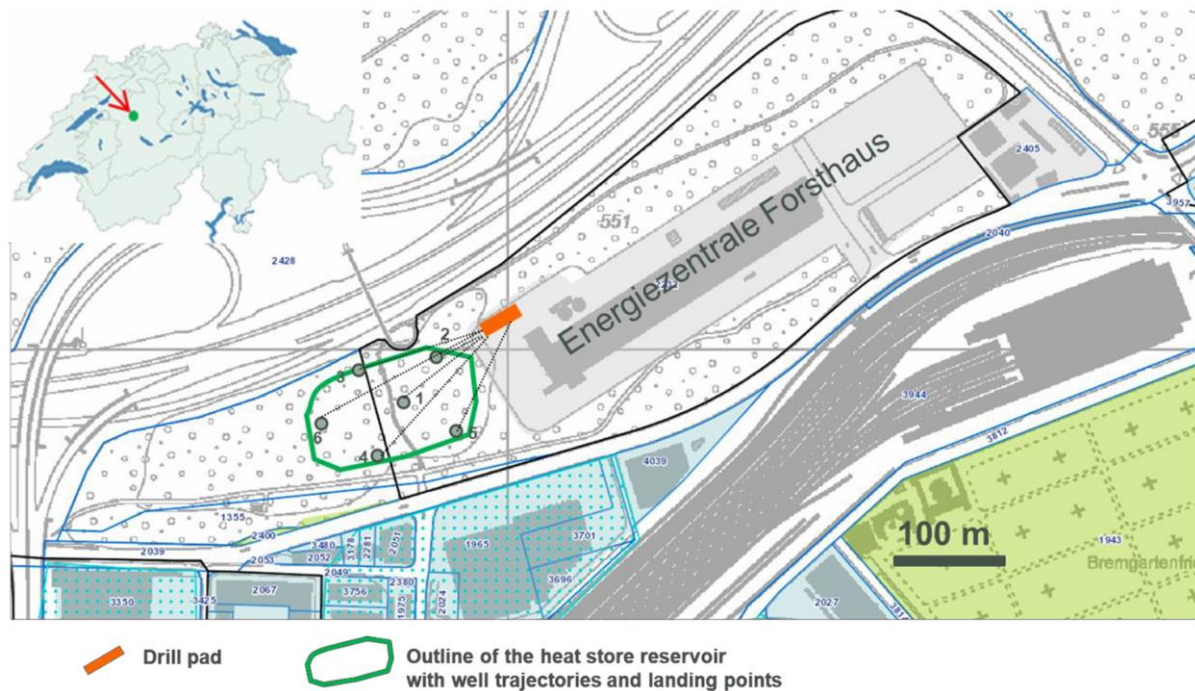
Figure 2.4.1 Location of the Aquifer Thermal Energy Storage project "Bern Forsthaus".

The purpose of the Forsthaus project is to create an Aquifer Thermal Energy Storage (ATES) where waste heat from the "Energiezentrale Forsthaus" will be stored during the summer instead of being dissipated into the atmosphere. That heat will be back-produced during the wintertime to feed into a district heating network.

The project design anticipates a main well at the centre of the system and peripheral auxiliary wells. The main well is used to inject and produce the energy in the form of hot water. The auxiliary wells are used to regulate the flow at the boundary, maintain the desired aquifer reservoir pressure and connect to the surface system, so that the underground geological formation, the wells and the surface facilities are acting as a closed loop system (Figure 2.4.2 and Figure 2.4.7).

2.4.1.2 Preliminary operation mode

The ATES Bern-Forsthaus is seasonally operated with loading cycles during summer time and unloading cycles during winter time (Figure 2.4.2).
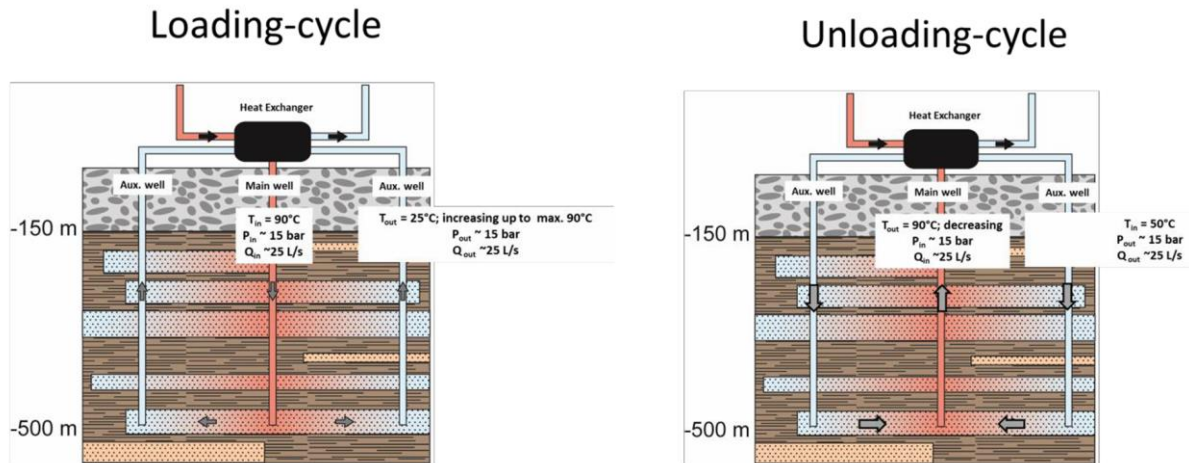

Figure 2.4.2 Preliminary operation parameters during loading cycles (left) and unloading cycles (right).

The preliminary operation parameters for loading- & unloading-cycles are:

	Loading cycle	Unloading cycle
Temperature:	90°C	Starting from 90°C down to 50°C
Duration:	216 days	149 days
Circulation rate:	25 L/s	
Heat losses:	ca. 40% (based on coupled thermos-hydraulic modelling	
Running time UTS:	20 years	

Under these preliminary assumptions the energy balance for the UTES Bern-Forsthaus was calculated:

- Total amount of lost heat stored in the reservoir: ca. 21.3 GWh/a
- Total amount of heat gained from the reservoir: ca. 12.8 GWh/a
- Reduction of CO_2 –output: 2'531 tons/a

2.4.1.3 Specific questions

In order to operate the future UTES in a safe and optimized manner, the following aspects are planned to be investigated by modelling / simulations:

Subsurface flow dynamics and heat transfer in relation to storage concept

To this end, a preliminary operation mode was defined (see section 2.4.1.2). Additionally, coupled hydraulic and thermal modelling will be performed with different operation parameters (changing temperature, loading- und unloading time) in order to optimize overall storage capacity and performance. Specific modelling questions are:

- What circulation rate can be applied between the main well and the auxiliary wells given a Δp (30 bar) and hydraulic reservoir properties?

- What is the amount of heat that can be stored in the reservoir and retrieved from the reservoir (= heat losses) for an assumed reservoir geometry and given hydraulic and thermal reservoir properties? During the course of drilling, knowledge on reservoir geometry and hydraulic reservoir properties will be improved continually.

- How many auxiliary wells are needed and where are these wells placed in order to gain maximum heat recovery?

- Concerning environmental /regulatory aspects the question of thermal disturbance, i.e., heating of shallow groundwater in the underground, has to be investigated. Swiss regulation restricts groundwater temperature changes to maximal 3°C at a distance of more than 100 m from the injection site. Temperature changes of more than 3°C are only allowed within a distance of 100 m from the site.

Additionally, Radial Jet Drilling is planned to improve reservoir transmissivity in the case that natural reservoir transmissivity turns out to be insufficient. Radial Jet Drilling allows drilling / jetting of small diameter laterals (Ø ~1") up to 100 m from a vertical wellbore. Up to six laterals can be horizontally jetted from one point in the wellbore in different directions (Figure 2.4.3). Specific modelling questions related to Radial Jet Drilling are:

- What is the impact of radial jetted laterals on the wellbore – reservoir connection and the overall reservoir performance?

- How do the number, length and geometrical configuration of laterals impact the wellbore-reservoir connection and the overall reservoir performance?
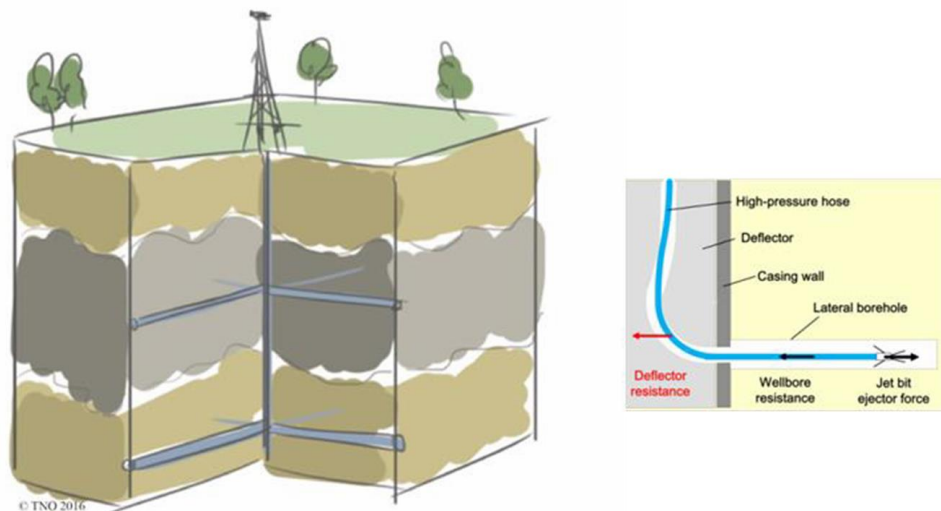

Figure 2.4.3 Radial Jet Drilling

Chemical reactions and their impact on environmental and operation: Understanding the chemical fluid-rock interaction during loading- and unloading cycles is a key task. It is well known from literature that fluid-rock interactions can affect overall system performance:

- Corrosion of chosen materials (casing, pipes, heat-exchanger) in presence of oxygen and highly saline fluids.

- Precipitation of calcite in the heat-exchanger at surface and/or within the near-field of the injection well.

- Dissolution of minerals (calcite or sulphides) within the reservoir and the mobilization of toxic metals like arsenic and cadmium.

- Dissolution of calcite in the targeted sandstone-layers with decreasing reservoir temperature may result in reduced sandstone-cohesion (sand production) and fine particles that can clog pore-space and wellbores.

- Precipitation of silicates due to fluid cooling.

- Clogging and corrosion due to microbial activity.

Coupled thermal-hydraulic-chemical models can be used to address each of these points. Examples of coupled THC simulations assessing chemical reactions and their impact on environmental and operation are presented in section 2.4.3.1.

Poro- and thermo-elastic effects and their impact:

- During loading- and unloading cycles the reservoir will experience poro- and thermo-elastic expansion and contraction. Modelling is expected to investigate the impact of expansion and contraction within the reservoir with respect to reservoir stability and shear processes and at surface with respect to uplift and subsidence. In addition, poro-elastic effects are modelled in order the investigate changes of effective stress within the reservoir. If these changes are high enough, innovative seismic surveys (3D-seismic, VSP) can help to image reservoir geometry.

Coupled thermal-hydraulic-mechanical models and how they can be used to assess mechanical implications of loading- and unloading cycles during the Forsthaus ATES operation are described in sections 2.4.3.2.and 2.4.3.3.

2.4.2 System Geometry and related Geology

2.4.2.1 Geology

The reservoir of the UTES project Bern-Forsthaus is located within the Lower Freshwater Molasse (USM) and belongs to the Swiss Molasse Basin (Figure 2.4.4). The Swiss Molasse is a thick Tertiary sedimentary body created by the detrital filling of a subsidence basin that was caused by the uplift of the Alps. At the project site the Lower Freshwater Molasse is covered by quaternary unconsolidated deposits (gravels, sands, clays) of about 150 m thickness. These unconsolidated deposits comprise a shallow fresh water aquifer from 8 to 10 m below surface.
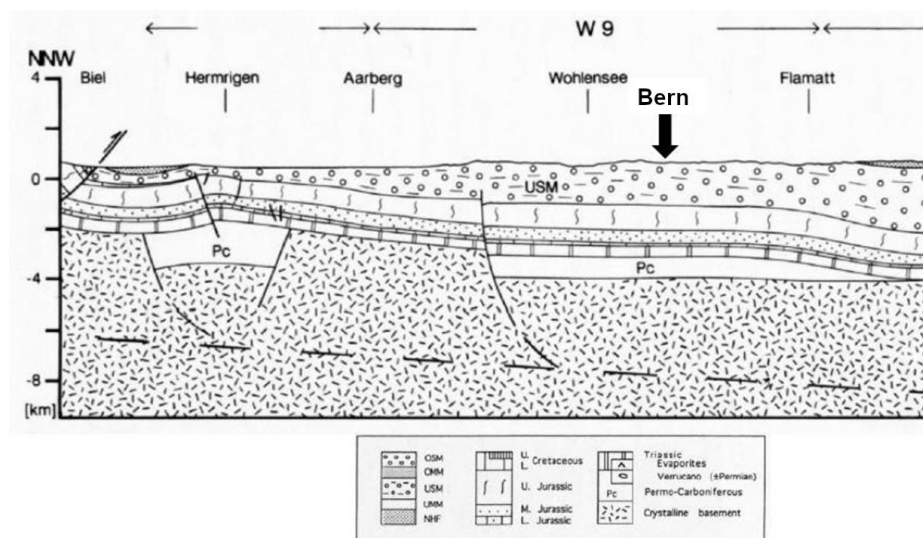

Figure 2.4.4 Regional NNW–SSE geological cross section across the project site in Bern. The acronym of the Lower Freshwater Molasse is "USM" (from Pfiffner et al., 1997).

Conceptual reservoir model

In the past the Lower Freshwater Molasse was the subject of detailed sedimentological and hydrogeological studies: NAGRA NTB 90-41, 1990; Platt et al., 1992; Keller, 1992; NAGRA NTB 92-03, 1993; Küpfer, 2005; Hölker, 2006. These defined specific architectural/facies elements (Figure 2.4.5).
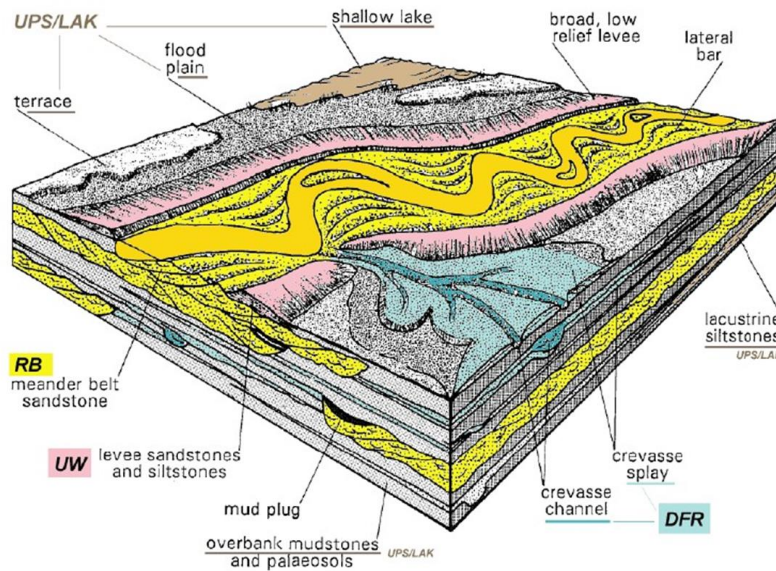

Figure 2.4.5 Summary facies model for the deposition of the Lower Freshwater Molasse (from Hölker, 2006).

These architectural elements have specific geometrical and hydrogeological properties:

Architectural element	Simplified geometry	Hydraulic conductivity Porosity (median)
RB (meander belt **sandstones**)	H = 2-15m B = 150-1500m L = n·10³ m	1E-04 to 1E-07 m/s 19.6%
DFR (crevasse splay and channel **sandstones and siltstones**)	H ≤ 4m B < 10m L = n·10³ m H = 1-2m B = n·10³ m L = n·10³ m	1E-06 to 1E-08 m/s 14.2%
UW (levee **sandstones and siltstones**)	H < 3m B = 10-30m L = n·10³ m	1E-07 to 1E-10 m/s 8.2%
UPS (overband **mudstones and palaeosols**)	H < 6m B = n·10³ m L = n·10³ m	1E-08 to 1E-11 8.1%
LAK (lacustrine **siltstones**)		No data, but very low values

(Modified from Keller, 1992)

Figure 2.4.6 Architectural elements of the Lower Freshwater Molasse

Based on the current state of knowledge, a conceptual reservoir model for the UTES Bern-Forsthaus was established consisting of mainly two elements: Porous and permeable sandstone-layers (RB-elements) embedded within a low-porosity and low-permeability matrix (UW-, UPS & LAK-elements). The permeable sandstone-layers are used for fluid and heat transport whereas heat will be stored within the sandstone layers and the surrounding matrix composed of marl- and mudstone (Figure 2.4.7).
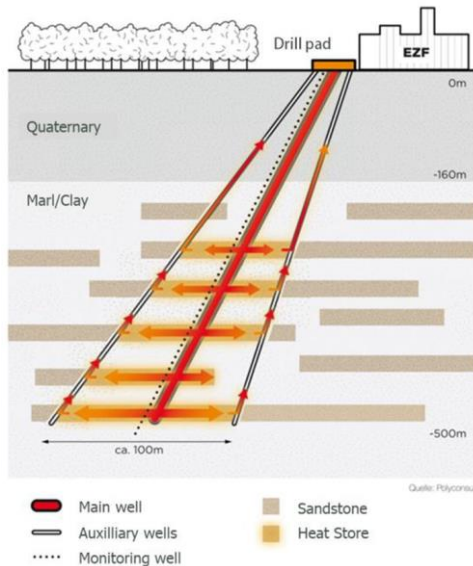

Figure 2.4.7 Expected conceptual reservoir model for UTES Bern-Forsthaus showing the RB-sandstones embedded within the matrix composed of marl- and claystone (UW-, UPS & LAK-elements).

Table 2.4.1 Specific material properties for "sandstones" and "matrix" of the Lower Freshwater Molasse and the overlaying unconsolidated sediments from the literature

	Heat capacity	Thermal conductivity	Density	E-Moduli	UCS	Mineralogy
	J/kg/K	W/m/K	kg/m^3	GPa	MPa	wt %
Sandstones	1037	2.67	2300	1 ± 0.3	6.5 ± 4	Quartz 35% Albite 18% Felspar 11% Calcite 12% Dolomite 2% Clay minerals, Mica 22% C_{org} 0.1%
Matrix	1037	2.67	2500	0.5 ± 0.5	23 ± 6 (mudstone) 8 ± 5 (marlstone)	Quartz 18% Albite 10% Felspar 7% Calcite 15% Dolomite 5% Clay minerals, Mica 45% C_{org} 0.1%
Quaternary unconsolidated deposits	840 - 1000	0.4 - 2.3	1800 - 2500	0.02 - 0.05	-	-

2.4.2.2 Local geothermal and groundwater conditions

The heat store reservoir will be placed between 200 to 500 m below surface. Applying the mean geothermal gradient of 3K/100 m, the natural reservoir temperature will be in the range of 17°C to 26°C. Horizontal groundwater flow is restricted to the discontinuous permeable sandstone layers. Vertical groundwater flow is highly inhibited due to almost impermeable matrix. The Lower Freshwater Molasse is therefore regarded as

an aquitard. From a near-by offset well (about 30 km to the east) it is known that in-situ pore pressures are different in different sandstone layers. All of them were found to be confined, but not artesian. Formation water found in the Lower Freshwater Molasse can be classified as Na-HCO₃ to Na-Cl-type. NAGRA (NTB 88-25) reported the hydrochemical composition for formation water from the Lower Freshwater Molasse as "Referenzgrundwässer USM" (Table 2.4.2). So far, no results from hydrochemical water-sample analysis are available for the project site. Water samples will be taken during the course of drilling and testing.

Table 2.4.2 Typical formation water compositions in the Lower Freshwater Molasse

Ca^{2+}	4.2E-3 mol/l
Mg^{2+}	2.8E-3 mol/l
Na^+	1.9E-1 mol/l
K^+	5.0E-4 mol/l
Cl^-	2.0E-1 mol/l
SO_4^{2-}	5.0E-5 mol/l
CO_3^{2-} (as HCO_3^-)	1.9E-3 mol/l
$H_2SiO_4^{2-}$	4.2E-4 mol/l
Temperature	40°C
pH	7.5
Eh	-240 mV
pCO_2	$10^{-2.47}$ bar
Alkalinity	1.84E-3 mol/l
Ion-Strength	0.207 mol/l
Saturated with	Calcite, Chalcedon, Dolomite

2.4.2.3 Planned Well Design and Testing

Well design

The main well and auxiliary wells are all foreseen with the same standard design, and are therefore interchangeable. The monitoring well architecture has not yet been defined, but will be lighter than that of the main/auxiliary well design. The construction of the wellbore will follow 3 phases of drilling and casing as described in Table 2.4.3 and Figure 2.4.8.

Table 2.4.3 Well design.

|	Phase 1	Phase 2	Phase 3
Hole size	26 in	20 in	14 ¾ in
Measured Depth	22 m	200 m	560 m
Vertical depth	20 m	180 m	500 m
Casing size	22 in	16 in	10 ¾ in
Casing weight	114.8 lbs/ft.	75 lbs/ft.	40.5 lbs/ft.
Connections	STC	LTC	Premium/LTC
Casing material	J55	J55	N80
Special equipment	Cemented with a stab-in shoe Cement basket for a potential top job	Cemented with a stab-in shoe Cement basket for a potential top job	Top 200 m equipped with thermally insulated casing and premium coupling. Bottom part with normal LTC using A fibre optic runs along the casing. The fibre is prepared for oriented perforating away from the fibre.
Comments	Section is slightly slanted to reach target	Main deviation section to reach the top of the reservoir at the set slant angle	Section will be entirely cored and successive testing will take place after each cored section.
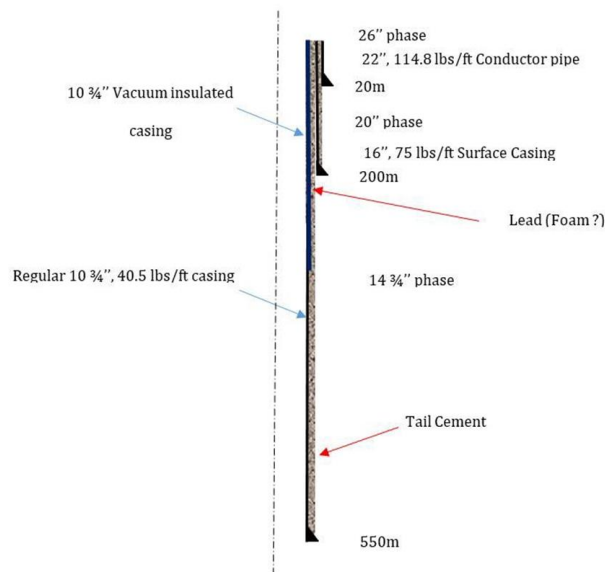
Figure 2.4.8 Planned well design

Coring and selective testing of the reservoir section (phase 3).

This phase is the reservoir section. It will be entirely cored and slanted towards the target zone and total depth within the USM at 500 m vertically. The coring and testing operations will be performed sequentially. Where the cored section exhibits good reservoir properties, the specially designed testing equipment (wireline packer system) will be run across that section through the coring bit, and a selective hydraulic test will be performed in order to characterize the test interval with respect to in-situ formation pressure, transmissivity, hydraulic boundaries and as soon as more than one well is available wellbore interconnectivity (hydraulic tomography). The procedure will allow establishing a geological and transmissivity profile for the entire reservoir section. This profile will be later used to select the zones to be perforated and used for the heat storage volume.

2.4.3 Modeling approach

Three different modelling groups are working on the UTES Bern-Forsthaus project having their own focus and approach.

Modelling group	Focus
University of Bern Rock-Water Interaction group	Thermo-Hydro-Chemical models (THC) with special focus on rock-water interaction
ETH Zürich Geothermal Energy and Geofluids (GEG)	Original focus on Thermo-Hydro-Mechanical models (THM) with special focus on surface uplift and thermo-poro-elasticity was altered to focus on Thermo-Hydro-Mechanical-Economic (THM$) model with focus on recommendations for optimal well spacing, flow rate, and minimum transmissivity
Universitat Politècnica de Catalunya (UPC)	Thermo-Hydraulic-Mechanical models (THM)

2.4.3.1 THC modelling, University of Bern

Conceptual simulation model

The reservoir of the Forsthaus "Geospeicher" is a sequence of permeable sandstones and low-permeability clayrocks. It is expected that fluid-rock reactions take place primarily in the more permeable, sand-rich layers of the USM. The less permeable clay-rich units play an important role in storing heat. Reactions in the permeable units are driven by fluid motion in response to injection or extraction cycles in combination with temperature changes. In addition to short-time variations related to pumping, there will be long-term, gradual or cumulative changes in reservoir properties. For instance, the reservoir will heat up over time as heat is conducted into the low-permeability clay units. Between injection and extraction cycles there are periods of rest without flow but with ongoing diffusion of heat. Mineral dissolution and precipitation reactions resulting from these changes in the reservoir affect the porosity and permeability of the aquifer material. If at any point in the reservoir the volume of minerals precipitating exceeds the volume of minerals dissolving, the permeability will be reduced. If this clogging of the reservoir rock becomes significant, additional, potentially costly, measures have to be taken to reverse this process and re-enhance permeability. In the worst case the operation can no longer be sustained.

Mineral precipitation or scaling may also occur in the wells and the heat exchanger due to changes in temperature and pressure. Aside from a potential re-dissolution of scales, no mineral dissolution reactions take place within the installation. To predict mineral precipitation in the installation, temperature and pressure conditions, the residence time of the fluid, as well as the rate at which minerals precipitate have to be known. The latter in turn is a function of temperature. Predicting mineral precipitation rates and hence of the distribution of mineral scale formation in the system is a difficult task because of a lack of published precipitation rate data, heterogeneities in the flow field, temperature and pressure conditions that cannot be captured at the scale of the model. In the wells, the precipitation rate may be limited by the low ratio of surface area to fluid flux that prevent minerals to effectively crystallize and grow on the inside wall of the well casing (i.e. heterogeneous nucleation).

In the heat exchanger, water undergoes significant heating or cooling very rapidly, typically under pressures lower than those in the reservoir. These steep gradients in physical conditions imply a strong potential for mineral scaling. Given that the heat exchanger is used for heating and cooling, the amounts and composition of mineral scales may change in time. Because the design of the heat exchanger used in the Forsthaus system is yet unknown, making reliable predictions about the implication of mineral scales on its performance is difficult at this point.

Corrosion of the casing or the surface installation is a risk that could induce significant additional operational cost. Corrosion is favored by certain chemical conditions, such as a low pH, dissolved gases such as O_2 or CO_2 or high TDS (total dissolved solids) in the production fluid or by bacterial activity in the system. Physical corrosion may occur when flow rates are high, in particular in the presence of suspended such as sand, sediment, corrosion by-products. Incipient chemical corrosion, however, can be detected by monitoring the composition of the circulating water. The risk of chemical corrosion and the implications of incipient corrosion on the water composition can be assessed with coupled THC simulations (e.g. Diamond and Alt-Epping, 2014), but corrosion is not considered in the examples presented below.

Chemical reactions between a fluid and a rock or between a fluid and a gas phase such as $CO_2(g)$ are a function of composition, temperature and pressure. In simulations involving the injection/extraction of waters into/from deep reservoirs, the effects of temperature and pressure on the equilibrium state and kinetic rates of reactions have to be considered explicitly. (Note that the effect of pressure on reactions can often be neglected as it is outweighed by the effect of temperature). To fully comprehend feedbacks between the flow of water, the thermal evolution and chemical reactions, a full-scale model of the ATES system needs to be constructed that includes and couples fluid flow, solute transport (diffusion and advection), heat transport (conduction and convection) and a chemical reaction network including all system-relevant reactions.

We use the high performance reactive transport code PFLOTRAN (www.pflotran.org) to carry out simulations flow and heat transport coupled with reactive transport. In PFLOTRAN, mass conservation equations have the form

$$\frac{\partial}{\partial t}(\varphi s \eta) + \nabla \cdot (\eta \boldsymbol{q}) = Q_w \qquad (2.4.1)$$

and the energy conservation equation can be written as

$$\frac{\partial}{\partial t}\left(\varphi s \eta U + (1-\varphi)\rho_r C_p T\right) + \nabla \cdot (\eta \boldsymbol{q} H - \kappa \nabla T) = Q_e \tag{2.4.2}$$

The Darcy flow velocity $\boldsymbol{q}$ is given by

$$\boldsymbol{q} = \frac{k k_r}{\mu} \nabla(P - \rho g z) \quad . \tag{2.4.3}$$

Here, φ denotes porosity, s saturation, ρ, η mixture mass density and molar density, respectively, of the brine, $\boldsymbol{q}$ Darcy flux, k intrinsic permeability, k_r relative permeability (here set to unity as only one fluid phase is expected), μ viscosity, P pressure, g gravity, and z the vertical component of the position vector. Water density and viscosity are computed as a function of temperature and pressure through an equation of state for water. The quantity ρ_r denotes the rock density, c_p, and κ denote the heat capacity and thermal conductivity of the porous medium-fluid system. The molar internal energy and molar enthalpy of the fluid, U and H, are obtained from an equation of state for pure water. These two quantities are related by the thermodynamic expression

$$U = H - \frac{P}{\eta} \tag{2.4.4}$$

Thermal conductivity κ is determined from the equation

$$\kappa = \kappa_{dry} + \sqrt{s_l}\left(\kappa_{sat} - \kappa_{dry}\right) \tag{2.4.5}$$

where κ_{dry} and κ_{sat} are dry and fully saturated rock thermal conductivities and s_l is liquid saturation. Here we consider fully saturated conditions at all times, hence the thermal conductivity is always κ_{sat}. Like in most continuum-based simulators, in PFLOTRAN thermal equilibrium is assumed between the liquid and solid within each cell of the model grid.

The governing mass conservation equations for the geochemical transport mode for a multiphase system is written in terms of a set of independent aqueous primary or basis species with the form

$$\frac{\partial}{\partial t}\left(\varphi \sum_a s_a \boldsymbol{\Psi}_j^a\right) + \nabla \cdot \sum_a \boldsymbol{\Omega}_j^a = Q_j - \sum_m v_{jm} I_m - \frac{\partial S_j}{\partial t} \tag{2.4.6}$$

and

$$\frac{\partial \varphi_m}{\partial t} = V_m I_m \tag{2.4.7}$$

for minerals with molar volume V_m, reaction rate I_m and volume fraction φ_m referenced to a single grid cell. The term involving S_j describes sorptive processes that are not considered here. Sums over α are over all fluid phases in the system, which in this study is only liquid H_2O. The quantity Ψ^α_j denotes the total concentration of the jth primary species A_j in the αth fluid phase defined by

$$\Psi_j^a = \delta_{la} C_j^l + \sum_{i=1}^{N_{sec}} v_{ji}^\alpha C_i^\alpha \tag{2.4.8}$$

In this equation the index l represents the aqueous electrolyte phase from which the primary species j with concentration C^l_i are chosen. The secondary species concentrations C^α_i are obtained from mass action equations corresponding to equilibrium conditions of the reactions

$$\sum_j v_{ji}^\alpha A_j^l \rightleftarrows A_i^\alpha \tag{2.4.9}$$

yielding the mass action equations

$$C_i^\alpha = \frac{K_i^\alpha}{\gamma_i^\alpha} \prod_j \left(\gamma_j^l C_j^l\right)^{v_{ji}^\alpha} \tag{2.4.10}$$

with equilibrium constant K^α_i and activity coefficients γ^α_k. Activity coefficients are calculated from the extended Debye-Hückel formulation.

The reaction rate I_m is based on transition state theory taken as positive for precipitation and negative for dissolution, with the form

$$I_m = -A_m\left(\sum_l k_{ml}(T) P_{ml}\right)\left|1 - (K_m Q_m)^{\frac{1}{\sigma_m}}\right|^{\beta_m} sign(1 - K_m Q_m) \tag{2.4.11}$$

where the sum over l represents contributions from parallel reaction mechanisms such as *pH* dependence etc., and where K_m denotes the equilibrium constant of the mineral, σ_m refers to Temkin's constant which is defined as the average stoichiometric coefficient of the overall reaction (Lichtner, 1996b), β_m denotes the affinity power, A_m refers to the specific mineral surface area, and the ion activity product Q_m is defined as

$$Q_m = \prod_j (\gamma_j m_j)^{v_{jm}} \qquad (2.4.12)$$

with molality m_j of the jth primary species. The rate constant k_{ml} is a function of temperature given by the Arrhenius relation

$$k_{ml}(T) = k_{ml}^0 \, exp\left[\frac{E_{ml}}{R}\left(\frac{1}{T_0} - \frac{1}{T}\right)\right] \qquad (2.4.13)$$

where k^0_{ml} refers to the rate constant at the reference temperature T_0 taken as 298.15 K, with T in units of Kelvin, E_{ml} denotes the activation energy (J/mol).

Permeability, tortuosity and mineral surface area may be updated optionally due to mineral precipitation and dissolution reactions through the change in porosity. The porosity φ is updated according to

$$\varphi = 1 - \sum_m \varphi_m \qquad (2.4.14)$$

where φ_m is the mineral volume fraction. Thus, although possible in principle, the full feedback between chemically induced porosity change and permeability is not included in the simulations presented below. In this study only the coupling between reactive surface area and porosity is considered and implemented as

$$A_m = A_m^0 \left(\frac{\varphi_m}{\varphi_m^0}\right)^n \qquad (2.4.15)$$

where φ^0_m is the initial mineral volume fraction. It should be noted, however, that this result only applies to primary minerals because of the restriction $\varphi^0_m > 0$.

Pre-processing workflow

Uni Bern is in the process of deriving experimental constraints for the pore fluid composition, mineralogical composition and for mineral reactivities of the rocks of the USM. These data will be used to construct the reaction network and the thermodynamic database and to constrain the input parameters for the chemical model. For each homogeneous and heterogeneous reaction included in the simulation the equilibrium constant has to be known as a function of temperature and pressure. The equilibrium constant will be computed from the thermodynamic databases *SUPCRT92* (Johnson et al., 1992).

As the true stratigraphic succession of sand and clay layers and their hydraulic and thermal properties are not yet known for the Forsthaus site, model values are taken from previous thermal-hydraulic simulations of the Forsthaus system (e.g. Driesner et al. 2017).

Computational approach and software

We use the open source, state-of-the-art massively parallel subsurface flow and reactive transport code PFLOTRAN (*www.pflotran.org*) to carry out these simulations. PFLOTRAN solves a system of generally nonlinear partial differential equations describing multiphase, multicomponent and multiscale reactive flow and transport in porous materials. The code is designed to run on massively parallel computing architectures as well as workstations and laptops. Parallelization is achieved through domain decomposition using the PETSc (Portable Extensible Toolkit for Scientific Computation) libraries. PFLOTRAN has been developed from the ground up for parallel scalability. The reactive transport equations are solved using a fully implicit Newton-Raphson algorithm.

PFLOTRAN uses a law-of-mass-action (LAM) approach for solving the chemical state of the system. The LAM approach is computationally efficient but it has limitations in terms of flexibility in that it is difficult to handle the effect of dynamic changes in both pressure and temperature on chemical conditions. PFLOTRAN can simulate 2-phase (gas and liquid) systems but here we assume fully liquid saturated conditions at all times. It is still possible to simulate processes such as degassing of CO_2 by using the approach proposed by Alt-Epping et al. (2013) in which the effect of CO_2 degassing was implemented via a pseudo-mineral precipitation reaction.

Two different model geometries are used to represent the Forsthaus system. The first model, presented in section 2.4.3.1.5.1, involves an axisymmetric model representing a single sequence of clay-sandstone-clay in the reservoir. Although the model geometry is simple, by modifying material properties and scaling parameters it is possible to increase realism and to consider processes that occur elsewhere in the system (e.g. in the heat exchanger). The simplicity of the model allows for the implementation of geochemical complexity and detail without limitations concerning computational performance. These axisymmetric simulations typically can be run on laptop PCs within less than one hour.

The second model (section 2.4.3.1.5.2) is a full scale 3D representation of the Forsthaus system. It spans the entire vertical and lateral extent of the system, comprising the main well and 5 supporting wells surrounding it. The model is designed, among other things, to test different well arrangements. It is constructed on the basis of a cartesian coordinate system and it is not limited by any symmetry constraints. This means that lateral heterogeneity in the stratigraphic sequence and hence in hydraulic conditions can be implemented easily. The model achieves perfect water balance between the flux through main well and total flux through all supporting wells by imposing a flux constraint for each supporting well.

Model Analysis

The models presented here are an extension of previous thermal-hydraulic models carried out by various groups, in that we couple flow and heat transport with solute transport and chemical reactions. The outcome of these simulations are valuable insights into geochemical processes that are expected to occur during the operation and an assessment of the risk of geochemical processes during a sustained operation.

The simple axisymmetric model, because of its short running time, is useful for sensitivity studies and parameter optimization. These are particularly useful to assess 1) processes or parameters affecting fluid-rock reactions in the reservoir and their implications for the transmissivity of individual sandstone layers, 2) processes related to cooling of water buffered by the reservoir rock, and 3) the implication of injecting water that is in thermal and geochemical disequilibrium with the reservoir rock.

The full scale 3D model is useful for design and performance optimization (e.g. well spacing, number of wells and pumping schedule) and to address issues related to spatial heterogeneity or asymmetries in the system (e.g. lateral pinching out of strata, background groundwater flow) .

Scenarios and results

Simplified models of the Forsthaus system

The simplified simulations presented below were originally designed as benchmark problems for reactive transport codes (Alt-Epping and Mindel, 2020). These simulations, despite their simplicity, are highly relevant for the Forsthaus system and are useful as a basis for the full scale 3D model.

1D simulation to constrain hot fluid composition at injection wellhead

This 1D flowpath simulation constitutes a preparatory step for the subsequent axisymmetric and 3D simulations. It models the closed-system chemical and thermal evolution of previously extracted USM groundwater as it passes through the surface heat exchanger, ready for pumping into the injection well during a heat storage cycle. The computed water composition is essential input for all models presented below. In the simulation USM groundwater at 15 $^\circ$C is fed into a 1D flowpath and heated to 90 $^\circ$C.

Water composition changes due to heating and mineral precipitation

USM Porewater

15 °C

Flow

90 °C

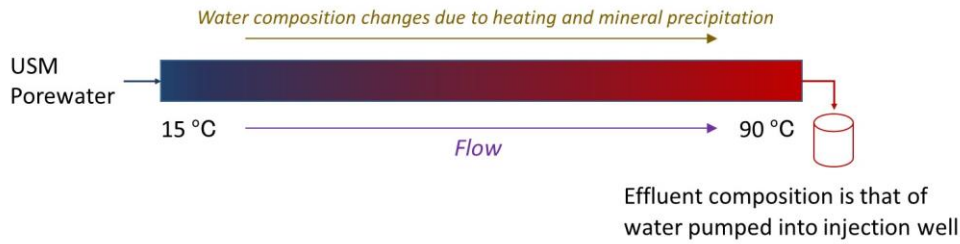Effluent composition is that of water pumped into injection well

Figure 2.4.9 Model of a 1D flowpath used to constrain the composition of the fluid injected into the injection well. Cold USM porewater (Table 2.4.4) enters on the left and is heated to 90 °C while reactions along the flowpath modify the water composition. The water extracted on the right has the temperature and composition of the water injected into the injection well in the scenarios presented below (Table 2.4.4).

The flowpath is arbitrarily 38 m long and discretized into 152 cells, each having a length of 0.25 m. At the inlet of the surface installation (production wellhead) the fluid composition is that of the USM sandstone porewater summarized in Table 2.4.4. A linear temperature gradient of 2 °C /m is imposed along the flowpath and the fluid composition at 90 °C is read out of the model. There are no dissolving minerals along the flowpath, only mineral precipitation is allowed. Mineral thermodynamic properties are summarized in Table 2.4.5. Fluid flow along the flowpath is slow enough to maintain local equilibrium. The total simulation time is 730 days.
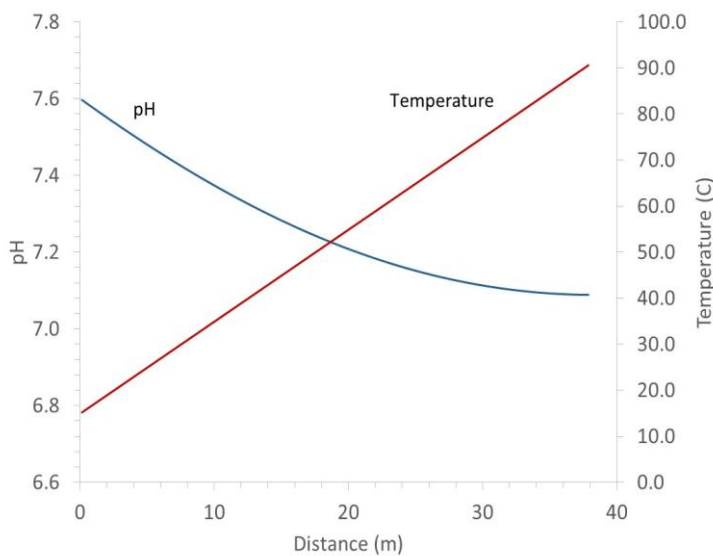
Figure 2.4.10: Profiles of temperature and pH
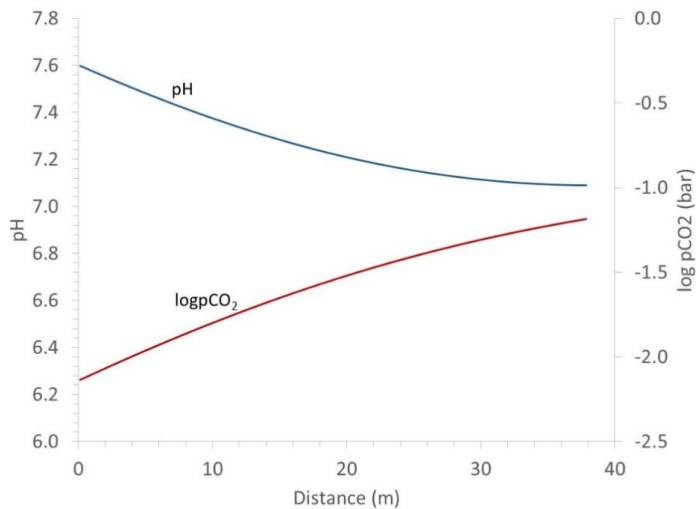
Figure 2.4.11: Profiles of pH and pCO2
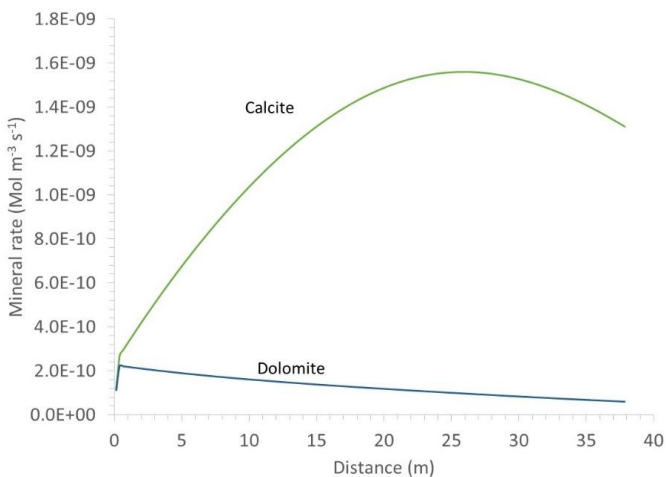
Figure 2.4.12: Profiles of carbonate mineral reaction rates. Heating the USM groundwater leads to precipitation of carbonate minerals due to their retrograde solubility with respect to temperature.

Heating of the USM groundwater to 90 °C leads to a slight decrease in pH, an increase in pCO_2 and to the oversaturation of carbonate minerals calcite and dolomite due to their retrograde solubility with temperature (Figure 2.4.10, Figure 2.4.11, and Figure 2.4.12). The composition of the water extracted at 90 °C is shown in Table 2.4.4. A comparison of columns 2 and 3 in that Table reveals the compositional changes of the water due to heating and carbonate precipitation.

Mass balance calculations reveal that for a model through flow of 4215.5 kgH_2O/yr, 1.01e-4 m^3 of carbonate scales (calcite plus dolomite) precipitate in total. If the flow rate in the real system amounts to 25 l/s or 7.89e8 kg/yr (using a density at 15 °C of 1001.21 kg/m^3_H_2O) then the total volume of carbonate scales produced could be as high as 18.9 m^3 per year. Assuming that a volume equivalent of 216 days or 0.59 years of pumping at 25 l/s has to be extracted from the aquifer and heated, the total amount of carbonate scales is 11.15 m^3. Taking into account the gradual heating of the aquifer and assuming that the injected temperature is actually 50 °C (instead of 15 °C) the total volume of carbonate minerals amounts to 6.57 m^3 for a fluid volume equivalent of 216 days of pumping at 25 l/s.

The simulations and mass balance calculations show that during loading cycles there is a substantial risk of carbonate precipitation with potentially serious consequences for a sustained operation when reservoir water is heated.

Table 2.4.4 Initial USM pore water compositions expressed as total concentrations and buffering mineral or gas phase, if applicable. The sandstone porewater corresponds to the water entering the flowpath in Figure 2.4.9 he composition of the 90 °C water is that of the outlet water in Figure 2.4.9, corresponding to the composition of the water injected at the well heads.

	Clay (15 °C)	Sandstone (15 °C)	Inj. water at well head (90 °C)
Tracer	1e-5	1e-5	1.0
SiO_2,aq	6.04e-5 (Quartz eq.)	6.04e-5 (Quartz eq.)	6.04e-5
pH	7.6	7.6	7.014
Na^+	Charge	Charge	Charge
Cl^-	8.69e-4	8.69e-4	8.69e-4
Ca^{++}	7.53e-5 (Calcite eq.)	7.53e-5 (Calcite eq.)	3.18e-4 (Calcite eq.)
Mg^{++}	5.68e-6 (Dolomite eq.)	5.68e-6 (Dolomite eq.)	1.3e-5 (Dolomite eq.)
K^+	7.16e-5	7.16e-5	7.16e-5
Al^{+++}	1e-12	1e-12	1e-12
$\log(pCO_2)$ (bar)	-2.15	-2.15	-1.1236
SO_4^{--}	2.34e-4	2.34e-4	2.34e-4

Table 2.4.5 Mineral kinetic properties

	Log rate constant (neutral) mol m^{-2} sec^{-1}	Activation energy (J/mol) (neutral)	Log rate constant (acid) mol m^{-2} sec^{-1}	Prefactor (H^+)	Activation energy (J/mol) (acid)	Reactive surface area m^2/m^3_bulk
Quartz	-13.4	90	-	-	-	1
Calcite	-5.81	14.4	-0.3	1	23.5	1
Dolomite	-7.53	52.2	-3.19	0.5	36.1	1
Albite	-12.56	70	-10.16	0.457	14.4	1
K-feldspar	-12.41	38	-10.06	0.5	51.5	1
Illite	-13.55	22	-11.85	0.37	22	1
Muscovite	-13.55	22	-11.85	0.37	22	1
Ca-Smectite	-12.78	35	-10.98	0.34	12.6	1
Na-Smectite	-12.78	35	-10.98	0.34	12.6	1
Kaolinite	-13.18	22.2	-11.31	0.777	65.9	1
Mg-chlorite	-12.52	88	-11.11	0.5	88	1
Gypsum	-2.79	0	-	-	-	1
Anhydrite	-3.19	14.3	-	-	-	1
SiO_2(am)	-9.42	49.8	-	-	-	100
CO_2(s)	-6	50	-	-	-	100

Injection/extraction scenarios with heat and tracer transport in an axisymmetric model

An important feature of regulatory and energetic concern is the spatial extent of the thermal and the geochemical plumes around the injection well. This is defined as the distance over which compositional changes of the original porewater induced by the operation are detectable around the well. An axisymmetric model of the reservoir (Figure 2.4.13 and Figure 2.4.14) is used to simulate the injection and extraction schedule summarized in Table 2.4.6. Simulations are carried out for an operation period of 10 years. The model comprises a vertical sequence of clay-sandstone-clay layers, each having a thickness of 5 m. Because of the symmetry of the reservoir in the upper panel of Figure 2.4.12 with respect to the horizontal plane at mid-depth, we only consider the lower half of the model in the simulation. Injection and extraction are performed alternately through the single well located in the center (i.e. along the center axis) of the cylindrical model. The injection/extraction rate is 25 l/s scaled by a factor that corresponds to the model thickness over the total thickness of the system. No reactions are included in this simulation yet, only solute and heat transport are considered. Solute transport is implemented via a non-reactive tracer dissolved in the injected water. No natural fluid flow in the reservoir is assumed. Outward transport of the tracer occurs due to this pressure differential upon injection and to diffusion and dispersion through the porewater. Heat is transported by convection and diffusion.
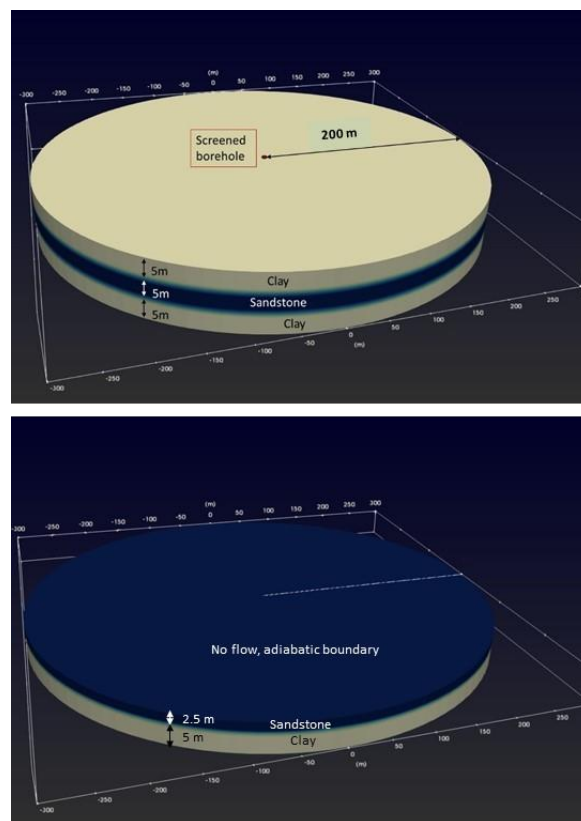
Figure 2.4.13 Simplified model of the Forsthaus system with a single permeable sandstone unit sandwiched between low-permeability clays (upper panel). Lower panel: actual model domain making use of the horizontal plane of symmetry at mid-depth.
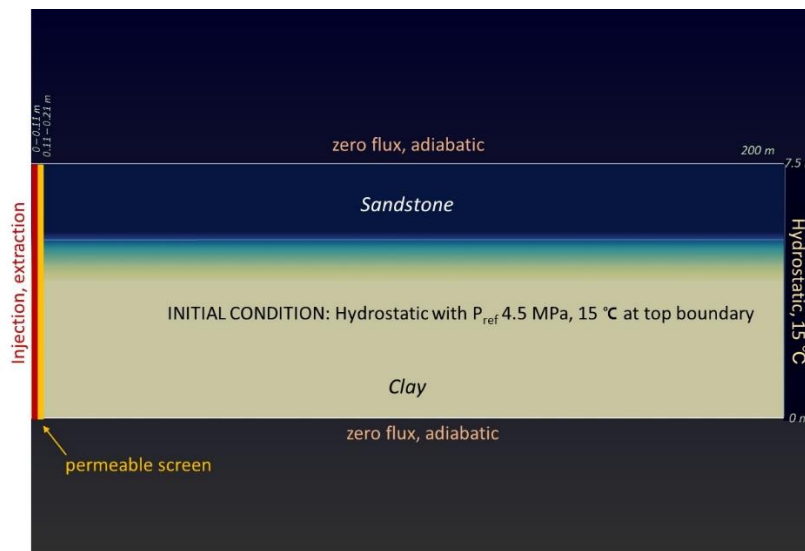
Figure 2.4.14 Model dimensions (not to scale) and boundary and initial conditions for flow and heat transport

Table 2.4.6 Annual schedule of injection/extraction cycles (note: PFLOTRAN requires a temperature condition at the extraction well which is set to be 50 ℃)

Time (d)	Q (l/s)	T (℃)	Inject	Extract
0-216	25	90	x	
216-365	25	50		x

Table 2.4.7 Physical properties of the materials

	Sandstone	Claystone	Screen	Borehole
Porosity	0.1	0.05	0.5	1.0
Tortuosity	0.05	0.05	0.05	1.0
Permeability (m^2)	3.45e-13	2.6e-17	1e-10	1e-10
Dispersivity (transverse and longitudinal) (m)	1e-3	1e-3	0.0	0.0
Heat capacity (J kg^{-1} K^{-1})	750	750	750	818
Thermal conductivity (W m^{-1} K^{-1})	2.67	2.67	1e-5	1.6
Density (kg/m^3)	2743	2743	2780	2000

The simulation output shows regular fluctuations of pressure according to injection/extraction cycles. The amplitude of these pressure fluctuations decreases with increasing distance from the well but the perturbation of fluid pressure due to pumping extends well beyond a distance of 100 m from the well (Figure 2.4.15).

The temperature increases and decreases upon injection and extraction, respectively, according to the pumping schedule in Table 2.4.6. While in close vicinity of the injection well the temperature of the sandstone aquifer acquires and maintains the injection temperature of 90 ℃ over each injection cycle, the extraction temperature increases over time. Likewise, further away from the well (e.g. at 50.25 m, Figure 2.4.15) the temperature exhibits a gradual increase over time. This temperature increase indicates a gradual heating of

the reservoir (which involves both the sandstone and the clay units). Thermal effects becomes weaker with increasing distance from the injection site – there is virtually no change in temperature at a distance of 100 m from the injection/production well over a period of 10 years.

In contrast, the tracer moves much faster and penetrates deeper into the reservoir than the temperature. This is because tracer transport is confined to the connected porosity while heat transport occurs through the bulk medium, consisting of liquid and solid. Hence, in PFLOTRAN for a given Darcy flux (i.e. volume of liquid per unit area per time) the tracer flow velocity scales inversely with porosity, while the thermal front moves at the rate of the Darcy flux. At observation points close to the well, the injection concentration of 1 mol/kg is attained rapidly and maintained during the 10 year operation period. During the first injection a fraction of the tracer migrates beyond 100 m into the reservoir. In the following extraction cycle much of the tracer mass is flushed out of the sandstone, as dilute water is drawn from the more distal part of the aquifer (note, the observation point at 100 m is not affected by the influx of water across the right-hand boundary). Because the injection period is longer than the extraction period, with each injection-extraction cycle, the tracer migrates deeper into the aquifer so that, ultimately, the tracer attains the injected concentration of 1 mol/kg at r = 100 m (Figure 2.4.15).

The results from this simulation are important because they demonstrate that the "radius of influence" of the operation, if defined on the basis of solute transport, far exceeds that defined by the thermal plume. This effect becomes even more pronounced if the volume of the injected water exceeds that of the extracted water.
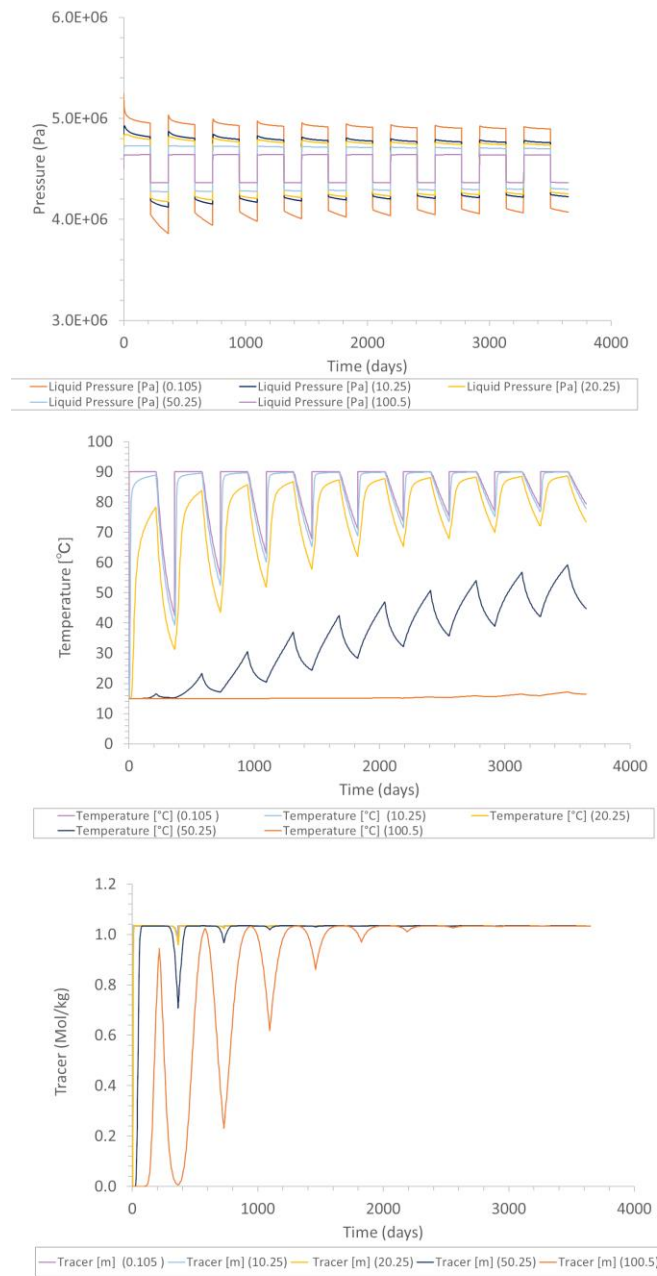
Figure 2.4.15 Time series of pressure, temperature and tracer concentration at different distances from the well. While the pressure fluctuates regularly (upper panel), the system heats up over time (e.g. temperature panel at 50.25 m). The thermal plume does not extend beyond 100 m after a 10 year period (middle panel). In contrast, solute transport (lower panel) affects a much larger region that extends well beyond 100 m (although it takes about 5 injection cycles to establish constant tracer concentrations at 100 m).

Implementing complex chemistry into the axisymmetric model

We use the same injection-extraction schedule, temperature constraints and domain geometry as in the previous simulation case. Here we couple the previous simulation with a full reaction network. The composition of the injected water is taken from Table 2.4.4. The primary mineralogy of the clay and sandstone units are given in Table 2.4.8. Note that the minerals amorphous silica and "CO_2,s" are omitted here as these minerals are specifically used to assess processes in the heat exchanger which are addressed in the next section.

Table 2.4.8 Mineral composition (volume fraction) of the clay and sandstone units in the USM

	Clay	Sandstone
Quartz	0.18	0.35
Calcite	0.15	0.12
Dolomite	0.05	0.02
Albite	0.10	0.18
K-feldspar	0.07	0.11
Illite	0.10	0.05
Muscovite	0.10	0.05
Ca-Smectite	0.10	0.05
Na-Smectite	0.10	0.05
Kaolinite	0.00	0.00
Mg-chlorite	0.05	0.02
Gypsum	0.00	0.00
Anhydrite	0.00	0.00
SiO_2(am)	-	-
CO_2(s)	-	-

Full list of component (primary) species, secondary species, minerals and gases:

Component species: SiO_2(aq), H^+, Na^+, Cl^-, Ca^{++}, Mg^{++}, K^+, Al^{+++}, HCO_3^-, SO_4^{--}

Secondary species: OH^-, CO_2(aq), CO_3^{--}, $H_3SiO_4^-$, $HSiO_3^-$, $MgOH^+$, $MgCO_3$(aq), $MgHCO_3^+$, $MgCl^+$, $MgSO_4$(aq), $CaCO_3$(aq), $CaHCO_3^+$, $CaCl^+$, $CaCl_2$(aq), $CaSO_4$(aq), KCl(aq), NaCl(aq), NaOH(aq), $NaCO_3^-$, $NaHCO_3$(aq), $AlOH^{++}$, $Al(OH)_2^+$

Gases: CO_2(g)

Minerals: Quartz, Calcite, Dolomite, Albite, K-Feldspar, Illite, Muscovite, Smectite-Na, Smectite-Ca, Kaolinite, Clinochlore-14A, Gypsum, Anhydrite, Amorphous silica, "CO_2(s)" (dummy mineral representing CO2(g) solubility at 3 bar)

Spatial profiles through the sandstone layer showing the tracer composition, temperature, pH and the rates of calcite and dolomite dissolution/precipitation after 214 days (at the end of the first injection period) and 363 days (at the end of the first extraction period) are shown in Figure 2.4.16, Figure 2.4.18 and Figure 2.4.19. The spatial profiles of the tracer and temperature in Figure 2.4.17 are consistent with the conclusion from the previous section, that the tracer front propagates much deeper into the aquifer than the thermal front.
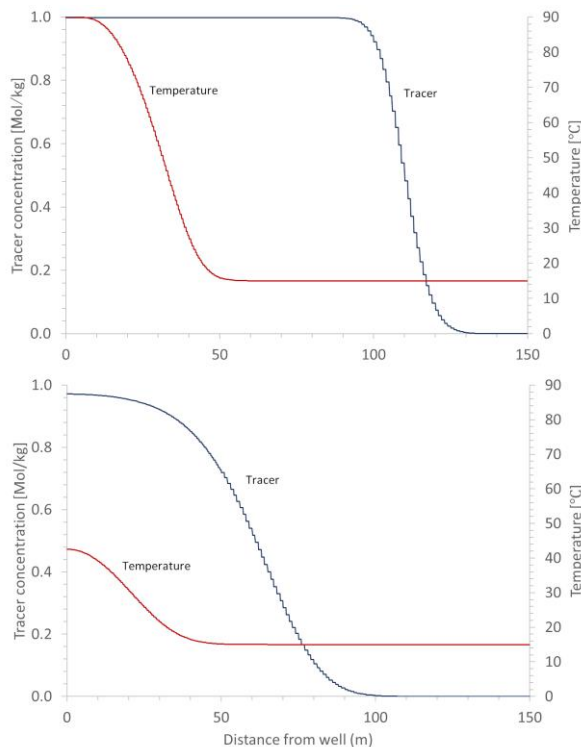
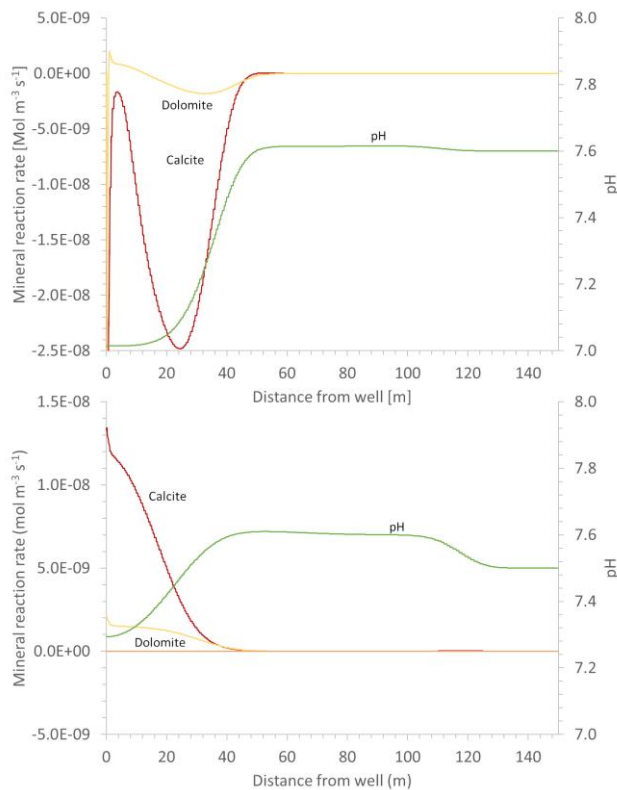**Figure 2.4.17 Spatial profiles of the tracer, temperature and pH after 214 days (end of first injection, upper panel) and 363 days (end of first extraction, lower panel. Tracer and pH perturbations advance and retract upon injection and extraction cycles. Owing to the fact that the injected water volume exceeds the extracted volume, over time the thermal and chemical fronts are pushed progressively deeper into the system. Note the slower breakthrough of the thermal plume compared with the tracer breakthrough.**

Mineral reactions are dominated by calcite dissolution and precipitation (Figure 2.4.18). All mineral reactions are confined within a radius of about 50 m from the well (Figure 2.4.18 and Figure 2.4.19). During injection, strong calcite and minor dolomite dissolution occurs while during extraction both minerals precipitate. This alternation between carbonate dissolution and precipitation also takes places at greater distance from the well, only at lower rates and with a certain time lag, as the injection zone (i.e. the zone affected by thermal or compositional changes due to injection) grows in size.

In contrast, the pH shows a slight drop towards the well, because the injected water is very slightly more acidic than the water in the reservoir (Table 2.2.2). There is little difference in the pH profiles between injection and extraction periods. The behavior of carbonate minerals is most likely controlled by thermal conditions, more specifically, by the slow evolution of the thermal conditions compared to solute transport. During injection, solutes are transported beyond the thermal front, implying that injected water undergoes cooling as it moves deeper into the aquifer. As the injected fluid is increasingly undersaturated with respect to carbonates at all temperatures below 90 °C, it dissolves carbonates as it cools. Upon extraction, cooler water from the distal parts of the aquifer is pumped towards the well, where the rock is relatively warm from the previous injection cycle. As a consequence, carbonate minerals precipitate due to their retrograde solubility with respect to temperature.

The reactivity of silicate minerals is orders of magnitude lower than that of the carbonate minerals (Figure 2.4.19). It is dominated by the hydration of feldspars to an assemblage of clay minerals. While all primary minerals dissolve continuously, regardless of whether water is pumped in or out, the composition of the clay assemblage is sensitive to the pumping conditions. During injection, the clay assemblage is dominated by muscovite, during extraction by smectite (Ca and Na endmembers).

Quartz dissolves at all times. The reason for this is that the injected water constitutes heated USM pore-water that has had no contact with quartz after leaving the reservoir. Because of its prograde solubility, quartz is strongly undersaturated in the hot injected water and hence it dissolves in the injection zone within the reservoir. During extraction relatively cool water is drawn from the distal parts of the reservoir towards the well where temperatures are higher (Figure 2.4.17). Here too, owing to its prograde solubility with temperature, quartz becomes undersaturated and dissolves from the reservoir rock.
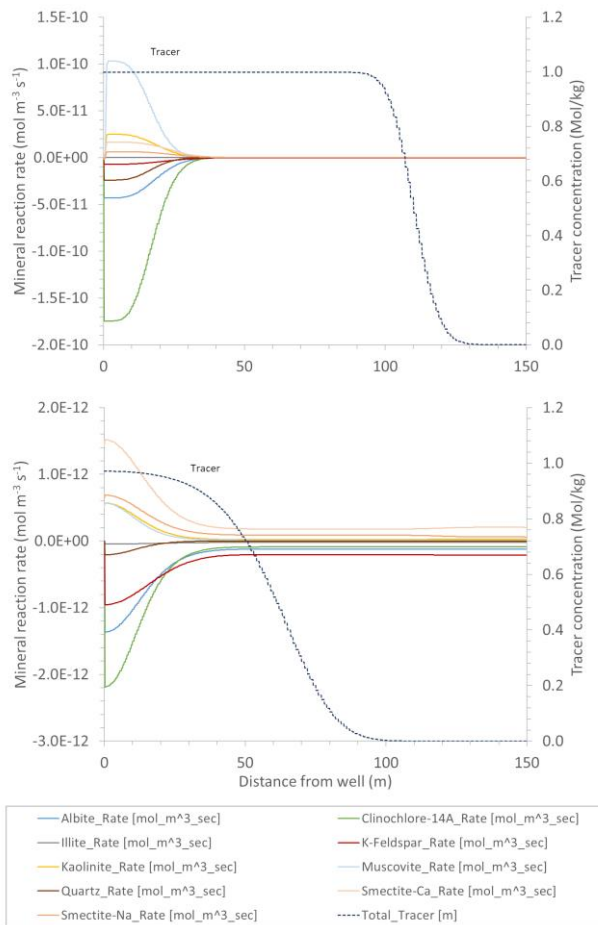
Figure 2.4.18 Carbonate mineral reaction rates after 214 days (end of first injection, upper panel) and 363 days (end of first extraction, lower panel. Both carbonate minerals precipitate dissolve and precipitate upon injection and extraction, respectively, within a radius of about 50 m. These reactions are controlled primarily by the direction of flow across isotherms: During injection the water is cooled as it moves away from the well inducing carbonate undersaturation. During extraction the water is heated as it moves towards the well inducing carbonate oversaturation.

Time series at observation points at different distances from the well (Figure 2.4.20 and Figure 2.4.21) show that at 100 m away from the injection well no mineral reactions take place over the simulated 10 year period. Very small fluctuation in the pH can be seen (Figure 2.4.21). At shorter distances from the well (20 - 50 m), chemical conditions change gradually over time. Superimposed on these gradual changes are fluctuations related to alternating periods of injection and extraction. For instance, the rate of quartz dissolution increases gradually (Figure 2.4.20), while the pH decreases (Figure 2.4.21). These gradual changes are caused by the heating of the reservoir. The thermal plume around the injection zone extends to a distance beyond 50 m but never reaches 100 m within the 10 year period (Figure 2.4.15, middle panel). The increase in quartz dissolution over time is an indication of its prograde solubility with respect to temperature and/or the temperature dependence of the rate constant (Eq. 2.4.13).

Closer to the well, the amplitude of pumping-related fluctuations in chemical conditions increases compared to the fluctuations in the more distal parts of the reservoir. However, the amplitude tends to decrease over time. For quartz (Figure 2.4.20), this decrease in amplitude is related to an increase in the dissolution rate during extraction. The behavior of quartz correlates with the temperature evolution in Figure 2.4.15, middle panel, indicating that the rate of quartz dissolution is temperature controlled.

One of the risks for a sustained operation related to chemical processes is that of clogging pore space and reducing permeability in the reservoir due to fluid-rock reactions. Porosity changes due to mineral reactions are readily predicted and they provide an indication of the expected change in permeability provided that a relation between porosity and permeability exists. Similarly, the dissolution of calcite cement may lead to the release of sandgrains that may clog flowpaths downstream or lead to physical corrosion in the wells or the surface installation. Although the behavior of calcite can be readily predicted with the THC model presented here, the potential release of sand as suspended load and its implication for the reservoir permeability or corrosion more difficult to predict and is beyond the scope of this modelling study.

Figure 2.4.18 and Figure 2.4.19 show the mineral dissolution and precipitation reactions that occur in the injection zone. Carbonate minerals are orders of magnitude more reactive than the silicate minerals. Aside from their low reactivity, the effect of reactions involving silicate minerals on porosity is negligible because the volume of dissolved primary minerals is partly compensated by the volume of precipitated clay minerals.

While silicate reactions are only mildly affected by alternating pumping scenarios, calcite and dolomite precipitate during extraction and (re)dissolve during injection. Although their reaction rates are high, because of alternating precipitation/dissolution the time-integrated effect of carbonate reactions on porosity is small (Figure 2.4.22) and there is virtually no risk of clogging. In fact, all reactions in the injection zone combined lead to a porosity increase. It follows that a serious decrease in permeability within the reservoir is very unlikely.

Figure 2.4.19 Reaction rates of alumino-silicates after 214 days (end of first injection, upper panel) and 363 days (end of first extraction, lower panel. Profiles show that kaolinite is the main alteration phase near the well, and muscovite occurs in small amounts. Kaolinite precipitates following the hydration of feldspars. Minor smectite forms during extraction and redissolves upon injection.
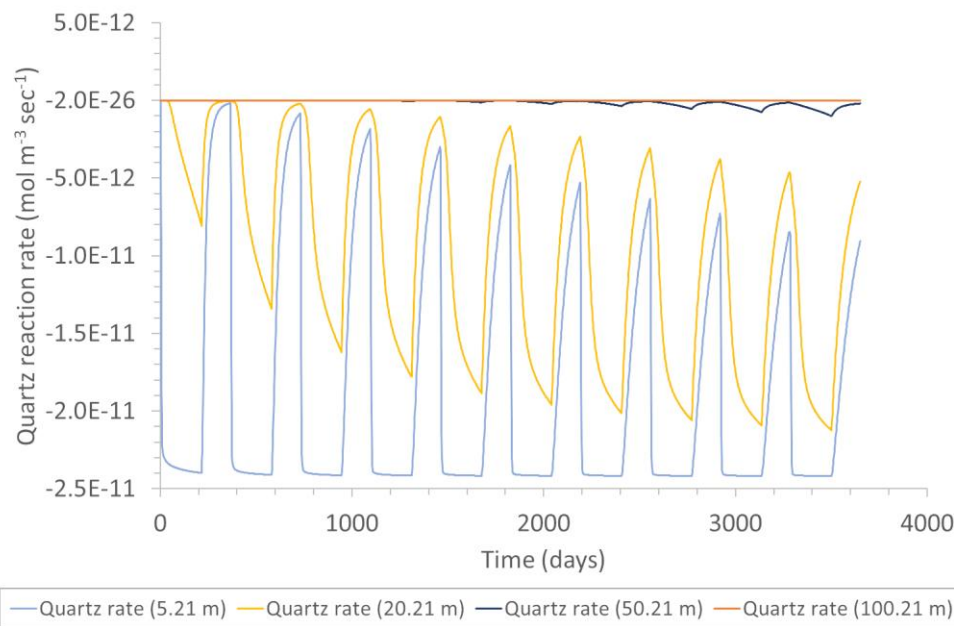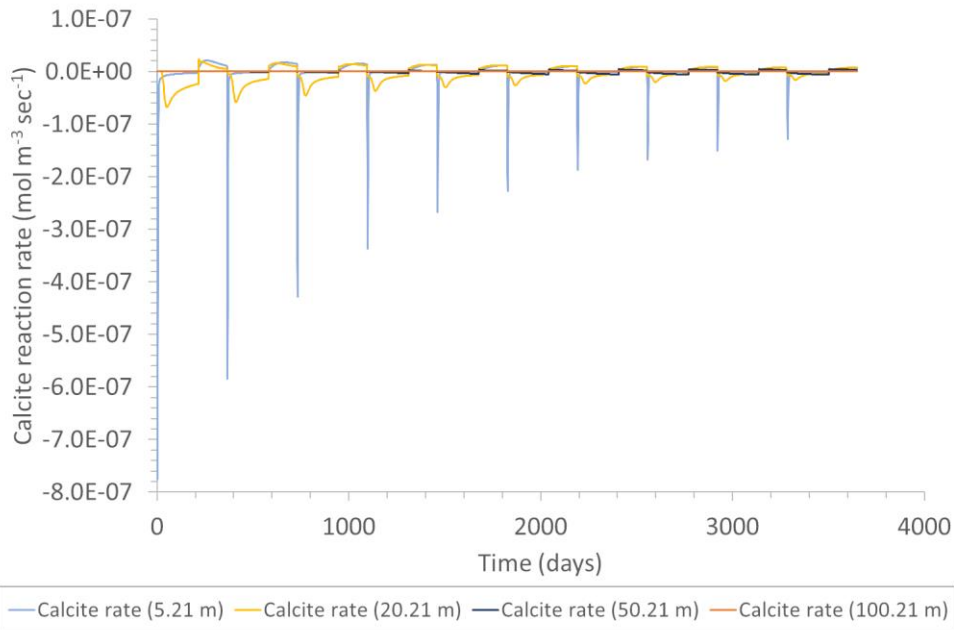
Figure 2.4.20 Upper panel: The alternating dissolution and precipitation of calcite upon injection and extraction as can be seen in Figure 2.4.17 can be seen here as well. Notable is the very short period of calcite dissolution at the beginning of each injection period. Lower panel: quartz dissolves in the vicinity of the injection site. Quartz undersaturation follows from the fact that the injected water constitutes heated USM groundwater. The dependence of the quartz reactivity on temperature is evident from the increasing dissolution rate at 20.21 m and 50.21 m.
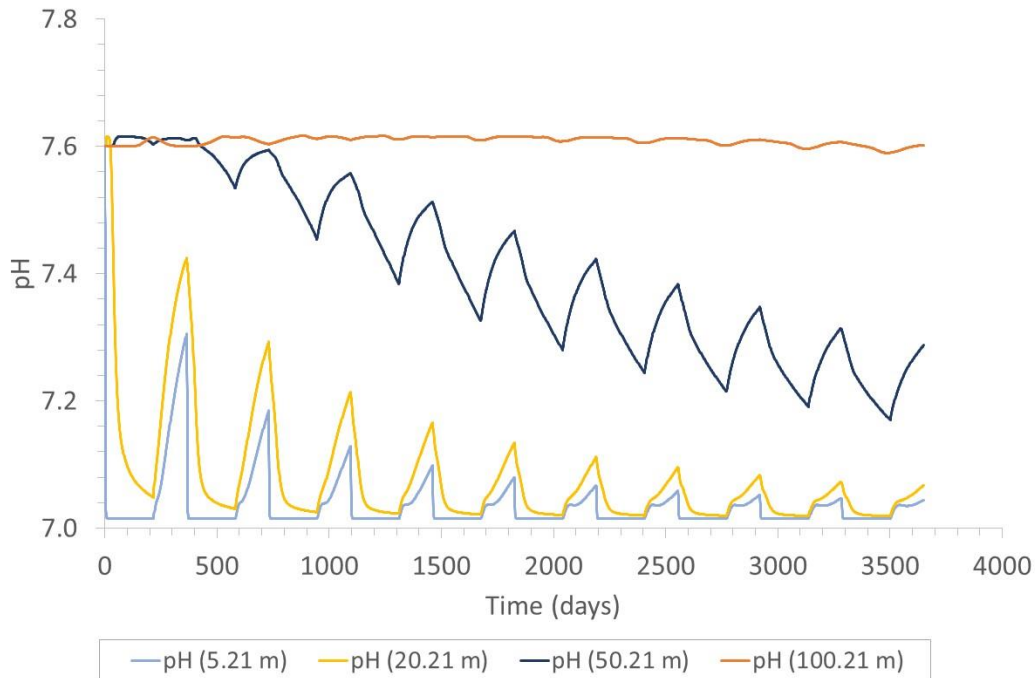
Figure 2.4.21 The pH of the initial, undisturbed sandstone is set to 7.6. This value is maintained (with slight fluctuations) in the distal parts of the domain (e.g. at 100.21 m). Closer to the injection well the pH decreases over time, consistent with a lower pH (7.09) of the injected water.
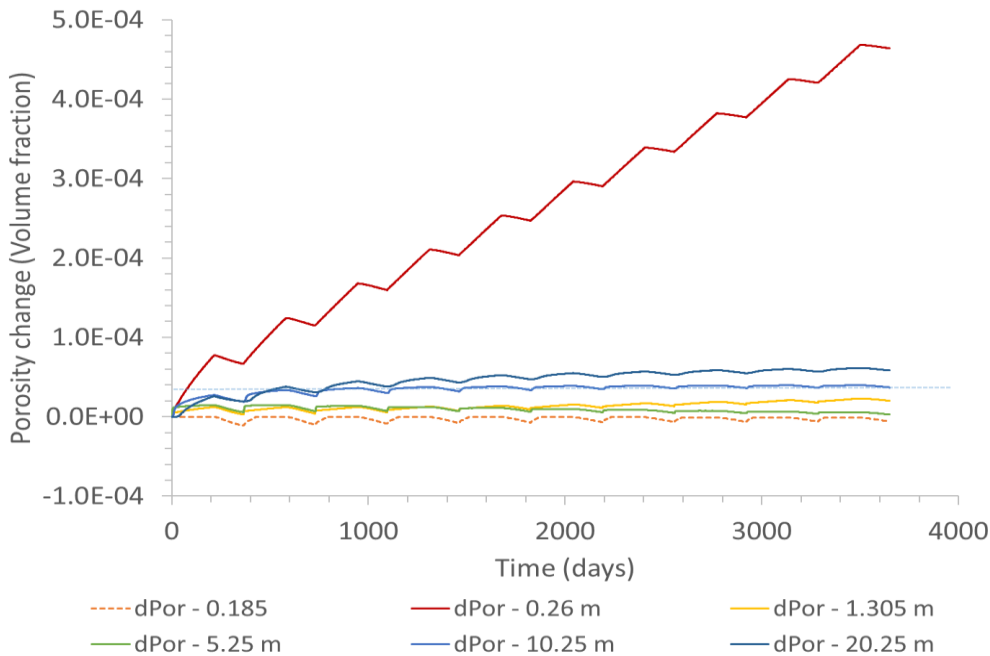
Figure 2.4.22 Porosity evolution at different observation points along the aquifer. Most of the porosity changes are due to carbonate dissolution/precipitation reactions. The porosity changes are very small and not likely to affect aquifer permeability and hence the operation of the system.

Implementing a heat exchanger into the axisymmetric model

Given the simplified geometry of the model, implementing the ascent of the water from the reservoir and its cooling in the heat exchanger can only be a crude approximation of reality. The heat exchanger constitutes a region where the fluid undergoes rapid cooling and heating during unloading and loading cycles, respectively. Here we only consider cooling in the heat exchanger during extraction. During injection we impose the same injection conditions, temperature and water composition, as in the previous section. A heat exchanger that accounts for these alternating conditions during injection and extraction is implemented by changing the properties of the borehole from an injection well to an extraction well in combination with a heat exchanger at the beginning of each injection and extraction cycle, respectively. The heat exchanger (the red area in Figure 2.4.23) is implemented in the model as follows:

1)   the thermal conductivity of the well is purposefully increased to an arbitrary high value

2)   the temperature along the section where the well meets the upper model boundary is set to the desired lowest temperature in the heat exchanger, which is assumed to be 20 °C

3)   the well attains the desired temperature of the heat exchanger throughout

4)   the heat capacity is set to an arbitrary high value

5)   Mineral precipitation reactions are turned on

6)   Mineral precipitation rates are increased by a factor of 100 to achieve mineral equilibration within the short interval of the model heat exchanger

Between each change from extraction to injection there is one day during which all properties of the well and heat exchanger are reset to injection conditions. To preserve those minerals that precipitated in the well and in the heat exchanger during extraction and to allow them to accumulate in time, during each injection period the reactivity of these minerals is is set to zero.

In addition, the well screen (the blue area in Figure 2.4.23) is used to mimic an extraction well. During extraction in the real system, water enters the well where it is no longer buffered by any dissolving minerals but undergoes pressure and temperature changes while ascending to the surface. Analogously to the real system, in the model screen the water moves from rock buffered conditions to unbuffered conditions. In the screen only mineral precipitation is allowed during extraction periods, mimicking the formation of scales in the real extraction well. Mineral precipitation rates are increased by two orders of magnitude to achieve instantaneous mineral equilibration within the interval of the screen which is much shorter than the real wells.
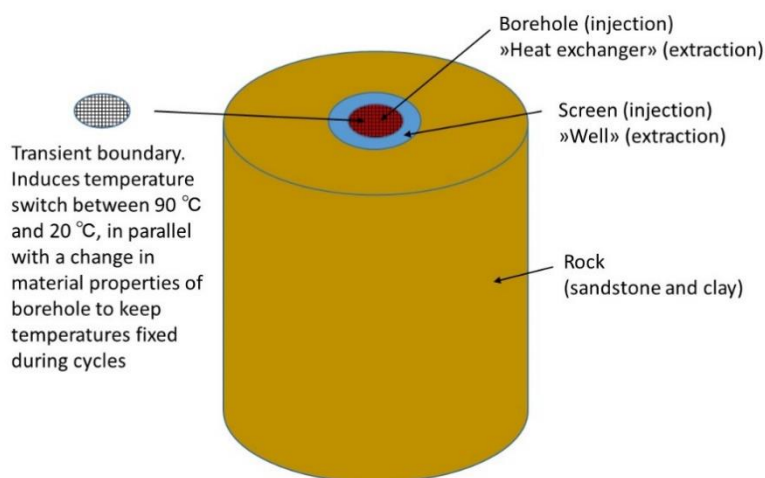
Figure 2.4.23 Concept of switching boundary conditions and material properties to approximate conditions in the installations (well and heat exchanger) in the real system.

However, because of the much shorter interval of the screen, we cannot model the pressure and temperature changes within a well in detail. Instead, we assume that the water ascends fast enough to maintain its reservoir temperature during ascent. Pressure changes are not accounted for.

We focus on processes in the immediate vicinity of the well, in the region r < 10.21 m. The innermost observation point (r = 0.105 m) is located within the region in which properties alternate between an injection well and a heat exchanger during injection and extraction cycles, respectively. The temperature–time series illustrates this behavior (Figure 2.4.24). During injection, the temperature of the borehole is that of the injected water (i.e. 90 °C). During extraction the borehole is cooled to 20 °C, assumed to be the lowest water temperature in the heat exchanger.
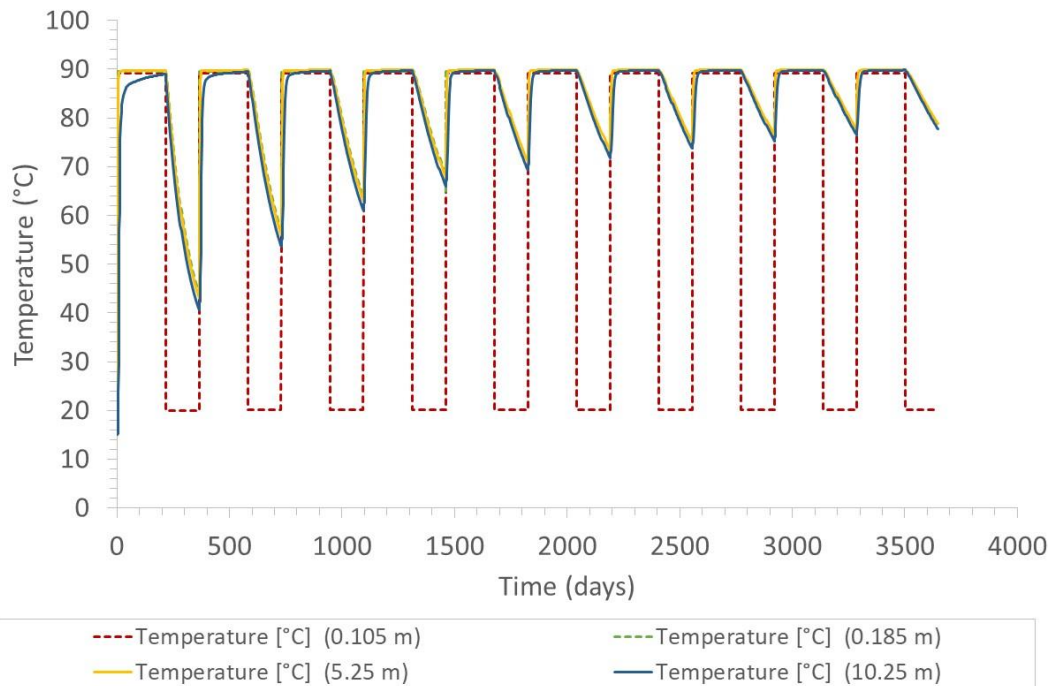
Figure 2.4.24 Temperature evolution in the injection well/heat exchanger (0.105 m) and at greater distance from the well.

The observation point at r = 0.185 m is located in the "screen" representing the well. The screen is thermally isolated from the heat exchanger, and the temperature is solely controlled by the movement of water (Figure 2.4.24). Chemical conditions are analogous to the borehole in the real system in that there are no primary minerals that can dissolve; only mineral precipitation is considered. The screen thus represents an interval in which the groundwater moves from rock buffered to unbuffered conditions. Precipitating minerals accumulate, mimicking the formation of scales.

Figure 2.4.25 shows the constant pH during injection periods (i.e. the pH of the injected water, Table 2.4.4) and the pH of the water extracted from the reservoir during extraction periods. The pH shows a general decrease in time, but there is a pH increase related to cooling in the heat exchanger (0.105 m). Calcite precipitation occurs in the "well" (i.e. the screen, 0.185 m). The water entering the screen is slightly oversaturated with calcite, owing to relatively high flow velocities in combination with heating in the vicinity of the well. The high precipitation rates in the screen that were imposed to scale the amounts of minerals precipitating in the screen to those precipitating along the length of the real well, lead to high rates of calcite precipitation. This indicates that calcite scaling in the well has to be expected during extraction (Figure 2.4.26 and Figure 2.4.27). There is no calcite precipitation in the heat exchanger during extraction due to its retrograde solubility. In the reservoir surrounding the well, calcite dissolution occurs during injection, consistent with Figure 2.4.18.

Cooling the water in the heat exchanger lowers the solubility of alumino-silicates leading to the precipitation of small amounts of clay minerals in the heat exchanger (Figure 2.4.28). It is interesting to note that neither quartz nor amorphous silica attain saturation. There may be two reason for this: 1) the extracted water is undersaturated with respect to quartz because the water temperature increases as the water is drawn

towards the well, and 2) the precipitation of clay minerals consumes SiO_2,aq such that it is no longer available for the formation of quartz.

The computed amounts of minerals in the "well" and the "heat exchanger" (i.e. the model screen and the model well, respectively), need to be scaled to the dimension of the real system to have any quantitative meaning. That is, model volume fractions have to be scaled by the extraction rates and bulk volumes in the real system. For instance, a volume fraction of 3.75e-3 of calcite accumulating in the screen over a period of 10 years (Figure 2.4.27) implies an absolute volume of about 0.078 m^3 for the 7.5 m vertical extent of the model. Recalculating for the entire thickness of the real system (350 m) yields a total volume of scales of 0.36 m^3 per year for the real system.
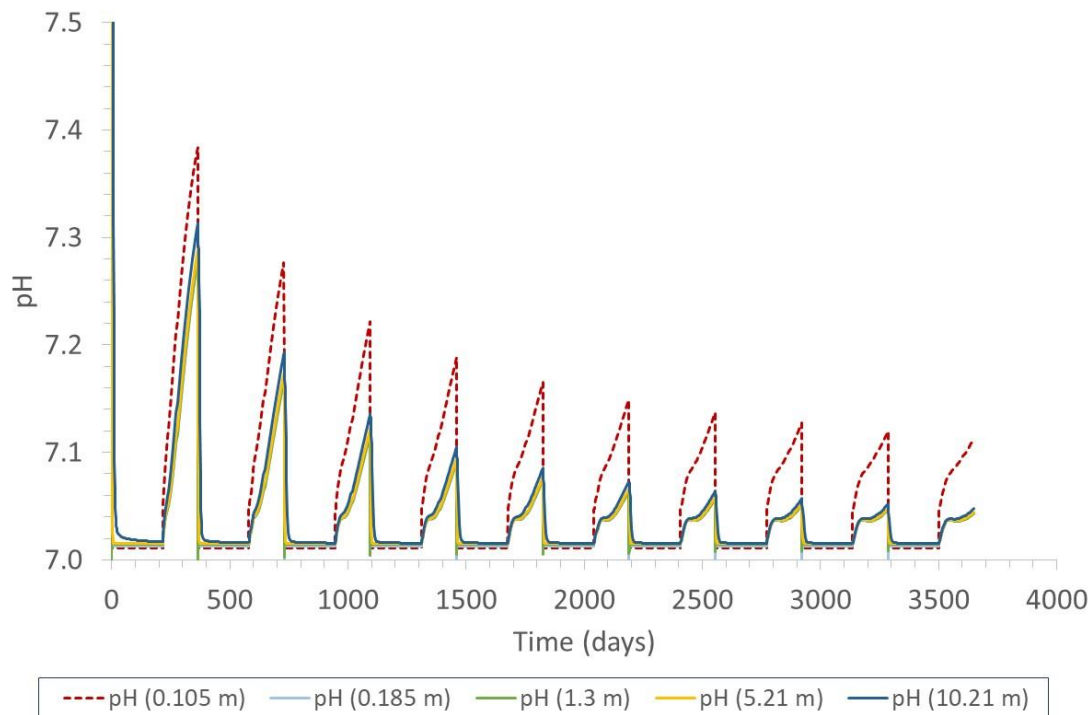
Figure 2.4.25 The pH shows fluctuations between that of the injected water (pH = 7.01) and that of the rock buffered water during injection and extraction cycles respectively.
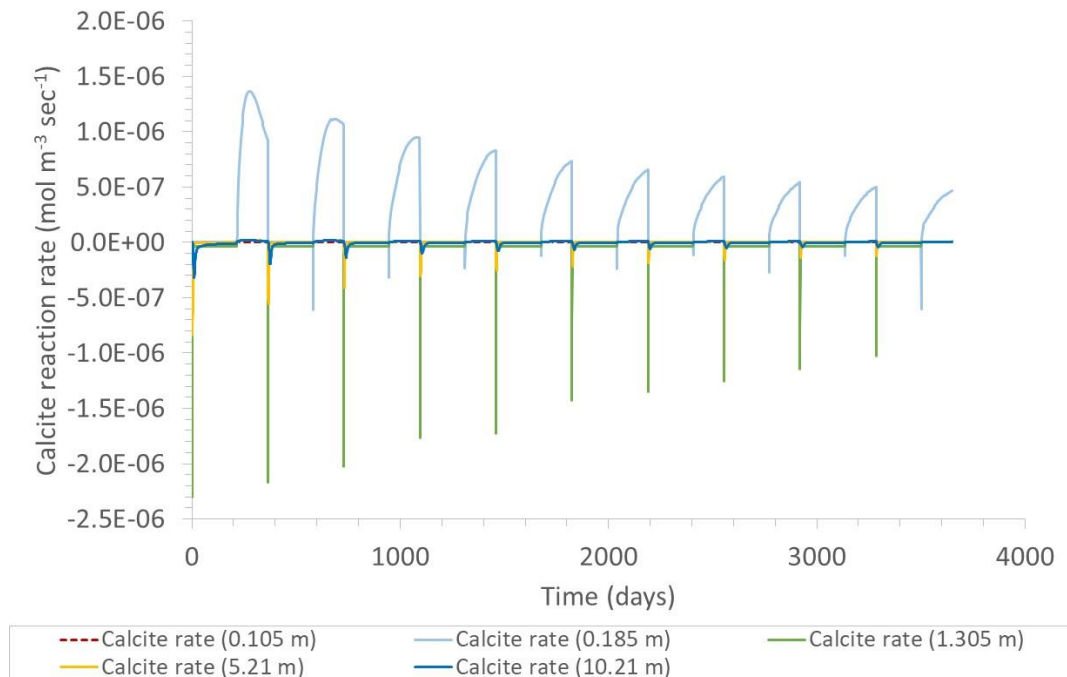
Figure 2.4.27 Calcite precipitates in the screen (representing the well in the real system) at r = 0.185 m during extraction and dissolves in the reservoir during injection.
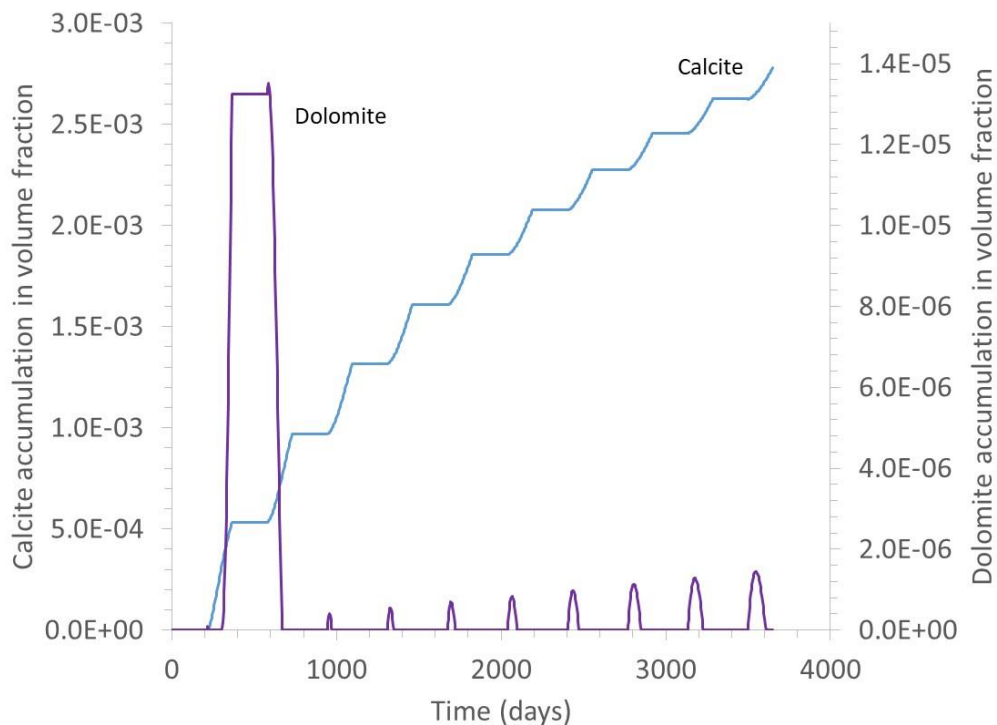
Figure 2.4.26 Accumulation of calcite and dolomite in the screen (representing scale formation in the well).
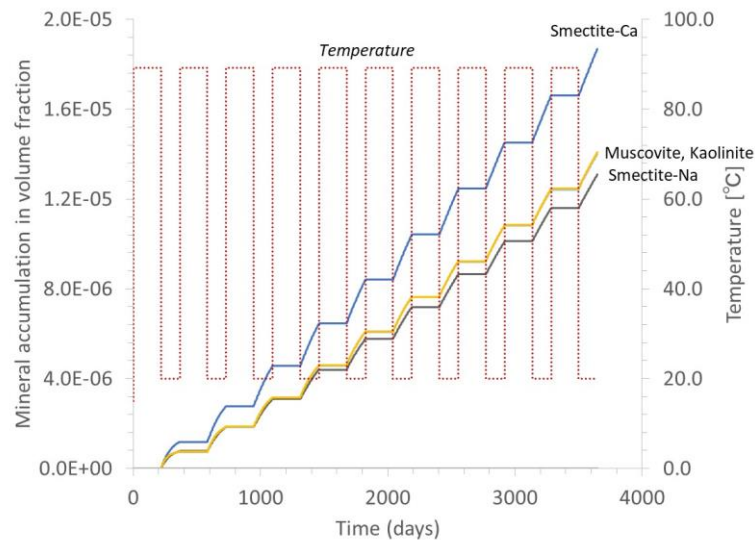
Figure 2.4.28 Minerals forming in the heat exchanger. Consistent with their prograde solubility with respect to temperature, clay minerals are the dominant scale-forming mineral phases.

The simulations included a dummy pseudo-mineral ($CO_2(s)$) to track the saturation state of the water with respect to CO_2 gas. The results suggest that degassing of CO_2 is not likely occur in the system. The computed reservoir pCO_2 and the assumed pressure drop to 3 bar overpressure in the surface installation are too low to cause CO_2 exsolution.

3D model of the Forsthaus system

Model design

A full scale 3D model of the Forsthaus heat storage system was constructed, which explicitly accounts for the envisaged arrangement of wells comprising the main injection/extraction well surrounded by supporting or auxiliary wells (Figure 2.4.29). However, because the Forsthaus project is still in its planning stage, the design of the model (specifically the stratigraphic succession, the lateral extent of individual strata or the distance between the wells) is still somewhat arbitrary. The main well is used to inject hot water into the reservoir during the warm months of the year and extract warm water during periods of demand. The supporting wells are used to regulate the flow, to maintain the desired reservoir pressure and to provide a connection to the surface installation, so that the reservoir, the wells and the surface installation (e.g. the heat exchanger) form a closed circulation system. The heat exchanger and closed-system circulation is not yet included in the simulations presented below.

To keep the model generic and allow for greatest flexibility in terms of updating the design or parameterization, it is constructed using a structured grid in a 3D cartesian coordinate system. Unlike axisymmetric models, which are in fact a 2D representation of the system, a Cartesian model is truly three-dimensional. The main advantage of a 3D model is to be able to include each well explicitly and to provide flexibility in terms of well design modifications, the implementation of geological heterogeneity in the reservoir and to account for asymmetric processes such as background groundwater flow.

The main disadvantage of a Cartesian coordinate system is that round features, such as the circular cross-section of the well, are represented by rectangles or blocks. The model wells for instance exhibit a square cross-section, whereby the cross-sectional area is scaled to match that of the real well. Similarly, because of regulatory constraints, the wellheads will be slightly offset from the target reservoir such that the wells will be slightly inclined (2 - 22°; Figure 2.4.7). This inclination is difficult to implement using a structured grid hence it is not considered here. All wells are assumed to be vertical. We do not expect that this affects the results significantly.

The model consists of a main well surrounded by five supporting wells at a distance of 50 m (Figure 2.4.29). The main and supporting wells have square cross-sectional areas of 0.09 m^2 and 0.058 m^2 corresponding to a diameter of an equivalent circular well of 13'' and 11'', respectively. We do not account for changes in diameter with depth. A more accurate representation of the wells (e.g. with decreasing diameter with depth) is planned in future simulations.

The domain extends to a depth of 495 m and horizontally more than 100 m beyond the circle of supporting wells (Figure 2.4.29 and Figure 2.4.30). The added lateral extent serves as a buffer to reduce the impact of the side boundaries, which are "open" with respect to flow and heat transport, on processes within the circle of wells. Open side boundaries are implemented using a constant hydrostatic pressure and a fixed thermal gradient of 35 °C/km. A constant background heat flux into the domain resulting in a geothermal gradient of 35 °C/km under conductive conditions is assigned to the bottom boundary of the domain. Note that a gradient of 35 °C/km is at the high end of estimated average gradients in the Molasse Basin. We assume a constant surface temperature of 15 °C which implies a temperature of 32.5 °C at a depth of 500 m, which is slightly above the estimated temperature range of 29 to 31 °C from the Swisstopo (*www.swisstopo.admin.ch*) GeoMol15 Temperature Model for the region of Bern. This slightly higher temperature gradient in the model should not significantly affect the results of this study.

The stratigraphy of the USM is based on previous modelling studies (e.g. Driesner et al., 2017) (Figure 2.4.30). It comprises alternating clay and sandstone layers of varying thickness. The thickness of individual layers ranges from 3 to 11 m. Each layer is horizontal, laterally continuous and of constant thickness. Given the generic design of the model, a more complex stratigraphic sequence representing the different lithotypes of the USM at the Forsthaus site more accurately will be easy to implement.

Thermal and hydraulic properties of the rock units are summarized in Table 2.4.9. Because the wells are planned to be cased throughout the Quaternary, all Quaternary rocks are considered "inactive", meaning that they are excluded from the simulation (Figure 2.4.30). In other words, Quaternary rocks are impermeable, adiabatic and inert. This assumption has a small impact on the distribution of heat in the system, because it prevents conductive heat loss into the Quaternary. We expect that this assumption has no impact on the results.

Injection and extraction follow the schedule presented in Table 2.4.10. The total simulated time is 2 years, spanning 2 injection-extraction cycles. Between periods of injection and extraction there are 2 days of resting.

Table 2.4.9 Thermal and hydraulic properties of the rock

	Quaternary	Sandstone	Clay
Porosity	**inactive**	0.1	0.05
Tortuosity		0.1	0.05
Dispersivity [m]		1e-3	1e-3
Density [kg/m^3]		2743	2743
Wet thermal conductivity [W m^{-1} K^{-1}]		2.67	2.67
Heat capacity [J kg^{-1} K^{-1}]		764	764
Permeability [m^2]		3e-13	2.3e-17

Table 2.4.10 Schedule of injection/extraction periods

Time (d)	Q (l/s)	T (ºC)	Inject	Extract
0-216	25	90	x	
216-365	25	50		x
365-581	25	90	x	
581-730	25	50		x

MW: Main well
SW: Supporting well
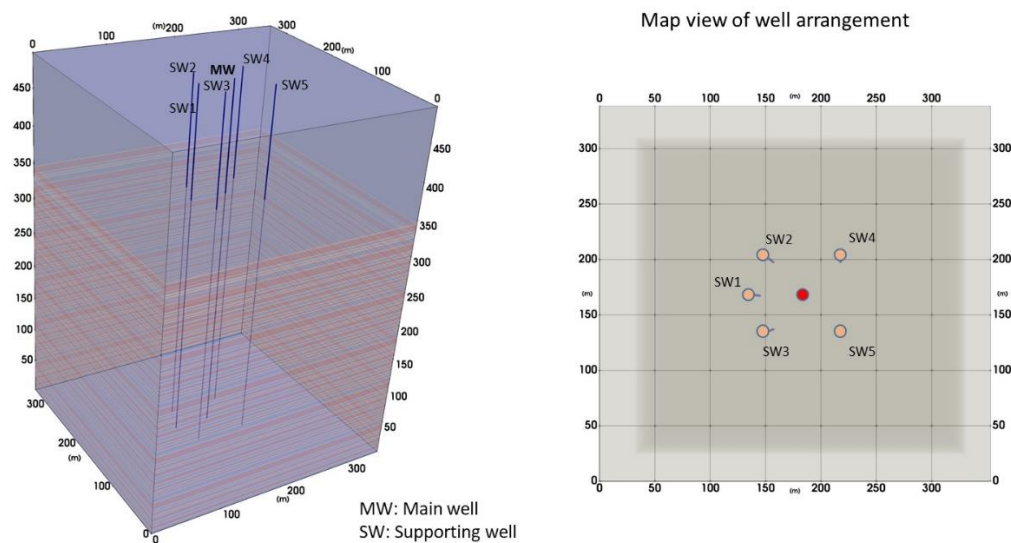
Figure 2.4.29 Model domain with stratigraphy and wells (left panel) and a map view of the well arrangement (right panel)

The main well constitutes the injection and extraction well through which active pumping occurs. Along with the supporting wells a water balance will be established so that the total volume of water in the reservoir remains constant. To achieve this in the model, the supporting wells are also "activated", that is, water balance is enforced by active pumping in these wells. Given a total of 5 supporting wells and assuming the same flow rate through each of them, the pumping rate through each well has to be 5 l/s to achieve water balance.

The domain is composed of a total of 3.2 Mio grid cells yielding a spatial resolution of less than 2 m within the circle of wells. All simulations were run on UBELIX, the HPC cluster at the University of Bern, with runtimes of up to 2 days.
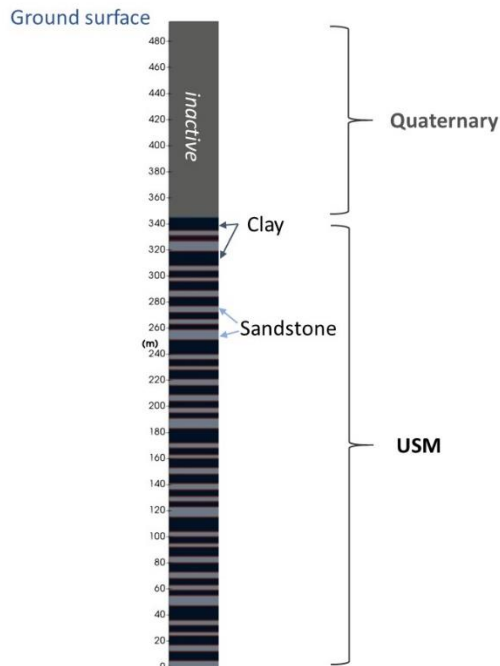
Figure 2.4.30 Stratigraphy of the model domain. The Quaternary is considered inactive, that is it is impermeable, adiabatic and inert. In this model, all sandstone and clay units in the USM are horizontal and laterally continuous. The thickness of individual layers ranges from 3 to 11 m.

Results

The fluxes through the wells (Figure 2.4.31) and the temperature at the wellheads (Figure 2.4.32) are consistent with the pumping schedule in Table 2.4.10. The injection temperature is 90 °C. The temperature of the extracted water decreases during withdrawal as more distal, cooler water is drawn from the reservoir. The lowest temperature at the end of the first and second extraction periods is 59 °C and 68.3 °C, respectively, indicating that the reservoir heats up over time. This gradual heating of the reservoir can also be seen in the water extracted from the supporting wells. The temperature of the water discharging from the supporting wells increases with each successive period of injection through the main well.

After the first injection, the thermal plume extends along the permeable sandstone layers driven by preferential flow along those layers (Figure 2.4.33, left panel). The edge of the thermal plume in the most transmissive layers extends to the supporting well SW1 which is 50 m away from the main well. This implies that there is a slight "thermal short circuit" causing the loss of heat that is being injected through the main well at the same time. This loss of heat is not very significant: during the injection through the main well the temperature of the water discharging through the supporting wells increases by 2-3 °C (Figure 2.4.32), but it could be easily avoided by increasing the distance between main and supporting wells. Figure 2.4.34 confirms that the circle of supporting wells with a radius of 50 m from the main well is situated at the very edge of the thermal plume. Increasing the radius by another 5 – 10 m would probably contain the thermal plume entirely even over a longer life times of the system.

Over time, heat diffuses vertically into the clay layers and the temperature distribution in the reservoir becomes more homogeneous and the reservoir as a whole heats up (Figure 2.4.33, right panel). The figure illustrates that, given the assumptions of the model, the concept of thermal storage in the Forsthaus "Geospeicher" works very well.
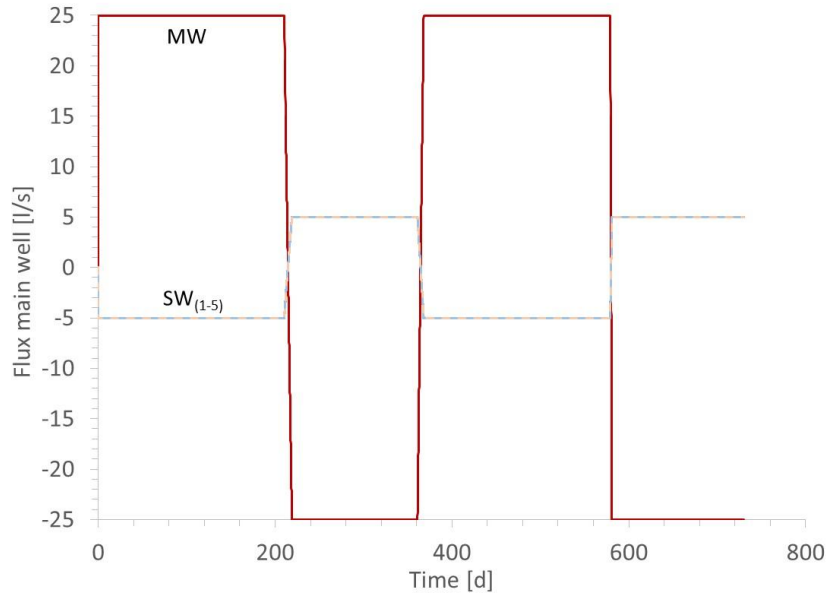
Figure 2.4.31 Pumping rates through the main well (MW) and supporting wells (SW) according to the schedule in Table 2.4.10 Pumping rate > 0 denotes injection and < 0 denotes extraction. It is assumed that the flow rate through each supporting well is the same, amounting to 5 l/s to achieve global water balance.
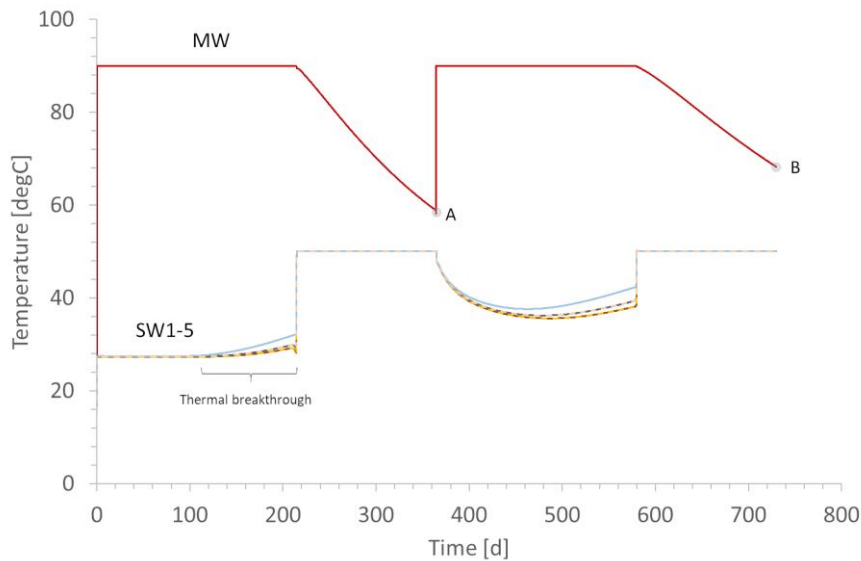
Figure 2.4.32: Temperature evolution at the wellheads. The temperature of the water extracted through the main well increases over time (see points A and B marking the ends of two successive extraction cycles) and so does the water discharging from the supporting wells in response to injection through the main well. This behavior indicates a gradual heating of the reservoir. Note the temperature increase of the water discharging from the supporting wells during injection into the main well, marking the thermal breakthrough. This is indicative of an unwanted "thermal short circuit".
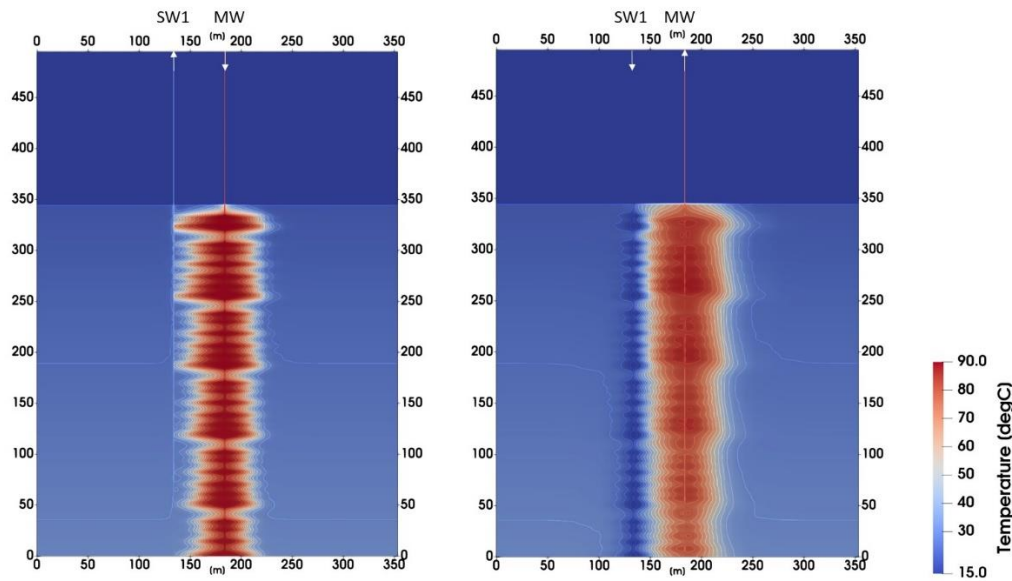
Figure 2.4.33 2D section through SW1 and MW showing the extent of the thermal plume after the first injection period (left panel) and after the second extraction period (right panel)

.
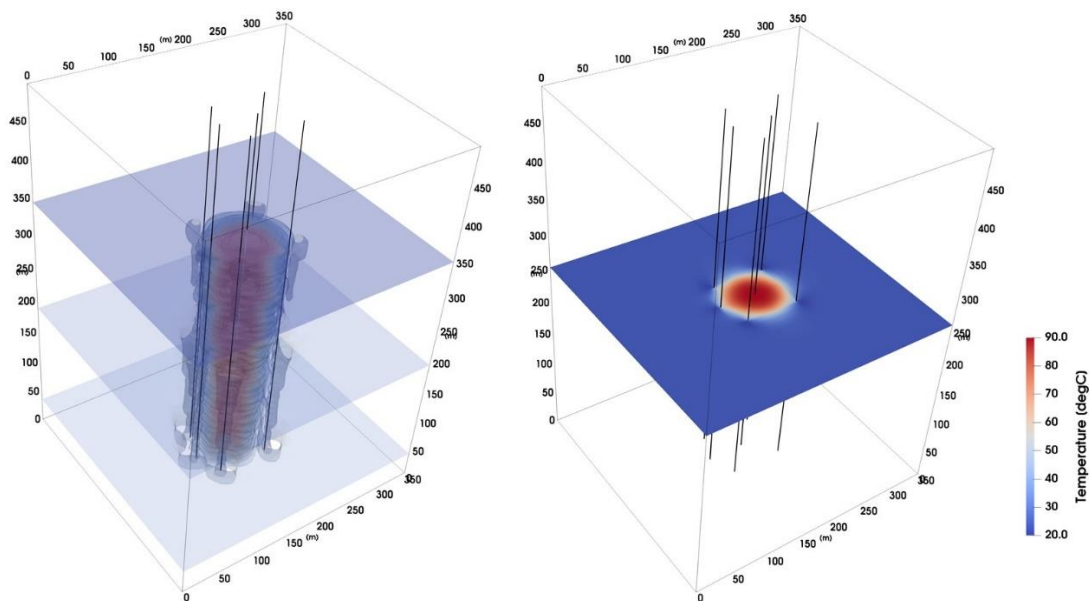
Figure 2.4.34 Extent of the thermal plume during the second injection period. The thermal plume stays within the circle of supporting wells, 50 m away from the main well.

A tracer was added to the injected water at a concentration of 1 mol/g. Figure 2.4.35 shows the arrival of the injected tracer at the wellhead of the supporting wells. Homogeneous conditions lead to a breakthrough of the tracer front in each supporting well at about the same time. In analogy to the (very weak) thermal "short circuit" discussed above (Figure 2.4.32 and Figure 2.4.33), the breakthrough of the tracer indicates a "short circuit" of water mass currently injected into the well head. Whereas the former is unwanted, the second is consistent with the design of the system. It takes 77 days for the breakthrough of 50% of the tracer concentration in the supporting wells. Unlike heat, there is little diffusive exchange of tracer mass between the transmissive sandstone layers and the over- and underlying clay units (Figure 2.4.36).

Consistent with the rapid breakthrough of the tracer is a much larger lateral extent of the tracer plume (Figure 2.4.36 and Figure 2.4.37). Figure 2.4.37 shows that a significant amount of tracer mass "escapes" the ring of supporting wells and migrates along the transmissive layers beyond the edge of the model domain, 175 m away from the main well. This escape can be prevented if the spacing between supporting wells is decreased. The spacing between supporting wells SW1-3 is closer than between SW4 and SW5 (Figure 2.4.29). The close arrangement of SW1-3 prevents the escape of the tracer as can be seen on the opposite side of the main well between SW4 and SW5 (Figure 2.4.37, right panel). In general, the tighter the ring of supporting wells, the more contained becomes the system.
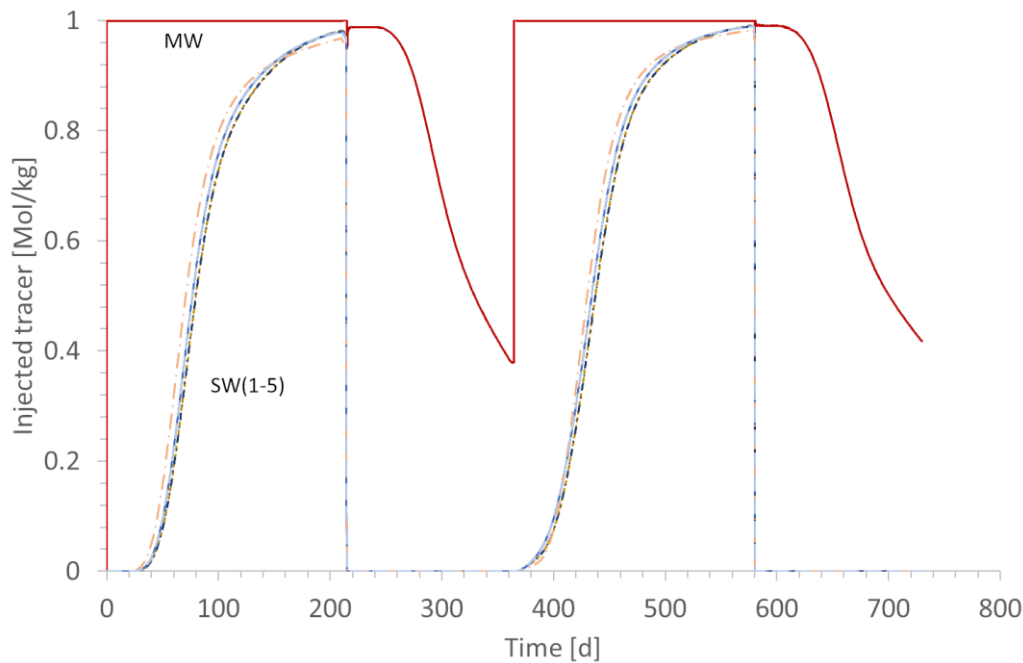
Figure 2.4.35 Injection of a tracer into the main well (MW) and breakthrough of the tracer in water discharging from the supporting wells. The breakthrough of 50 % of the tracer concentration takes about 77 days.
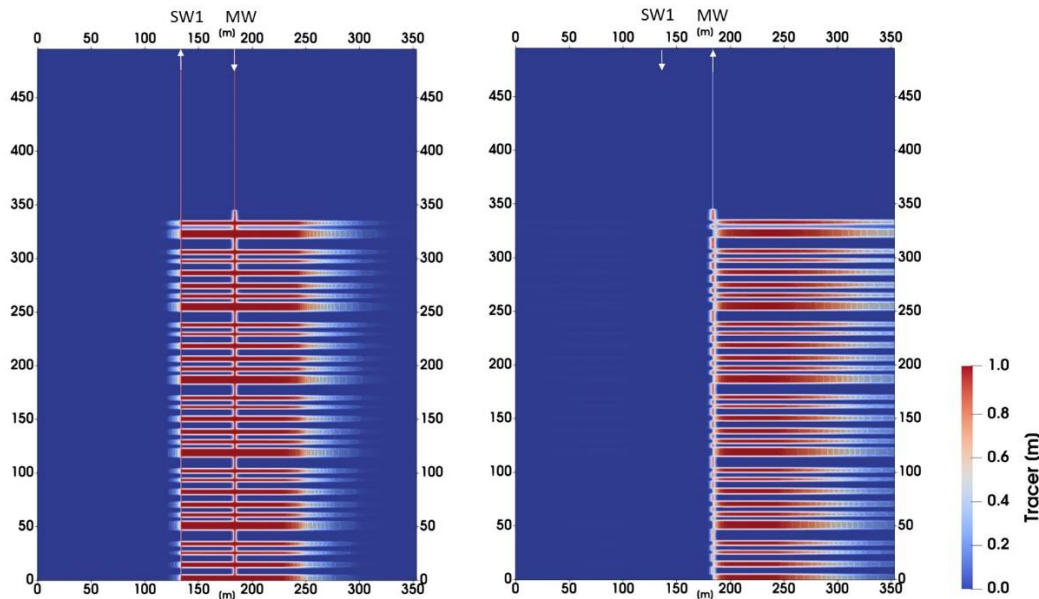
Figure 2.4.36 2D section through SW1 and MW showing the concentration of the injected tracer after the first injection and second extraction period (left and right panels, respectively). The tracer distribution shows preferential flow and transport along the permeable sandstone layers and the extent of the tracer plume to the boundary of the model.
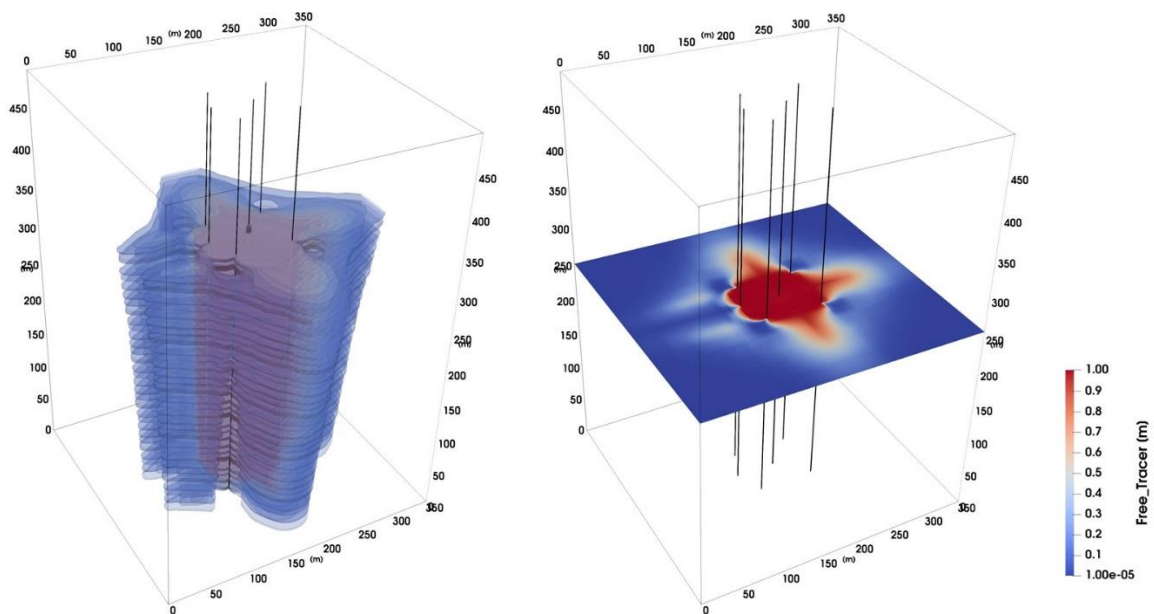
Figure 2.4.37 3D distribution of the tracer during the second injection period (left panel). Unlike the thermal plume, the tracer is not contained within the circle of supporting wells (right panel).

The pH distribution after 2 years of operation shows a similar pattern as that of the tracer. Changes in pH are restricted to the transmissive layers and within these layers, changes in the pH extend beyond the model boundary. Unlike the tracer, the pH is affected by chemical reactions between the water and the rock. Hence the pH changes as a function of the pumping scenario and temperature, so that, after 2 years, the pH of the reservoir water around the main well is highly heterogeneous as a result of time-integrated, overlapping processes (Figure 2.4.38). However, for conditions as they apply to the Forsthaus system, spatial and

temporal changes in pH are very small (Figure 2.4.38 and Figure 2.4.39, respectively) and these are not likely to cause problems such as enhanced mineral reactions or corrosion.
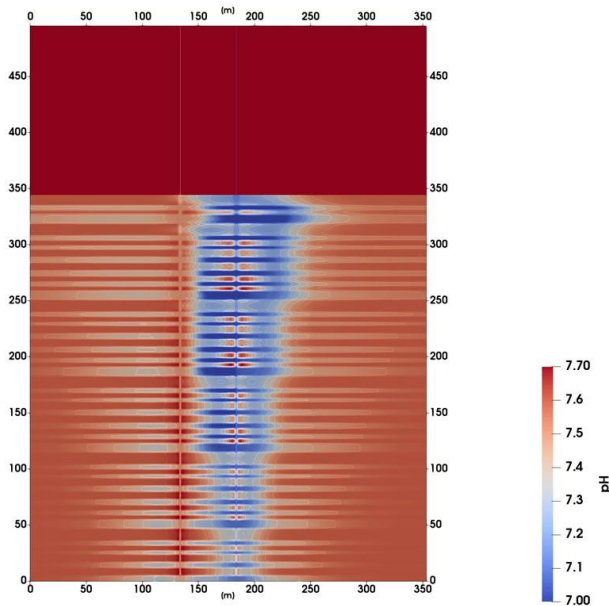
Figure 2.4.38 The pH after 730 days, at the end of the second extraction cycle.
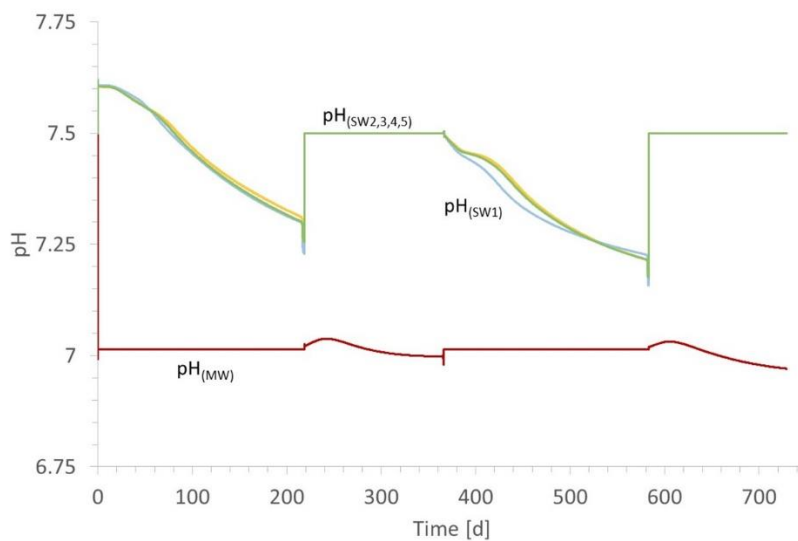
Figure 2.4.39 The pH evolution at the wellheads

The behavior of mineral reactions is consistent with that described for the axisymmetric model. Significant mineral reactions are restricted to the region within the circle of supporting wells, that is within a radius of 50 m around the main well (Figure 2.4.40 and Figure 2.4.41), which corresponds roughly to the extent of the thermal plume (Figure 2.4.33). Carbonate minerals calcite and dolomite dissolve during injection and precipitate during extraction (cf. Figure 2.4.18 and Figure 2.4.40), while quartz and other primary silicate minerals dissolve, regardless of the pumping scenario. The size of the zone involving silicate alteration (or

the local intensity of silicate reactions) increases and decreases during injection and extraction periods, respectively, consistent with the fluctuations in the quartz reaction rate seen in Figure 2.4.20.

Figure 2.4.40 Calcite reaction rate (<0: dissolution ; >0 precipitation) after the first injection and
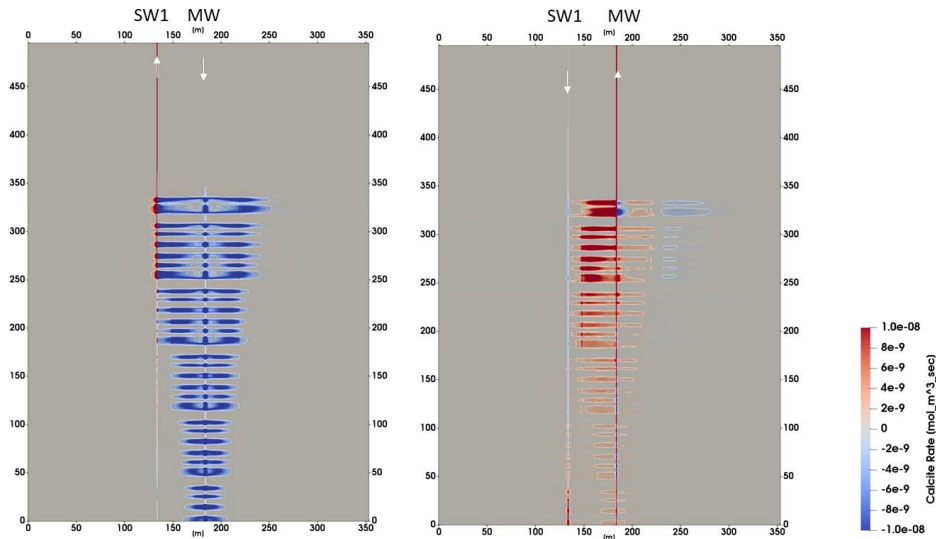
second extraction period (left and right panel, respectively).
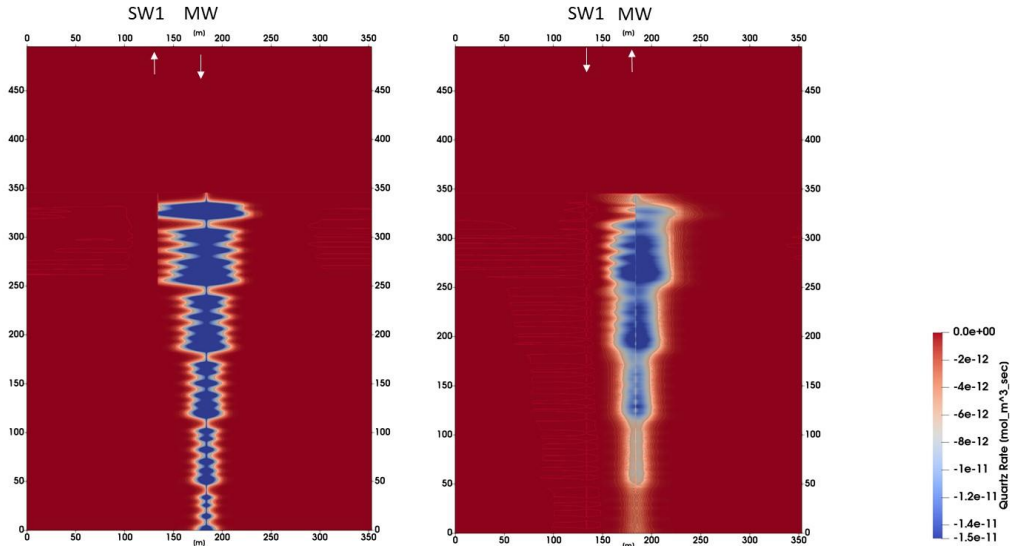
Figure 2.4.41 Quartz reaction rate after the first injection and second extraction period (left and right panel, respectively)) showing only dissolution. During injection: the injected water is undersaturated with respect to quartz (as it is in-situ pore water heated to 90 ºC). During extraction distal, cooler reservoir water is drawn towards the relatively warm injection zone, thereby heating up and becoming undersaturated with respect to quartz.
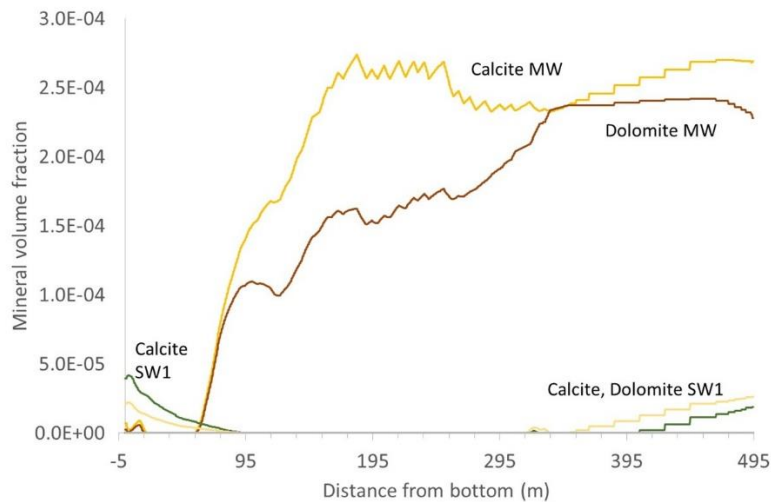
Figure 2.4.42 Snapshot of mineral scales along the main well (MW) and supporting well 1 (SW1) after 486 days (second injection)

Consistent with the axisymmetric model, carbonate minerals calcite and dolomite precipitate in the wells, whereby the amounts forming in the main well far exceed those in the supporting wells (Figure 2.4.43). Clay minerals may also form as accessories (Figure 2.4.44). Scale forms in the wells only during periods of extraction (Figure 2.4.43) but these scales are largely preserved during subsequent injection periods (Figure 2.4.42). However, the total amount of scales remains low (Figure 2.4.44) and there is little risk of rapid clogging of the well. Even if scale formation in the well turns out to be a problem (for instance if mineral precipitation occurs rapidly within a short interval of the borehole or if it results in turbulent flow and thus reduced flow rates), given that scales are predominantly composed of calcite and dolomite, the formation of these scales could be prevented with relatively little effort by injecting appropriate inhibitors.
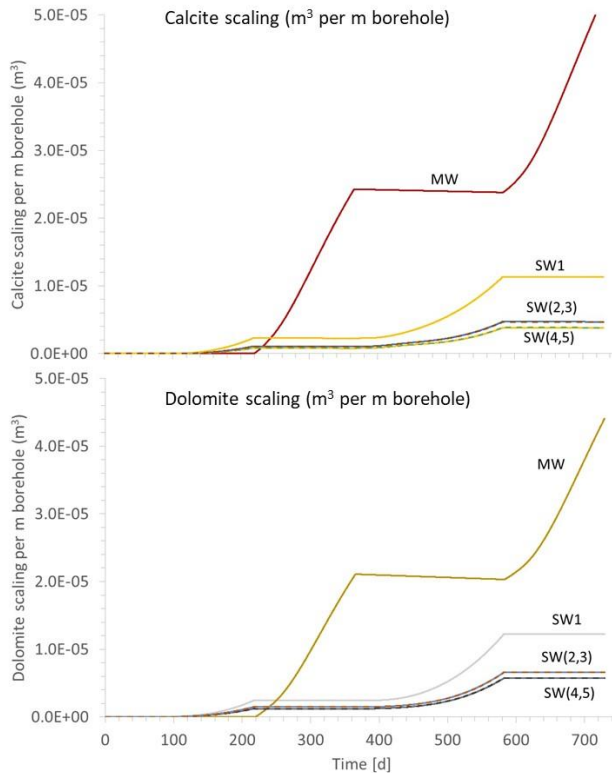
Figure 2.4.43 Carbonate scale formation at the well head.
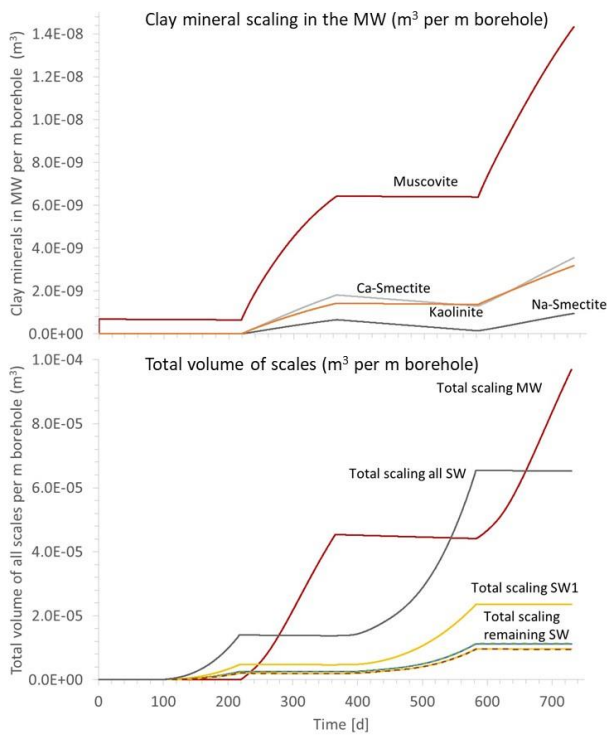
Figure 2.4.44 Formation of silicate scales (upper panel) and total volume of mineral scales (lower panel)

Analysis and discussion

We use two modelling approaches to gain insight into processes that may occur in the Forsthaus "Geospeicher" during the operation stage. One approach is to use a simple axisymmetric model with a single injection and extraction well in the center that includes a single permeable sandstone layer sandwiched between two clay layers. The reduced dimension, simplified geometry and reduced complexity of the flow system allows for the implementation of a relatively large and complex chemical reaction network without compromising computational performance. The purpose of this simple model is to run suites of parameter and scenarios tests. The other approach is that of a full-scale 3D model of the system. The model is designed to allow for easy adaptation of the well design, operation schedule and implementation of geological heterogeneity as soon as new information becomes available.

These two approaches complement one another because they operate on different scales and on different levels of detail. Furthermore, results from the simple model, in particular those concerning the chemical system or geochemical processes, e.g. the optimal composition and parameterization of the chemical reaction network, can be used to constrain input for the large scale simulations.

With simple modifications of the axisymmetric model, realism can be greatly enhanced. We conducted a study in which we use the simple axisymmetric model to address critical geochemical issues in various parts in the system. The simulations show that the "radius of influence" of the Forsthaus operation may exceed 100 m during a 10 year period if it is defined in terms of solute transport. Chemical constituents injected or released from the aquifer material can travel far beyond the radius of the thermal plume and up to several hundreds of meters away from the Forsthaus site. This could be a problem if unwanted constituents are released and transported into aquifer systems outside the Forsthaus site, which are utilized for other purposes. However, these considerations neglect the effect of the supporting wells, which may limit the spread of a solute plume, provided that the spacing between these wells is sufficiently close. Hence, this assessment requires confirmation with simulations involving the large scale model and appropriate well arrangements.

Although solutes may travel relatively large distances, the region of fluid-rock reactions where noticeable mineral dissolution and precipitation reactions take place, is restricted to a radius of less than 50 m. The zone of strong mineral alteration is limited to a radius of about 20 m. It is not likely that these zones will expand significantly if the operation time of the system increases beyond the simulated 2 years. One reason for this is the circular geometry of the plume which implies lower flow velocities and stronger dilution of the chemical perturbation induced by the injection with increasing distance from the well. This in turn implies a relatively rapid dissipation of chemical disequilibrium and transition to a rock buffered water composition with increasing distance from the well. Geochemical processes within the 50 m radius are controlled by two overlapping processes: the long-term heating of the reservoir and short-term reversals in the direction of flow in combination with heating and cooling due to pumping. Heating of water in the injection zone occurs during periods of extraction when water is drawn from distal, cooler parts of the reservoir towards the well, where temperatures are still high owing to the preceding injection. Cooling occurs during injection when the direction of flow is reversed and warm water is pumped into cooler regions of the aquifer.

One of the main concerns regarding geochemical processes in the reservoir is that of permeability reduction due to mineral precipitation. Results suggest that this is not likely to be a problem in practice. Mineral reactions involving alumino-silicates are slow and porosity changes are small as volume changes due to the precipitation of secondary clay phases is balanced by those caused by the dissolution of primary minerals. Similarly, the precipitation of carbonates, which is a major concern in the installation, does not seem to greatly affect reservoir permeability because carbonate precipitation during extraction is followed by a carbonate redissolution during injection. Hence, the behavior of carbonate minerals is strongly dependent on the pumping scenario and the pumping schedule. It is possible, in principle, to influence the distribution of carbonate reactions in the reservoir by designing an appropriate pumping schedule.

Carbonate precipitation during extraction occurs in the vicinity of and within the main well. It is caused by the higher temperature around the injection/extraction well in combination with retrograde solubility. That is, carbonate enriched water that is drawn towards the well becomes oversaturated with respect to calcite or dolomite which subsequently precipitate. Given that flow velocities increase as the water approaches the well, it is likely that the water entering the production well is oversaturated with respect to calcite. This leads to the formation of carbonate scales on the inside wall of the production well.

There is little risk of carbonate precipitation in the heat exchanger when the produced warm water is cooled. Instead, silicate minerals which have prograde solubility with temperature precipitate, albeit in small amounts. The dominant minerals that form in the heat exchanger upon cooling are clay minerals. This conclusion is based solely on the assumption of thermodynamic equilibrium. It is not known if precipitation kinetics will play a role, in which case the amounts of clay minerals forming in the heat exchanger could be even lower.

One important result of these simulations is that quartz or amorphous silica scaling does not seem to be an issue during extraction and cooling in the heat exchanger. Apparently, the same process causing calcite oversaturation in the production well, that is heating of the water approaching the well in combination with fast flow velocities near the well, also lead to quartz undersaturation in the production fluid and thus prevent quartz (or amorphous silica) precipitation in the heat exchanger. The suite of simulations involving the simple axisymmetric model did not reveal any obvious problem or risk related to geochemical processes that would hinder a sustained operation.

The 3D model is a much more accurate representation of the geometry of the system. Nevertheless, it is reassuring that the results from the 3D simulations of the Forsthaus system are largely consistent with the insights gained from the simpler axisymmetric model in particular concerning those of chemical processes near the main well. Even the composition and the amount of scales that may precipitate in the main well during extraction could be predicted with the simpler model with reasonable accuracy.

Results from the 3D simulations show that based on the extent of the thermal plume, a radius of 50 m for the circle of supporting wells is an absolute minimum and should not be any lower. In fact, for an optimal heat exploitation this radius should be increased if possible. The optimal distance is yet to be determined, but the results suggest that an additional 5 meters would be sufficient to eliminate the "thermal circuit" that occurs in the most transmissive sandstone layers.

With the current design of the system it is not possible to contain the chemical plume, that is compositional changes to the original reservoir water induced by the operation, within the circle of supporting wells. To achieve chemical containment the spacing between the supporting wells need to be reduced, meaning that more wells are required. Because this is not feasible, it is important to assess the implications of the operation for the composition of the groundwater and how these changes may affect any groundwater usage within a radius of hundreds of meters around the Forsthaus system. Currently, there is no groundwater usage in the vicinity of Fortshaus and the USM groundwater is not classified as drinking water. Experimental results and the simulations presented here suggest that these compositional change are small. The pH changes only slightly and there is no indication that unwanted compounds could be released from the aquifer rock into the groundwater.

Consistent with the results from the axisymmetric model, the risk of significant scaling in the wells or clogging of the reservoir is low. Carbonate minerals are far more reactive than silicate minerals and dominate the composition of scales in the wells and volume changes in the reservoir rock. The amount of carbonate scales in the main well is small over 2 injection extraction cycles. The effect of carbonate reactions on porosity and permeability in the reservoir is reduced due to opposing behavior during injection and extraction: carbonate minerals dissolve during the former and precipitate during the latter.

The simulations have verified the feasibility of the heat storage principle in deep aquifers of the sandstones in the USM (Figure 2.4.33). From a geochemical perspective and with the current knowledge, there is little risk for failure. Perhaps the greatest risk for the operation are the unknown geological and hydraulic conditions in the subsurface. The stratigraphy used for the USM in this model is based on data from the NAGRA drilling campaign at Burgdorf near Bern and not the specific stratigraphy at Forsthaus. Likewise, the pore water composition is from another site. Furthermore, little is known about active groundwater flow in the USM. All modelling results are based on the assumption that natural groundwater flow does not occur. The models presented here will be adapted as soon as site-specific data or information become available.

2.4.3.2 THM$ model, ETH Zürich

In the plan outlined in the interim version of D2.1 (Driesner 2019), ETHZ laid out ambitious goals to model the Bern-Forsthaus and Geneva sites. We planned to investigate the mechanical impacts, especially surface deformation, caused by HT-ATES operations using a MOOSE thermo-hydro-mechanical (THM) numerical model. Our goal was to first run predictive THM models in the early stages of the project. As the project

progressed, we would incorporate more data about the geology and operational conditions, provided by other work packages, into our models. And finally we would calibrate and validate the THM models against field data, such as pumping tests.

MOOSE simulations were run to understand surface deformation at the Geneva site according to the plan described in the previous paragraph, but MOOSE simulations were not conducted at the Bern site for two reasons. Firstly, there were COVID-related delays in drilling at the Bern site, which delayed some of the site-specific input parameters and pumping test calibration and validation data that would have entered into a numerical model. Secondly, the THM simulations for the Geneva site only converged for a subset of geological and operational parameters provided, and it was not within the time allotted for the project to identify the cause of poor convergence. Instead, the THM simulations raised questions about what are reasonable combinations of geological and operational parameters. For example: (a) what are optimal well spacing and flow rate and (b) how does reservoir transmissivity affect HT-ATES operations and is there a minimum value for HT-ATES to be feasible?

Despite the lack of MOOSE THM simulations at the Bern site, we developed a novel thermo-hydro-mechanical-economic (THM$) approach that answered questions about optimal flow rate, well spacing, depth, and minimum economically-viable transmissivity (MEVT) (Birdsell et al., 2021). The MEVT is the transmissivity below which HT-ATES is sure to be economically unattractive, and it can be used as a pre-screening criteria. By analysing a generic HT-ATES system, we found in Birdsell et al. (2021) that the MEVT can be approximated as one value ($5 \cdot 10^{-13}$ m^3) for a broad range of HT-ATES reservoirs. Additionally, the THM$ is adapted specifically for the Bern site, which allows us to make recommendations of optimal well spacing and flow rate at Bern. The THM$ approach has the advantage of being analytical and computationally efficient so that a large parameter space can be explored for pre-screening studies.

Conceptual simulation model

The THM$ approach considers a HT-ATES doublet (see Figure 2.4.45 The four stages of the conceptual model: (a) Injection, (b) Storing, (c) Extraction, and (d) Resting.) that has four stages: (a) heat injection, (b) storing, (c) heat extraction, and (d) resting, each lasting one-quarter of a year. The stages correspond roughly to summer, fall, winter, and spring, respectively. The HT-ATES system is connected to an idealized district heating network (DHN).

The THM$ approach balances three reservoir-engineering and economic constraints on HT-ATES operations. Constraint I is hydro-thermal and ensures that the reservoir has enough capacity to hold the heat provided. Constraint II is hydro-mechanical and ensures that hydraulic fracturing (HF) is avoided. Constraint III is related to economics and ensures that the flow rate that minimizes the levelized cost of heat (LCOH) is selected. The LCOH takes the following variables into account: (a) heat recovered; (b) the capital cost, which increase with depth due to well construction costs; and (c) the operating cost, which is based on the cost of electricity to run pumps. If Constraints I and II limit the flow rate and well spacing, the HT-ATES system is in the "reservoir-constrained regime", but if Constraints I and III limit the flow rate and well spacing, the HT-ATES system is in the economic-constrained regime.

A number of assumptions were made:

1) Heat is lost irrecoverably from the reservoir to the overlying and underlying rock (at a background geothermal temperature) during the Storing stage according to one-dimensional conduction, and advective heat loss is assumed to be negligible.

2) We neglect costs related to the construction and maintenance of a district heating network (DHN), which are necessary for most large-scale HT-ATES systems.

3) We also neglect maintenance costs of the HT-ATES system.

4) We assume a reverse faulting regime for the base-case scenario, which allows for higher flow rates without HF.

5) The reservoir is homogeneous and isotropic.

These assumptions are conservative in the sense that they ensure the MEVT is a lower-bound on the transmissivity that could be economically attractive.

As this is a new methodology, we only present an overview here. More details can be found in Birdsell et al. (2021).
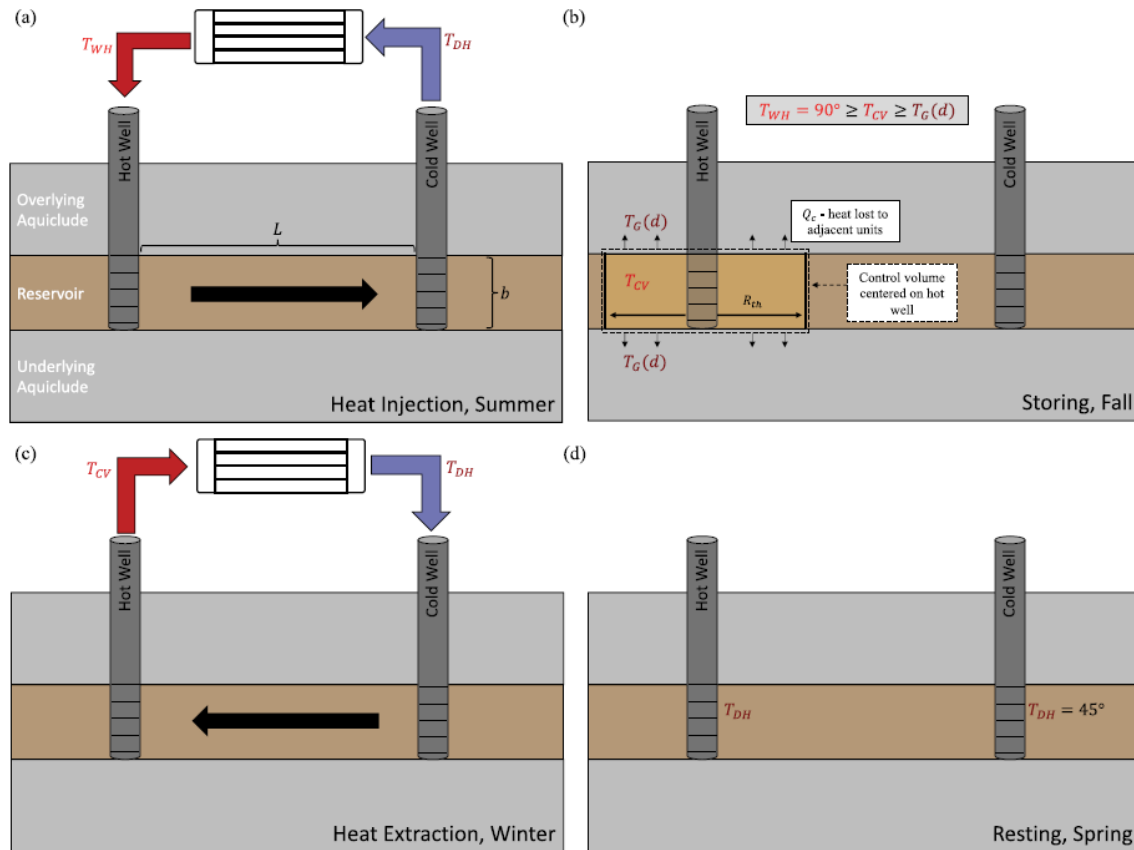

Figure 2.4.45 The four stages of the conceptual model: (a) Injection, (b) Storing, (c) Extraction, and (d) Resting.

Pre-processing workflow

The THM$ approach reflects a generic HT-ATES doublet. Unless otherwise specified, the parameters match Table 1 of Birdsell et al. (2021), and the generic approach is useful because it allows us to present a sensitivity analysis on reservoir thickness, permeability and depth and find a widely-applicable screening tool, the MEVT.

Furthermore, we adapt the THM$ approach specifically to the Bern-Forsthaus site to make recommendations for optimal well spacing and flow rate. Namely, we employ the reservoir properties from the Bern site and change the model to account for the many permeable target layers interspersed within low-permeability units. Firstly, we use the cumulative permeable thickness as the effective reservoir thickness, which we assume captures the approximate hydraulic response. Secondly, we consider two bounding cases for heat loss from the reservoir layers to the aquitards. In the first scenario, we consider heat is lost from each target layer, which likely approximates the early years of operation. In the second scenario, we consider that heat is lost only from the top of the topmost target layer and the bottom of the bottom target interval. This may reflect the behavior after several annual cycles. Interestingly, it can be shown analytically that the optimal flow rate and well spacing do not depend on the amount of heat loss (Birdsell et al., 2021). However, the heat loss effects other performance metrics like the amount of heat recovered, the thermal efficiency, and the LCOH.

Computational approach and software

While the THM$ approach can be expressed entirely analytically, we created an open-source python code for variable passing, interpolation, plotting, and to solve implicit equations (Birdsell, 2020). A block diagram of the algorithm is depicted in Figure 2.4.46. First, reservoir and economic parameters are specified. Then, two estimates of the well spacing and flow rate are calculated. One estimate corresponds to the reservoir-constrained regime and one corresponds to the economic-constrained regime. The optimal well spacing and flow rate are assigned as the minimum of the reservoir-constrained and economic-constrained values. Finally, additional performance metrics, such as the LCOH, thermal efficiency, and MEVT are calculated.

<div>

Specify Reservoir and Economic Parameters
From Table 1

↓

Calculate the well spacings and flow rates from reservoir and economic constraints
L_{res} from Eq. 10 balances Constraints *I* and *II*
L_{econ} from Eq. 11 balances Constraints *II* and *III*
$m_{res} = m_I(L_{res})$ from Eq. 3
$m_{econ} = m_I(L_{econ})$ from Eq. 3

↓

Calculate optimal well spacing and flow rate
$L^* = \min(L_{res}, L_{econ})$
$m^* = \min(m_{res}, m_{econ})$

↓

Calculate additional performance metrics
LCOH from Eq. 6
Thermal efficiency η from Equation 13
Heat lost during storage stage, Q_c from Equation 14
Reservoir temperature at end of storing stage T_{CV} from Eq. 15
MEVT from Sec. 2.5

</div>

Figure 2.4.46 Block diagram describing the THM$ algorithm steps. Note that table and equations numbers refer to Birdsell et al. (2021).

Model Analysis

The THM$ approach is analytical, which leads to benefits when exploring large parameter spaces. For example, some parameters, such as the optimal well spacing and the flow rate that corresponds to a minimum LCOH, can be expressed analytically (see Eqs. 8, 10, and 11 from Birdsell et al. (2021)). By inspecting these analytical expressions, it is clear how a change in one parameter leads to a change in another parameter, even without running any calculations. Secondly, THM$ calculations are computationally inexpensive, and therefore a wide range of parameters can be explored. Examples of this are shown in the next section (see Figure 2.4.48,Figure 2.4.50 and Figure 2.4.52) where the optimal well spacing and flow rate are plotted as a function of permeability and depth, the LCOH is plotted as a function of depth and thickness, and the minimum economically-viable transmissivity is plotted as a function of depth and thickness.

Scenarios and results

In this subsection, we first analyze and conduct a sensitivity analysis on a generic HT-ATES system following Birdsell et al. (2021). This leads to broadly-applicable insights about optimal well spacing, flow rate, depth, and MEVT for HT-ATES systems. Second, we adapt the THM$ approach and apply it to focus specifically on the Bern site, which gives insights about the well spacing, flow rate, and thermal efficiency at Bern.

Insights for generic HT-ATES systems

The three constraints are plotted together in Figure 2.4.47. One key takeaway is that the optimal flow rate and well spacing occur at the intersection between two or more of the constraints, and two regimes emerge. The reservoir-constrained regime happens when the flow rate and well spacing are dictated by the thermal capacity of the reservoir (Constraint 1) and the HF threshold (Constraint 2). The economic-constrained

regime occurs when the flow rate and well spacing are curtailed to reduce the LCOH (Constraint 3), while Constraint 1 is still honored. Figure 2.4.47 (a) shows a shallow reservoir, which is in the reservoir-constrained regime. Figure 2.4.47 (c) shows a deep reservoir that is in the economic-constrained regime. The main difference between Figure 2.4.47 (a) andFigure 2.4.47 (c) is the overburden stress, which changes the pressure and flow rate that leads to HF. Figure 2.4.47 (b) is the base-case scenario, which was chosen at a depth (575 m) where all three constraints imply the same flow rate and well spacing.
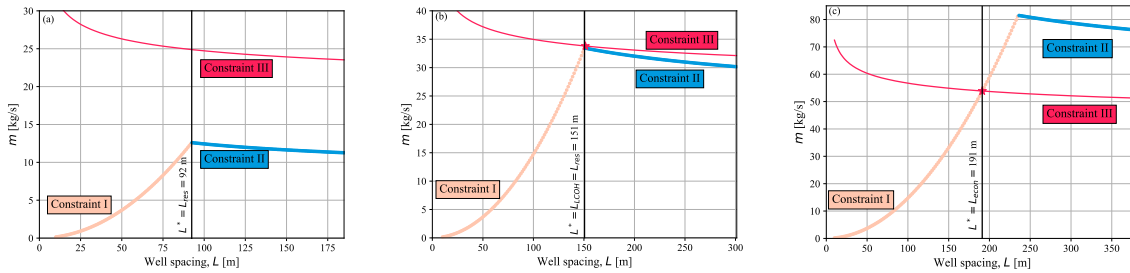
Figure 2.4.47 The flow rate versus well spacing implied by each of the three constraints for reservoir depths of (a) 200 m, (b) 575 m (the base case), and (c) 1500 m.

Figure 2.4.48 shows the optimal well spacing and flow rate as a function of depth and permeability. We found that the optimal well spacing, flow rate, and thermal radius all increase with respect to depth. Interestingly, the optimal well spacing is 1.8 times the thermal radius at all depths investigated. The optimal flow rate and well spacing also increase with permeability.
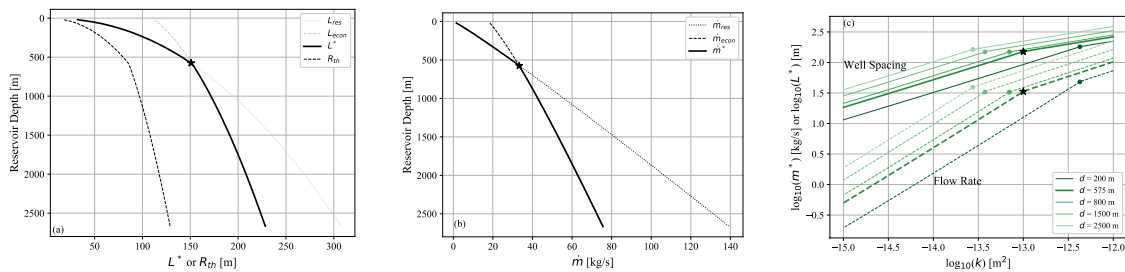
Figure 2.4.48 Optimal well spacing and flow rate. (a) Optimal well spacing (L*) and thermal radius (Rth) as a function of reservoir depth. (b) Optimal mass flow rate (m*) as a function of reservoir depth. (c) Optimal well spacing and flow rate versus the logarithm of permeability at various depths.

The thermal efficiency and the per-doublet heat injection, heat recovery, and heat loss are functions of depth, as seen in Figure 2.4.49. The heat injection increases monotonically with depth because the optimal flow rate and well spacing increase with depth. The thermal efficiency also increases monotonically with respect to depth because the background geothermal temperature increases with depth, and therefore the temperature difference that drives conductive heat losses decreases with depth. At the greatest depth investigated (2667 m), the background geothermal temperature (T_G) equals the waste-heat injection temperature (T_{WH}) and the thermal efficiency is 100%. The heat recovery, which is the heat injection minus the heat loss, also increases monotonically with depth.

Interestingly, the heat loss per doublet is non-monotonic, due to trade-offs between the thermal radius and the geothermal temperature. The thermal radius (R_{th}) dictates the area over which heat losses occur (see Figure 2.4.48 (b)), and a smaller radius corresponds to less heat loss if all else is equal. The background geothermal temperature increases with depth and a higher temperature corresponds to less heat loss, if all else is equal. The maximum heat loss occurs near 600 m, the depth at which: (a) the thermal radius is large

enough to have a large heat-loss area and (b) the geothermal temperature is small enough to encourage large heat fluxes.
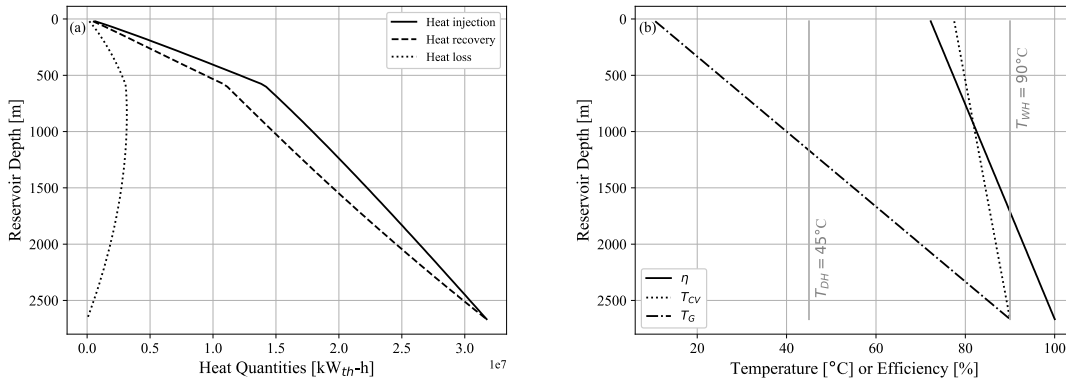

Figure 2.4.49 a) Heat injection, recovery, and heat loss per doublet as a function of depth and (b) thermal efficiency (η), the temperature of the reservoir control volume at the end of the resting stage (T_{CV}), and the background geothermal temperature (T_G) as a function of depth.

Figure 2.4.50 (a) shows that the levelized cost of heat (LCOH) has a minimum at an intermediate depth. This occurs because of the rate of change with depth in the heat produced, capital cost, and operating cost as a function of depth, as seen in Figure 2.4.50 (b).
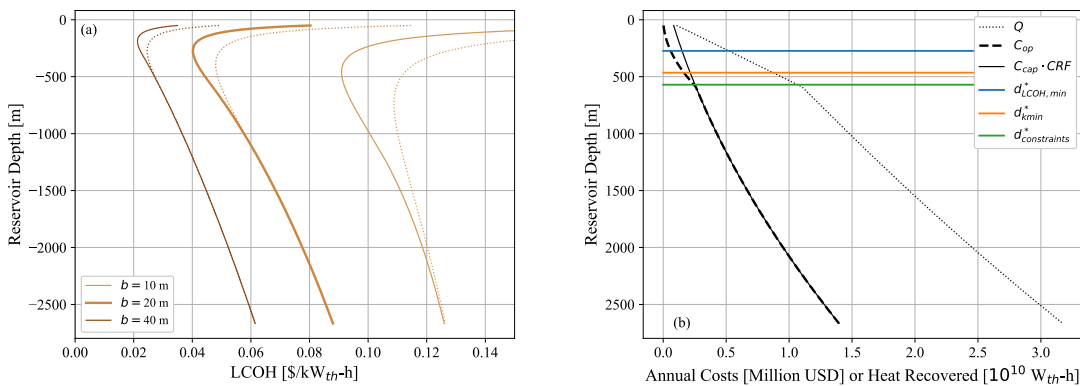
Figure 2.4.50 (a) The LCOH versus depth for various reservoir thickness (i.e., $b = 10$ m, $b = 20$ m, and $b = 40$ m). (b) The heat recovered (Q), annual operating cost (C_{op}), and equivalent annualized capital cost ($C_{cap} * CRF$) as functions of depth.

Figure 2.4.51 (a) shows that the LCOH increases with decreasing permeability and decreasing reservoir thickness. We define the permeability where the LCOH equals the cost of electricity as k_{min}, the minimum economically-viable permeability (MEVP). Any HT-ATES reservoir below this permeability would surely be economically unattractive because electricity could be used directly for electrical resistance heating at a lower cost than from the HT-ATES. We assume an electricity cost of $0.10/kWh, so the MEVP is the intersection between the horizontal dashed line in Figure 2.4.51 (a) and the LCOH curves.
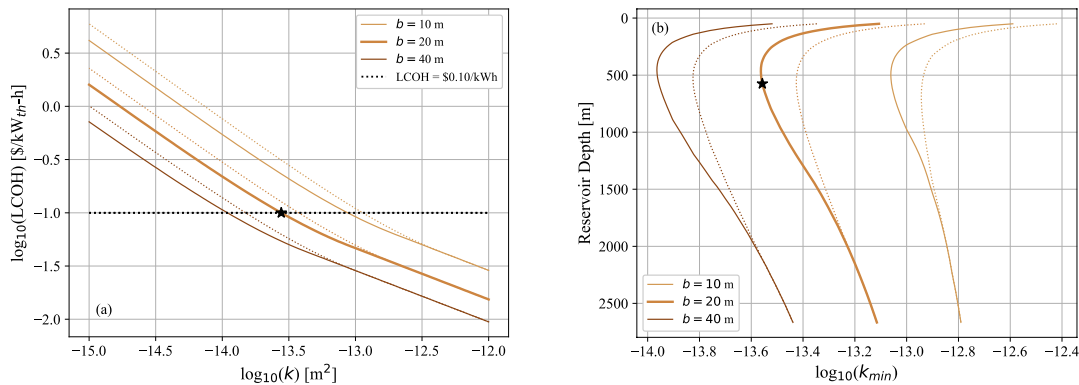
Figure 2.4.51 (a) The LCOH versus permeability for various reservoir thickness (i.e., b=10 m, b = 20 m, and b = 40 m) and the LCOH curves. (b) The MEVP (kmin) as functions of depth.

Figure 2.4.52 (a) shows the combinations of permeability and reservoir thickness that result in different values of γ, the ratio of the electricity cost to the amount of HT-ATES heat recovered. The red curve corresponds to the MEVP, which varies substantially with respect to reservoir thickness and therefore cannot make a good heuristic. On the other hand, Figure 2.4.52 (b) shows the combinations of transmissivity and reservoir thickness that result in different values of γ, and the red curve corresponds to the minimum economically-viable transmissivity (MEVT), which can also be expressed as the MEVP times the reservoir thickness. Unlike the MEVP, the MEVT does not vary by much with respect to reservoir thickness. Figure 2.4.52 (c) shows contour plots of LCOH. Again, the red curve corresponds to the MEVT, which is relatively insensitive to depth.
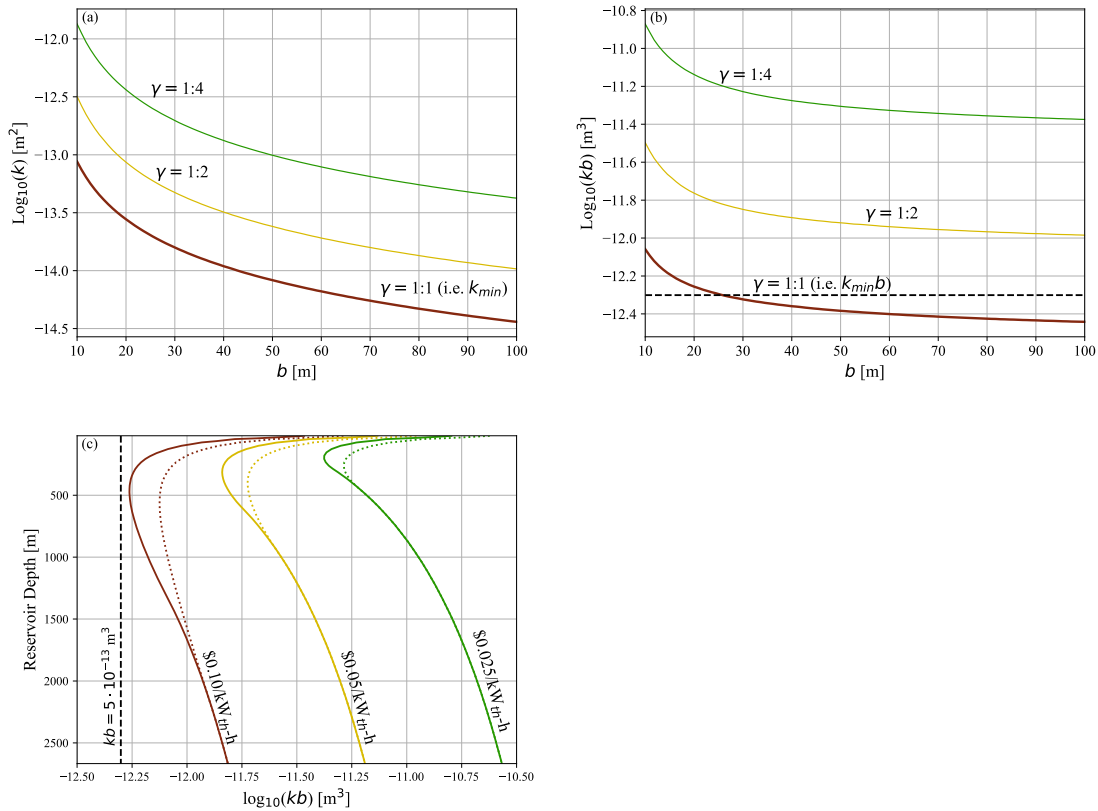
Figure 2.4.52 (a) Combinations of the logarithm of permeability and the reservoir thickness that lead to different values of γ, the ratio of electricity cost to HT-ATES heat cost. (b) Combinations of the logarithm of transmissivity and the reservoir thickness that lead to different values of γ. (c) Contour of LCOH for a range of reservoir depth and transmissivity.

Optimal well spacing and flow rate for Bern-Forsthaus

In this subsection, we assign the reservoir properties and number of reservoir layers to reflect the Bern-Forsthaus site. Based on input from GES, we use the following parameters for the Bern-specific base case: hydraulic conductivity = $3.3 \cdot 10^{-6}$ m/s, rock thermal conductivity = 2.67 W/m-K, porosity = 0.1, cumulative target thickness = 58 m, number of target layers = 12, and rock heat capacity = 1037 J/kg/K. We consider a range of depths from 150 to 500 m.

The optimal well spacing and flow rate for the Bern site base case are shown in Figure 2.4.53. The spacing increases with depth from 98 m to 121 m, and the flow rate increases from 47 to 71 kg/s. Except for the top 20 meters, the system is in the economic-constrained regime, meaning that the well spacing and flow rate is dictated by: (a) the available heat storage capacity of the reservoir and (b) the capital and operating costs. In the economic-constrained regime, the flow rate is kept relatively low to reduce the pumping costs, which ensures that the HF pressure is not approached. However, if one accepts a higher operating cost and corresponding lower LCOH, then a larger well spacing and flow rate could be used, as shown by L_{res} and m_{res} in the Figure 2.4.53. In this case, higher pore pressures would be encountered, and it would be prudent to monitor pressure to avoid HF.
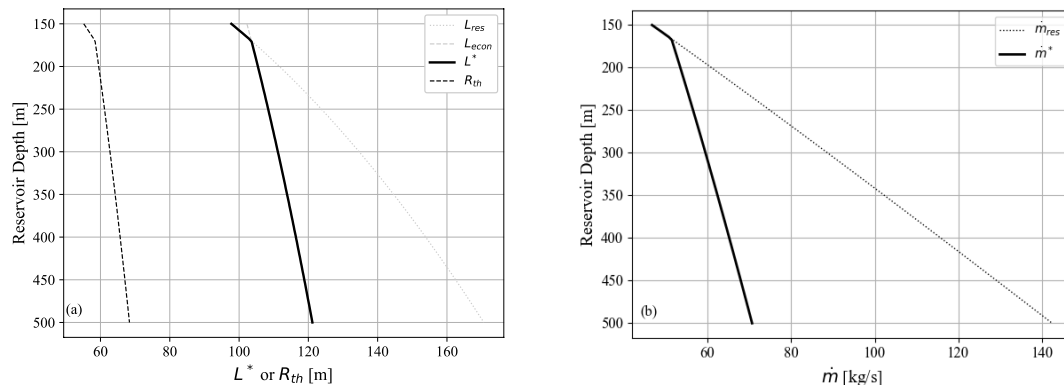
Figure 2.4.53 (a) Optimal well spacing and (b) optimal flow rate with respect to depth. Subscript "res" indicates the reservoir-constrained value, subscript "econ" indicates the economic-constrained value, and superscript "*" denotes the optimal value, which is the smaller of the previous two.

The thermal efficiency, heat loss, and LCOH depend on the heat loss from the reservoir layers. We run scenarios wherein either: (a) all twelve target units experience heat loss or (b) the reservoir layers act together as one layer and only experience heat loss from the top of the top layer and the bottom of the bottom layer. If all 12 layers experience heat loss, which may represent the early year(s) of operation, then the thermal efficiency increases with depth from 26% to 37%. On the other hand, if only the top and bottom layer lose heat, then the efficiency is >90%.

There is uncertainty in the hydraulic conductivity of the target layers and the cumulative thickness. Therefore we present a small sensitivity analysis to show the sensitivity of optimal well spacing and flow rate to conductivity and thickness (see Table 2.4.11). The hydraulic conductivity and the cumulative reservoir thickness are each doubled and halved from their base-case values.

Table 2.4.11 Sensitivity analysis on hydraulic conductivity and reservoir thickness

Hydraulic Conductivity [m/s]	Cumulative reservoir thickness [m]	Optimal well spacing range [m]	Optimal flow rate range [kg/s]
$1.6 \cdot 10^{-6}$	58	71-103	25-51
$3.3 \cdot 10^{-6}$	58	98-121	47-71
$6.6 \cdot 10^{-6}$	58	121-143	70-99
$3.3 \cdot 10^{-6}$	29	98-143	23-49
$3.3 \cdot 10^{-6}$	58	98-121	47-71
$3.3 \cdot 10^{-6}$	116	87-103	72-101

Analysis and discussion

Our THM$ approach provided many valuable and practical guidelines for the HT-ATES operations at Bern-Forsthaus (and for other HT-ATES systems). The THM$ approach is useful because it combines constraints from different fields, namely THM reservoir engineering and heat and energy economics. We used the THM$ approach to find the optimal well spacing, flow rate, depth, and MEVT. There is certainly room to further refine these values with additional work that focuses on reservoir simulation or the heating system, and many other HEATSTORE partners have contributed in this sense. However, the optimal well spacing, flow rate, and depth and the MEVT that we calculated can be taken as useful guidelines to start with. In the

subsections below we describe the practical insights that were learned and the interface with other work packages.

Predictive and sensitivity-related learnings

Transmissivity

Transmissivity is an important parameter for the technical and economic success of HT-ATES, and it can be used as a pre-screening criteria. We showed that permeability and thickness are both important to a successful HT-ATES system, but their product, transmissivity, may be even more important than either permeability or thickness. Furthermore, the LCOH of a system is more sensitive to the reservoir transmissivity than the depth or the faulting regime. In fact, the transmissivity could be used as a pre-screening tool for HT-ATES systems at Bern-Forsthaus and elsewhere. The MEVT can be approximated as one value, $5 \cdot 10^{-13}$ m^3, because it is relatively insensitive to depth, reservoir thickness, and faulting regime (see Figure 2.4.52). If a reservoir's transmissivity is below the MEVT, then the reservoir can be removed from consideration for HT-ATES.

Optimal well spacing and flow rate

To decide on the well spacing and flow rate at the Bern-Forsthaus site, many uncertain aspects can be considered. There is uncertainty in the reservoir properties, the number of wells that will be installed, and the configuration of those wells. Given these uncertainties, any recommendation on optimal well spacing and flow rate will be preliminary at this point, and the THM$ approach is well-suited to provide preliminary guidance.

In the analysis of the general HT-ATES system, we found that the optimal well spacing and flow rate are dictated by either the reservoir constraints (Constraints I and II) for shallow or low-permeability reservoirs, or by the economic constraints (Constraints I and III) for deep or high-permeability reservoirs. The well spacing and flow rate increase with depth, and the well spacing was always 1.8 times the thermal radius for the parameters considered. This suggests that the deviated well design that is proposed for Bern-Forsthaus could be advantageous. Under this deviated design, the effective well spacing increases with respect to depth and could be nearly optimal for all depths, depending on the angle of deviation.

In the Bern-specific base-case, we found that the optimal well spacing and flow rate range from 98 to 121 m and from 47 to 71 kg/s, respectively. The optimal well spacing is fairly insensitive to hydraulic conductivity and cumulative reservoir thickness. For example, doubling the hydraulic conductivity only increases the optimal well spacing by 22 m, or 21%, and doubling the reservoir thickness only reduces the optimal well spacing by 15 m, or 13%. Over the entire range of hydraulic conductivity, reservoir thickness, and reservoir depth considered, the optimal well spacing ranges from 71 m to 143 m. The optimal flow rate is more sensitive to the conductivity and reservoir thickness. Doubling the hydraulic conductivity increases the optimal flow rate by 25 kg/s, or 43%, and doubling the thickness increases the optimal flow rate by 27 kg/s, or 46%.

Since our Bern-specific well spacing recommendation are relatively insensitive to the reservoir parameters, they could be used to choose the location of a second well at Bern-Forsthaus. Alternatively, our well spacing recommendation could be used as the base-case value for a future numerical sensitivity study to further understand well placement at Bern, wherein the number of wells, their spacing, and orientation are varied.

Optimal depth

We showed in our generic HT-ATES model that the LCOH and the MEVT are both minimized at intermediate depth due to trade-offs in the heat produced and the costs (see Figure 2.4.50 Figure 2.4.52). The minimum LCOH and MEVT occur at approximately 500 m for a 10-m-thick reservoir. This seems to be good news for the Bern-Forsthaus site, since the reservoir(s) are located near that depth.

2.4.3.3 UPC THM model

Conceptual simulation model

Mechanical effects can be found, when thermal and hydraulic loads induce rock deformations. Thermal expansion of water and rock are different. Depending on the permeability considered, the expansion/contraction of the water can affect pore pressures. This in turn can affect effective stress, which leads to volumetric deformations. On the other hand, the hydraulic effect caused by pressure increments to inject the water into the system may also lead to deformations. Overall, it is expected that injection of hot water may induce uplift of the surface and local stress variations.

THM models are TH model extended with the mechanical equations. One has to bear in mind that TH problem requires 2 degrees of freedom per node (usually pressure and temperature) while THM requires ($2 + nd$) degrees of freedom per node (usually pressure, temperature and nd displacement components (u_x, u_y, …), where nd corresponds to number of dimensions, for instance, $nd = 3$ for a three-dimensional problem).

Pre-processing workflow

Based on the information described above, a 3D THM model of of the HT-ATES pilot project in Bern has been made. The model simulates one year of operation of the system. For simplicity, completely vertical wells are assumed and only a quarter of the domain with one auxiliary well is considered (Figure 2.4.54). Missing data of rock properties has been completed with data from literature for similar geological materials.
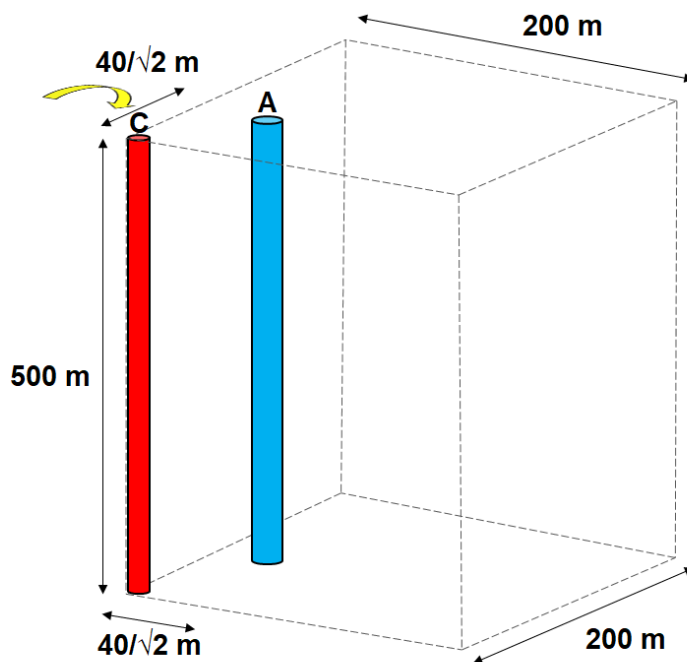
Figure 2.4.54 Model geometry including the central well and one auxiliary well. Symmetry is assumed, so the model represents a five-well system.

Modelling the wells with the actual shape and/or size implies meshing difficulties and numerical problems associated with heat losses in the pipeline. The model proposed here does not incorporate the complete wells. It only includes a permeable zone representing the filter around the well in the injection section.

The model boundaries are far enough so that they do not affect the results near the wells. The size in the horizontal direction is equal to 200 m and the height is 500 m. The length of the wells is 500 m (Figure 2.4.54).

For the geometry developed here, the finite element mesh is semi-structured, that is, unstructured at the top and bottom surfaces and structured in the vertical direction. The elements of the mesh are hexahedral. Different element sizes are used for accuracy and affordable calculations times. The mesh is displayed in Figure 2.4.55.
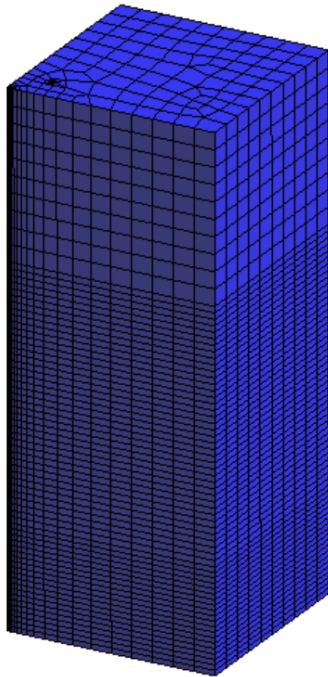
Figure 2.4.55 Semi-structured mesh.

Water is either injected in the central or the auxiliary well. The total flow rate (25 l/s) is divided by four to account for the fact that only a quarter of the domain is modeled. The well is simulated by elements of high permeability, located at a depth between 400 and 500 m. Injection in the central well is carried out at 90°C while injection at the 4 auxiliary wells (25/4 l/s at each one) is carried out at 50°C. It is assumed that injection in the central well takes place during 2/3 of the year (injection phase). Flow is reversed during the remaining 1/3 of the year (back injection phase).

The pressure and temperature at the upper surface of the domain are considered at atmospheric conditions. We impose pressure and temperature on top surface at atmospheric pressure (0.1 Ma) and 20 ^{0}C, respectively. Restriction of vertical displacements on the bottom surface and a restriction for the lateral displacements at the lateral boundaries of the model are applied. The mechanical boundary conditions for both wells are represented in the Figure 2.4.56. We assume that the vertical boundaries and bottom surface are impervious.
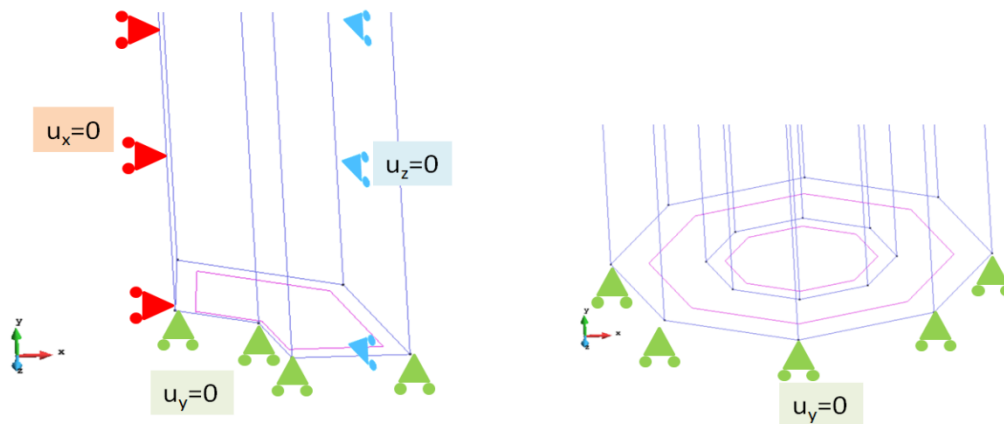
Figure 2.4.56 Mechanical boundary conditions for the Central well (left) and Auxiliary well (right).
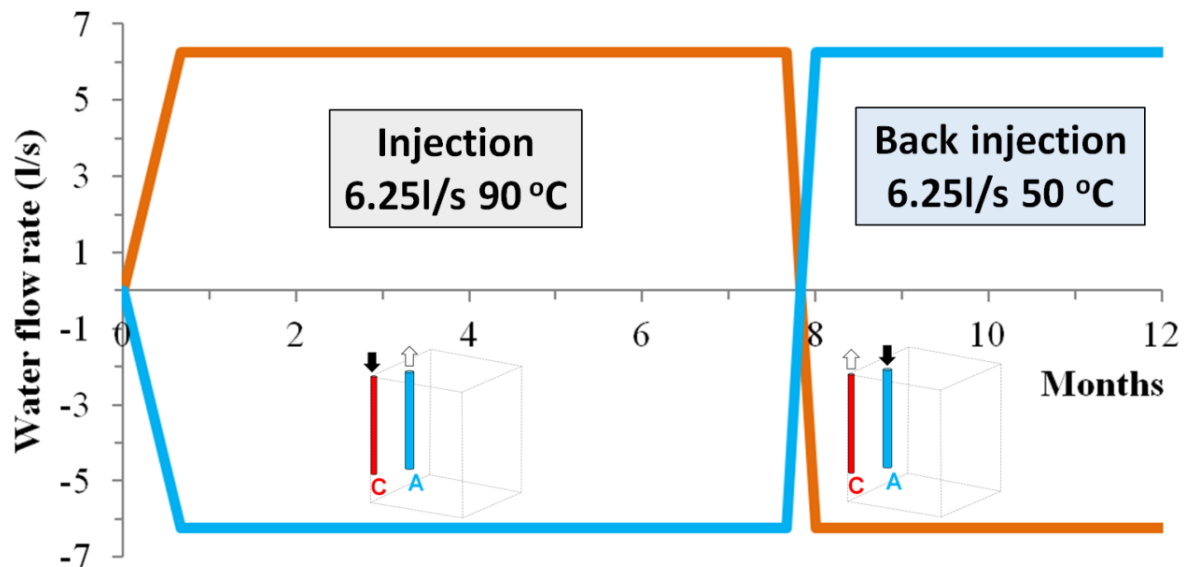
Figure 2.4.57 Simulated stages: Injection and Back Injection.

The initial temperature in the entire model is 20°C and the liquid pressure is assumed hydrostatic starting on the upper surface at atmospheric pressure.

The simulated time is one year. It consists of 3 calculation phases:

- Phase 1: Initial interval of 10 days (time: -10 – 0 days). It is used to calculate the initial stresses and the initial liquid pressure of the model.

- Phase 2: Injection (time: 0 – 8 months). Water is injected with a flow rate of 6.25 l/s and a temperature of 90°C in the central well (Figure 2.4.57). The design flow rate is divided by 4 because the geometry corresponds to 1/4 of the domain.

- Phase 3: Back Injection (time: 8 – 12 months). It consists of an injection of water with 50°C and a flow rate equal to 6.25 l/s in the auxiliary well (only one auxiliary well in the domain). The water is extracted in the central well (Figure 2.4.57).
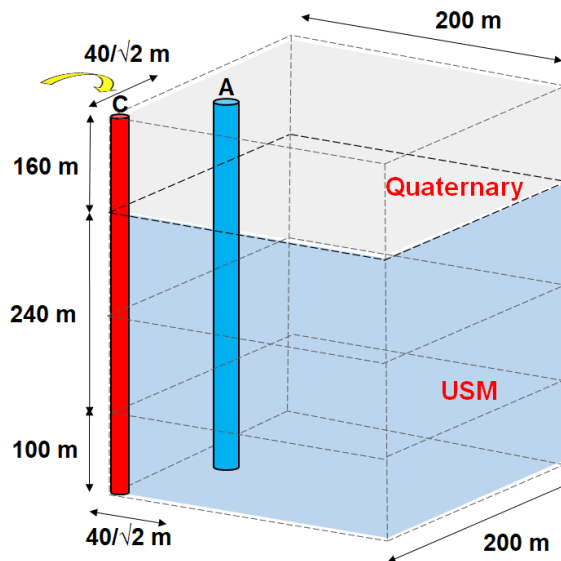
Figure 2.4.58 Model with the different geological materials.

The domain represents two geological formations: Quaternary materials (in the first 160 m) and an aquifer, named Lower Freshwater Molasse or USM (in the rest of the model). The model considers the Quaternary materials as one material layer. The Molasse formation is represented by 2 layers, a shallow with a thickness of 120 m and a deep one with a thickness of 100 m thick. The layers for the Molasse or USM have the same properties in the base case model (Figure 2.4.58). All the materials are saturated.

A summary of the main parameters of the geological materials is shown in Table 2.4.12. This table corresponds to a base case model in which only permeability is the only parameter that is different for each geological section. Mechanical properties are the same for all geological materials, except for the filter at the injection zone.

Table 2.4.12. Parameters for preliminary calculations

Material	Intrinsic permeability (m^2)	Thermal conductivity (W/m·k)	Dispersivities (longitudinal and transversal) (m)	Solid heat capacity (J/ kg·K)	Porosity (-)	Density (kg/m^3)	Elastic Modulus (MPa)	Poisson's ratio (-)
Quaternary	1.0×10^{-16}	2	1/0.1	1000	0.3	2700	5000	0.3
Molasses2	1.0×10^{-15}	2	1/0.1	1000	0.3	2700	5000	0.3
Molasses1 (aquifer)	1.0×10^{-13}	2	1/0.1	1000	0.3	2700	5000	0.3
Filter at injection zone	1.0×10^{-9}	2	100/10	1000	0.3	2700	500	0.3

Computational approach and software

We use Code_Bright (Olivella et al., 1996) for the modeling. This code has been developed at the Department of Civil and Environmental Engineering of the Polytechnic University of Catalonia (UPC).

Code_Bright is a Finite Element Method (FEM) program capable of performing coupled thermo-hydro-mechanical (THM) analysis in geological media. It can handle 1D, 2D and 3D elements. The method of Newton-Raphson is used to solve the nonlinear equations. It has been coupled to the pre/post-processor GiD, developed by the International Center for Numerical Methods in Engineering (CIMNE).

Model Analysis

Scenarios and results

We first present the base case, followed by the sensitivity analysis. In all the scenarios, we focus on the following results: liquid pressure, temperature, displacements and stresses.

Results for the base case

The behaviour of liquid pressure depends on the simulated stage. During injection, liquid pressures are higher in the central well than in the auxiliary wells, indicating flow water from the central well to the auxiliary well. The behaviour is inverted during back Injection (Figure 2.4.59).
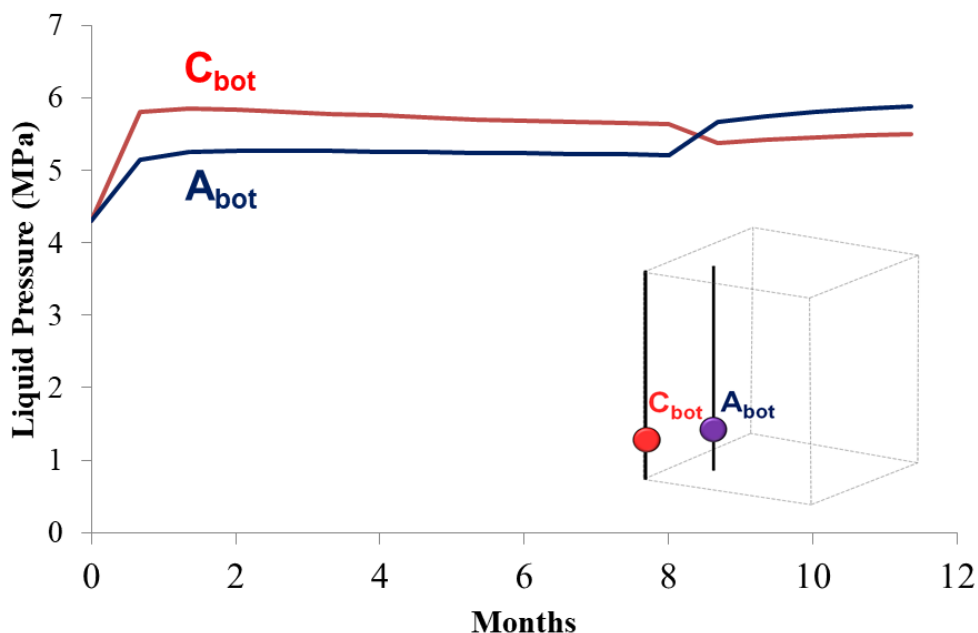
Figure 2.4.59 Liquid pressure for the Central and Auxiliary Well at 400 m depth.

During the Injection, the temperature in both wells increases (Figure 2.4.60). At the end of this phase, the maximum temperature in the central well is close to 90 °C (temperature of the injected water). During back injection, the temperature in the central well decreases to 60 °C. In the auxiliary well it remains nearly constant. In this phase, water is injected at 50 °C.

The volume of aquifer affected by increase of temperature (above 20 degrees) obtains its maximum temperature at the end of the injection, but reaches its maximum size during the back injection. This means that in one year there has been an accumulation of energy (Figure 2.4.61).
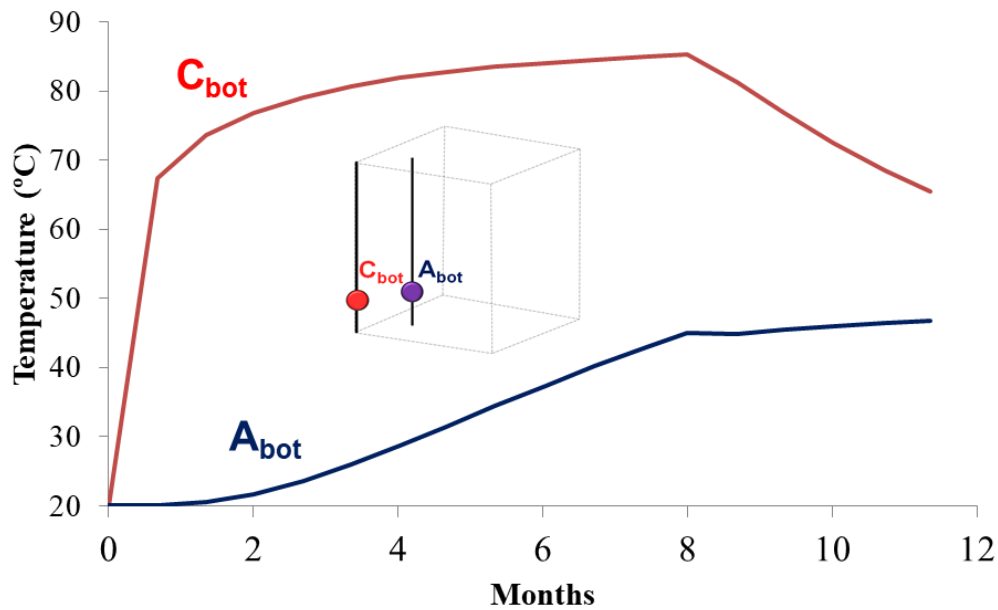
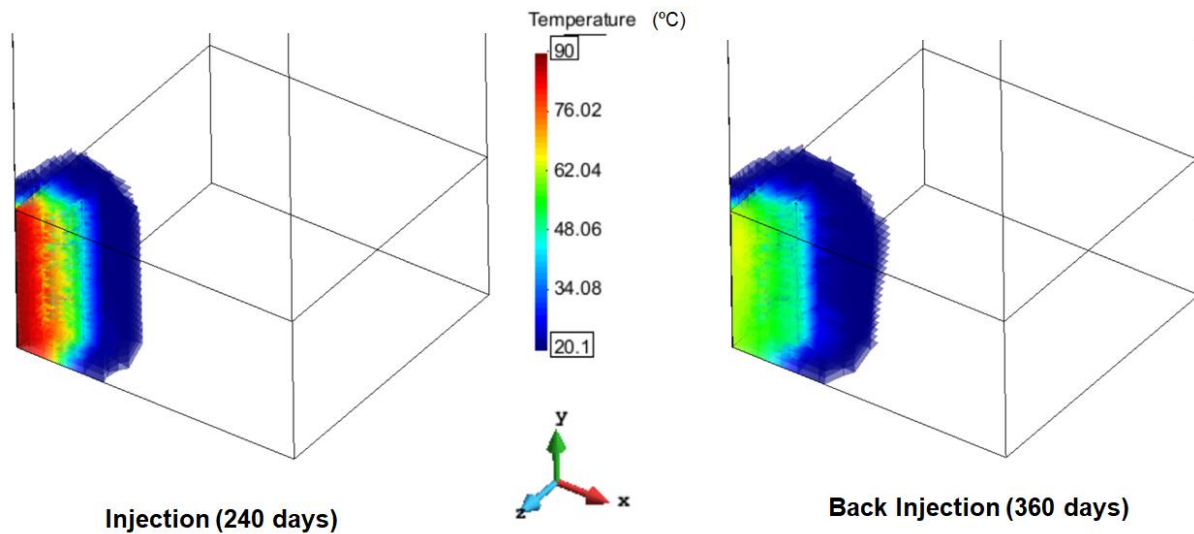**Figure 2.4.60 Temperature in the Central and Auxiliary Well at a depth of 400 m.**

Figure 2.4.61 3D representation of the aquifer affected by the injected temperature at the end of the injection (240 days) and back injection (360 days).

The vertical total stresses increase with depth and remain constant in time. There are no large differences between the end of the injection and the back injection (Figure 2.4.62). This is expected as there are not external loads and equilibrium of forces is satisfied during the whole time.

C A

C A

Injection (240 days)   **Back Injection (360 days)**
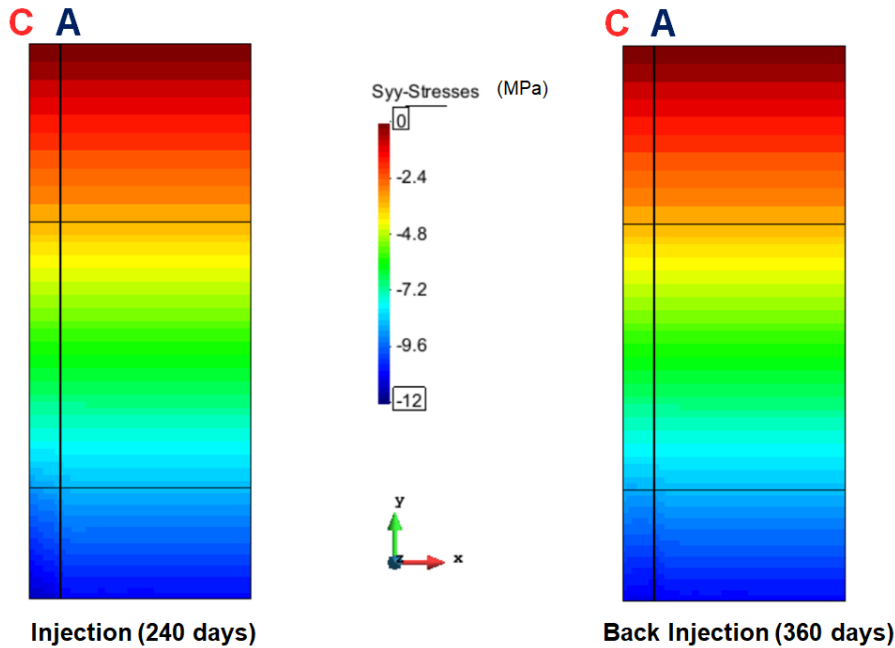
Figure 2.4.62 Vertical total stresses in a central cross section.

The vertical displacements are positive during the whole simulated time. The vertical displacements reach their highest values at the end of the injection. Displacements are a consequence of both hydraulic and thermal loads.

For hydraulics, if strain is estimated using the volumetric modulus in a simplified one dimensional way, it results in:

$$\Delta\varepsilon = \frac{\Delta p_w}{K} = \frac{1.5}{4166} = 3.6 \times 10^{-4} \tag{2.4.16}$$

with $K = \frac{E}{3(1-2v)} = \frac{5000}{3\times(1-2\times0.3)} = 4166 \text{ MPa}$ (2.4.17)

where Δp_w is the increment of the liquid pressure (MPa), K is the bulk modulus (MPa), E is the elastic modulus (MPa) and v is the poisson's ratio (-).The same can be done with the thermal expansion:

$$\Delta\varepsilon = \alpha\Delta T = 1.0 \times 10^{-5} \times (90 - 20) = 7.0 \times 10^{-4} \tag{2.4.18}$$

where α is the linear thermal expansion coefficient (°C^{-1}) and ΔT is the increment of temperature (°C).
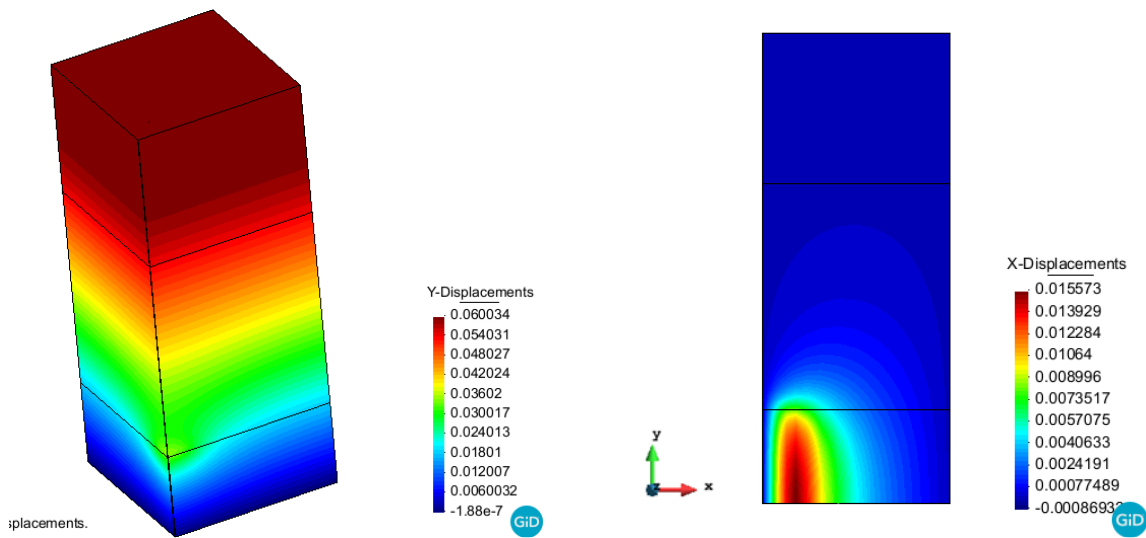
Figure 2.4.63 Vertical displacements (y direction) and horizontal displacement (x direction) at 240 days.

This leads to the conclusion that pressure and temperature variations produce deformation (and consequently displacements) in the same range. This is true for the ranges of variations of pressure and temperature in this type of problem. During the second phase, the displacements increase further.

There are no significant differences between the vertical displacements at the same depth in the central and auxiliary well (**Figure** 2.4.64).
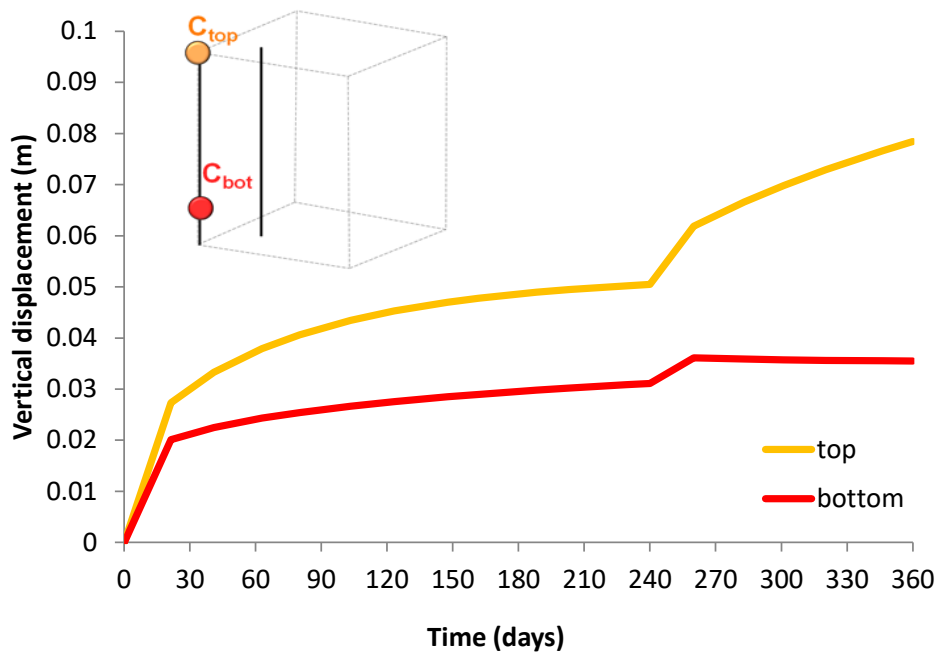
Figure 2.4.64 Vertical displacements at 0 m (Ctop) and 400 m (Cbot) depth in the central well.

Sensitivity to boundary conditions and geometry

In this part, the boundary conditions for vertical displacement applied to the vertical surface (only normal prescribed displacement) lead to an upper bound of vertical displacements. If the vertical displacements are also prescribed, then movements are smaller. This model is also 100 m deeper than the base case model. But the injection section is maintained.

Temperature distribution and evolution (Figure 2.4.65 and Figure 2.4.66) is not significantly different, as the environmental boundary conditions (excluding the injection and extraction) are only applied to the top surface for heat and water flow. Actually, water and heat flow take place in the region limited by the wells.

The stress distribution (Figure 2.4.67) reflects the effect of gravity but it is not as uniform as in the base case (Figure 2.4.62). However, differences appear in the vicinity of the injection borehole. This is explained by the boundary conditions which for the base case permit free vertical movement to the complete mass of materials while for the sensitivity case, the movement is restricted in the vertical direction on the outer boundaries.

In contrast, the displacements (Figure 2.4.68 and Figure 2.4.69) are quite different as compared to the displacements in the base case (Figure 2.4.63 and Figure 2.4.64). Comparison of Figure 2.4.68 with Figure 2.4.63 clearly shows that the displacement field is different. In general less uplift is calculated when the vertical boundary has fixed displacement in all directions. And the movements concentrate around the central well.
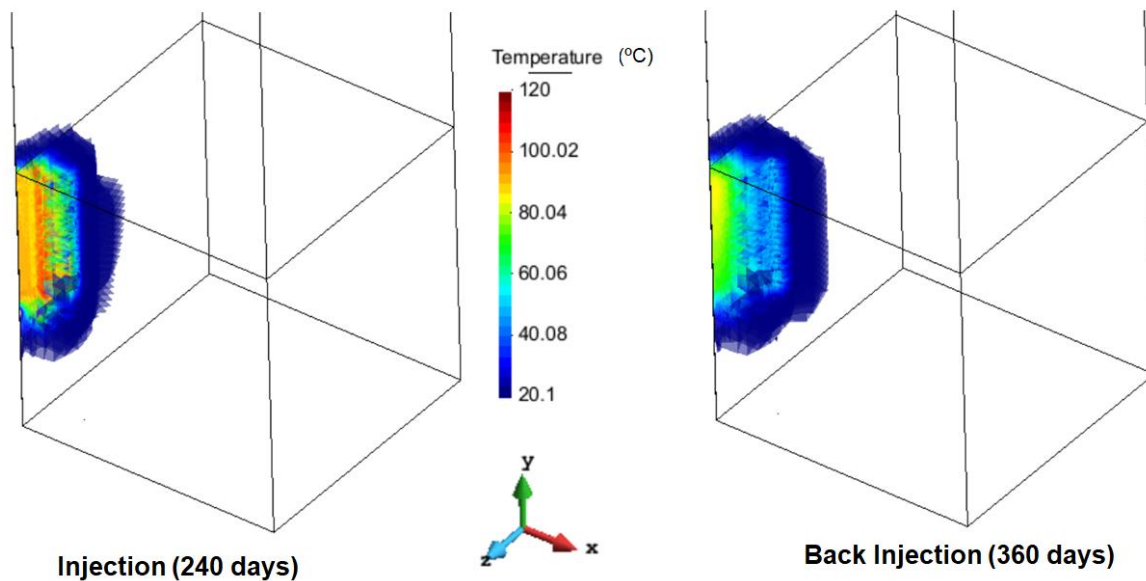

Figure 2.4.65 3D representation of the aquifer affected by the injected temperature at the end of the injection (240 days) and the back injection (360 days).
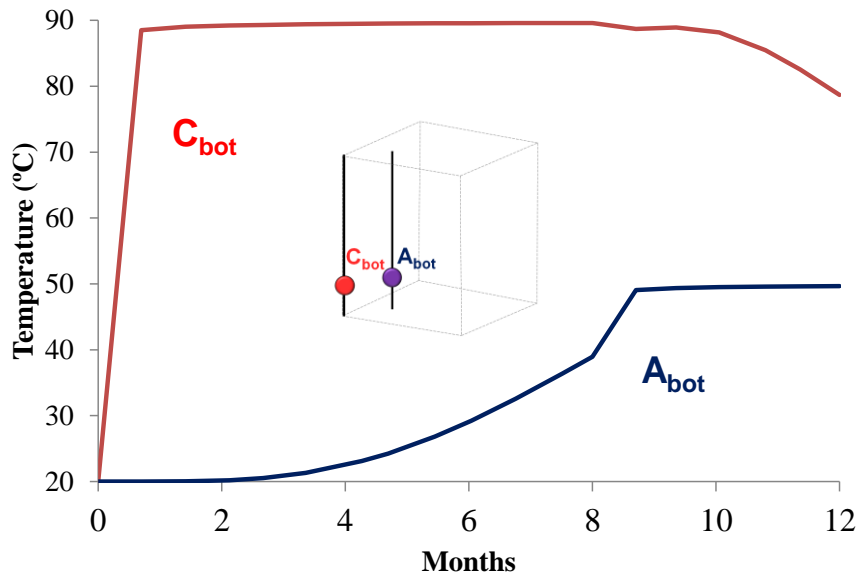
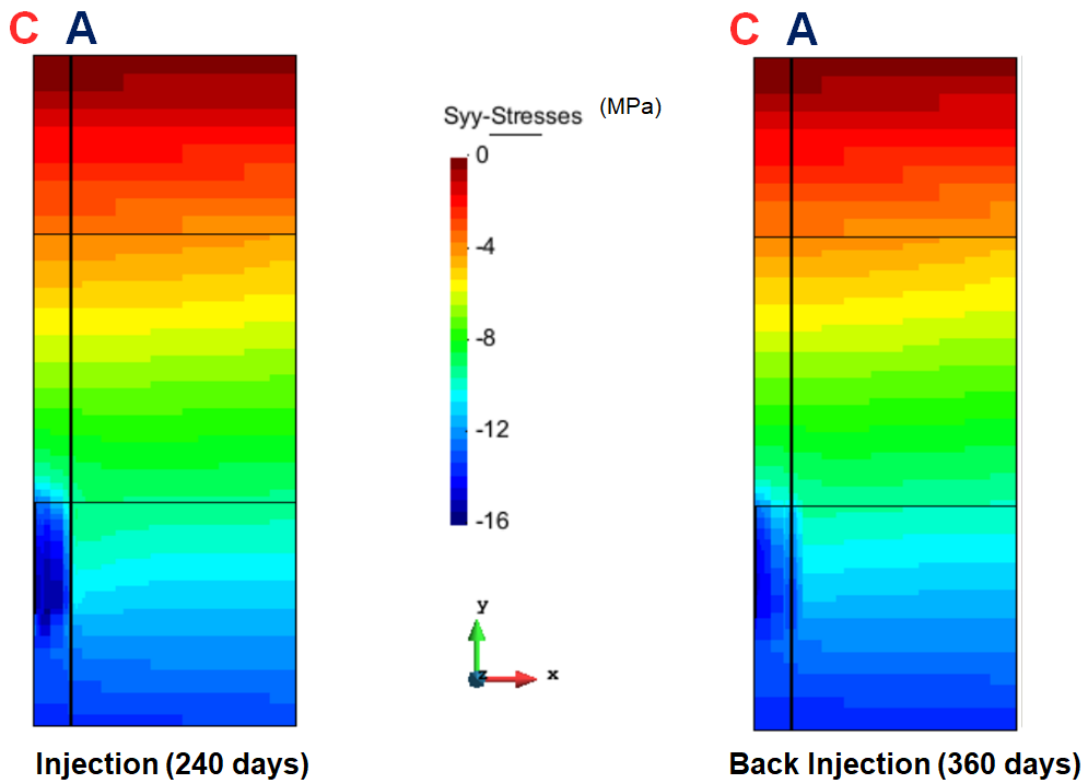**Figure 2.4.66 Temperature in the Central and Auxiliary Well at 400 m deep.**

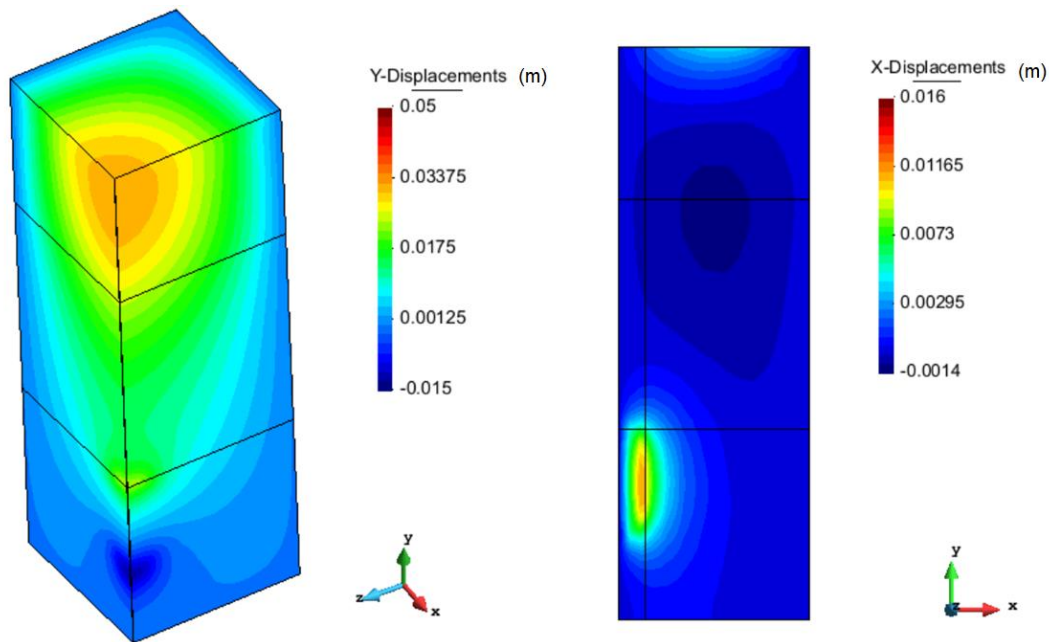**Figure 2.4.67 Vertical total stresses in a central cross section.**

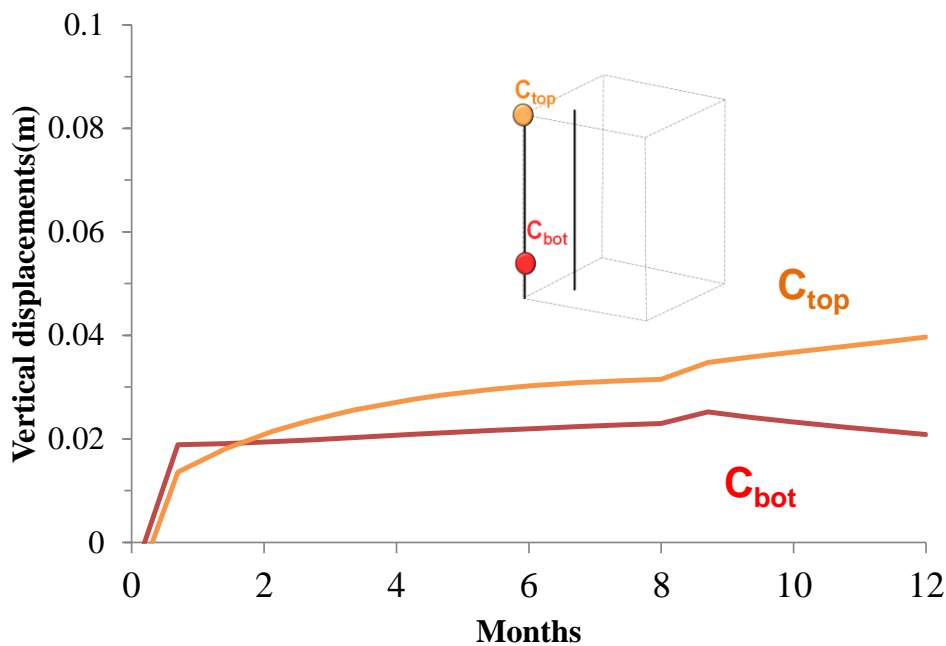**Figure 2.4.68 Vertical displacements (y direction) at 240 days and 360 days.**

Figure 2.4.69 Vertical displacements at 0 m (Ctop) and 400 m (Cbot) depth in the central well.

Analysis and discussion

In this chapter/section, a Thermo-Hydro-Mechanical modelling has been presented based on the Forsthaus Heat Storage project to be developed in Bern. The model is 3D and only considers a quarter of the entire domain. The model reproduces a period of injection (first 8 months) and back-injection (last 4 months) during one year. The material parameters are uniform, except that for intrinsic permeability. The representation of the filters has been done using specific properties.

The liquid pressures of the model are consistent with the flow rate injected in each well. At the end of the year, the temperature in the injection zone is higher than the initial temperature, so there has been accumulation of energy. Vertical total stresses increases with depth and remain quite constant during de calculations. Vertical displacements are a consequence of the hydraulic and thermal loads. A maximum of 8 cm has been detected at the central borehole surface for the base case.

A sensitivity analysis has been done. The vertical dimension of the model has been enlarged and the vertical and horizontal displacements in the outer vertical boundaries have been fixed. The results are somewhat similar to the previous calculation, with the exception of total stresses, that increase by up to 5 MPa between both boreholes in the injection zone, and the vertical displacements, which are in the range of 4 cm.

2.4.4 Work Package Interfaces

2.4.4.1 WP1: Specifications and characterization for UTES concepts

The Forsthaus project is exemplary in how laboratory and experimental analysis, geological field work (by studying analoguous sites), engineering expertise, technological know-how, and the numerical modelling presented here can be used to decrease uncertainly and risk before and during an UTES operation.

The Uni Bern THC model can help with crucial design issues. For instance, the model has shown that a spacing of 50 m between main and supporting wells is not optimal in terms of heat storage and should be extended. The model has shown that the chemical plume arising from the operation cannot be contained with the envisaged well design. But given the predicted reactions and changes in groundwater composition, this effect is not serious for conditions at the Forsthaus site. However, this situation could be deifferent at other locations.

The model has shown that adverse effects of carbonate reactions on the transmissivity in the reservoir can be controlled and prevented by properly adjusting the pumping schedule.

The results of the ETHZ THM$ interface well with WP1, particularly Task 1.3, which focuses on screening the national potential of UTES. The MEVT can be used as a pre-screening value, especially since it can be approximated as one value ($5 \cdot 10^{-13}$ m³). Any reservoirs that have a transmissivity below the MVET can be removed from consideration, and the capacity of the remaining reservoirs would act as an upper bound on national HT-ATES potential. Daniel Birdsell regularly attended and contributed these ideas to T1.3 meetings.

In a similar screening approach vein, some of the concepts and equations in the THM$ approach and behind the MEVT were used by GES and EWB in one iteration of the decision tree analysis for a second well at the Bern-Forsthaus site. The decision to drill a second well is an important and costly proposition, and will be guided by many factors. To take these many factors into account, GES created an Excel tool for EWB and incorporated estimates of pumping power and heat recovery from the THM$ work. In the end, an alternative decision criteria was elected, but the THM$ approach was considered as one candidate for screening.

Due to the computational speed of the THM$ approach, it was possible to evaluate a large range of uncertainty in the parameter space. We showed the HT-ATES response for permeabilities that vary over three orders of magnitude, reservoir thickness that varies by a factor of two, and depth ranging from 50 to 2667 m. Furthermore, the code is free and open source so that others can plug their own range of parameters corresponding to future potential HT-ATES scenarios.

2.4.4.2 WP3: Heating System integration and optimization of design and operation

Suppose there are similar reservoirs at different depths. The results from the ETH simulations shown in Figure 2.4.50 suggest there are two ways to choose the depth of a HT-ATES reservoir. One, possibly naive, approach is to select the depth based on the amount of heat storage desired. This would involve reading the depth from Figure 2.4.50 (b) and would have the benefit of storing the desired heat. An alternative, likely better approach, is to select the depth that minimizes the LCOH as seen in Figure 2.4.50 (a). Then the number of doublets can be scaled to match the heat demand. In this way the LCOH is minimized and the heat demand is met.

We also offered insight into HT-ATES thermal efficiency. For example, our generic THM$ HT-ATES model showed that thermal efficiency increases with depth. Furthermore, in the Bern-specific model we showed that

the thermal efficiency is low if each target layer experiences heat loss, but the efficiency is high if the USM acts as one collective reservoir. The former likely reflects the early years of operation, before heat can diffuse into the intermediate aquitards, while the later likely reflects the later years when a large interval of the USM is heated. This suggests that thermal efficiency will increase from year to year.

2.4.4.3 WP5: Monitoring and validation to assess system performance and workflow

Pre-operation modelling was used in the Uni Bern simulations to identify potential risks during the operation and knowledge gaps in the model parameterization, that is, that lack or uncertainty of specific data that are needed to make reliable predictions using numerical simulations. Identifying these will help optimize the monitoring strategy before the start of the operation and define a strategy for sampling and data collection prior to and during operation.

The models can easily accommodate and adapt to new data and information when they become available as the project progresses. Results from these model updates will be used to improve the monitoring and data collection strategy.

2.4.5 Potential issues related to IP

PFOTRAN, used by Uni Bern, is open source software and can be download following the links at www.pflotran.org.

The ETHZ THM$ approach is free and open source and can be found at https://github.com/danielbi-ETHZ/THM-Econ.

CODE_BRIGHT of UPC is a free software and it can be downloaded from https://deca.upc.edu/en/projects/code_bright. Updates of the code with respect to the HEATSTORE project will be free as well and available on the same web sites.

2.4.6 References

Alt-Epping, P.; Waber, Niklaus; Diamond, L. W.; Eichinger, L. (2013). Reactive transport modeling of the geothermal system at Bad Blumau, Austria: Implications of the combined extraction of heat and CO2. Geothermics, 45, S. 18-30. Pisa: Pergamon 10.1016/j.geothermics.2012.08.002

Alt-Epping, P. & Mindel, J., (eds.) 2020: Benchmarking and improving models of subsurface heat storage dynamics, GEOTHERMICA – ERA NET Cofund Geothermal, 104 pp.

Birdsell DT. (2020). Thermo-hydro-mechanical-economic (THM$) code for HT-ATES. http://dx.doi.org/10.5281/zenodo.4075425, *Zenodo.org*.

Birdsell, D. T., Adams, B. M., & Saar, M. O. (2021). Minimum transmissivity and optimal well spacing and flow rate for high-temperature aquifer thermal energy storage. *Applied Energy*, 289, 116658.

Diamond, L.W. and P. Alt-Epping (2014), Predictive modelling of mineral scaling, corrosion and the performance of solute geothermometers in a granitoid-hosted, enhanced geothermal system. Applied geochemistry, 51, S. 216-228. Pergamon 10.1016/j.apgeochem.2014.09.017

Driesner, T., Manatschal, L., and Mindel, J. (2017) Finaler Berich numerische Simulationen «Geospeicher Forsthaus», ETHZ, Department Erdwissenschaften

Driesner, T. (ed.) (2019). Initial report on tools and workflows for simulating subsurface dynamics of different types of High Temperature Underground Thermal Energy Storage. GEOTHERMICA – ERA NET Cofund Geothermal, unpublished report, 143 pp.

Hölker, A. (2006). Lower Freshwater Molasse. Stochastic Modelling of hydraulic conductivity. Report for Hauptabteilung für die Sicherheit von Kernanlagen CH-5232 Villigen-HSK by Andreas Hölker Proseis AG.

Johnson, J.W., Oelkers, E.H., Helgeson, H.C., (1992). SUPCRT92: a software package for calculating the standard molal thermodynamic properties of minerals, gases, aqueous species and reactions from 1 to 5000 bar and 0 to 1000□C, Comput. Geosci., v. 18, 899-947

Keller, B. (1992). Hydrogeologie des schweizerischen Molasse-Beckens: aktueller Wissensstand und weiterführende Betrachtungen. Eclogae Geologicae Helvetiae, 85.

Küpfer, T. (2005). Arbeitsbericht NAB 04-09. Hydrogeologie der Unteren Süsswassermolasse.

Lasaga, A.C., J. M. Soler, J. Ganor, T. E. Burch, and K. L. Nagy (1994). Chemical weathering rate laws and global geochemical cycles, Geochimica et Cosmochimica Acta, 58(10), 2361-2386. https://doi.org/10.1016/0016-7037(94)90016-7

Leu, W., Mégel, T., Schärli, U. (2006). Schlussbericht – Geothermische Eigenschaften der Schweizer Molasse (Tiefenbereich 0 -500 m). Datenbank für Wärmeleitfähigkeit, spezifische Wärmekapazität, Gesteinsdichte und Porosität. Überarbeitung 2006. Im Auftrag des Bundesamtes für Energie.

Li, L., C. I. Steefel, L. Yang (2008). Scale dependence of mineral dissolution rates within single pores and fractures, Geochimica et Cosmochimica Acta, 72, 360-377. https://doi.org/10.1016/j.gca.2007.10.027

NAGRA NTB 88-07 (1990). Hydrochemische Synthese Nordschweiz: Tertiär- und Malm-Aquifere.

NAGRA NTB 88-25 (1988). Sedimentstudie – Zwischenbericht 1988.

NAGRA NTB 90-41 (1990). Sedimentäre Architektur der distalen Unteren Süsswassermolasse und ihre Beziehung zur Diagenese und den petrophysik. Eigenschaften am Beispiel der Bohrungen Langenthal.

NAGRA NTB 92-03 (1993). Untere Süsswassermolasse im Erdsondenfeld Burgdorf. Charakterisierung mittels Geologie, Petrophysik und Fluid Logging.

Olivella, S., Gens, A., Carrera, J., Alonso, E.E., 1996. Numerical formulation for a simulator (CODE_BRIGHT) for the coupled analysis of saline media. Eng. Comput. 13(7), 87–112 (1996). https://doi.org/10.1108/02644409610151575

Palandri, J. and Y.K. Kharaka (2004) A compilation of rate parameters of water–mineral interaction kinetics for application to geochemical modeling. US Geol. Surv. Open File Report 2004-1068. 64 pp.

Parkhurst, D.L., Appelo, C.A.J. (2013), Description of input and examples for PHREEQC version 3—A computer program for speciation, batch-reaction, one-dimensional transport, and inverse geochemical calculations: U.S. Geological Survey Techniques and Methods, book 6, chap. A43, 497 p., https://pubs.usgs.gov/tm/06/a43/

Pfiffner, O.A., Lehner, P., Heitzmann, P., Müller, St. & Steck, A. (1997). Results of NRP 20. Deep Structure of the Swiss Alps. Birkhäuser.

Platt, N.H., Keller, B. (1992). Distal alluvial deposits in a foreland basin setting – the Lower Freswater Molasse (Lower Miocene), Switzerland: sedimentology, architecture and palaeosols. Sedimentology 39, 545-565.

2.5 Icelandic case study: seasonal extra heat storage to aquifers used for district heating

Sigrún Tómasdóttir, Gunnar Gunnarsson, Thomas Ratouis

Reykjavik Energy

2.5.1 Conceptualization

Extensive geothermal activity is found in Iceland. Geothermal systems in the country are conventionally divided into two categories; high-temperature systems, where temperature at 1 km depth is above 200 °C, and low-temperature systems, where temperature at 1 km depth is below 150 °C (Böðvarsson, 1961). The high-temperature areas are found within the youngest parts of the country (Figure 2.5.1), the active volcanic zones, but the low-temperature areas are mainly located outside the volcanic zones (Axelsson et al., 2010).
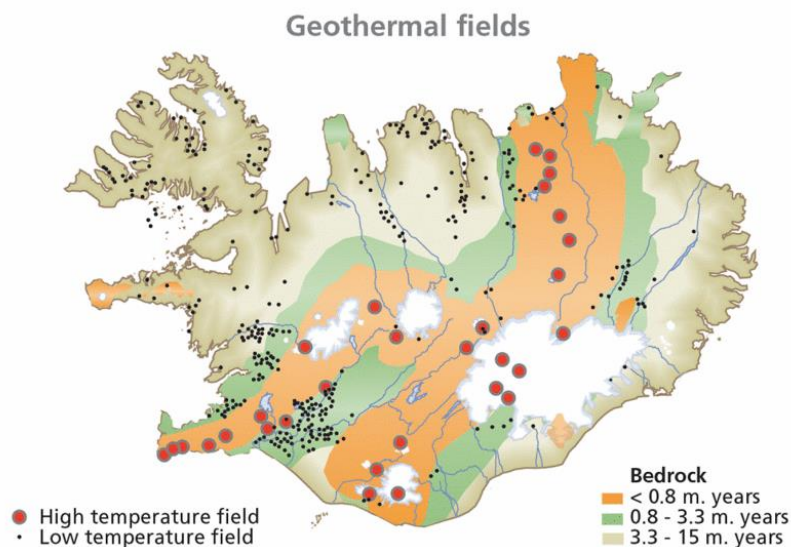
Figure 2.5.1 Distribution of geothermal fields in Iceland (Orkustofnun, n.d.).

Comparing these temperatures with the definition of high temperature systems within the HEATSTORE project (~25°C to ~90°C) clearly shows how the Icelandic geothermal conditions differ from the central European conditions. The harnessing of geothermal energy has played a large role in improving the quality of life in Iceland. About 90 % of space heating requirements in the country (Figure 2.5.2) are supplied by geothermal energy (Orkustofnun, 2019a).

Reykjavík Energy operates the district heating utility in the capital area. It is the world's largest geothermal district heating service, serving about 58 % of the country's population (Gunnlaugsson and Ívarsson, 2010). The water for the district heating system comes from two different sources. On one hand, from low temperature fields in the city´s vicinity and on the other hand from two high-temperature fields in the Hengill area, about 30 km east of Reykjavík (Figure 2.5.3). The water from the low temperature fields has a low chemical content and can thus be used directly. Geothermal water from the high-temperature fields, however, has a higher chemical content and cannot be used directly due to the risk of scaling in pipes and radiators. Because of this, the geothermal fluid from the high-temperature systems is used to heat up colder groundwater which is then supplied to the district heating system.
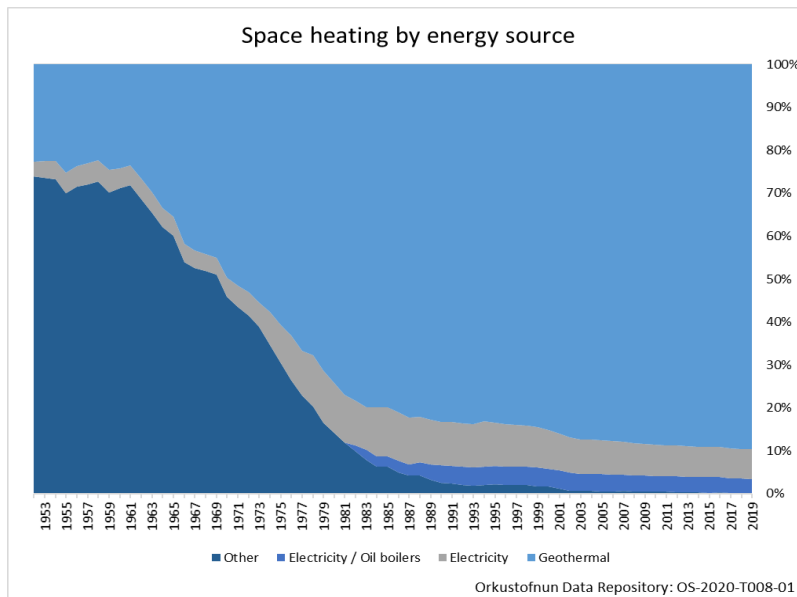
Figure 2.5.2 Space heating in Iceland by energy source (Orkustofnun Data Repository: OS-2020-T008-01).

Mixing of these two water types can cause precipitation of magnesium silicates in the distribution system and therefore, the two water types are kept separate within the system. That is, certain parts of the city rely only on water from low temperature fields and other parts only on heated groundwater from the Hengill Area. There is a fast-growing demand for hot water in the capital areas, especially within areas that rely on water from the low temperature fields. The low temperature fields, however, have a finite production capacity. The thermal plants in the high-temperature fields in the Hengill Area can, however, and will be expanded. This discrepancy between demand and supply requires new solutions.

One solution could be to inject excess water that is produced from the Hengill Area during summer, when space heating demands are lower, into one of the low temperature systems. This would imply storing the heat underground for later usage. The effect of such injection into low temperature systems is the subject of this study. The aims of the study, the possible challenges of the heat storage scheme and the conceptual model will be described in further detail in the following chapters.
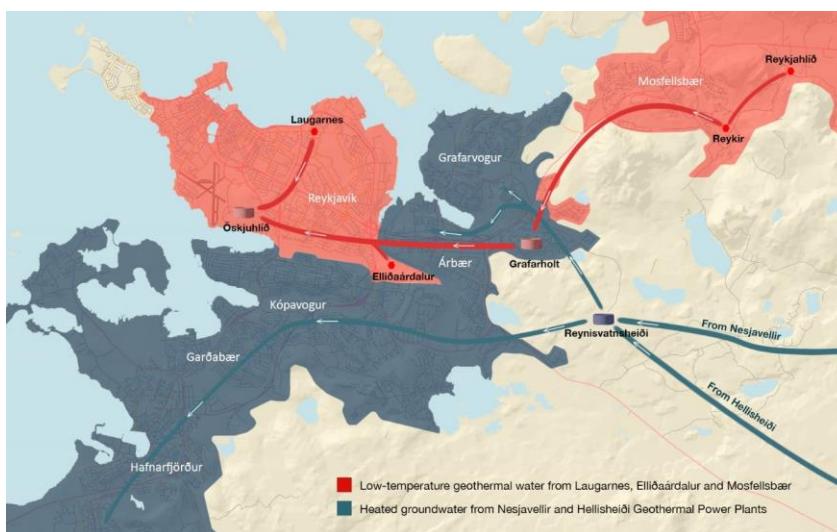

Figure 2.5.3 A map showing how the hot water will from now on be distributed throughout the capital. The low temperature fields are marked with red circles. The red shaded areas receive water from the low temperature areas and the blue shaded areas receive water from Hellisheiði and Nesjavellir.
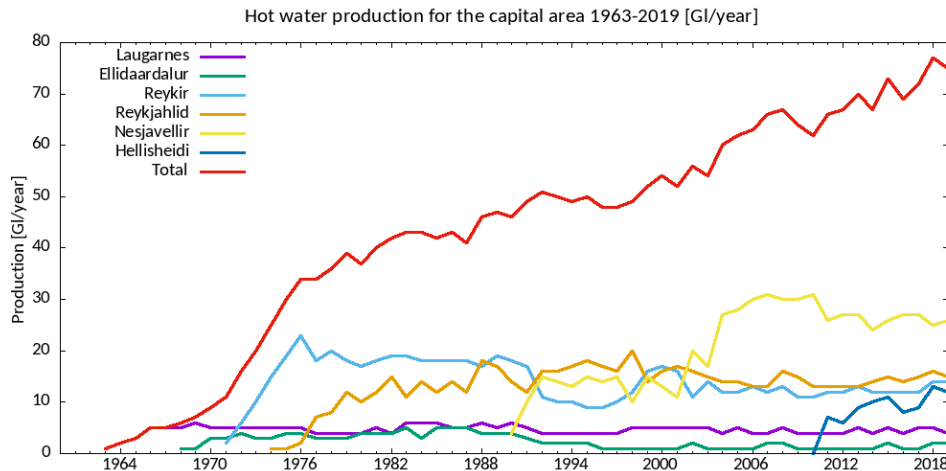
Hot water production for the capital area 1963-2019 [GI/year]

Figure 2.5.4 Hot water production for the capital area from 1963-2019 [Gl/year] (Data from Ívarsson, 2020).

2.5.1.1 UTES concept and specifications, scope and aims of the study

Reykjavík Energy utilizes three low temperature fields; Laugarnes, Elliðaárdalur and Reykir/Reykjahlíð, and two high temperature fields in the Hengill area; Hellisheiði and Nesjavellir, for supplying hot water for the capital area. As previously mentioned, the water from the low and high temperature fields cannot be mixed without precipitation occurring and the waters are thus kept separate in the distribution system (Figure 2.5.3). Figure 2.5.4 shows the hot water production for the capital area from 1963 until 2019, from the individual areas and the total production. The production from the low temperature fields was intentionally decreased in 1990, when Nesjavellir was commissioned, to protect the systems. In 2019, the Reykir/Reykjahlíð field supplied 38,9 % of the total produced hot water, the Hengill area 51,9 % and the two fields in Reykjavík 9,3 %. The Reykir/Reykjahlíð field supplied 39,6 % of the power (MW$_{thermal}$) in 2019, the Hengill areas supplied 45,5 % and the Reykjavík areas supplied 15 %. This difference comes from the fact that the average temperature of the water from the low temperature systems is higher than the temperature of the water from Hengill, which is maintained at 80°C (Ívarsson, 2020).

The water from Hellisheiði and Nesjavellir comes from two combined heat and power plants that operate on base-load all year round. Because of less heating demand during the summer time, 250 – 300 l/s of hot water from Nesjavellir have routinely been disposed of during the summer months. The water is injected into shallow wells located between Nesjavellir and Reykjavík. Considering the production pressure on the low temperature systems, wasting hot water is not considered an acceptable long-term option.

In search of better ways to use the resource, the idea of injecting the excess water into a utilized low temperature system for storage came up. This would reduce energy wasting and thus improve the efficiency of the hot water production at Nesjavellir and provide pressure support in the low temperature system. A simple schematic is shown in Figure 2.5.5. But before trying this, simulations need to be carried out to explore the effects of such an injection.

Two low temperature systems can be considered as possible injection locations; the Reykir/Reykjahlíð system and the Elliðaárdalur system. Figure 2.5.6 shows the location of these areas, hot and cold-water wells in the capital area and the main pipes in the distribution system. Flow models have been developed to test the effect of injecting 80 °C warm water from Nesjavellir on pressure and temperature in the Reykir/Reykjahlíð system. Emphasis was put on the Reykir/Reykjahlíð system since that system is under much more production than the Elliðaárdalur system and water levels in the Elliðaárdalur system already rise to the surface during normal summer operations.

The aim with the model simulations is to understand the system´s response to introducing fluid injection into the system, which currently has no injection wells. The first aim is to analyse whether injection in summer will provide pressure support that can then be utilized in the winter and thereby increase the areas production capacity during periods of high demand. We assess the sensitivity of the modelled production characteristics
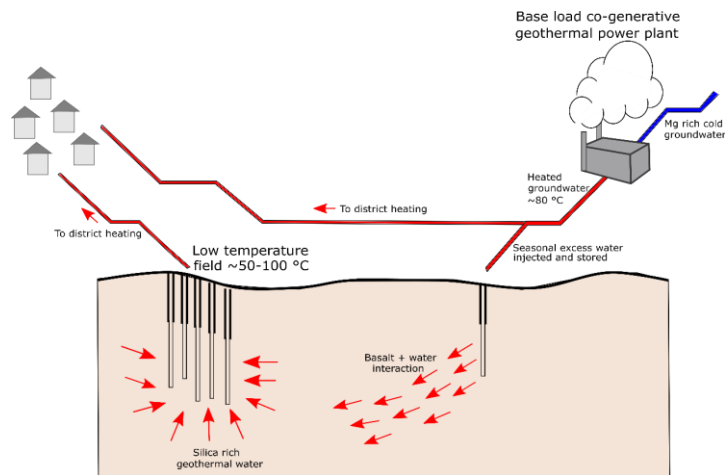
Figure 2.5.5 Schematic for seasonal injection of excess heat from Nesjavellir

to the model parameters. This includes injection rates and volumes as well as varying the hydraulic and thermal properties of the host rocks within plausible ranges. The second aim is to assess via chemical simulations the effects of mixing of the two water types in the subsurface. Can the same types of precipitates be expected when in mixing happens in the presence of rock and, if so, can clogging be expected around the injection sites? Or will the presence of reservoir rocks positively affect interaction such that the chemical problems that occur when the waters are mixed within the distribution system (precipitation of magnesium silicates) are reduced or eliminated? Existing wells or hypothetical well locations are used for different injection scenarios.
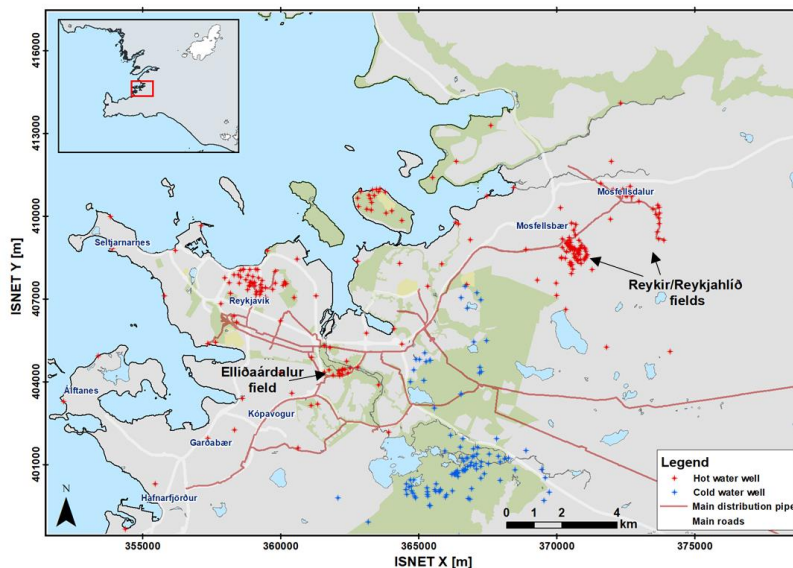

Figure 2.5.6 Map of the capital area showing the location of hot and cold water wells, the main distribution pipes and the location of the Reykir/Reykjahlíð and Elliðaárdalur fields (Data source: National Land Survey of Iceland and Reykjavík Energy).

2.5.1.2 System Geometry and related Geology

The Reykir/Reykjahlíð system is located on the western edge of the active rift zone that runs through Iceland. The main rock types on the surface at Reykir/Reykjahlíð are Pleistocene basaltic and intermediate lavas, eruptive materials and sediments. (Figure 2.5.7) (Hjartarson and Sæmundsson, 2014).
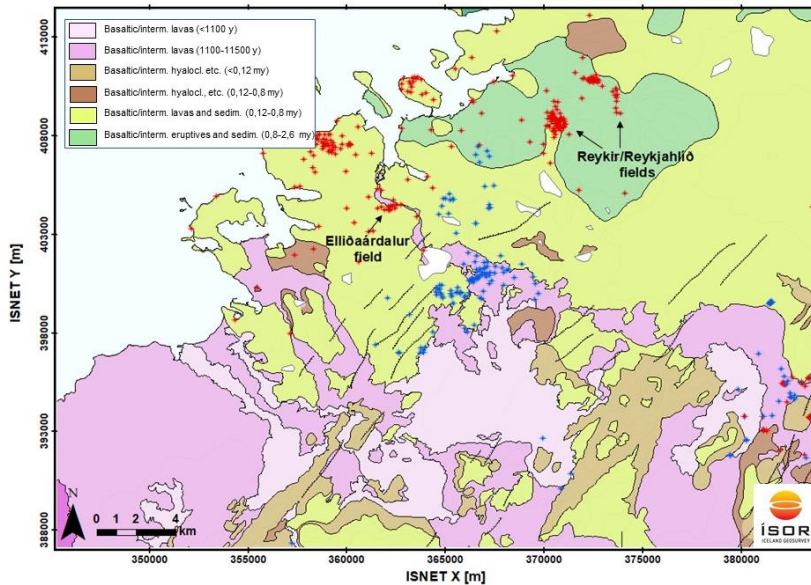
Figure 2.5.7 A simplified geological map of the area. Pink shades are basaltic and intermediate Holocene lavas, brown shades are hyaloclastites, pillow lavas and associated sediments younger than 0.8 Ma and green shades are basaltic and intermediate Pleistocene lavas, eruptive materials and sediments. The hot and cold water wells are shown in red and blue, respectively (Source for geological map data: Hjartarson and Sæmundsson, 2014).

The Reykir/Reykjahlíð geothermal system covers about 10 km^2. The system is separated into two subareas, Reykir and Reykjahlíð. They are both at an elevation of about 20-80 m above sea level (m a.s.l.). They lie 2-3 km apart from each other and are separated by hills which rise to 220-250 m a.s.l. The stratigraphy in the area is characterized by alternating sequences of subaerial basaltic lava flows and hyaloclastite formed during glacial periods (Tómasson, 1997). Einarsson (2018) constructed a lithological model of the Reykir/Reykjahlíð areas (Figure 2.5.8). The model shows these alternating sequences. Extensive geothermal alteration is found in the area, both low temperature and high temperature alteration, which indicates that the system used to be a high temperature geothermal system.
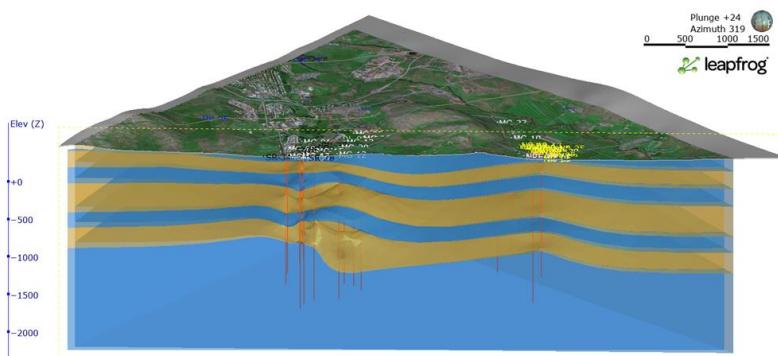

Figure 2.5.8 A lithological model of the Reykir/Reykjahlíð areas. The azimuth of the slice is 140 ° and the slice dip is 90 °. Orange layers represent hyaloclastite and blue layers represent basalt. The red traces are well paths. (Adjusted from Einarsson, 2018).

Specific data for porosity, permeability, density, heat capacity and thermal conductivity for each layer in the system does not exist. However, studies have been done on these parameters for different rock types in Iceland (see e.g. Sigurðsson and Stefánsson, 1994). General parameter values for basalt and hyaloclastite are presented in Table 2.5.1. These values are measured matrix values and therefore not completely representative for the geothermal systems due to the fractured and altered nature of the rocks within them.

Table 2.5.1 Average values for active porosity, permeability, density, thermal conductivity and heat capacity in basalt and hyaloclastite.

Rock type	Active porosity [%]	Permeability [m²] *	Density (kg/m³)	Thermal cond. [W/m°C]	Heat capacity [J/kg°C]
Basalt	7 [1]	3,75 * 10⁻¹⁵ [1]	2890 [1]	1,8 [2]	1050 [2]
Hyaloclastite	28 [1]	3,67 * 10⁻¹³ [1]	2780 [1]	0,85 [3]	1100 [4]

[1] Sigurðsson and Stefánsson, 1994
[2] Wohletz and Heiken, 1992
[3] Frolova, 2010
[4] Bacon, 1977
* These are measured matrix values. The formation values would likely be higher due to fractures.

2.5.1.3 Local geothermal and groundwater conditions

Low temperature systems in Iceland are considered to form through one or more of the following processes (Arnórsson, 1995):

- Deep hydraulic gradient driven flow of groundwater from highland to lowland areas through permeable structures

- Convection in young fractures in older bedrock

- Drift of high-temperature areas from the active rift zone

- Magma intrusion into bedrock close to the active volcanic belts

The Reykir/Reykjahlíð field is believed to have formed through a mixture of the above-mentioned processes. The field is a part of an ancient high-temperature system formed through volcanic activity 2 million years ago in the extinct Stardalur volcano (Friðleifsson, 1985). High-temperature alteration indicating much higher temperatures than observed in the system today supports this theory. Active fissure swarms from the Krísuvík and Trölladyngja volcanic system in the Reykjanes Peninsula reach into the field and have caused recent fracturing in the older bedrock. The current geothermal system is thought to have developed through convection in such fractures (Arnórsson, 1995). Permeability in the system is largely affected by the presence of these fractures which extend mainly in a SW-NE direction. Water level changes in nearby wells accompanying pumping during pressure tests conducted between 1972-1977 showed greater hydrological connection between wells in the main fracture direction than perpendicular to it. The overall results from the tests showed that the field can be roughly split up into different sections that are aligned in the main fracture direction. They are called Helgafellssvæði, Vestursvæði and Austursvæði (Thorsteinsson and Einarsson, 1990). The hydrological connection towards the SW/NE is also confirmed by seasonal water level fluctuations in wells as far as 20 km northeast of the production zone (Vatnaskil, 1994; Björnsson and Steingrímsson, 1995). Wells in the area show a levelled temperature over a long depth range due to convection. The highest temperature is however found at 500-600 m depth and then the temperature decreases slightly making the temperature profiles reversed (Figure 2.5.9). One explanation for such reverse temperature profiles is that rising warm water spreads out horizontally once it finds a horizontal permeable layer and overlays colder water (Björnsson and Steingrímsson, 1995). Another explanation is cooling at depth due to recharge of cold water at depth (Arnórsson, 1995).
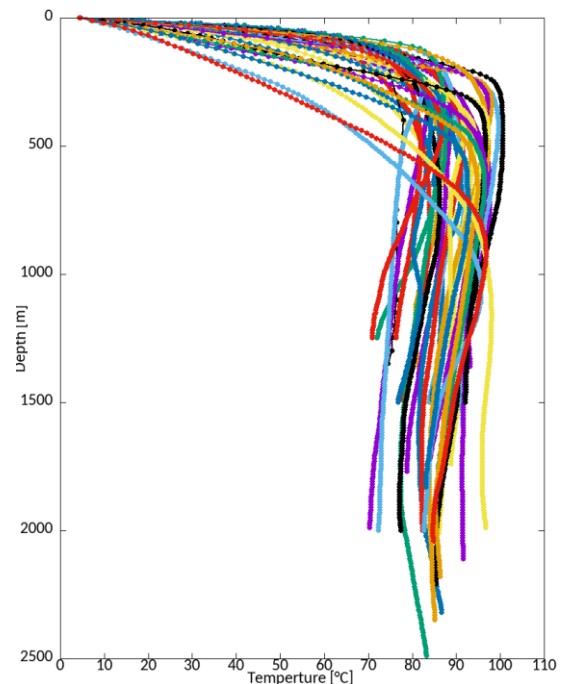

Figure 2.5.9 Rock temperature profiles in production wells in Reykir and Reykjahlíð.

Recharge into the geothermal system is considered to come mainly from two directions. On one hand, about 100 °C warm water flows in from the northeast and on the other hand colder water from the southwest, likely from the Elliðaárdalur region, sinks to great depths through fractures, warms up and then rises towards the southern part of Reykir and enters the system. There appears to be a colder groundwater system on the western edge of Reykir, separated from the geothermal system by an impermeable barrier. The hydrological connection at least seems to be much poorer towards the west (Björnsson and Steingrímsson, 1995). The temperature of the water produced from Reykjahlíð has maintained stable throughout the production history. This implies that recharge into the system from the northeast must be sufficiently warm when it enters the system (Björnsson and Steingrímsson, 1995).

Temperature distribution maps provide a good way to visually see the extent of the geothermal system. They are constructed using formation temperature profiles that are meant to represent the temperature in the system before production started. Figure 2.5.10 shows formation temperature contours in the capital area at 500 m depth as depicted by Björnsson et al. (1999). It clearly shows sharp temperature structures towards the west and south and a warm inflow from the northeast.
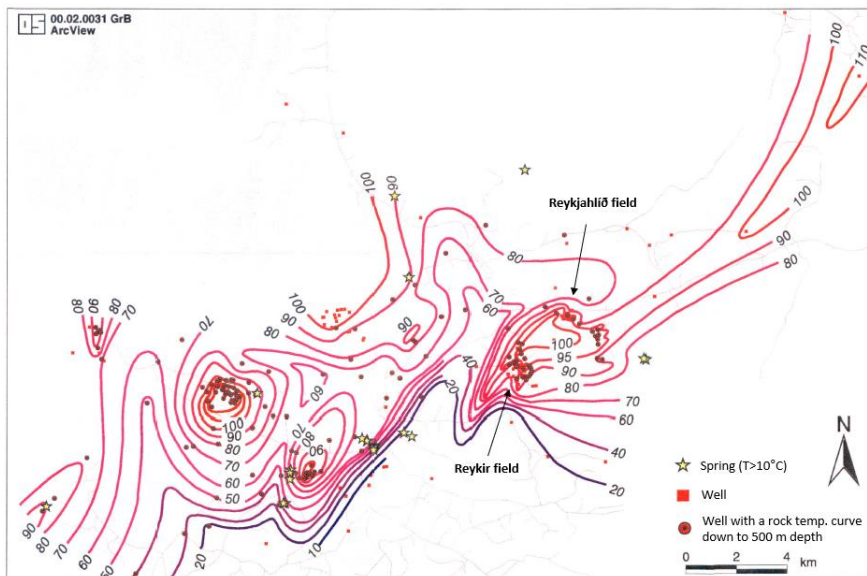

Figure 2.5.10 Formation temperature distribution at 500 m depth (adjusted from Björnsson et al., 1999).

2.5.1.4 Well operation and history

Drilling in the Reykir/Reykjahlíð area started in 1933 with the drilling of numerous, shallow (<600 m deep) free flowing wells, named SR and NR wells. The production from these wells amounted to about 360 L/s but precise production data for this period does not exist. Drilling of deeper wells (> 1km deep) started in 1959 but properly took off in 1970. These wells, named MG, are equipped with pumps and with them the average combined production from the two subareas is about 1000 L/s of 86 °C warm water. Deep production caused a decline in system pressure, free flowing from shallower wells stopped and water level dropped down to a depth of 50-100 m below sea level (Björnsson and Steingrímsson, 1995). The shallower wells (SR and NR) were cemented and closed once production from deeper wells started. Today, active production wells are 34, 22 in Reykir and 12 in Reykjahlíð (Figure 2.5.11).

Generally, most wells in the southern and western part of Reykir have suffered some cooling over the last 50 years in response to the production. Two deep wells at the southern edge of the system, wells MG-07 and MG-10 were cemented and closed in 1987 and 1991 because of cold water inflow from the southwest and casings were deepened in three other wells, wells MG-04, MG-17 and MG-23 (Björnsson and Steingrímsson, 1995). The temperature of the water produced from Reykjahlíð has however been relatively stable throughout the production history (Ívarsson, 2020). This implies that recharge into the system must be sufficiently warm when it enters the system (Björnsson and Steingrímsson, 1995).

Figure 2.5.12 shows the monthly production from the two areas from 1985 until 2019 along with water level in monitoring wells. It is apparent that the water level fluctuates with the production.
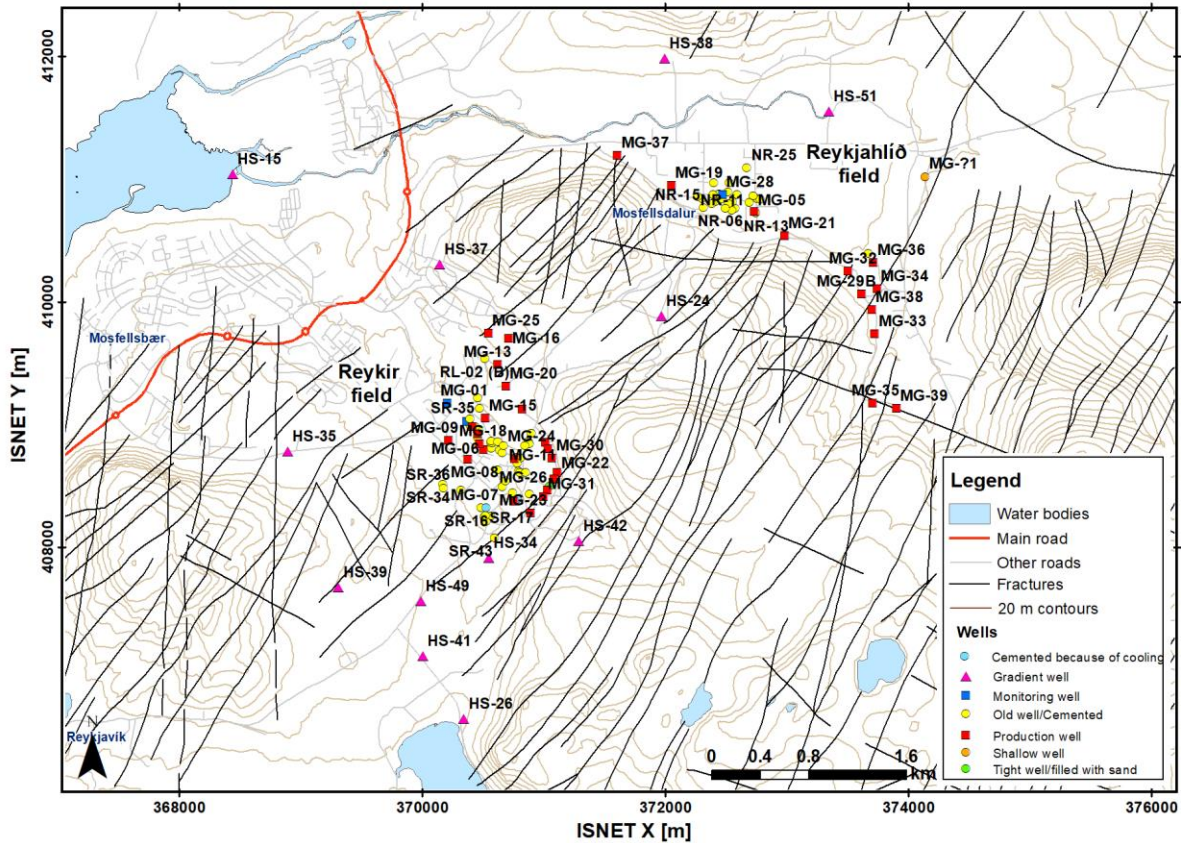

Figure 2.5.11 Map of the Reykir/Reykjahlíð fields showing wells, roads, elevation contours, and fractures that have been mapped on the surface for this specific area. Active production wells are shown with red squares (Data source: National Land Survey of Iceland, Reykjavík Energy and Iceland Geosurvery, ÍSOR).
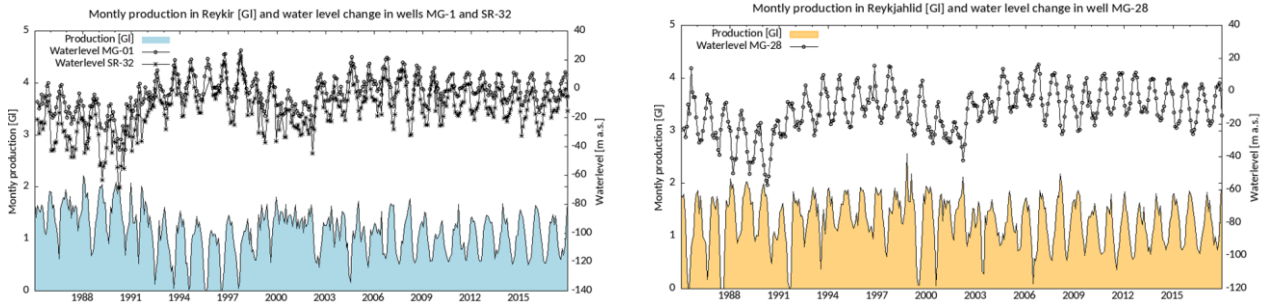
Figure 2.5.12 Monthly production in Reykir from 1985-2019 [Gl] along with water level measurements in monitoring wells MG-01 and SR-32 (left) and monthly production in Reykjahlíð from 1985-2017 [Gl] along with water level measurements in monitoring well MG-28 (right) (Data from Ívarsson, 2020).

Few, sporadic water level measurements exist in research wells (HS-wells) outside the main production zone. These measurements show that the drawdown resulting from production in Reykir/Reykjahlíð is spread out, but anisotropic. To get a better feeling for the water level changes in the vicinity of the production wells and the extent of the system, pressure sensors were placed in two wells in 2018, well HS-35 which is located west of the Reykir production zone and well HS-34 which is located at the southern edge of the Reykir production zone. In addition, pressure sensors were placed in monitoring wells SR-32 and MG-01 in Reykir and monitoring well MG-28 in Reykjahlíð in 2019 but these wells had previously only been measured manually. Figure 2.5.14 shows data collected from the sensors in 2019 compared to production data and water level measurements from monitoring wells. Data from well UF-04 for the first months of the year was included in addition to get a comparison with a cold groundwater well at a greater distance from the production zone. The data clearly shows that well HS-35 maintains a high water level and behaves more like the cold groundwater well UF-04. It doesn´t appear to be influenced by to the production. It thus seems to be located on the other side of the hypothetical permeability barrier mentioned above. Well HS-34 on the other hand shows fluctuating water level like the systems monitoring wells and is therefore well connected to the geothermal system.
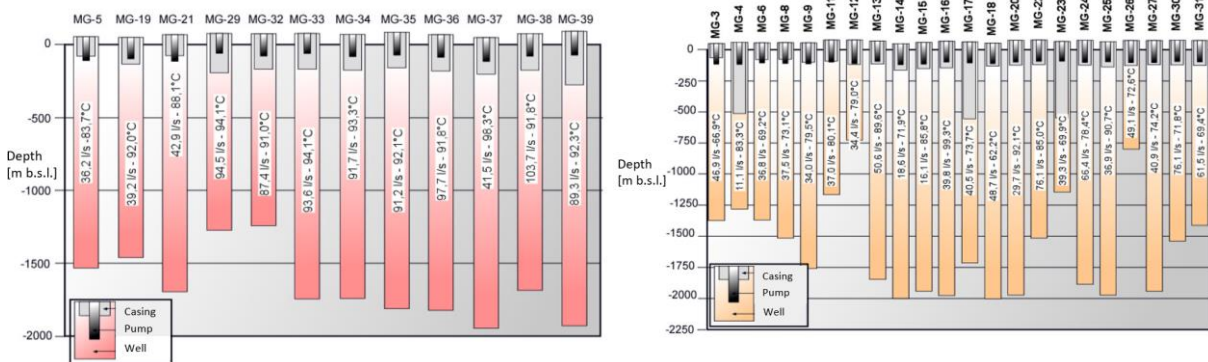

Figure 2.5.13 Main characteristics of production wells in Reykjahlíð; well depth, casing depth, pump depth, average flow rate and average temperature of produced water (left) and main characteristics of production wells in Reykir; well depth, casing depth, pump depth, average flow rate and average temperature of produced water (right) (Modified from Ívarsson, 2018).

Water level measurements in shallow groundwater wells in Mosfellsdalur NE of Reykjahlíð show water level close to the land surface (Elefsen, 2016) despite the wells being located very close to monitoring
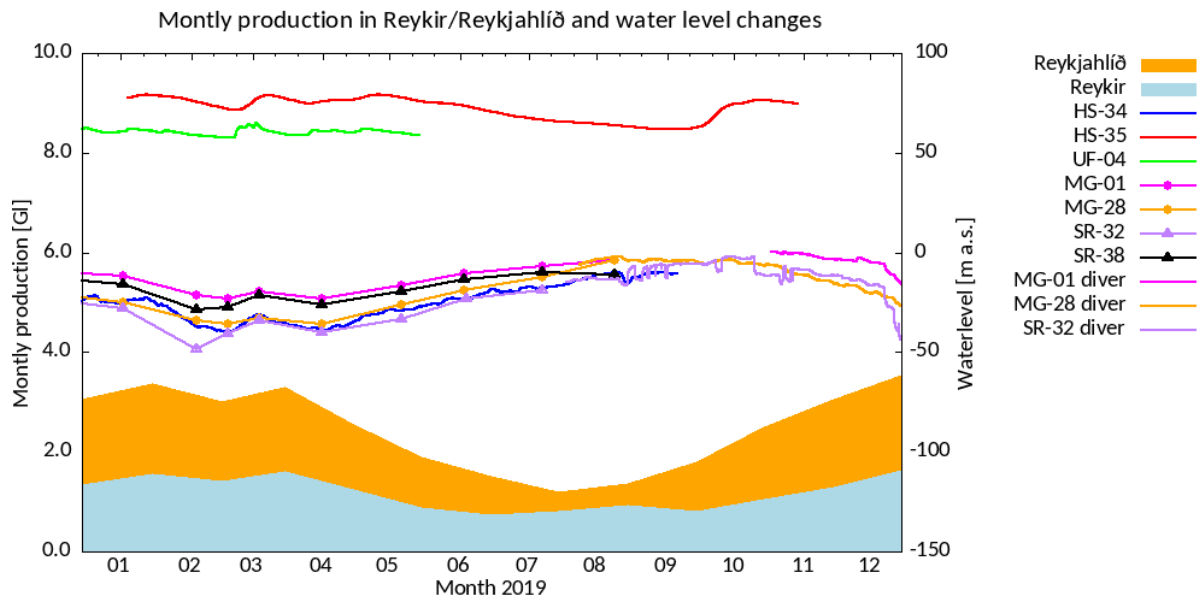
Figure 2.5.14 Water level measurements in different wells from December 2018 until September 2019 compared to production data for 2019.

wells that show water level below sea level. This could indicate that the geothermal system is somewhat closed off from a colder groundwater system above it by a low permeability lateral layer. Figure 2.5.13 show the main characteristics of the current production wells. The wells are generally cased off to a depth of about 150-250 m.

2.5.1.5 Fluid chemistry and bedrock chemical analysis

The geothermal water from the low temperature areas has a different chemical composition than the heated groundwater from the power plants. Table 2.5.2 shows the composition of water from well MG-25 and MG-23 in Reykir, well MG-39 in Reykjahlíð and heated groundwater from Nesjavellir. Most notable are the differences in Silica (SiO_2) content which is almost double in the geothermal waters and the Magnesium (Mg) content in the heated groundwater but Magnesium is absent in the geothermal water.

The composition of geothermal water in geothermal systems is controlled by primary mineral dissolution and secondary mineral precipitation. The degree of alteration and type of minerals formed will be dependent on the temperature of the system.

Many studies indicate that groundwater, at least when above 100 to 150°C, is close to equilibrium with various secondary minerals (Gíslason and Eugster, 1987, Gíslason and Arnórsson, 1990, Gíslason and Arnórsson, 1993, Arnórsson et al., 2002). Consequently, the solubilities of the secondary minerals control the aqueous concentrations of the components that form these minerals. The formation of secondary minerals corresponds with the breakdown of primary phases, as shown in Figure 2.5.15. High pH groundwaters are usually under-saturated with respect to olivine and plagioclase. Subsurface alteration of basalts by high pH waters will, accordingly, largely affect the plagioclase and olivine. Alteration products from plagioclase are expected to be mostly zeolites but clay minerals from the olivine.

Table 2.5.2 Fluid chemistry data for well MG-25 and MG-23 in Reykir, well MG-39 in Reykjahlíð and heated groundwater from Nesjavellir.

		Reykir MG-25	Reykjahlíð MG-39	Reykir MG-23	Nesjavellir Heated groundwater
Date		1.3.2018	5.2.2018	1.3.2019	8.3.2018
Temperature	°C	90.3	92.2	69.5	80
pH		9.75	9.81	9.79	8.49
pH-temperature	°C	23.1	22.4	22.3	22.7
Conductivity	µS/cm	231	193	179	207
Conductivity-temperature	°C	22.4	22.3		22.3
CO_2	mg/kg	24.45	24.8	23.1	40.75
H_2S	mg/kg	0.76	1.278	0.12	0.41
SiO_2	mg/kg	96.73	97.42	52.4	54
Na	mg/kg	45.37	47.82	34.7	22.2
K	mg/kg	0.91	1.034	0.45	2.87
Ca	mg/kg	2.436	1.963	2.55	9.329
Mg	mg/kg			0.001	4.423
Fe	mg/kg	0.01		0.01	0.006
Al	mg/kg	0.159	0.186	0.115	0.178
Cl	mg/kg	15.85	13.15	9.2	16.8
SO_4	mg/kg	15.43	16.34	7.2	15.21
F	mg/kg	0.69	0.824	0.214	0.155
B	mg/kg	0.038	0.036	0.017	0.148

The formations within the Reykir geothermal system consist of heavily altered basalts. Alteration minerals found in the system provide insights into the evolution of the geothermal system. The presence of high temperature alteration minerals (smectite, chlorite, prehnite, epidote) indicate that the system was once a
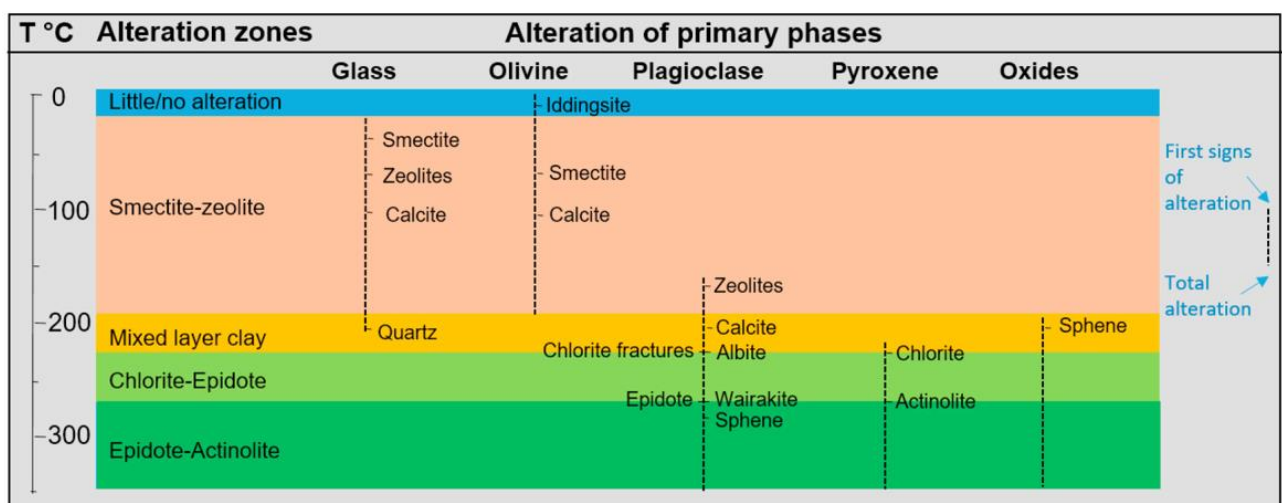

Figure 2.5.15: The alteration zones and the breakdown of the primary phases (Snæbjörnsdóttir et al., 2018)

high temperature system (>230°C). The presence of minerals stable at intermediate temperature (laumonite) are representative of the cooling of the system down to temperature between 120-150°C. During a sea

intrusion at the end of the last glacial period salts such as anhydrite and zeolites (gyrolite) formed. Some of the minerals found are then formed at temperatures representative of the system today (mainly stilbite and mesolite) (Tómasson, 1999). The geothermal fluid present in the system today is in equilibrium with lower grade alteration minerals. The history and the mineral assemblage at the Reykir geothermal system is very complex and many minerals found are not in equilibrium with the current temperature of the system.

Chemical analysis of total rock samples exists for different depth intervals in well MG-27 in Reykir (Gunnlausson, 1977). The data is listed in Table 2.5.3.

Table 2.5.3 Chemical analyses of total rock samples from well MG-27 in Reykir. Major elements (Gunnlaugsson, 1977).

Sample	120 m	318 m	6161 m	1036 m	1316 m	1920 m
SiO_2	45.38	43.77	44.28	47.15	46.5	45.79
Al_2O_3	14.1	13.72	12.92	12.27	12.24	12.54
TiO_2	2.01	1.78	2.71	2.66	2.87	3
Fe_2O_3	5.97	3.46	4.3	3.27	2.61	3.36
FeO	5.68	6.83	7.86	7.9	10.35	10.01
MnO	0.19	0.18	0.22	0.22	0.22	0.23
MgO	6.41	5.85	5.96	4.79	4.69	5.36
CaO	11.45	11.8	11.75	10.16	9.27	10.75
Na_2O	2.24	1.76	2.43	2.65	2.57	2.31
K_2O	0.18	0.17	0.1	0.24	0.43	0.43
P_2O_5	0.31	0.3	0.43	0.43	0.46	0.48
Loss of ignition	5.74	9.69	5.03	7.1	6.15	6.2
Sum	99.66	99.31	97.99	98.84	98.36	100.46

The past sections have described the concept and aims of the study as well as the general features of the selected location; the Reykir/Reykjahlíð geothermal system. This information makes up the foundation for the numerical model setup and the reactive transport model that will be described in the following sections.

2.5.2 Modelling approach

From the above descriptions we derive the need for performing two general directions of modelling, the first assessing flow and heat transfer on the field scale and the second addressing the possible chemical consequences of injecting heated groundwater from the Hengill area into a low-temperature geothermal system.

2.5.2.1 Field scale flow model

Conceptual simulation model

A flow model of the Reykir/Reykjahlíð site has been developed. This is a field scale model based on the TOUGH2 simulator, which is calibrated by fitting observed data and production history. The model has a hexagonal grid which is refined around the production areas and has coarser blocks towards the edges. The model reaches from 320 m above sea level down to 3500 m below sea level. It has 26 layers, about 76 thousand elements and about 300 thousand connections. The model domain (30x30 km) is shown on Figure 2.5.16. An effective continuum method is used to model the fractured medium so individual fractures are not specifically represented. Possible effects from fluid injection on rock mechanics are neglected in the model. This is considered reasonable since the injected water is at a similar temperature as the formation temperature and because the bedrock has high permeability and thus there will be limited pressure build-up. TOUGH2 uses various "equation of state" (EOS) modules which are designed for different applications. This

model uses EOS1 which describes water in liquid, vapor and two-phase state. Standard TOUGH2 does not take dispersion into account. The numerical grid, however, generates some dispersion.
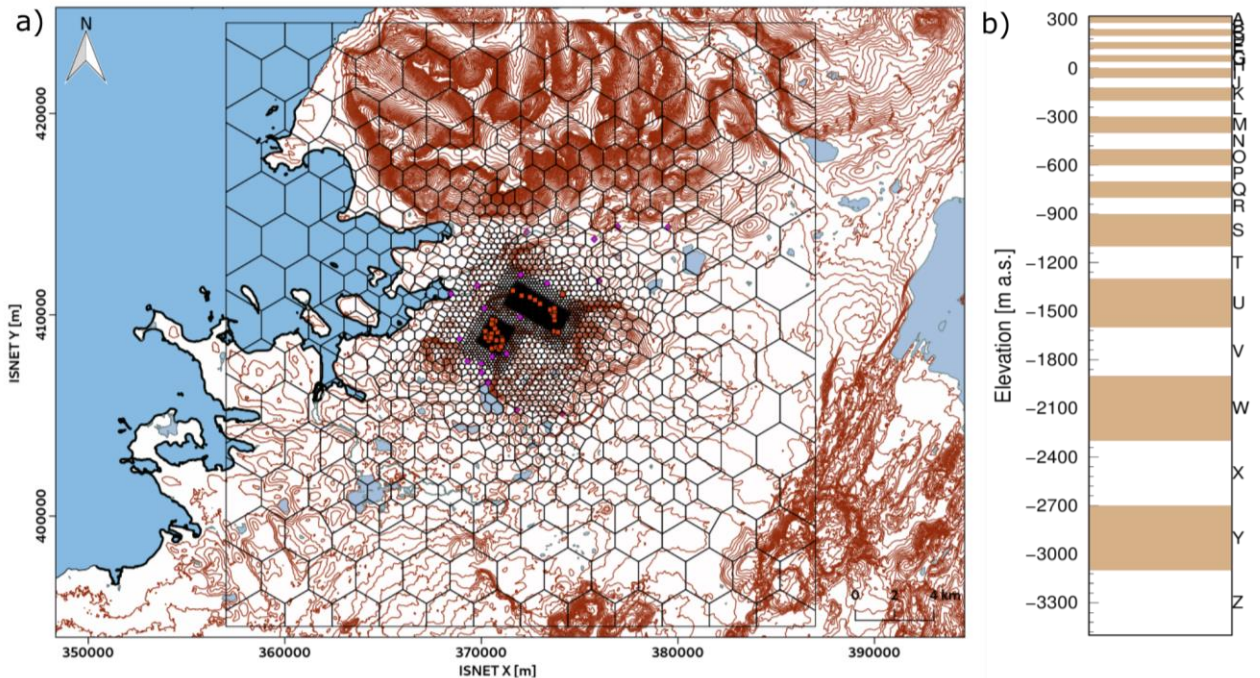

Figure 2.5.16 a) Plan view of the numerical grid for the Reykir/Reykjahlíð area, b) The layering structure of the model. The white and beige colors show the thickness of the layers and the letters on the left are used to identify each layer (Data Source: Reykjavík Energy and Nation Land Survey of Iceland).

Pre-processing workflow

The workflow for model development and scenario simulations can be summarized as follows:

- A numerical grid was generated to break the continuous volume into blocks for which calculations of mass and energy balance could be performed.
- Polygons describing the boundaries of the geothermal system were used to assign rock types to the grid blocks. Each rock type was assigned hydrogeological parameters. The model grid covers a much larger area than the geothermal system itself. Most emphasis was placed on the processes within the system itself.
- Current understanding of heat flow and recharge into the system was used to set up boundary conditions. The model was allowed to run for a long time to generate stable initial conditions that represent the natural state in the system before the start of deep production. Rock temperature profiles from wells in each area were used to calibrate the initial state model.
- Production history data for each well was gathered and compiled into monthly production averages and introduced as sinks in the model. The model elements that correspond to aquifer locations within wells were used as sinks. Estimates on the proportion of flow that comes from each stratigraphic unit in each well (Tómasson, 1997) were used to divide the flow rate over the wells depth interval.
- Water level and temperature measurements were used to calibrate the model. The permeability and porosity were varied to get a good match. Density, thermal conductivity and heat capacity were kept constant.
- Once the flow model had been constructed and calibrated, different injection scenarios were simulated. This included injection at different distances from the active production zones, on one hand at the system periphery and on the other hand into rarely used production wells, within the production field. The injection was simulated over the summer months. The scenarios were run

along normal summer production as it was in 2019 and along so-called summer resting of the fields where production was decreased or stopped.

Computational approach and software

The TOUGH2 numerical simulator was used for the simulations (Pruess, Oldenburg and Moridis, 2012) as implemented in forward and inverse mode within the iTOUGH2 code (Finsterle, 2007). TOUGH2 is a multiphase flow and transport simulation program for fractured and porous media. It is widely used in the geothermal industry (Pruess, Oldenburg and Moridis, 2012).

Conceptually, the model simulates the transport of fluid and heat in a single-phase liquid geothermal system. It solves governing equations that describe the conservation of mass and energy. The change in mass/energy in a given subdomain V_n across enclosing surface Γ_n is represented as:

$$\frac{d}{dt} \int_{V_n} M^k dV_n = \int_{\Gamma_n} F^k \bullet nd\, \Gamma_n + \int_{V_n} q^k dV_n$$

where M^k stands for the mass/energy of the mass/heat component k present in that subdomain. $F^k \bullet n\, d\Gamma_n$ stands for the flux of component k into domain V_n normal to surface Γ_n. Lastly, q^k stands for sinks or sources of component k in domain V_n. Conduction and convection control the heat flow. Thermodynamic conditions are based on local equilibrium of all phases. Advection controls the mass flow and a multiphase version of Darcy's law is used to calculate advective mass fluxes in each phase (Pruess, Oldenburg and Moridis, 2012).

The program AMESH was used for the numerical grid generation (Haukwa, 1998). The program uses the Voronoi or Thiessen tessellation method to create the elements which have mainly a hexagonal shape.

Model development and calibration

Due to the fractured and altered nature of the system, the basalt/hyaloclastite stratigraphy does not realistically represent the system's permeability structure. Therefore, simplifications were made on the stratigraphic structure of the model. Water level fluctuations and temperature profiles from surrounding wells, temperature distribution maps as well as results from previous modelling studies (Verkfræðistofan Vatnaskil, 2000) were used to estimate the extent of the geothermal system. The parts of the model that lie outside the geothermal system were given other rock types than the parts of the model that lie within it. Based on water level measurements well HS-35 for example falls outside of the geothermal system rock types. The system itself was then split up into the subsections Helgafellssvæði, Vestursvæði and Austursvæði according to the division presented by Thorsteinsson and Einarsson (1990) based on pump test results. The system inflows from the southwest and the north eastern edge were given other rock types as well. The system rock types were further split up into two depth intervals. The geothermal system was assumed to be separated from the

colder groundwater system above it by a less permeable layer. A plan view of the general rock type distribution within the system is shown on Figure 2.5.17.
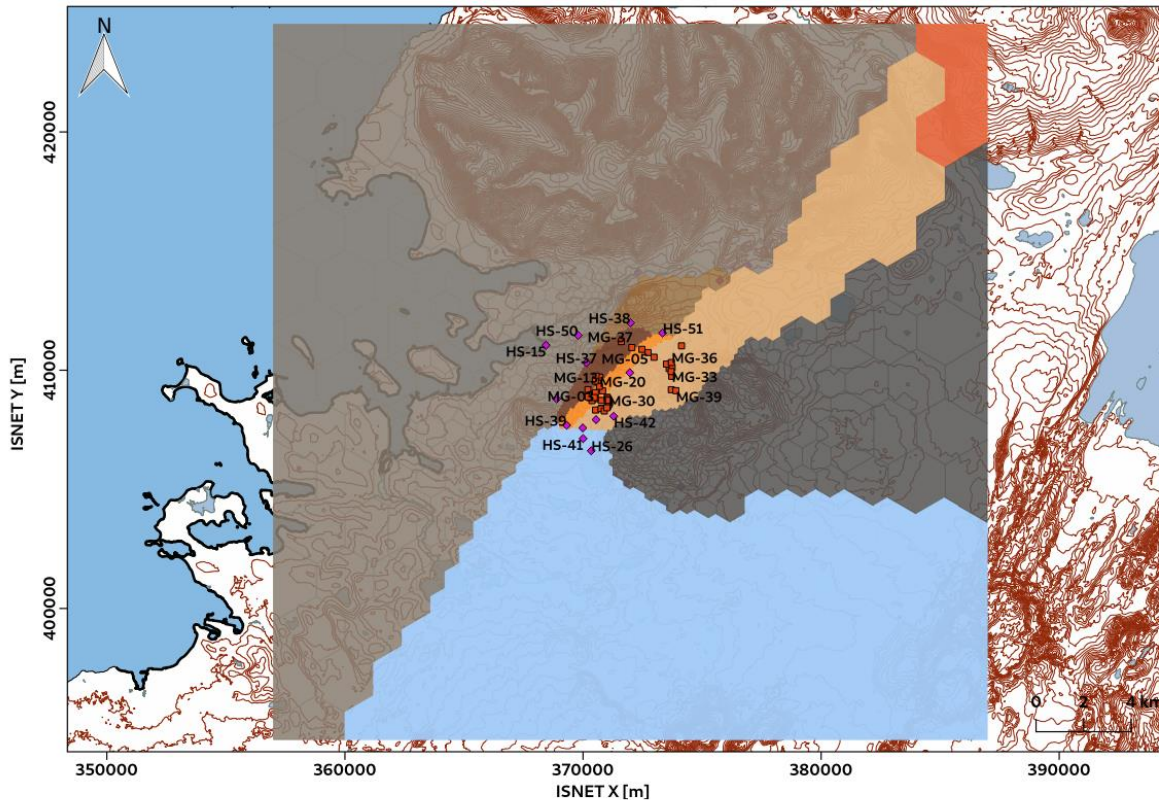

Figure 2.5.17 Overview of rock type distribution within the geothermal system. Inflow from the NE is shown in orange, inflow from the SW in blue, less permeable edges in grey, the system and its subsections in brown, light orange and beige. Wells are shown with red and pink markers (Data Source for map data: Reykjavík Energy and Nation Land Survey of Iceland).

The model elements that lie above the elevation of the water table were given an atmospheric rock type which has a constant pressure of 1 bar and temperature of 4 °C. The elevation of the water table in each element was approximated by interpolating between shallow groundwater elevation contours (Verkfræðistofan Vatnaskil, 2017) and extracting the value in the element center. The shallow water level is assumed to be constant and with a temperature of 4 °C. The initial pressure profile is hydrostatic. A temperature gradient of 50 °C/km was applied as initial conditions. The conditions in the bottom layer were assumed to be constant. Higher permeability within the system than outside of it and temperature in the bottom layer cause convection within the geothermal system.

Starting from the above-mentioned initial conditions the evolution of the system driven by the above-mentioned boundary conditions was simulated. A long period of time was simulated in order to generate stable conditions that represent the natural state of the system before the start of deep production. This is standard procedure in geothermal modeling (O'Sullivan et al., 2001). Formation temperature profiles from wells in each area were used to calibrate the initial state model. Examples of formation temperature comparisons are shown in Figure 2.5.18.
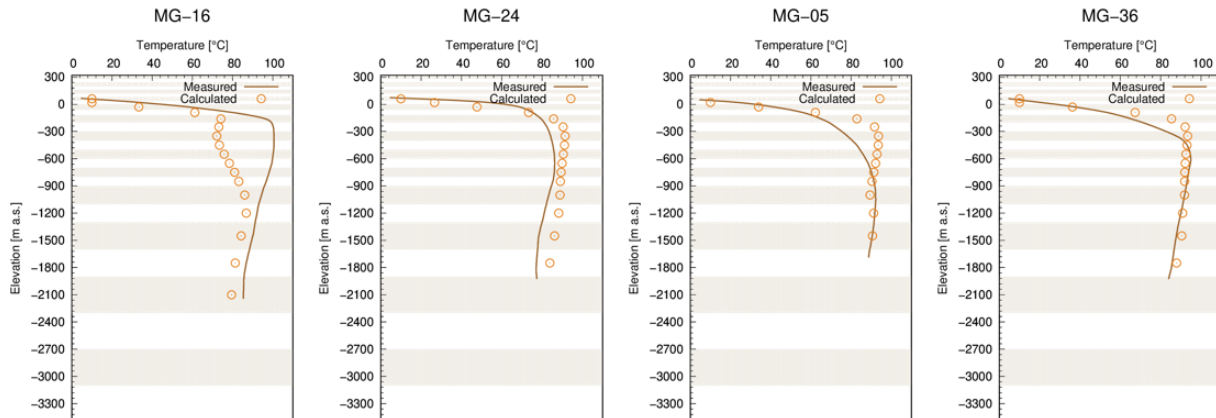
Figure 2.5.18 Example of steady state matching. In wells MG-24 and MG-36 there is a good match for formation temperature but wells MG-16 and MG-05 show a poorer fit but they are located closer to system edges.

Production history data for each well was gathered and compiled into monthly production averages and introduced as sinks in the model. Model elements that correspond to aquifer locations within wells were used as sinks. Estimates on the proportion of flow that comes from each stratigraphical unit in each well (Tómasson, 1997) were used to divide the flow rate over the wells depth interval. The production history was calibrated against reservoir pressure draw-down in the geothermal system and temperature of produced fluid. The horizontal and vertical permeability in the different rock types was varied to get a good match. Rock density, thermal conductivity and heat capacity were kept constant. This is an iterative process that requires multiple runs to get a satisfactory match both with regards to initial state and production history and system response.

Figure 2.5.19 shows simulated and measured reservoir pressure draw-down derived from water level measurements for 3 monitoring wells; SR-32 and MG-01 in Reykir and MG-28 in Reykjahlíð. Data for pressure drawdown in monitoring wells is used to monitor the response of the system to production. These wells are cased down to the geothermal reservoir and thus reflect the system pressure. A good fit is obtained for formation temperature and pressure draw-down in many of the wells. The poorest fits are for the wells located closest to the system edges (see e.g. well MG-16 in Figure 2.5.18). This is due to lack of deep wells towards the edges and further away from the production areas. Data from such wells would give a more accurate representation of the temperature distribution away from the production areas. For the same reason, comparisons between measured and simulated changes in the temperature of produced fluid in wells close to the edges give the poorest results. Temperature distribution in the model outside the geothermal system itself needs to be better represented in order to model cooling which has been observed in some of these wells, especially wells located at the southwestern edge of the Reykir field. Possible

downflow through rarely used wells in Reykir, from colder aquifers closer to the surface down to hotter aquifers at greater depth, also plays a role in the observed cooling which makes it more difficult to simulate.
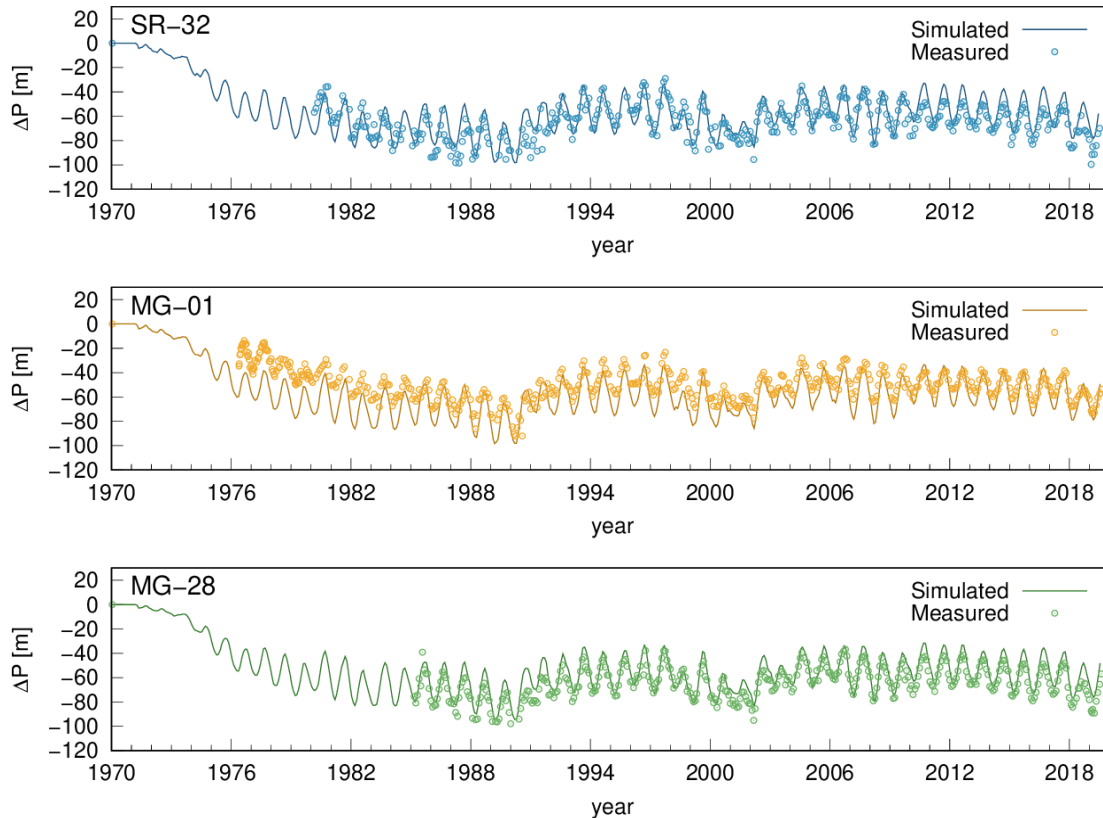

Figure 2.5.19 Simulated and measured draw-down for monitoring wells SR-32, MG-01 and MG-28 during the period 1970-2019.

Calibration of the model to available data shows that the system is very permeable. The horizontal permeability values for the geothermal system rock types range from $8 \cdot 10^{-13}$ to $5 \cdot 10^{-12}$ m^2 and the vertical permeability from $7 \cdot 10^{-14}$ to $1 \cdot 10^{-13}$ m^2. With a calibrated numerical model, different production and injection scenarios were simulated.

Scenarios and results

The aim with the model simulations was to investigate the system´s response to introducing fluid injection into the system, which currently has no injection wells. The aim was to analyse whether injection of excess water during the summer could provide pressure support that could then be utilized during the winter.

Numerous hypothetical injection scenarios have been simulated over the course of the project. A selection of them will be presented here. They can be divided into two different categories; injection at the system periphery (by well HS-34) and injection into rarely used production wells within the system. These wells have it in common to have suffered from cooling or decreased productivity since production started. Because of the cooling, those wells have not been used much as the water from them is cooler than the desired delivery temperature of hot water. But not using them in some cases enhances their cooling as production stop can allow downflow between feed zones, from colder aquifers to hotter ones. In three of the presented scenarios, the production as it was in 2019 was used as a baseline and then injection of 80°C warm water was introduced from either the 1st of May until the 1st of August or from the 1st of June until 1st of September. This cycle was repeated each year from 2020 until 2024. In the other two presented scenarios, we changed how the production scheme was simulated over the summertime inspired by recent changes in the operation of the district heating system.

A new idea and an expansion of the thermal plant in Hellisheiði in 2020 have made seasonal operational changes in the district heating system possible. These changes could also open possibilities for injection of heated groundwater with less costly infrastructure than constructing pipes all the way from the Nesjavellir pipeline (approx. 5 km). The expansion of the thermal plant in 2020, and the seasonal excess water routinely available from Nesjavellir, meant that the production capacity of heated groundwater from the power plants in the Hengill area was sufficient to meet the entire hot water demand in the capital region over 2 months in the summertime. In the summer of 2020, it was therefore decided to rest the low temperature systems and supply the entire capital region with heated groundwater. This scheme involves minimal mixing of the two water types as the geothermal water is pushed out of the system and replaced with heated groundwater. Smaller scale experiments had been performed in 2019 for individual neighbourhoods.

With this operation, there is still excess production capacity of heated groundwater that could be injected into Reykir for enhanced pressure support. With this setup, the water would have already been transported to the area via the current distribution system so the need for new pipe construction would be greatly reduced.

The different hypothetical injection sites used in the simulations are shown with green stars in Figure 2.5.20. The monitoring wells used to estimate the pressure effect are shown with orange stars (MG-01, SR-32 and SR-38 in Reykir and MG-28 in Reykjahlíð). The plots shown in the following sections show a comparison between simulated drawdown when no injection takes place and when injection/summer resting takes place and the difference between the two for wells SR-32 and MG-28.
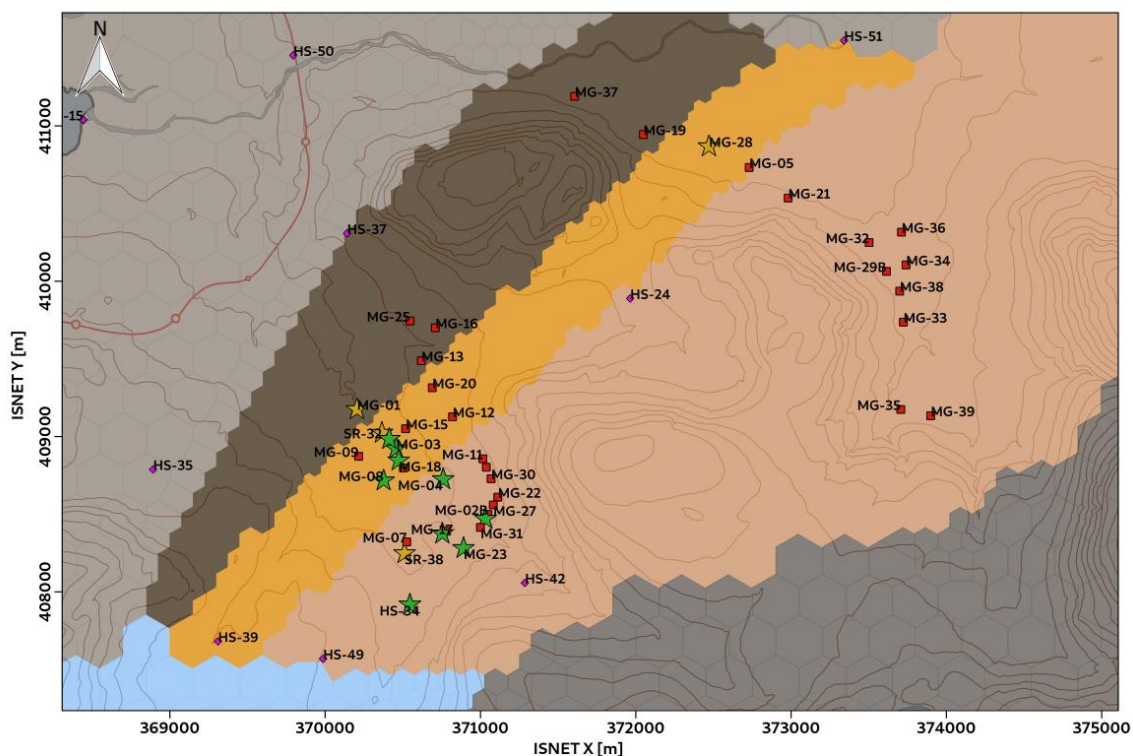

Figure 2.5.20 A map showing the injection locations used in the scenarios (green stars); well HS-34 at the system periphery and production wells MG-03, MG-04, MG-08, MG-14, MG-17, MG-18, MG-23 and MG-26 as well as the areas monitoring wells SR-32, MG-01, MG-28 and SR-38. The colors show the rock type distribution within the geothermal system (Data Source: Reykjavík Energy and Nation Land Survey of Iceland).

Injection at system periphery

In the first scenario, all water that has routinely been disposed of into shallow wells on Mosfellssheiði, 250 l/s is injected into well HS-34 at the Reykir system periphery from 1st of May until 1st of August while maintaining normal summer production (as it was in 2019) from other wells (Figure 2.5.21). The same pattern is apparent for all monitoring wells but the pattern is the sharpest in the closest wells, SR-38 and SR-32. A rise in pressure is seen immediately when the injection is started and after 3 months, the water level lies 20 m higher than in the case of no injection. The water level starts dropping again once injection is stopped but pressure support still lasts until the end of the year. Almost no pressure support is seen after the new year, that is, the support dissipates.
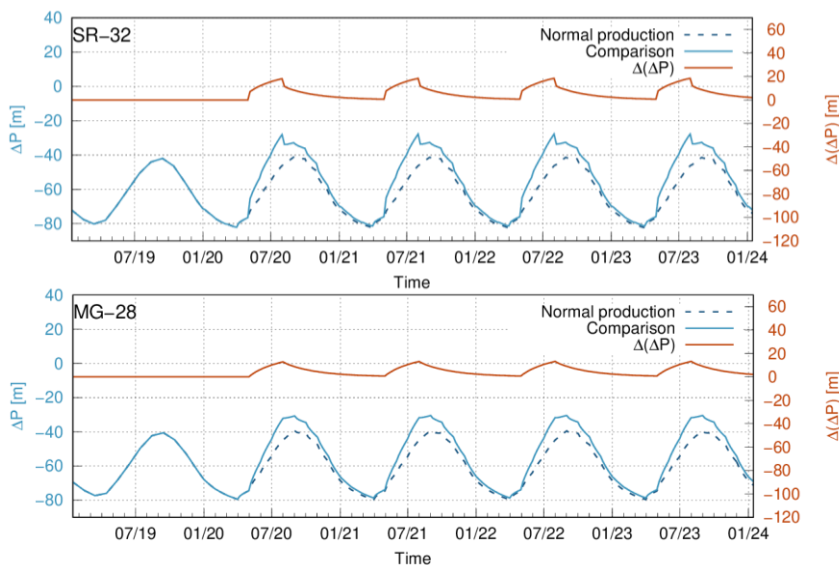

Figure 2.5.21 Comparison between simulated drawdown when no injection takes place (dashed blue line) and when 250 l/s injection takes place (solid blue line) and the difference between the two (orange line) for two monitoring wells (SR-32 and MG-28).

In the second scenario, half of the water that has routinely been disposed of into shallow wells on Mosfellssheiði, 125 l/s is injected into well HS-34 at the Reykir system periphery from 1st of May until 1st of August while maintaining normal summer production (as it was in 2019) from other wells (Figure 2.5.22). A similar pattern is seen here as with the 250 l/s injection but the effect is much smaller. The pressure support is negligible from the start of November, 3 months after the end of injection.
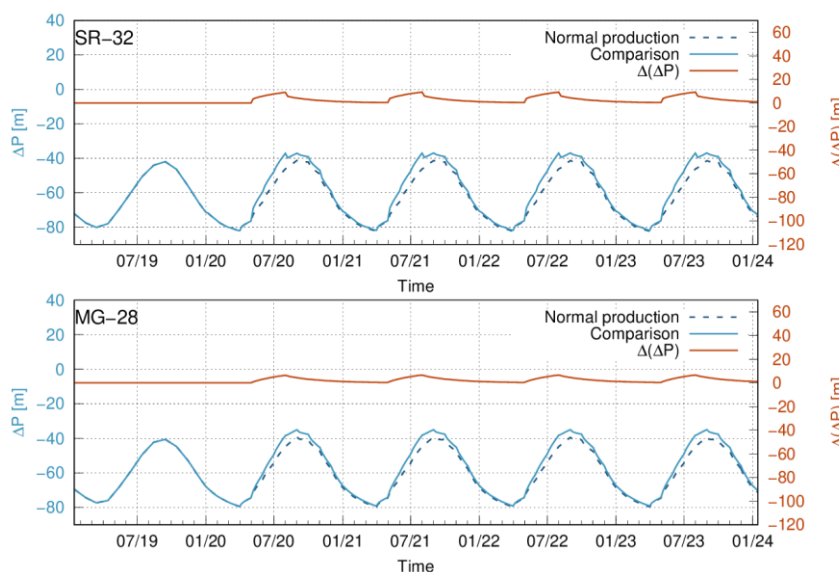

Figure 2.5.22 Comparison between simulated drawdown when no injection takes place (dashed blue line) and when 125 l/s injection takes place (solid blue line) and the difference between the two (orange line) for two monitoring wells (SR-32 and MG-28).

In the third scenario, all water that has routinely been disposed of into shallow wells on Mosfellssheiði, 250 l/s, is injected into well HS-34 at the Reykir system periphery, now from 1st of June until 1st of September. In addition to that, the production from the Reykir system is stopped from the 1st of June until the 1st of August and production from the Reykjahlíð area is maintained at 20 % of its normal (2019) summer production over that period (Figure 2.5.23). This scenario is inspired by the new production scheme described above where heated groundwater can be supplied to the whole capital region for a period of two months and the low temperature fields are rested in the meantime. In this case the rise is much sharper than in the previous cases as there is both injection and greatly decreased production. After 2 months, the water level lies about 40 m higher than in the case of no injection and no summer rest and reaches 10 m below the levels it was at before the start of production. The water level is maintained high while the injection still takes place even though production has started, until the beginning of September, but then starts dropping again. Pressure support lasts until the following summer.
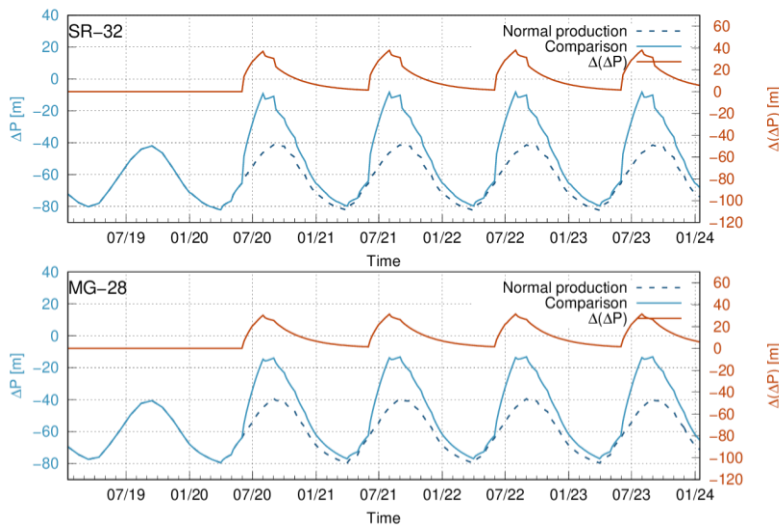

Figure 2.5.23 Comparison between simulated drawdown when no injection takes place (dashed blue line) and when 250 l/s injection takes place from the 1st of June until the 1st of September at the system periphery as well as summer resting from 1st of June until 1st of August (solid blue line) and the difference between the two (orange line) for two monitoring wells (SR-32 and MG-28).

Injection into rarely used wells in Reykir

A few wells within the Reykir field have been somewhat abandoned due to cooling (MG-03, MG-14 and MG-18) or decreased productivity (MG-04). The cooling in these wells however seems to be greatly enhanced by production stops. Other wells have suffered from long term cooling (MG-08, MG-17, MG-23 and MG-26), likely more due to cooling of the aquifers themselves rather than downflow between aquifers. In the following scenarios summer injection into these wells is simulated.

In the fourth scenario, all water that has routinely been disposed of into shallow wells on Mosfellssheiði, 250 l/s, is injected into wells MG-03, MG-04, MG-14 and MG-18 from 1st of May until 1st of August while
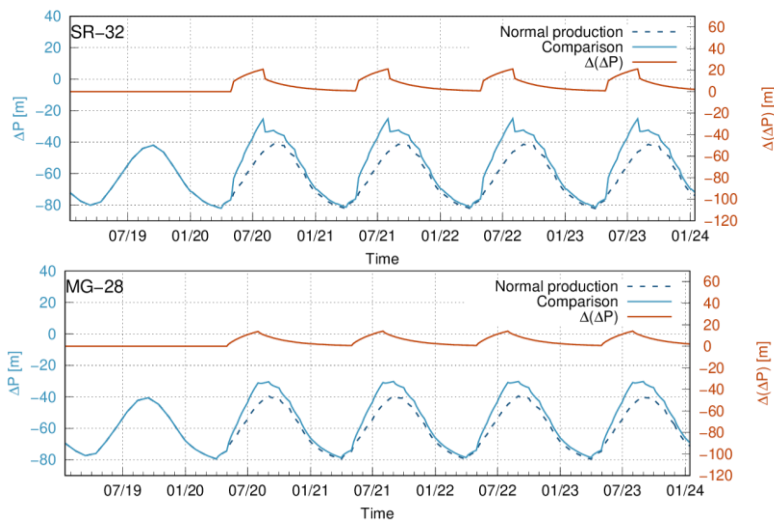

Figure 2.5.24 Comparison between simulated drawdown when no injection takes place (dashed blue line) and when 250 l/s injection into rarely used production wells takes place (solid blue line) and the difference between the two (orange line) for two monitoring wells (SR-32 and MG-28).

normal (2019) production is maintained in other wells in the area. The fluid is evenly distributed between the four wells (Figure 2.5.24).

The overall effect of this case is very similar as for the first case, the difference lies in the response of the closest wells. The pressure in well SR-32 increases more in this case as it now lies closer to the injection wells. Pressure support lasts until the end of the year but limited pressure support is seen after the new year, that is, the support dissipates.

In the fifth scenario, all water that has routinely been disposed of into shallow wells on Mosfellssheiði, 250 l/s, is injected into wells MG-08, MG-17, MG-23 and MG-26 from 1st of June until 1st of September. The fluid is evenly distributed over the four wells. In addition to that, the production from both Reykir and Reykjahlíð is stopped from the 1st of June until the 1st of August (Figure 2.5.25). The overall effect of this case is very similar as for the third case but the effect is slightly greater in well MG-28 as production is now completely stopped in Reykjahlíð but not maintained at 20 % of normal summer production. Pressure support lasts until the following summer.
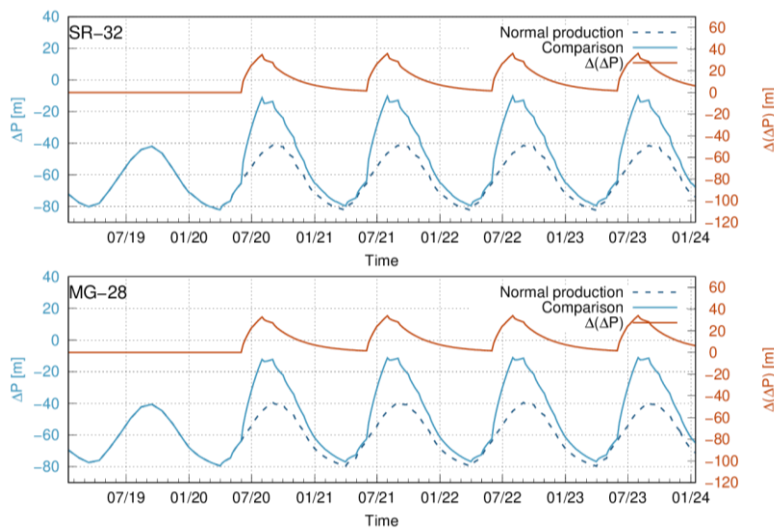

Figure 2.5.25 Comparison between simulated drawdown when no injection takes place (dashed blue line) and when 250 l/s injection into wells MG-08, MG-17, MG-23 and MG-26 takes place from the 1st of June until the 1st of September as well as summer resting from 1st of June until 1st of August (solid blue line) and the difference between the two (orange line) for two monitoring wells (SR-32 and MG-28).

Figure 2.5.26 shows a comparison between simulated drawdown in well SR-32 for different scenarios to attempt to illustrate the benefits of different utilization strategies. The figure shows a comparison between simulated drawdown when no injection takes place (dashed blue line), when 250 l/s injection into wells MG-08, MG-17, MG-23 and MG-26 takes place from the 1st of June until the 1st of September (orange line), when no injection takes place but production from Reykir and Reykjahlíð is turned off from 1st of June until 1st of August (red line), when these two cases are combined (purple line) and lastly when the injection in the combined case is shifted to the 1st of July until the 1st of October (gray line). These results show that past September, the effect of summer resting for two months is very comparable to the effect of a 3 month long injection from the 1st of June until the 1st of September. Combining the two understandably gives a greater pressure support. If the injection can be shifted longer into the fall months, the pressure support is slightly greater.
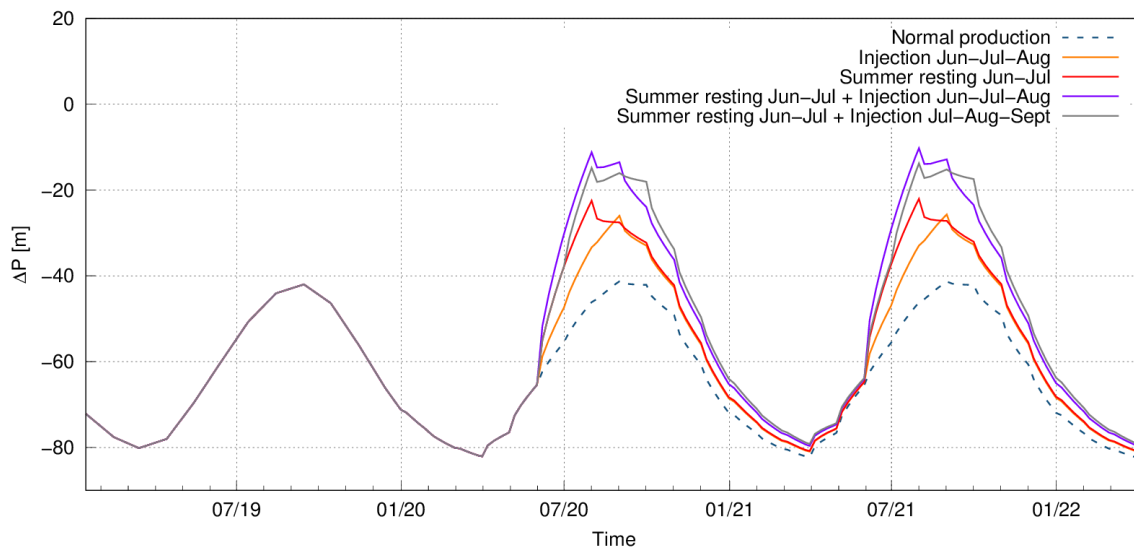
Figure 2.5.26 Comparison for well SR-32 between simulated drawdown when no injection takes place (dashed blue line), when 250 l/s injection into wells MG-08, MG-17, MG-23 and MG-26 takes place from the 1st of June until the 1st of September (orange line), when no injection takes place but production from Reykir and Reykjahlíð is turned off from 1st of June until 1st of August (red line), when these two cases are combined (purple line) and lastly when the injection in the combined case is shifted to the 1st of July until the 1st of October (gray line).

2.5.2.2 Reactive chemistry model

Conceptual simulation model

Reactive transport models of the injection of heated groundwater into the Reykir geothermal system were developed to explore the effects of mixing heated groundwater and geothermal water in a low enthalpy geothermal system.

Previous experiments have shown that mixing the two fluids within the distribution system causes precipitation of magnesium silicates clogging the pipes. The objective of the modeling study was to understand if similar behaviour would be observed if the two fluids were mixed within a basaltic reservoir. Would magnesium silicate precipitate around the injection well causing clogging of the well? Would the magnesium not react with the reservoir rocks and rather be transported to neighbouring production wells risking magnesium silicates in the distribution system? Precipitation of additional secondary minerals or dissolution of minerals in place and their impact on the system (both in term of resulting reservoir water composition and rock porosity) were also of interest. Injection of heated groundwater for heat storage and pressure support has the potential to increase the efficiency and flexibility of our district heating system but it may not be feasible if the mixing of the two fluids triggers magnesium silicate, clays, or other minerals to precipitate within the wellbore or in the immediate vicinity of the well. Mineral precipitation may clog the system due to porosity decrease dampening the heat recovery from the injection well or neighbouring wells or pressure support potential of the injection well. On the other hand, if magnesium silicates form at a further distance from the well and do not impact adversely the porosity and permeability of the system, the mixing of the two fluids within the reservoir may become beneficial. Both in terms of heat storage but also in terms of chemical storage; the magnesium silicate dropping from the liquid phase into the mineral phase would eliminate the issue of mixing the two waters.

As part of this study, one-dimensional reactive chemistry models were developed of the injection of heated groundwater into an injection well. These represent a permeable pathway intersecting the injection well and can be considered a small sub-volume of a more extensive three-dimensional reservoir. The model was centred on well MG-23 located in the Reykir geothermal system (Figure 2.5.11). MG-23 was drilled in 1986 and has a depth of 1175 m. Reservoir temperatures are approximately 70°C and pressure follows the hydrostatic curve.

The composition of the background geothermal water was based on the chemistry of well MG-23 (Table 2.5.2). Elected secondary minerals stable under present basaltic reservoir conditions were included in the model as the basis for the reactive chemistry (see section 2.5.1.5). Porosity and permeability values assigned to the rock were set to 15% and $1*10^{-11}$ m^2 to represent a fracture in the geothermal reservoir. Other hydrogeological parameters were taken from the large-scale flow model presented above. The modelling work focused on the solubilities of secondary minerals and which minerals may precipitate or dissolve when magnesium-rich heated-groundwater is injected into a low enthalpy geothermal system depleted in magnesium and rich in dissolved silica (Table 2.5.2).
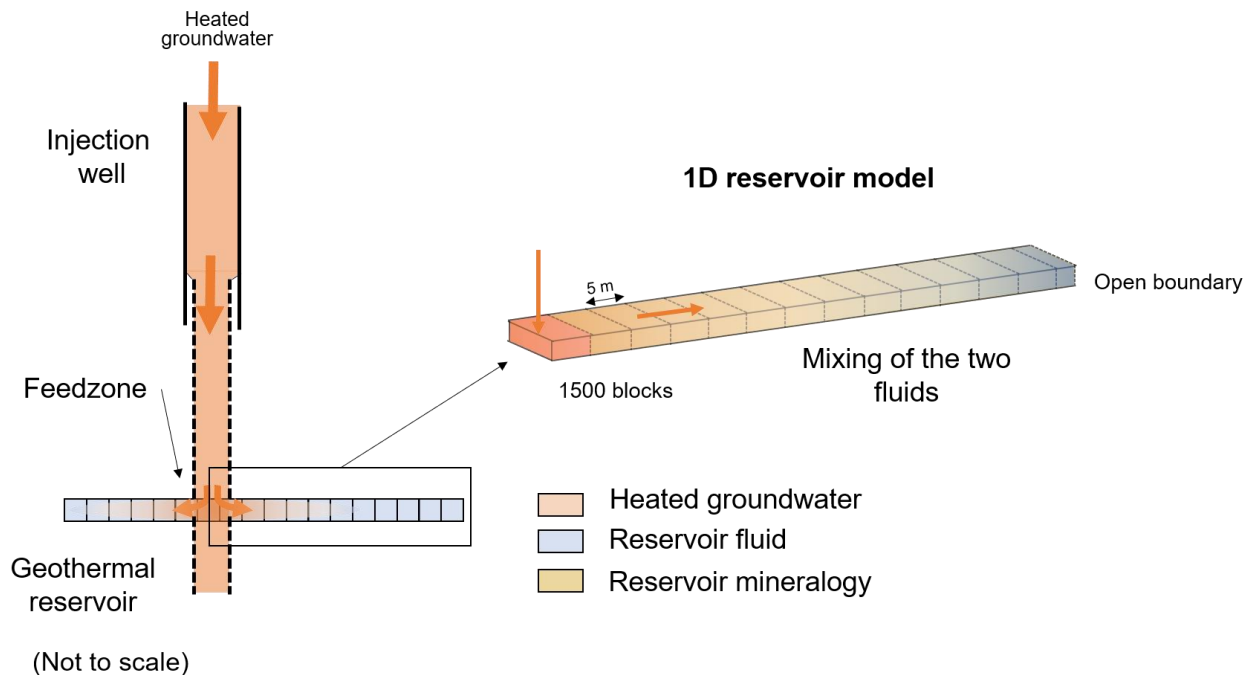

Figure 2.5.27: Conceptual model of the one-dimensional reactive transport model.

Simulations were performed with TOUGHREACT, a fully coupled reactive transport modelling software used to simulate subsurface solute transport, multiphase fluid and heat flow and chemical reactions (Xu et al. 2006, Sonnenthal et al. 2018).

Modeling workflow

The workflow for the reactive transport model and scenario simulation can be summarized as follows:

- A single block model is built to equilibrate the geothermal reservoir mineralogy with the reservoir fluid. The resulting geothermal water composition and mineralogy will be used as the initial geo-chemical conditions for the one-dimensional models. This initial step ensures the water-rock interactions simulated in the one-dimensional model reflect the impact of the injection of heated groundwater and not internal reservoir equilibrium changes.
- A one-dimensional grid is generated, and hydrogeological parameters are assigned to the rocktype of the model based on values from the large-scale model. The model blocks measure 5x50x50 m^3 in the x,y,z direction. The model is refined in the x direction to capture the mixing between the two fluids and fluid-rock interaction associated.
- Initial conditions are set to reservoir pressure and temperature.
- Injection of heated groundwater is represented by a mass generator in the first block of the reservoir model. The injected fluid will flow through the model due to formed pressure gradient.
- Reservoir chemistry and mineralogy from the single block model is used as input.
- The chemistry of the heated groundwater is assigned to the injected water from the mass generator.
- The simulation is run for one year with the injection active for three months (summer months).

- Long term effect is simulated over a 20-year simulation with the injection turned on for three months each year.
- The simulation(s) results are plotted.

Computational approach and software

A reactive transport model, such as the one developed here, relies on a mathematical formulation to describe geochemical processes involving fluid-rock interactions. The general governing equation can be written as:

$$\frac{\partial}{\partial t}(\phi C_i) = \frac{\partial}{\partial x}\left(\phi D \frac{\partial C_i}{\partial x}\right) - \left(\phi v \frac{\partial C_i}{\partial x}\right) + \phi \sum_k \left(\frac{\partial C_i}{\partial x}\right)_k \tag{1}$$

Where C_i is the concentration of a specific species in the pore fluid, D is the combined diffusion and dispersion coefficient term, v is the linear fluid flow rate, and ϕ is the porosity. The first two terms on the right describe the transport process (diffusion, dispersion, and advection) while the last term describes the effect of geochemical reactions on the concentration of a specific species over time. Due to complex boundary conditions and complicated coupling between the transport and reaction terms, it is impossible to provide analytical solutions to equation (1) for even the simplest geochemical system. Therefore, numerical solutions have to be used.

The simulations in this study were carried out using the non-isothermal reactive geochemical transport code TOUGHREACT (Xu et al. 2006, Sonnenthal et al. 2018). The program treats multi-phase fluid and heat flow, advection and diffusion. It models geochemical reactions including aqueous complexation, mineral dissolution and precipitation, dissolution and exsolution, and ion exchange. TOUGHREACT was developed by introducing multi-component reactive transport into the framework of the existing multi-phase 3-D finite volume fluid and heat flow code TOUGH2. It is a THC (Thermo-Hydro-Chemical) simulator applicable to a wide range of reactive fluid and geochemical transport subsurface conditions. Flow, transport, and chemistry are coupled in a sequential manner.

TOUGHREACT includes the following processes required to model the mixing of two waters within a low enthalpy geothermal reservoir:

- fluid flow in liquid phases occurring under pressure, viscous, and gravity forces;
- heat flow by conduction and convection;
- thermophysical and geochemical reactions as a function of temperature, such as fluid density and viscosity, and thermodynamic and kinetic data for mineral-water-gas reactions;
- transport of aqueous species by advection and molecular diffusion in liquid;
- Temporal changes in porosity, permeability, and unsaturated hydrologic properties owing to mineral dissolution, precipitation and clay swelling.

Geochemical computations are carried out using a mass balance/mass action approach. By default, activity coefficients are computed using an extended Debye-Hückel model (Helgeson et al., 1981) applicable to NaCl-dominant, moderately saline solutions. The thermodynamic database used for the TOUGHREACT simulations presented here makes use of equilibrium constants from the Carbfix database developed at the University of Iceland (Voigt et al., 2018). Mineral dissolution and precipitation can proceed either subject to local equilibrium or kinetic conditions.

The mineral saturation ratio can be expressed as:

$$\Omega_m = K_m^{-1} \prod_{j=1}^{N_C} c_j^{v_{mj}} \gamma_j^{v_{mj}} \tag{2}$$

where m is the equilibrium mineral index, and K_m^{-1} is the corresponding equilibrium constant. Where at equilibrium:

$$log_{10}\Omega_m = 0 \tag{3}$$

Reactions are under kinetic constraint, mineral dissolution and precipitation, a general form of rate law (Lasaga, 1984; Steefel and Lasaga, 1994; Palandri and Kharaka, 2004) is used:

$$r_n = f(c_1, c_2, \dots c_{Nc}) = \pm k_n A_n |1 - \Omega_n^\theta|^\eta \tag{4}$$

The positive values of r_n in equation (4) indicate dissolution and negative values stand for precipitation, k_n is the rate constant which is temperature and pH dependent. A_n is the specific reactive surface area per kg H_2O

of each mineral and Ω_n^θ is the kinetic mineral saturation ratio. The reaction rate constants considered here were calculated based on the reaction rate constant at 25°C, k_{25}, and activation energy E_a.

$$k = k_{25} \exp\left[\frac{-E_a}{R}\left(\frac{1}{T} - \frac{1}{298.15}\right)\right] + k_{25}^{H+} \exp\left[\frac{-E_a^{H+}}{R}\left(\frac{1}{T} - \frac{1}{298.15}\right)\right]a_{H+}^{n_{H+}} + k_{25}^{OH-} \exp\left[\frac{-E_a^{OH-}}{R}\left(\frac{1}{T} - \frac{1}{298.15}\right)\right]a_{OH-}^{n_{OH-}} \qquad (5)$$

The mechanisms include the neutral, acid, and base mechanisms. For the acid and base mechanisms, dissolution and precipitation of minerals are catalyzed by H^+ and OH^- respectively. In equation (5), R is gas constant, T is absolute temperature, and superscripts or subscripts, $H+$, and $OH-$ indicate acid and base mechanisms, respectively; α is the activity of the species and η is the power term.

Changes in porosity during the simulation are calculated from changes in mineral volume fractions.

Similar to TOUGH2 (Pruess, Oldenburg and Moridis, 2012), the input files mainly include rock properties, time stepping information, geometric grid information, initial and boundary conditions, and data related to multi-phase fluid and heat flow simulation. An additional data block "TREAC" is present to control high-levels parameters for reactive transport simulation. In addition to the flow input file, a "solute.inp" file is required. It includes the input parameters for calculations of reactive transport, such as diffusion coefficients, tolerance limits for convergence of transport and chemical iterations, mineral and aqueous species, and the configuration of model zones with different chemical composition. The geochemical system (i.e. the type and number of aqueous component species, minerals, considered in the simulation) is defined in the "chemical.inp" input file. It also includes the initial compositions of water, mineral, and gas zones configured and kinetic data for minerals (rate constants, surface areas, etc.). In addition, the program needs a thermodynamic database file. This file contains reaction stoichiometries, dissociation constants (log (K)), and regression coefficients of log (K) as a function of temperature.

Batch model

Input

The origin of geothermal water in low enthalpy fields in Iceland has been thoroughly researched (see e.g. Gíslason and Eugster, 1987, Gíslason and Arnórsson, 1990, Gíslason and Arnórsson, 1993, Arnórsson et al., 2002). The composition is the result of rock-fluid interaction between meteoric water and basalt. The amount or presence of basaltic glass and crystalline basalt (pyroxene, feldspar, olivine) will depend on the alteration degree, temperature, and age of the basalt. Meteoric water will dissolve minerals for which it is under-saturated or secondary minerals will precipitate moving the system towards a new equilibrium. Alteration in MG-23, consists of palagonite, smectite, quartz, zeolites; kabasite, analcime, mesolite, stilbite, haulandite, modenite, epistilbite, laumonite, iron-oxide, calcite, opal, chalcedony, mixed layer clays, chlorite, pyrite and epidote (Tómasson, 1999). Overall descriptions of alteration in the area describe heavy alteration of glass. It is mentioned that no trace of olivine is found in the area meaning that either there was none to begin with or that it has all been altered.

In this study, we used a more general mineral description of the rock and select secondary minerals in equilibrium with the geothermal water (Figure 2.5.28). The mineral assemblage for the temperature (<100°C) and pH range considered (~9) usually includes:

- silicates (Chalcedony and Celadonite predominantly)
- clays
- zeolites
- carbonates

Primary minerals and high-temperature alteration minerals were therefore not included. Zeolites have been found to induce high numerical instability, therefore only thomsonite and analcime were used (Figure 2.5.28). Stilbite and mesolite which are likely to be present should be included in future studies.

The minerals considered in this study are listed in **Table 2.5.4** with the formation reaction and the stability field (when available). Solid solutions were considered for saponite end members. The kinetic rate expression of different minerals used in the simulation can be found in Table 2.5.5. Mineral reactive surface areas in the subsurface are generally unknown. In the current study, reactive surface area for all minerals was assumed to be 100 cm^2/g, in agreement with the work of Sonnenthal et al. (2005). When the aqueous phase supersaturates with respect to a certain secondary mineral, a small volume fraction of 1×10^{-6} is used

for calculating a seed surface area for the new phase to grow (Xu et al. 2006). The precipitation of secondary minerals is represented using the same kinetic expression as that for dissolution. As precipitation rate data for most minerals are unavailable, parameters for neutral pH rates were employed to describe precipitation.
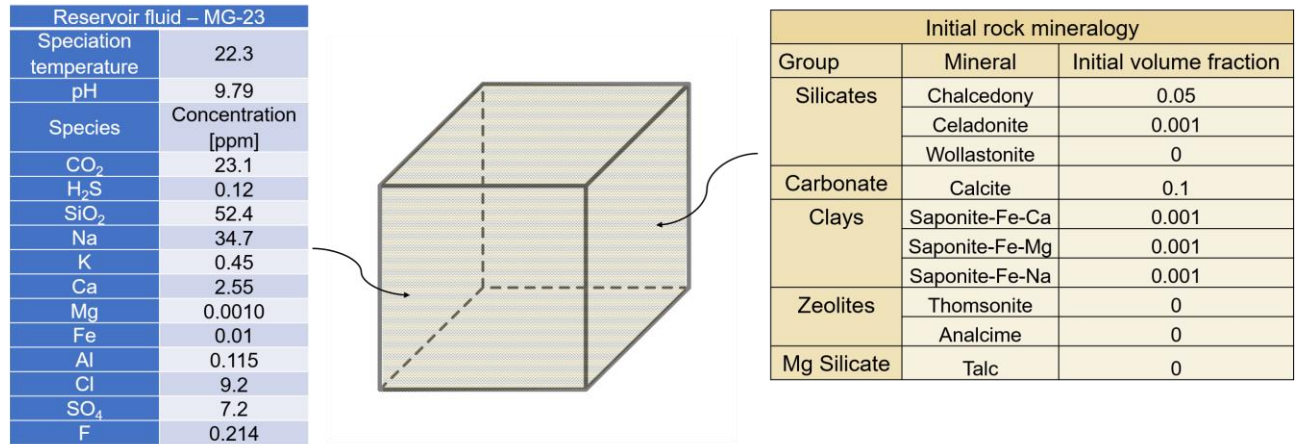
Reservoir fluid – MG-23	
Speciation temperature	22.3
pH	9.79
Species	Concentration [ppm]
CO_2	23.1
H_2S	0.12
SiO_2	52.4
Na	34.7
K	0.45
Ca	2.55
Mg	0.0010
Fe	0.01
Al	0.115
Cl	9.2
SO_4	7.2
F	0.214

Initial rock mineralogy		
Group	Mineral	Initial volume fraction
Silicates	Chalcedony	0.05
	Celadonite	0.001
	Wollastonite	0
Carbonate	Calcite	0.1
Clays	Saponite-Fe-Ca	0.001
	Saponite-Fe-Mg	0.001
	Saponite-Fe-Na	0.001
Zeolites	Thomsonite	0
	Analcime	0
Mg Silicate	Talc	0

Figure 2.5.28: Initial geothermal water composition and reservoir mineralogy used as input for the single block model (based on well MG-23 in the Reykir geothermal system).

Table 2.5.4: Summary of the secondary phase included in the reaction transport simulations. The composition and reaction are presented along with the mention if the minerals are considered as an ideal solid solution (as defined in Sonnenthal et al. 2018), and the stability field (indicative formation temperature).

Phase	Reaction	Solid Solution	Stability field
Secondary Mineralogy			
	Magnesium silicate		
Talc	$Mg_3Si_4O_{10} + 6H^+ = 3Mg^{+2} + 4SiO_2 + 4H_2O$		
	Carbonates		
Calcite	$CaCO_3 + H^+ = Ca^{+2} + HCO_3^-$		
	Clay minerals		
Saponite-Fe-Ca	$Fe_{3.175}Al_{0.35}Si_{3.65}O_{10}(OH)_2 + 7.4H^+ = 0.175Ca^{2+} + 0.35Al^{+3} + 3Fe^{+2} + 3.65SiO_2 + 4.7H_2O$	1	<200 °C
Saponite-Fe-Mg	$K_{0.35}Fe_3Al_{0.35}Si_{3.65}O_{10}(OH)_2 + 7.4H^+ = 0.175Mg^{2+} + 0.35Al^{+3} + 3Fe^{+2} + 3.65SiO_2 + 4.7H_2O$		<200 °C
Saponite-Fe-Na	$K_{0.35}Fe_3Al_{0.35}Si_{3.65}O_{10}(OH)_2 + 7.4H^+ = 0.35Na^{2+} + 0.35Al^{+3} + 3Fe^{+2} + 3.65SiO_2 + 4.7H_2O$		<200 °C
	Silicates		
Chalcedony	$SiO_2 = SiO_2$		
Celadonite	$Mg_3Si_4O_{10} + 6H^+ = Al^{+3} + K^+ + Mg^{+2} + 4SiO_2 + 4H_2O$		
Wollastonite	$CaSiO_3 + 2H^+ = Ca^{+2} + SiO_2 + H_2O$		
	Zeolites		
Analcime	$Na_{0.96}Al_{0.96}Si_{2.04}O_6{:}H_2O + 0.92H_2O = 0.96Al(OH)_4^- + 2.04SiO_2 + 0.96Na^+$		<200 °C
Thomsonite	$Ca_2NaAl_5Si_5O_{20}{:}6H_2O + 4H_2O = 5Al(OH)_4^- + 2Ca^{+2} + 5SiO_2 + Na^+$		≤100 °C

Table 2.5.5: Kinetic rate parameters for mineral dissolution and precipitation.

Mineral		Parameter for kinetic rate law							
Initial rock mineral composition		Neutral mechanism		Acid mechanisms			Base mechanism		
Primary	Area (cm^2/g)	k_{25} (mol/m^2/s)	E_a (kJ/mol)	k_{25} (mol/m^2/s)	E_a (kJ/mol)	$n(H^+)$	k_{25} (mol/m^2/s)	E_a (kJ/mol)	$n(H^+)$
Secondary									
Calcite[a]	100	1.549×10^{-6}	23.5	5.012×10^{-1}	23.5	1.000			
Talc[a]	100	1.0×10^{-12}	56.6						
Chalcedony[a]	100	3.8×10^{-10}	49.8						
Saponite-Fe-Ca[b]	100								-
Saponite-Fe-Mg[b]	100	1.659×10^{-13}	35.0	1.047×10^{-13}	23.6	0.340	3.020×10^{-17}	58.9	0.400
Saponite-Mg-Na[b]	100								
Analcime[c]	100	1.590×10^{-12}	58.0	2.000×10^{-08}	58.0	0.700	5.50×10^{-15}	58.0	- 0.300
Thomsonite[c]	100								
Celadonite[a]		1.66×10^{-13}	35	1.05×10^{-11}	23.6	0.34	3.020×10^{-17}	58.9	- 0.400
Wollastonite[a]	100	1.585×10^{-09}	54.7	7.244×10^{-08}	50.8	1.000			

[a] From Palandri and Kharaka (2004).

[b] Based on smectite ($K_{0.04}Ca_{0.5}(Al_{2.8}Fe_{0.53}Mg_{0.7})(Si_{7.65}Al_{0.35})O_{20}(OH)_4$) from Palandri and Kharaka (2004).

[c] All zeolites assumed to have the same rate law as heulandite.

One dimensional simulation

Input

Initial reservoir fluid composition and mineral assemblage were obtained from the batch model described above and used as the initial conditions for the time dependent simulations (Figure 2.5.29). The injection of a fluid with a different chemical composition disrupts the equilibrium in place and causes mineral dissolution and precipitation.

Equilibrated reservoir fluid - MG23	
Temperature	69
pH	8.76
Species	Concentration [ppm]
CO_2	12.4
H_2S	0.12
SiO_2	57.29
Na	20.26
K	0.61
Ca	5.59
Mg	0.00009
Fe	0.00007
Al	0.22
Cl	9.23
SO_4	7.17
F	0.21

Initial rock mineralogy		
Group	Mineral	Initial volume fraction
Silicates	Chalcedony	0.05
	Celadonite	0.0009999
	Wollastonite	0
Carbonate	Calcite	0.1
Clays	Saponite-Fe-Ca	0.0009723
	Saponite-Fe-Mg	0.0010004
	Saponite-Fe-Na	0.0010276
Zeolites	Thomsonite	0
	Analcime	0
Mg Silicate	Talc	0

Figure 2.5.29: Equilibrated geothermal water composition and reservoir mineralogy. This was used as input for the one-dimensional transient simulations (based on well MG-23 in the Reykir geothermal system).

To investigate the impact of the injection of heated groundwater, two transient simulations were run:

- One-year simulation, which included the injection of heated groundwater for three months before stopping the injection.
- 20-year simulation: One-year simulation is repeated 20 times for the long-term effect.
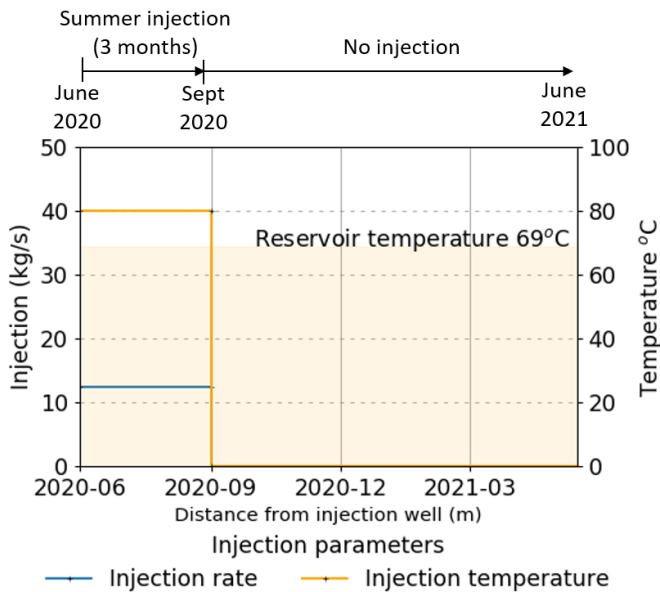
Figure 2.5.30: Injection rate and temperature used for the one-year simulation. This represents injection of heated groundwater into well MG-23 during the summer months.

Simulation results – short-term impact: June 2020 to June 2021

Simulations were carried out from June 2020 to June 2021. The results presented below are from the one-dimensional model based on the data from well MG-23 with a reservoir temperature of 69°C.

The modelled temperature distribution and pH change along the one dimensional model at different times are shown in Figure 2.5.31. The heated groundwater is warmer and has a lower pH. The temperature increases in the vicinity of the injection well from 69°C to 80°C and the pH decreases from 8.75 to 7.8. The mixing of the two fluids is the area located where the pH rises, this propagates away from the injection well. The plots also illustrate the higher speed of the chemical front compared to the thermal front.
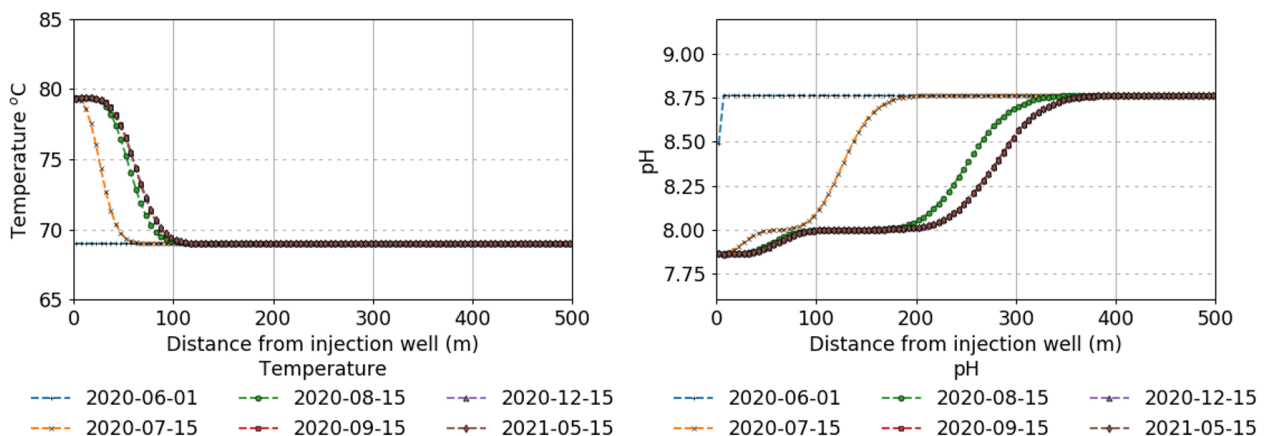
Figure 2.5.31: Model result for the 1-year simulation – Temperature (left) and pH (right) vs. distance from the injection well at different times.

Figure 2.5.32 shows the changes in volume fraction of magnesium silicate and pH (left) and the concentration of magnesium and aqueous silica (right) along the x-axis of the reservoir at the end of the one year simulation. The precipication of magnesium silicate is represented by the following equation:

$$3Mg_{(aq)}^{2+} + 2H_4SiO_{4(aq)} + H_2O_{(l)} \rightarrow Mg_3Si_2O_5(OH)_{4(s)} + 6H_{(aq)}^+$$

197
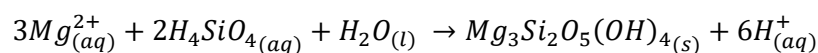
This reaction is controlled by the pH. As the magnesium enriched fluid (4 ppm) enters the reservoir it mixes with the fluid depleted in magnesium (<0.001 ppm). Combined with an increase in pH, the resulting water becomes supersaturated with respect to magnesium silicate and it begins to precipitate.This behaviour can be seen in the plot as the area of maximum magnesium silicate precipitation. It is located 300m away from
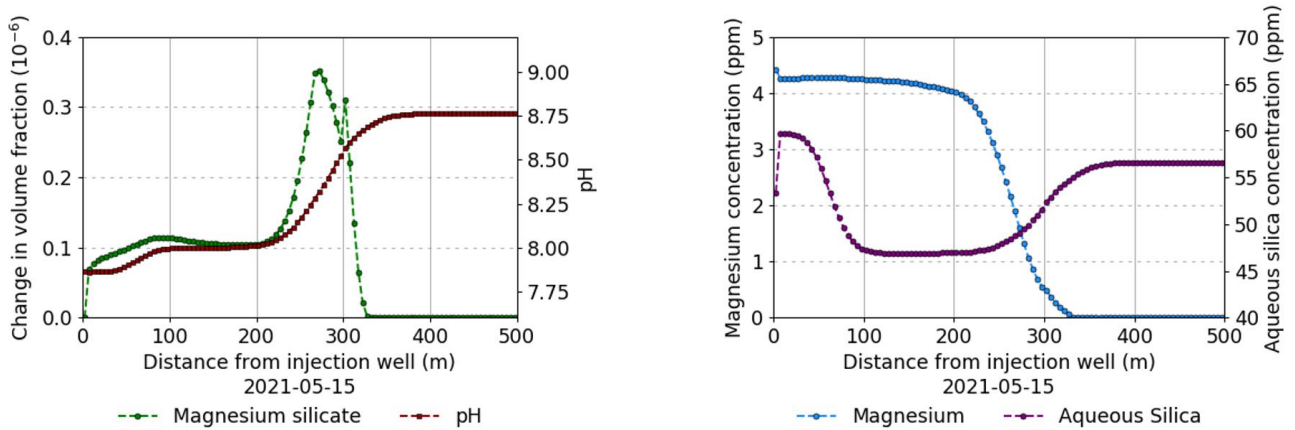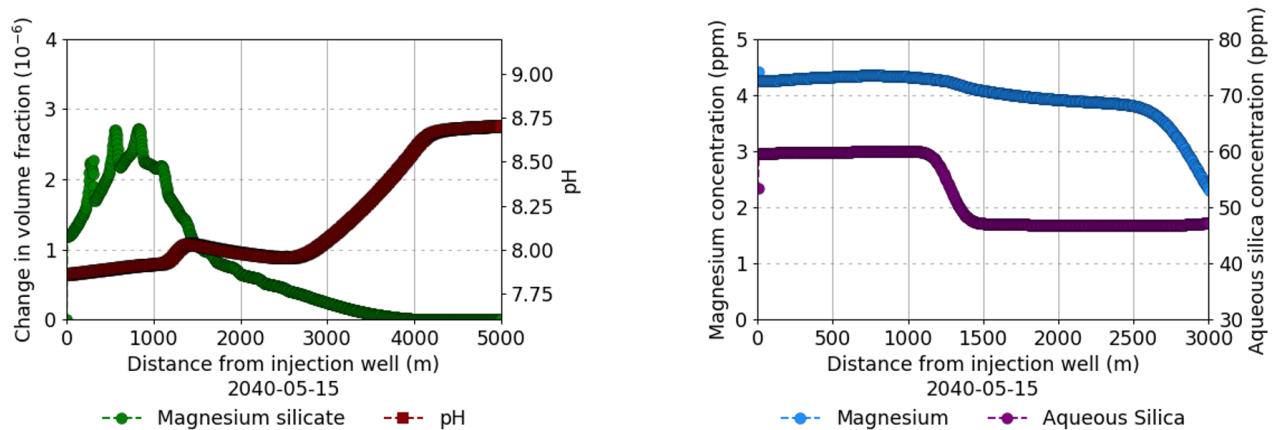

Figure 2.5.32: Model result for the 1-year simulation – Changes in volume fraction of magnesium silicate and pH (left) and the concentration of magnesium and aqueous silica (right) vs. distance from the injection well at the end of the 1-year simulation.

the injection where the pH is highest. The pH controls the formation of magnesium silicate which is beneficial as it limits its precipitation in the immidiate vicinity of the injection well.

Figure 2.5.33 shows the changes of volume fraction for selected minerals. The injected fluid is undersaturated in chalcedony and it dissolves in the immediate vicinity of the wells while 20 to 100m away it precipitates. Celadonite precipitates around the injection well and very small amounts of clay minerals precipitate around the wellbore. Carbonates' dissolution and precipitation is very irregular and may be linked to changes in pH. Carbonates participate the most to changes in volume fraction followed by chalcedony, celadonite, magnesium silicates and saponite. It can be noted that magnesium silicate and clay are formed but only very small amounts.
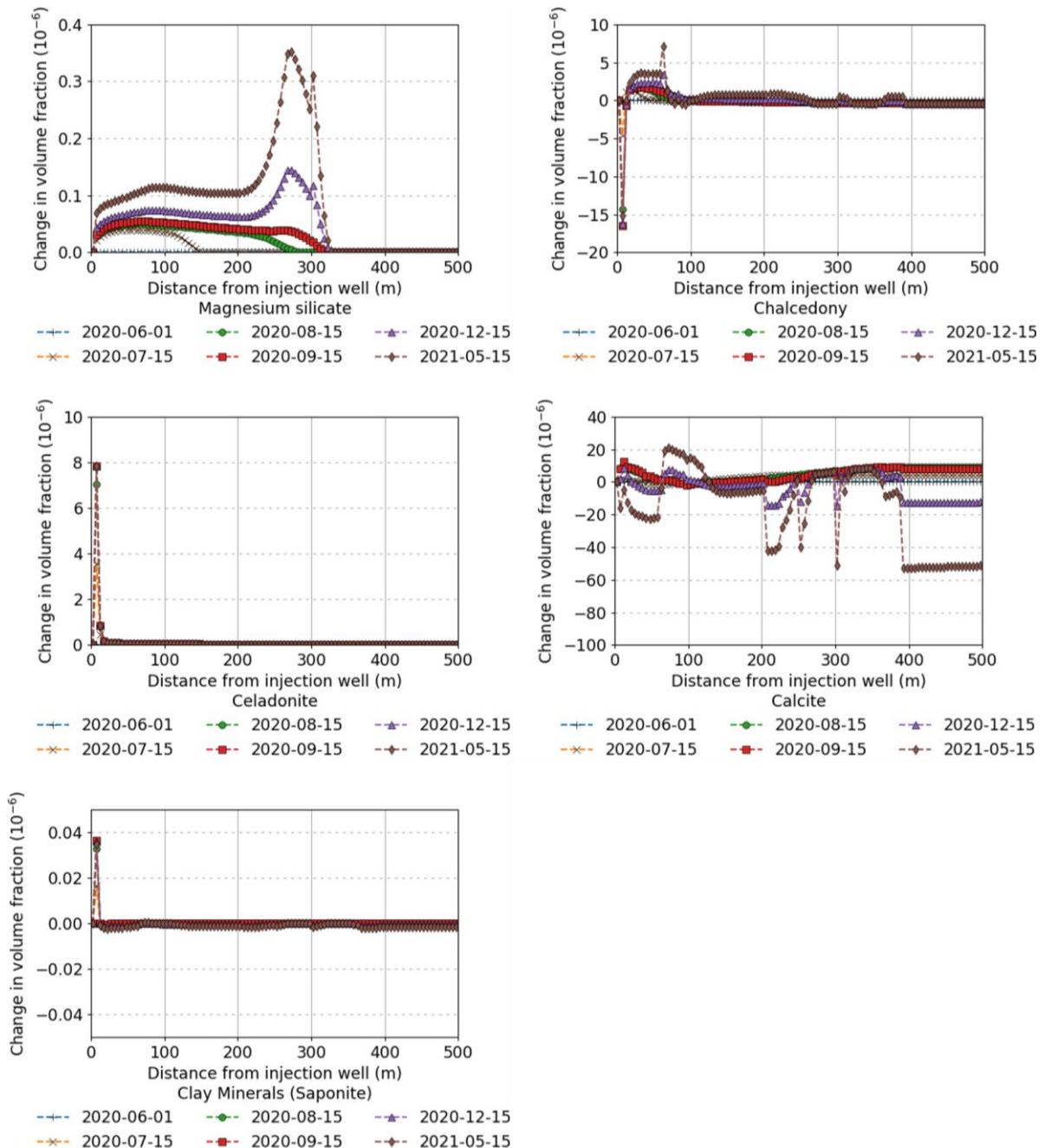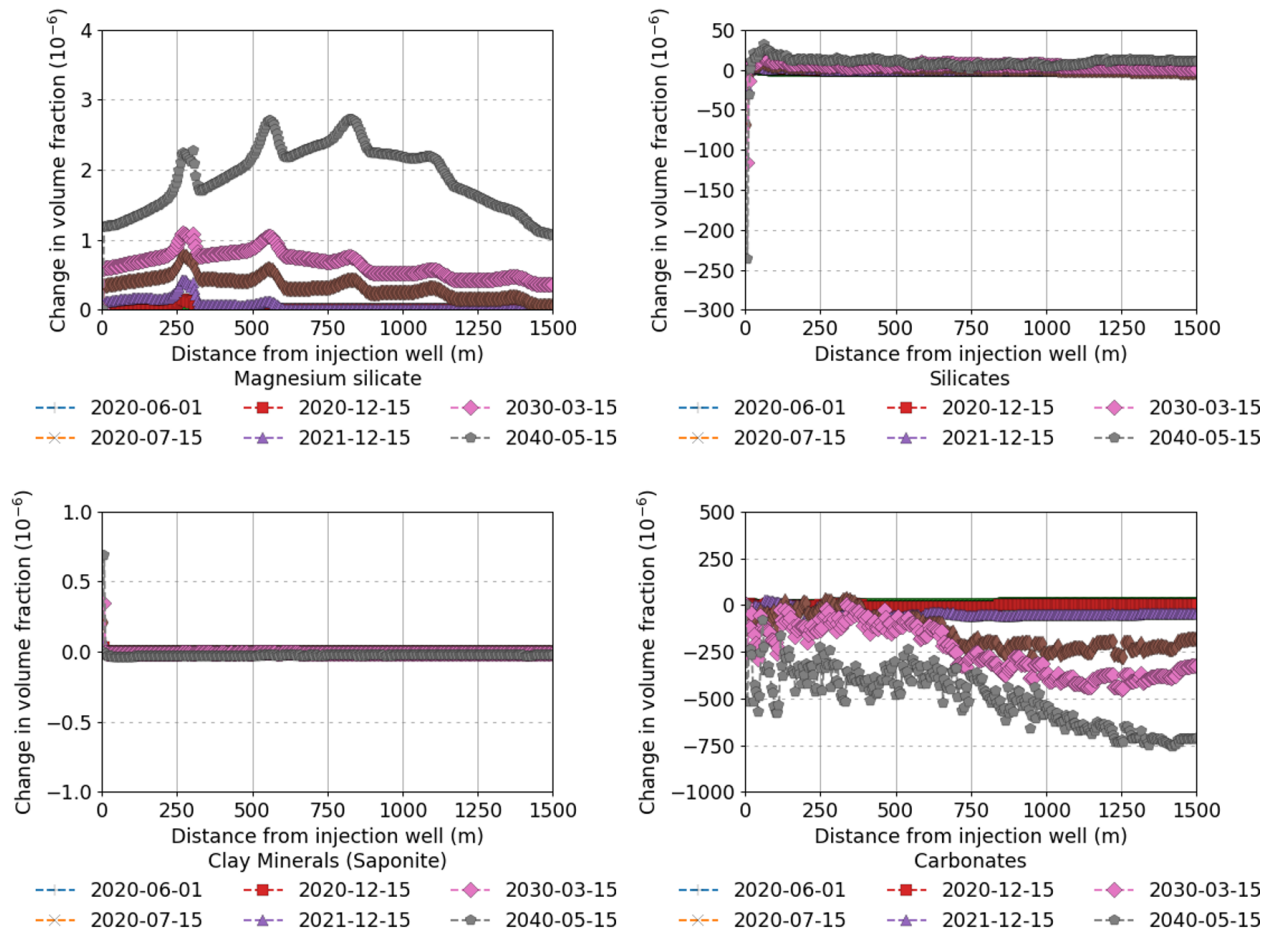
Figure 2.5.33: Model result for the 1-year simulation - Change in volume fraction for selected minerals vs. distance from the injection well at different times.

Simulation results – long-term impact: 2020 to 2040

Long-term simulations were carried out from 2020 to 2040 with injection of heated groundwater for 3 months each year. The results presented below are from the one-dimensional model.

Figure 2.5.34 shows the changes in volume fraction of magnesium silicate and pH (left) and the concentration of magnesium and aqueous silica (right) along the x-axis of the model at the end of the 20 year simulation. The model shows successive peaks of magnesium silicate precipitation linked with the propagation of the pH increase.The most magnesium silicate preciptation occurs in the first 1500m from the injection well. Little magnesium silicate precipitation occurs further away even if pH values are good. This may be due to the shortage of aqueous silica which is also incorporated in silicates (chalcedony and celadonite).

Figure 2.5.34: Model result for the 20-year simulation - Changes in volume fraction of magnesium silicate and pH (left) and the concentration of magnesium and aqueous silica (right) vs. distance from the injection well at the end of the 20-year simulation.

Figure 2.5.36 shows the changes of volume fraction for selected mineral groups for the first 1500 m from the injection well. Other silicates (chalcedony and celadonite) are undersaturated in the immidiate vicinity of the well but oversaturated away from the well. These minerals will compete for the aqueaous silica with the magnesium silicate. Figure 2.5.36 shows a similar behaviour as for the short term simulation which is little clay precipitation in the immediate vicinity of the injection well and unstable calcite behaviour.

Figure 2.5.36: Model result for the 20-year simulation - Change in volume fraction for selected minerals vs. distance from the injection well at different times. Results for magnesium silicate, silicates (chalcedony and celadonite), clays (saponite), and carbonates are shown from left to right and top to bottom.

Under these reservoir conditions and fluid composition the change in volume fraction is negligible and no adverse impact on the reservoir porosity is noted as can be seen in Figure 2.5.35.
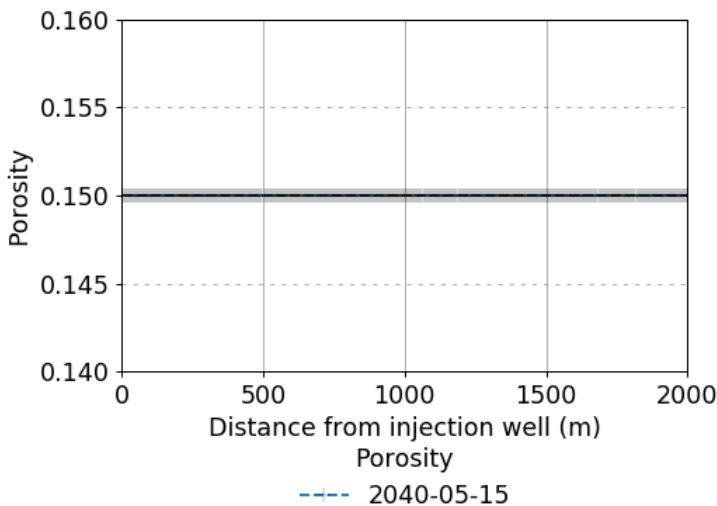

Figure 2.5.35: Change in porosity over the 20 years simulation time. Negligible change in porosity is observed through the simulation time.

2.5.3 Analysis and discussion

The aim with the presented simulations was to see whether a production scheme including the injection of surplus hot water from the Hengill area into the Reykir/Reykjahlíð system would be realistic and feasible.

The results from the field scale flow model simulations indicate that injection of 250 l/s of 80°C warm water from the 1st of May until the 1st of August into a well at the system periphery along with normal production would provide pressure support in the systems until the end of the year. In this case the water level at the end of injection in the beginning of August lies about 20 m higher than in the case of no injection. For a field that is operated with downhole pumps that are either switched on or off, a higher water level simply means greater production capacity. Based on experience on what the combined production capacity from the fields is at different water levels, the capacity would be about 180 l/s (calculated to 80°C) greater at the end of injection than without injection. This increased capacity would however have decreased down to about 40 l/s in the beginning of December. Even though this is a substantial decrease, 40 l/s is similar to what an average well gives. The problem is, however, that according to this scenario, the increased production capacity doesn´t last beyond December but the heaviest cold spells can be expected in the few months before and after the new year. As previously mentioned, the Reykir/Reykjahlíð field doesn´t have any injection wells as injection has not been a part of the systems utilization scheme. Injecting substantial amounts of water (250 l/s) at the periphery of the system would require the drilling of a specific injection well and the construction of an over 5 km long pipe to transport the heated groundwater from the pipe that transports water from Nesjavellir to the capital area. The cost of drilling an injection well and the construction of a 5 km long pipe, compared to the persistence of benefits from injection that the numerical simulations show, make that option unfeasible.

Resting the systems by decreasing or stopping production from other wells for two months during the summer along the injection greatly enhances the pressure support. Scenarios three and five simulated this scheme. The third scenario indicated that a combination of two months of stopped or decreased production, and injection of 250 l/s into a well at the system periphery from the 1st of June until the 1st of September, resulted in a 40 m higher water level after two months than in the case of no injection and no summer rest. Based on experience on what the combined production capacity from the fields is at different water levels, the capacity would be about 400 l/s (calculated to 80°C) greater after two months of summer resting and injection than without injection and summer resting. In the beginning of February the following year, this increased capacity would have decreased down to about 60 l/s. This is a greater and a more long lasting support than in the case of solely injecting and starting the injection earlier (May instead of June). The combined results from the simulations therefore show that being able to inject water alongside of summer resting can increase the production capacity of the fields until the following summer. While the pressure support lasts, the systems are in better shape to handle increased demand. The results also show that shifting the start of injection to the later summer months results in a longer lasting effect. Because of high cost related to drilling and pipe construction, the suggested way to implement injection is to use rarely used production wells. Implementing injection and summer resting is, however, not enough to permanently decrease pressure drawdown in the systems. That is, the water level in the wintertime reaches the same depths year after year, despite decreased netto uptake from the systems, because the uptake in the wintertime remains the same.

The injection of 80 °C water did not cause a temperature decrease in any well except the injection wells themselves in the cases where the temperature in the injection well was higher than 80 °C. That is, the temperature effect is very local.

One dimensional reactive transport models of the injection of heated groundwater into the Reykir geothermal system were developed to explore the effects of mixing heated groundwater and geothermal water in a low enthalpy geothermal system. The formation of magnesium silicate in the model is controlled by the pH which controls where it may precipitate. Additionally, it appears to compete for aqueous silica with chalcedony and celadonite. This effect should be further investigated for confirmation. The simulations indicate that under these reservoir conditions and fluid composition the change in volume fraction due to mineral precipitation is negligible and no adverse impact is seen on the reservoir porosity. These are positive results as they mean that mineral precipitates would not cause clogging of the injection well. However, the long-term simulations indicate that, because of little precipitation, the magnesium in the fluid would be transported long distances and could thus reach production wells risking magnesium silicates forming in the distribution system. This is a preliminary study of the geochemical and hydrogeological effects of the injection of heated groundwater into a

low enthalpy geothermal system in Iceland. One dimensional simulations always include simplifications of the actual conditions. The fluid can in reality flow in all directions which obviously changes the results. The results should therefore be interpreted qualitatively and not quantitatively. With these results we are now at the stage of being able to verify the effect on porosity with laboratory tests and the general effect on site. For later stages it would be interesting to understand the reason for the instability of calcite, to add more minerals such as zeolites (stilbite and mesolite) but also minerals that are present in the system but not in equilibrium under the current thermo and hydrodynamic state of the reservoir. It would also be important to test injection into various reservoir settings and chemical composition to get a better understanding of the sensitivity of the results and to upscale the model to including production wells as well.

As the previous paragraph clearly states, there would always be very high uncertainty in the effects of injecting heated groundwater into the Reykir geothermal system. However, some wells in the area have almost been abandoned due to cooling or lowering productivity. Using such wells for testing this idea would reduce the risk of such a trial as the wells are not considered an integral part of the production field anymore.

Future plans aim at integrating the low temperature geothermal water and heated groundwater by making pseudo low temperature water already at the power plants by precipitating magnesium-silicates before the water is transported to the city. The idea is that then the water types can theoretically be mixed without problems. When those changes have been implemented, reinjection would also be less risky because the precipitation risk in the system would be reduced. Injection could then be used for heat storage to top up the systems because there will still be fluctuation in demand and need for maximum production capacity from the low temperature fields during winter. These simulations have shown that this method could be one part of a combined solution to the capital region's future heating demand.

2.5.3.1 Work Package Interfaces

WP1: Specifications and characterization for UTES concepts

The literary and data review described in chapter 1 provides key inputs for the simulations regarding geological setting, material properties and boundary conditions.

WP3: Heating System integration and optimization of design and operation

This study is a case study but not a demonstration site. If/when the project will be realized, optimization of design and operation will use results from the simulations.

WP5: Monitoring and validation to assess system performance and workflow

Monitoring in the low temperature fields that Reykjavík Energy operates consists of:

- Monthly water level measurements in monitoring wells to monitor drawdown in the systems. Over the course of the project, these measurements were changed to continuously logging pressure sensors

- Flow and temperature measurements at well head in all wells every two weeks

- Total chemical analysis of water samples from all wells once a year

- Quality control on the water within the distribution system, every two weeks

The monthly water level measurements were used for the model calibration, the flow and temperature measurements were used to assign production rate values and for calibration, the chemical analysis was used to get average values for water composition for the reactive chemistry simulations. The quality control data was used for comparison with simulated chemical concentration of mixed water.

2.5.4 References

Arnórsson, S. (1995). Geothermal systems in Iceland: Structure and Conceptual models – II. Low-temperature areas. *Geothermics,* vol. 24 (5/6), pp. 603-629. DOI: 10.1016/0375-6505(95)00026-7

Arnórsson, S., Gunnarsson, I., Stefánsson, A., Andrésdóttir, A., Sveinbjörnsdóttir, A.E. (2002). Major element of surface and ground waters in basaltic terrain, N-Iceland: I. Primary mineral saturation. *Geochim. Cosmochim. Acta*, vol. 66, pp. 4015 – 4046.

Axelsson, G., Gunnlaugsson, E., Jónasson, Th. and Ólafsson, M. (2010). Low temperature geothermal utilization in Iceland, Decades of experience. *Geothermics*, vol. 39 (4), pp. 329–338. DOI: 10.1016/j.geothermics.2010.09.002

Bacon, C. R. (1977). High temperature heat content and heat capacity of silicate glasses: experimental determination and a model for calculation. *American Journal of Science*, vol. 277, pp. 109–135.

Björnsson, G. and Steingrímsson, G. (1995). *Hitalíkan af Reykjasvæðunum í Mosfellsbæ* [Temperature model of the Reykir areas in Mosfellsbær]. OS-95016/JHD-02. Reykjavík: Orkustofnun

Björnsson, G., Thordarson, S. and Steingrímsson, B. (1999*). Hiti í berggrunni og hugmyndalíkan af jarðhitakerfum á höfuðborgarsvæðinu* [Rock temperature and conceptual model of geothermal systems in the capital area]. OS-99112. Reykjavík: Orkustofnun

Bödvarsson, G. (1961). Physical characteristics of natural heat resources in Iceland. *Jökull,* vol. 11, pp. 29-38.

Einarsson, D. (2018). *3D modelling of the Reykir geothermal areas in Mosfellssveit, Iceland*. M.Sc. Reykjavík University.

Elefsen, S.Ó. (2016). *Vatnafarsrannsókn í Mosfellsdal – upplýtsingar úr borun, fyrstu mæliniðurstöður og viðbótarkostnaður vegnar aukinnar vöktunar við Geldingatjörn og Leirvogsvatn, minnisblað*. Kópavogur: Mannvit. Available at: http://ibuagatt.mosfellsbaer.is/meetingsearch/display-document.aspx?itemid=03636005410454992681&meetingid=201606019F%20%20%20%20&filename=1431234-000-CMO-0001.pdf&cc=Document [2019-01-03]

Finsterle, S. (2007). *iTOUGH2 User's Guide.* (LBNL-40040). California: Lawrence Berkeley National Laboratory. Available at: https://static1.squarespace.com/static/57b526322994ca46e44b1da6/-t/5aa16391085229dea8c15bd7/1520526232928/iTOUGH2_Users_Guide.pdf [2018-11-21]

Friðleifsson, I. B. (1985). Jarðsaga Esju og nágrennis [The geological history of Mt. Esja and surroundings]. *Iceland Travel Association Yearbook of 1985*, pp. 141-172.

Frolova, Yu. V. (2010). Patterns of Transformation in the Compositions and Properties of Icelandic Hyaloclastites during Lithogenesis. *Moscow University Geology Bulletin*, vol. 65 (2), pp. 104-114.

Gíslason S. R. and Eugster H. P. (1987). Meteoric water-basalt interactions. II. A field study in N.E. Iceland. *Geochim. Cosmochim. Acta,* vol. 51, pp. 2841–2855.

Gíslason S. R. and Arnórsson S. (1990). Saturation state of natural waters in Iceland relative to primary and secondary minerals in basalt. Fluid-Mineral Interactions: A Tribute to H. P. Eugster (ed. Spencer and Chou). *The Geochemical Society*, Special Publication 2, pp. 373–393.

Gíslason S. R. and Arnórsson S. (1993). Dissolution of primary basaltic minerals in natural waters: Saturation state and kinetics. *Chem. Geol.* vol. 105, pp. 117–135.

Gunnlaugsson, E. (1977). The origin and distribution of sulphur in fresh and geothermally altered rocks in Iceland. Ph.D. thesis, Univ. Leeds, U.K., 192 pp.

Gunnlaugsson, E. and Ívarsson, G. (2010). Direct Use of Geothermal Water for District heating in Reykjavík and Other Towns and Communities in SW-Iceland. *Proceedings World Geothermal Congress 2010*. Bali, Indonesia. Available at: https://www.geothermal-energy.org/pdf/IGA-standard/WGC/2010/3418.pdf [2018-02-01]

Haukwa, C.B. (1998*). AMESH—A Mesh Creating Program for the Integral Finite Difference Difference Method.* (LBNL-45284). California: Ernesto Orlando Lawrence Berkeley National Laboratory. Available at: http://esd1.lbl.gov/files/research/projects/tough/documentation/AMESH_Users_Guide.pdf [2018-11-16]

Helgeson, H. C., Kirkham, D. H., Flowers, D. C. (1981). Theoretical prediction of the thermodynamic behavior of aqueous electrolytes at high pressures and temperatures: IV. Calculation of activity coefficients, osmotic coefficients, and apparent molal and standard and relative partial molal properties to 600 C and 5 kb. *Am. J. Sci.,* vol. 281, pp. 1249–1516.

Hjartarson, Á. and Sæmundsson, K. (2014). *Berggrunnskort af Íslandi* [Bedrock map of Iceland], 1:600000. Reykjavík: Iceland Geosurvey

Ívarsson, G. (2018). *Hitaveita í Reykjavík, Vatnsvinnslan og efnafræði vatnsins 2017* [District heating in Reykjavík, Water production and chemistry in 2017]. Report 2018-014. Reykjavík: Reykjavík Energy and Veitur utilities.

Ívarsson, G. (2020). *Hitaveita í Reykjavík - Vatnsvinnsla 2019* [District heating in Reykja1981 vík, Water production in 2019]. Report 2020-005. Reykjavík: Reykjavík Energy and Veitur utilities.

Lasaga, A. C. (1984). Chemical kinetics of water-rock interactions, *J. Geophys. Res.*, vol. 89, pp. 4009-4025.

National Land Survey of Iceland (2018). *Niðurhalsþjónusta* [Download service]. Available at: https://www.lmi.is/en/licence-for-national-land-survey-of-iceland-free-data/ [2018-11-18]

Orkustofnun (2019a). *Orkustofnun data repository OS-2020-T008-01: Proportion of energy source in space heating based on heated space in Iceland 1952-2019.* Available at: https://nea.is/the-national-energy-authority/energy-data/data-repository/ [2021-04-20]

Orkustofnun (n.d.). *The Resource.* Available at: https://nea.is/geothermal/the-resource/ [2018-11-21]

O'Sullivan, M.J., Pruess, K. and Lippmann, M.J. (2001). State of the art of geothermal reservoir simulation. *Geothermics*, vol. 30 (4), pp. 395–429. DOI: https://doi.org/10.1016/S0375-6505(01)00005-0

Palandri, J., and Kharaka, Y. K. (2004). A compilation of rate parameters of water-mineral interaction kinetics for application to geochemical modeling, US Geol. Surv. Open File Report 2004-1068, 64 pp.

Pruess, K., Oldenburg, C. and Moridis, G. (2012). *TOUGH2 User's guide, Version 2.* (LBNL-43134). California: Lawrence Berkeley National Laboratory. Available at: http://esd1.lbl.gov/files/research-/projects/tough/documentation/TOUGH2_V2_Users_Guide.pdf [2018-11-21]

Sigurðsson, Ó. and Stefánsson, V. (1994). *Forðafræðistuðlar – Mælingar á bergsýnum* [Reservoir properties – Sample Measurements]. Report OS-94049/JHD-28 B. Reykjavík: Orkustofnun.

Snæbjörnsdóttir, S.Ó., Tómasdóttir, S., Sigfússon, B., Aradóttir, E.A., Gunnarsson, G., Niemi, A., Basirat, F., Dessirier, B., Gislason, S.R., Oelkers, E.H. and Franzson, H. (2018). The geology and hydrology of the CarbFix2 site, SW-Iceland. *Energy Procedia*, vol. 146, pp.146-157.

Sonnenthal, E., Ito, A., Spycher, N., Yui, M., Apps, J., Sughita, Y., Conrad, M. and Kawakami, S. (2005). Approaches to modeling coupled thermal hydrological and chemical processes in the Drift Scale Heater Test at Yucca Mountain. *Int. J. Rock Mech. Min. Sci.* vol.42, pp. 684–719.

Sonnenthal, E., Spycher, N., Xu, T., Zheng L. (2018). *A parallel simulation program for non-isothermal multiphase geochemical reactive transport. TOUGHREACT V3.6-OMP reactive transport user guide.* Energy Geosciences Division, Lawrence Berkeley National Laboratory, California, USA.

Steefel, C. I., and Lasaga, A. C. (1994). A coupled model for transport of multiple chemical species and kinetic precipitation/dissolution reactions with applications to reactive flow in single phase hydrothermal system, *Am. J. Sci.*, vol. 294, pp. 529-592.

Thorsteinsson, Þ. and Einarsson, K. (1990). *Áhrif þrýstiprófana 1972-1977 á vatnsborð í borholum í Mosfellssveit* [The effect of pumping tests 1972-1977 on waterlevel in wells in Mosfellssveit]. OS-90023/JHD-11 B. Reykjavík: Orkustofnun.

Tómasson, J. (1997). *Megin jarðlagasyrpur í borholum á Reykjasvæðunum í Mosfellsbæ* [Main lithological sequences in wells in the Reykir areas in Mosfellsbær]. JT-97-02. Reykjavík: Orkustofnun.

Tómasson, J. (1999). Borholur á Suður-Reykjum. Jarðfræði og ummyndun [Wells in Southern Reykir. Geology and alteration]. OS-99043. Samvinnuverk Hitaveitu Reykjavíkur og Orkustofnunar. Reykjavík: orkustofnun

Verkfræðistofan Vatnaskil (1994). *Reykjavík, reiknilíkan af jarðhitasvæðum*. Reykjavík: Verkfræðistofan Vatnaskil.

Verkfræðistofan Vatnaskil (2000). *Reykjavík, þrívítt reiknilíkan af jarðhitasvæðum*. Reykjavík: Verkfræðistofan Vatnaskil.

Verkfræðistofan Vatnaskil (2017). *Höfuðborgarsvæði – Grunnvatns- og rennslislíkan. Árleg endurskoðun fyrir árið 2016.* [Capital area- Groundwater and discharge model. Yearly revision for the year 2016], Report 17.15. Reykjavík: Vatnaskil Consulting Engineers

Voigt, M., Marieni, C., Clark, D.E., Gislason, S.R., Oelkers E.H. (2018) Evaluation and refinement of thermodynamic databases for mineral carbonation. *Energy Procedia*. vol. 146, pp. 81-91.

Wohletz, K. & Heiken G. (1992). *Volcanology and Geothermal Energy*. Berkeley: University of California Press.

Xu, T., Sonnenthal, E., Spycher, N., Pruess, K. (2006). TOUGHREACT – a simulation program for non-isothermal multiphase reactive geochemical transport in variably saturated geologic media: applications to geothermal injectivity and CO2 geologic sequestration. *Comput. Geosci.,* vol. 32, pp. 146–165.

3 Borehole Thermal Energy Storage (BTES)

3.1 French pilot site

Charlotte Rey[1], Charles Maragna[2], Patrick Egermann[1]

[1]Storengy, [2]BRGM

3.1.1 Conceptualization

3.1.1.1 UTES concept and specifications, scope and aims of the study

The report is based on the initial version of the French pilot: a coupling between a borehole field and thermal solar panels to store heat on a seasonal pattern (Figure 3.1.1). It was supposed to deliver heat to 3 administrative buildings of STORENGY main natural gas storage, located in Chémery, France.
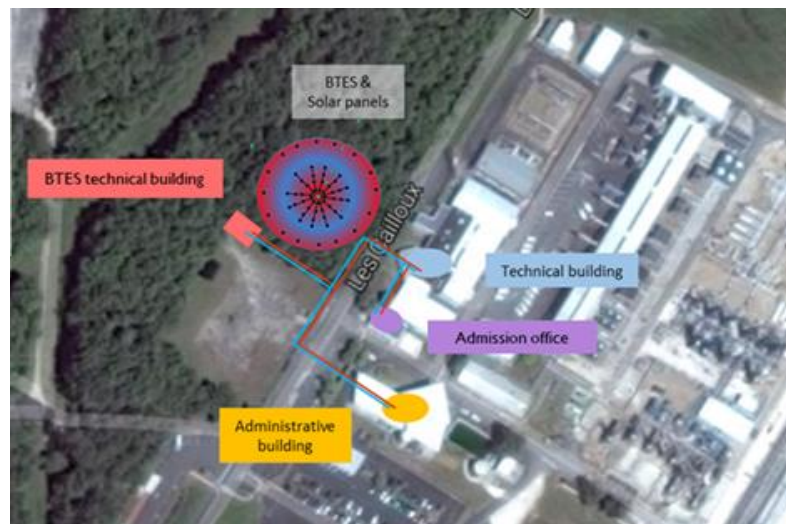
Figure 3.1.1 French pilot, BTESmart.

The initial design included a BTES made of 48 boreholes of 12 m, with 4 boreholes linked in series to form a "radius" (Figure 3.1.2). The heat carrier fluid was supposed to circulate in parallel in the 12 radii. When no heating was required in the buildings, the heat collected at the solar thermal panels would go to the BTES, flowing into the different radii from the centre of the field to its periphery. The heat carrier fluid would flow in the opposite direction when discharging the BTES.

The initial design also included 16 recovery boreholes (25 m) in a circular arrangement around the BTES at about 20 meters distance from the centre, intended to help reducing the heat losses at the periphery of the BTES.

The initial idea was that at the beginning of autumn, the recovery boreholes would be used to bring their temperature level back to its initial value. When the measured temperature at the recovery boreholes would be greater than the initial temperature of, for example, 10°C, water would be sent to these boreholes to recover some of the heat. They would be stopped when the ground temperature would be back to/close to its initial value and not far below so as not to drive the heat still stored in the centre of the BTES to its periphery. The extracted heat would be either used for heating or reinjected in the BTES, which would improve the system efficiency.
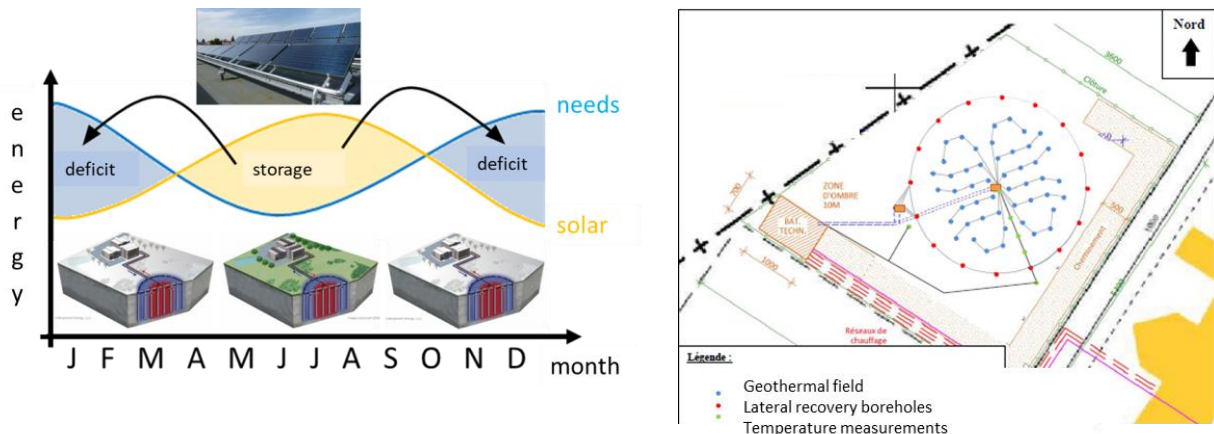
Figure 3.1.2 Concept of the French pilot (left figure) and <u>initial BTES design</u> with the 12 "radius" of boreholes (blue dots on the right figure).

The main objective for modelling is the best possible description of subsurface flow dynamics and heat transfer in relation to the storage concept, including the impact of subsurface heterogeneities. The ability of the simulation tools to be used for design and optimization of performance and sustainability will also be tested.

3.1.1.2 System Geometry and related Geology

There are differences between the initial design presented in the previous section and the system modelled in the report:

- The boreholes of the (main) BTES field and the lateral recovery boreholes are 20 m deep.
- The underground is composed of a first layer of soil, followed by homogeneous rock.

Some heterogeneity will however be later added. An insulation layer is also present at the top surface. Main characteristics of the BTES elements are described in Table 3.1.1.

Table 3.1.1 System Geology

Stratigraphic columns				
Description	Top depth [m]	Bottom depth [m]	Thermal conductivity [W.K^{-1}.m^{-1}]	Heat Capacity [MJ.K^{-1}.m^{-3}]
Soil	0	0.5	0.25	1.50
Insulation	0.5	1.0	0.20	2.00
Rock	1.0	Inf.	1.90	2.30

The initial temperature of the ground is set to 13.0 °C.

3.1.1.3 Local geothermal and groundwater conditions

Before any heat injection, the temperature of the underground is supposed to be constant, with no geothermal gradient. No underground water flow is considered.

3.1.1.4 Well operation and history

All the boreholes have the same characteristics (see Table 3.1.2).

Table 3.1.2 BHE characteristics.

Borehole depth	Grout thermal conductivity	External pipe radius	Internal pipe radius	Spacing between pipes	Pipe thermal conductivity	Fluid heat capacity	Fluid Thermal conductivity
20 m	2.0 $W.K^{-1}.m^{-1}$	16.0 mm	13.1 mm	40.0 mm	0.40 $W.K^{-1}.m^{-1}$	4 000 $kJ.K^{-1}.kg^{-3}$	0.48 $W.K^{-1}.m^{-1}$

3.1.2 Modelling approach

3.1.2.1 Conceptual simulation model

The processes to be simulated are mainly related to heat transfer, first in homogeneous but then in heterogeneous media using two simulating approaches (analytical and 3D models).

In the 3D model, the borehole heat exchangers are represented as embedded 1D elements and linked to the nodes along join edges. Cauchy-type boundary conditions are then applied to the nodes to represent the interactions with the borehole controlled by the heat transfer coefficient between the soil and grout material zones of the boreholes. Heat transfer relationships for the BHE models can then be determined with numerical [1] or analytical (Eskilson and Claesson's) solutions. Flow in the boreholes in not explicitly simulated. Effects of thermal expansion to assess possible ground uplift will not be included/studied.
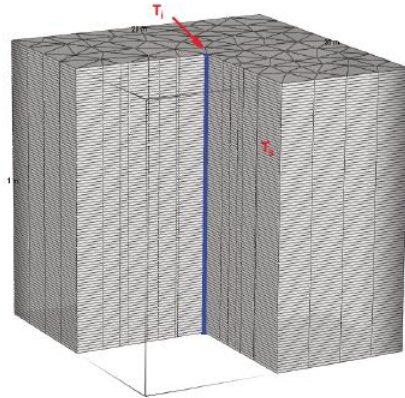
Figure 3.1.3 Example of a single BHE in a 3D mesh (exaggerated view).

An alternative to fully discretized models is the use of analytical solutions to the heat equations. Analytical solutions, also known as *step responses* or *g-functions* (after the pioneering work on BHEs by Eskilson [2]) and often denoted $G(t^*)$, describe the evolution of the normalized temperature of the borehole or pile perimeter under a constant power applied by unit length p
(W.m^{-1}). G-functions are usually configured so that the temperature computed is that at the borehole (or pile) wall. The evolution of the temperature change ΔT is then given by:

$$\Delta T = \frac{p}{\lambda_m} G(t^*)$$

Where t^* is a dimensionless time factor (Fourier number) and λ_m the ground thermal conductivity (W.K^{-1}.m^{-1}). Analytical solutions only hold when the physical properties of the materials do not change with the temperature. The change of the dynamic viscosity of underground water from 1.31×10^{-3} at 13 °C (initial temperature) to 6.5×10^{-3} Pa s at 40 °C (maximal injection temperature) is significant. Besides, previous monitoring on Neckarsulm BTES shown an increase of ground thermal conductivity from 2.0 W.K^{-1}.m^{-1} at initial temperature to 2.4 W.K^{-1}.m^{-1} at c.a. 60 °C [3]. Therefore, the effect of the dependence of the thermal

properties upon the temperature is tested for a few materials. Note that conductivity may increase or decrease with the temperature, depending on the material properties [4]. At normal temperatures for uniform crystals, thermal conductivity is inversely proportional to absolute temperatures, while amorphous materials exhibit a linear increase of thermal conductivity with temperature.

3.1.2.2 Pre-processing workflow

For the 3D model, the desired location of the boreholes, as well as the surface of the insulation layer were calculated in Excel based on the chosen distance between the boreholes of the (main) BTES and the chosen distance between the main fiend and the lateral recovery boreholes. The points set were then uploaded in the simulation software.

3.1.2.3 Computational approach and software

FEFLOW model

The software that is used here for the numerical simulations is FEFLOW (DHI, 2010 & 2015). The user manual is freely available online. It simulates flow via standard (saturated) groundwater-flow equation. The steady-state flow in the underground will be combined with a transient transport of heat.

A specific mesh around each borehole was defined as recommended in FEFLOW White Paper V (DHI, 2010). In FEFLOW, a BHE is reduced to an internal boundary condition occupied at a single node in a horizontal view on the 3D finite element mesh of the global problem. If inserting a heat flow Q_b at a singular node i, the resulting head value h_i in a flow simulation do not usually represent the head exactly at the
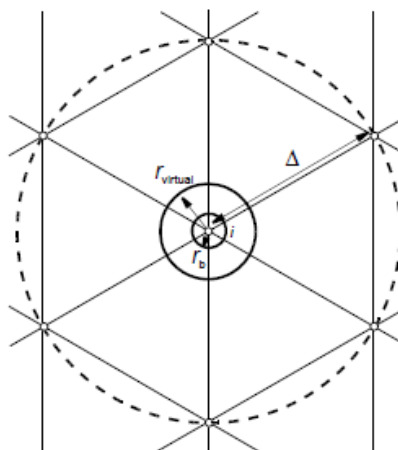
Figure 3.1.4 Spatial discretization (n =6) around a BHE 'well' node.

physical borehole radius r_b: The computed head h_i at the node i is to be deemed on a different radius, which is called virtual radius, $r_{virtual}$. It can be shown that the virtual radius is primarily dependent on the mesh discretization around the node i, represented by a nodal distance Δ. An optimal mesh (=optimal accuracy) is obtained when $r_b = r_{virtual}$.

The following equation can be used to determine the required nodal distance:

$$\Delta = \exp(\alpha)\, r_{virtual} \qquad \alpha = \frac{2\pi}{n \tan\left(\frac{\pi}{n}\right)}$$

With n the spatial discretization around the BHE, Δ the nodal distance (Figure 3.1.4).

Thanks to the symmetry of the system, only a quarter of the system was simulated, to gain a non-negligible amount of simulation time.
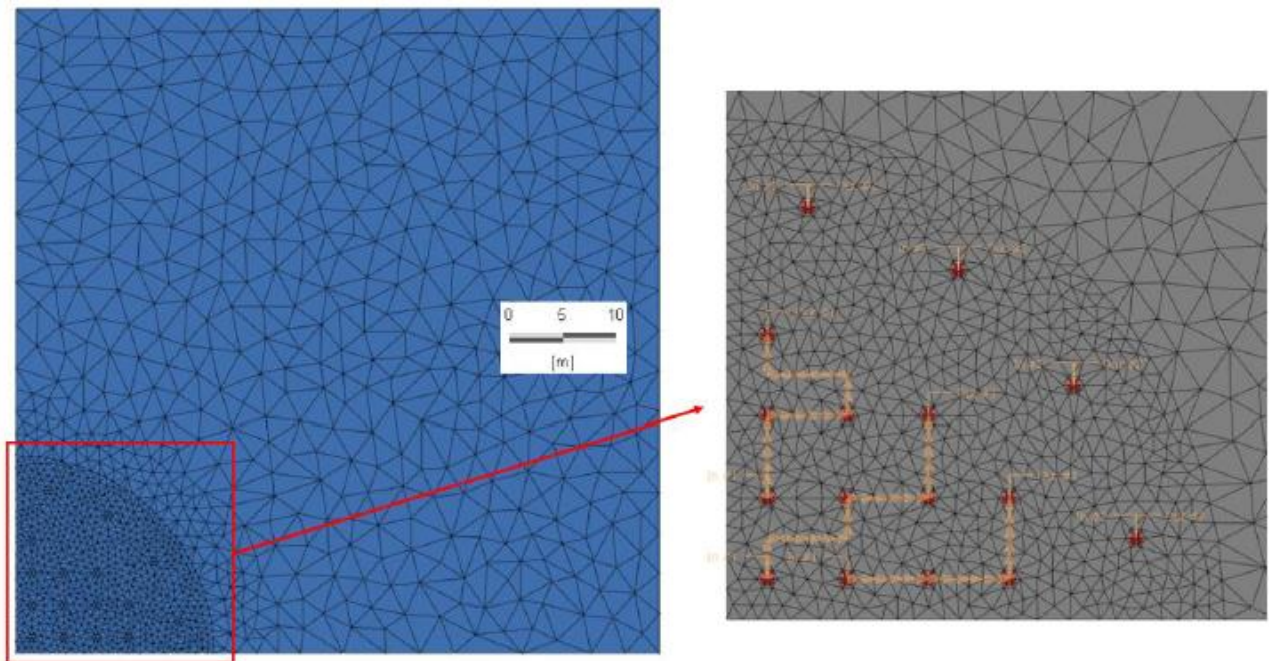
Figure 3.1.5 Mesh used in FELOW and hydraulic connections between boreholes. Only one quarter of the BTES simulated, with 48/4 = 12 inner boreholes and 16/4 = 4 lateral boreholes.
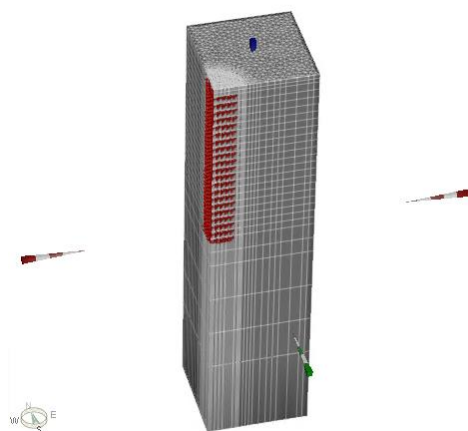

Figure 3.1.6 FEFLOW model.

The coordinates of these nodes were also calculated in Excel. A 2D supermesh, which forms the framework for the generation of the finite-element mesh, is then created using the imported points sets from Excel. A mesh is generated that considers the points and lines defined in the supermesh.

In case of a layered approach, the 2D mesh is extended to the third dimension by extruding the 2D mesh, resulting in prismatic 3D elements. Another approach exists, which consists in directly importing 3D supermeshes and mesh them in FEFLOW. Structured or unstructured grids, made outside FEFLOW, can also be directly input. However, the format needs to be supported by FEFLOW.

Within FEFLOW's BHE configuration dialog, the Eskilson and Claesson's analytical solution BHE was chosen, as it is a better alternative to the general Al-Khoury et al.'s numerical strategy for long term predictions in terms of accuracy. Only one iteration is performed per each time, but a stronger RMS error tolerance of 10^{-6} concerning the AB/TR automatic time-stepping control was selected. The streamline upwinding option was also preferred to the default no upwinding (Galerkin-FEM) option.

An optimal BHE nodal distance of 0.38 m (by using n = 6) was chosen for the unstructured mesh. Finally, the total study area of 60 m x 60 m was discretized in 1,500 triangular prismatic element per layer. In the vertical direction, the used finite element mesh consists in 28 layers with a thickness between 0.5 and 10 m; within the BTES the slice thickness is 1 m.

Semi-analytical (SA) model

Analytical models are more suitable for routine use than fully discretised models. Indeed, analytical models can run over reasonable time frames, i.e., performing simulations over 30 years with hourly time step.

Common *G*-functions consider that heat is transferred by conduction. The simplest BHE G-function, the *infinite line source* (*ILS*) model, represents the borehole as an infinite line emitting a constant heat flux [5]. Further improvements of the geometrical representation include the *finite line source* (*FLS*) model [2] and the *hollow*

211

infinite cylindrical source (*HICS*) [6] [7] and solid cylindrical heat source [8]. The convection is taken into account by the *moving infinite line source (MILS), moving finite line source (MFLS)* [9]. In the MILS model the borehole geometry is assimilated to an infinite line located in a homogenous media where groundwater flows with a constant velocity. Molina-Giraldo et al. (2011) presented a *moving finite line source* (MFLS) that takes into account the finite length of the borehole [10]. For this work, we used the *moving finite line source model with Cauchy-type top boundary conditions* since it deals with the heat exchange at the surface [11]. It relies on the following assumptions:

1. The underground media is assumed homogenous, see the geological description above.
2. A Cauchy-type boundary condition is applied at the interface between the atmosphere and the ground. The air temperature oscillates between $T_{min,air}$ and $T_{max,air}$; the heat transfer coefficient h is assumed to be constant in time and space. Practically, the insulation layer is assumed to be of infinite radial extent, and the following contributions to the heat balances are overlooked: convection, infrared, incoming and reflected radiations [12].

The step response used reads:

$$G(t^*) = \lambda_m R_b + \frac{1}{8\pi} \int_{\frac{1}{4t^*}}^{\infty} \frac{1}{\varphi} \exp(-\varphi) \left\{ 4 \operatorname{erf}\left(H^*\sqrt{\varphi}\right) - 2 \operatorname{erf}\left(2H^*\sqrt{\varphi}\right) \right.$$
$$\left. + \frac{1}{H^*\sqrt{\pi\varphi}} \left[4 \exp\left(-\varphi H^{*2}\right) - \exp\left(-4\varphi H^{*2}\right) - 3 \right] \right\} d\varphi + \frac{1}{h^* H^*} \int_{\frac{t^*}{4}}^{\infty} \frac{1}{\varphi} \exp[-\varphi]\, \psi(h^*, H^*, \varphi) d\varphi$$

Note that Rivera et al. assumes a constant underground water flow accounted for through a Peclet number *Pe* [11]. Since there is no underground water flow in our study, *Pe* has been set to zero. The underground media is therefore assumed impervious. As a result, the advection is neglected, the heat is transferred only through conduction. This assumption holds only for the model analysis and comparison with experimental data. The term $\lambda_m R_b$ has been added to account for the heat transfer inside the borehole. R_b is the borehole resistance and has been set to $R_b = 0.095$ K.m.W^{-1}, a value measured in-situ trough a thermal response test. H^* and h^* are normalized expressions for the BHE depth H and heat transfer coefficient at the surface h [W.K^{-1}.m^{-2}]:

$$H^* = H/r_b$$

$$h^* = (h\, r_b)/\lambda_m$$

$h \to 0$ and $h \to \infty$ respectively correspond to an adiabatic condition (perfectly insulated surface) and no insulation at all. h can be estimated through:

$$h = \frac{1}{\left(\frac{e}{\lambda}\right)_{layer\,1} + \left(\frac{e}{\lambda}\right)_{insulation}} = \frac{1}{\frac{0.50}{0.25} + \frac{0.50}{0.20}} = 0.222 \text{ W.K}^{-1}.\text{m}^{-2}$$

ψ is a function defined by:

$$\psi(h^*, H^*, \varphi) = 2 \operatorname{erf}\left(H^*\sqrt{\varphi}\right) - \operatorname{erf}\left(2H^*\sqrt{\varphi}\right) + \kappa(h^*, H^*, 0) - \kappa(0,0,0) - \kappa(h^*, H^*, H^*)$$
$$+ \kappa(h^*, 0, H^*)$$

$$\kappa(h^*, \mu, \nu) = 2\sqrt{\frac{\varphi}{\pi}} \int_0^{\infty} \exp\left[-\left((\nu + \mu + \varepsilon)\sqrt{\varphi}\right)^2 - h^*\varepsilon \right] d\varepsilon$$

The fluid temperature is different in each circuit, but within a circuit it is assumed to be the same in every BHE. As a result, the mean fluid temperature $T_{fl,J}$ in every hydraulic circuit J (j = 1,2) at every time step n ($t^n = n\,\Delta t$) is given by:

$$T_{fl,J}{}^n = \frac{T_{in,B,J}{}^n + T_{out,B,J}{}^n}{2} = T_0 + \frac{1}{\lambda_m N_J H_J} \left(P_{B,J}{}^1 G_{B,J}{}^n + \sum_{l=1}^{n-1} \left(P_{B,J}{}^{l+1} - P_{B,J}{}^l\right) G_{B,J}{}^{n-l} \right) + \delta T_{J' \to J}$$

Where $T_{in,B,J}$ and $T_{out,B,J}$ are the BTES inlet and outlet temperatures of the Jth circuit, T_0 the averaged initial ground temperature, λ_m the ground thermal conductivity (W.K^{-1}.m^{-1}), N_J and H_J the number of boreholes and depth in the Jth circuit, $P_{B,J}{}^n$ the exchanged power between the surface installation and the ground (positive values corresponding to some heat being injected into the BTES). $\delta T_{J' \to J}$ accounts for the thermal interaction between the circuits. $G_{B,J}(t^*)$ is the global response function of the Jth circuit defined by:

$$G_{B,J}(t^*) = \lambda_m R_b + G_1(t^*) + \frac{1}{N_J}\left(\sum_{i=1}^{N}\sum_{\substack{j=1\\i\neq j}}^{N} G_{i\to j}(t^*)\right)_{BHE\ i\ in\ J^{th}\ circuit}$$

where the 1^{rst} term on the right represents the internal thermal transfer in the borehole, the second term the interaction of a borehole with the surrounding ground, while the last term accounts for the interaction between all the boreholes of a given circuit. As the underlying equations are linear, the resulting temperature change from several sources (here BHE) can be obtained by simply adding the temperature change from each BHE. Note that the dimensionless time factor t^* (Fourier number) characterizes the ratio of diffused heat to stored heat:

$$t^* = \frac{\lambda_m}{(\rho C_p)_m r_b^2}t$$

With $(\rho C_p)_m$ the ground thermal capacity (J.K^{-1}.m^{-3}) and r_b the borehole radius.

A power balance on each circuit gives:

$$P_{B,J}{}^n = \dot{m}_{B,J}C_p\left(T_{in,B,J}{}^n - T_{out,B,J}{}^n\right)$$

TRNSYS is a famous software to simulate transient systems, where components (or "Types") are inter-connected. It has been widely applied to energy systems. A famous BTES Type is the Duct Storage Thermal (DST) Type 557, which relies on a mix of analytical and numerical solutions. DST has been validated against monitoring data over several years of operation in Solar Drake Landing [13] and Crailsheim [3] BTES. However, DST considers the fluid temperature to be same throughout the BTES while smartBTES has 2 independent hydraulic circuits. A BTES type for TRNSYS with independent hydraulic circuits is under development and will be finalized in the framework of the prolongation of the French project. Here is reported the validation of the analytical approach and the comparison with the fully discretized model

3.1.3 Scenarios and results

Heat is stored for 214 days by circulating fluid at 40 °C and unloaded for 151 days by circulating fluid at 13 °C, so a full cycle is 1 year and 10 cycles are simulated. Each branch of the inner core is fed with a volume flow-rate Q = 0.5 m.h^{-3}, so that 6.0 m.h^{-3} circulates in the inner core or 1.5 m^3.h^{-1} in the modelled fourth of the BTES. Note that as the discharge temperature is low, a heat pump will be necessary to increase the fluid temperature to a level usable for heating (e.g., 35-30 °C).

Several comparisons were performed:

- The SA model has been benchmarked against the FEFLOW model in the case there is no circulation in the lateral boreholes.
- The addition of flow through the lateral recovery boreholes was compared with the case with no flow in FEFLOW.
- The impact of some heterogeneity was assessed using FEFLOW, on both cases: with and without active lateral recovery boreholes.

The heterogeneity in the model lies in the top half of the borehole length (= 10 m – layer 3 to 12) in a rock with a thermal conductivity of soil of 1 W.K^{-1}.m^{-1} and the bottom half of the borehole length (= 10 m – layer 13 to 22) in a rock with a thermal conductivity of soil of 3 W.K^{-1}.m^{-1}; the thermal conductivity of soil of the same 20 m being 2 W.K^{-1}.m^{-1} in the homogeneous case.

The lateral boreholes are active during the first 3 months of the discharging period, with an inlet temperature of 13°C and a flowrate per borehole of 0.125 m^3/h.

The impact of the temperature dependence of the ground conductivity, initially planned, was not evaluated as not possible with the current version of FEFLOW, without using the Python interface to implement this new functionality.

Case: Homogeneous ground without recovery boreholes.

Note that the borehole resistance has been set to R_b = 0.08 K.m.W^{-1} instead of R_b = 0.095 K.m.W^{-1} for this test. Both models are in good agreement (see Figure 3.1.7), though the error on the BTES outlet temperature is about 0.9 °C after 10 h of operation. The influence of the FE mesh on the result quality must be further investigated. The error on the energy exchanged between the fluid and the ground over the 10 years of operation is 0.25% (energy in absolute value). If one defines the BTES efficiency η as the ratio of unloaded to stored heat, the BTES reaches a pseudo-periodic state after a few years of operation and η converges towards 67.0 % at the 10th year of operation.
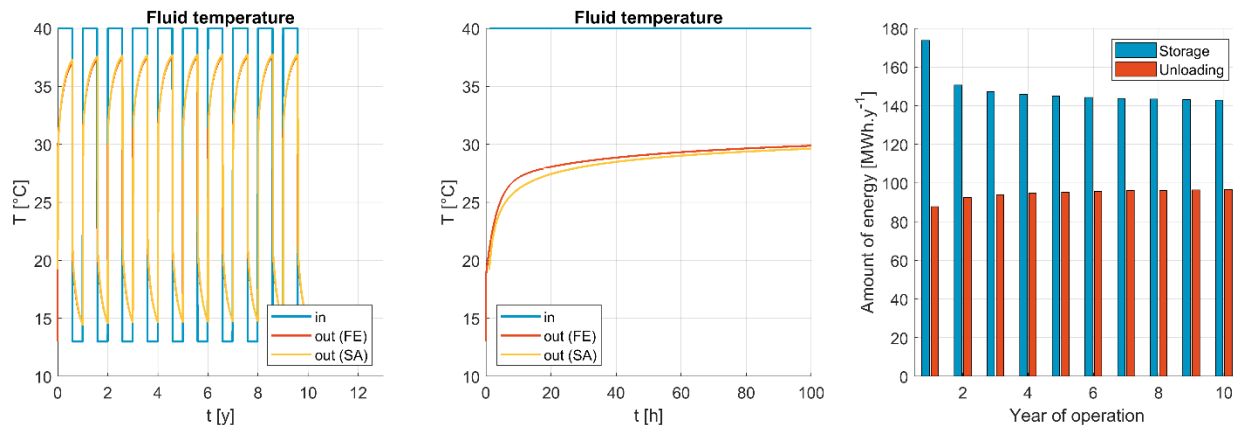
Figure 3.1.7 Benchmark: Evolution of the fluid temperature for 10 years (left) and at the early stage (middle). Yearly energy stored and unloaded (right), as computed by the SA model.

Case: With and without lateral recovery boreholes.

The temperature profiles and the system efficiency of both cases are presented below.

The efficiency of the (main) BTES field grows to 65% 10 years after running the system. When the lateral recovery boreholes are active, the heat injected in the field is bigger, but the amount of recovered heat is lower, resulting in a slightly lower efficiency of the system. Indeed, the external BHE cool down the BTES core. Therefore, the temperature difference between the fluid and the surrounding ground is a bit higher than in the reference case, leading to an increased transfer of heat from the BHE to the ground. Conversely, the lower core temperature leads to a lower recovery rate from the core. The amount of heat recovered through the lateral recovery boreholes, added to the one from the (main) BTES field results however in a slightly higher amount of heat overall. Note that the heat from the outer part is however recovered at a lower temperature and the HP with require more electricity to operate it.

One of the noticeable impacts of activating the lateral recovery boreholes is the decrease of the temperature around the (main) BTES field (Figure 3.1.8).

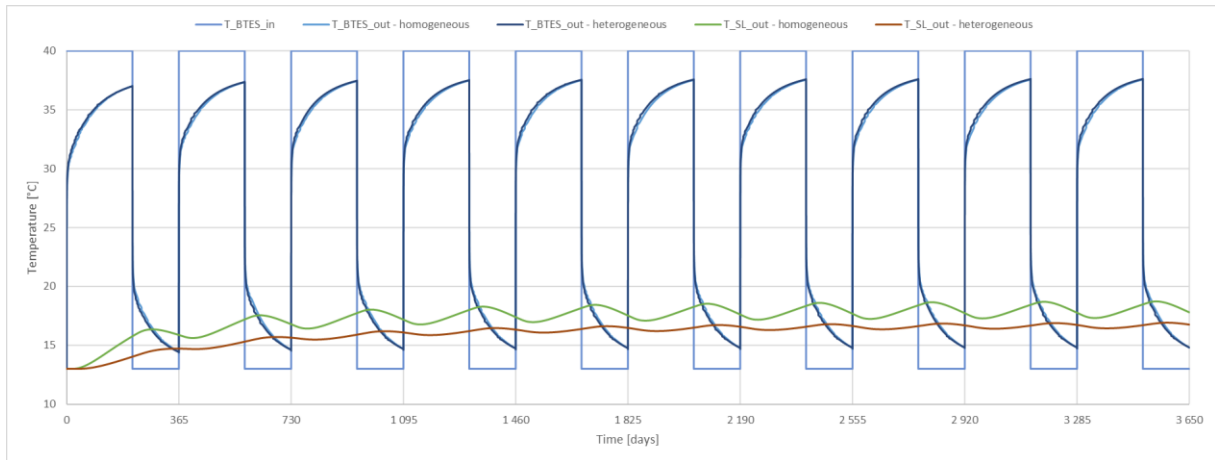More cases still need to be tested to find an optimal way to use the lateral recovery boreholes.
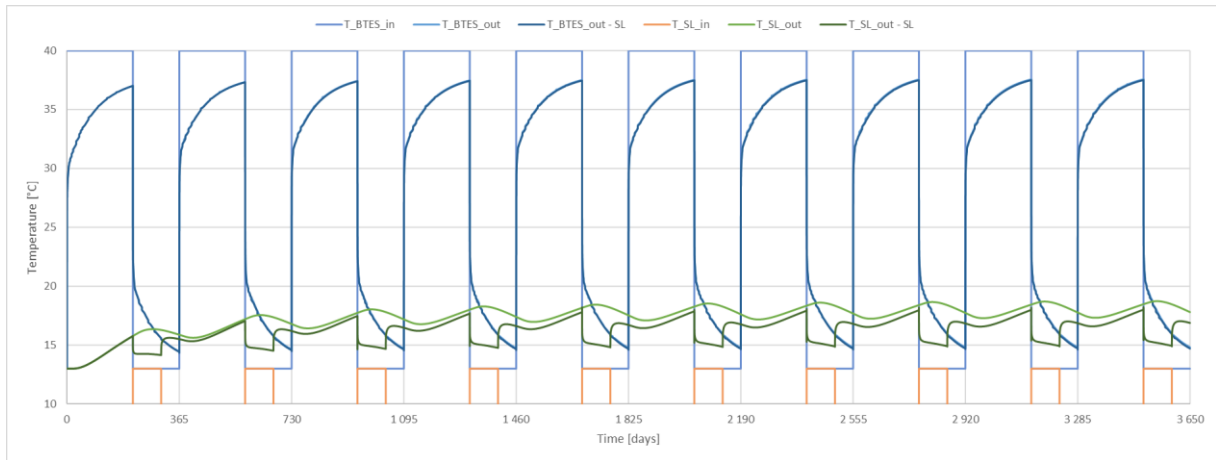
Figure 3.1.8 Inlet temperature of the (main) BTES field ; outlet temperatures of the (main) BTES field for homogeneous cases with and without lateral recovery boreholes (SL) ; inlet temperature for the lateral recovery boreholes when active; mean temperature along the 4 lateral recovery boreholes when active and non-active.

Table 3.1.3 Energies injected and recovered from the (main) BTES field in cases with and without lateral recovery boreholes. Additional energy recovered through lateral recovery boreholes (SL).

| Year | Homogeneous case | | | Homogeneous case with SL | | | | | |
	E_BTES_in [MWh]	E_BTES_out [MWh]	BTES efficiency	E_BTES_in [MWh]	E_BTES_out [MWh]	BTES efficiency	E_SL_out [MWh]	E_BTES+SL_out [MWh]	Total efficiency
1	78.0	37.0	47%	78.0	36.8	47%	0.7	37.4	48%
2	67.9	39.5	58%	68.3	38.8	57%	0.9	39.8	58%
3	66.0	40.3	61%	66.9	39.7	59%	1.0	40.7	61%
4	65.2	40.7	62%	66.1	39.9	60%	1.1	41.0	62%
5	64.7	41.0	63%	65.6	40.4	62%	1.1	41.5	63%
6	64.5	41.0	64%	65.4	40.3	62%	1.1	41.4	63%
7	64.1	41.3	64%	65.3	40.7	62%	1.1	41.8	64%
8	64.0	41.4	65%	65.2	40.5	62%	1.2	41.7	64%
9	63.9	41.5	65%	65.1	40.6	62%	1.2	41.7	64%
10	63.8	41.7	65%	65.0	40.6	62%	1.2	41.8	64%

Case: Homogeneous vs. heterogeneous media.

The temperature profiles and the system efficiency of both cases are presented below.

The efficiencies of both cases are the same, but the energy injected in the (main) BTES is higher in the homogeneous case.

The mean temperature along the 4 lateral recovery boreholes (here with no flow) is lower for both the heterogeneous case, compared to the homogeneous one.

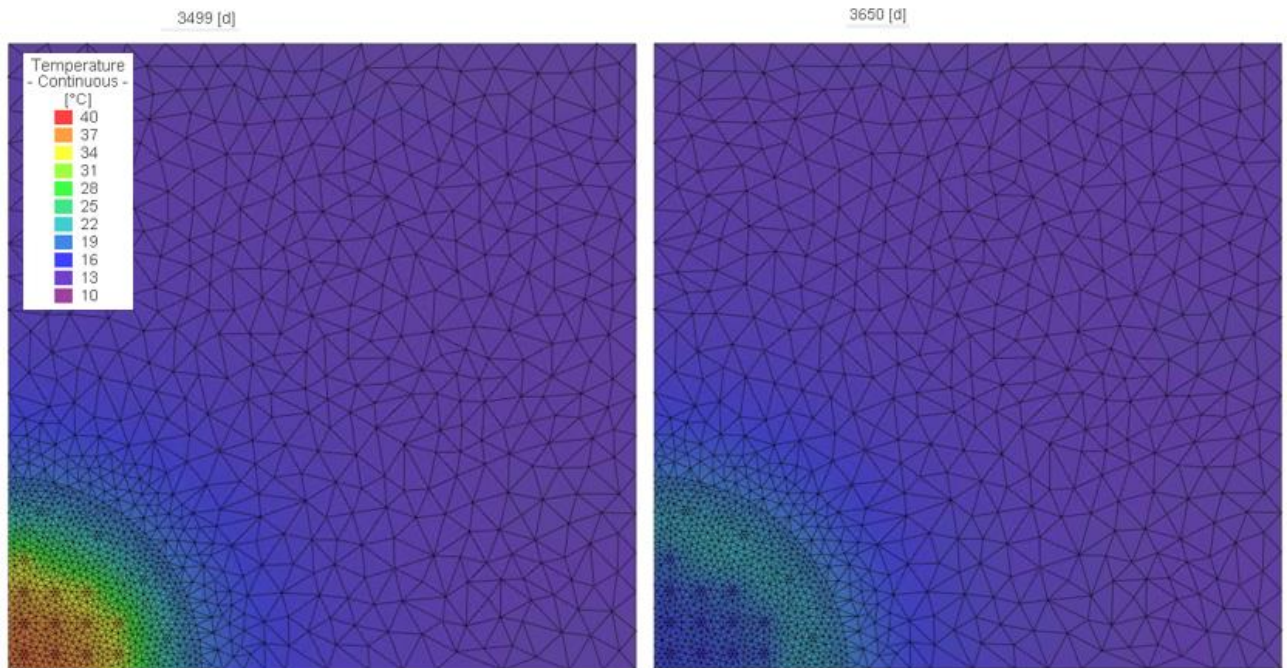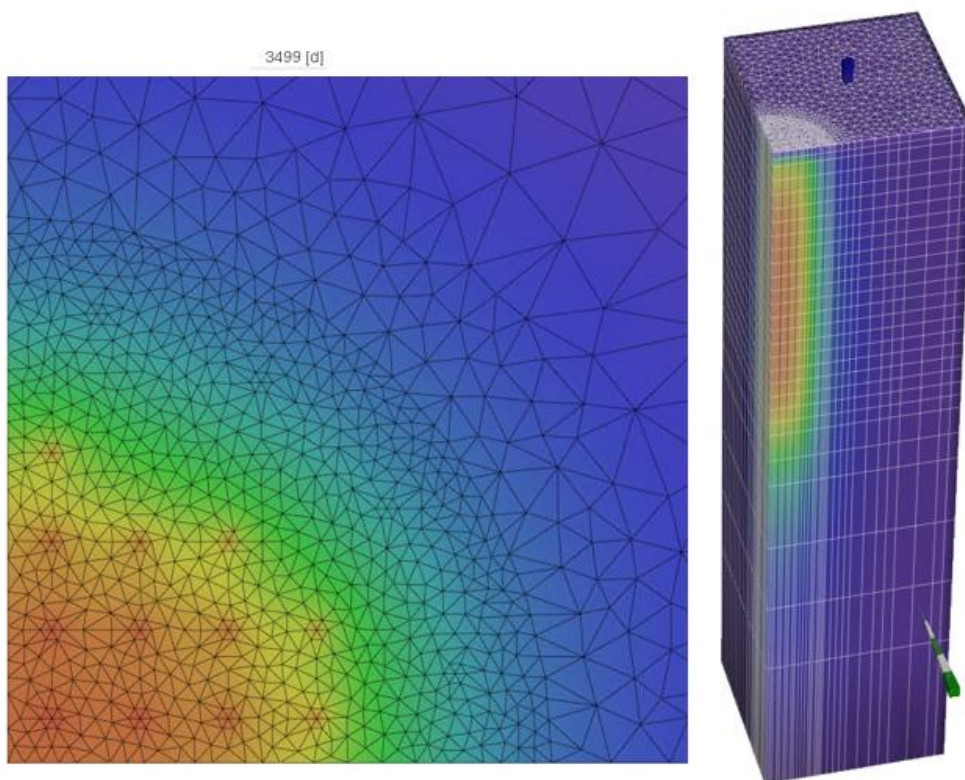The temperature maps at the end of the charging (3 499 days) and the discharging (3 650 days) of the 10th year, for the homogeneous case are also shown in Figure 3.1.10 and Figure 3.1.11.
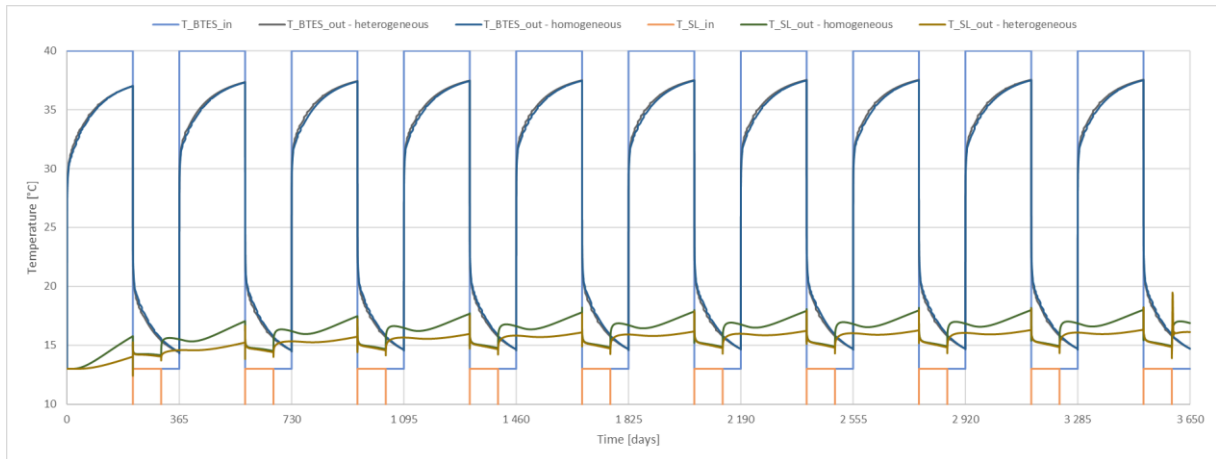
Figure 3.1.9 Inlet temperature of the (main) BTES field ; outlet temperatures of the (main) BTES field for both homogeneous and heterogeneous cases ; mean temperature along the 4 lateral recovery boreholes (no flow) for both homogeneous and heterogeneous cases.

Table 3.1.4 Energies injected and recovered from the (main) BTES field in homogeneous and heterogeneous cases.

Year	Homogeneous case			Heterogeneous case		
	E_BTES_in [MWh]	E_BTES_out [MWh]	BTES efficiency	E_BTES_in [MWh]	E_BTES_out [MWh]	BTES efficiency
1	78.0	37.0	47%	75.6	34.5	46%
2	67.9	39.5	58%	65.2	37.4	57%
3	66.0	40.3	61%	63.2	38.2	60%
4	65.2	40.7	62%	62.3	38.7	62%
5	64.7	41.0	63%	61.7	39.0	63%
6	64.5	41.0	64%	61.3	39.2	64%
7	64.1	41.3	64%	61.1	39.4	64%
8	64.0	41.4	65%	60.9	39.6	65%
9	63.9	41.5	65%	60.7	39.6	65%
10	63.8	41.7	65%	60.6	39.7	65%

Figure 3.1.10: Temperature maps at the end of the charging (3 499 days) and the discharging (3 650 days) of the 10th year, for the homogeneous case – middle depth of the field.

Figure 3.1.11: Temperature map at the end of the charging (3 499 days) of the 10th year, for the homogeneous case – middle depth of the field and 3D view.

217

Case: Homogeneous vs. heterogeneous media, with lateral recovery boreholes.

The temperature profiles and the system efficiency of both cases are presented in Figure 3.1.12. Despite the different temperature level, the energy recovered through the lateral recovery boreholes in both cases are similar.

Figure 3.1.12 Inlet temperature of the (main) BTES field ; outlet temperatures of the (main) BTES field for homogeneous and heterogeneous cases with and without lateral recovery boreholes (SL) ; inlet temperature for the lateral recovery boreholes; mean temperature along the 4 lateral recovery boreholes for homogeneous and heterogeneous cases when lateral recovery boreholes are active.

Table 3.1.5 Energies injected and recovered from the (main) BTES field in homogeneous and heterogeneous cases with active lateral recovery boreholes. Additional energy recovered through lateral recovery boreholes (SL).

Homogeneous case with SL						Heterogeneous case with SL					
E_BTES_in [MWh]	E_BTES_out [MWh]	BTES efficiency	E_SL_out [MWh]	E_BTES+SL_out [MWh]	Total efficiency	E_BTES_in [MWh]	E_BTES_out [MWh]	BTES efficiency	E_SL_out [MWh]	E_BTES+SL_out [MWh]	Total efficiency
78.0	36.8	47%	0.7	37.4	48%	75.6	34.4	46%	0.6	35.1	46%
68.3	38.8	57%	0.9	39.8	58%	65.7	36.9	56%	0.9	37.7	57%
66.9	39.7	59%	1.0	40.7	61%	63.7	37.5	59%	1.0	38.5	60%
66.1	39.9	60%	1.1	41.0	62%	63.0	38.0	60%	1.0	39.0	62%
65.6	40.4	62%	1.1	41.5	63%	62.6	38.3	61%	1.1	39.3	63%
65.4	40.3	62%	1.1	41.4	63%	62.3	38.2	61%	1.1	39.3	63%
65.3	40.7	62%	1.1	41.8	64%	62.2	38.7	62%	1.1	39.8	64%
65.2	40.5	62%	1.2	41.7	64%	62.0	38.5	62%	1.1	39.7	64%
65.1	40.6	62%	1.2	41.7	64%	61.9	38.7	62%	1.1	39.8	64%
65.0	40.6	62%	1.2	41.8	64%	61.8	38.7	63%	1.1	39.8	64%

3.1.4 Analysis and discussion

3.1.4.1 Predictive and sensitivity-related learnings

The following conclusions can be drawn:

- Analytical solutions are an efficient and accurate approach to BTES hydrothermal modelling, provided that the physical phenomena at stake remain linear. They lead to similar results to a fully discretized 3D model, but with a much shorter execution time.
- Though most analytical solutions assume the ground is homogeneous, the comparison of the 3D model without or with two layers exhibiting a large discrepancy of thermal conductivity shows that the heterogeneity has little effect on the evolution of the BTES thermal regime. However, this holds only

for impervious layers. If one layer exhibits underground water flow, even relatively slow (e.g. Darcy velocity ≈ 15 m.y^{-1}), the BTES recovery may be greatly affected [14].

- The benefit of the lateral recovery boreholes could not be exhibited from the simulations. Indeed, the circulation of cooler fluid tends to slightly cool down the BTES inner core. Further investigations are still needed, as planned in the prolongation for the French demo site.

3.1.4.2 Work Package Interfaces

WP1: Specifications and characterization for UTES concepts

The UTES systems are known for their heat losses. For BTES, that is the reason why the favoured geology are clayed materials. Nevertheless, even in this context, heat losses remain high typically in the order of 25-45% depending on the size and the shape of the bore field, and the loading/unloading temperatures. The BTESmart design will provide some indications about the ability of lateral recovery boreholes to recover a larger part of these heat losses making BTES more efficient.

WP3: Heating System integration and optimization of design and operation

For the system integration, one of the keys is the ability of coupling the subsurface and surface modelling tools and to obtain results is a reasonable calculation time. The BTESmart analytical component for TRNSYS will enable to perform such integration for the work planed in WP3.

WP5: Monitoring and validation to assess system performance and workflow

The monitoring plan has been already transmitted to WP5 and once the demo will start the monitoring data will be shared.

3.1.5 References

[1] R. Al-Khoury and P. G. Bonnier, "Efficient finite element formulation for geothermal heating systems. Part II: Transient," *Int. J. Numer. Methods Eng.*, vol. 67, no. 5, pp. 725–745, 2006.

[2] P. Eskilson, "Thermal analysis of heat extraction boreholes," University of Lund, Sweden, 1987.

[3] J. Nussbicker, W. Heidemann, and H. Mueller-Steinhagen, "Monitoring results and operational experiences for a central solar district heating system with Borehole Thermal Energy Store in Neckarsulm (Germany)," in *Ecostock - 10th International Conference on Thermal Energy Storage. Richard Stockton College of New Jersey 31.05.-02.06.2006*, 2006.

[4] Z. Abdulagatova, I. M. Abdulagatov, and V. N. Emirov, "Effect of temperature and pressure on the thermal conductivity of sandstone," *Int. J. Rock Mech. Min. Sci.*, vol. 46, no. 6, pp. 1055–1071, Sep. 2009.

[5] L. R. Ingersoll and H. J. Plass, "Theory of the ground pipe heat source for the heat pump," *Heating, Pip. Air Cond.*, 1948.

[6] H. S. Carslaw and J. C. Jaeger, *Conduction of Heat in Solids*. Oxford: Oxford University Press, 1947.

[7] P. Eslami-nejad and M. Bernier, "Coupling of geothermal heat pumps with thermal solar collectors using double U-tube boreholes with two independent circuits," *Appl. Therm. Eng.*, vol. 31, no. 14–15, pp. 3066–3077, Oct. 2011.

[8] Y. Man, H. Yang, N. Diao, J. Liu, and Z. Fang, "A new model and analytical solutions for borehole and pile ground heat exchangers," *Int. J. Heat Mass Transf.*, vol. 53, no. 13–14, pp. 2593–2601, Jun. 2010.

[9] M. G. Sutton, D. W. Nutter, and R. J. Couvillion, "A Ground Resistance for Vertical Bore Heat Exchangers With Groundwater Flow," *J. Energy Resour. Technol.*, vol. 125, no. 3, p. 183, Sep. 2003.

[10] N. Molina-Giraldo, P. Blum, K. Zhu, P. Bayer, and Z. Fang, "A moving finite line source model to simulate borehole heat exchangers with groundwater advection," *Int. J. Therm. Sci.*, vol. 50, no. 12, pp. 2506–2513, Dec. 2011.

[11] J. A. Rivera, P. Blum, and P. Bayer, "Influence of spatially variable ground heat flux on closed-loop

geothermal systems: Line source model with nonhomogeneous Cauchy-type top boundary conditions," *Appl. Energy*, vol. 180, pp. 572–585, 2016.

[12] M. Chalhoub, M. Bernier, Y. Coquet, and M. Philippe, "A simple heat and moisture transfer model to predict ground temperature for shallow ground heat exchangers," *Renew. Energy*, vol. 103, pp. 295–307, 2016.

[13] B. Sibbitt *et al.*, "Measured and Simulated Performance of a High Solar Fraction District Heating System With Seasonal Storage," 2007.

[14] A. Nguyen, P. Pasquier, and D. Marcotte, "Borehole thermal energy storage systems under the influence of groundwater flow and time-varying surface temperature," *Geothermics*, vol. 66, pp. 110–118, 2017.

4 Mine Thermal Energy Storage (MTES)

4.1 German pilot site Markgraf II

Christoph M. König, Torsten Seidel, Timo König

delta h Ingenieurgesellschaft

4.1.1 Conceptualization

4.1.1.1 UTES concept and specifications, scope and aims of the study

The aim of the German HEATSTORE sub-project is to create a technically and fully functional seasonal mine thermal energy storage pilot plant for the energetic reuse of the abandoned coal mine Markgraf II, with the emphasis on a two-year operating and monitoring phase. The generated data can be exploited for the implementation and dissemination of future deep geothermal storage systems.

The pilot plant aims at utilizing the abandoned coal mine Markgraf II, which is directly located under the premises of the International Geothermal Centre (GZB) in Bochum, as a seasonal mine thermal energy storage. Seasonal unutilized surplus heat from solar thermal collectors is shall be stored during the summer within the mine layout and produced during the winter for heating buildings of the GZB.

The area also includes the drilling and test facility site, on which the Bo.REX (Bochum Research and Exploration Drilling Rig) is currently located. This leads the way of a very cost-effective exploration (less than 5 %, when compared to standard industry drilling rates) of the flooded Markgraf II mine in a depth of approx. 63 m below ground. The injection and production well and the additional ten monitoring wells will be drilled with our own drilling rig.

The Markgraf II mine produced 37.043 tons of coal during 1953 to 1958. Based on a calculation with a coal density of 1,35 g/cm3, we can assume a void volume of approx. 27.439 m³. This volume does not include any drifts and shafts, which need to be analysed based on the mine layout. Considering the effect of mine subsidence, the remaining void volume will most likely be in the range of approx. 10 %. Utilizing a ΔT of 50 K within the mine water, a heat capacity of approx. 165 MWh, which resembles the yearly heat demand of the GZB compound, could be stored within dedicated drifts and former mining areas of Markgraf II for the heating season.

Based on this first evaluation the yearly GZB heat demand could be substituted by emission free solar thermal energy. After the two-year pilot phase is concluded the integration of the Markgraf II MTES into the district heating network of the "unique Wärme GmbH" can be tackled, as two CHP plants (7,2 MWth) are going to be put in operation by 7/2018 in a very close proximity of approx. 350 m to the GZB pilot plant.

4.1.1.2 System Geometry and related Geology

The site is located at the southern edge of the northerly dipping "Münster Cretaceous Basin". It is one of the biggest continuous sedimentary basins in Germany with sediments consisting primarily of Upper Cretaceous layers (Figure 4.1.1). Among these, the argillaceous marls of the Emscher Formation are of particular importance because they seal the upper aquifer. The Emscher Formation comprises Campanian, against the lower aquifer which lies within Upper Carboniferous and Cenomanian/Turonian strata. The Emscher Formation shields because of its sealing characteristics, the underlying hard-coal deposit of Carboniferous age. Close to the pilot plant location Carboniferous rocks are cropping out at the surface.

Geological Units

- Aquifer 1
- Tertiary
- Cretaceous, above Emscher-Formation
- Cretaceous, Emscher-Formation
- Cretaceous, Cenomanian/Turonian
- Lower Cretaceous
- Buntsandstein
- Zechstein (Upper Permian)

Figure 4.1.1 Geological units of the "Münster Cretaceous Basin"

4.1.1.3 Local geothermal and groundwater conditions

Hydrogeological Conceptualization

The groundwater flow in the "Münster Cretaceous Basin" can be schematized considering two different types of aquifers.

The first aquifer type is constituted by shallow aquifers: they are spatially discontinuous if the whole basin is considered; they are generally outcropping but can be locally overlapped and vertically bounded by impervious strata e.g. Emschermergel (Coniac/Santon).

The second is a deep aquifer, hundreds of meters thick in the central region, which corresponds to the intensely fissured Cenomanian-Turonian carbonate basement, which extends over the whole basin; it is hereinafter called deep aquifer. This aquifer is affected by a southward directed regional flow coming from the "Teutoburger Wald" mountains.

Thermal Rock and Groundwater Features

Thermal conductivity, thermal diffusion and volumetric heat capacity of rocks will be determined by laboratory tests using rock samples by the project partner GZB later on. The results of thermal conductivity and thermal diffusion measurements can then be determined by performing a statistical analysis of various measurements for each parameter and sample.

4.1.2 Modelling approach

4.1.2.1 Conceptual simulation model

In this study numerical groundwater flow and heat transport modelling is used to estimate the influence of a mine thermal energy storage pilot plant on the groundwater aquifer, the prediction of the physical environment and the assessment of the impacts of different pumping rates. Later on, monitoring programs will be developed and competing demands on the groundwater resource can be evaluated.

Understanding heat transport during the planning of geothermal plants is complicated by heterogeneities in the subsurface and cyclical plant loads. Based on the extensive mining situation in the Ruhr area within a complex geologic setting a stepwise modelling concept was developed (Figure 4.1.2).

The conceptual model was developed using maps and cross sections, existing data and data gathered during the field investigation of this study. It forms the basis for the understanding of the groundwater occurrence and flow mechanisms of the HEATSTORE site, and is used as basis for the numerical groundwater modelling.

The conceptual model as discussed includes the underground mining works (Figure 4.1.3), which are also part of the numerical groundwater model.

The concept comprises the following 3 scales with an increasing level of detail:

- Regional scale (>10.000 km²)

   The Regional scale includes geology and the transient mining (dewatering) influence in the regional area. Large scale transient groundwater models have been built to analyse the regional flow system. They deliver boundary conditions for the site scale.
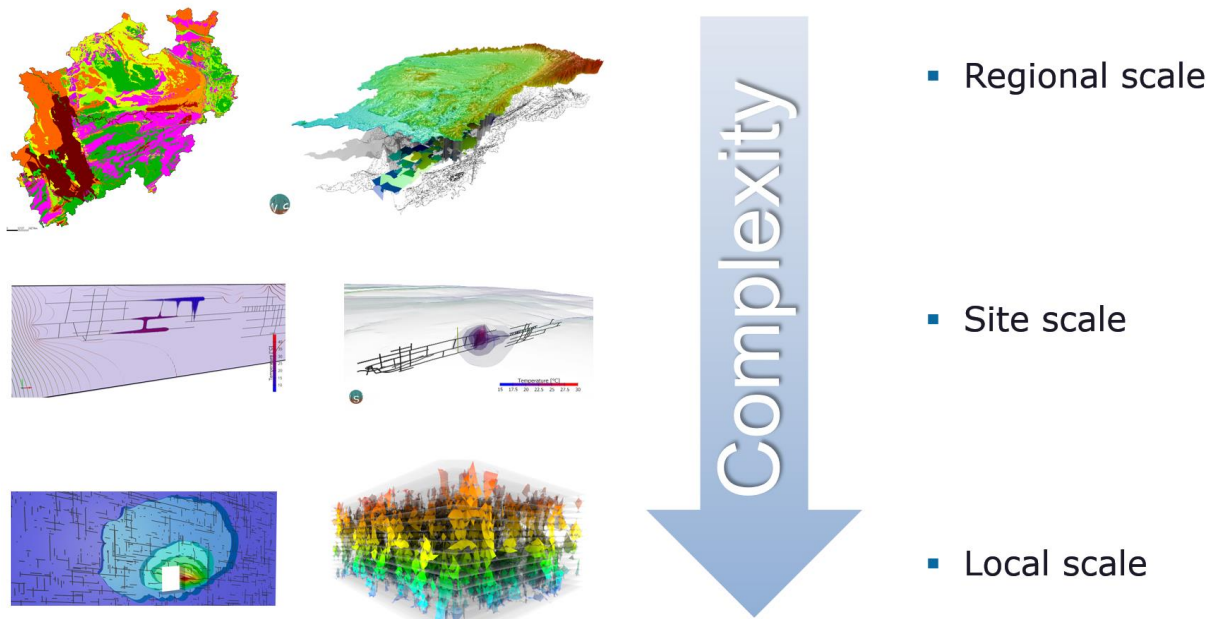
Figure 4.1.2 Stepwise modelling concept

- Site scale (~10 km²)

  The Site scale models the detailed underground mining works at the HEATSTORE site within a local geological setting. It enables planning, dimensioning and optimization of the energy storage pilot plant in terms for heating and cooling cycles.

- Local scale (<1 km²)

  At the local scale different parts of the pilot plant are modelled with a high detail. It is used to estimate local effects like the influence of fractures or different (residual) mine void volumes.
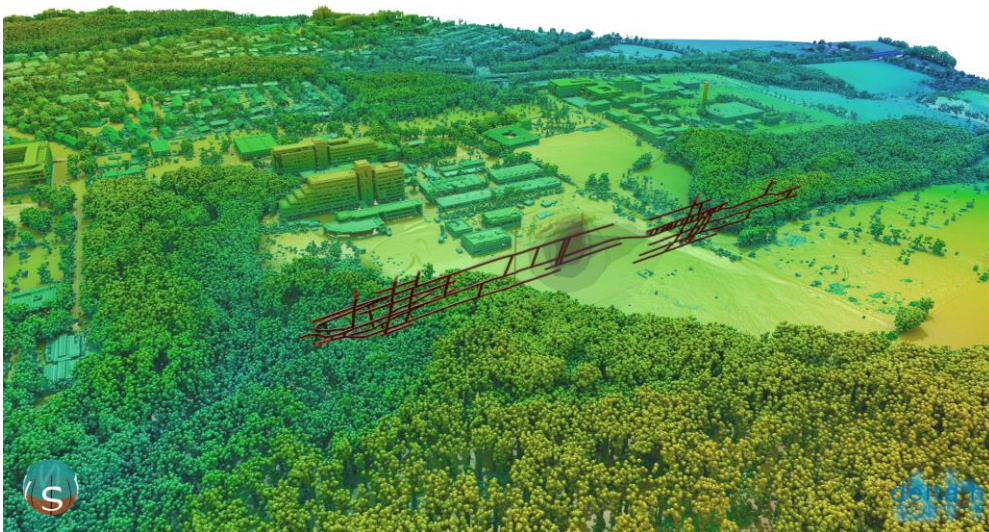
Figure 4.1.3 3D model of the local mining system.

Significant influence parameters are shown in Figure 4.1.4

Hydraulic permeabilities:
- (K1) Mine void – open
- (K2) Mine void – back filled
- (K3) Carboniferous rock (roof)
- (K4) Carboniferous rock (floor)
- (K5) Fault system
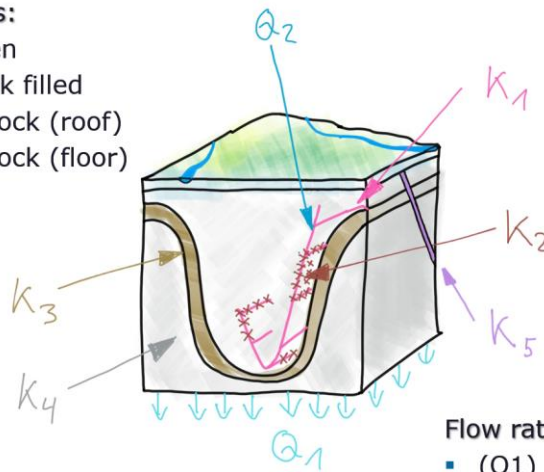
Flow rates:
- (Q1) Bottom outflow
- (Q2) Infiltration/production
- GW-recharge

Figure 4.1.4 Significant influence parameters

4.1.2.2 Pre-processing workflow

Regional scale

The regional scale consists of the two existing models *"Groundwater Model Northrhine-Westfalia"* (Figure 4.1.5) and groundwater model *"Münster Cretaceous Basin" (*Figure 4.1.6*).* The "Groundwater model Northrhine-Westfalia" was built by delta h for GROWA+ NRW 2021 and characterizes the upper aquifer of the whole federal state Northrhine-Westfalia (König 2017). The 2D horizontal model covers an area of about 33.000 km^2. It delivers regional information about geometry, conductivities, monitoring data and the upper groundwater surface.

The groundwater model "Münster Cretaceous Basin" (König et.al. 2017) was built by delta h for „Mine thermal energy storage Bochum" project – MTES (Figure 4.1.6).

With an area of about 14.000 km^2 the 3D groundwater model covers the whole Cretaceous Basin in the area "Münsterland"
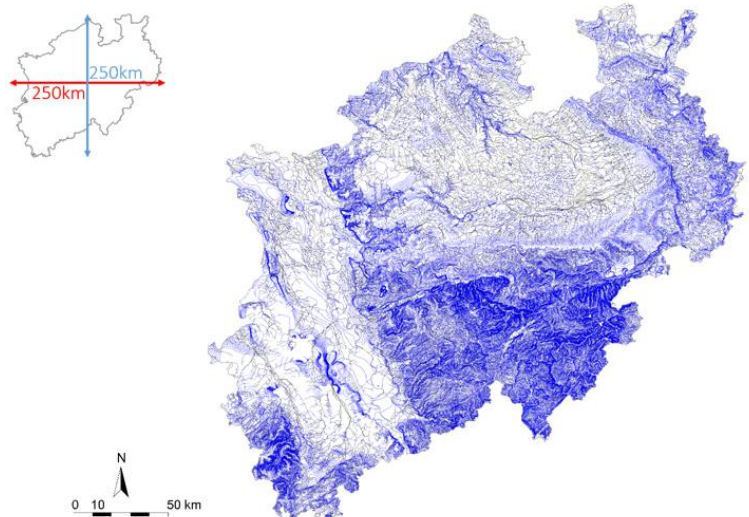
Figure 4.1.5 Groundwater model Northrhine-Westfalia

and delivers information about the regional geology as well as the influence of the complex mining setting (Figure 4.1.7). Modelling the impacts of mine dewatering and flooding on a regional scale as for the basin presents many challenges including the appropriate discretization of mine voids and the accurate modelling of layered aquifer systems. To predict the environmental impacts of both the historic mining activities and future operations, a detailed conceptual model of the aquifer systems and a 3-dimensional model of the mining areas were incorporated into a numerical groundwater model. This model was used to simulate the dewatering and post-closure rebound of the water tables in the vicinity of the mine.
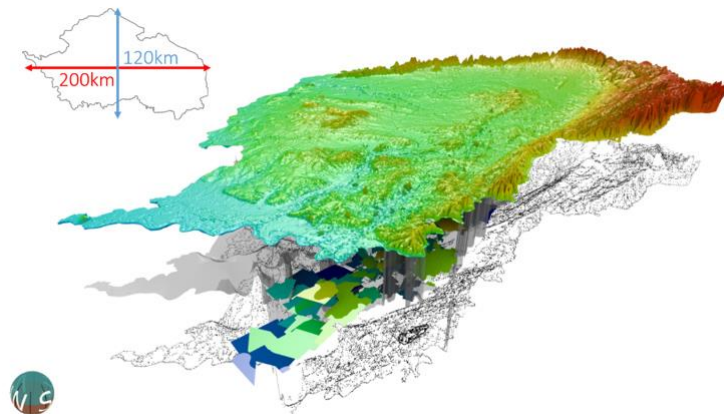
Figure 4.1.6 Groundwater model "Münster Cretaceous Basin"

Groundwater enters the model domain as direct recharge from rainfall. The deeper aquifer is recharged by limited vertical seepage from the quaternary aquifer. Water leaves the model domain via perennial and non-perennial rivers and "shallow" groundwater flow in the upper aquifer system. Notwithstanding the type, all surface water drainages were classified as continuously gaining river courses with no exfiltration of water allowed.

The underground mine workings were integrated into the model domain as drains on a separate model layer aligned to the depth of the mine voids. Groundwater is only allowed to discharge into the underground mine voids and it is assumed that any groundwater entering the mine voids is removed (pumped out) from the model domain.
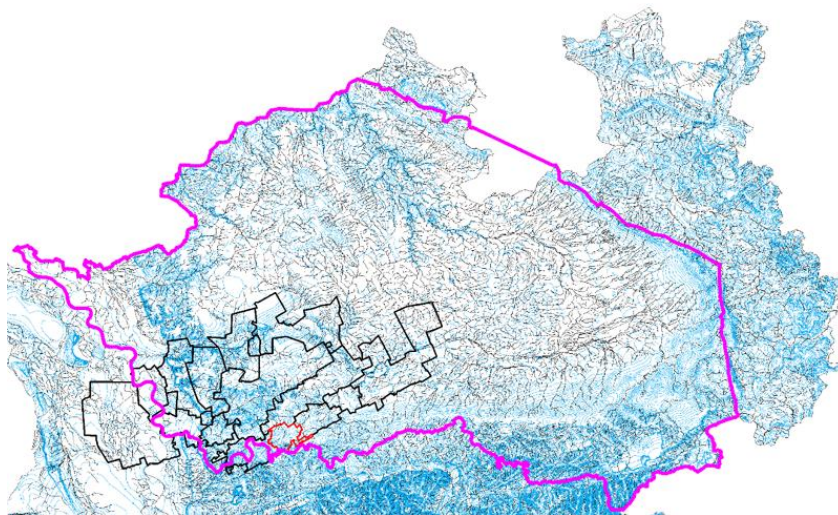
Figure 4.1.7 Dewatering provinces at different flooding levels (black lines, Heatstore site located in the red province) and boundary of the regional model (purple)

As the Carboniferous rock crops out in Bochum the model had to be extended in the South to cover the HEATSTORE site.

It includes a detailed geologic layer distribution with the local syncline structure and coal seams at the site (Figure 4.1.10). In accordance with the developed conceptual model, the upper model layer simulates the upper aquifer system and the lower layers represent the deeper underlying aquifers and aquicludes.

Groundwater enters the model domain as direct recharge from rainfall. Water leaves the model domain via perennial and non-perennial rivers and "shallow" groundwater flow in the upper aquifer system. Notwithstanding

the type, all surface water drainages were classified as continuously gaining river courses with no exfiltration of water allowed. The regional mining influences are assigned as boundary conditions taken over from the regional scale.

In contrast to the regional scale, underground mine workings were integrated into the model domain as 1D fracture elements aligned to the depth of the mine voids.

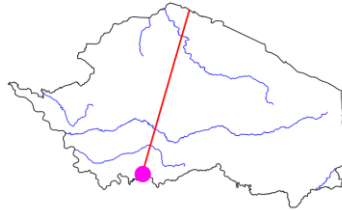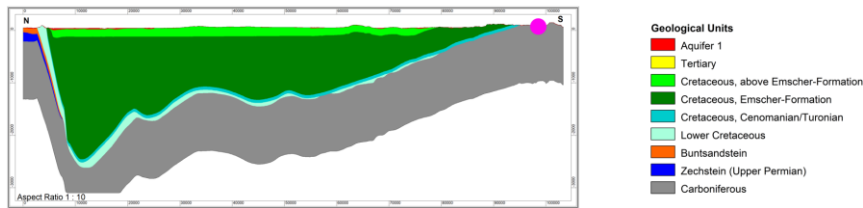- Expansion to „Heatstore" site
- Boundary conditions for site model

Figure 4.1.8 Cross section through extended groundwater model "Münster Cretaceous Basin"; colored by regional geology

Geological Units
- Aquifer 1
- Tertiary
- Cretaceous, above Emscher-Formation
- Cretaceous, Emscher-Formation
- Cretaceous, Cenomanian/Turonian
- Lower Cretaceous
- Buntsandstein
- Zechstein (Upper Permian)
- Carboniferous

Site scale

The 3D site scale model covers an area of ~10 km² with a vertical resolution of 18 layers. It models the local aquifer system and includes the digitalized mine void model (Figure 4.1.9 and Figure 4.1.10).
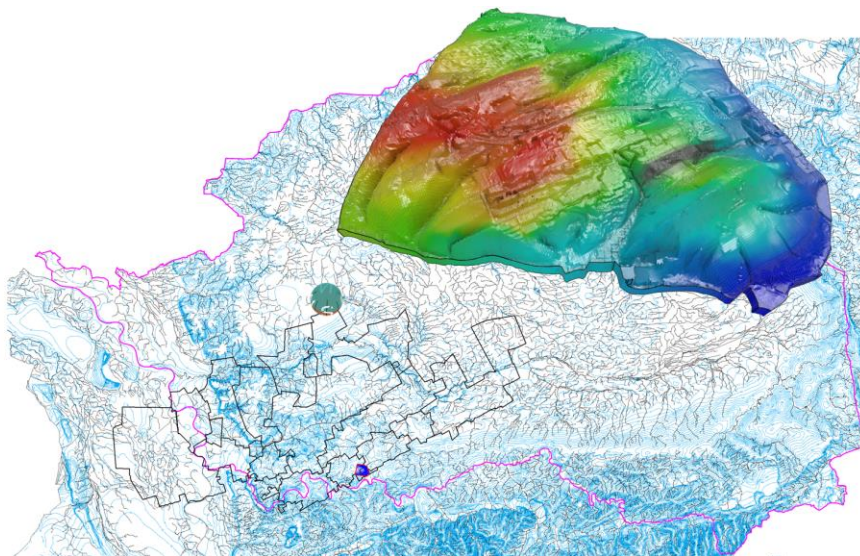
Figure 4.1.9 Location of the site scale model (inset at the top) in correlation to the regional model (blue area in the background map)
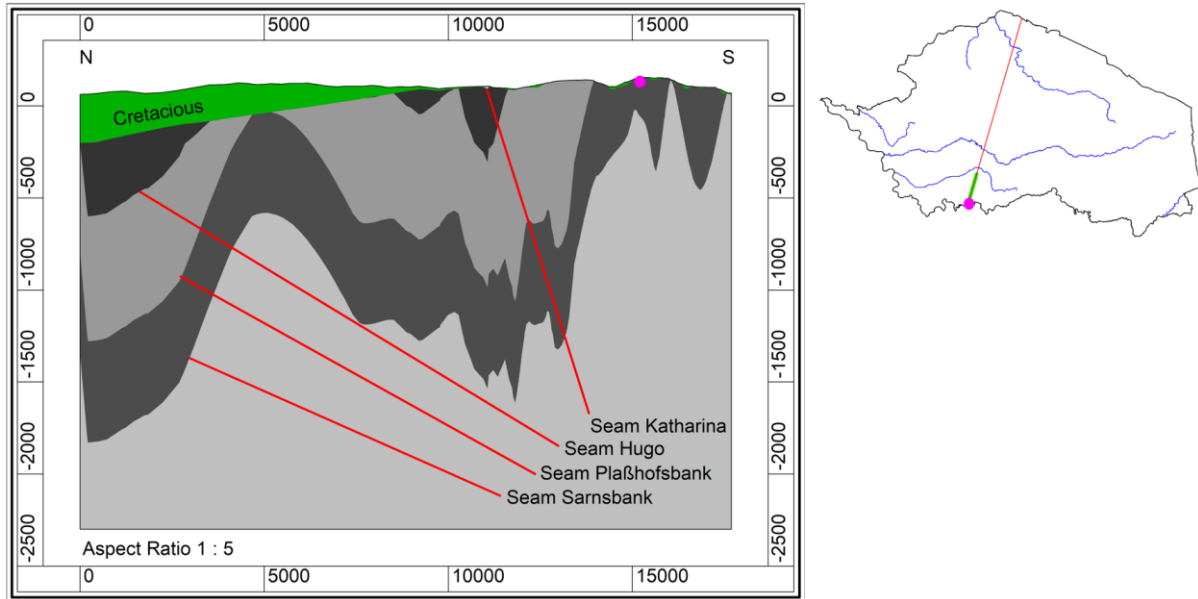
Figure 4.1.10 Cross section through the local geological system

Local scale

Carboniferous rock at the site is highly fractured. Groundwater flow takes place in the fracture network where advection and gravity forces are the dominant processes. For characterizing the flow and transport phenomena in the fractured rock on a local scale, it is necessary to model a discrete fracture matrix system (König 1998).

The local fractured Carboniferous rock is exposed in a sandstone pit close to the site. Measurements of the local carboniferous fracture data have been performed by Witthüser and Himmelsbach (1997) including a tracer test between two boreholes. The results were analysed to get the statistic parameters for a stochastic fracture generation which was performed in a local model domain:

Table 4.1.1 Statistical parameters of the measured clusters

cluster	orientation in space	spherical angle Q	spherical variance φ	concentration parameter k
I	(a,f) = (274°,88°)	8.2°	0.95	16
II	(a,f) = (71°,6°)	8.2°	0.95	17
III	(a,f) = (309°,4°)	12.3°	2.35	16

The clusters of preferred orientations are determined by identifying their respective maximum densities and choosing an appropriate selection angle for each cluster. A symmetrical Fisher (i.e. spatial normal) distribution is assumed for each cluster. The Fisher distribution is based on a unimodal distribution function, which describes the variation of vector orientation from a principal direction. The basis for this function is a spherical normal distribution that is characterized by a circular symmetrical arrangement of data around a vector (Wallbrecher 1986). It has the density function f. The spherical angle φ is the angle between the mean value and the observed value. The concentration parameter κ depends on the number of random samples.

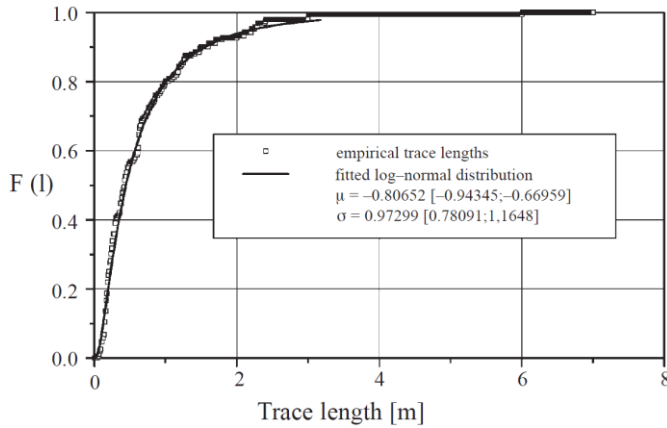$$f(\phi, \kappa) = \frac{\kappa^{\kappa \cos \phi}}{4\pi \sinh \kappa}$$

Figure 4.1.11 Fitting of the empirical trace lengths by log-normal distribution (Witthüser 1996)

The lengths are generated stochastically using log-normal distribution. Figure 4.1.11 shows the fitting of fracture trace length by log-normal distribution. To give the fracture an irregular shape the distance the four lengths l1 to l4 are generated separately to define the corners of the fracture plane.

In the local model fractures are generated by using the analysed statistical data and are approximated by plane elements. The volume elements of the surrounding porous rock matrix are generated by means of a layer technique (Figure 4.1.12).
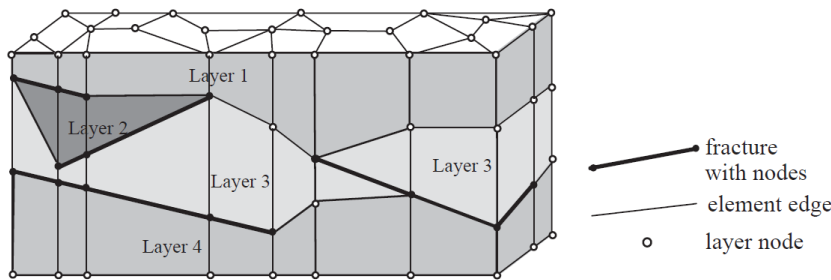
Figure 4.1.12 Fractures in a three-dimensional mesh using layer technique

With a fixed potential head assigned at the inflow and outflow boundary a combined hydraulic conductivity (porous media/fractures) can be calculated and transferred to the site model.
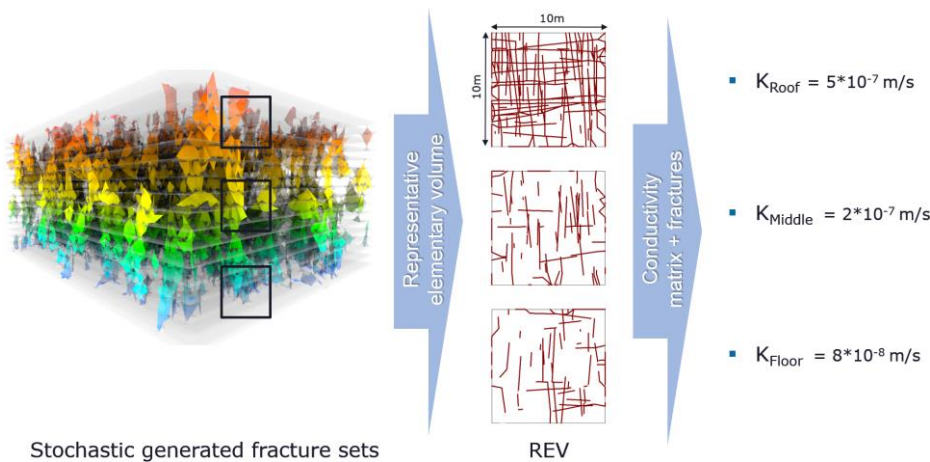
Figure 4.1.13 By stochastic fracture generation estimated hydraulic conductivities (Carboniferous)

$K_{Roof} = 5*10^{-7}$ m/s

$K_{Middle} = 2*10^{-7}$ m/s

$K_{Floor} = 8*10^{-8}$ m/s

4.1.2.3 Computational approach and software

The software code chosen for the numerical modelling work was the 3D groundwater flow and transport model SPRING, developed by the delta h Ingenieurgesellschaft mbH, Germany (König, 2014). The program was first published in 1970, and since then has undergone a number of revisions. SPRING is widely accepted by environmental scientists and associated professionals. SPRING uses the finite-element approximation to solve the groundwater flow and transport equations. This means that the model area or domain is represented by a number of nodes and elements. Hydraulic and thermic properties are assigned to these nodes and elements and an equation is developed for each node, based on the surrounding nodes. A series of iterations are then run to solve the resulting matrix problem utilizing a pre-conditioning conjugate gradient (PCG) matrix solver for the current model. The model is said to have "converged" when errors reduce to within an acceptable range. SPRING is able to simulate steady and non-steady flow, contaminant transport, density dependent transport as well as heat transport, in aquifers of irregular dimensions and different model layers with varying thicknesses as well as out-pinching model layers are possible.

4.1.3 Scenarios and preliminary results

4.1.3.1 Groundwater flow calculation

A steady-state calibration of the site groundwater flow model was performed using 8 groundwater level data points within the model domain. Only water levels observed in groundwater monitoring boreholes were considered representative of the shallow and deep aquifers and used for the calibration. Figure 4.1.14 shows the modelled groundwater surface of the upper aquifer (steady state).

4.1.3.2 Mine site heat transport calculations

Heat transport in groundwater is driven by advection, hydromechanical dispersion and the heat conduction in fluid and matrix. It can be mathematically described by the generalized heat transport equation:

$$\underbrace{\frac{\partial(n\rho S_r c_w T)}{\partial t}}_{\substack{\text{storativity term} \\ \text{in the fluid}}} + \underbrace{\frac{\partial((1-n)\rho_s c_s T)}{\partial t}}_{\substack{\text{storativity term} \\ \text{in the matrix}}} + \underbrace{\nabla\left(n\rho S_r c_w (\vec{J_k} + \vec{J_d} + \overrightarrow{J_{m,w}}) \right.}_{\substack{\text{energy flux} \\ \text{in the fluid}}} + \underbrace{\left. (1-n)\rho_s c_s \overrightarrow{J_{m,s}}\right)}_{\substack{\text{energy flux} \\ \text{in the matrix}}} = \underbrace{q(T_{in} - T)}_{\substack{\text{source} \\ \text{terms}}}$$

Material parameters:

n   porosity [-]

ρ, ρ_s density fluid, density matrix [kg/m³]
S_r saturation [-]
c_w, c_s specific heat capacity of fluid and matrix [(Ws)/(kgK)]]

Variables:
v   distance velocity [m/s]
T   temperature [K]
T^{in} temperature in- and outflow [K]
t   time variable [s]
q   = div v [1/s]

Energy flux:
$\vec{J_\kappa} = \vec{v}\,T$ advection
$\overrightarrow{J_m} = -D\nabla T$ hydro mechanical dispersion, D is the symmetrical dispersion tensor [m²/s]]
$\overrightarrow{J_{m,w}} = -\lambda_w \nabla T$ heat conduction in fluid, λ_w is the heat conductivity of the fluid [W/(mK)]
$\overrightarrow{J_{m,s}} = -\lambda_\vartheta \nabla T$ heat conduction in matrix, λ_s is the heat conductivity of the matrix [W/(mK)]

The first terms on the left hand side are the storativity term in the fluid and the matrix followed by the energy flux in the fluid and the matrix. The right hand side is the source term. For steady-state modelling the storativity term vanishes.
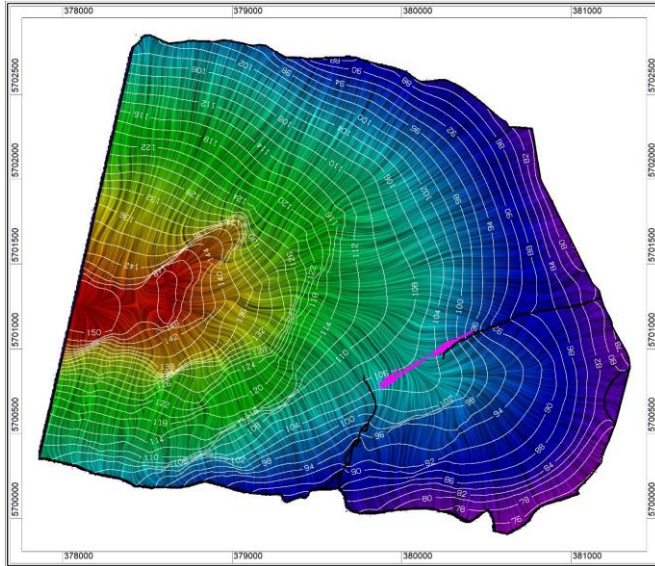

Figure 4.1.14 Calculated groundwater surface of the upper aquifer (white contour lines) and flow field colored by potential head from red=high to purple=low, mine site in magenta

Scenario A

Figure 4.1.15 shows the setup for a steady state heat transport calculation (scenario A). Warm water with a temperature of 35 °C and a flow rate of 1.600 m³/a is infiltrated at level 4 (MP1) while cool water is extracted with the same flow rate at level 1 (MI1).

- Steady state
  (flow and heat transport)

- MI1 cool site Ort 1
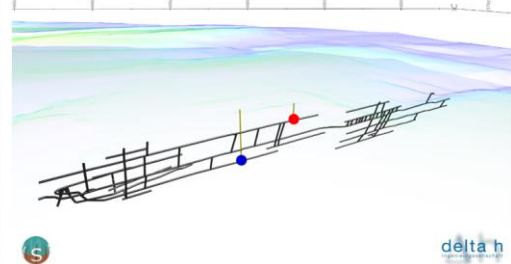
- MP1 hot site Ort 4 (35°C)

- 1.600 m³/a
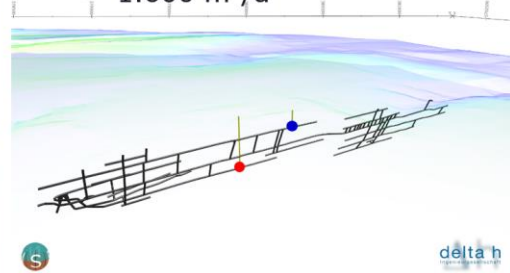
Figure 4.1.15 Site setup for heat transport calculations (scenario A)

Figure 4.1.16 shows the calculated temperature distribution of the steady state flow and heat transport calculation (scenario A). A temperature plume is developing from the infiltration point to the West in direction
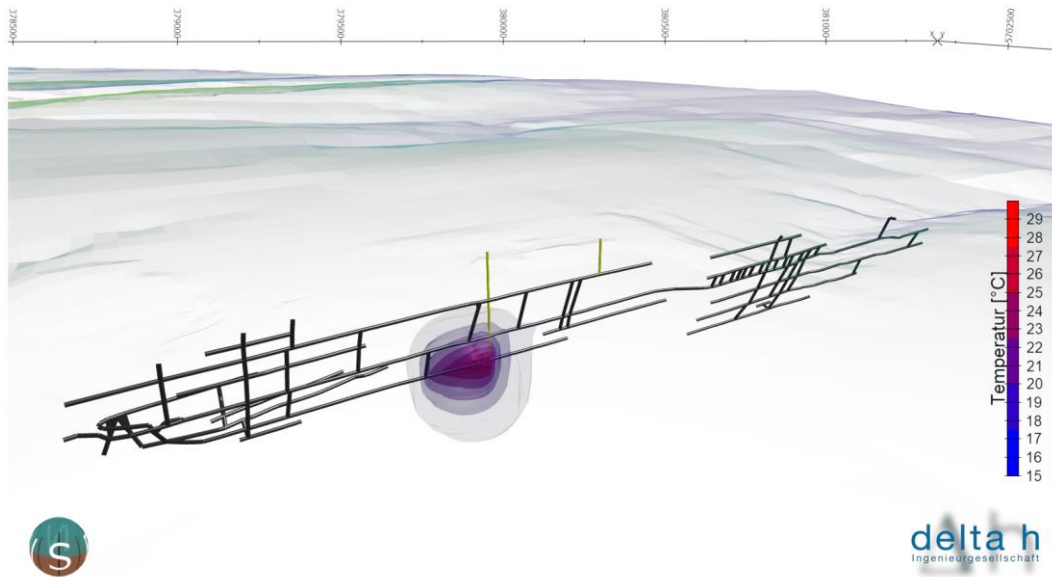
Figure 4.1.16 Steady state temperature distribution (scenario A)

of the (open) mine void. Because of the steady state calculation type the result can be classified as "worst case" as the plume is much bigger than it would be under transient conditions.
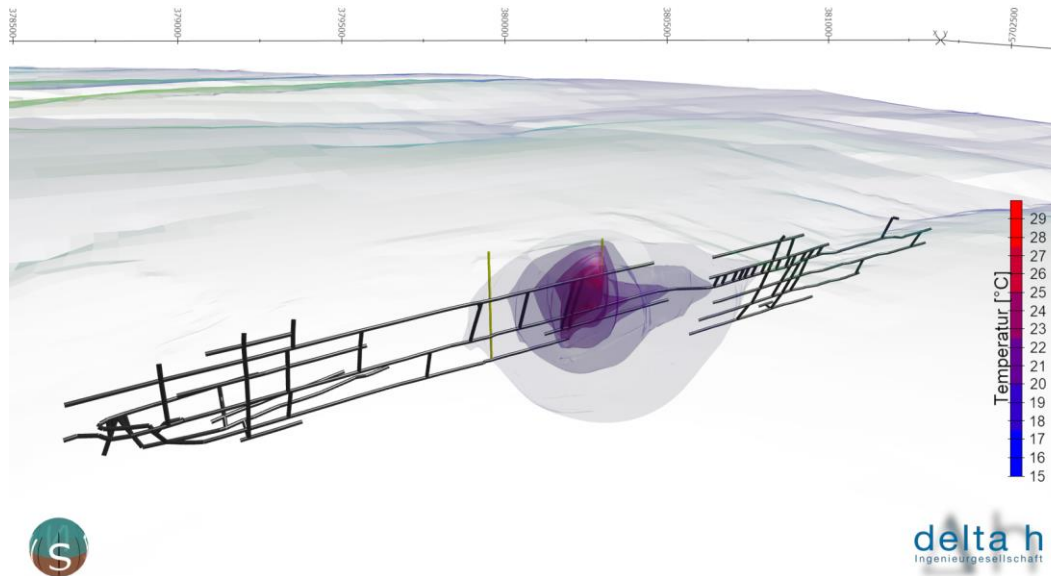
Scenario B

To estimate the impact of different pumping locations and for optimization the model can be used to calculate different scenarios. Figure 4.1.17 shows the setup for an alternative scenario B. Warm water with a temperature of 35 °C and a flow rate of 1.600 m^3/a is infiltrated at level 1 (MI1) while cool water is extracted with the same flow rate at level 4 (MP1).

- Steady state (flow and heat transport)
- MI1 hot site Ort 1 (35°C)
- MP1 cool site Ort 4
- 1.600 m^3/a

Figure 4.1.17 Site setup for heat transport calculations (scenario B)

Figure 4.1.18 shows the calculated temperature distribution of the steady state flow and heat transport calculation (scenario B). A temperature plume is developing from the infiltration point following the mine void down and to the East. Because of the steady state calculation type the result can be classified as "worst case" as the plume is much bigger than it would be under transient conditions.

Figure 4.1.18 Steady state temperature distribution (scenario B)

Scenario C

Figure 4.1.19 shows the setup for an alternative scenario C. Warm water with a temperature of 35 °C and a flow rate of 1.600 m^3/a is infiltrated at level 4 (MO1) while cool water is extracted with the same flow rate at the same level (MI1).
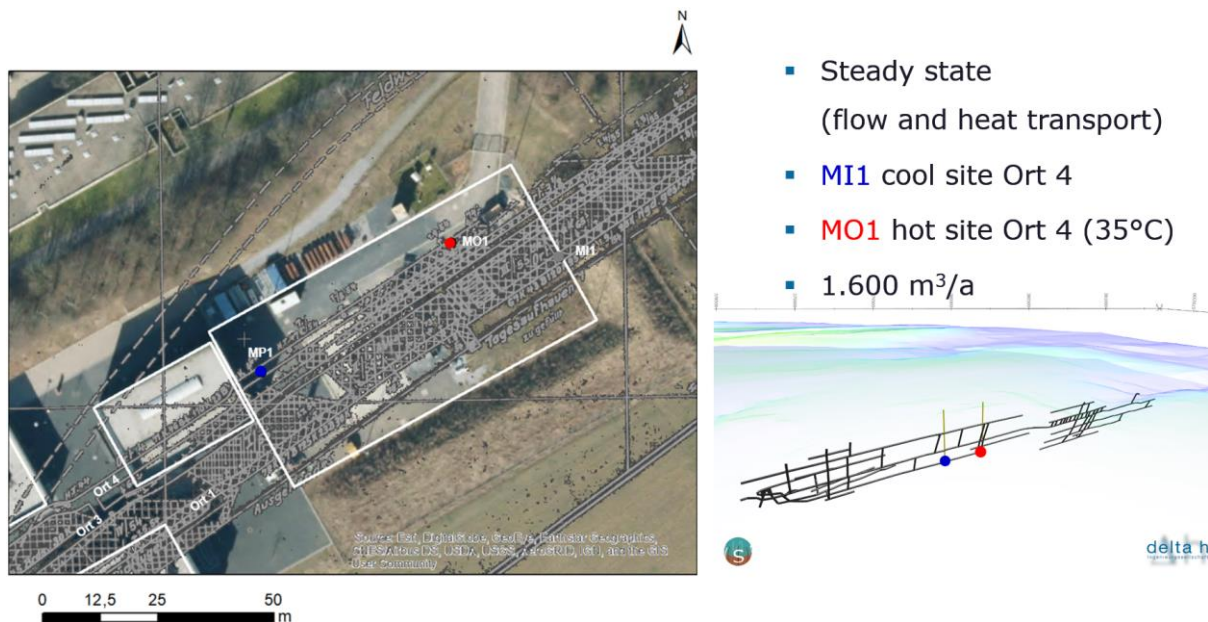

- Steady state (flow and heat transport)
- MI1 cool site Ort 4
- MO1 hot site Ort 4 (35°C)
- 1.600 m^3/a

Figure 4.1.19 Site setup for heat transport calculations (scenario C)

Figure 4.1.20 shows the calculated temperature distribution of the steady state flow and heat transport calculation (scenario C). A temperature plume is developing from the infiltration point following the mine void to the West. Because of the configuration with both infiltration and production wells at the same level the result shows a hydraulic and thermic "shortcut".
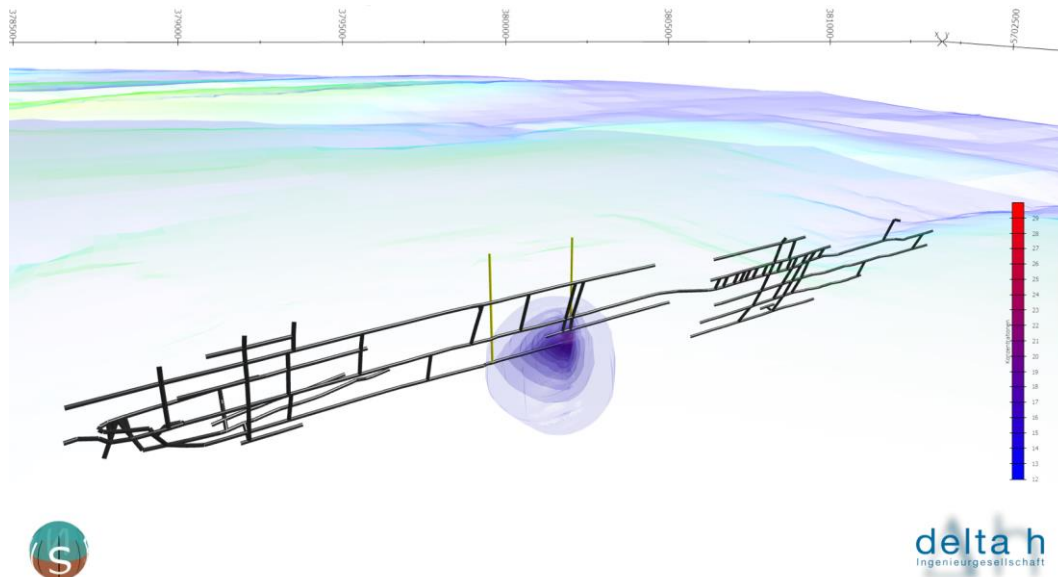
Figure 4.1.20 Steady state temperature distribution (scenario C)

The results of pumping tests showed that borehole MI1 Ort 1 (scenarios A and B) only provides a relatively low productivity. For this reason the circulation concept was changed to scenario C, which was used as reference scenario for further investigation.

Sensitivity analysis

The challenge in modelling the fracture system lies in the large number of unknown parameters and the small number of measured and known parameters for the Upper Carboniferous of the Ruhr district. The aim of the sensitivity analysis at this point is to assess the understanding of the hydraulic model and the dynamics of the system, as well as to identify sensitive parameters which have a critical effect on the system.

Basic parameters influencing the numerical model described above are the hydraulic conductivity, boundary inflows and outflows as well as the position and flow rate of the two-well system.

Reliable parameters of the model are the geometry of the mining system as well as the geological layers (stratigraphy).

Unknown, however, is the exact permeability of the local Carboniferous layers, for which a bandwidth can be defined.

The sensitivity analysis has been conducted to assess the impact of uncertainty associated with assigned model parameters. The calibrated groundwater flow model was used as the basis with the following input parameters varied:

- Mine system permeability (opening width)
- Saturated hydraulic conductivities of the Upper Carboniferous
- Flow rates of the injection-/production wells

The values of these parameters were subsequently varied within reasonable boundaries and reassigned to the numerical model to reflect the uncertainty associated with their determination. The standard approach of numerical model sensitivity analysis was followed by multiplying the parameter with fixed constant values according to Table 4.1.2.

Table 4.1.2 Parameter variations for the sensitivity study, Bochum site (*reference scenario).

Hydraulic conductivities Carboniferous [m/s]	Mine opening width b [m]	Injection and production rate [m³/a]
x0.1	x0.1	x0.1
-	x0.5	x0.5
x1*	4*	1600*
-	x2	x2
x10	x10	x10

Figure 4.1.21 - Figure 4.1.26 show the results of the sensitivity analysis by three dimensional temperature plumes and temperature breakthrough curves at the production well.
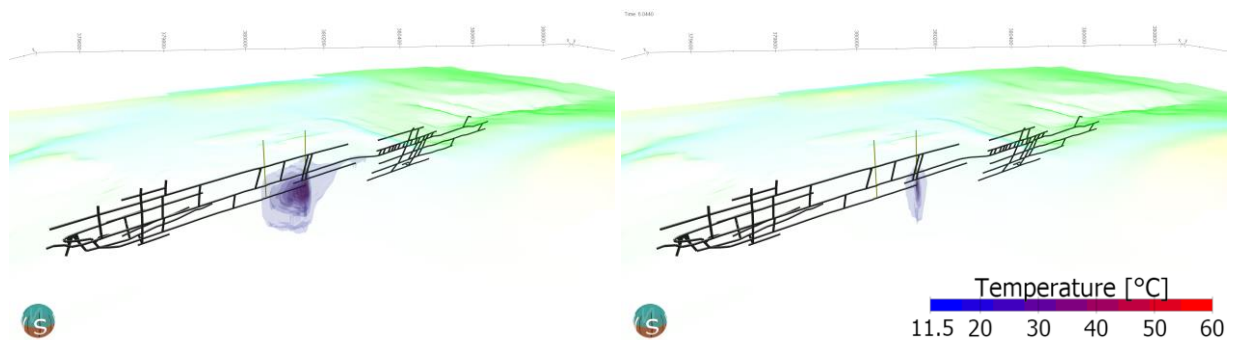

Figure 4.1.21 Modelled temperature distribution after 6 months reflecting 2 times lower (left) and 2 times higher (right) mining system permeabilities
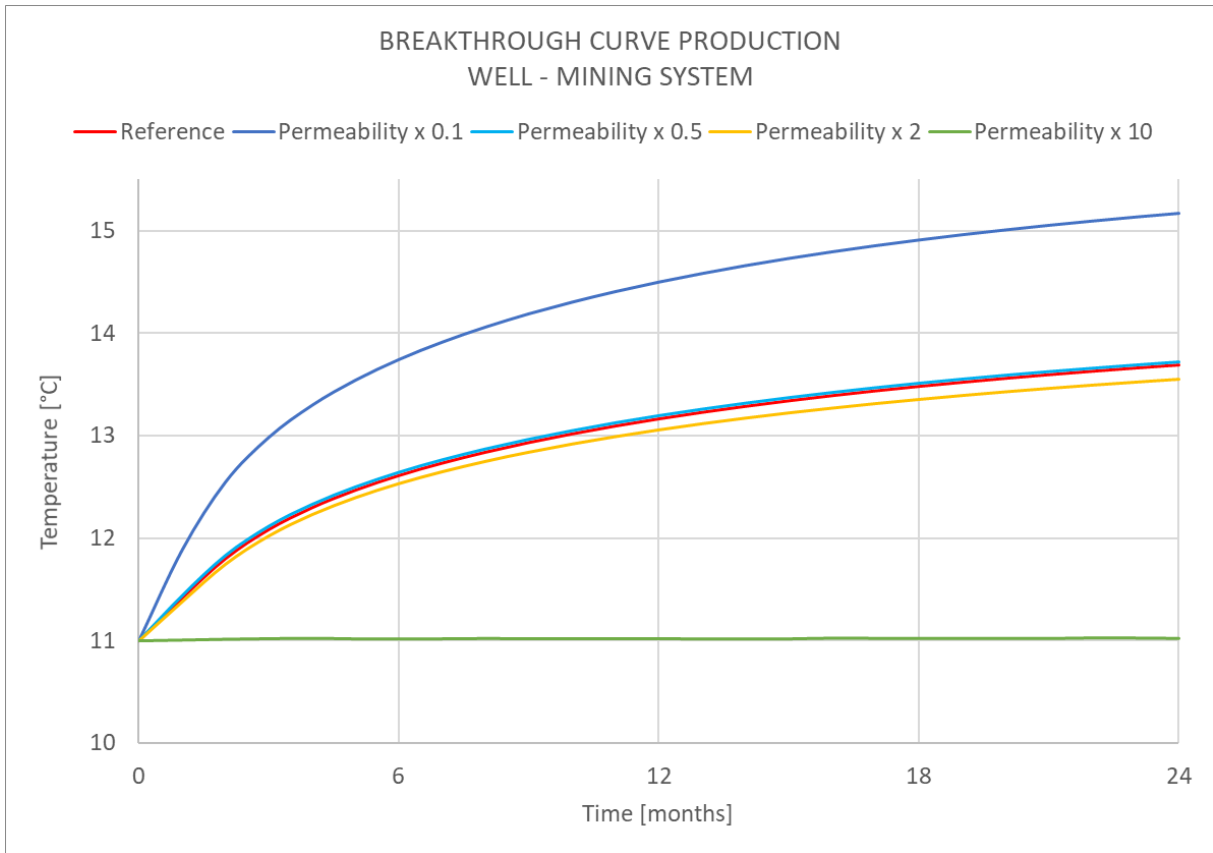
Figure 4.1.22 Modelled temperature breakthrough curve at the production well by variation of mining system permeability (scenario C).

Figure 4.1.22 shows temperatures at the production well (scenario C) in comparison to different mine system permeabilities. As expected, low permeabilities lead to low volumes that produce a high water velocity with increased recovery rates while high permeabilities cause lower recovery rates at the production well. The reason for the expansion of the temperature plume with a lower permeability is that the mining system works as a preferential pathway. It generates specific migration routes that support higher fluxes compared to the surrounding rock. If the effective diameter of such pathways are limited, the volume also decreases and migration along the mining system increases.
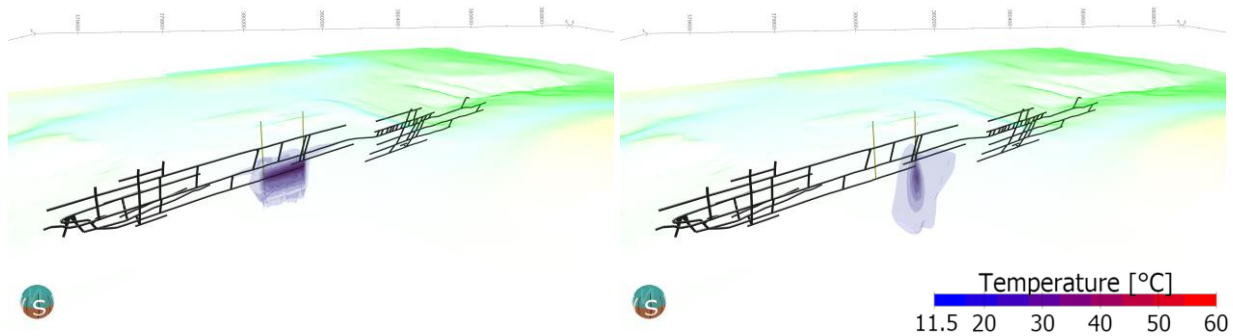

Figure 4.1.23 Modelled temperature distribution after 6 months reflecting 10 times lower (left) and 10 times higher (right) hydraulic conductivities of the Carboniferous rock
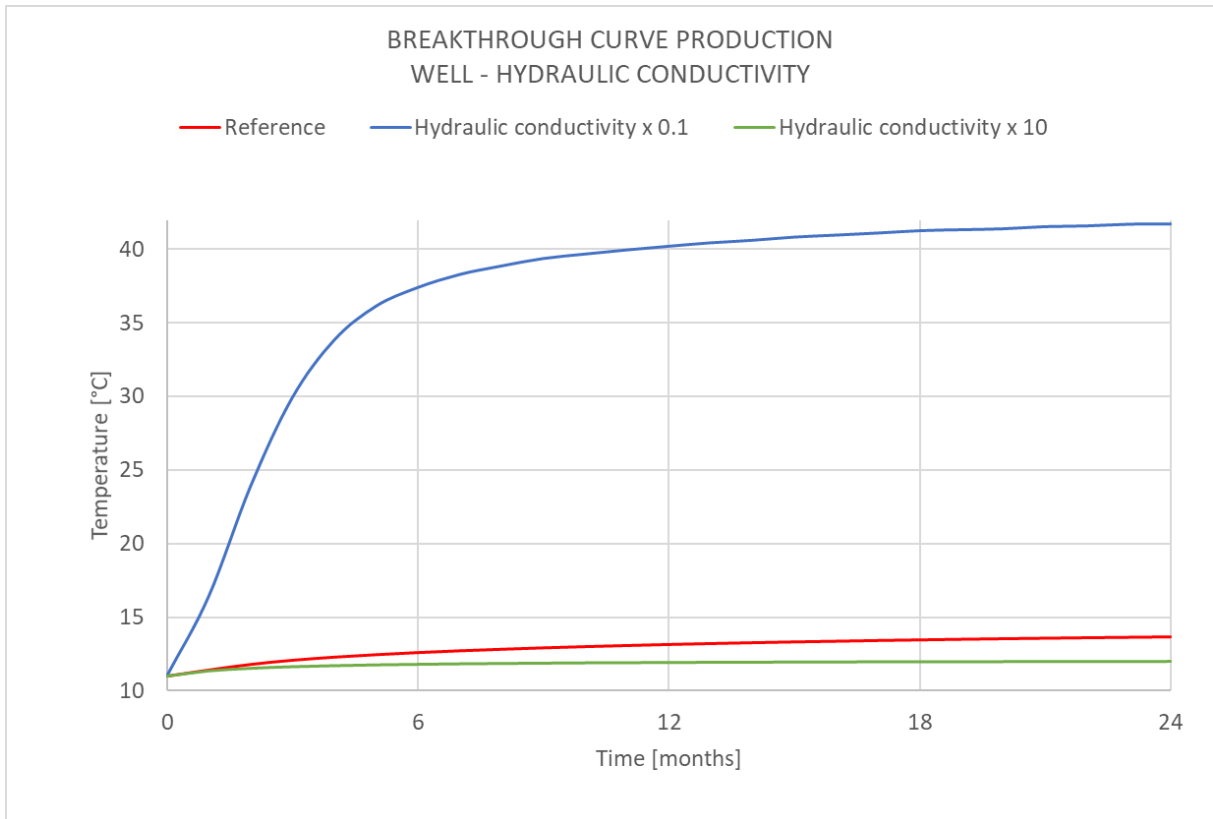
Figure 4.1.24 Modelled temperature breakthrough curve at the production well by variation of hydraulic conductivities (scenario C).

Figure 4.1.24 shows the effect of varying hydraulic conductivities to the temperature distribution. A scenario with globally 10 times higher hydraulic conductivities leads to lower recovery rates at the production well as a higher amount of the infiltrated warm water is distributed into rock matrix.

A globally 10 times lower permable rock matrix increases the permeability contrast between mining system and surrounding rock, preferential pathways dominate even more and the plume can migrate faster in the direction of the production well.
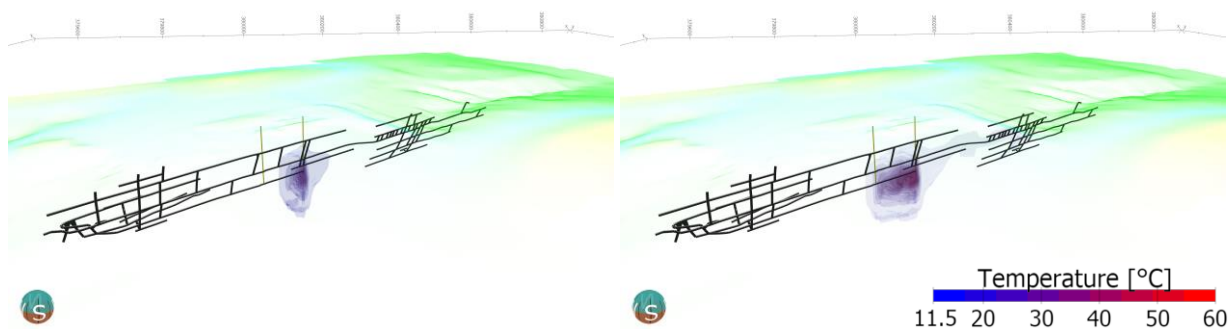

Figure 4.1.25 Modelled temperature distribution after 6 months for 800 m³/year (left) and 3200 m³/year (right) system flow rates
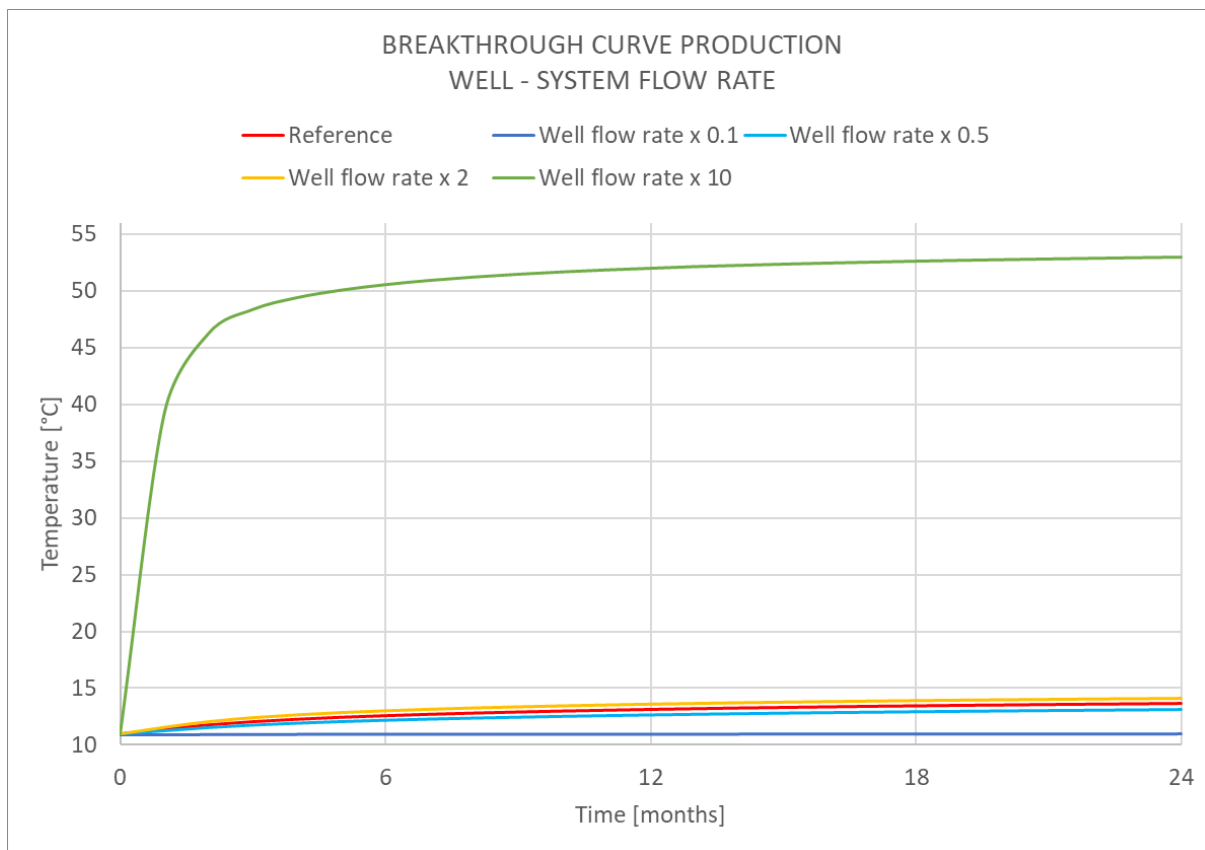
Figure 4.1.26 Modelled temperature breakthrough curve at the production well by different system flow rates (scenario C).

Figure 4.1.26 shows the effect of different system flow rates to the temperature distribution. Higher flow rates lead to an increased temperature plume migration along the mining system and result in higher recovery rates. Lower flow rates also decrease the migration in the direction of the production well. For a practical field-experiment (0) high injection rates are recommended, since the temperature can be recovered within a short period of time.

In-situ tests

In December 2020 in-situ tests were carried out to predict the plant operation accurately and update the model. The provided data sets were used to calibrate the SPRING model. Over a period of 7 days 46 °C warm water was pumped into to the system with a flow rate of 5.8 m^3/h. It was circulated between injection well MO1 and production well MI1 (Ort 4 - scenario C). After 7 days, pumping was stopped and the system was continuously monitored. The injection test, or transient state data set, reflects the desired response to injection.

The SPRING model should ideally be able to follow the steady-state data and also accurately model the change in temperature during the transient state.

For the transient state the proposed injection scenario was simulated using the model by keeping infiltration and production rates constant. The model was set to inject 46 °C warm water at the injection well and extract the same amount of water at production well. The initial temperature of the system was set at 11 °C.

Figure 4.1.27 shows the modelled temperature distribution for the injection test between MO1 (infiltration) and MP1 (production) wells. Figure 4.1.28 shows the temperature response of the calibrated model at the production well.
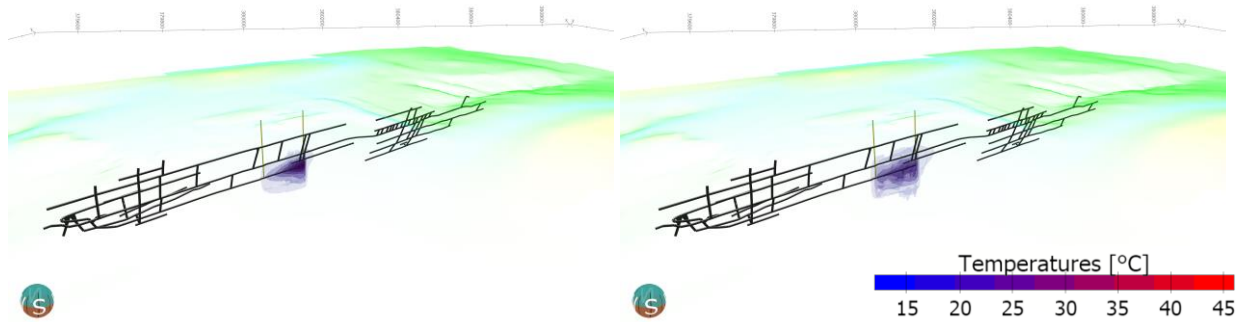
Figure 4.1.27 Modelled temperature distribution after 3 days (left) and 7 days (right) of the in-situ test
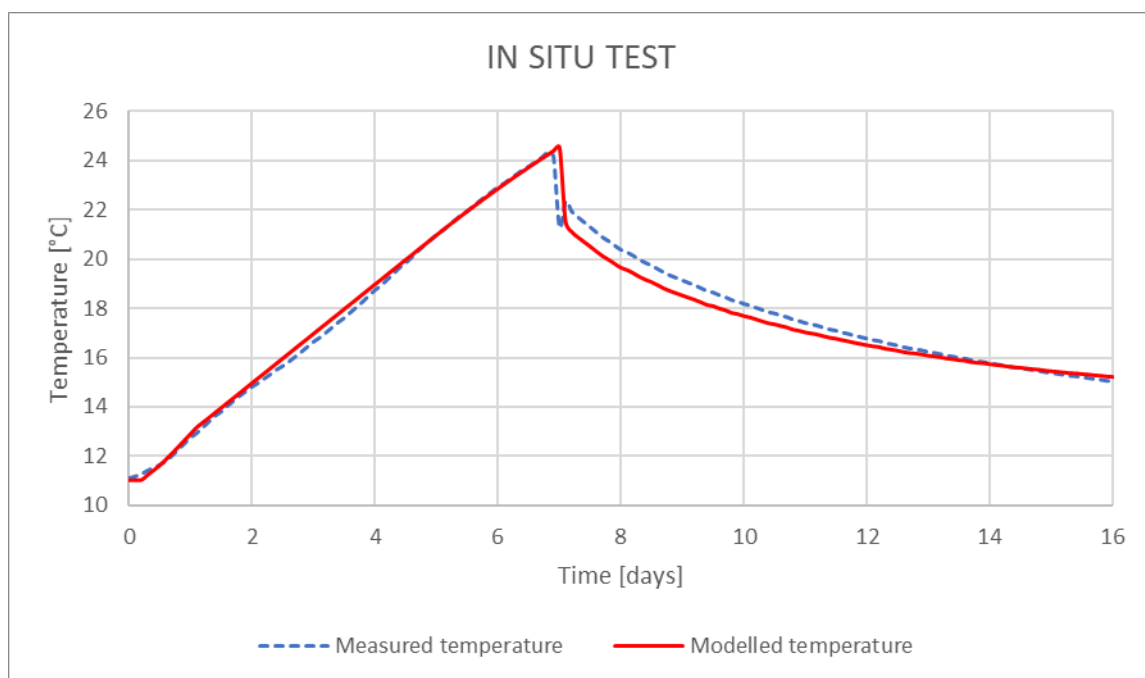

Figure 4.1.28 Modelled temperature distribution compared to measured in-situ temperature profile.

As the injection rate is much higher in comparison to the sensitivity analysis, temperature at the production well increases more rapidly. After 7 days infiltration was stopped and temperatures decreased as expected. In comparison to the infiltration phase the system reacts with a slower temperature decrease.

4.1.4 Analysis and discussion

4.1.4.1 Predictive and sensitivity-related learnings

Geothermal storage systems are a promising technology for heating and cooling buildings with renewable energy sources. The energy performances of these systems depend on the properties of the mine, the surrounding rock and the groundwater flow. In this work, the operation of a seasonal mine thermal energy storage pilot plant has been simulated, using a finite-element subsurface flow and heat transport modelling code (SPRING).

The relative influence of the regional and local mining system, hydrogeological and thermal rock property has been investigated running a set of simulations and analysing the resulting fluid temperatures.

The results of a sensitivity analysis show that the simulated temperature distribution proved to be highly sensitive to parametrisation of the mining system as well as the assigned hydraulic conductivity values of the different formations, which are at this stage not yet sufficiently assessed for the wider area of interest.

A hydraulically open mining system (in contrast to the surrounding rock) can dominate the system. Despite this, migration requires two conditions, pressure and flow. Reducing flow rates at both wells also reduces the migration radius. A relocation of the production well closer to the infiltration well could also supress migration.

However, if the permeability contrast between mining system and surrounding rock increases (higher mining permeability and/or lower rock permeability), preferential pathways dominate even more and the plume can migrate faster in the direction of the production well.

At this time, we observe that the condition of the mine is a very important property for the hydraulic pathways and should be further investigated to optimise the overall performance of the system. Besides that, heat conductivity of the surrounding rock heavily influences the resulting fluid temperatures, as in-situ tests showed.

4.1.5 References

König, C., Becker, M., Diehl, A., Seidel, T., Rosen, B., Rüber, O. & Zimmermann, C. (2018): SPRING - Simulation of Processes in Groundwater. - 5. Aufl.: 478 S.; Witten.

König, T., Rüber, O. & König, C. (2017): Erstellung der Grundwasseroberfläche für das gesamte Bundesland NRW als Datengrundlage für das Kooperationsprojekt GROWA+ NRW 2021 (unveröffentlicht). - Im Kooperationsprojekt GROWA+ NRW 2021, Im Auftrag vom Landesamt für Natur, Umwelt- und Verbraucherschutz Nordrhein-Westfalen; Witten (delta h Ingenieurgesellschaft mbH).

König, C., Rüber, O., Seidel, T., Zimmermann, C. (2017): Geo-Mine Thermal Energy Storage - Studie zur thermischen Nachnutzung von Steinkohlebergwerken am Beispiel des Bergwerks Prosper-Haniel am Standort der Innovation City Bottrop; Teilvorhaben: Numerische Modellierung (FKZ 03ET1193B), Witten

Ch. König, B. Rosen (1998): Calculation and Mesh Generation of a Three-Dimensional Matrix-Fracture-System; J. Hydraulic Res. 36, 867 - 884.

Witthüser, Kai (1996): Geostatistische Methoden der Trennflächenanalyse geklüfteter Sandsteine – mit Beispielen aus dem Ruhrkarbon – Diplomarbeit Fak. XVII Geowissenschaften, Ruhr–Universität Bochum

Witthüser, Kai, Thomas Himmelsbach (1997): Evaluation of fracture parameters for stochastic generation of fracture networks. In: Gottlieg, J. et.al. (Eds.): Field Screening Europe, pp. 183–186, Kluver Academic Publishers, Dordrecht

5 Other subsurface activities

5.1 Danish deep subsurface reconnaissance study

Carsten Møller Nielsen, GEUS

5.1.1 Conceptualization

Denmark has large potential for use of geothermal energy in the country energy mix, both in a direct use concept and in a storage concept. District heating grids are developed in many of the larger and minor municipalities. The subsurface contains several geological formations with excellent reservoir properties for geothermal energy utilization, especially in the depth range 500 m – 2500 m. The reservoirs are considered low enthalpy reservoirs, but with district heating well developed in Denmark and the advancing technology of heat pumps the market is obvious.

At present, no UTES (Underground Thermal Energy Storage) are in operation in the stated depth range. A single ATES (Aquifer Thermal Energy Storage) and two BTES (Borehole Thermal Energy Storage) are in operation. GEUS will focus on the potential for UTES in the above mentioned depth interval in the present WP in the HEATSTORE project. The potential for thermal heat storage will be investigated both as a standalone storage operation and in combination with geothermal energy operations in order to evaluate the potential for heat storage in synergy with geothermal energy production.
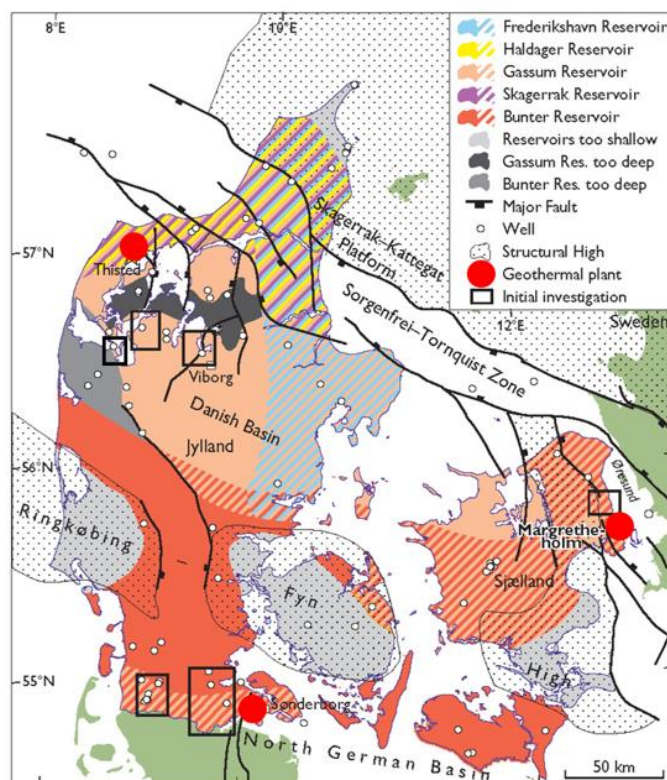

Figure 5.1.1 Map of potential geothermal reservoirs in Denmark. Location of the three Danish operating geothermal plants (red dots). Thisted geothermal plant in the northern part of Denmark, Sønderborg in the most southern part and Margretheholm in the Copenhagen area.

Three geothermal plants are in production in Denmark (Figure 5.1.1). All three plants are operated in a doublet well configuration mode and with capacities of 4 – 8 MW. The producing reservoir intervals are in the depth range of 1100 m – 2600 m and with production temperatures of 44°C – 75°C. The temperature of the produced geothermal water is boosted with help of heat pumps before entering the district heating grid.

The present geothermal plants are producing from two main reservoir formations; the Triassic Bunter Sandstone Formation (Margretheholm) and the Gassum Sandstone Formation of upper Triassic – Lower Jurassic age (Thisted and Sønderborg).

The experiences from the three plants will be used to investigate the potential for UTES in Denmark and to constrain the modelling work in WP 2 in the HEATSTORE project for GEUS' part.

As indicated in Figure 5.1.1 potential geothermal reservoirs exists in most of the country and in several areas there are more than one reservoir (dashed areas), which can lower the exploration risk.

5.1.1.1 UTES concept and specifications, scope and aims of the study

As stated above there are no plan for deep UTES projects in Denmark at present. But, as discuss above the potential is assessed to be large for using the subsurface; reservoirs of good quality and a developed district heating grid in many cities/municipalities.

In an ongoing research project (CONvert, EUDP 2017, DK) with the objective to evaluate the entire energy system in the municipality around the city of Aalborg, the fourth largest city in Denmark, the use of subsurface heat storage is included. Seasonal excess heat from waste incineration, cement production and the city power plan can potential be stored in the Gassum Formation. Preliminary reservoir simulation results indicate that a doublet well configuration can provide a storage efficiency of 70-90% depending on the geology and the operation scheme (loading/un-loading and temperature).

Two of the active geothermal plants (reservoirs) will be used in the present modelling work; the Margretheholm and the Sønderborg geothermal plants. The two locations give a span in depth, geology and temperature. The Thisted plant will not be included, as the reservoir geology and depth are similar to the Sønderborg plan.

Sønderborg is producing from the Gassum Sandstone Formation from a depth interval of 1100 – 1200 m and a reservoir temperature of 48°C. The Margretheholm plant is producing from the Bunter Sandstone Formation at a depth Interval of 2500 – 2600 m and with a production temperature of approx. 75°C. Both the Bunter and the Gassum reservoirs have good to very good reservoir quality with respect to porosity and permeability, the Gassum reservoir has the highest permeability, due to a lower burial depth and the Bunter reservoir has higher formation water temperature due to deeper burial.

The objectives for GEUS' modelling in WP2 are to evaluate the efficiency of a UTES operation as a function of reservoir temperature (depth), permeability and reservoir architecture (vertical variation in sandstone/shalestone layers) and the operation mode (loading/un-loading time and temperature).

Experiences from the Danish operating geothermal plants indicate that the flow rate (production/injection) should not exceed 150 m^3/h in order to avoid deterioration of the well completion and the near well bore reservoir area. Therefor the flow rates for the present study will be in the range of 100 – 150 m^3/h. The loading temperature will be in the range of 60 – 90°C, which is the temperature interval of the excess heat output from e.g. vast incineration plants.

For the two geothermal plants GEUS has constructed static (geological) and dynamic (reservoir simulation) models. The models are to some degree history matched to historical production data and are assessed to bring reliable and realistic models in to the HEATSTORE project.

5.1.1.2 System geometry and related geology

As stated above GEUS has geological models for the two geothermal plants, Sønderborg and Margretheholm. The models are constructed as layer-cake models but reflects the actual vertical distribution in the geology/lithology. The vertical variation in lithology and porosity are interpreted from wireline logs, the
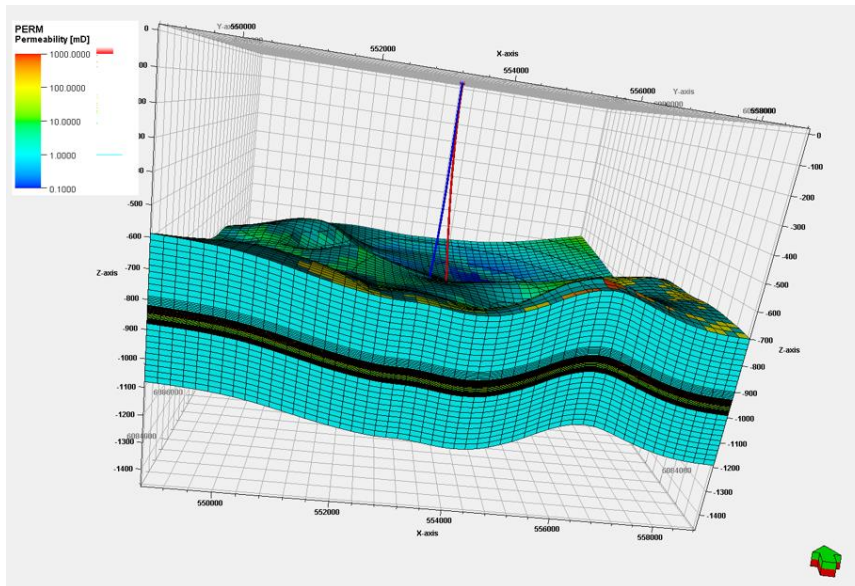
Figure 5.1.2. Permeability distribution in the Sønderborg model.

Sønderborg model is shown in Figure 5.1.2 and the interpreted wireline log for the Sønderborg well in Figure 5.1.3. The permeability is derived from a permeability-porosity relation as the permeability cannot be derived directly from wireline logging tools. The permeability-porosity relation is established from laboratory measurements on core samples.
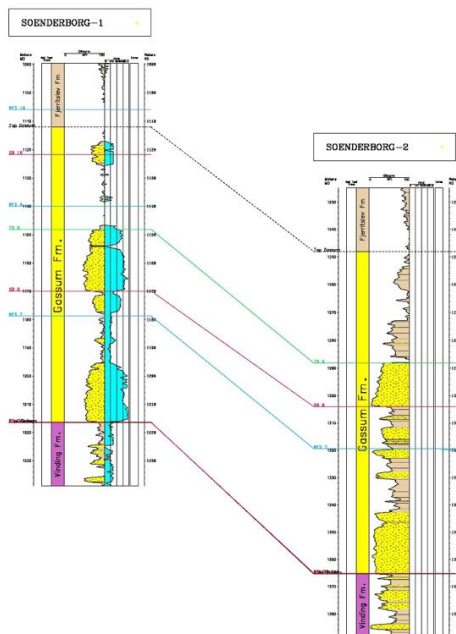

Figure 5.1.3 Well panel for the two Sønderborg wells. A porosity log is interpreted in Sønderborg-1. The well panel shows a 25 m depth offset between the wells.

Thermal properties are taken from the literature and previous research projects on thermal properties in the Danish subsurface (e.g. Fuchs, 2015). The reservoir properties (porosity, permeability, heat conduction, heat capacity) are distributed in to the grid by the Petrel software (Petrel, 2015), cf. section 5.1.2.2 below. The Petrel software provides a fast workflow for updating individual parameters in the model-grid.

The layer-cake approached is assessed to be sufficient, as the geology is relative "calm" for the two areas, so only heterogeneity in the vertical direction. If necessary anisotropy can be applied for the parameters in the lateral directions, both for the thermal – and the flow properties.

A model domain of 10 km x 10 km is assessed to be sufficient in order to have full control on the lateral boundary conditions for the dynamic modelling. In the vertical direction, 200 m of over- and underburden are applied to secure proper boundary conditions for the top and bottom of the model(s).

Initially the wells will be placed vertically in the model. If an increased connectivity between the wells and the reservoir is needed the well trajectories can alternatively be deviated. (Drilling experience dictated an inclination angle of max 45 deg.).

The geological models were constructed from interpreted seismic horizons and all available well data. 3D models use corner point grids. Porosity values were interpreted from well logs and permeability values were calculated from a porosity permeability relation determined from core laboratory flooding experiments. Thermal properties are taken from various research project results for the Danish area constrained with literature values.

The Petrel software allows for fast update on individual parameters and matching procedures to integrate any new information or interpretations.

5.1.1.3 Local geothermal and groundwater conditions

The depth interval in interest for the modelling part is 1100 m – 2600 m, so any regional pre-existing shallow groundwater flow can be disregard. Some evidence for regional pressure gradients in the respective depth interval exist from interpretation on non-equilibrium conditions in the Danish oil & gas province in the North Sea, but this is due to fast deposition above the Cretaceous chalk interval. The very low permeability in the chalk preserves pressure gradients over long time. For the sandstones in question in the present work the permeability is almost three order of magnitude higher, and any pressure gradient and non-equilibrium conditions due to geological process can be neglected with respect to seasonal heat storage.

The subsurface temperature gradient for the Danish onshore area is typical in the range of 25 – 30°C/km; for the Margretheholm area a temperature gradient of 27°C/km is determined and 34°C/km for the Sønderborg area. The relative high gradient in the Sønderborg area are caused by a short distance down to the Zechstein salt and Röt salt due to salt tectonics in the area.

The salinity of the of the formation water increases linearly with depth for the areas, a higher than normal salinity is observed in the Sønderborg area, caused by the salt deposit explanation as above.

5.1.1.4 Well operation and history

Pre-existing wells for the geothermal operations are both vertical and deviated wells. Deviated wells in order to obtain well distance at reservoir level, when drilled from the same spud location and also to increase the well contact to the reservoir in order to obtain increased injectivity/productivity.

Some wells are completed with screens and gravel packs and some are completed with guns (holes in the cemented liner).

The present work has access to all relevant well data for the two geothermal plants; i.e. well trajectories, completion intervals and methodology, operational - and production history and workover operations.

Two of the three operating geothermal plants are experiencing injectivity problems; fines migrations or geochemical instability resulting in precipitation in well completions or in the near well bore area. Research and investigations are ongoing to resolve the problems but at present no definite conclusions.

At the Margretheholm plant the production well is drilled as a vertical well and the injection well is drilled deviated with an inclination of approx. 30 deg. The two wells are drilled from the same spud location and drill pad. Both wells are completed with guns, and only completed in the best sand intervals. The Margretheholm wells have experienced some decrease in productivity and injectivity; especially on the injection side there have been challenges to sustain the flow rate. Several attempts have been tried to sustain injectivity; acid treatment, "rock-the-well" operations and new completions with heavier guns/explosives. The plant was original planned for flow rates above 300 m^3/h but is operated at approximate 100 m^3/h.

At Sønderborg both the injection well and the production well are all drilled as deviated wells with an inclination of 30 – 35 deg. Both wells are completed with gravel packs and screens. They are completed over the entire reservoir interval; i.e. the screens cover both the sandstone intervals and interbedded shale layers. Sønderborg has also experienced decreasing injectivity over time; only acid treatment has been used to establish injectivity, but with minor success. The plant is at present operated at 70 – 100 m^3/h.

5.1.2 Modelling approach

5.1.2.1 Conceptual simulation model

For both direct geothermal energy production and the use of the subsurface for thermal heat storage mass and heat transfer are the main governing processes to be modelled, especially when modelling relative deep reservoirs, where the lithostatic pressure is more than double than the hydrostatic pressure. For both the geothermal reservoirs to be used in the present work the pressure increase can be sustained well below the estimated fracture pressure of the formation(s) during operation. The formation fracture pressure for the sandstones is set to be 80% of the lithostatic pressure for the reservoir.

Geochemical effects are neglected; as a first order approximation of the storage operation the time span for the mass and heat transfer are much faster than the geochemical processes in the reservoir rock (this could be challenged).

- Mass transport (or flow) is solved by use of Darcy's equation.

  - Mechanical dispersion is handled by anisotropy in the lateral permeabilities,

  - Viscous dissipation is handled through the mobility ratio of the cold and hot water,

  - Diffusivity, ratio between permeability and compressibility.

- Heat transfer is solved by the heat equation.

  - Convection is handled by a build in "tracer option" in the dynamic solver (Eclipse 100). The injected water (cold or hot) is tracked by the solver when entering a single grid block. The temperature of the grid cell will be averaged by a volume weighted average of the injected water and the water already in the individual grid cells. Mixing is instantaneously in the time domain, which can cause numerical dispersion, but can be handled by proper gridding and time stepping.

  - Dispersion is handled by anisotropy in the lateral heat conduction coefficients.

  - Diffusivity, ratio between heat conduction and capacity.

5.1.2.2 Pre-processing workflow

The static models are constructed in the Petrel software (Petrel, 2015). The software offers a full suite of applications to construct detailed grids and populate the grids with properties. Petrel is fully coupled with the Eclipse 100 software (Eclipse, 2015), which will be used for the dynamic modelling. Both softwares are developed in the oil & gas industry and regarded as state-of-the-art for deep subsurface multi-phase transport modelling.

In an ongoing research project, GEOTHERM (DK, Innovation Fund Journal: 6154-00011B) the Eclipse software was benchmarked to the FEFLOW software. Results from comparable conceptual modelling schemes showed very good agreement between the two software.

The Petrel software uses corner point grids allowing for complex geometries, and grid refinement processes for CPU optimization and handling of numerical dispersion effects.

The following workflow will be used:

1. QC of all input data; stratigraphic framework, geophysical data (seismic data and interpretation, fault identification and other structural complexity), petrophysical data (wireline log interpretation), thermal properties and any available production data.
2. Import of seismic interpreted horizons/layers.
3. Import of well trajectories and well pics.
4. Adjustment of the seismic horizons to the well pics. (well pics are regarded as hard data
5. Gridding and discretization. Number of layers are determined by relevant well pics and resolution requirement.
6. Distribution of reservoir properties in to the individual grid cells. For "layer cake" modelling the interpreted well(s) are used to guide the vertical distribution and the lateral.
7. Export of grid and properties to the Eclipse software.
8. Calibration; the geological model is updated from the validated output from the dynamic simulations in an iterative process (e.g. identification of flow restrictions and grid refinement).

5.1.2.3 Computational approach and software

The Eclipse 100 software (Eclipse, 2015) will be used for the dynamic modelling. Eclipse is a finite difference solver and as stated above developed for use in the oil & gas industry. It is designed to solve multi-phase flow problems, but can easily be adopted to solve for single phase transport and temperature. The finite difference solver requires that the numerical domain is gridded in boxes, but through the corner point gridding process even very complex structures can be approximated. Further, the CPU time for even very fine gridded models with millions of cells is relative low (in the hour range).

Eclipse is fully integrated with the Petrel software and seamless export/import facilities make any adjustments of the static and dynamic models easy and transparent.

Several techniques are available for setting up boundary conditions to solve the differential equations; e.g. a "well option", numerical - and analytical aquifers.

For the present project, the "tracer option" mentioned in Section 5.1.2.1 and used to model convective heat transport is import to evaluated. The accuracy of this approach is assessed to depend largely on both time and grid discretization. It will be of great interest to compare convective heat transport with the other simulation software/codes used in the GEOTHERM project.

As mentioned in the section above the Eclipse software was benchmarked with the FEFLOW software, but only on a single conceptual model, further benchmarking will be of great importance for future modelling with Eclipse.

5.1.2.4 Model Analysis

Preliminary studies on deep UTES for relevant Danish geological settings have indicated that the storage efficiency is very dependent on the vertical variation in lithology's; sandstones with varying degree of interbedded claystone's show differences in storage efficiency. Claystone's with a lower heat conduction tend to isolate the system in an efficient manner. A drawback of having many interbedded clay layers are the reduction in the systems overall transmissibility and continuity and therefor difficult to load and un-load. Reservoir architecture and its implications (sensitivity) for optimal operation of the UTES system will be an important issue to examine in the project.

As mentioned above the two reservoir models that will be used as start models, i.e. the Sønderborg and Margretheholm models. The models are to some degree history matched to the production data from the direct geothermal energy production. But setting up a more detailed re-calibration scheme based on data (modelled) from a seasonal UTES operation will be beneficial for reliable predictions for UTES performance.

Finally, synergetic effect in combining UTES with direct geothermal energy production can be examined, i.e. well configurations operation modes.

5.1.3 Scenarios and results

This section gives an introduction to how the model analysis (section 5.4.2.4) can be performed with the existing models for the Sønderborg and Margretheholm geothermal plants. As described in section 5.1 the two geothermal reservoirs are of different geology, depth and initial temperature giving an opportunity to span the model analysis.

The geothermal plants in Denmark are operated in a classical doublet well configuration; one production well and one injection well. Potential UTES systems are to be modelled with a similar well configuration, at least for an initial guess of an optimal well configuration. The inter-well distance for the geothermal plants are in the range of 900 – 1400 m.

For stand-alone UTES systems the well distance can be much shorter; the distance will depend on the distribution of the hot water plume spreading around the operating "hot" well. The "cold" well must deliver formation water, when the system is loaded with hot water and receive cooled water when the system is un-loaded. The optimized well distance will depend on the acceptable pressure (flow) and temperature interference between the wells. A practical issue for the UTES well configuration is the flow reversal, when shifting from loading to un-loading mode. The deep wells need a production pump (Electrical Submersible Pump, ESP) placed at some depth in the well bore in order to produce at a certain depth of the reservoir. The ESP is difficult to pull whenever the well has to shift to injection mode, where the injection well is placed at the surface.

For the deep UTES systems, a setup with a classical geothermal operation may bring synergetic effect for both systems; i.e. shared well(s).

The above discussions point to a number of scenarios to be modelled/simulated (preliminary list):

- Study on the reservoir architecture/lithology variations effect on the storage efficiency,

- Study on well configuration and operational mode implication on storage performance,

- Study on synergy effects, when UTES is combined with direct geothermal energy production.

5.1.4 Analysis and discussion

5.1.4.1 Predictive and sensitivity-related learnings

Understanding the sensitivity in the input parameters and in the governing physics for the dynamic modelling results can certainly strengthen the predictiveness of the model(s).

Future development and re-development decisions for deployment of UTES systems in Denmark (as well as other countries) rely strongly on predictive tools and reliable projections.

First pass simulation results, obtained in a similar project, indicate that for deep UTES in low enthalpy areas, like Denmark, a crucial parameter is the reservoir architecture, i.e. the variation in sand and clay content. This call for sensitivity analysis in the modelling work, but also emphasizes the need for proper site/reservoir characterization, and a workflow to secure full update of the models. This goes directly in the Section 5.1.4.2 of the project.

5.1.4.2 Work Package Interfaces

For an optimal performance of an UTES system not only the subsurface must be evaluated but the operational schemes for the system are to be characterized and optimized.

WP1: Specifications and characterization for UTES concepts
To be completed in M35.

WP3: Heating System integration and optimization of design and operation
To be completed in M35.

WP5: Monitoring and validation to assess system performance and workflow
To be completed in M35.

5.1.5 Potential issues related to IP

- The software to be used (Petrel, Eclipse 100) are both commercial and contracted to GEUS with no restrictions in use.

- Subsurface data to be used in the static models are available in the public domain; the seismic surveys and wireline well log data are all more than 5 years old, which release the data from company confidentiality. GEUS, as being the national data centre, has full access to the data.

- Production data (pressure, fluid rate, temperature and operational schemes) and system description, used to calibrate the dynamic models are made available to GEUS to be used in the HEATSTORE project by company agreement.

5.1.6 References

ECLIPSE 100 Technical Description (2015). Version 2015.1. Schlumberger.

Petrel (2015). Version 2015.3. Schlumberger.

Fuchs, S., Balling, N., & Förster, A. (2015). Calculation of thermal conductivity, thermal diffusivity and specific heat capacity of sedimentary rocks using petrophysical well logs. *Geophysical Journal International, 203*(3), 1977-2000. doi:10.1093/gji/ggv403.

5.2 Danish district heating systems with existing large thermal energy storages

Geoffroy Gauthier, PlanEnergi

Between 2000 and 2020, Solar District Heating (SDH) systems have known a very fast development in Denmark (see Figure 5.2.1) and can typically supply 20% of the yearly local heat demand from solar heat. During the same years, the will to increase this solar fraction by means of seasonal thermal energy storage grew, and several projects were started after 2008. The thermal design of heat storages as a part of a heating system is crucial to determining the feasibility of a project. In Denmark, several TES have been implemented, coupled with a variety of heat sources, which require a specific modelling phase to assess behavior, performance and resulting costs of heat. This has been done in the following examples for two different types of TES, in 3 different locations, by PlanEnergi and with the modelling program TRNSYS.
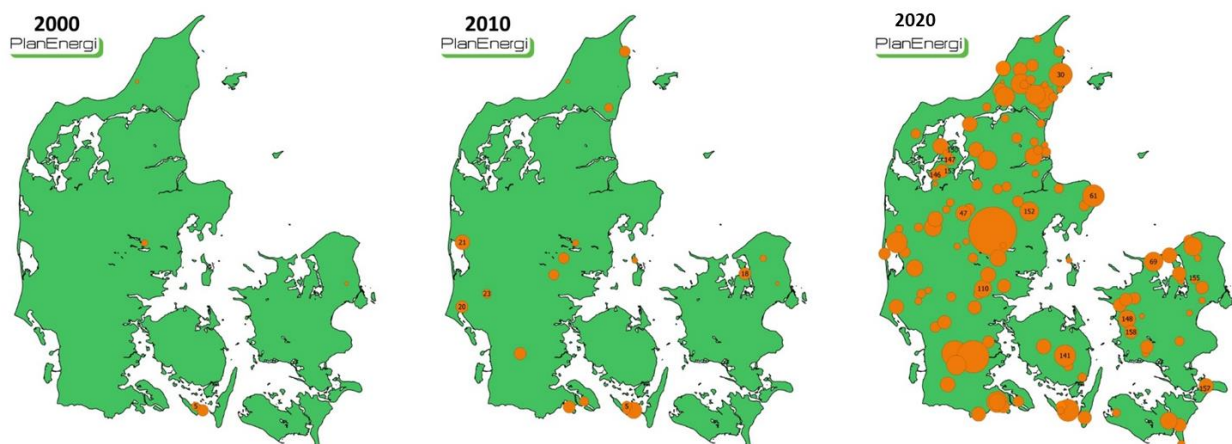

Figure 5.2.1. Evolution of the SDH installations in Denmark between 2000 and 2020[5]. Each circle represents a SDH system and its area is proportional to the surface area of the solar collectors. The figures in the circles show the order in which the SDH systems have been put into operation.

5.2.1 Pit Thermal Energy Storage (PTES)

This part of the report presents the studies carried out for 2 Danish cases: a PTES based in Dronninglund (Denmark), as a part of the EUDP project *SUNSTORE 3[6]*, and a PTES based in Marstal (Denmark), as a part of EU project *SUNSTORE 4[7]*.

5.2.1.1 Danish pilot site in Dronninglund

UTES concept and specifications, scope and aims of the study

The PTES project implemented in Dronninglund is a pilot project, meant to demonstrate a full-scale pit heat storage in combination with solar thermal and a heat pump. It was supported as EUDP project *SUNSTORE 3[6]* and implemented in 2014. Initially, the objective was for the system to cover 50% of the district heat consumption in Dronninglund (40'000 MWh/year) with solar thermal. The objective of the study presented

---

[5] Source: www.planenergi.dk.

[6] *SUNSTORE 3 – Slutrapport, Fase 1 - Projektering og udbud*, 2011, EUDP project number 63011-0178.

[7] *SUNSTORE 4 - Innovative, multi-applicable and cost efficient hybrid solar (55 %) and biomass energy (45 %) large scale (district) heating system with long term heat storage – and Organic Rankine Cycl*

here was to assess feasibility through modelling and system economics optimization, and the results obtained were used during the tender phase.

A preliminary study had determined the main elements of the solar heating system:

- A thermal solar collector field of 35'000 m^2 (gross area).
- A solar heat exchanger defined by a coefficient UA = 5 MW/K.
- A 60'000 m^3 water volume PTES.
- A district heating heat exchanger defined by a temperature difference ΔT = 3 K.
- A 3 MW$_{th}$ (heating capacity) electrical heat pump.

Prior to this solar heating system, the main heat sources comprised of:

- 4 gas engines, for a total of 6 MW$_{th..}$
- 2 bio-oil boilers, for a total of 10 MW$_{th..}$

System geometry and related geology

The geometry of the PTES is that of an inverted truncated pyramid (see Figure 5.2.7). Using an internally developed excel-based tool, the optimal depth of 16 m was determined. Using a slope of 1:2 (26.6°), this sets to 26 m the side length of the square at the base of the pyramid (Figure 5.2.2) and to 90 m the side length of the square edge at the top of the pyramid. Reusing the soil dug out to build up the sides of the PTES, it is possible to obtain a water depth of 16 m by digging only 11.7 m under the soil surface, elevating the sides by 4.3 m.
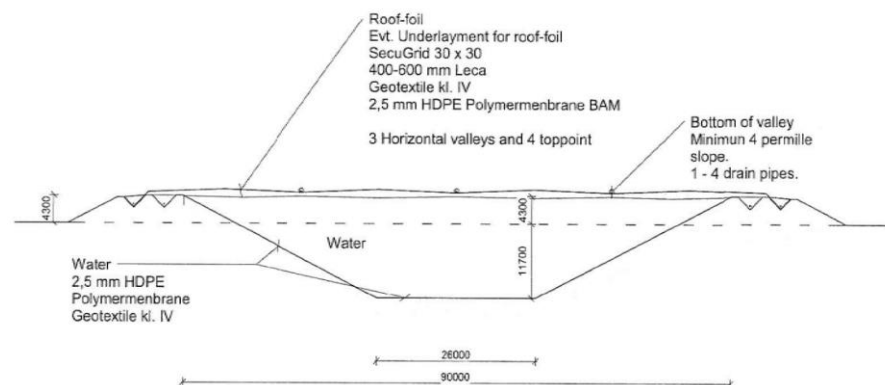

Figure 5.2.2 Cross-section view of the original PTES concept in Dronninglund .

The PTES was built in a former gravel pit, close to the location of the solar collector field (see Figure 5.2.4), after a series of geological studies of the possible locations. A first geological study, carried out in 2009, showed that the original location identified to build the PTES was unfavorable to establishment of the PTES. Both digging and rebuilding of the sides would have been complicated due to:

- High groundwater level, requiring cumbersome and expensive water-lowering measures in order to dig properly the PTES.
- Presence of silt in most of the digging area, making the rebuilding of the sides impossible (silt doesn't hold to ground compression operations) for 60% of the soil.

Therefore, a second geological study was carried out in 2010, North of the original studied location. This second study also showed unfavorable conditions, as a high groundwater level and high silt content were encountered in the soil.

Finally, in a third study from 2010, 5 different locations were studied (see **Figure 5.2.3**). These 5 locations are located North of the solar collector field and are mainly characterized as a mixture of sand and gravel. Groundwater levels revealed that locations A, B, D (from **Figure 5.2.3**), and possibly also E would be suitable for digging (levels being 2 to 3 meters below the bottom of the PTES). Out of these four possibilities, an environmental screening revealed that location A would be most suitable, and a more detailed study of the soil confirmed that the ground could be dug without draining the groundwater, and slopes could respect

the geometry plans of 1:2 inclination both for digging and rebuilding the sides of the PTES. The dry sand around the PTES also showed interesting low conductivity properties in the range of 0.3 to 0.5 W/(m·K). The measured ground properties were however only used for finding the proper location to establish the PTES, and not for detailed modelling, as the ground thermal properties don't have a decisive impact on the overall feasibility of the project (as long as there isn't a groundwaterflow), and knowing precisely these properties wouldn't change the results obtained from a sensitivity or parametric study carried out through modelling.

This site was, however, located in a site with some protected historical sites, as well as close to a forest, and derogations have therefore been necessary to obtain to enable the construction process (see **Figure 5.2.4**).
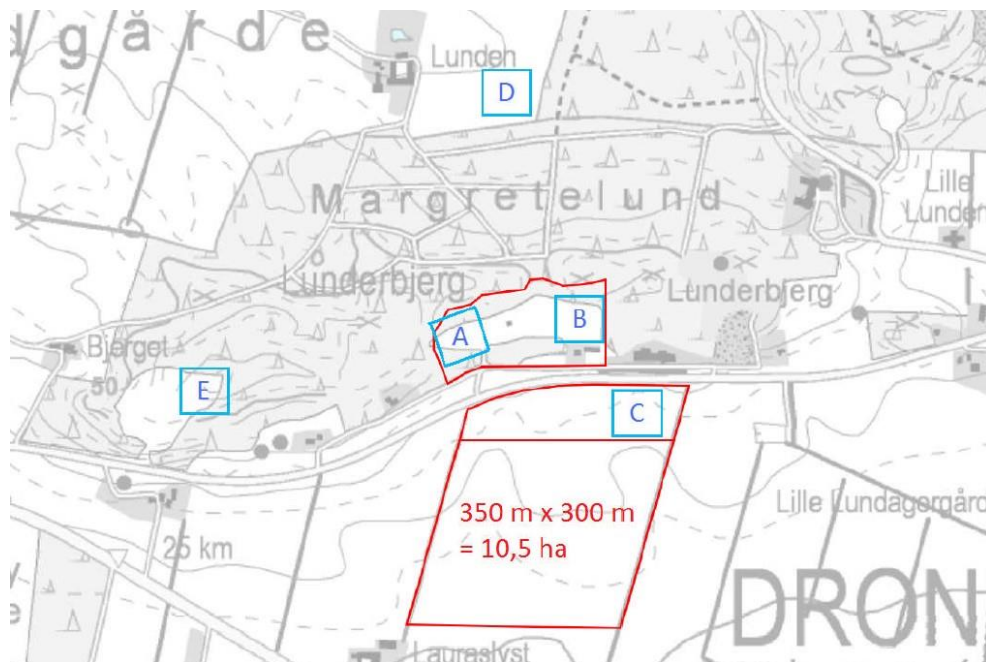

Figure 5.2.3. Alternative locations for the PTES studied during the third geological study. A and B are in a gravel pit, C is located just North of the solar collector field, between the road and the field. D is located North of the Margretelund forest, while E is in another gravel pit.

Once the location of the PTES was properly established, plans for connecting the solar collector field and the PTES to the main district heating network in Dronninglund were made through district heating pipes (see **Figure 5.2.5**).

Local geothermal and groundwater conditions

Local groundwater conditions have been presented in the previous section and have not been used in detail as inputs to the modelling phase. The groundwater levels for the targeted location have been found at 3 meters depth below the PTES bottom. The ground thermal properties from this depth have been estimated to have a thermal conductivity of 1.0 W/(m·K). However:

- Since the PTES is going to be used as a seasonal storage, the bottom of the storage will be the coldest.
- And because of its geometry (with a much smaller bottom surface area compared to the top surface area).

Then most of the heat losses will occur through the top and the sides of the storage, meaning that potentially increased heat losses at the bottom of the PTES can be, in the design phase, neglected.
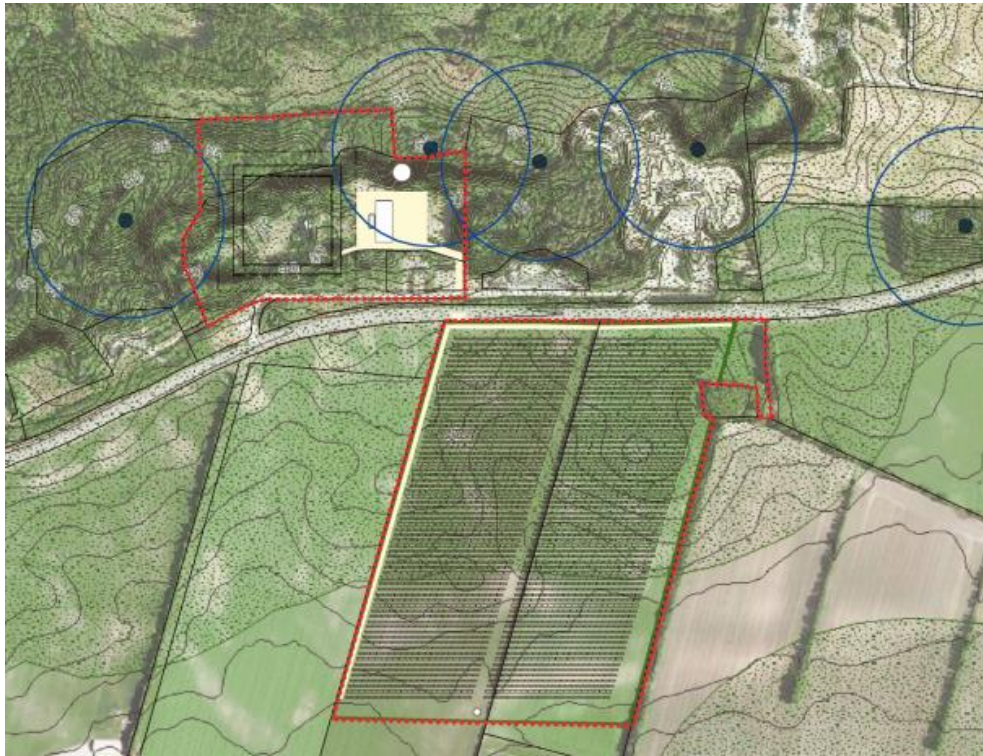
Figure 5.2.4. Area chosen to implement the system (surrounded by red stripes). Blue dots are protected historical areas (burial mounds) where no digging is allowed within a 100 m distance.
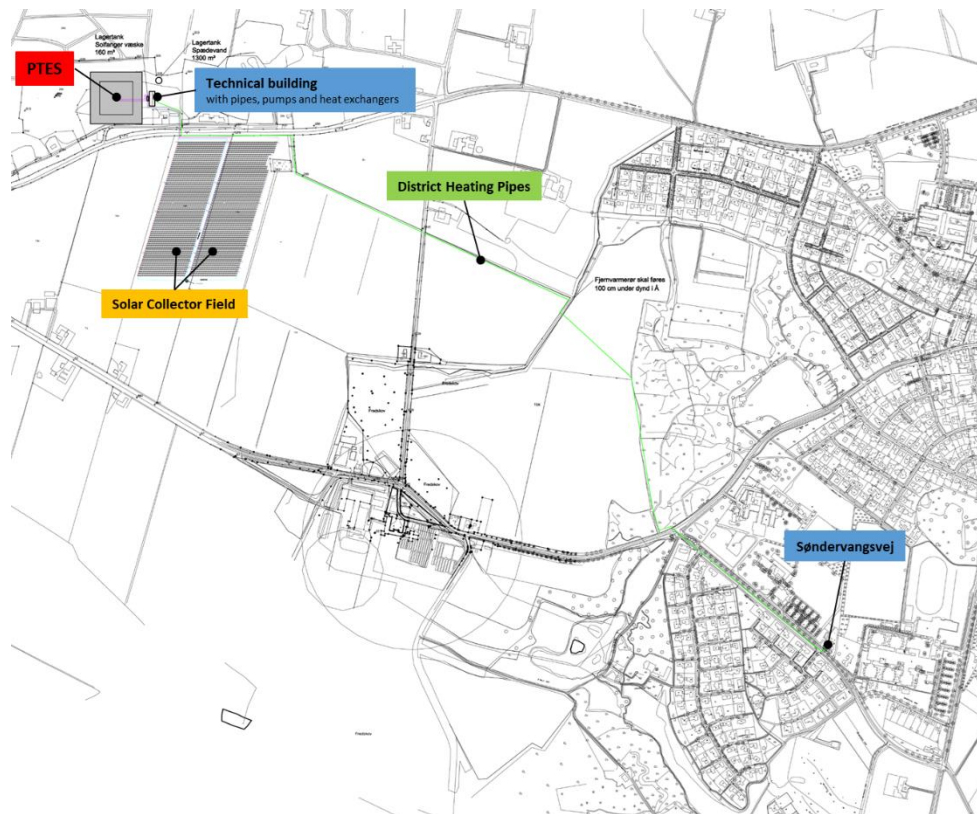
Figure 5.2.5. Location of the solar heating system project and the (green) transmission line to the district heating network of Dronninglund at the boiler plant at Søndervangsvej.

Modelling approach

Calculations of the energy production of the solar heating system and the economy for the SUNSTORE 3 project were carried out through a simulation model, set up in TRNSYS 16.

Conceptual simulation model

The elements mentioned have been included in the model shown in Figure 5.2.6. The gas motors ('Motor'), the solar collector field ('SCF'), the PTES, the heat pump, the bio-oil boilers and the heat exchangers ('HX-1&2') are the main components. Table 5.2.1 gathers the legend for the connections between the components. The gas motor is coupled to a buffer tank (Tank Thermal Energy Storage, TTES) of 865 m^3, 10 meters high and with a constant loss coefficient 3.0 kJ/(h·m^2·K) (uniform losses assumption).

Component 'Control' ensures the balance between the sources of heat, depending on which are cheapest and/or available. 'Motor-ON' determines when the gas-motors should run. 'Load' determines the flowrate for the district heating forward and return pipes. 'Splitter-4' decides which port the water should go through for the PTES discharging when using the heat pump. 'Type 109' provides the radiation to the solar collector field. 'Elspot' contains the time series of the electricity spot prices for a year. 'Pipe-1' & 'Pipe-2' estimate the heat losses from the pipes between the SCF and the PTES.
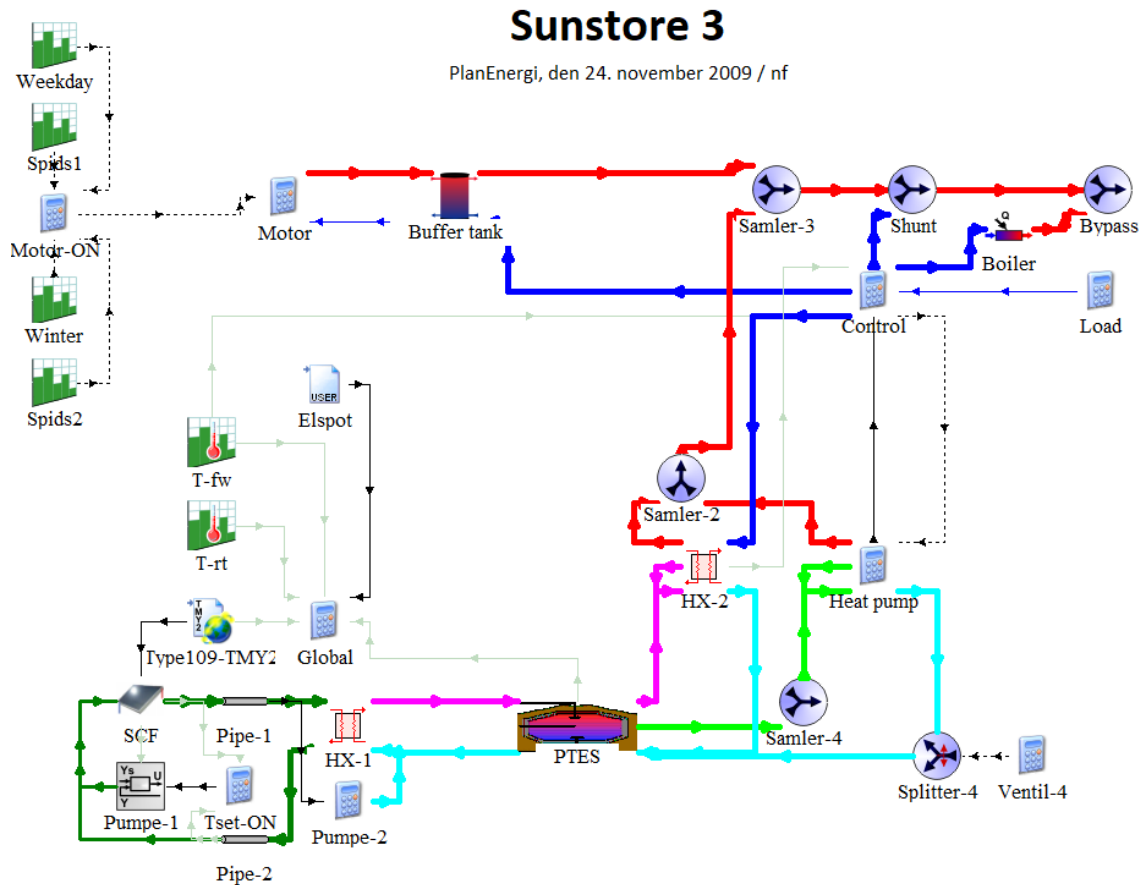
Figure 5.2.6. Components and connections in the TRNSYS model for Dronninglund. Thick lines represent water flows, and thin lines represents the control signals.

Table 5.2.1 Legend for the Dronninglund TRNSYS model connections shown in Figure 5.2.6.

Line thickness	Color	Explanation
Thick	Dark green	Water-glycol mixture loop
Thick	Light blue + magenta	Water loop between the PTES and the heat exchangers (HX)
Thick	Light green	Water loop between the PTES and the heat pump evaporator
Thick	Dark blue	District heating return loop
Thick	Red	District heating forward loop
Thin	Gray green	Temperature signals
Thin	Dotted-black	Control signals
Thin	Plain black	Other signals/information
Thin	Dark blue	No connection (information transmitted remotely or not needed)

Pre-processing workflow

The way the TRNSYS model is controlled is done through the following components and setups.

Solar collector field (SCF)

The SCF should have the highest yield possible. This is ensured by the control of the flowrate going through this component to obtain a temperature increase of 35 K (with an imposed max output temperature of 95°C). The SCF aperture area is 35'000 m^2. It is assumed the SCF panels are divided into a number of parallel strings each with 10 panels in series. Max flowrate is set to 500'000 kg/hr, minimum flowrate is set to 70'000 kg/hr. Thermal and optical parameters are gathered in Table 5.2.2. The SCF is assumed to have a slope of 30° and oriented south (azimuth 0°).

Table 5.2.2. Main thermal and optical parameters for the SCF.

Parameter	Fluid specific heat	η0	a1	a2	1st order IAM	2nd order IAM
Value [unit]	3.973 [kJ/(kg·K)]	0.815	8.748 [kJ/(h·m^2·K)] (= 2.43 [W/(m^2·K)])	0.0432 [kJ/(h·m^2·K^2)] (= 0.012 [W/(m^2·K^2)])	0.1008	0

Weather file – Type 109 TMY2

The solar radiation and air temperature are provided by Type 109, which reads inputs from the meteonorm file (format TMY2) from the city of Aalborg (closest location with an available dataset).

Heat exchangers

For both heat exchangers, the mass flowrate is controlled to have a matched heat capacity rate ($\dot{m} \cdot cp$) on both sides of the heat exchanger.

For 'HX-1' (see Figure 5.2.6), the flow is determined by the SCF flowrate, and the flow on the other side is modulated to have a matching heat capacity rate, as long as the PTES can be charged. Water on the PTES side has a heat capacity of cp$_{water}$ = 4.19 kJ/(kg·K). The water inlet temperature for the PTES is limited to 85°C, and the flow on the PTES side of HX-1 can therefore be further modulated (up to 1.5 times the flowrate on the SCF side) to moderate the PTES inlet water temperature. HX-1 has a constant global heat transfer coefficient UA = 5.0 MW/K = 18'000'000 kJ/(hr·K).

For 'HX-2', the flow is determined by the flow from the district heating network loop to obtain a matching heat capacity rate on both sides of the heat exchanger (matching mass flowrates, because the same fluid heat capacity is assumed on both sides). This heat exchanger is defined by a constant temperature difference $\Delta T = 3\ K$. This sets the outlet temperatures in the following way:

$$T_{HX2,PTES}^{out} = T_{HX2,city}^{in} + 3$$

$$T_{HX2,city}^{out} = T_{HX2,PTES}^{in} - 3$$

The temperature returning to the PTES is the district heating return temperature plus 3 degrees Celsius. The temperature returning to the district heating network is the PTES discharging temperature minus 3 degrees Celsius.

PTES

The pit thermal energy storage is modelled by Type 342 (XST model), which uses a cylindric geometry (see Figure 5.2.7). This model assumes the PTES is divided into a given number of segments of equal volume and homogenic temperature. Because of the geometry (cylinder), each segment has the same height.

In this model, the PTES was divided into 30 segments. The PTES is set up to have 3 pipes to extract water from the PTES: one at the segment most at the top (segment # 1), one at the middle volume of the PTES (segment # 15), and a last at the segment most at the bottom (segment # 30). The water sent into the PTES

is sent to the segment with closest temperature (it acts almost as if the water sent into the PTES was sent through a movable pipe, but instead of having to choose between 3 pipe heights, it chooses between the 30 segments). That's how this TRNSYS component is built, and it behaves close to how the PTES would be operated in reality.

Water inside the PTES is assumed to have a heat capacity of cp_{water} = 4.19 kJ/(kg·K), a density of 980 kg/m^3, and it is assumed to be insulated at the top by a 0.54 m thick material of conductivity 0.36 kJ/(hr·m·K) (or 0.1 W/(m·K)). The soil surrounding the water is consisting of one ground layer of 100 m depth, 2.3 W/(m·K) conductivity, and 2'300 kJ/(m^3·K) volumetric heat capacity.

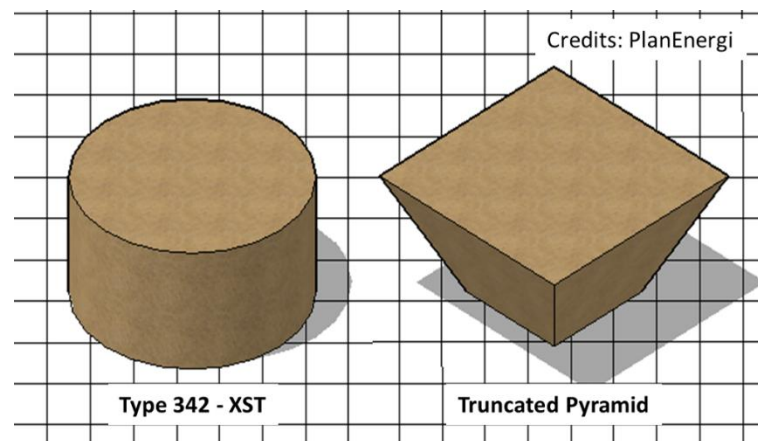**Figure 5.2.7. Geometry used in the TRNSYS PTES model (left) and real geometry of the PTES (right).**

The PTES model has a volume of 60'000 m^3, and a height of 7.345 meters. This height is much smaller than the actual PTES height (16 meters), which is built as an inverted truncated pyramid (see Figure 5.2.7). The TRNSYS PTES model height was determined to keep the same PTES lid area between modelling and reality: $90 \times 90 = 8'100$ m^2 in reality corresponds to $\frac{V_{PTES}}{h_{PTES}} = \frac{60000}{7.345} = 8'169 \ m^2$ in the model. 7.345 meters corresponds to a top edge of $\sqrt{\frac{60000}{7.345}} = 90.38 \ m$, which is the precise edge length at 16 m water depth in the PTES design dimensions.

Heat pump – evaporator side

The water that arrives to the evaporator side of the heat pump is determined based on the temperature of the middle of the PTES, $T_{PTES,middle}$:

- If $T_{PTES,middle} > 20°C$, then water is taken from the middle of the PTES.
- If $T_{PTES,middle} \leq 20°C$, then water is taken from the top of the PTES.

This control is ensured by the component 'Ventil-4', which controls the valve 'Splitter-4'.

Shunt

The component 'Shunt' (see top right part of Figure **5.2.6**) is used to dilute the flow of hot water sent to the forward temperature of the district heating network for it to match the required forward temperature (for example, water coming from the gas motors is produced at a temperature of 90°C, which is higher than the max forward temperature of 75°C).

Control

The component control choses which heat source (gas motors, heat pump, PTES and boiler) to use in priority, according to availability of the given heat sources, and the following order:

1. Heat from the buffer tank (gas motors).
2. HX-2.
3. Heat pump combined with direct heat from HX-2.
4. Heat pump alone.
5. Boiler.

Motor

This component simulates the gas motors. It runs only in peak-load periods, in the winter, and during weekdays, determined by the components 'Weekday', 'Winter', 'Spids1' & 'Spids2', and if the buffer tank isn't fully charged.

Winter is from November to February. Weekdays are Monday through Friday. Peak load 1 ('Spids-1') corresponds to from 7:30 am to 12:15 pm, with 15 minutes ramps from 0% to 100% (and vice-versa), and peak load 2 is from 5:00 pm to 8:45 pm, with 15 minutes ramps from 0% to 100% (and vice-versa). These ramps were used for model stability and translate real behavior of the gas motors that cannot start and stop instantaneously. Outside of these periods, the gas motors are not used.

These inputs are gathered in the component 'Motor-ON' and the general control is sent to the component 'Motor', which set the flowrate sent to the buffer tank.

The way the buffer tank is charged is the following: the gas motors' outlet temperature is set to 90°C, and the thermal power produced by the gas motors is regulated depending on the buffer tank bottom temperature. The gas motors run at full power (6 MW) as long as the buffer tank temperature is under 50°C. Then it is linearly reduced from 100% to 0% when this buffer tank bottom temperature increases from 50°C to 80°C.

Heat pump

The heat pumps are turned on when the electricity price is low enough. This information is provided by component 'Elspot', which reads a dataset giving the electricity spot prices (with 1-hour interval) for the year 2007 in Denmark. These prices are multiplied by 1.5 to estimate the price rate for 2010-2015. The heat pumps' condenser flowrate is regulated such that the condenser produces hot water at 80°C maximum (if the heat pump has enough power), and the condenser cools down the water to between 5°C and 10°C, depending on inlet temperature following the formula:

$$T_{HP,evap}^{out} = max\left(min\left(\frac{T_{HP,evap}^{in}}{2};10\right);5\right)$$

The heat pump' COP is calculated based on the data sheet of an existing heat pump, and has been approximated with the following formula:

$$COP_{heat-pump} = 2.81 + max\left(-0.8; min\left(1; 0.05 \cdot (40 - T_{rt})\right)\right) + max\left(-1.0; min\left(0; 0.05 \cdot \left(T_{HP,evap}^{in} - 20\right)\right)\right)$$

Then the heat pump is assumed to have a nominal electrical capacity of 475 kW, and it is assumed that a given number of those heat pumps are used in parallel.

Boiler

The boiler has the last priority to provide the necessary heat to the district heating network. It makes sure that the forward temperature is always met for the load. For instance, if the heat provided by the other heat sources reaches 70°C, and the district heating network forward temperature is 75°C, it heats up the flow up to 75°C.

Load

The component 'Load' sets the mass flowrate required by the district heating network. The forward and return temperatures are set by the components 'T-fw' and 'T-rt' according to the following parameters:

- Summer (May to October) forward temperature: 72°C, return temperature: 39°C.
- Winter (November to April) forward temperature: 75°C, return temperature: 35°C.

The load profile is calculated to provide a yearly load of 40'000 MWh, with a constant base load of 35% (GUF=35%, see formula below), and an (ambient) temperature-dependent part of 65%. For the temperature-dependent part, a reference temperature of 17°C is used to calculate the variable "load factor" on an hourly basis. The formula used is:

$$load\ factor\ = GUF + (1 - GUF) \cdot \frac{\max(0; 17 - T_{amb})}{24} \cdot \frac{8760}{N_{degree-days}}$$

Where:

- T_{amb} is the ambient temperature for the given hourly timestep.
- GUF is the base-load percentage.
- $N_{degree-days}$ is the number of degree-days, calculated with an excel-based tool to obtain a total yearly heat demand of 40'000 MWh, when summing all hourly load over a year (using the ambient temperature time series). It was calculated to be $N_{degree-days} = 3457.45288$.

For instance, if a given hour has an ambient temperature of 16°C, then the load factor would be
$load\ factor\ = 0.35 + 0.65 \cdot \frac{\max(0;17-16)}{24} \cdot \frac{8760}{3457.45288} = 0.35 + 0.65 \cdot \frac{1}{24} \cdot \frac{8760}{3457.45288} = 0.35 + 0.0686 = 0.4186$. Any hour with an ambient temperature above 17 degrees would give a load factor of 35%.

The hourly heat demand/load is then calculated with:

$$Load\ [MW] = \frac{40000 \cdot load\ factor}{8760}$$

Finally, the load is translated into a mass flowrate with knowledge of forward and return temperatures.

Scenarios and results

Phase 1 calculations

Using the model presented in the previous section, the temperatures and mass flowrates of the system are calculated with a timestep of 15 minutes for 5 years, and using 2 different cases: one with the heat pump turned off, and the other with the heat pump turned on.

Phase 2 calculations

In a second version of the model, the electrical heat pump is replaced by an absorption heat pump. This adapted model is also run over 5 years with a timestep of 15 minutes. A principle diagram of the way the absorption heat pump is integrated into the system is shown in Figure 5.2.8.
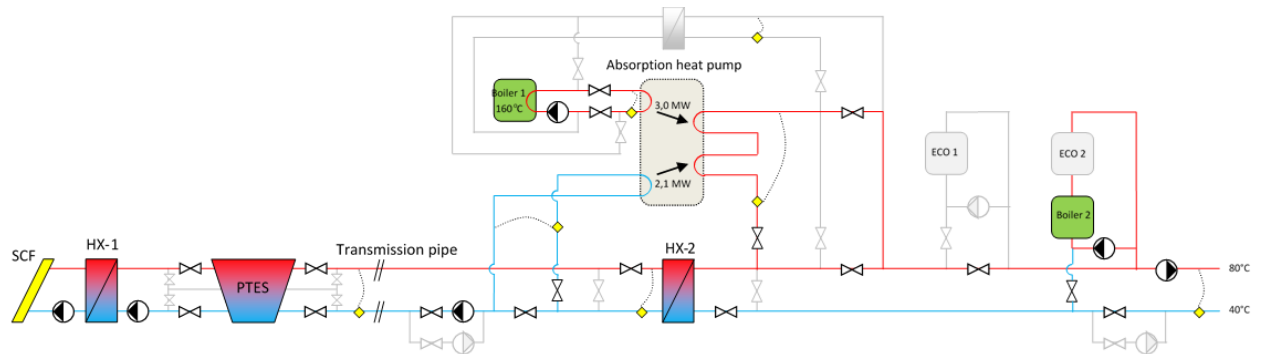
Figure 5.2.8. Principle diagram of the absorption heat pump integration into the system.

The way the absorption heat pump works is detailed in Figure 5.2.9.
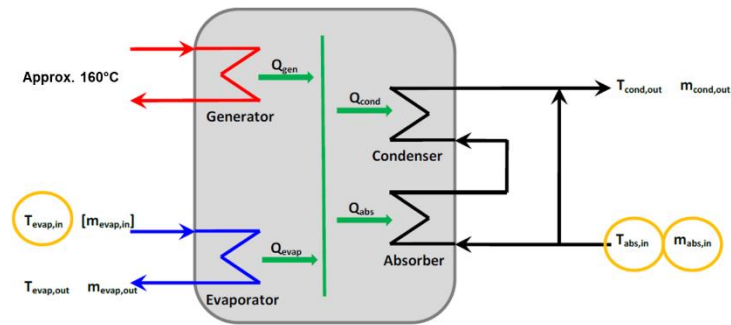

Figure 5.2.9. Principle diagram of the absorption heat pump. T are temperatures, m are mass flows and Q are heat flows.

At the right-hand side of Figure 5.2.9, a bypass is shown. This is used when the mass flow at a given temperature increase exceeds the heating capacity of the heat pump.

The inputs to the model are marked with yellow circles. $m_{evap,in}$ is not used as an input, but it is equal to $m_{evap,out}$. The main outputs are $T_{evap,out}$, $m_{evap,out}$, $T_{cond,out}$ and $m_{cond,out}$.

It is assumed that the heat input into the generator is hot water at approximately 160°C, produced by a bio oil boiler.

The main parameter in the model of the heat pump is Q_{out} which is the sum of the heat output through the absorber and the condenser ($Q_{out} = Q_{abs} + Q_{cond}$), which equals the heat input through the evaporator and the generator ($Q_{out} = Q_{evap} + Q_{gen}$).

The absorption heat pump is modelled in the following way:

• $T_{evap,out} = T_{abs,in} - 35$ K.

• $m_{evap,out}$ is calculated from $T_{evap,in}$, $T_{evap,out}$ and Q_{evap} (energy conservation).

• $T_{cond,out}$ is calculated from $T_{abs,in}$, $m_{abs,in}$ Q_{out} (energy conservation).

• $m_{cond,out} = m_{abs,in}$ (mass conservation).

• Q_{out} is not allowed to exceed the capacity of the heat pump (e.g. 3 MW).

• $T_{cond,out}$ is not allowed to exceed 90°C.

• The heat pump is bypassed when $T_{evap,in} < T_{abs,in} - 30$ K.

- $Q_{evap} = Q_{out} * 76 / 176$ ($COP_{cooling} = 0.76$).

- $Q_{gen} = Q_{out} – Q_{evap}$ (energy conservation, $COP_{global} = 1.76$).

Figure 5.2.10 presents the main components of TRNSYS model with the absorption heat pump (AHP). Additional pipe components were added between the PTES and the AHP.
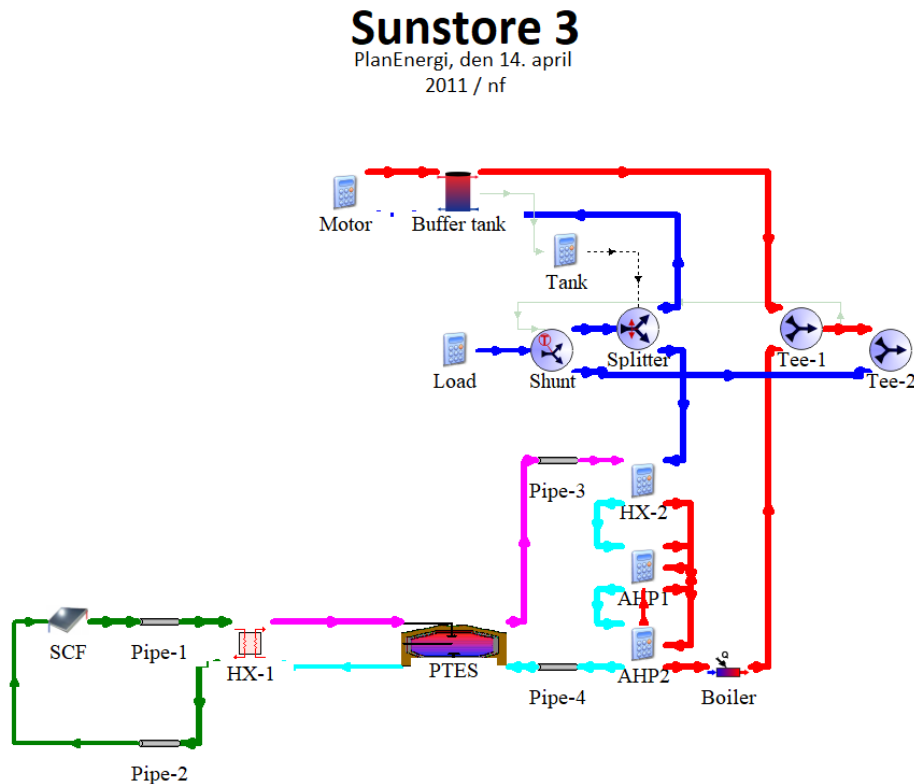

Figure 5.2.10. Main components of the 2nd TRNSYS model used for Dronninglund calculations (phase 2).

Analysis and discussion

Predictive and sensitivity-related learnings

First TRNSYS study – with & without electrical heat pump

Figure 5.2.11 shows the evolution of the temperatures inside the PTES during year 2 of the simulation, with the electrical heat pump activated. The top calculated PTES temperature reaches 90°C, while the minimum bottom PTES temperature is 12°C. This low bottom temperature clearly shows the impact of the heat pump cooling effect. Without the heat pump, the minimum achievable temperature inside the PTES is limited by the district heating network's return temperature (35°C).
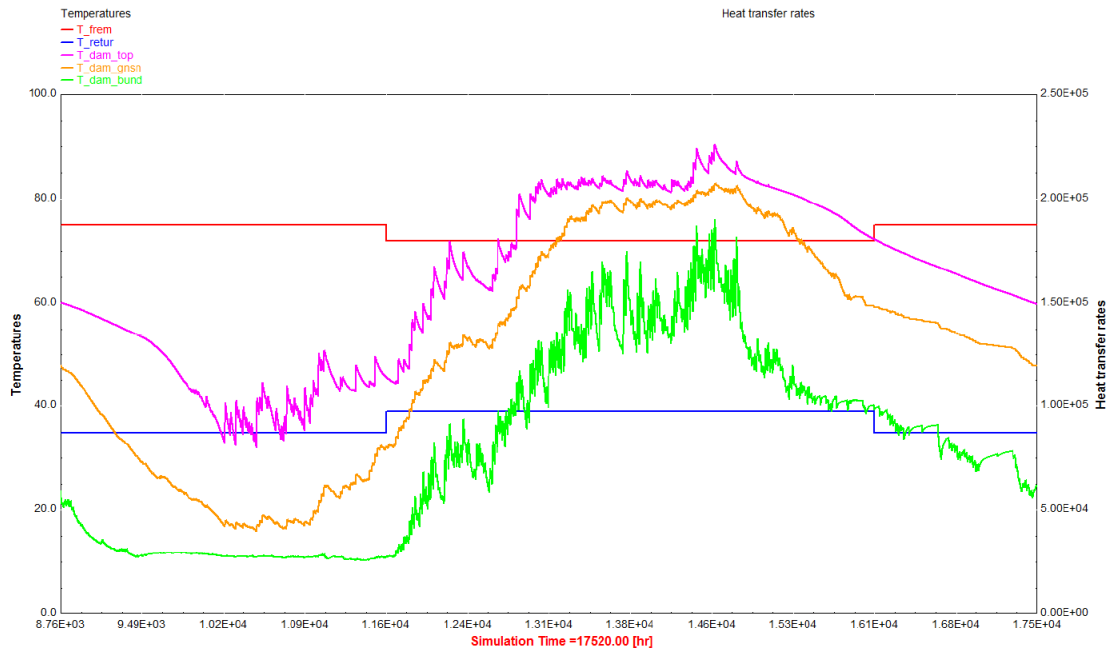
Figure 5.2.11. Evolution of the PTES temperatures – TRNSYS simulation results.

Monthly results for year 5 are presented in **Figure 5.2.12**, and show that the gas motors are not needed when using the heat pump.
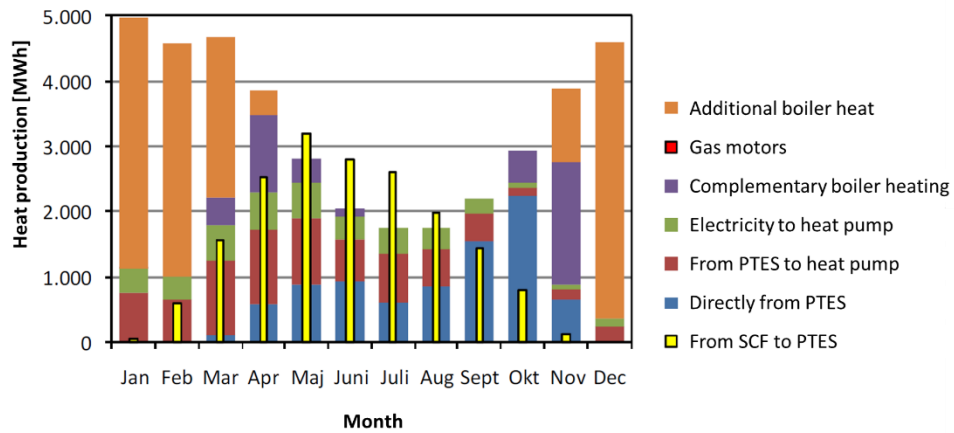

Figure 5.2.12. Monthly energy contribution by source for year 5 calculated.

Then the different scenarios can be compared, see Table 5.2.3. The 'reference' scenario is the one where only the bio-oil boiler is used to supply heat to the system. Then comes the scenario with PTES, SCF and without heat pump 'Without HP'. The same scenario but with use of the heat pump is called 'With HP'.

Table 5.2.3. Summary of the energy contributions for the different scenarios simulated with the first phase of TRNSYS calculations.

Description	Unit	Reference	Without HP	With HP
Solar collectors yield (to PTES)	MWh/year	0	13'207	16'215
Solar collectors yield (to PTES)	kWh/m^2/year	0	377	463
PTES heat losses	MWh/year	0	2'893	2'235
Heat directly from the storage*	MWh/year	0	10'315	5'816
Heat pump, evaporator	MWh/year	0	0	8'164
Heat pump, electricity	MWh/year	0	0	4'107
Heat pump, condenser*	MWh/year	0	0	12'271
Heat pump, full load hours	hours/year	-	-	4'323
Heat pump, yearly COP	-	-	-	2.99
System-COP = net heat produced/el.	-	-	-	1.89
Gas motor production*	MWh/year	0	0	0
Boiler production*	MWh/year	39'998	29'681	21'912
Boiler production	-	100%	74%	55%
Total heat delivered (sum of all "*")	MWh/year	39'998	39'996	40'000

Without the heat pump, the solar heating system can provide 10.3 GWh per year, which corresponds to 26% of the total heat demand. With the heat pump, the solar collector field (SCF) yield increases, the PTES losses decrease; the contribution of the solar heating system increases to 18.1 GWh[8] (45% of the heat demand). This is due to lower temperatures in the solar and storage loops of the heating system.

The yearly COP of the heat pump is close to 3.0, while the system COP is close to 1.9. The system COP is defined as the net heat produced (how much more energy is produced by the solar system with the heat pump compared to the amount of energy produced by the solar system without heat pump) divided by the amount of electricity consumed by the heat pump.

From an economical point of view, the yearly costs of heat have been estimated for 3 cases, and the case with heat pump (HP) has been divided into 2 sub-scenarios (see Table 5.2.4). The 2 heat pump scenarios differ by the way the tax over the heat pump's electricity consumption is calculated.

The first scenario, referred to as 'With HP-Heat tax', corresponds to the taxation rules at the time the study was made (in 2009-2010). Taxation on electricity for the heat pump (HP) was proportional to the amount of heat produced by the HP, with a fixed rate of 208 DKK/MW$_{heat}$.

The second scenario, referred to as 'With HP-El. tax', corresponds to a taxation scheme, where electricity is taxed proportionally to the amount of electricity consumed by the heat pump, with a fixed rate of 208 DKK/MW$_{el}$.

---

[8] Including the heat pump's electricity consumption.

Table 5.2.4. Costs of heat for the different scenarios simulated with the first phase of TRNSYS calculations.

Description	Unit	Reference	Without HP	With HP-Heat tax	With HP-El. tax
Heat production costs	mio. DKK/year	18.8	14.1	14.6	12.9
Operations savings	mio. DKK/year	0	4.73	4.18	5.87

As shown in Table 5.2.4, the first HP scenario generates less savings than the case without HP. With the electricity taxation scheme at the time of the study, it was not economical to invest in a heat pump for that system. The direct consequence of this is that the amount of renewable-energy production in the system is reduced by 7'800 MWh per year[9]. The second HP scenario shows that, with a change in the taxation scheme, the scenario with HP would become more economical and enable a higher production from the solar heating system.

A request to the government had been made at the time of the study to change the taxation scheme, but these did not take place before the beginning of project implementation. It was therefore chosen to study an absorption heat pump instead of a compressor heat pump, through a second TRNSYS model.

Second TRNSYS study – with an absorption heat pump

The second TRNSYS model uses an absorption heat pump instead of an electrical heat pump. This model was used during phase 2 of the SUNSTORE 3 project[10].

In the second phase of the project, a new way of assembling connecting pipes for the solar collector field made it possible to have a more compact layout and gave room for extra solar collectors. The collector aperture area thus ended at 37'573 m^2 instead of 35'000 m^2. Calculations showed that it would be feasible to extend the solar collector area if the existing natural gas fired CHP plant should join the open electricity market and therefore have only a few running hours in the summer period[11].

The purpose with the simulation was to gain as much heat as possible from the solar plant and the PTES and to optimize the economy. In Figure 5.2.13.a the amount of heat from the solar heating system can be seen, depending on the size of the heat pump generator.

The amount of heat from the solar plant and the PTES can be increased from 11'503 MWh/year without heat pump to 14'322 MWh/year (+24.5%) as maximum with a heat pump[12].

If the substitution heat price is 350 DKK/MWh, the absorption heat pump specific investment costs are 2 mio. DKK/$MW_{cooling}$ and the capital costs are calculated as a 5% p.a., 15-year annuity loan, the extra value of different cooling capacity can be calculated. This is illustrated in Figure 5.2.13.b.

---

[9] At the time of the study, carbon footprint of electricity was higher, which explains the lower number compared with total heat produced at the condenser.

[10] *SUNSTORE 3 - Phase 2 - Implementation*, 2015, EUDP project number 64009-0043 and 64010-0447.

[11] For more details, refer to HeatStore deliverable D3.3 – Allaerts K. et al., 2021, *UTES and its integration in the heating system -Defining optimal design and operational strategies for the demonstration cases*, GEOTHERMICA – ERA NET Cofund Geothermal.

[12] These results have been obtained with an intermediate version of the TRNSYS model (not fully optimized in terms of control strategy), using 35'000 m^2 of solar collectors.
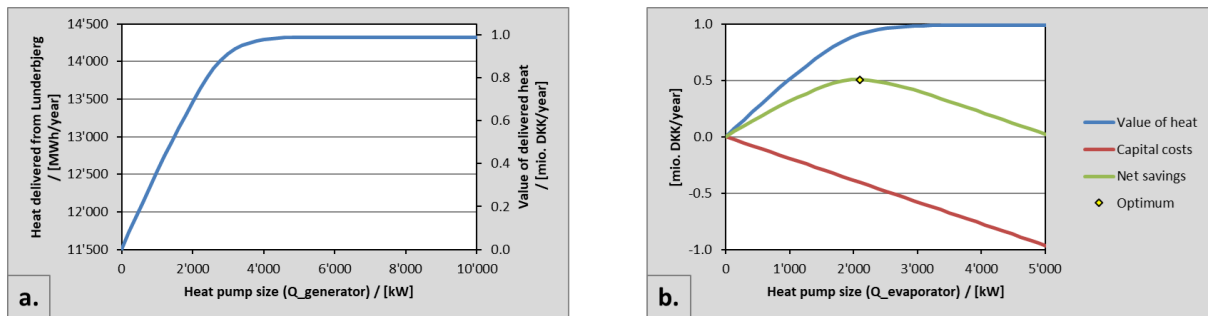
Figure 5.2.13. a. Heat from the solar heating system depending on absorption heat pump size (to the left). b. Value of the extra solar heat from the solar heating system as a function of absorption heat pump size (to the right).

As can be seen from **Figure 5.2.13.b**, the optimal size of the heat pump is approximately 2.1 MW cooling capacity. Sensitivity analysis of heat price and depreciation period showed optimal heat pump capacities between 1.9 and 2.3 MW$_{cooling}$.

With the use of the pipe components in the model (see Figure 5.2.10), calculations showed that if the heat exchanger and the heat pump are moved from the buildings close to the PTES to the existing boiler plant at Søndervangsvej (see Figure 5.2.5), heat delivery from the solar heating system (SCF + PTES) is 577 MWh extra per year.

If the substituted heat production price is 350 DKK/MWh, the extra income will be 208'950 DKK/year. For these reasons, the 2.1 MW$_{cooling}$ absorption heat pump was implemented at Søndervangsvej.

Final calculation of yearly energy balance for the system are presented in Table 5.2.5.

Table 5.2.5. Calculated heat contributions from the TRNSYS calculations, phase 2.

	Reference	With AHP
Preconditions		
Natural gas, calorific value, kWh/Nm^3	11	11
Bio oil, calorific value, MWh/ton	10.076	10.076
Engines, electricity efficiency, %	35	35
Engines, heat efficiency, %	59	59
Engines, heat capacity, MW	5.9	5.9
Bio oil boiler, efficiency, %	92	94
Energy		
Heat demand, MWh	40'000	40'000
Degree day dependent heat, %	65	65
Max. heat demand, MW	11.3	11.3
Min. heat demand, MW	1.4	1.4
Heat production, engines, peak load, MWh	7'086	7'086
Heat production, engines, high load, MWh	6'626	6'626
Heat production, bio oil boilers, MWh	26'288	9'986
Heat from solar collectors, MWh	0	18'500
Heat loss from storage, MWh	0	-1'602
Energy change in storage, MWh	0	38
Heat deliverer by the SHS (SCF + PTES), MWh	0	16'860
Heat loss from transmission line, MWh	0	-558
Heat delivered at Søndervang, MWh	0	16'302
Heat via heat exchanger, MWh	0	10'478
Absorption heat pump, cooling, MWh	0	5'824
Electricity production, peak load, MWh	4'204	4'204
Electricity production, high load, MWh	3'931	3'931
Natural gas consumption, MWh	23'240	23'240
Bio oil consumption, MWh	28'574	10'623

During contract negotiation with ARCON Solar it was discussed if it was feasible to avoid the insulating foil in the first solar collectors in the rows. Therefore, the solar system was calculated in TRNSYS with two solar fields connected in series.

The first solar field was without foil ($\eta_0 = 0.845$, $a_1 = 2.94$, $a_2 = 0.013$) and the second with foil ($\eta_0 = 0.817$, $a_1 = 2.205$, $a_2 = 0.0135$). The total aperture area was 36'897 m^2. Results can be seen in Figure 5.2.14.
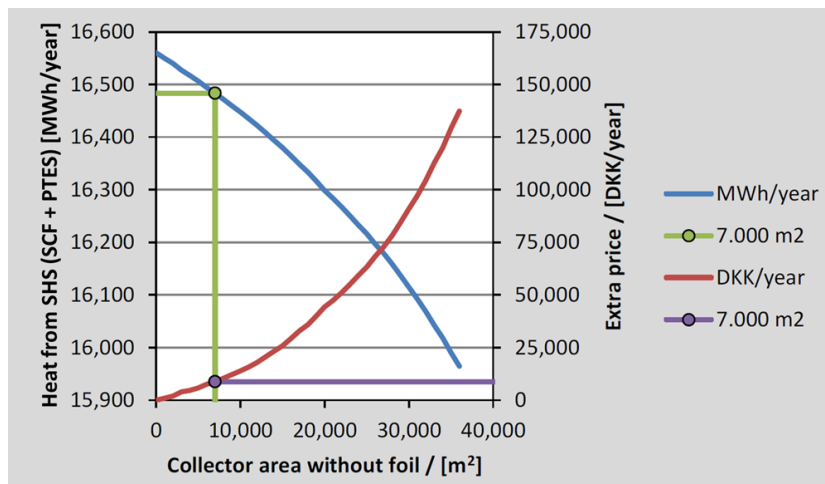
Figure 5.2.14. Comparison between cases with and without foil.

The blue curve shows the yearly heat delivered from the solar heating system (SCF + PTES) as a function of the solar area without foil. The slope of the curve shows that the amount of produced heat is reduced with 11 kWh/m²/year if there is no foil in the first solar collectors in a row and with 26 kWh/m²/year if there is no foil in the last solar collectors in a row. The foil price is 10.6 €/m². Yearly cost is calculated with a 25 years annuity loan with a 1.5 % p.a. real interest. The price of substituted heat is expected to be 62 €/MWh (bio oil).

The red curve shows the extra price for produced heat if foil is removed and the green line shows the result if 7'000 m² solar collectors are without foil:

- Reduction in investment 7'000 m² x 10.6 €/m² = 74'200 €.
- Capital cost reduction (4.8 % of investment) 3'562 €/year.
- Reduction in heat production 77 MWh/year.
- Extra cost bio oil 77 MWh/year x 62 €/MWh = 4'774 €/year.

With the conditions in Dronninglund, it was therefore not feasible to remove SCF foil since the red curve shows that the lowest price is obtained if all solar collectors have foil. It was therefore decided to have foil in all solar collectors in Dronninglund. If the price for substituted heat is more than 50 €/MWh, foil is still feasible for the total plant. And if the price for substituted heat is below 20 €/MWh foil is not feasible for the total plant.

Comparison of system design figures and first monitoring results

The global system design figures as well as measurement figures from 2016 are represented in Figure 5.2.15 in a graphical way.

Monitoring results 2016, numbers in MWh/a
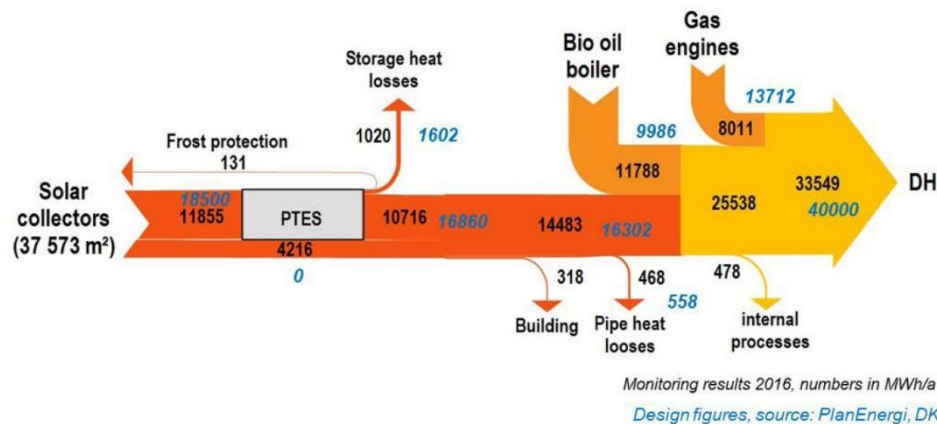*Design figures, source: PlanEnergi, DK*

Figure 5.2.15. Yearly energy flow diagram for the SDH plant in Dronninglund. A fuel change from bio-oil to natural gas in October 2016 is not considered here[13].

The design figures differ mostly from the measurement due to 3 factors:

- The actual heat demand differs quite largely from the design numbers.
- In the model, all the solar heat produced by the solar collector field goes through the PTES, whereas in reality, a portion is directly sent to the district heating network.
- The actual solar radiation received by the solar collector field is lower than the one used for the design, which explains why the solar collectors produce 16'071 MWh in 2016 instead of 18'500 MWh/year.

This partially explains the differences encountered between measurements and design figures. If we focus on the operations of the PTES, we can see that the design figures give a charge of the PTES with 18'500 MWh, a discharge with 16'860 MWh (91.1% of the charged energy) and 1'602 MWh of heat losses (8.7% of the charged energy, internal energy change of +38 MWh). Whereas measurements show a charge of 11'855 MWh, a discharge of 10'847 MWh (91.5% of the charged energy) and 1'020 MWh of heat losses (8.6% of the charged energy, internal energy change of -12 MWh), which is very close to the annual behavior of the modelled PTES and validates the use of the tool for design optimization.

Conclusions

With the help of TRNSYS calculations, the full design of the solar heating system with an absorption heat pump was optimized. The type and size of the heat pump, the type of solar collectors, the location of the PTES heat exchangers and the heat pump were all determined by calculations made with TRNSYS.

A solar heating system (SHS) comprising of a SCF of over 37'000 m^2 and a 60'000 m^3 PTES, together with a 2.1 MW$_{cooling}$ absorption heat pump were implemented in Dronninglund. Calculations showed that solar heat could cover a total of 41% of the heat demand, which is lower than the initial objective, but can be explained by the fact that an absorption heat pump was used instead of the electrical heat pump, and that the electricity consumption from the electrical heat pump was initially counted as a part of the solar heat production.

5.2.1.2 Danish pilot site in Marstal

The PTES project implemented in Marstal is a demonstration project, further developing a smaller pilot project implemented by Marstal District Heating that already had a PTES. The new system comprises a full-

---

[13] Schmidt and Sørensen – *Monitoring Results from Large Scale Heat storages for District Heating in Denmark* – EnerSTOCK2018, 14th International Conference on Energy Storage, 25-28 April 2018.

scale PTES in combination with solar thermal, a heat pump, a wood chip boiler and an Organic Rankine Cycle plant (ORC). It was supported as EU project SUNSTORE 4[14] and implemented in 2012.

The solar energy system in Marstal was established between 1996 and 2012, the second part of the project being supported under EU's 7th framework programme project SUNSTORE 4 between 2010 and 2014.

UTES concept and specifications, scope and aims of the study

First solar heating system (1996-2003)

The first part of the project has been implemented between 1996 and 2003, as a part of the project SUNSTORE 2. It was used as a starting point to the study being reported here. It consisted of the following elements:

The old boiler plant at Jagtvej with 3 oil boilers, 18.3 MW_{th} total capacity. The fuel had until 2006 been waste oil, but caused by problems with emission of heavy metals, Marstal changed the fuel to bio-oil from 2007.

The solar plant at Skolevej with:

- 9'000 m^2 solar collectors (ARCON HT1996).
- 8'019 m^2 ARCON HT2002.
- 881 m^2 G3-Teknik2002 (Now Sunmark).
- 103 m^2 Wagner, roof elements.
- 108 m^2 Termomax, evacuated tubes.
- 211 m^2 IST, focusing collectors.
- 2'100 m^3 steel tank (TTES).
- 10'340 m^3 pit heat storage (PTES).
- 100 kW_{el} propane heat pump.

The total aperture area of solar collectors was 18'300 m^2, see the right-hand side of Figure 5.2.16. The solar thermal plant runs with an adjustable flow on both the primary and the secondary side of the heat exchangers. By measuring the sun radiation (W/m^2) and the return temperature to the collectors, it is possible using the efficiency curve for the solar collectors to calculate the necessary flow to achieve a desired outlet temperature (typically 75-80°C during summer and lower in winter).

Marstal district heating had 1'460 end users and a yearly heat production of 28'000 MWh. The solar fraction was approximately 30% and the solar heat covered 100% of the demand in the 3 summer months (see Figure 5.2.17).

---

[14] *SUNSTORE 4 - Innovative, multi-applicable and cost efficient hybrid solar (55 %) and biomass energy (45 %) large scale (district) heating system with long term heat storage – and Organic Rankine Cycle electricity production,* 2014, funded by the EU's Seventh Framework Programme - Theme 5 - Energy, under grant agreement number 249800.
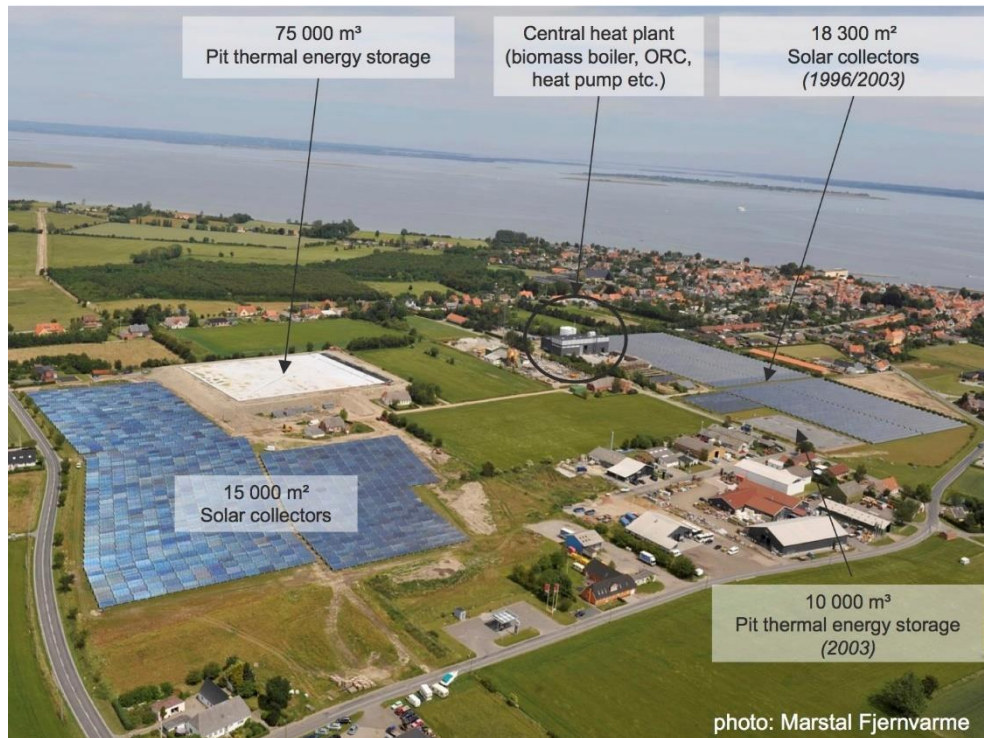
Figure 5.2.16. Aerial overview photo of the renewable energy heating system in Marstal.
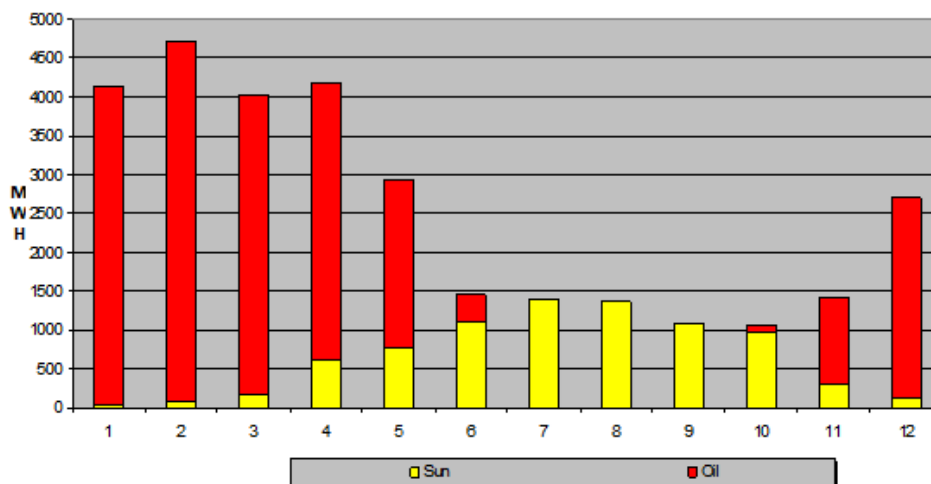

Figure 5.2.17. Measured monthly solar production in Marstal in 2006.

Second solar heating system (2011-2012)

The second part of the project has been implemented between 2011 and 2012. It was intended to increase the solar fraction from 30% to 55% and reach 100% coverage from renewable energy sources. This was calculated as achievable by adding the following elements (see the mid and left-hand side of Figure 5.2.16):

- 15'000 m² additional thermal solar collectors.
- A 75'000 m³ PTES.
- A 4 MW$_{th}$ wood chip boiler with:
  - 3.25 MW$_{th}$ heat output.
  - and 750 kW electrical output from an ORC.
- A 1.5 MW$_{th}$ heat pump using CO_2 as a refrigerant.

This was based on a yearly heat load demand from the district heating network of 28'000 MWh. The yearly load was increased to 32'000 MWh. The aim of the study presented here was to demonstrate a technical reliable energy system with 100 % renewable energy sources (55 % solar and 45 % biomass) and a heat production price of 50 – 55 €/MWh.

System geometry and related geology

The PTES in Marstal has a maximum water depth of 16.385 m, a bottom rectangular area of 22.6 m width for 47.6 m length and a top rectangular area of 88.14 m length for 113.14 m length (see Figure 5.2.18 and Figure 5.2.19). The sides of the PTES are elevated by 4.6 m[15] compared with the ground surface level.
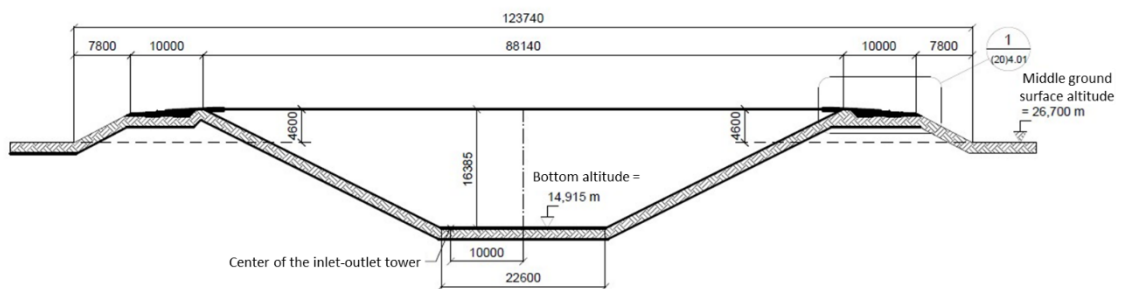

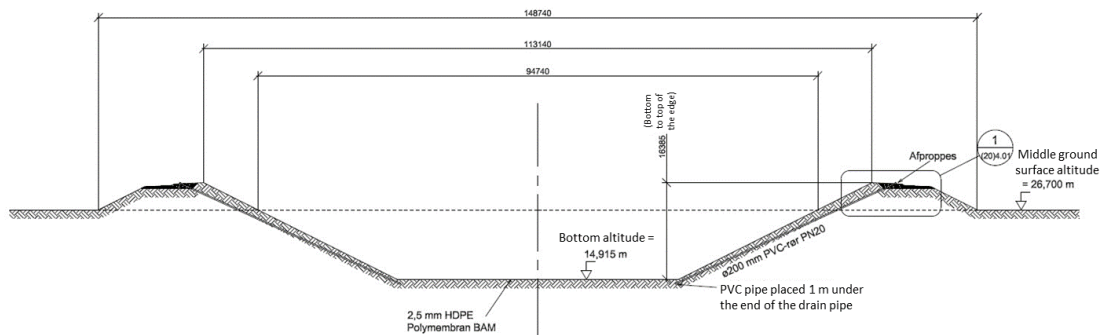**Figure 5.2.18. Cross-section view of the PTES in Marstal, along the width.**

Figure 5.2.19. Cross-section view of the PTES in Marstal, along the length.

Regarding the local geological conditions, several reports have been carried out by Geo. These reports showed that the soil was mostly sand, boulder clay and fat clay. For the layers containing fat clay that will be in contact with the inner slopes of the PTES, it was recommended to dig it out and replace it with locally available boulder clay (see Figure 5.2.20). Between all the sides, the report estimates an extra digging of

---

[15] On a theoretical flat surface.

5'000 m3 of soil, totalling 45'000 m^3 instead of 40'000 m^3. No thermal response tests have been carried out for this geotechnical study, but the soil thermal conductivity has been estimated between 2 and 3 W/(m·K).
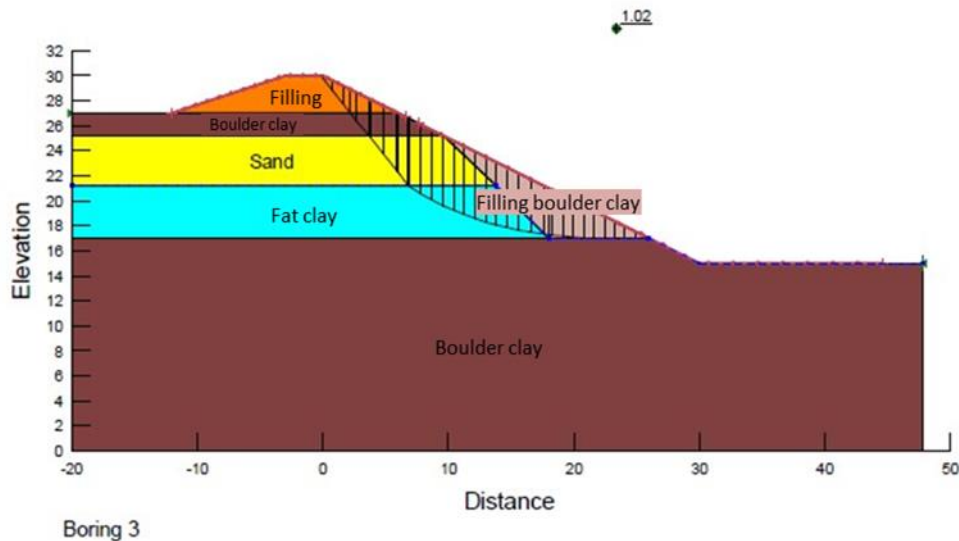

Boring 3

Figure 5.2.20. Cross-section sketch of the recommended setup around boring number 3.

Local geothermal and groundwater conditions

Besides from the special soil conditions, the geotechnical reports revealed presence of groundwater beneath the surface, at different depths. The surface of the PTES is situated between levels +26.3 m and +27.2 m. Figure 5.2.21 shows an overview of all the borings that have been drilled for the study, and Table 5.2.6 shows the groundwater levels encountered.

Table 5.2.6. Levels of the different groundwater layers for borings 1 to 9.

Boring number	1	2	3	4	5	6	7	8	9
Upper layer	+26.5	?	+26.5	+25.0	+26.5	-	+26.4	+26.3	+25.6
Lower layer	+23.6	?	+17.0	<+12.7	+23.2	<+13.0	+23.7	+18.2	<+12.3

The borings revealed 2 different groundwater levels, separated by the fat clay layers, and located between 0.2 meters depth and over 14 meters depth. Since the PTES bottom will be located 12 meters under the soil surface, a necessary groundwater sinking was recommended during the construction phase, by digging borewells with a minimum diameter of 250 mm, all around the PTES, as well as at the center/bottom area of the PTES. These groundwater conditions have not been used in detail as inputs to the modelling phase, but besides from the groundwater levels, the study has shown that no groundwater flow was identified, and therefore no extra heat loss was to expect.
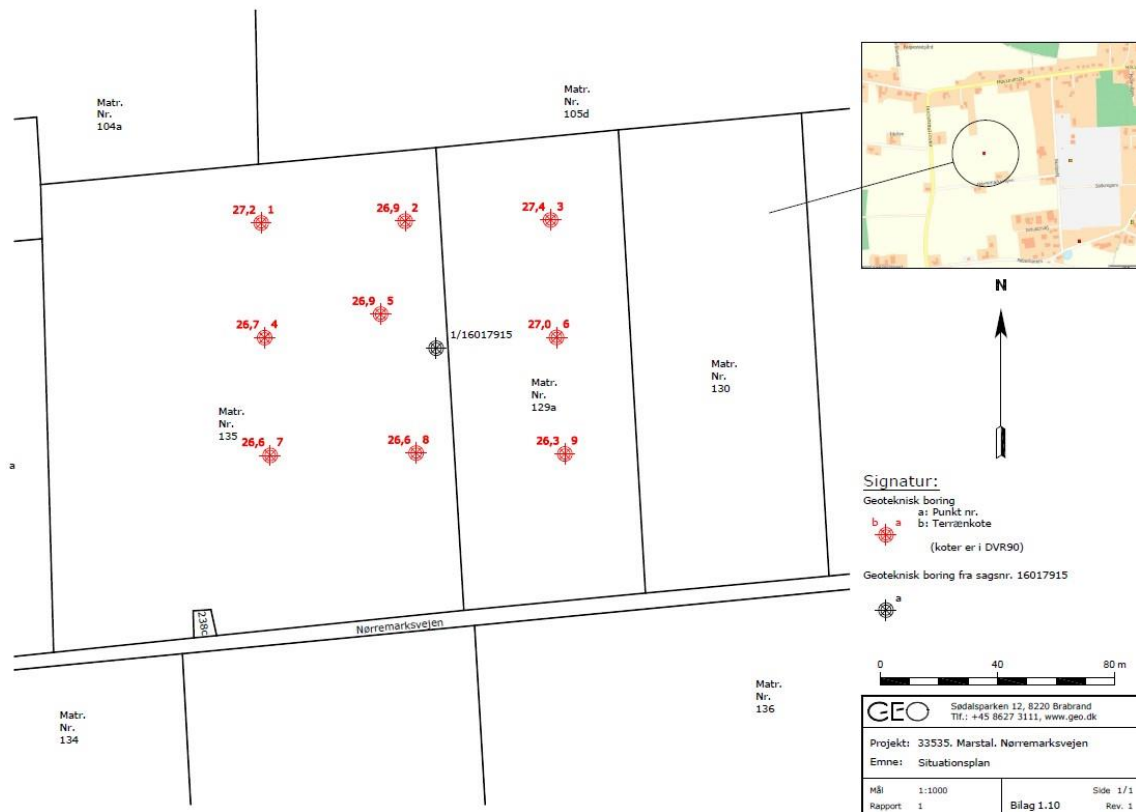
Figure 5.2.21. Location of the borings made by Geo in Marstal.

Modelling approach

In order to calculate the energy production of the solar heating system and the economy for the SUNSTORE 4 project, a model was set up in TRNSYS 16.

Conceptual simulation model

The model is displayed in the simplified diagram of Figure 5.2.22. This diagram will be used in the next section to describe control strategy of the TRNSYS model. These main components have been included in the TRNSYS model shown in Figure 5.2.23. The 3 solar collector fields ('9.000 m2', '9.300 m2' and '15.000 m2'), the 2 PTES ('10.000 m3' and '75.000 m3'), the new heat pump ('HP-CO2'), the propane heat pump ('HP-R290'), the wood chip boiler (with ORC), the Tank Thermal Energy Storage (TTES, '2.100 m^3') the bio-oil boilers ('Biooil') and the heat exchangers (HX-1 to 6). Table 5.2.7 gathers the legend for the connections between the components in the TRNSYS model.
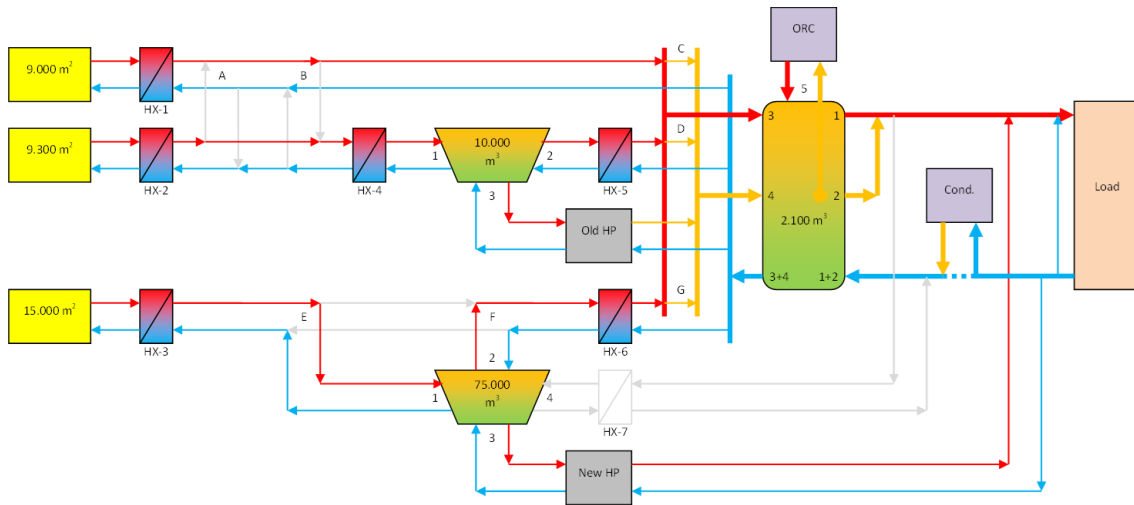
Figure 5.2.22. Functional diagram of the TRNSYS model. Light grey arrows indicate connections that have not been implemented in the TRNSYS model.

Table 5.2.7. Legend for the Marstal TRNSYS model connections shown in Figure 5.2.23.

Linked to	Color	Explanation
Solar Collector Field	Dark green	Water-glycol mixture loops
PTES	Light blue	Cooled water from the heat pump evaporators
PTES	Red	(Warm) Water arriving at or coming from the top of the PTES
PTES	Blue	(Cold) Water arriving at or coming from the bottom of the PTES
Condenser and ORC	Red	(Warm) Water coming out of the ORC
Condenser and ORC	Blue	(Cold) Water arriving at or coming from the boiler condenser
TTES – '2.100 m^3'	Red	(Warm) Water arriving at or coming from the top of the PTES
TTES – '2.100 m^3'	Blue	(Cold) Water arriving at or coming from the bottom of the PTES
TTES – '2.100 m^3'	Yellow	(Lukewarm) Water arriving at or coming from the middle of the TTES

Sunstore 4

PlanEnergi, September 11th, 2010 /
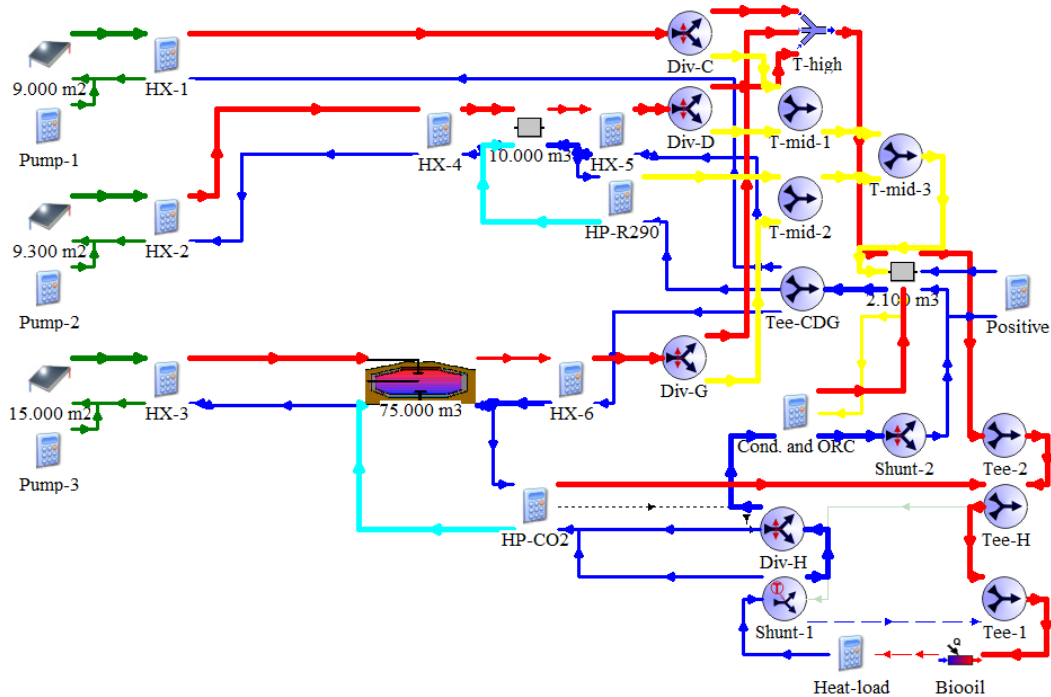Niels From

Figure 5.2.23. Graphical view of the water loops in the TRNSYS model (layers with controllers, weather, data files and outputs have been switched off).

PTES

The 75'000 m³ pit thermal energy storage is modelled by Type 342 (XST model), which uses a cylinder geometry (see Figure 5.2.7), the same as used for the PTES study in Dronninglund.

In this model, the PTES was divided into 11 segments. The PTES is set up to have 3 pipes to extract water from the PTES: one at the segment most at the top (segment # 1), one at the middle of the PTES (segment # 6), and a last at the segment most at the bottom (segment # 11). The water sent into the PTES is sent to the segment with closest temperature (it acts almost as if the water sent into the PTES was sent through a movable pipe, but instead of having to choose between 3 pipe heights, it chooses between the 11 segments).

Water inside the PTES is assumed to have a heat capacity of cp_{water} = 4.19 kJ/(kg·K), a density of 980 kg/m³, it is assumed to be insulated at the top by a 0.5 m thick material of conductivity 0.1 W/(m·K). The soil surrounding the water is consisting of one ground layer of 100 m depth, 2.3 W/(m·K) conductivity, and 2'300 kJ/(m³·K) volumetric heat capacity.

The PTES model has a volume of 75'000 m³, and a height of 7.8 meters. This height in the model is much lower than the actual PTES height (16.385 meters), which is built as an inverted truncated pyramid (see Figure 5.2.7). The TRNSYS PTES model height was determined to keep the same PTES lid area between modelling and reality: $88 \times 113 = 9'944$ m² in reality corresponds to $\frac{V_{PTES}}{h_{PTES}} = \frac{75000}{7.8} = 9'615 \, m^2$ in the model. This is due to a difference between early design dimensions and actual implemented dimensions.

The 10'000 m³ PTES is modelled as a steel tank storage, 10 meters high, containing water (cp_{water} = 4.19 kJ/(kg·K), a density of 992 kg/m³) and with fixed heat loss capacity rates:

- 900 kJ/(hr·K) at the bottom of the storage.
- 1'200 kJ/(hr·K) to the sides of the storage.
- 1'800 kJ/(hr·K) at the top of the storage.

Pre-processing workflow

Load - Heat demand

In 2009 the heat demand was 28'862 MWh ab plant of which 7'351 MWh (25%) was delivered from the current solar collector fields / heat storage system (SHS). The monthly heat demand is shown in Figure 5.2.24. More than 90% of the heat demand from May to September is covered by the SHS.
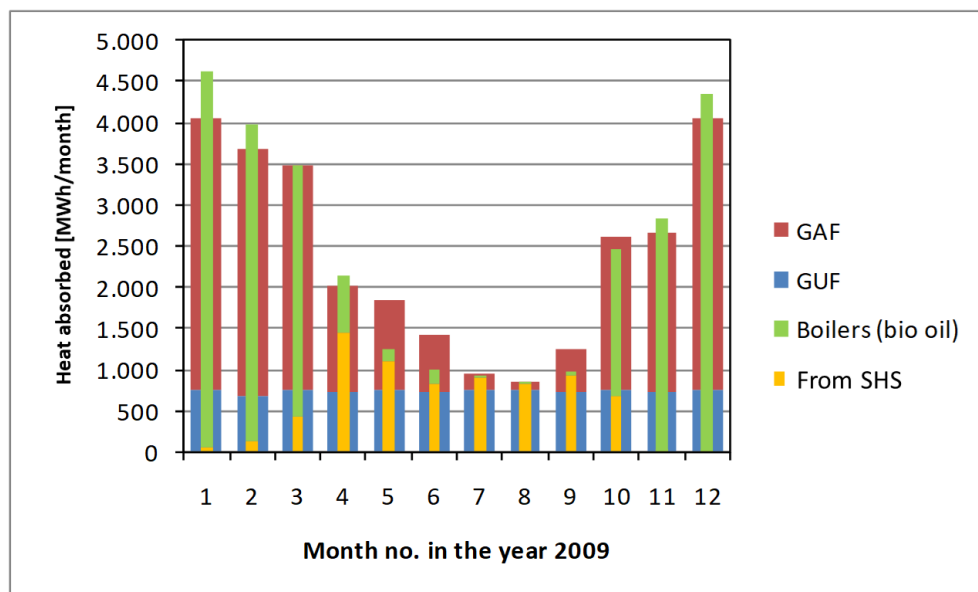

Figure 5.2.24. Monthly heat demand in 2009. 'GAF' and 'GUF' are explained in the text. GAF and GUF are calculated. Heat production from boilers and SHS are measured.

The heat demand is divided into the following two parts:

- GAF, which is the part of the heat demand that is <u>dependent</u> of the number of "degree-days" (the number of degree-days in 24 hours are defined as 17°C minus the average ambient temperature).
- GUF, which is the part of the heat demand that is <u>independent</u> of the number of degree-days.

The number of degree-days (for Fynen, DK) is taken from www.emd.dk. In 2009 there were 3'101 degree-days. In the 'emd normal year' (average from 1987 to 1998) there are 3'333 degree-days. Taking this into account, the heat demand in a normal year is 30'364 MWh of which 70.9% are GAF.

In 2010, the district heating area in Ommel would soon be connected to Marstal District Heating. The heat demand of Ommel is approximately 2'000 MWh/year. It has therefore been chosen to set the future average heat demand to 32'000 MWh/year (with 70.9% GAF).

In the original funding application, the heat demand was set to 28'000 MWh/year, so compared to this, the heat demand is increased by 14%. A representation of the resulting load profile is shown in Figure 5.2.29

Load - Forward and return temperatures

The forward and return temperatures are shown in Figure 5.2.25 and Figure 5.2.26. Forward temperatures are more transient compared to the return temperatures. The reason for this is that the forward temperature is controlled by the actual demand of year 2009.
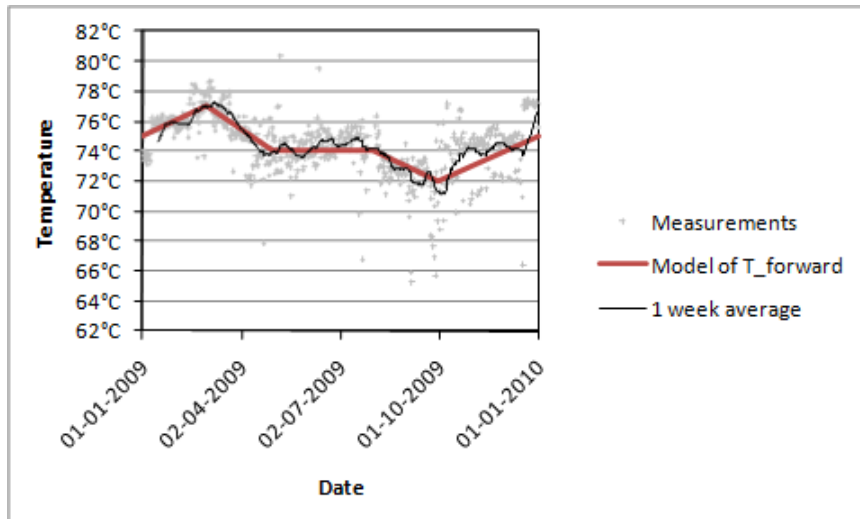

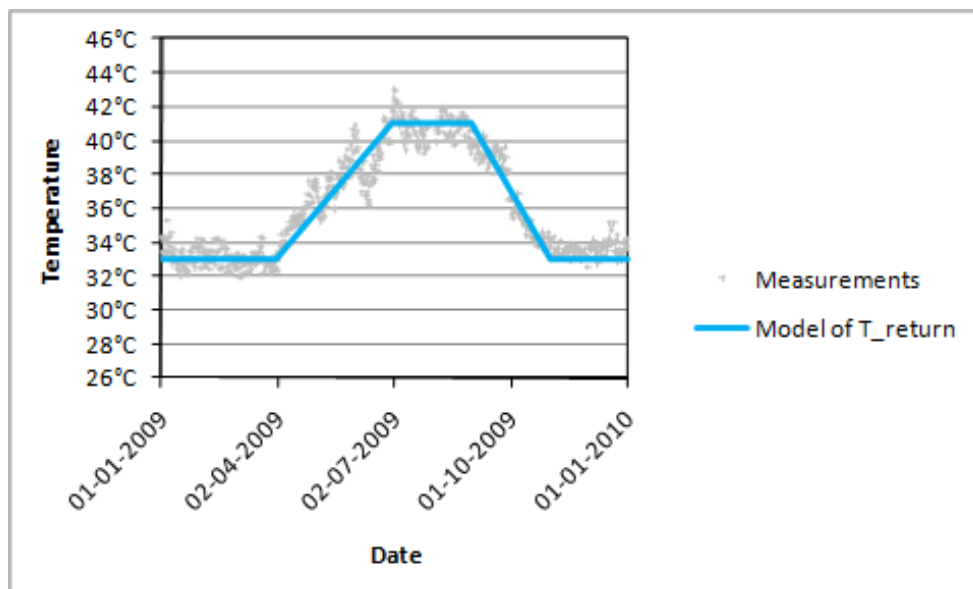**Figure 5.2.25. District heating forward temperatures for year 2009 and chosen model.**

Figure 5.2.26. District heating return temperatures for year 2009 and chosen model.

Based on the models shown in Figure 5.2.25 and Figure 5.2.26, the heat load, forward and return temperatures have been used as inputs to the TRNSYS model, through the component 'Heat-load' (see Figure 5.2.23). Heat load was translated into mass flowrates with the use of forward and return temperatures.

Control strategy – Solar collectors

The TRNSYS model works in the following way. The oldest collector field (9'000 m^2) charges the steel tank (2'100 m^3). The SUNSTORE 2 collector fields (9'300 m^2) charges the old pit heat storage (10'000 m^3), and the new SUNSTORE 4 collector field (15'000 m^2) charges the new pit heat storage (75'000 m^3). Table 5.2.8 gather the main optical parameters of the solar collector fields.

Table 5.2.8. Main thermal and optical parameters for the Solar Collector Fields (SCF).

Parameter Value [unit]	Fluid specific heat [kJ/(kg·K)]	η0	a1 [W/(m^2·K)]	a2 [W/(m^2·K^2)]	Row distance	Collector slope
SCF1	3.973	0.76	3.5	0.002	4.5	35
SCF2	3.973	0.81	2.577	0.0079	4.5	35
SCF3	3.973	0.85	3.07	0.01	4.5	35

Weather data from Meteonorm is used as inputs for ambient air temperature and solar irradiation. It corresponds to the typical meteorological year for 1995 (file format TMY2), for Copenhagen. In real life, all collector fields will be connected not only to their respective units, but also to the steel tank. Moreover, it will be possible to charge the pit heat storages from the steel tank. These two features have not been implemented in the TRNSYS model.

The way the flowrate is regulated for each solar collector field follows the same principle and is controlled by a specific pump component Pump-i, where i is either 1, 2 or 3 (see Figure 5.2.23).

The pump component has been internally developed at PlanEnergi and uses as inputs the total shaded radiation (calculated from geometry parameters, beam and diffuse radiation) together with the water inlet temperature from the previous timestep.

The way the flowrate is calculated in this component follows 4 direct control constraints:

1. A minimum temperature increase through the solar collectors.
2. A minimum outlet temperature for each solar collector field.
3. A maximum flowrate allowed to flow through the solar collector field.
4. A minimum flowrate allowed to flow through the solar collector field (defined as a fraction of the maximum flowrate).

These parameters differ for each solar collector field, and Table 5.2.9 gathers the main information used.

Table 5.2.9. Main parameters used for the solar collector fields' pump component.

Parameter\Pump	Pump-1	Pump-2	Pump-3
Minimum temperature increase ΔT_{min}	5°C	5°C	5°C
Minimum outlet temperature $T_{coll, out, min}$	33°C	25°C	20°C
Maximum flowrate	180'000 kg/hr	200'000 kg/hr	300'000 kg/hr
Minimum flowrate (fraction of max flowrate)	15%	15%	15%

For each timestep, the Pump-i component evaluates the solar collector efficiency based on current timestep total (shaded) solar radiation, outlet targeted temperature and ambient air temperature, using the following formula:

$$\varepsilon_i = G_{tot,shaded} \cdot (\eta_{0,i} - a_{1,i} \cdot \Delta T - a_{2,i} \cdot \Delta T^2)$$

Where:

- $G_{tot,shaded}$ is the total shaded radiation at the current timestep.
- $\eta_{0,i}, a_{1,i}$ and $a_{2,i}$ are the optical parameters of the given solar collector field.
- $\Delta T = \frac{T_{Coll\,i,out}+T_{Coll\,i,in}}{2} - T_{amb}$.
- $T_{Coll\,i,out}$ is the collector output temperature determined by the previous temperature constraints.
- $T_{Coll\,i,in}$ is the collector inlet water temperature from the previous timestep.
- T_{amb} is the ambient air temperature.

Then, the optimal flowrate is calculated by energy balance over the solar collector array, and the actual output flowrate is the optimal flowrate, limited by maximum and minimum flowrates:

$$Coll\,i_{\dot{m}} = \max\left(Pump_{i,\dot{m},min}; \min\left(Pump_{i,\dot{m},max}; \frac{Coll\,i_{area}}{cp_{water,glycol}\cdot\left(T_{Coll\,i,out}-T_{Coll\,i,in}\right)}\cdot\varepsilon_i\right)\right)$$

Where:

- $Pump_{i,\dot{m},min}$ is the minimum flowrate allowed through solar collector field i, while $Pump_{i,\dot{m},max}$ is the maximum flowrate.
- $Coll\,i_{area}$ is the total gross area of the solar collector field i.
- $cp_{water,glycol}$ is the heat capacity of the glycol-water mixture running through the solar loops.

This calculation/formula enables to calculate beforehand if, with the given temperature targets and temperature inlets, the solar collector field can produce heat for the next timestep. If $Coll\,i_{\dot{m}}$ is lower than $Pump_{i,\dot{m},min}$, then the pump i doesn't send any flow to the given solar collector field.

As mentioned, a delay component feeds in the collector field inlet temperature from the previous timestep to each pump. This is done to improve model stability, as with this input, it is possible to evaluate the minimum solar collector average temperature, and thus calculate an upper boundary of solar collector efficiency. If the inlet collector temperature is too high, for a given solar radiation, the upper boundary efficiency of the solar collector could be negative, in which case the calculated flowrate $Coll\,i_{\dot{m}}$ will be 0.

Once the flowrates have been calculated, the hot water flow coming out of the solar collector fields is sent to the other component of the model through heat exchangers "HX-i", i taking values 1, 2 or 3. In each heat exchanger, a constant temperature drop of 3°C is assumed between hot and cold sides (temperature difference between the hot-side inlet and cold-side outlet, and temperature difference between the cold-side inlet and the hot-side outlet). Flowrates on the cold side (opposite to the solar collector fields) are calculated based on energy balance and knowledge of the inlet/outlet water temperatures. This assumption is the same one as used for the model in Dronninglund.

Control strategy - Heat Pump (HP)

The pit heat storages can be discharged either by heat exchangers or by heat pumps. Heat from the heat exchangers and from the old propane (R290) heat pump[16] is sent to the steel tank.

The warm side of the new CO_2 (R744) heat pump is connected directly to the district heating network. The main reason for this is that the efficiency of a CO_2 heat pump is very dependent of the inlet temperature to the gas cooler (at the warm side of the heat pump). An example of the efficiency of a CO_2 heat pump is shown in Figure 5.2.27.

---

[16] The propane heat pump has been considered in the calculations, although it doesn't contribute significantly to the heating system and wasn't used after 2010.
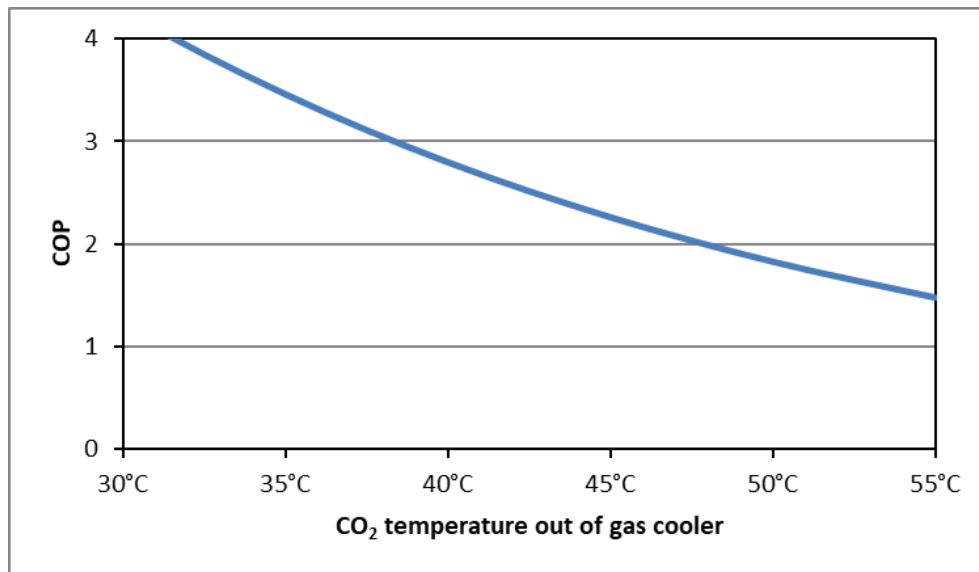
Figure 5.2.27. Coefficient Of Performance (COP) as a function of the refrigerant temperature out of the gas cooler in a CO_2 heat pump (the COP is calculated with the tool *CoolPack*[17], with an evaporation temperature of 10°C).

If the temperature of the water to the gas cooler gets too high (above 40-45°C) the CO_2 heat pump will not operate at all.

Control strategy - Wood chip boiler and ORC

The flue gas scrubber, in which water vapor in the flue gas is condensed, has second priority to the cold return water from the district heating network. As for the CO_2 heat pump the reason for this is that the fuel efficiency of the wood chip boiler is affected by the temperature of the cooling water as shown in Figure 5.2.28.

The electrical efficiency of the Organic Rankine Cycle (ORC) is relatively insensitive to the temperature of the cooling water into the cold side of the ORC unit. The ORC is therefore cooled by water from the mid outlet of the steel tank (TTES). The temperature of this water will be between the forward and return temperatures, typically around 60°C.

On the other hand, the electrical efficiency of the ORC is sensitive to the outlet temperature of the cooling water on the cold side of the ORC unit, because this temperature determines the pressure in the ORC condenser. In the TRNSYS model the flow rate of the cooling water in the ORC condenser is controlled so the outlet temperature of the cooling water from the ORC condenser will be 5 K above the forward temperature to the district heating network.
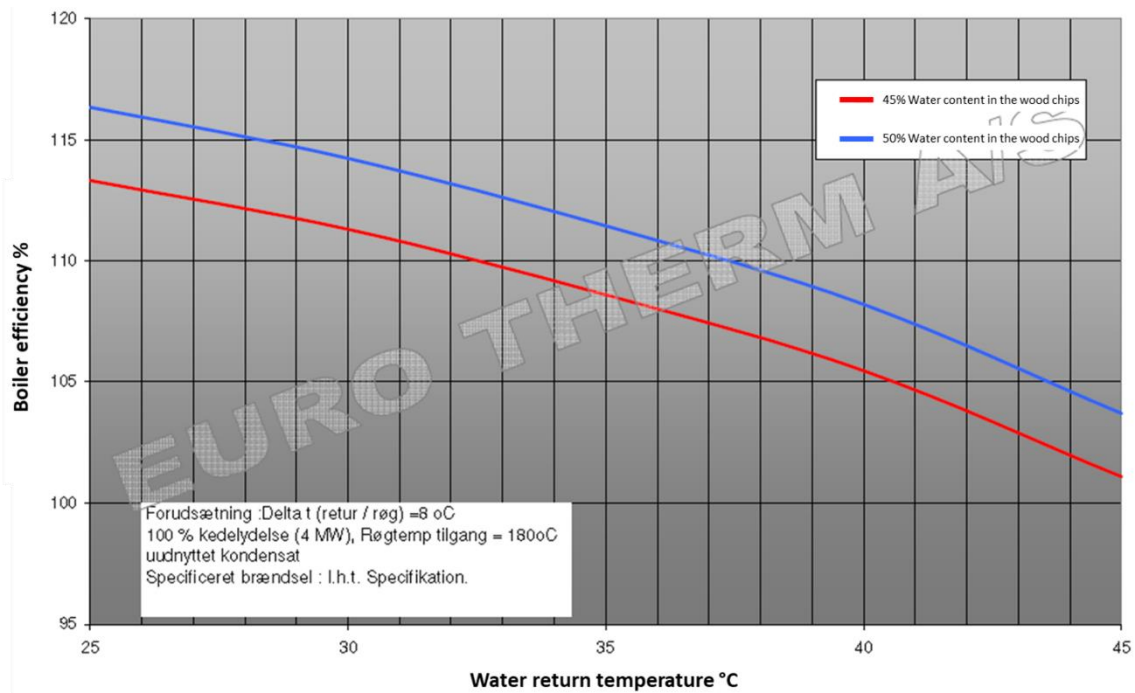
---

[17] https://www.ipu.dk/products/coolpack/

Figure 5.2.28. Wood chip boiler system efficiency as a function of the temperature of the cooling water into the flue gas scrubber. This figure is made by Euro Therm A/S.

Scenarios and results

Validation of the reference model

To validate the TRNSYS model of the SUNSTORE 4 energy system, the new parts of the SUNSTORE 4 have been disabled. This reduces the model to consist of the following parts:

- 9'000 m² + 9'300 m² solar collector fields.
- 10'000 m³ PTES.
- 2'100 m³ TTES.
- 100 kW$_{el}$ propane HP.

There is no wood chip boiler system in the reference. Key figures are listed in Table 5.2.10**.**

Full system simulation and optimization

The TRNSYS model was run for 2 years with a timestep of 1 hour. First results are obtained and used as a base for further optimization of the system (through testing various operational control strategies). Part of the optimization was aimed to reduce the designed fuel consumption of the bio-oil boilers.

Analysis and discussion

Results from the reference model

The simulation calculates the solar production to be 7.6% less than measured in 2009. The main reason for this might be that the simulation uses weather data (including solar radiation) from a 'typical' year, whereas the actual weather data in 2009 might depart from this.

The deviation for the 9'000 m² collector field is greater than the deviation for the 9'300 m² collector field. This might be caused by the fact that the first charges only the steel tank in model, and that the steel tank might be too small for this, leading to increased collector temperatures in the summertime.

The heat losses from the 10'000 m^3 pit heat storage were abnormally high in 2009 because the lid was not intact. The calculated heat losses were therefore much lower than the measured heat losses (close to 48% deviation).

The measured solar production minus the heat losses in the pit heat storage equals 7'600 MWh/year, which is 249 MWh/year or 3.4% more than measured heat delivered by the SUNSTORE 2 solar heating system. A part of this might be heat losses from the steel tank, but it might also indicate measurements' inaccuracies.

Table 5.2.10. Simulation results of the reference vs. measurements from 2009.

Reference		Solar production		Heat losses		Heat delivered
		9'000 m^2	9'300 m^2	PTES	TTES	
Measurements 2009	**MWh/year**	4'049	4'323	-772	?	7'351
Simulation	**MWh/year**	3'640	4'097	-402	-89	7'245
Deviation from meas.	**-**	**-10.1%**	**-5.2%**	**-47.9%**	**n/a**	**-1.4%**

Simulation results from the full system simulation

The TRNSYS model was then run for 2 years with a timestep of 1 hour. Results from year # 2 are presented in the following. The load profile and duration curves for the wood chip boiler heat production are shown in Figure 5.2.29.
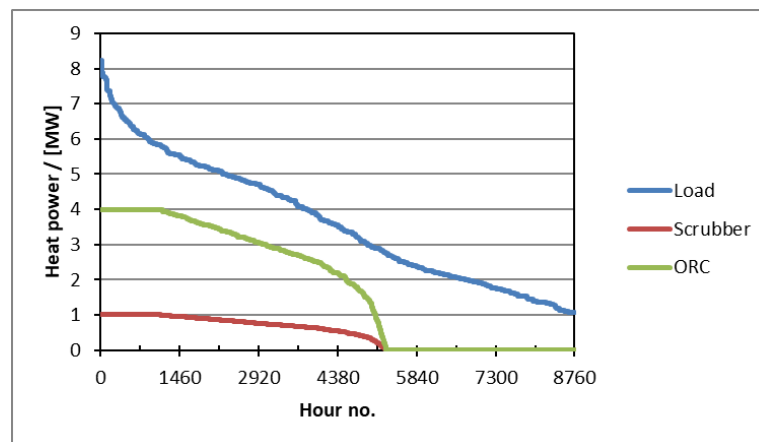

Figure 5.2.29. Duration curves for the heat load and the wood chip boiler system.

On the district heating side, the wood chip boiler system consists of a scrubber and an ORC. Key figures for these are given in Table 5.2.11 and Table 5.2.12.

The wood chip boiler system is shut down from day # 160 to day # 280 (from June 10th to October 8th). This means that the boiler is limited to max. 5'880 running hours per year. In the simulation the boiler gets 1'108 full load hours, 4'176 part-load hours and 596 hours with no load. The operation corresponds to 4'008 full load hours with a heat production of 16'028 MWh/year.

The reason for the part load operation of the boiler is that the capacity of the boiler is reduced in the model if the cold water flow rate to the scrubber is limited, or if the temperature of the cooling water to the ORC gets too high. The last rule ensures that the boiler is only running if heat is needed.

Table 5.2.11. Key figures for the district heating water to the scrubber.

Scrubber	T_{in}	T_{out}	$\dot{m}$	Q	Delta-T
	°C	°C	m³/h	MW	K
Max.	38.5	46.2	167	**1.00**	**8.0**
Avg.	33.5	41.2	94	0.83	7.5
Min.	**33.0**	37.6	55	**0.50**	3.9

Table 5.2.12. Key figures for the district heating water at the cold side of the ORC.

ORC	T_{in}	T_{out}	$\dot{m}$	Q	Delta-T
	°C	°C	m³/h	MW	K
Max.	61.9	82.0	129	**3.00**	42.3
Avg.	46.8	80.1	64	2.48	33.3
Min.	38.7	77.7	36	**1.50**	**20.0**

The heat pumps are allowed to run 12 hours per day in the 6-months period from October 1st to April 1st (2'196 hours/year). The propane heat pump gets 2'142 full load hours (97.5%) and the CO_2 heat pump gets 2'195 full load hours (>99.9%). The heat pumps have an electrical power consumption of 100 kW and 475 kW respectively for the propane and the CO_2 heat pump, and the direct heat production is 1'257 MWh/year.

The 33'300 m² solar collector fields produce 13'545 MWh/year (407 kWh/m²/year). The heat losses from the storages represent 2'833 MWh/year. The heat production from the solar collectors, the heat pumps, the scrubber and the ORC minus the heat losses from the storages equals 28'000 MWh/year. The remaining heat (4'000 MWh/year) is produced by the existing bio-oil boilers.

An overview of the calculated annual heat production is given in Table 5.2.13. Temperatures from the 3 storages are shown in Figure 5.2.30, Figure 5.2.31 and Figure 5.2.32.

Table 5.2.13. Overview over the calculated heat production.

Calculated heat production	MWh/year
9.000 m^2	3'383
9.300 m^2	3'727
15.000 m^2	6'435
Collectors total	**13'545**
Propane heat pump	214
CO_2 heat pump	1'043
Heat pump total	**1'257**
ORC	12'023
Scrubber	4'008
Wood chip total	**16'031**
2.100 m^3	-119
10.000 m^3	-520
75.000 m^3	-2'193
Storage losses total	**-2'833**
Bio oil boilers	4'000
Total	**32'001**
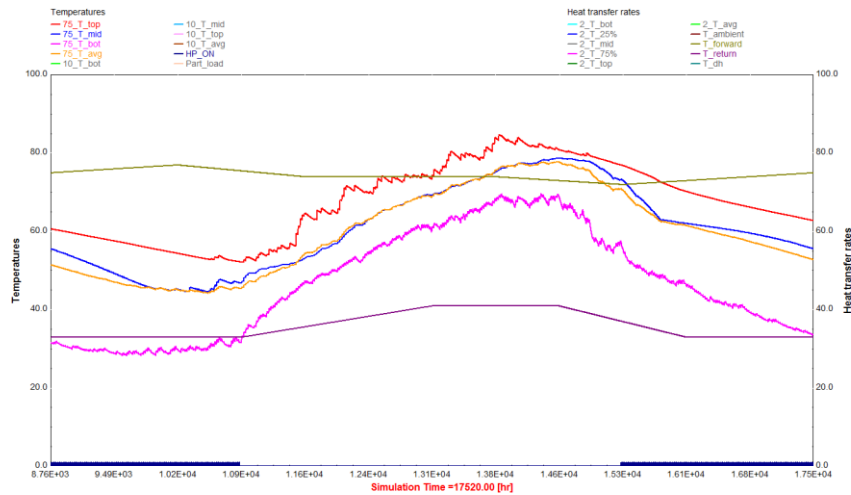
Figure 5.2.30. Top, mid, bottom and average temperatures in the 75'000 m^3 pit heat storage as well as forward and return temperatures in the district heating system (simulation year # 2). The dark blue line in the bottom of the diagram shows the operation time of the heat pump.
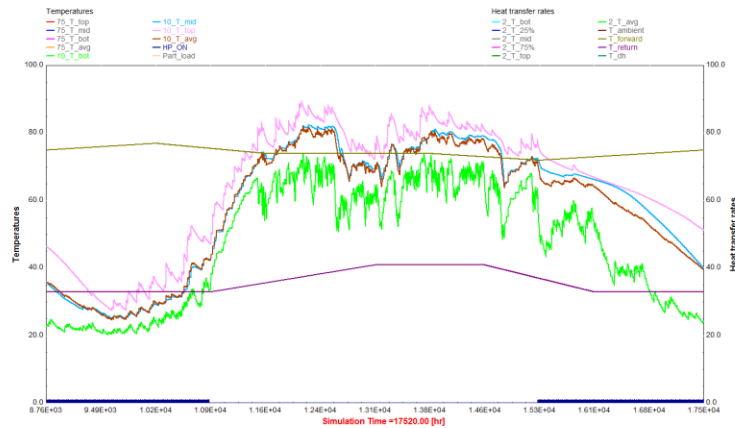
Figure 5.2.31. Top, mid, bottom and average temperatures in the existing 10'000 m³ pit heat storage as well as forward and return temperatures in the district heating system (simulation year # 2).
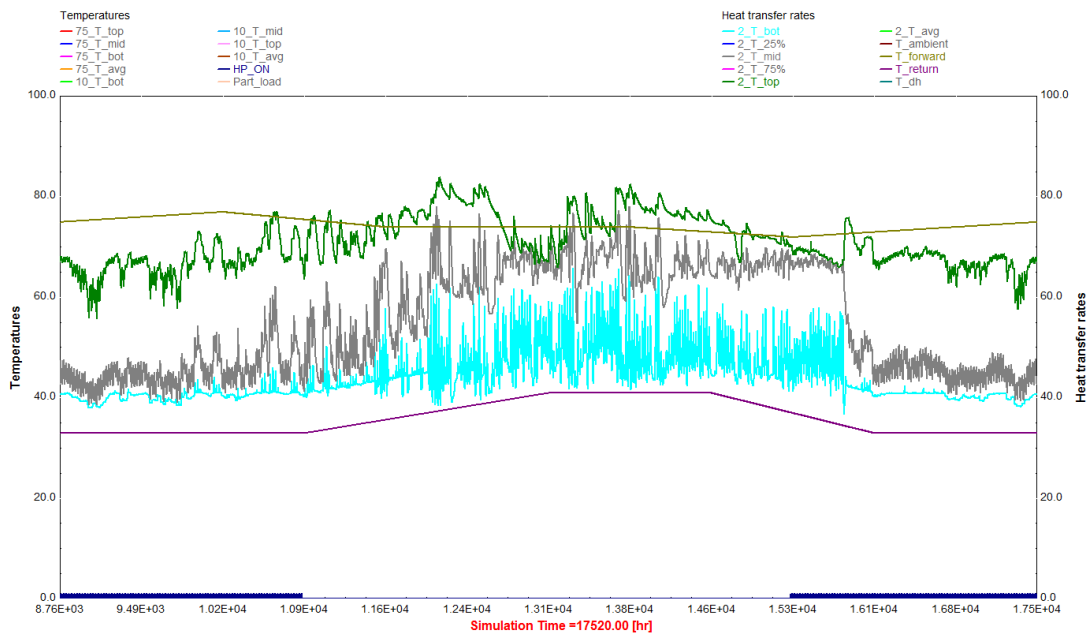

Figure 5.2.32. Top, mid and bottom temperatures in the 2'100 m³ steel tank as well as forward and return temperatures in the district heating system (simulation year # 2). Note what happens to the mid temperature when the wood chip boiler is started at about hour # 15'800.

The part load ratio for the wood chip boiler system is shown in Figure 5.2.33.
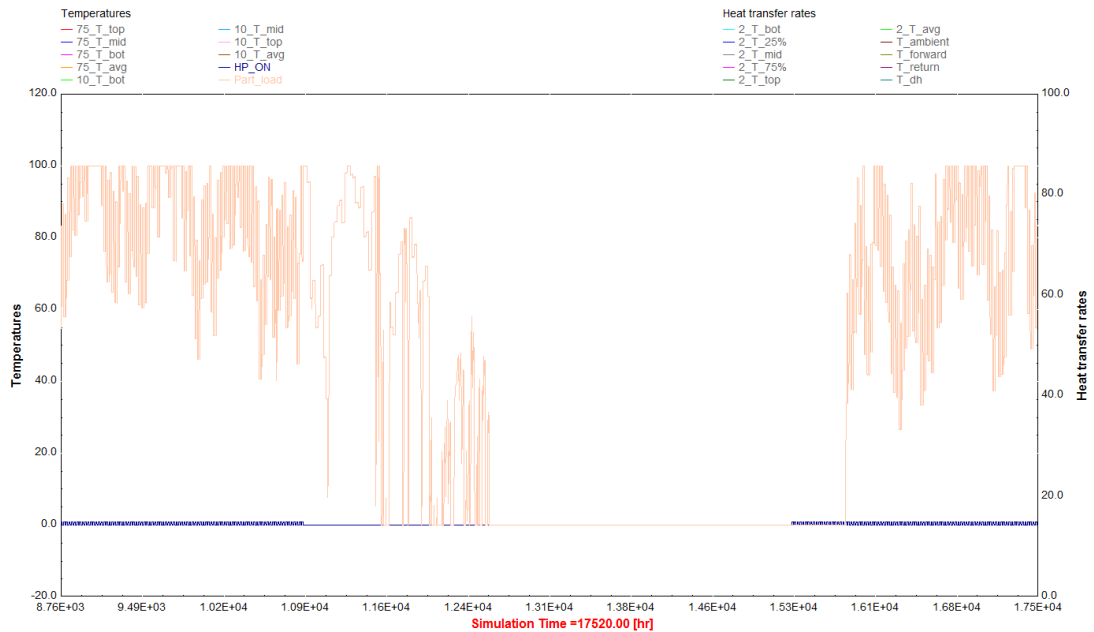
Figure 5.2.33. Part load (actual load over max. load in [%]) for the wood chip boiler system. These data are linked to the duration curves in Figure 5.2.29. When the CO$_2$ heat pump is ON the boiler load is reduced due to priority of the cooling (return) water.

Extreme temperatures in the storages are shown in Figure 5.2.34 and in Table 5.2.14. Calculated temperature exploitation range of the 75'000 m^3 pit heat storage is 34 K, which is only 60% of the 57 K in the 10'000 m^3 pit heat storage.

The main reason for this might be the difference in the ratios between the installed heat pump cooling capacities (approximately 1'000 kW and 400 kW respectively for the 75'000 m^3 PTES and the 10'000 m^3 PTES) and the storage volumes: approximately 13 W/m^3 and 40 W/m^3 respectively.
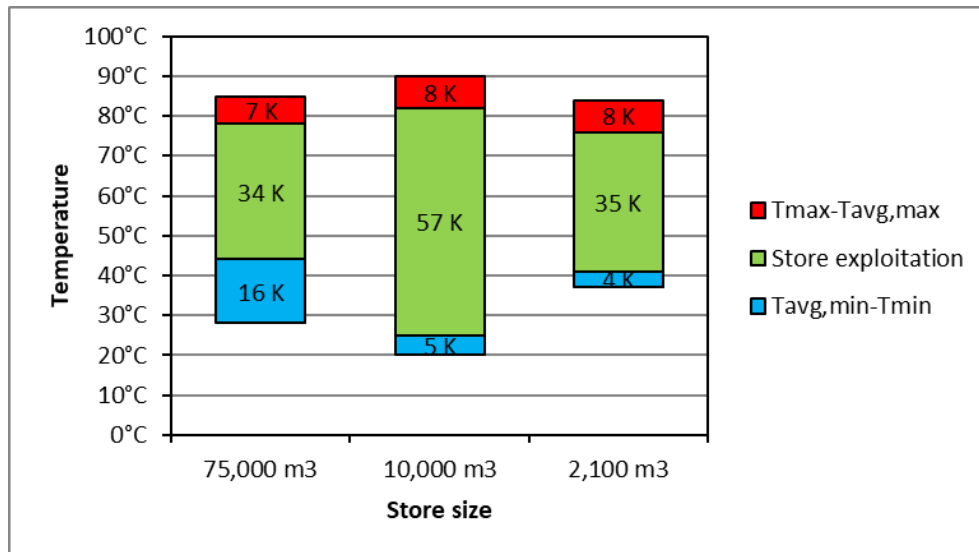
Figure 5.2.34. Extreme temperatures in the storages (simulation year # 2).

Table 5.2.14. Extreme temperatures in the storages (simulation year # 2). T_{avg} is the average temperature in the store at a given time.

Storage size	75'000 m³	10'000 m³	2'100 m³
T_{max}	85°C	90°C	84°C
$T_{avg,max}$	78°C	82°C	76°C
$T_{avg,min}$	44°C	25°C	41°C
T_{min}	28°C	20°C	37°C

System and control strategy optimization

The description given previously is based on design at the time of the first design group meeting, i.e. September 2010. In this design the heat production from the existing bio oil boilers was approximately 4'000 MWh/year (Table 5.2.13). In the control strategy, the bio oil has the lowest priority because this production unit has the highest heat production price.

At the first design group meeting the heat production from the bio oil boilers was discussed: what was the origin of the relatively high share (12.5% of the annual heat production) and what could be done to reduce the bio oil consumption. The following study presents the analysis of the bio-oil consumption and the different scenarios tested to reduce this fuel consumption.

Up to the second design group meeting the bio oil consumption was analyzed. Figure 5.2.35 shows the heat production from the bio oil month by month. The figure shows that 8% of the bio oil is used in the summertime (from May to October), and 92% is used in the wintertime (from November to April).
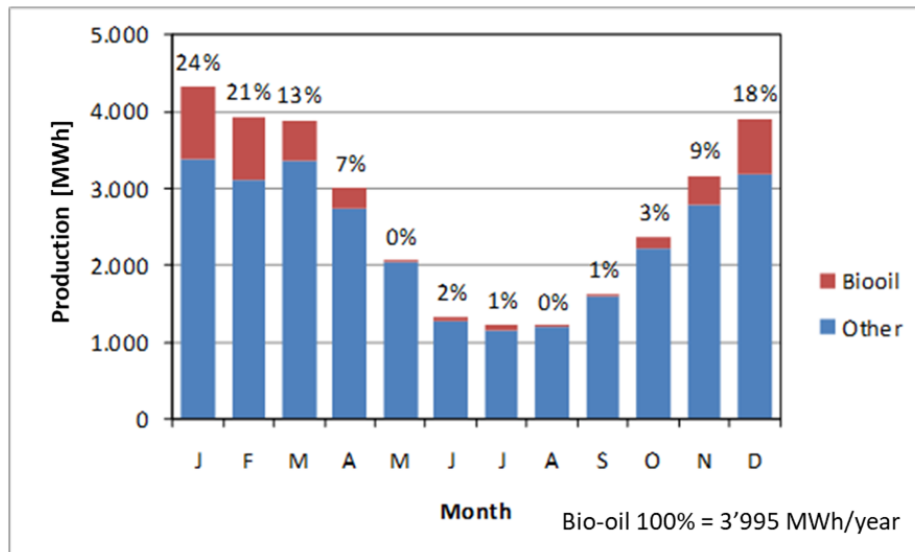
Figure 5.2.35. Monthly distribution of the heat production from the bio oil boilers.

Figure 5.2.36 shows the heat production from bio oil under different conditions. 'Reference' corresponds to the design explained above. 'Solar + 5'000 m2' corresponds to a design where the solar collector area is increased by 5'000 m^2 compared to the reference design. This reduces the heat production from the bio-oil boiler by nearly 1'000 MWh/year.
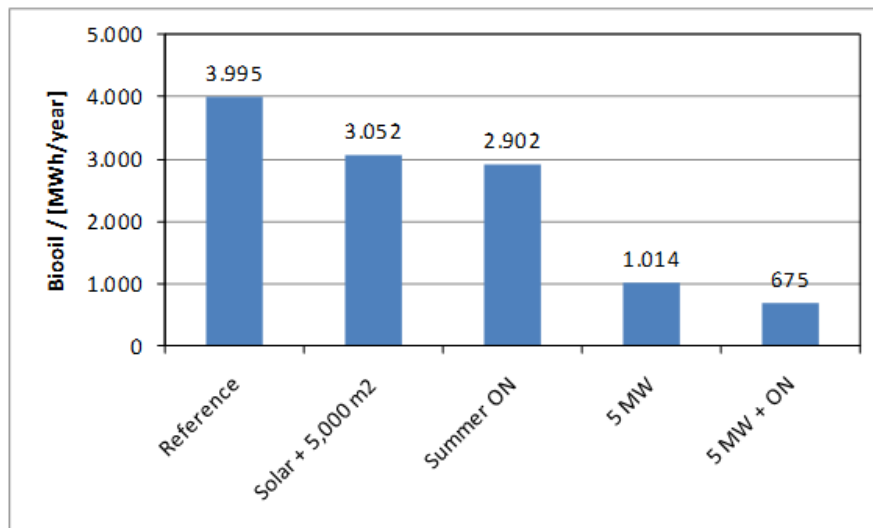

Figure 5.2.36. Reduction of bio oil consumption as a result of different actions.

'Summer ON' corresponds to a situation where the biomass boiler is allowed to run at any time of the year. In the reference design this boiler was forced off in the summer period (from May 10th to October 8th). This change in the operation strategy reduces the heat production from bio oil with 1'100 MWh/year, or a little more than the extra 5'000 m^2 of solar collectors.

'5 MW' corresponds to a design where the heat output from the biomass boiler system is increased from 4 MW in the reference design to 5 MW. This action reduces the bio oil consumption by 75%.

'5 MW + ON' corresponds to the combination of '5 MW' and 'Summer ON'. In this case the reduction of heat from bio oil is only 339 MWh/year or 1/3 of 'Summer ON' with the 4 MW biomass boiler in the reference design.

Between the 2nd and 3rd design group meetings the bio oil consumption was further analyzed. Figure 5.2.37 and Figure 5.2.38 show the results of this.

The 'Reference' corresponds to the initial design, i.e. the figures in Table 5.2.13.

'Wood chip incr.' corresponds to a design where the heat output from the 4 MW biomass boiler system (including the ORC) is increased from 4.0 MW to 4.6 MW. This is not because the biomass boiler system capacity is increased, but because more detailed information has become available as a result of the detailed design of the biomass boiler system.

'HP improved' corresponds to a change in operation strategy for the heat pump, which makes it more flexible.

'Flue gas DT incr.' corresponds to a change in operation strategy for the scrubber. In the original design the water in the scrubber was limited to a max. temperature increment of 8 K. This resulted in a lot of part load of the biomass system. In this calculation, water is allowed to be heated up to 16 K before part load is forced.
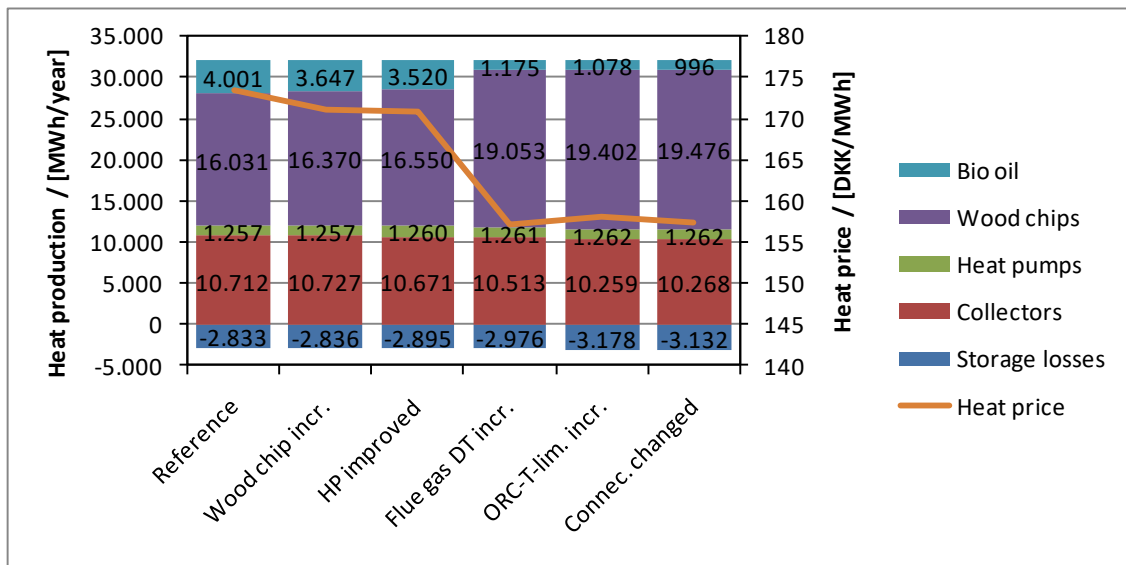

Figure 5.2.37. Heat production in [MWh/year] for the different production units as well as the heat production price. Note that collector production is the sum of 'Collectors' and 'Storage losses', and that the different actions are accumulated from left to right.
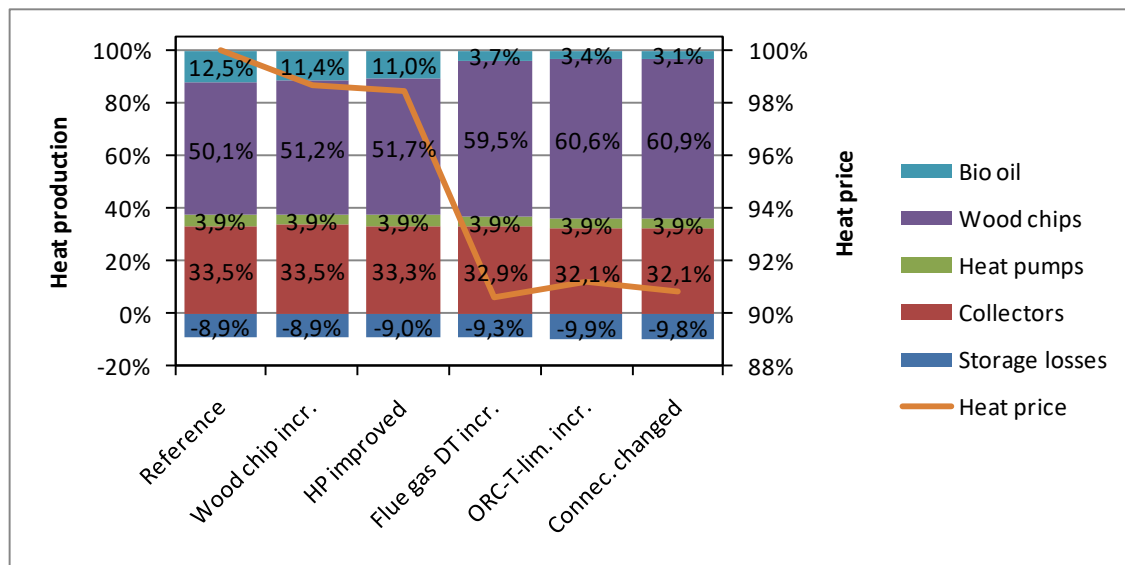
Figure 5.2.38. Relative heat production for the different heat production units as well as the heat production price relative to the reference.

'ORC-T-lim incr.' corresponds to a change in the operation strategy where the max. inlet temperature to the ORC condenser is increased from 64.5°C to 67.0°C before part load operation is forced.

'Connec. changed' corresponds to a change in the design where the scrubber, the grate cooling and the ORC are serial connected.

As the last column of Figure 5.2.37 has the lowest heat production from bio oil, this is defined as the final design data. The calculations result from the optimized model are presented in Table 5.2.15, together with measurements result from the first year of operation (2013).

Table 5.2.15. Main yearly energy contribution to the load for original design calculations (left), optimized design calculations (middle) and measurements from first year of operations (right).

Production part [MWh/year]	Original design	Optimized design	Realised (2013)
Solar heat (SCF + PTES + HP)*	12'927	13'400	14'326
Heat pump el. consumption*	2'931	1'262	1'190
Wood chip boiler*	11'304	19'476	17'182
Existing oil boiler*	190	996	3'794
Heat loss, storages*	-978	-3'132	-3'093
ORC electricity production	2'600	3'175	2'133
SHS heat (solar heat + HP el.)	14'880	11'530	12'423
Total heat (sum of *)	26'374	32'002	33'399
SHS share [%]	56.4%	36.0%	37.2%

The wood chip boiler was still not in normal operation in the first months of 2013. That explains the low realized production from the boiler and the ORC. The solar production is better than expected in design calculations, most likely because of the difference between the weather dataset used (weather for

Copenhagen, typical meteorological year 1995) and the actual local weather conditions (Marstal in 2013). Nevertheless, the solar fraction was below the original objective of 55% mainly because the heat demand in Marstal had been extended since 2009, when the SUNSTORE 4 application was made.

Conclusions

Measurements (see Table 5.2.15) indicate that the demonstration plant uses 100 % RES and demonstrates the elements mentioned in the objectives.

The solar fraction is lower than the 55% objective (36% for the calculations, 37% for measurements from 2013). This is mainly due to the extension of the heat demand compared with the start of the project.

The calculations made for the solar heating system (former SCF and new SCF, PTES, TTES and heat pump) are in good accordance with the measurements.

An optimization of the system design and of the control strategy has shown how to reduce both the bio-oil boiler consumption and the heat price. Improvement in the way the wood chip boiler is operated (both the scrubber and the ORC), the understanding of the boiler specifications and in the HP flexibility showed how the heat price could be reduced by 9%, and that the bio-oil boiler heat use could be reduced from 3'995 MWh/year to 675 MWh/year. This hasn't been realized in 2013 because the wood chip boiler was still not in normal operation in the first months of 2013.

The optimization study has been carried out in TRNSYS and has shown how useful this tool could be for system design. The model has also been tested against measurements data, both for the system without the new installations (from SUNSTORE 4 project) and the full system. Good accordance has been found for most of the parameters (10% or less deviation), and clear explanations can be advanced for the parameters that differ more from the measurements.

5.2.2 Borehole Thermal Energy Storage (BTES)

5.2.2.1 Danish pilot site in Brædstrup

Brædstrup Totalenergianlæg (Brædstrup Total Energy Plant) is the production plant for Brædstrup District Heating. During the summer 2009 the board of directors in Brædstrup Totalenergianlæg decided to extend their existing solar collector field on their way to 100 % RES, by adding extra solar collectors, a heat pump and a seasonal thermal energy storage (a BTES and a Buffer Tank). Applications were sent to Energinet.dk's support program 'ForskEL' for support to design and implementation of such an extension. It was supported by both Energinet.dk's ForskEL program and EUDP[18].

UTES concept and specifications, scope and aims of the study

When the project 'Boreholes in Brædstrup' started, Brædstrup Total Energy Plant already had:

- 8'000 m^2 thermal solar collectors.
- 2 natural gas fired engines (8.2 MW$_{th}$ total capacity).
- 2 gas boilers.
- 2'000 m^3 accumulation tank for the heating system.

In the original application, the new system should add, as a first step to covering 50% of the yearly heat consumption with solar (approximately 40'000 MWh):

- A pilot borehole storage of approximately 8'000 m^3 soil volume.
- A 2'000 m^3 buffer tank.
- A heat pump of 1 MW$_{th}$ capacity approximately.

Since the pilot plant should only be the first step towards 50 % solar fraction, the design of the pilot plant started with design of the full-scale plant including solar collectors, accumulation tank, a full-scale borehole storage and heat pumps.

In the area identified for new field of solar collectors, 42'000 m^2 was available, and the accumulation tank for the full-scale plant was expected to be 5'000 m^3. Therefore, these two parameters were fixed in the design calculations for the full-scale plant. An overview is shown in Figure 5.2.39. The size of the other component of the system have been determined afterwards by the design modelling study:

- The size of the heat pump.
- The volume of the full-scale BTES.
- The volume of the pilot BTES.

---

[18] *Boreholes in Brædstrup – Final report, 2013*, ForskEL project number 2010-1-10498 and EUDP project number 64012-0007-1.
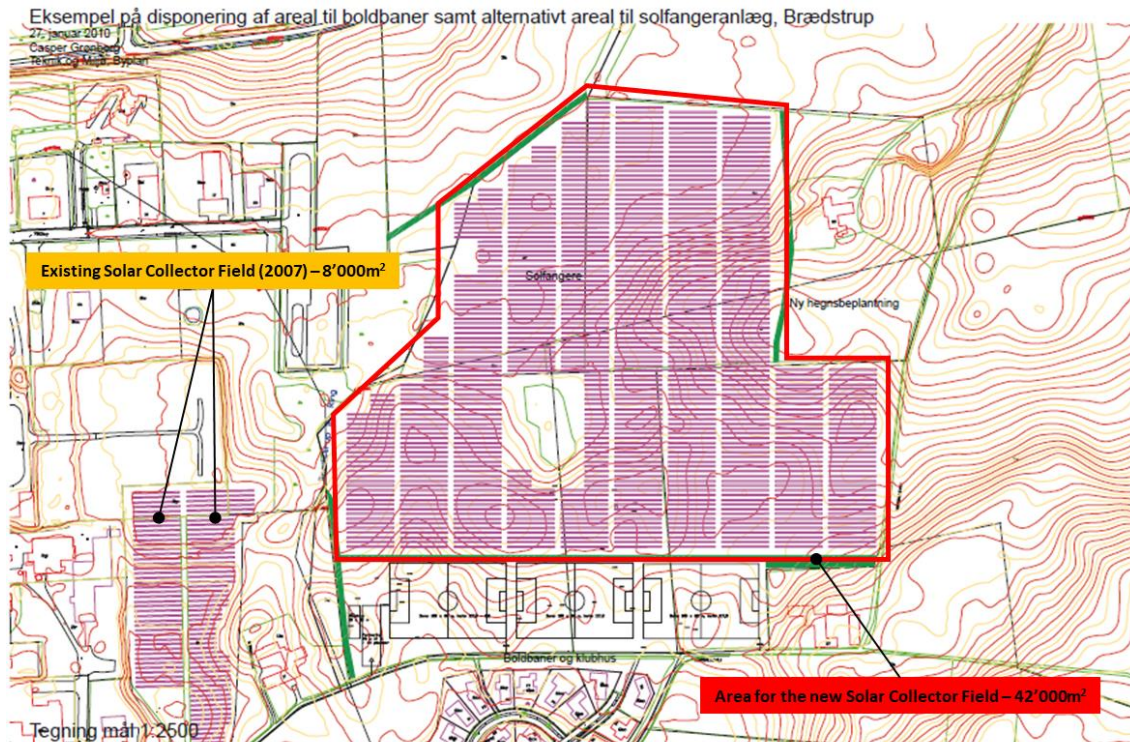
Figure 5.2.39 Land area available for new solar collectors in Brædstrup, in 2009.

System geometry and related geology

The company GEO has performed a geological and geotechnical site investigation for the BTES project[18]. The main results from this study is described in the following.

The site investigation comprises 8 Cone Penetration Test (CPT)-soundings, 2 borings, 1 thermal response test in a boring and laboratory tests. The location of the borings and CPTs are presented in **Figure 5.2.40**. The CPTs were penetrated unto maximum possible depth of 9.3 to 20.6 meters (90 kN thrust). Boring "no. 3" was carried out as Ø6" cased boring (dry rotary drilling) unto 25 meters depth. Boring "no. 4" was carried out as Ø10" cased boring (dry rotary drilling) unto 51 meters depth, where groundwater was encountered.
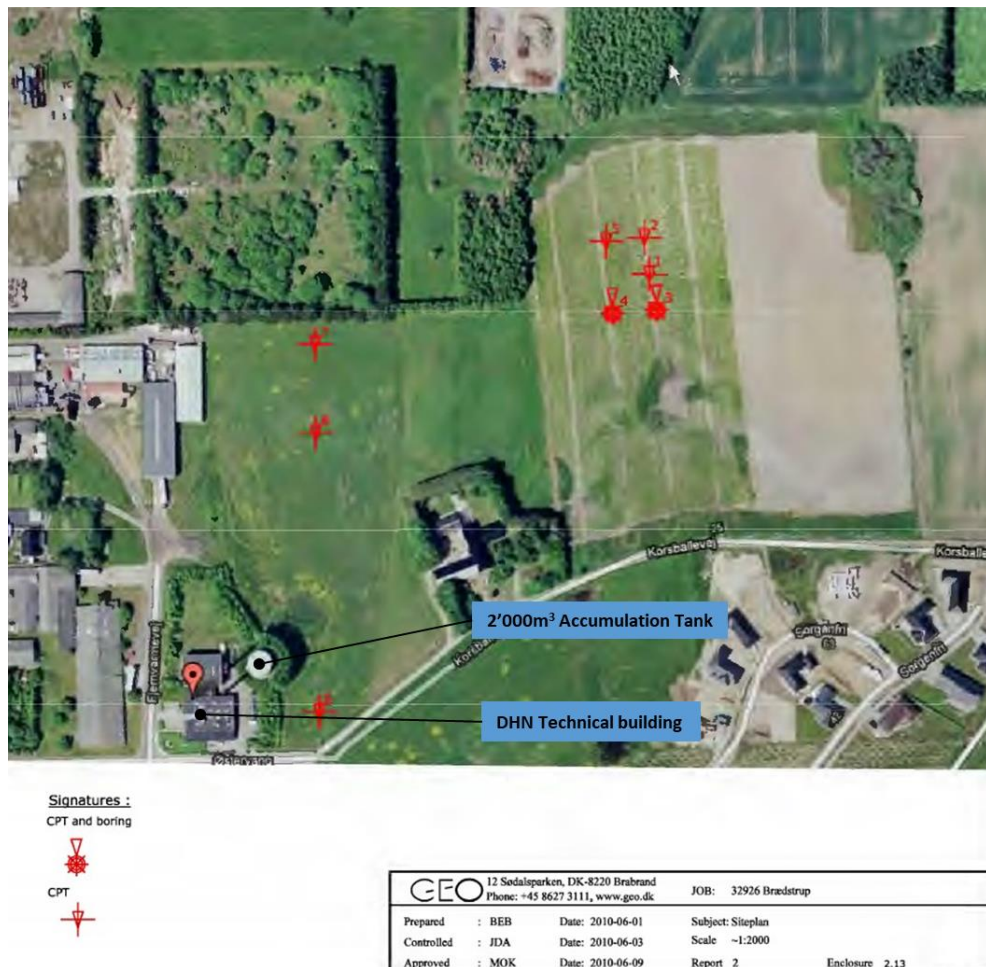
Figure 5.2.40. Map placing the CPTs and borings next to the original District Heating Network building in Brædstrup.

Local geothermal and groundwater conditions

The geological site investigation has found that the groundwater table is at approximately 50 meters depth, with no groundwater flow. During drilling seepage of ground water were registered in the upper clay till, but the standpipes were dry at later soundings of groundwater tables. The borings were made in the late Winter and early Spring, whereas water from e.g. melting snow presumably has weathered the upper soil (seasonal secondary groundwater).

Below this the different soils were dry down to nearly 50 meters depth. During drilling groundwater was encountered in 49.3 meters depth. At a later sounding in the deep standpipe no groundwater table was recognized. Therefore, the groundwater table in the primary reservoir may be deeper than 51 meters (Danish Vertical Reference 1990 - DVR90 - level +69). A study of other borings in the neighborhood (using the national database of borings at http://www.geus.dk) indicates a groundwater table in approx. DVR90 level +65 in the primary groundwater reservoir. These observations were confirmed by the measured natural water content, which generally was very low (w = 2 – 8 %) in the sand deposits.

A thermal response test was also carried out. The average thermal conductivity down to 45 meters was measured to 1.42 W/(m·K) and the average volumetric heat capacity is 1.8 – 2.0 MJ/(m³·K). Thermal resistance of the borehole was also measured to R_b = 0.172 m·K /W. It was therefore concluded that the soil was relatively well suited for energy storage.

Modelling approach

The original plan was to design the pilot plant as a first step to a bigger renewable heat production system. The pilot plant should later be extended to reach a 50% solar heat coverage of the demand. Therefore, the pilot plant was designed after designing the full-scale solution. During the project period the project group has utilized experiences from a similar BTES project in the German city Crailsheim.

Full-scale renewable energy (RE) system design

The full-scale RE system is designed in steps, as illustrated by Figure 5.2.41.
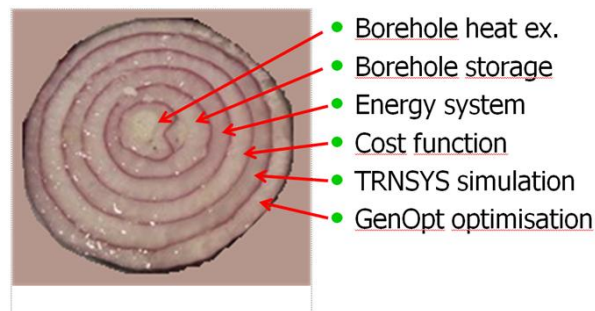

Figure 5.2.41. 'Onion rings approach to designing the system, starting from the center.

Borehole heat exchanger

The design of the borehole heat exchanger is similar to the heat exchanger in Crailsheim:

- Borehole diameter: 150 mm.
- Number of U-tubes per borehole: 2.

A calculated value of the thermal resistance is used (see BTES model below).

Borehole storage

Calculation of the borehole storage is carried out in TRNSYS with the DST-model, Type 557a. The calculation methodology is explained in the DST manual[19].This model assumes that a given number of boreholes are placed uniformly within a cylindrical storage volume of soil. There is convective heat transfer within the pipes, and conductive heat transfer to the storage volume. The temperature in the ground is calculated from three parts: a global temperature, a local solution, and a steady-flux solution. The global and local problems are solved with the use of an explicit finite difference method. The steady flux solution is obtained analytically. The temperature is then calculated using superposition methods. The geometry used by the model is represented in Figure 5.2.42.

The model parameters were set to the following, after the geological investigation of the site:

- The soil properties (heat conduction and heat capacity) are homogeneous inside the storage volume (or 'boreholes area', see Figure 5.2.42) 1.4 W/(m·K) and 1.9 MJ/(m3·K) as well as outside the boreholes area.
- The boreholes will be 45 m deep since the ground water level is expected to be at least 50 m below the surface.
- Outside the boreholes area, the soil is divided into 9 layers of 5 meters.
- Borehole thermal resistance was taken equal to 0.01755 m·K·hr/kJ.

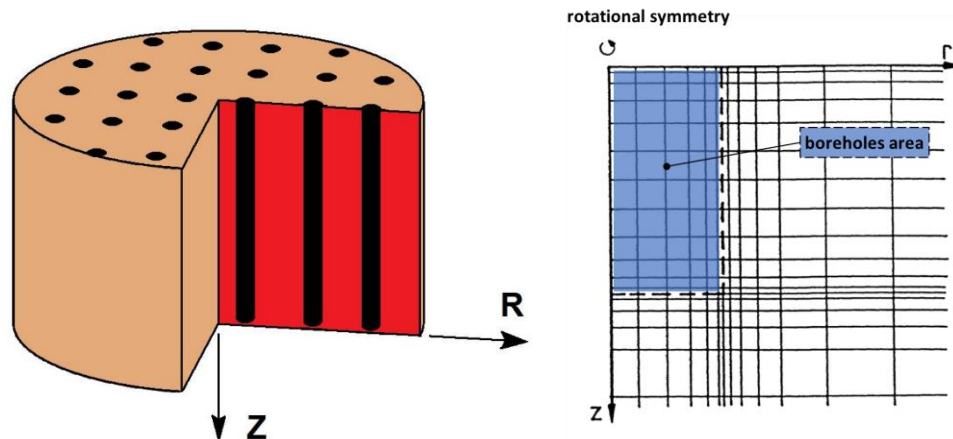[19] *Duct ground heat storage – Manual for computer code*, 1989, Göran Hellström.

Figure 5.2.42. Geometry used to model the BTES in the DST TRNSYS model (left figure) and example of mesh (right figure, taken from the DST Manual for Computer Code[19]) used for the soil modelling in TRNSYS DST model.

Energy system – main components

Having found the component needed to model the BTES, a principle diagram for the full-scale energy system has been established and can be seen in Figure 5.2.43. From this, a corresponding TRNSYS model was developed (see Figure 5.2.44).

Main components of the energy system are:

- The 50'000 m^2 solar field, 'collector field'.
- The main solar heat exchanger 'HX-1'.
- The 2'000 + 5'000 m^3 TTES, named '5000m3'.
- The BTES.
- The gas boiler, 'gas-boiler-1'.
- The heat pump, 'heat-pumps'.
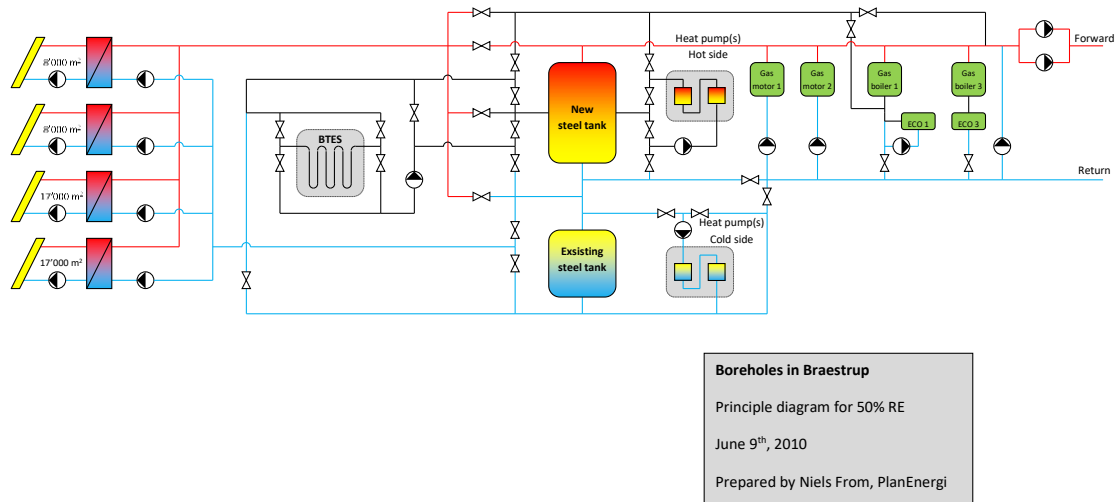- The heat load 'heat-load', with a yearly demand of 45'000 MWh.

Figure 5.2.43. Principle diagram for the full-scale plant.
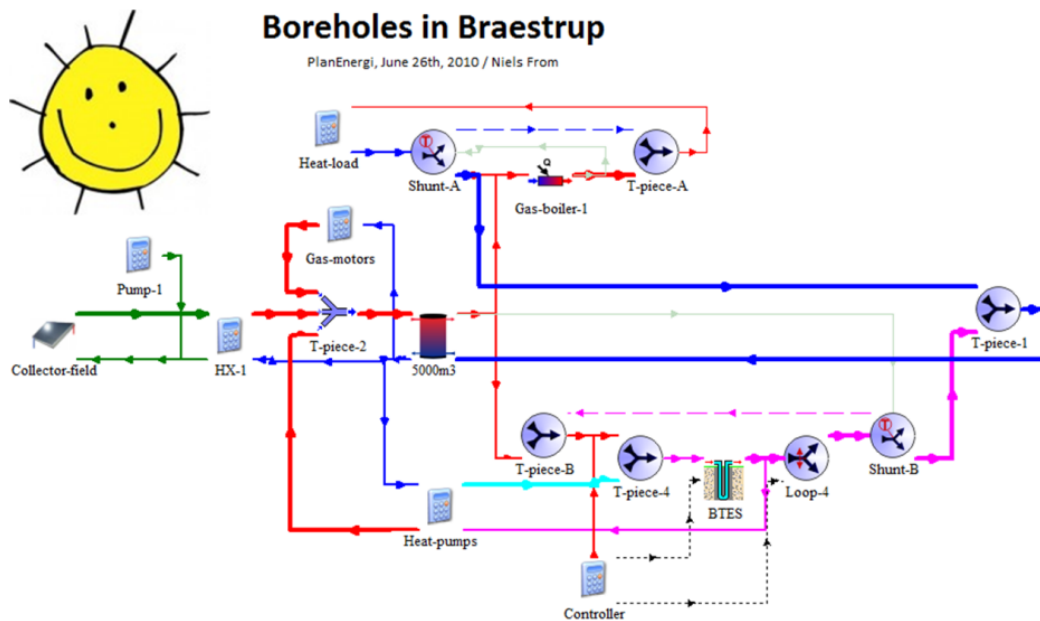

Figure 5.2.44. TRNSYS model for the full-scale plant.

Pilot energy system design

The pilot plant calculations were performed using the same model as used for the full-scale RE system, using the following figures:

- Solar collector area 16'000 m^2 (8'000 m^2 + 8'000 m^2).
- Steel tanks 5'000 m^3 + 2'000 m^3.
- Number of 1.2 MW$_{th}$ heat pumps: 1.
- 19'200 m^3 soil volume for the BTES, with 48 boreholes.
- Investment 20'000'000 DKK.
- Capital costs of 7%/year = 1'400'000 DKK/year.

Pre-processing workflow

First version of the TRNSYS model

The way the TRNSYS model is controlled is done through the following rules and formulas.

Solar Collector Field (SCF)

The way the flowrate is regulated is following the same principle as used in the Marstal model, with a target temperature increase of 10°C, a minimum outlet temperature of 40°C, and a max flowrate of 250'000 kg/hr. Optical parameters of the collector field are gathered in Table 5.2.16. The heat produced by the solar collectors is sent to the tank TES through a heat exchanger assuming a constant temperature drop of 3°C is assumed between hot and cold sides (same design as the Marstal model).

Table 5.2.16. Main thermal and optical parameters for the SCF.

Parameter [unit]	Fluid specific heat [kJ/(kg·K)]	η0	a1 [W/(m²·K)]	a2 [W/(m²·K²)]	Row distance	Collector slope
Value	3.973	0.815	2.43	0.012	5	30

Weather data from Meteonorm is used as inputs for ambient air temperature and solar irradiation. It corresponds to the typical meteorological year for 1995 (file format TMY2), for Copenhagen.

Load – Heat demand

The load is calculated the same way as it has been done with the TRNSYS model in Dronninglund, with a GUF of 0.33, a yearly heat load of 45'000 MWh, a reference temperature of 17°C. The number of degree days for this district heating network (using air temperatures from the meteonorm file) has been calculated to 3409.81.

Load – Forward and return temperatures

The forward and return temperatures are set according to the following parameters:

- Summer (May 2nd, hour 2'920 to November 1st, hour 7'300) forward temperature: 70°C, return temperature: 35°C.
- Winter (November 1st to May 2nd) forward temperature: 80°C, return temperature: 33°C.

Control strategy – Heat pump

The heat pump is set to be able to run only if spot-prices allow it. This has been calculated beforehand from a spot-price time series from 2010 and has determined 2'500 hours where it's interesting to use the heat pump and 1'500 hours where the gas motors can be used. Gas boilers and solar heat are used to complement the rest. The hours from the time series have been given a number from 1 to 8'760 in an input file, such that all hours labeled with a number higher than 2'500 cannot make use of the heat pump.

Then the heat pump has been implemented based on the data sheet of an existing heat pump, and has been approximated with the following formulas:

$$HP_{power}[kW] = N_{heat\ pumps} \cdot \max\left(100; \min\left(300; 13.8 + 1.3 \cdot T_{HP,evap}^{out} + 3 \cdot T_{HP,cond}^{out}\right)\right)$$

Where:

- $N_{heat\ pumps}$ is the number of heat pumps used in the model (varied for optimization).
- $T_{HP,evap}^{out} = T_{HP,evap}^{in,step} - 5$ is the evaporator outlet temperature.
- $T_{HP,evap}^{in,step}$ is the evaporator inlet temperature from the previous timestep.
- $T_{HP,cond}^{out} = \max\left(80; T_{HP,cond}^{in,step}\right)$ is the condenser outlet temperature.
- $T_{HP,cond}^{in,step}$ is the condenser inlet temperature from the previous timestep.
- HP_{power} is the electrical power (in kW).

This means that the model accounts for a given number of a 300 kWel heat pump, where the objective at the evaporator is to cool down the inlet water temperature by 5 K, and at the condenser, the temperature should be increased by 10 K, with a maximum outlet temperature of 80°C.

The COP of the heat pump is calculated from the following formula:

$$HP_{COP} = \max\left(1; \min\left(6; 6.82 + 0.085 \cdot T_{HP,evap}^{out} - 0.06 \cdot T_{HP,cond}^{out} + C\right)\right)$$

Where:

- $C = \begin{cases} 0.7 \ if \ N_{heat\ pumps} = 2 \\ 1.7 \ if \ N_{heat\ pumps} \geq 3 \\ \quad 0 \ otherwise \end{cases}$

The COP depends both on the temperatures of the evaporator and condenser outlets, as well as the number of heat pumps used, and is limited to 1 as a minimum, and 6 as a maximum.

Then, the heat pump is turned off if the tank bottom temperature is below 10°C and turned back on if it exceeds 15°C (hysteresis control).

Using these parameters, the cooling effect on the evaporator and the heating effect on the condenser side are calculated, as well as the flowrates for each side of the heat pump.

Control strategy – Gas motors and gas boiler

The gas motors are only used when the spot-prices allow for it, the same way it has been determined for the heat pump, but for 1'500 hours. Moreover, these hours have been labeled backwards in the time series input file, which means that for the gas motors to be turned on, the timestep need to have an hour labeled with over 8'760-1'500 = 7'260.

Then the gas motors are assumed to have a constant heating capacity of 8.2 MW, and have a maximum output temperature of 90°C, with a minimum temperature increase of 20°C. From the output temperature and the heating capacity, the mass flowrate required is calculated.

The gas boiler is a theoretical 100% efficiency boiler, that is used only to reach the required forward district heating temperature. It therefore has a theoretical maximum heating capacity of 20 GW.

Control strategy – Charge and discharge of the BTES

To control the charge and discharge of the BTES, a single charge/discharge total flowrate was chosen as a free parameter for optimization. Then the charge or discharge of the BTES is determined following 2 hysteresis controllers each.

For the charge of the BTES:

- The tank's top temperature needs to exceed 71°C, and stay above 70°C.

- The tank's top temperature needs to exceed the BTES average soil temperature with 10°C, and remain above the BTES average soil temperature with 1°C.

For the discharge of the BTES:

- The tank's top temperature needs to drop below 60°C, and stay under 65°C.
- The BTES average soil temperature needs to exceed the tank's top temperature with 10°C, and remain above the tank's top temperature with 1°C.

Second version of the TRNSYS model

Previously described control strategy was used for the first version of the TRNSYS model. It was further improved to obtain better operation of the BTES with the following modifications:

- The solar collector field forward temperature was cooled down by the heat pump, thus higher solar production was achieved.
- Control of charging flow to the BTES was optimized.

Cost function

The TRNSYS model is run, and then the heat price is calculated based on a given number of assumptions, with the following formula:

$$Heat\ Price = \frac{Operation\ costs + Capital\ costs}{Heat\ demand}$$

The assumptions are:

- Prices are in DKK, assuming 1 € = 7.45 DKK.
- Operation costs are calculated for the 2nd year of the operation.
- Yearly capital costs are calculated as 7% of the investment (Based on a 20-year annuity loan with real interest rate of 3% p.a.).
- Heat demand is still 45'000 MWh/year.
- Heat production price for the natural gas boiler is calculated to 450 DKK/MWh (see Table 5.2.17).
- The heat production price from the motors is calculated as an average 400 DKK/MWh.

Table 5.2.17 Calculation of heat production price from natural gas boilers (2010).

Boiler	Specification	DKK/MWh
Natural gas	2.50 DKK/Nm^3	217.17
Energy tax		208.00
NO$_x$ tax	0.008 DKK/Nm^3	0.69
CO$_2$ quotas	100 DKK/ton	19.61
O&M		5.00
Heat price		**450.47**

GenOpt optimization

The cost function is implemented directly in TRNSYS, such that the optimization program GenOpt can be used to iterate calculations while varying some parameters. GenOpt will launch the TRNSYS model and vary parameters in order to find the lowest resulting heat price.

In the optimization the collector area (50'000 m^2) and the capacity of the accumulation tanks (7'000 m^3) are frozen parameters. The optimization parameters are the following:

- BTES geometry (soil volume, depth of boreholes, number of boreholes).
- BTES operation strategy (time for starting and stopping charging and discharging the BTES), flowrate.
- Number of heat pumps (each with a heating capacity of 1.2 MW$_{th}$).

This optimization was used to:

- Find the full-scale system providing the best (lowest) heat price, including:
    - The optimal number of boreholes per surface area of the BTES lid.
    - The optimal insulation thickness.

Scenarios and results

Reference, full-scale RE and pilot systems scenarios

A first version of the TRNSYS model was run to calculate the heat produced by the initial system configurations (where only the existing heat production means - boilers, motors and existing solar collector field - are used), with the corresponding heat price. This is the 'reference' case.

Then the first version of the TRNSYS model was used to make calculations for both the full-scale RE system and the pilot plant with initial components sizes.Then GenOpt was used to find the optimized full-scale RE system, based on the first TRNSYS model.

Final design scenario

To finish, a second version of the model, improved in terms of BTES operations, was run and new heat prices were determined. The following sections present the detailed initial calculations results, results obtained from the optimization, and then the detailed results for the final full-scale RE and pilot plant designs.

Analysis and discussion

Initial design detailed results

The first case studied is the reference case. This provides a heat price of 405 DKK/MWh (see Table 5.2.18). Then, calculations with TRNSYS show, for the initial full-scale RE system design, a heat price of 461 DKK/MWh (see Table 5.2.19). This is achieved by a 400'000 m^3 BTES (soil volume), with 1'000 boreholes of 45 m depth, and 50'000 m^2 total solar collector field. The capital costs of the RE system are detailed in Table 5.2.20.

Table 5.2.18. Calculation of the reference case heat price.

Reference	DKK/MWh		MWh/y		DKK/year
Boilers	450	*	29'550	=	13'297'429
Motors	400	*	12'300	=	4'920'000
Thermal solar	5	*	3'572	=	17'860
Heat pumps, O&M	10	*	0	=	0
Heat pumps, elec.	600	*	0	=	0
Operational costs	**405**	*	**45'000**	=	**18'235'289**
Capital costs	**0**	*	**45'000**	=	**0**
Total	**405**	*	**45'000**	=	**18'235'289**

Table 5.2.19. Calculation of the initial full-scale RE system design heat price.

Initial design full-scale	DKK/MWh		MWh/y		DKK/year
Boilers	450	*	15'522	=	6'984'983
Motors	400	*	12'300	=	4'920'000
Thermal solar	5	*	16'845	=	84'227
Heat pumps, O&M	10	*	10'405	=	104'050
Heat pumps, elec.	600	*	2'066	=	1'239'805
Operational costs	**296**	*	**45'000**	**=**	**13'333'064**
Capital costs	**165**	*	**45'000**	**=**	**7'409'306**
Total	**461**	*	**45'000**	**=**	**20'742'370**

Table 5.2.20. Calculation of the capital costs for the full-scale RE system initial design.

Initial design - Full-scale RES	Unit price			No. of units			Price	
BTES volume				400'000	m³			
BTES depth				45	m			
BTES no. of boreholes				1'000	pcs.			
BTES (heat exchangers)	365	DKK/m	*	45'000	m	=	16'425'000	DKK
BTES (lid)	385	DKK/m²	*	8'889	m²	=	3'422'222	DKK
Solar collectors	1'500	DKK/m²	*	42'000	m²	=	63'000'000	DKK
Heat pumps	1'500'000	DKK/pcs.	*	6	pcs.	=	9'000'000	DKK
Steel tank (5'000 m³)							4'000'000	DKK
Miscellaneous							10'000'000	DKK
Total investments							**105'847'222**	DKK
Payback rate[20]							7	%/y
Capital costs	**165**	**DKK/MWh**	*	**45'000**	**MWh/y**	**=**	**7'409'306**	**DKK/y**

For the initial pilot plant design, calculations show a heat price of 411 DKK/MWh. This is achieved by a 19'200 m³ BTES (soil volume) with 50 boreholes of 45 m depth. Table 5.2.21 shows the heat price calculation details.

---

[20] Based on a 20-year annuity loan with effective rate of interest of 3% p.a.

Table 5.2.21. Calculation of the initial pilot plant design heat price.

Reference	DKK/MWh		MWh/y		DKK/year
Boilers	450	*	26'669	=	12'001'052
Motors	400	*	12'300	=	4'920'000
Thermal solar	5	*	6'480	=	32'400
Heat pumps, O&M	10	*	688	=	6'881
Heat pumps, elec.	600	*	247	=	148'246
Operational costs	**380**	*	**45'000**	=	**17'108'580**
Capital costs	**31**	*	**45'000**	=	**1'400'000**
Total	**411**	*	**45'000**	=	**18'508'580**

The result of the initial design was thus that neither the pilot plant nor the full-scale plant was economically feasible compared to the reference situation. But it could also be seen that the solar production was quite low (approximately 340 kWh/m^2/year) for the full-scale plant and for the pilot plant (405 kWh/m^2/year). Therefore, the TRNSYS model was optimized with GenOpt, and further improved (see following sections).

Optimization results

First step to improving the RE system had been the optimization with GenOpt for the full-scale case. By running GenOpt, varying BTES dimensions, the heat price was reduced from 461 to 442 DKK/MWh.

Table 5.2.22 shows the optimized parameters next to the initial design parameters and Figure 5.2.45 shows the heat price evolution using GenOpt.

Table 5.2.22. Results of the optimization: new parameters (to the right) vs. initial parameters (left).

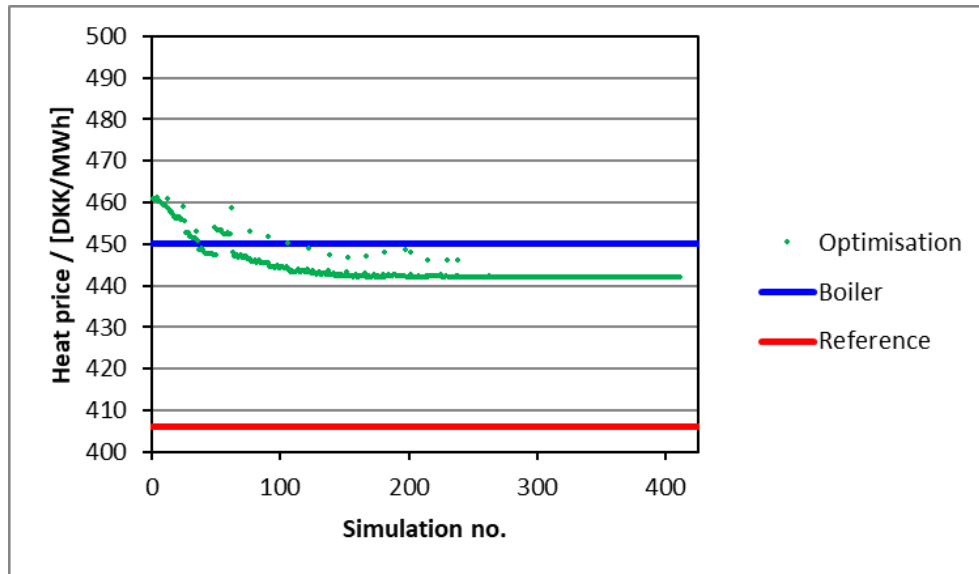| Design parameter	Unit	Initial	Optimized
BTES volume	m^3	400'000	210'000
BTES no. of boreholes	pcs.	1'000	553
BTES charge flow	kg/h	400'000	100'000
No. of heat pumps	pcs.	6	3
Charge start time	hr	2'800	3'303
Charge stop time	hr	6'600	6'706
Discharge start time	hr	7'000	6'950
Discharge stop time	hr	2'500	2'813
Heat price	**DKK/MWh**	**461**	**442**

Figure 5.2.45. Heat price evolution during GenOpt optimization process.

BTES design optimization

For a BTES, the volume is defined as:

$$V_{BTES}[m^3] = A_{BTES,lid} * (Depth_{borehole} + 5)$$

Where $A_{BTES,lid}$ is the BTES lid area in m², and $Depth_{borehole}$ is the depth of a borehole in meters.

This optimization study shows that the appropriate number of boreholes for 210'000 m³ is 553 (see Table 5.2.22). This corresponds to a ratio of 7.6 m² of lid surface area per borehole. This parameter has been independently studied in another optimization study using GenOpt, and showed an optimal value of 7.76 m² per borehole (see Figure 5.2.46). Therefore, a general design rule of 8 m² per borehole was used for the pilot storage.
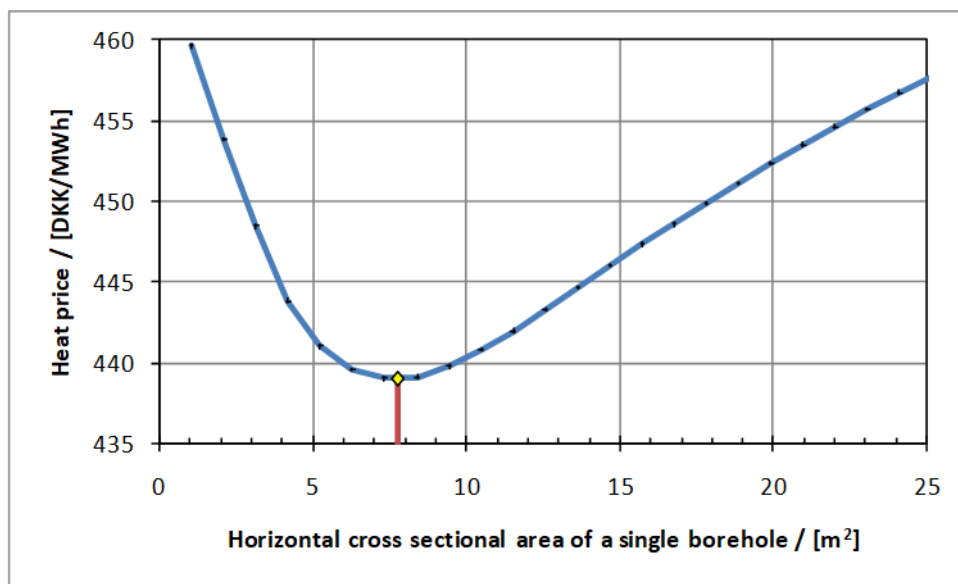
Figure 5.2.46. Heat price as a function of the cross-sectional area of the boreholes[21].

GenOpt has also enabled optimization of the lid insulation thickness and showed 50 cm insulation with mussel shells was the best option.

Although lower prices have been achieved with GenOpt optimization, the solar yields remained quite low (approximately 320 kWh/m²/year), and the heat price was still inferior to the reference heat price. Therefore, it was chosen to improve system operations to find a better economy with the solar heating system coupled with a BTES and a heat pump.

Final design detailed results

Further improvement of the TRNSYS model showed that the initial design and GenOpt-optimized designs could lower the heat prices of the full-scale RE system and the pilot plant.

Table 5.2.23 shows the detailed result for the full-scale RE system heat price, while Table 5.2.24 shows the detailed result for the pilot plant heat price.

---

[21] These results have been obtained with an intermediate version of the TRNSYS model (not optimized in terms of control strategy), hence the slightly higher heat price compared with the final full-scale results.

The full-scale RE system shows an improved heat price of 434 DKK/MWh (vs. 461 DKK/MWh for the initial design), as well as an improved yield for the solar collector field: approximately 360 kWh/m^2/year, compared to the 340 kWh/m^2/year of the initial design.

The pilot plant shows an improved heat price of 403 DKK/MWh (vs. 411 DKK/MWh for the initial design), as well as an improved yield for the solar collector field: approximately 465 kWh/m^2/year, compared to the 405 kWh/m^2/year of the initial design.

Table 5.2.23. Calculation of the final full-scale RE system design heat price.

Final design full-scale (50.000 m^2)	DKK/MWh		MWh/y		DKK/year
Boilers	450	*	16'759	=	7'541'371
Motors	400	*	12'300	=	4'920'000
Thermal solar	5	*	17'927	=	89'633
Heat pumps, O&M	10	*	4'101	=	41'011
Heat pumps, elec.	600	*	783	=	469'646
Operational costs	**290**	*	**45'000**	=	**13'061'661**
Capital costs	**143**	*	**45'000**	=	**6'451'412**
Total	**434**	*	**45'000**	=	**19'513'073**

Table 5.2.24. Calculation of the final pilot plant RE system design heat price.

Pilot plant – final design	DKK/MWh		MWh/y		DKK/year
Boilers	450	*	25'928	=	11'667'727
Motors	400	*	12'300	=	4'920'000
Thermal solar	5	*	7'421	=	37'105
Heat pumps, O&M	10	*	560	=	5'602
Heat pumps, elec.	600	*	191	=	114'308
Operational costs	**372**	*	**45'000**	=	**16'744'742**
Capital costs	**31**	*	**45'000**	=	**1'400'000**
Total	**403**	*	**45'000**	=	**18'144'742**

The results showed that the pilot plant was economically feasible. The electricity price for the heat pump and the natural gas price are important for the calculations results, and therefore sensitivity calculations were made for these parameters.

The results were that a gas price of 3.00 DKK/Nm^3 would reduce the difference between the reference and the full-scale plant with 14 DKK/MWh, and that an electricity price of 1.00 DKK/kWh would increase that difference with 7 DKK/MWh.

Conclusions

The calculations carried out in TRNSYS have enabled an improvement of operation strategy for the charge and discharge of the BTES, the use of the solar collector field, and therefore the resulting heat price. Calculations predict an improvement of the solar yield by approximately 60 kWh/m^2 for the pilot plant.

From the optimization study done on the full-scale RE system, certain design parameters have been optimized:

- Charge-discharge flowrate of the BTES.
- Number of boreholes (general rule of approximately 1 borehole per 8 m^2 of lid area).
- Insulation thickness.

These parameters were then used as design rules for the pilot plant of Brædstrup (that was later implemented[18]) and have shown the opportunity for a good potential economy for the project.

Calculations have proven to be crucial in the design of a novel system, for which little reference was available at the time. They have been used to prove feasibility of the project and find the ideal design for the given situation. Detailed design tools should therefore be used as often as possible to accompany feasibility and implementation projects involving seasonal heat storages such as BTES.

Work package interfaces

The studies presented in the current report have been made during the design phase of various UTES projects in the early 2010s and have been directly used for implementation. There has therefore been no revision of the calculations based on improved site characterization.

5.2.3 Conclusion

The calculations carried out in TRNSYS for renewable energy systems involving both PTES and BTES storages have proven crucial in all 3 Danish examples presented in this report. These calculations have been used to:

- Determine overall economic feasibility of the project.

- Design and optimize the overall energy system including:
  - Sizing of the main components.
  - Location of the main components.
  - Choice of the type of technology used.
  - Improvement of the control strategy.
  - Improvement of solar collector field yield.

- Design and optimize specific components:
  - Optimal cross-section surface of a borehole.
  - Optimal charge/discharge flowrate through the boreholes.
  - Possibility of removing foils from part of the solar collector field.
  - Optimal BTES lid insulation thickness.

Similar calculations could and should also be used to:

- Find the ideal PTES storage volume and solar collector field area for a given solar fraction target.
- Identify the PTES storage volume and solar collector field area providing the lowest possible cost of heat (not necessarily providing the target solar fraction).

A good collaboration between system design engineers and project developers can make the difference between a feasible project and a non-feasible one. It can help make savings at an early stage and should always be considered when studying a project involving a multitude of components in interaction with each other, and especially when one or several of those are thermal storages. This kind of approach is necessary if we want to widely spread the use of renewable energies within heat networks, because each case has a specific configuration for which an off-the-shelf solution cannot be used. To this purpose, it is of high importance to have tools that can model TES in a realistic way, in order to include this as a central part of the renewable heating system.

5.3 Azores study

Fátima Viveiros[1], Daniela Matias[1], Catarina Silva[1], José Virgílio Cruz[1], Luísa Pereira[1], Vittorio Zanon[1], Lucia Moreno[1], Thomas Driesner[2], Thierry Solms[2], Jessica Uchôa[1], Pedro Freire[1]

[1]IVAR, University of the Azores, [2]ETH Zürich

5.3.1 Conceptualization

Caldeiras da Ribeira Grande area (Figure 5.3.1) is located in the north flank of Fogo Volcano (São Miguel Island, Azores archipelago) and shows several manifestations of volcanism, such as hydrothermal fumaroles, thermal and cold CO_2-rich springs as well as thermal and soil diffuse degassing anomalies, namely in what concerns carbon dioxide and radon. In 2009 the local geothermal company (*EDA Renováveis S.A.*) attempted to drill in the area for high enthalpy geothermal production, however during the drilling process an incident (blow-out) interrupted the drilling and the project was stopped.

Preliminary surveys in the area used essentially geophysical data to decide the drilling project. In the current project we aim to use a geochemical approach with multi-data from different techniques that will complement the known geological background and contribute to define a conceptual model that will eventually support future activities in the area. The modelling pretends to contribute to produce a roadmap with geochemical tools for definition of conceptual models that can be used to select future areas for geothermal exploitation.
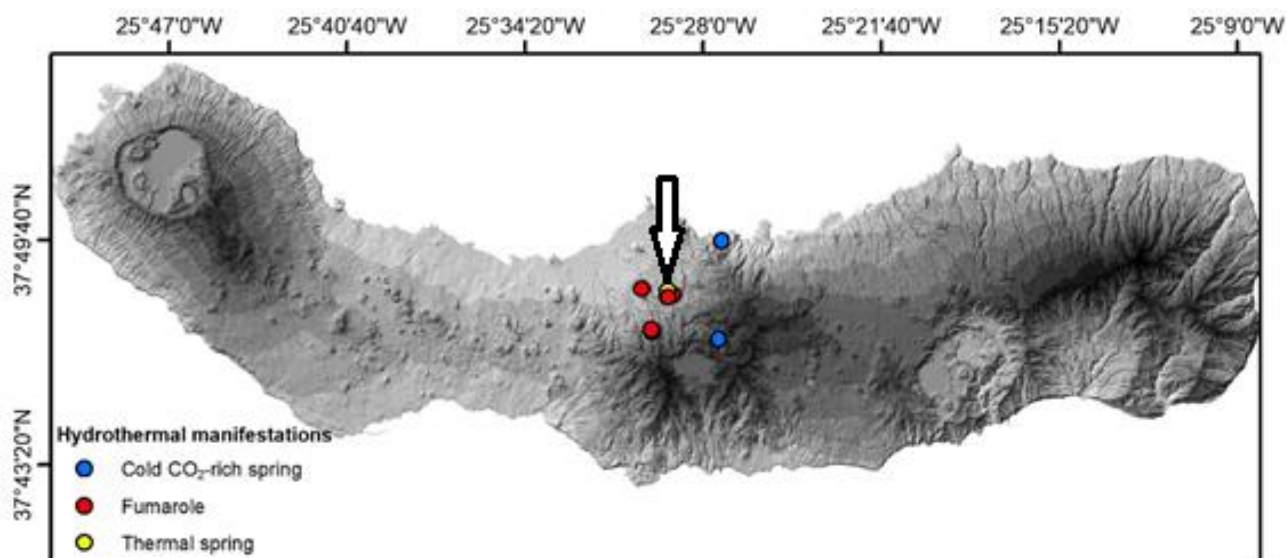
Figure 5.3.1 São Miguel Island digital elevation model with the location on the visible manifestations of volcanism in the north flank of Fogo Volcano. The arrow points to Caldeiras da Ribeira Grande study site.

5.3.1.1 Scope and aims of the study

The selected area to study in the current project is located in the north flank of the active Fogo Volcano (São Miguel Island, Azores archipelago, Portugal). An existing reservoir model is restricted to the drilled extent of the exploited geothermal field (Franco et al., 2018) but the larger-scale structure of the geothermal field as well as the driving forces and possibly larger extent are essentially unknown. The aim of the study, therefore, was deriving and simulating conceptual models of the volcano-scale subsurface fluid flow that represents the reservoir that feeds the hydrothermal manifestations observed at the surface. Two complementary approaches to understand the thermodynamic conditions and the fluid flow at Fogo Volcano, at different geographical scales, were carried out:

1) General fluid flow model for the Fogo Volcano site;

2) Detailed characterization of the Caldeiras da Ribeira Grande study site and model thermodynamic conditions in the area.

The above-mentioned approaches were based on the use of the available geochemical and geological parameters, such as:

- gas geothermometers (H_2S/Ar, H_2/Ar, H_2O-CO_2-H_2-CO-CH_4-O_2) based on the composition of the gases emitted by the fumaroles;

- geochemical indicators (quartz, chalcedony, amorphous silica, Na/K, Na/Li, Mg/Li, Li, Mg/Na, Fe/K^2) measured on the main thermal springs from the study area; their applicability depend on the specific conditions of each water;

- soil temperature at the surface, 10 cm depth and from some wells drilled in the surrounding area, which showed temperatures up to 100 m;

- soil diffuse degassing maps with the spatial variability of carbon dioxide and radon on the area;

- temperature of formation of the minerals (calcite, pyrite, quartz, chlorite, just to name some of the possible minerals) found out across a drilled well in the area (up to a depth of 1343 m);

- In addition to the geochemical parameters, geological and volcanological characterization of the area (main tectonic structures, geology) as well as the topography were available to complement and characterize the site.

The main objectives of the modelling are to:

- Understand, for which conceptual model would a subsurface flow dynamics result that explains the asymmetric geothermal activity at Fogo, i.e., the restriction to the Northern flak

- Provide a framework for follow-up projects to

  - understand chemical fluid-rock interaction and its impact on the environment;

  - estimate the thermal energy and gas fluxes emitted from the study area;

  - build the roadmap to define conceptual models for geothermal exploitation and avoid future incidents;

  - integrate all the available data in a common database that will be useful not only for research scopes but also for decision makers;

  - check if the modelling tools used for HEATSTORE project are adequate for high enthalpy projects.

5.3.1.2 System Geometry and related Geology

The Caldeiras da Ribeira Grande geochemical study site has an area of about 0.5 km^2 that accomplishes with the secondary manifestations of volcanism existent in the area, and the geothermal RG5 drilled well (Figure 5.3.2).

The model can go deep to the reservoir accounting with several layers that will be superimposed. Even if most of the layers will be built based on superficial data (soil degassing, location of the secondary manifestations of volcanism, soil temperature, location of water lines, topography), some information from the drilled wells will be used and will contribute to better define the model with precise depths. These deep layers will include essentially information about temperature obtained by direct measurements and indirect information from the altered minerals. A wider area was studied aiming at understanding the fluid flow in the north flank of the volcano, and will account with information from the boarder of the caldera (at about 580 m height) to the sea level.

The geology of the area is dominated by the presence of trachytic (*s.l.*) material, which includes lavas and pumice material with different dimension (essentially from ashes to *lapilli*) (Wallenstein *et al.,* 2015 and references therein). The main tectonic structures in the area have a general NW-SE direction, similar to the Ribeira Grande Graben that dominates the local tectonic (Carmo *et al.*, 2015 and references therein). Fogo Volcano was formed more than 200 000 ago and has produced major trachytic explosive activity in the last 10 000 years, including two Plinian scale events. The last eruption occurred in 1563 and corresponded to a sub-

Plinian eruption inside the summit caldera. Four days later a Hawaiian event occurred in the northwestern flank of the volcano. A phreatic explosion was reported in 1564, in the same site of the 1563 sub-Plinian eruption (Wallenstein *et al.*, 2015 and references therein).
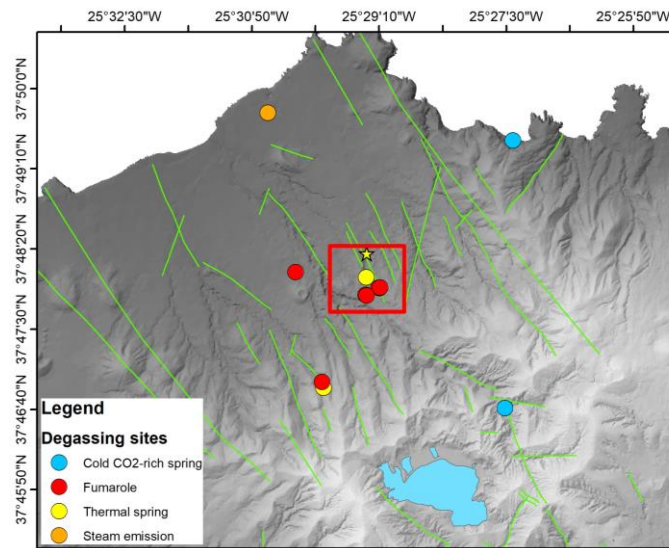

Figure 5.3.2 North flank of Fogo Volcano with the location of the main visible degassing sites. The yellow star corresponds to the location of RG5 geothermal well. The green lines represent the tectonic structures identified in the area by Carmo et al. (2015). Red square highlights the Caldeiras da Ribeira Grande study site.

All the visible hydrothermal manifestations are located in the north flank of the volcano, where the geothermal power plants have been set up. Recent studies (Andrade *et al.*, 2020) highlighted the absence of volcanic degassing on the caldera lake.

No unambiguous geophysical signals of a magma body in the Fogo subsurface have so far been recorded. Current knowledge of high-enthalpy geothermal systems implies that these are driven by magmatic heat but that their activity can last beyond the full solidification of magma. Numerical modelling may therefore also help to constrain possible locations of active or solidified magma bodies in Fogo's subsurface.

5.3.1.3 Fogo Volcano geothermal power plants

Three high enthalpy geothermal power plants are currently running in the Azores, in two of the nine volcanic islands that form the archipelago. The installed geothermal capacity is 23 and 3.5 MW at São Miguel and Terceira islands, respectively (Franco *et al.*, 2017; 2019). After a period of initial exploration, SOGEO (now called EDA Renováveis S.A.) started the main geothermal program on São Miguel Island in 1990 (Rangel *et al.*, 2015). At Terceira Island, the power plant started operating in 2017 and new geothermal wells are programmed for the current year.

Two geothermal power plants are located in Fogo Volcano, in the so-called Ribeira Grande geothermal field. The Cachaço-Lombadas power plant is located at higher altitude, while the Pico Vermelho power plant is located in the northern area of the geothermal field, at lower altitude. At least 25 wells were drilled in the last decades in this volcanic system (Figure 5.3.3), and currently eight wells are in production. The program is now expanding with additional drilling in São Miguel Island. Both vertical and directional wells have been drilled with a maximum depth of 2029 m depth (CL1). RG5 well, located close to the study site has a depth of 1343 m and corresponds to an observation well drilled in 2009. A maximum temperature of 240 °C was measured during drilling (Rangel, 2014). RG5 is considered a quite impermeable well since, despite the strong veining of the lithologies intersected, no fluid losses occurred during drilling in the reservoir sector, as observed in the cuttings studied in the current project.
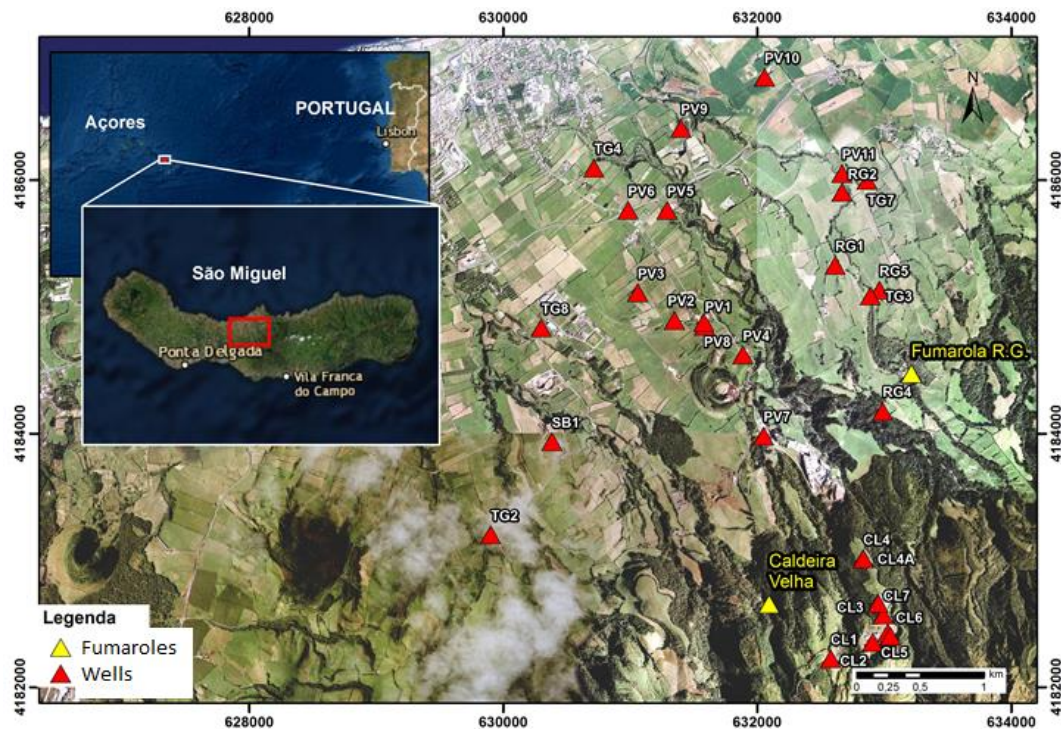
Figure 5.3.3 Location of the fumaroles and geothermal wells drilled in the north flank of Fogo Volcano.

5.3.1.4 Local geothermal and groundwater conditions

Three fumarolic fields can be found in the north flank of Fogo Volcano, namely the Caldeiras da Ribeira Grande, Caldeira Velha and Pico Vermelho fumaroles. These hydrothermal manifestations are low-temperature fumaroles with maximum outlet temperature of 100 ºC. Water vapour is the main component and CO_2 the most abundant dry gas (more than 93%). Minor amounts of H_2S, N_2, H_2, CH_4, He, Ar and CO can also be detected (Truesdell *et al.*, 1984; Ferreira, 1994; Ferreira and Oskarsson, 1999; Ferreira *et al.,* 2005; Caliro *et al.*, 2015).

Application of the geothermometer based in the gas equilibria in the H_2-CO_2-CO-CH_4-H_2O system (Chiodini and Marini, 1998) to Caldeiras da Ribeira Grande fumarolic field showed equilibrium temperatures ranging from 260 to 280ºC for the reservoirs that feed these fumaroles (Caliro *et al*., 2015). Truesdell *et al.* (1984) estimated temperatures around 240 ºC for the Caldeiras da Ribeira Grande fumarole, based on D'Amore and Panichi (1980) geothermometer applied to gases collected in 1977. Truesdell *et al.* (1984) estimated an equilibrium temperature of 221 ºC for gas samples from Caldeira Velha fumarolic field, using also the D'Amore and Panichi (1980) geothermometer. These inferred temperatures are in similar order of magnitude of the temperatures measured in geothermal wells drilled in the area. The geothermal reservoir is liquid-dominated with maximum temperatures around 245 ºC (Ponte *et al.,* 2010; Rangel, 2014; Franco, 2016; Rangel *et al.*, 2017; Franco *et al.*, 2018).

Despite hydrothermal fumaroles, thermal and cold CO_2-rich springs are also found out in the area. Thermal springs located on the north flank of Fogo Volcano, namely associated with the Caldeiras da Ribeira Grande fumaroles, present Na-SO_4 dominated compositions and correspond to the more acidic springs measured in the Azores, with pH ranging between 2.02 and 2.27 (Cruz and França, 2006).

5.3.1.5 Available data

In order to integrate all the available information for the current project, a geodatabase was prepared with data both from the literature, as well as the information obtained during the current project. Table 5.3.1 shows the available data on the database organized on the HEATSTORE Project.

Table 5.3.1 Information available on the database organized on the HEATSTORE project.

Data information	Excel file	Shapefile	Geodatabase	Vector type
Location of the geothermal well	X	X	X	point
Type of geothermal well	X	X	X	point
Depth of the geothermal well	X	X	X	point
Maximum temperature measured in the geothermal wells (at different depths)	X	X	X	point
Geothermal wells temperature (-400 bsl)	X	X	X	point
Temperature of the well (at different depths)		X	X	line
Location of the permeability areas in the geothermal wells	X	X	X	point
Stratigraphy identified on the geothermal well	X	X	X	point
Topographic data (10 m intervals)		X	X	line and point
Water lines		X	X	line
Tectonic data		X	X	line
Lakes		X	X	polygon
Degassing sites (visible emissions)	X	X	X	point
Geology		X	X	polygon
Temperature (at different depths - just on the RG4 area)	X	X	X	point
Soil temperature (20 cm depth - RG4 area)	X	X	X	point
Radon concentration (50 cm depth - RG4 area)	X	X	X	point
Soil CO_2 flux (RG4 area)	X	X	X	point

5.3.2 Modelling approach – general fluid flow model for Fogo Volcano

5.3.2.1 Conceptual simulation model

Since little information is available on the details of the local underground geology, the conceptual simulation approach will focus on deriving possible generic scenarios for the reservoir hydrology. Given that the systems are located on a volcanic island with significant topography, priority will be given to study the influence of key parameters governing geothermal flow in such settings:

- location, size and depth of a possible magmatic heat source

- topography

- plausible permeability distributions in the underground

For a given magmatic heat source, the thermal structure and flow patterns in high- and medium enthalpy magma-driven geothermal resources are a sensitive function of large-scale permeability (Driesner & Geiger, 2007; Scott *et al.*, 2016). Therefore, we expect that already simulating a limited set of possible configurations will allow deriving first order conclusions about plausible configurations of the reservoirs. The above approach is depicted in Figure 5.3.4.
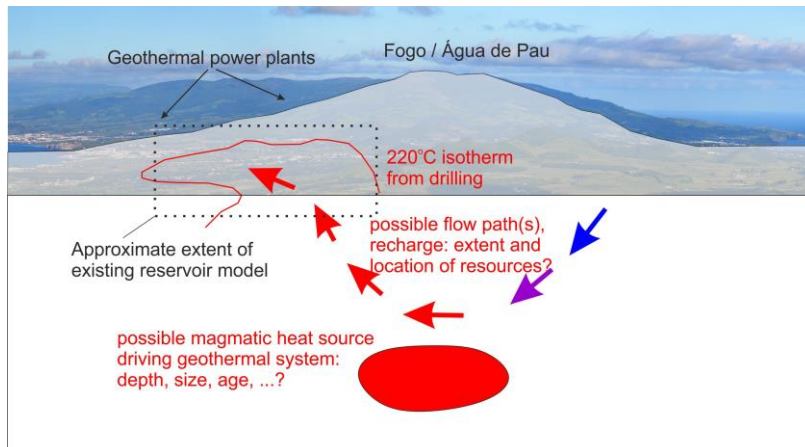
Figure 5.3.4 Conceptual modelling approach: the available reservoir model covers approximately the drilled extent of the geothermal reservoir (dotted black line) but does not include the heat source and volcano-scale geothermal hydrology. HYDROTHERM (2D) and CSMP++ (3D) simulations were performed to identify geological scenarios in which a geothermal reservoir with the location and thermal structure of the Caldeiras da Ribeira Grande field would emerge naturally.

Reconnaissance simulations were performed with the HYDROTHERM interactive software (Kipp et al., 2008; available at https://volcanoes.usgs.gov/software/hydrotherm/) that allows simulating simplified 2D models efficiently to obtain a working hypothesis about the role of the different parameters listed above. Subsequently, ETH's CSMP++ code was used to perform advanced 3D models that focused on the role of magma body location. As of the writing of this report (October 2021) efforts with the CSMP++ code are still ongoing as the simulations are computationally intense. It should, however be noted that these are the first ever 3D simulations of a hydrothermal system in a volcano with the full properties of water and explicitly represented magma bodies. This demonstrates that the HEATSTORE modelling toolset has a superior performance also when applied beyond HT-UTES applications, thereby fulfilling the main goal of HEATSTORE's Task 2.3.

5.3.2.2 HYDROTHERM simulations

HYDROTHERM simulations were carried out in 2D section with topography that resemble a N-S section through Fogo's center. An example setup is shown in Figure 5.3.6. Previous research (Hurwitz et al., 2003) had shown that the water table in hydrothermally active volcanoes is often depressed significantly below the surface; as these relations have remained undetermined for large parts of Fogo, the elevation seen in the models represents a generic water table, represented as a constant pressure and temperature boundary condition.
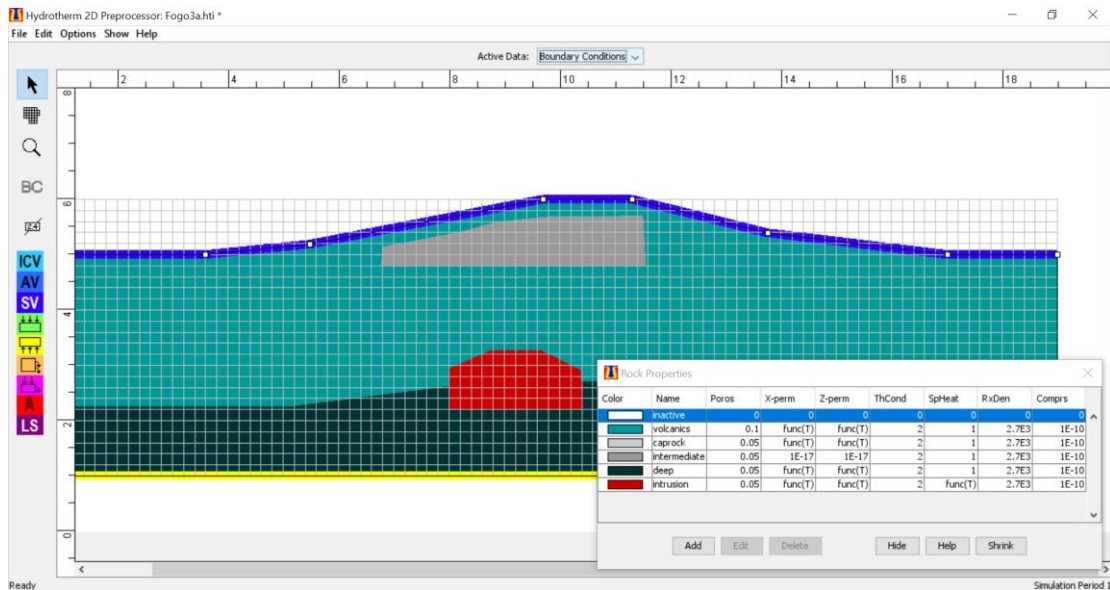
Figure 5.3.6 Example setup of a HYDROTHERM simulation for a Fogo-like conceptual model. Three different host rock types (dark green: low permeability, turquoise: medium permeability, grey: low-permeability cap-rock) and one magmatic intrusion (red). Top boundary condition with fixed temperature (20°C) and pressure (1.013 bar), bottom boundary: constant heat flux (100 mW/m2).

Exploring the parameters space in ca. two dozen simulations revealed that a magmatic heat source placed asymmetrically to the North below the volcanic edifice could generate a geothermal system that closely resembles the drilled one (Figure 5.3.5). It should be noted that for the lack of detailed subsurface geologic data, the model assumes a homogeneous permeability in each rock unit, which ignores the presence of faults and potential aquifers and aquitards except for the possible presence of a low-permeability cap-rock above the geothermal system.
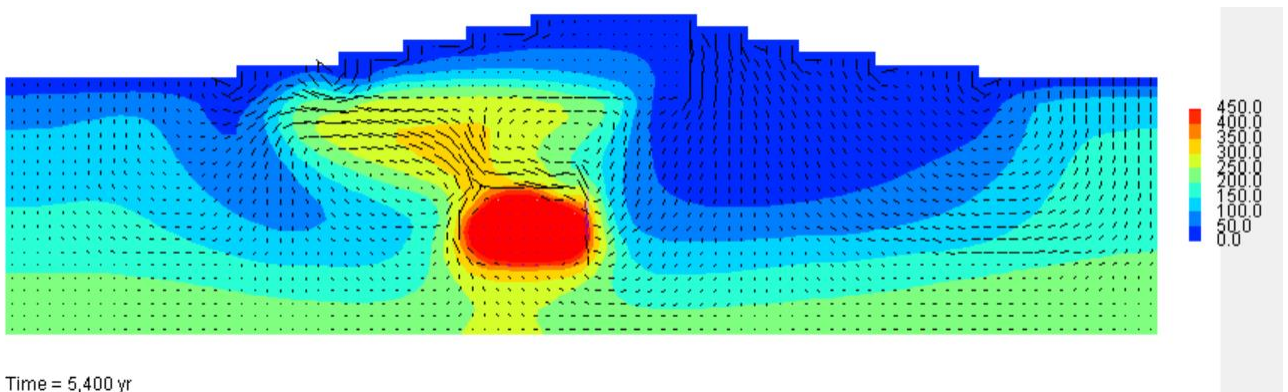
Time = 5,400 yr

Figure 5.3.5 Simulation result for the setup shown above.

The pictured simulation would imply a bulk permeability in the order of $5 \times 10^{-15}\,m^2$ for the Fogo subsurface with reasonable model results obtained for the range from ca. $1 \times 10^{-15}\,m^2$ to $1 \times 10^{-14}\,m^2$ in related simulation setups. In the pictured simulation, a Fogo-like geothermal system would be in place when the magma body is still active in the subsurface a few thousand years after intrusion and would persist beyond the full solidification of the intrusion. The learnings from these 2D simulations were then used to constrain the 3D models employing the CSMP++ code.

5.3.2.3 CSMP++ simulations

Preprocessing workflow

For the CSMP++ simulations, two different approaches for generating the computational geometries were, employed (Figure 5.3.7):

- A Digital Elevation Model of the island was used to generate computational meshes with precise local topography for detailed site-specific simulations (not yet carried out).
- For the reasons given above (suppressed water table inside the volcanic edifice), a series of geometries was created that are based on a more generic and regular, shallow cone on the top of the model.

In both cases, geologic units in the subsurface were manually created in the Rhino3D CAD software. The procedures for meshing, initial and boundary condition assignments etc. have been detailed in HEATSTORE's deliverable D2.2 (Tómasdóttir. & Gunnarsson, 2021).
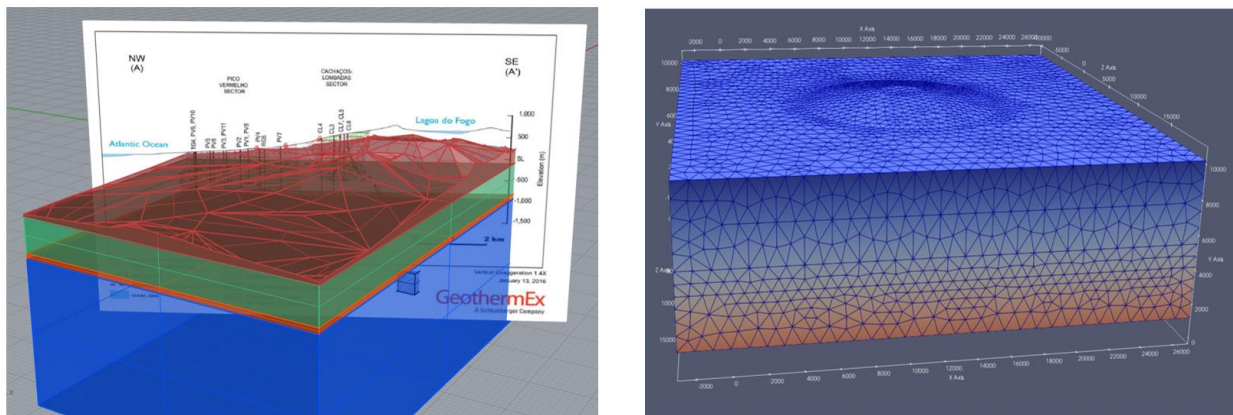
Figure 5.3.7 Two geometric setup options utilized in the study. Left: Topography generated from a Digital Elevation Model and showing how drill data from the actual geothermal field could then be compared to simulation results. Right: a more regular, generic geometry of a volcanic edifice that represents the water table inside the edifice.

Computational approach and software

The simulation study utilized ETH's CSMP++ computing platform to demonstrate its relevance for better defining geothermal reservoirs for which comparatively little data are available but for which we expect that meaningful generic scenarios may be developed. We will utilize the hydrothermal flow implementation with a control-volume-finite-element (CVFE) approach that has been described and benchmarked in detail by Weis et al. (2014). For the HEATSTORE context this had been extended to 3D by A. Yapparova and B. Lamy-Chappuis (unpublished). For more details the readers are referred to HEATSTORE's deliverable D2.2 (Tómasdóttir. & Gunnarsson, 2021).

A key advantage of CSMP++ is the ability to explicitly represent magmatic heat sources in the model, which is a key element in reducing the possible parameter space by eliminating the need to place and adjust non-natural boundary conditions as in industry standard TOUGH2-based workflows. Flow patterns can evolve naturally in response to driving forces such as topography and magmatic heat.

Model Analysis

Model analyses were restricted to manual visual inspection of the .vtu outputs for temperature and vapor saturation for the most straightforward comparison to the drilled reservoir geometry. Visualization for such analyses is done using Paraview (www.paraview.org).

Scenarios and results

To this end, CSMP++ simulation were run for generic small magma bodies (ca. 2 - 4 km^3 in size) in either a central position below the crater or shifted underneath one of the flanks. Parameters varied include magma body depth and lateral position, permeability of the host rock, and topography of the water table.

As of the writing of this report (end of October, 2021), the simulation studies are ongoing and only the simulation with results that most closely resemble the actual field evidence is discussed. Individual simulations require up to two weeks such that exploring a larger set of configurations is very time-demanding.

An example of a simulation that resulted in a Fogo-like scenario is shown in Figure 5.3.8 to Figure 5.3.10. The initial configuration has a magma body at about 2.5 km depth below the surface of the Northern volcano flank (Figure 5.3.8). Bulk permeability of the host rock was assumed to be homogeneous and set as 1 x 10^{-15} m^2; a basal heat flux of 100 mW/m^2 was applied. Due to the relatively low permeability, the geothermal system evolves relatively slowly over several thousand years while the magma body is gradually cooling and solidifying, i.e., the active heat source is decreasing in size.

Figure 5.3.9 shows the thermal state of the system after about 8'000 years: a geothermal system is active on the Northern flank (left) although the temperature distribution shows that the magmatic heat source has already fully solidified. Given that geophysical evidence for an active magmatic source is lacking, this may be an interesting scenario for understanding the current state of the system. Figure 5.3.10 reveals that the upper parts of the geothermal system are steam-rich, in accordance with the observed strong geothermal degassing activity in the area.
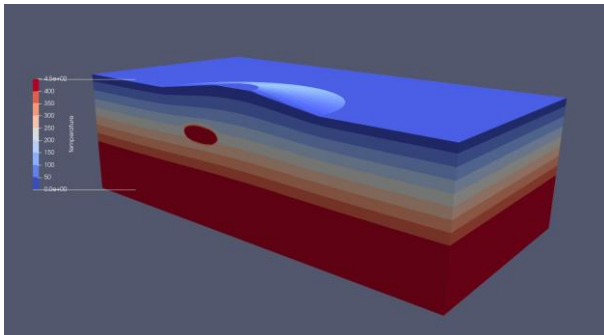
Figure 5.3.8 Initial configuration of a plausible conceptual model, showing the initial position and state of a magma body, as it would have been several thousand years before present.
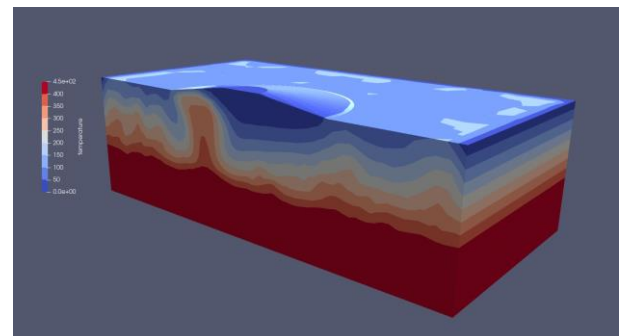
Figure 5.3.9 Simulated thermal state of the geothermal system that evolved from the above initial configuration after 8'000 years: the magma body is fully solidified but the thermal structure closely resembles today's system.
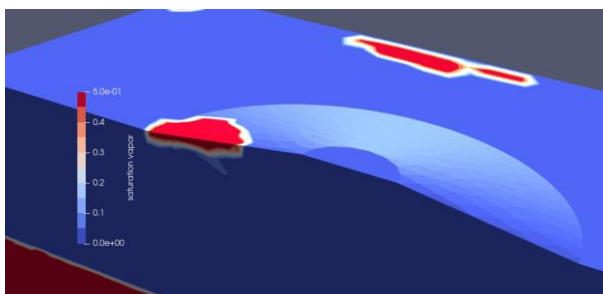

Figure 5.3.10 Near-surface steam saturation on the Northern flank (at 8'000 yrs after magma intrusion) occurs where active geothermal degassing has been detected in the area. Steam zone in background low-lands should be considered a modelling artifact.

5.3.3 Geochemical approach – thermodynamic conditions at Caldeiras da Ribeira Grande site

Characterization of the Caldeiras da Ribeira Grande geothermal system was done based on several geochemical parameters. Chemical, isotopic and temperature, petrographic and mineralogical data were integrated in order to contribute to reservoir modelling.

5.3.3.1 Geochemical data

5.3.3.2 Hydrothermal fumaroles

As mentioned-above, three main fumarolic fields are located in the north flank of Fogo Volcano. Gases collected on the Pico Vermelho emissions mostly consist of water vapour, with minor amounts of CO_2. High concentrations of nitrogen (N_2) and oxygen (O_2) indicate air contamination. For this reason, these fumaroles have been excluded from the current project.

Gases collected in the Caldeiras da Ribeira Grande and Caldeira Velha fumaroles were analysed and showed typical hydrothermal composition. A total of 150 gas analyses were done at both fumarolic fields for the period between 2015 and 2021. Gases were sampled on the fumaroles and geothermal wells following the so-called Giggenbach methodology (Giggenbach, 1975; Giggenbach and Gogel, 1989). The dry gases (Ar, O_2, N_2, CH_4, He and H_2) were analysed by gas chromatography (Perkin Elmer Clarus 580 GC), using a thermal conductivity detector (TCD). The acid gases dissolved in the basic solution were determined by titrimetric methods. CO_2 was quantified with automatic titration using hydrochloride acid (HCl) and the H_2S with mercury acetate ($Hg(CH_3COO)_2$) by manual colorimetric titration using dithizone for end point detection.

A detailed review of the gas geothermometers available in the literature was done and several geothermometers were applied to the gas compositions from the two fumarolic fields. The H_2/Ar gas geothermometer defined by Arnórsson et al (1998) showed to be the most adequate, considering the gas composition of the fumaroles and the requested assumptions. Even if previous studies applied the geothermometer defined by Chiodini and Marini (1998) to the Caldeiras da Ribeira Grande gas data (Caliro et al., 2015), the lack of facilities in the University of the Azores to detect CO does not allow the use of this geothermometer.

Based on the H_2/Ar geothermometers, an average temperature of 256 ºC was estimated for the hydrothermal system reservoir feeding the Caldeiras da Ribeira Grande fumaroles, and an equilibrium temperature of 229 ºC was estimated for the Caldeira Velha fumaroles. Equilibrium temperatures ranged between 245 and 262 ºC, and between 223 and 232 ºC for Caldeiras da Ribeira Grande and Caldeira Velha, respectively. The lower temperature inferred for the reservoir feeding Caldeira Velha fumarole is in agreement not only with the results obtained previously by Truesdell et al. (1984), but also with the temperatures measured in the geothermal wells located in the upper part of the volcanic system. These wells (CL1, CL5, CL6 and CL7), located closer to Caldeira Velha fumarole, show maximum temperatures ranging between 229 and 235 ºC (Franco, 2016; Franco et al., 2018) Figure 5.3.11.

In addition, the hydrothermal mineral assemblage identified in the RG5 well, nearby the Caldeiras da Ribeira Grande fumarolic field, is in agreement with the inferred reservoir temperatures. Application of the H_2/Ar geothermometer to the fluids collected in the RG5 well during a survey carried out in 2016 showed equilibrium temperatures around 252 ºC, i.e. in the same order to magnitude of the temperatures measured in this well Figure 5.3.11.
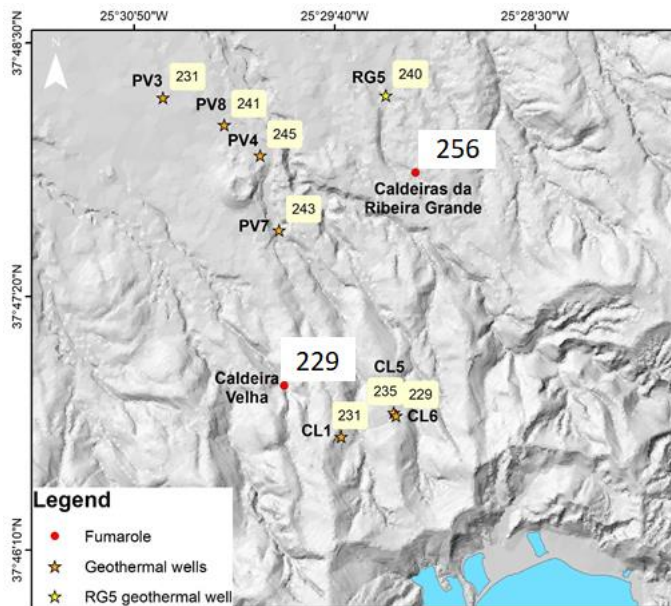
Figure 5.3.11 Maximum temperatures (yellow squares) measured in the geothermal wells and inferred reservoir temperatures (white squares) based on the Arnórsson et al. (1998) geothermometer applied to the gas released from the fumaroles

Despite the application of geothermometers to infer thermodynamic conditions of the reservoir, even before the drilling, the equilibrium temperatures may also be applied on the monitoring and management of the reservoir. Temporal variation of the estimated reservoir temperatures, using the H_2/Ar Arnórsson *et al.* (1998) geothermometer was evaluated for the Caldeiras da Ribeira Grande and Caldeira Velha fumaroles Figure 5.3.12. The distribution of the projected values reflects an equilibrium state in the geothermal system during the studied period (from July 2015 to February 2021).
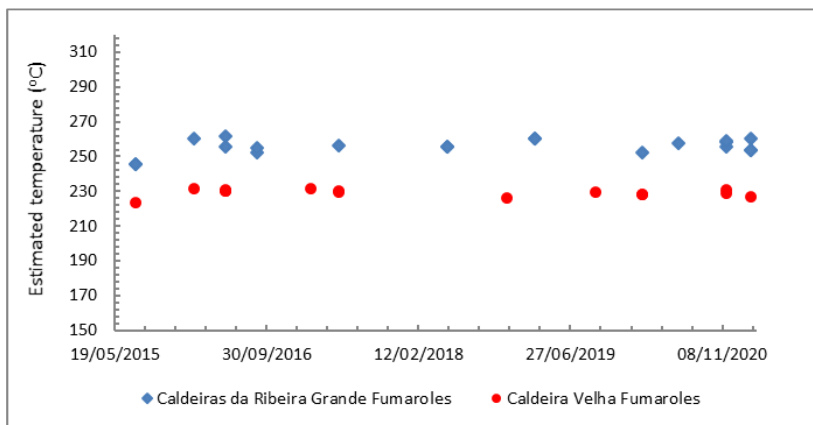
Figure 5.3.12 Temporal variation of the equilibrium temperatures estimated by the H2/Ar Arnórsson et al. (1998) geothermometer for the reservoir feeding the Caldeiras da Ribeira Grande and Caldeira Velha fumaroles.

5.3.3.3 Thermal and cold CO₂-rich springs

Similarly to what was mentioned for the fumaroles, a set of geothermometers (*e.g.*, Na-K-Ca, Na/Li, Mg/Li, Rb/Na, Sr/K[2], Serra and Sanjuan, 2004 and references therein) was applied to the chemical composition of the thermal waters and a wide range of values (from 180 to 230 ºC) were inferred even for the same spring. This variability is justified by the immature composition of the waters and, consequently, the application of geothermometers to the data collected on the Fogo Volcano springs is challenging and needs to be done carefully. Disequilibrium conditions and oversaturation regarding silica solid phases constitute major challenges and difficulties.

Stable isotopic composition of the springs confirms a meteoric origin for the water present in the system and a magmatic origin for the carbon and sulphur elements, in agreement with previous data for Furnas Volcano (Cruz *et al.,* 1999), and even with the isotopes measured in the gas fraction (Caliro *et al.*, 2015).

315

For the other side, the composition of the thermal and cold CO_2-rich springs allows establishing the hydrogeochemistry processes dominating in the area, showing both water-rock interaction and the steam heating processes. Despite these subsurface controlled processes, sea salts dry deposition is also identified from the interpretation of the groundwater geochemistry.

Chemical and isotopic compositions of the springs may be used essentially to define the main sources of the different elements, as well as to identify the main hydrogeochemistry processes occurring in the area. These are relevant aspects to understand the fluid paths and the holistic conceptual models.

5.3.3.4 Diffuse degassing areas

Permanent and not visible gas emissions also characterize volcanic and geothermal areas. CO_2 and the radioactive gas radon (^{222}Rn) are the main volatile species released in these areas, and are detected only using specific instruments. Previous surveys carried out at Fogo Volcano showed anomalous soil CO_2 concentrations mainly in the north flank of the volcano, essentially associated with the Pico Vermelho degassing area and the Ribeira Seca village (Marcos, 2006; Viveiros *et al.*, 2015).

Soil CO_2 flux surveys using the accumulation chamber method (Chiodini *et al.*, 1998) were carried out at the Caldeiras da Ribeiras Grande area in 2012 and 2016. A total of 1093 measurements were carried out in an area with about 0.218 km^2 and gas fluxes varied between 0 and 20 780 g m^{-2} d^{-2}. Carbon isotopic composition of the soil CO_2 flux in the 2016 survey showed a mixture of volcanic and biogenic contribution for the released gas (Fig. 6). The total CO_2 emitted in the surveyed area was estimated to be 70 t d^{-1}, with 90 % of the gas showing a deep-derived origin.

^{222}Rn measurements, at about 50 cm depth in the soil, were performed in July 2019 and values ranged between 17 and 298 500 Bq m^{-3}. The 133 measured sites showed anomalous gas concentrations spatially correlated with the soil CO_2 fluxes (Fig. 6). Soil temperature, at about 15 cm depth, was measured in all the surveys and values varied from 10.5 to 98.6 ºC. A positive correlation between soil temperature and the soil gases is also highlighted, showing that the main geochemical anomalies are located in thermal anomalous zones.

The degassing maps show lineaments of gas anomalies (for both CO_2 and ^{222}Rn) along general NW-SE trends, defining the so-called diffuse degassing structures (DDS) by Chiodini *et al.* (2001). Previous structural studies (Carmo *et al.*, 2015) carried out in the area did not identify tectonic structures crossing Caldeiras da Ribeira Grande area, what can be explained by the existing vegetation together with the thick pumice deposits that hide eventual structures. However, the consistent lineament of gas anomalies for the different gas surveys point to a deep structural control and suggest the existence of tectonic structures in the study area. In addition, the integration of these maps with previous geological data, confirm similar trends for the gas lineaments and the identified faults (Carmo *et al.*, 2015) (Figure 5.3.13).

Considering the positive correlation between soil CO_2 fluxes and soil temperature, the thermal energy released in the study area was estimated following the method defined by Chiodini *et al.* (2005). Integration of deep-derived CO_2 fluxes with the fumarolic composition allows to estimate the thermal energy in the studied area, similarly to what was also done at Furnas do Enxofre fumaroles (Terceira Island, Viveiros *et al.*, 2020). At Caldeiras da Ribeira Grande area, an hydrothermal CO_2 emission of 63 t d^{-1} together with the mass ratio H_2O/CO_2 of 4.07 allows to estimate a thermal energy of about 7.7 MW for the sampled area (0.218 km^2).

Data obtained through diffuse degassing processes give information about the permeability and the fluid paths in the area. In addition, the isotopes applied to the released gases may also contribute to understand the origin of the gases and consequently can constitute relevant tools to spatially identify the location of potential reservoirs. The heat released in the area may be estimated through the thermal energy released.
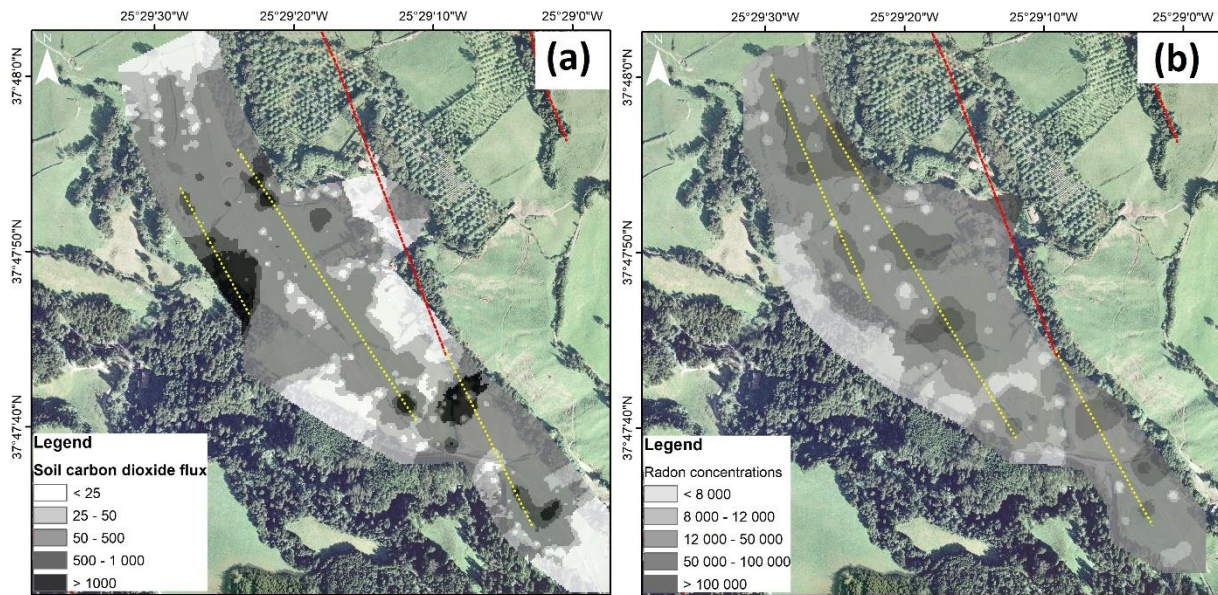
Figure 5.3.13 Soil CO2 flux (a) and soil radon (b) distribution maps for Caldeiras da Ribeira Grande area. Data were interpolated using the deterministic IDW method (6 neighbor points). The red line represents a tectonic lineament previously mapped by Carmo et al. (2015). The yellow lines represent degassing lineaments inferred with the diffuse degassing data (Viveiros et al., 2020+1).

5.3.3.5 Petrography and mineralogy data

As well as geochemical data obtained from the secondary manifestations of volcanism existing in the study area, the mineralogy of the cuttings from the RG5 observation well was also studied. The description and analysis of RG5 cuttings is an important contribute to a better characterization of the subsurface geology, hydrothermal alteration, main hydrothermal zones, and structure of the reservoir of the Ribeira Grande Geothermal Field in the Caldeiras da Ribeira Grande study site.

As previously mentioned, RG5 well is located close to Caldeiras da Ribeira Grande area, at about 800 m from the main fumaroles. EDA Renováveis S.A. supplied the drill cuttings that allowed to characterize the mineral assemblages of this well, down to a depth of 1343 m. Characterization of the samples was done with stereomicroscope (Nikon SMZ1000) and aid of the light KLC 1500 LCD. In addition, a total of 36 samples were analysed through X-ray diffraction (XRD) in Activation Laboratories Ltd (Ontario, Canada). Qualitative and quantitative XRD analysis as well as clay speciation analysis were done.

The local subsurface lithologies, which correspond to eruptive products of Fogo Volcano, are recognized in the RG5 well. The upper part of the well comprises pyroclastic units interbedded with trachyte lavas. Below sea level, in the reservoir sector, basaltic lava flows are predominant along with lava breccia rich in hematite. In the deepest sector, a transition sequence from a subaerial to submarine environment is found similarly to what was observed by Muecke *et al.* (1974) and McGraw (1976). This sequence, 107 meters thick, comprises altered lithic tuffs and altered breccia tuffs interbedded with fine-grained basalt lavas and lava breccia.

The mineralogy results, along with the formation temperature profile, are useful to understand the geothermal field structure. From the surface to 280 m depth, there is a significant increase in the geothermal gradient. Around a depth of about 280 m, the temperature approaches isothermal behaviour, nearby the cap rock that goes until 301 m (Figure 5.3.14). It comprises a well-consolidated lithic tuff, impermeable and strongly silicified, associated with a unit of altered lava. A tuff breccia follows until 323 m. This zone marks the transition to the top of the reservoir, where a steam cap exists, as documented previously (Henneberger and Nunes, 1990; GeothermEx, 2008; Pham *et al.*, 2010; Ponte *et al.*, 2010; Rangel, 2014; Franco, 2016). A significant abundance of adularia (K-feldspar) occurs around 305 m, being this mineral a good steam indicator and, therefore, reflects the existence of a boiling zone on the top of the reservoir (Browne, 1970; Browne and Ellis,

1970; Keith and Muffler, 1978). In RG5, adularia associates with high contents of quartz, illite, and increasing calcite. The reservoir itself is characterized by an isothermal formation temperature and a maximum temperature of 240°C is reached, as measured during tests carried out in the area (Rangel, 2014). Around 620 m depth, a reversal of temperature marks the end of the reservoir and suggests absence of upflow in the RG5 area.

In the entire well, the main alteration minerals are chlorite, smectite, illite, mixed-layer illite-smectite, kaolinite, quartz, hematite, calcite, dolomite, pyrite, anatase and titanite. No zeolites, epidote or prehnite crystals were identified. The hydrothermal minerals occur replacing the primary minerals or filling open-space voids, directly
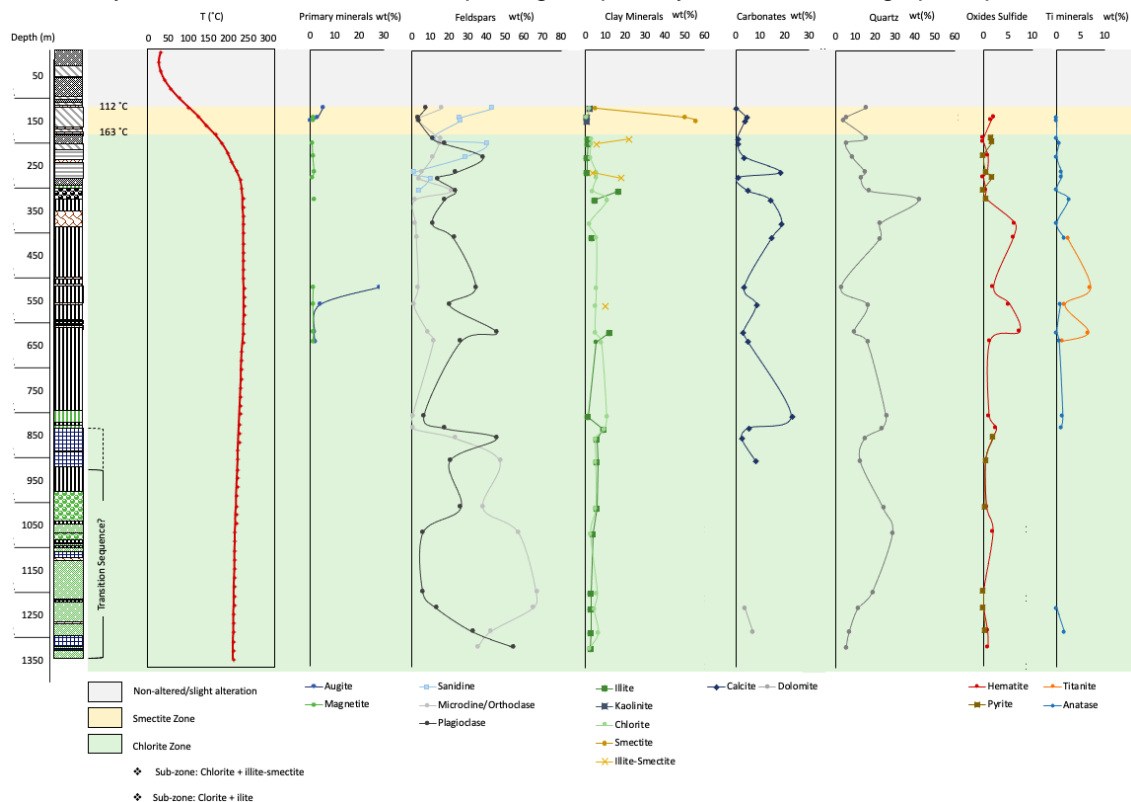
Figure 5.3.14 Main alteration zones and XRD analysis results – minerals in bulk samples (wt. %) vs. depth (m).

precipitating from the geothermal fluid. The abundance of hydrothermal minerals in RG5 is greatly dependent on temperature, fluid composition and on the composition and texture of the host rock. No linear variation with depth was observed.

Chlorite, identified in XRD analysis as clinochlore, is stable for a wide range of temperatures and in RG5 appears at temperatures lower than 120ºC, contrarily to what expected (*e.g.*, Reyes, 1990; Lagat, 2009). This distribution seems to agree with the hypothesis that the hydrothermal fluid was in upper levels in the past (Franco, 2016). Other evidence for this is the presence of illite below 200ºC, also in an unusual thermal stability area (*e.g.,* Utami and Browne, 1999; Harvey and Browne, 1991).

In what concerns the clay minerals, their correlation with temperature occur as expected (Browne and Ellis, 1970, Browne, 1978). In the superficial levels with lower temperature, smectite coexists with kaolinite, evidencing acidic conditions. The mixed layer illite-smectite seems to be controlled by the fluid flow, since is abundant in tuffs (diffuse flow) comparing to the lava flows, where the fluid circulation is controlled by factures.

Pyrite occurs for a wide range of temperatures and seems to be controlled by the lithology, being more common in pyroclastic units and altered rocks. The amount of hematite is more relevant in the reservoir sector, mainly in the lava breccia units. The occurrence of anatase, which reaches its peak in the upper part of the reservoir (325 m – 236ºC), points out for a system rich in Ti. When anatase disappears, titanite (a sphene with Ti)

precipitates (maximum amount at 519 m depth and 239ºC). Titanite decreases again with the reappearance of anatase highlighting that both minerals abundance is correlated and inter-dependent. Titanite is also considered a low-permeability indicator (Reyes, 1990; Lagat, 2009).

Calcite is more abundant in lava and lava breccia. Similar to quartz, it appears filling open-spaces and veins reflecting a former high permeability. Chlorite and anatase also reflect more permeable conditions in the past. Calcite disappears and another carbonate, the dolomite, appears and is firstly identified at 1221 m depth. The occurrence of this mineral at so high temperature is unusual (Cathelineau *et al.*, 1985; Elders *et al.,* 1981). We interpreted this behaviour with two hypothesis: the precipitation of dolomite could be related with the precipitation of gypsum at 1183 m depth that lowered the amount of Ca and the Ca/Mg ratio in the system favouring the precipitation of dolomite instead of calcite (Konari and Rastad, 2016). Other option could be that the identified dolomite would be instead ankerite (Fe), which can be found on shear zones as transformation product of calcite, or can result from the decomposition of chlorite (Mackenzie and Craw, 2007).

The main alteration zones are defined according to the abundance in clay minerals and chlorite. A shallow unaltered to weakly altered zone is identified until 123 meters, where the altered smectite zone begins (112-168ºC). At about 183 m a chlorite zone (temperature > 168°C) begins and persists up to the end of the well. Discontinuous sub-zones can be considered inside the chlorite zone, as the chlorite + illite-smectite mixed-layer sub-zone that marks the transition of a smectite zone to a chlorite zone or, deeper in the well, low permeability conditions and/or augite's alteration. The chlorite + illite sub-zone appears in the top of the reservoir in the steam cap sector and exists after the reservoir sector, throughout the entire RG5 well.

The hydrothermal mineral assemblages can be indicative of the system temperature. Smectite + kaolinite point out for temperatures lower than 160°C, since around 180°C smectite and kaolinite are inexistent. On the other hand, the mineral assemblage chlorite + quartz + hematite ± calcite ± anatase ± titanite + albite ± adularia (± dolomite) indicates temperatures higher than 235°C. Study of the RG5 mineralogy is useful not only to characterize the reservoir structure and permeability, but also to complement and confirm inferred information by using surficial geochemical data.

In addition, all this information may be used to validate the flow model simulated for Fogo Volcano.

5.3.3.6 Conclusions and Outlook

As of the writing of this report, the study is ongoing. Due to COVID-delays and key staff leaving the ETH group as well as the unexpectedly long simulation run times, conclusion of the study will be pursued after the official termination of HEATSTORE. Nevertheless, even the reconnaissance results presented here successfully demonstrate that original aim, i.e. that ETH's unique numerical modelling capabilities are able to provide field-testable and geologically plausible models, has been reached.

The plethora of (a) relevant field *data obtained* in the study (e.g., the derived thermal heat output constraints) will allow testing and selectively refining competing numerical modelling results. On the other hand, another plethora of *lacking data* (e.g., thermal gradients in deep boreholes, water table data inside the volcano, and geologic information about the volcano architecture) remain a challenge. Yet, the models allow to rank the relevance of such data for identifying the most plausible subsurface concepts. This will a valuable contribution to elaborate the roadmap for the definition of conceptual models for future high-enthalpy geothermal projects based on this first-time combination of advanced modelling and essential geochemical data.

Caldeiras da Ribeira Grande site was selected to evaluate the applicability of studying several geochemical parameters on the characterization of geothermal reservoirs both in a pre-drilling phase and after drilling to support the reservoir management.

Information obtained based on the surficial hydrothermal manifestations contribute to recognize percolation paths and identify permeable zones, infer thermodynamic conditions at depth, identify the source of the fluids emitted and characterize sub-superficial processes, such as water-rock interaction or steam heating. Mapping deep-derived gases (*e.g.* CO_2 and radon) released on the surface may be valuable to deduce not only permeability structures but also the reservoir location. In addition, CO_2 flux studies integrated with fumarolic composition can be used to estimate the thermal energy released in an area, and consequently contribute to understand the geothermal potential of the study site.

The use of petrography and hydrothermal mineralogy highlighted their relevance to better understand the structure of the reservoir, namely by establishing alteration zones, infer temperatures at depth and define the

permeability zones. The minerals assemblages in the RG5 geothermal well showed agreement with the low permeability found during drilling operations and with the maximum temperatures measured in the well.

As mentioned above, time series of the main geochemical parameters can be used for monitoring purposes and reservoir management in order to identify possible changes on the deep feeding system. Some successful examples for the Caldeiras Ribeira Grande area seem to be the use of the H_2/Ar from the fumaroles or the total CO_2 emitted by diffuse degassing processes.

All these geological data are useful to constrain a holistic geothermal reservoir model for the area and shows the potential of these relatively "low cost" tools to any geothermal exploitation area.

5.3.4 References

Andrade, C., Cruz, J.V., Viveiros, F., Coutinho, R.: CO_2 emissions from Fogo intracaldera volcanic lakes (São Miguel Island, Açores): a tool for volcanic monitoring, *Journal of Volcanology and Geothermal Research* 400, (2020), 106915.

Arnórsson, S. Gunnlaugsson, E. (1985). New gas geothermometers for geothermal exploration - calibration and application. *Geochimica et Cosmochimica Acta* 49, 1307-1325.

Arnórsson, S., Fridiksson, T., Gunnarsson, I. (1998). Gas chemistry of the Krafla geothermal field, Iceland. *International Symposium on Water-Rock Interaction*, Auckland, New Zealand, 613-616.

Browne, P.R.L. (1970). Hydrothermal alteration as an aid in investigating geothermal fields. *Geothermics* 2(2), 564-570.

Browne, P.R.L., Ellis, A.J. (1970). The Ohaki-Broadlands hydrothermal area, New-Zealand: Mineralogy and related chemistry. *American Journal of Science* 269, 97-133.

Browne, P.R.L., (1978). Hydrothermal alteration in active geothermal fields. *Annual Review Earth and Planetary Sciences* 6, 229–250.

Caliro, S., Viveiros, F., Chiodini, G., Ferreira T. (2015). Gas geochemistry of hydrothermal fluids of the S. Miguel and Terceira Islands, Azores. *Geochimica et Cosmochimica Acta* 168, 43-57.

Carmo, R., Madeira, J., Ferreira, T., Queiroz, G., Hipólito, A. (2015). Volcano-tectonic structures of S. Miguel Island, Azores, Volcanic Geology of S. Miguel Island (Azores archipelago), *Geological Society of London Memoir* 44, 65-86.

Cathelineau, M. Oliver, R., Nievat D., Garfias, A. (1985). Mineralogy and distribution of hydrothermal mineral zones in Los Azufres (Mexico) geothermal field. *Geothermics* 14(1), 49-57.

Chiodini, G., Cioni, R., Guidi, M., Raco, B. and Marini, L.: Soil CO_2 flux measurements in volcanic and geothermal areas, *Applied Geochemistry* 13, (1998), 543-552.

Chiodini, G., Marini, L. (1998). Hydrothermal gas equilibria: The H_2O-H_2-CO_2-CO-CH_4 system. *Geochimica et Cosmochimica Acta* 62, 2673-2687.

Cruz, J.V., and França, Z.: Hydrogeochemistry of thermal and mineral springs of the Azores archipelago (Portugal), *Journal of Volcanology and Geothermal Research* 151, (2006), 382–398.

D'Amore, F., Panichi, C. (1980). Evaluation of deep temperatures in hydrothermal systems by new gas geothermometer. *Geochimica et Cosmochimica Acta* 44, 549-556.

Driesner, T., Geiger, S. (2007). Numerical simulation of multiphase fluid flow in hydrothermal systems. In Fluid-Fluid Interactions (A. Liebscher and C.A. Heinrich, eds.) *Reviews in Mineralogy and Geochemistry* 65, pp. 187-212.

Elders, E. A., Hoagland, J. R., Williams, E. (1981). Distribution of hydrothermal mineral zones in the Cerro Prieto geothermal field of Baja California. *Geothermics* 10 (3/4), 245-253.

Ferreira, T., 1994. *Contribuição para o estudo das emanações gasosas associadas a processos de vulcanismo no arquipélago dos Açores*. Master thesis, University of the Azores [in Portuguese].

Ferreira, T., Oskarsson, N. (1999). Chemistry and isotopic composition of fumarole discharges of Furnas caldera. *Journal of Volcanology and Geothermal Research* 92, 169-179.

Ferreira, T., Gaspar, J.L., Viveiros, F., Marcos, M., Faria, C., Sousa, F. (2005). Monitoring of fumarole discharge and CO_2 soil degassing in the Azores: contribution to volcanic surveillance and public health risk assessment. *Annals of Geophysics* 48 (4-5),787-796. doi: https://doi.org/10.4401/ag-3234.

Franco, A. (2016). Subsurface geology and hydrothermal alteration of Cachaços-Lombadas sector, Ribeira Grande geothermal field, São Miguel Island, Azores. *United Nations University Geothermal Training Programme (UNU-GTP) 2015 annual book*, chapter 10, 113-160.

Franco, A., Guimarães, T., Henneberger, R. (2018). Geothermal geology of the outflow of the Ribeira Grande geothermal system. *Geothermal Resources Council Transactions 2018 Conference*, Reno, Nevada 42, 1316- 1326.

Franco, A., Ponte, C. (2019): The role of geothermal in the energy transition in the Azores, Portugal. *European Geologist Journal* 47.

Giggenbach, W.F. (1975). A simple method for the collection and analysis of volcanic gas samples. *Bulletin of Volcanology* 39, 132-145.

Giggenbach, W.F., Goguel, R.L. (1989). Collection and analysis of geothermal volcanic water and gas discharges. Chemistry Division, DSIR, New Zealand. *Report no. CD 2401.*

GeothermEx (2008). Update of the conceptual and numerical model of the Ribeira Grande geothermal reservoir, São Miguel, Açores. GeothermEx Inc., *Report for Sociedade Geotérmica dos Açores, S.A. (SOGEO)*, pp.190.

Harvey, C.C., Browne, P.R.L. (1991): Mixed-layer clay geothermometry in the Wairakei geothermal field, New Zealand. *Clay Minerals* 39, 614-621.

Henneberger, R., Nunes, J. (1990). A new discovery well in the upper Água de Pau geothermal system, São Miguel Island, Azores: results of drilling and testing. *Geothermal Resources Council Transactions* 14, 1449-1452.

Hurwitz, S., Kipp, K.L., Ingebritsen, S.E., Reid, M.E., 2003. Groundwater flow, heattransport, and water table position within volcanic edifices: Implications forvolcanic processes in the Cascade Range. J. Geophys. Res. 108, 2557.

Keith, T.E.C., Muffler, L.J. (1978). Minerals produced during cooling and hydrothermal alteration of ash flow tuff from Yellowstone drill hole Y-5. *Journal of Volcanology and Geothermal Research* 3: 373-402.

Kipp KL Jr, Hsieh PA, Charlton SR, (2008) Guide to the revised ground-water flow and heat transport simulator: HYDROTHERM – version 3. Techniques and Methods, 6-A25, pp. 160, US Geological Survey, Reston, Va, USA.

Konari, M. B., Rastad, E. (2016): Nature and origin of dolomitization associated with sulphide mineralization: new insights from the Tappehsorkh Zn-Pb(-Ag-Ba) deposit, Irankuh Mining District, Iran. *Geological Journal* 53(1), 1-21.

Lagat, J. (2009): Hydrothermal alteration mineralogy in geothermal fields with the case example from Olkaria Domes Geothermal Fields, Kenya. *Presentation – Short Course IV on Exploration for Geothermal Resources, UNU-GTP*, KenGen and GSC, Kenya, 2009, pp. 24.

MacKenzie, D.J., Craw, D. (2007): Contrasting hydrothermal alteration mineralogy and geochemistry in the auriferous Rise and Shine Shear Zone, Otago, New Zealand, *New Zealand Journal of Geology and Geophysics* 50(2), 67- 79.

Marcos, M. (2006). *Estudo dos processos de desgaseificação difusa nos Açores, com base na análise de variações espaciais de CO_2 e temporais de ^{222}Rn*, Master Thesis, University of the Azores, (2006), 135p. [in Portuguese].

McGraw, P. (1976). *A petrological/geochemical study of rocks from the São Miguel drillhole, São Miguel, Azores*. MSc dissertation, University of Dalhousie, 194 pp.

Muecke, G., Ade-Hall, J., Aumento, F., MacDonald, A., Reynolds, P., Hyndman, R., Quintina, J., Opdyke, N., Lowrie, W. (1974). Deep drilling in an active geothermal area in the Azores. *Nature* 252, 281-285.

Pham, M., Klein, C., Ponte, C., Cabeças, R., Martins, R., Rangel, G. (2010). Production/injection optimization using numerical modeling at Ribeira Grande, São Miguel, Azores, Portugal. *Proceedings of the World Geothermal Congress 2010*, Bali, Indonesia, pp. 6.

Ponte, C., Cabecas, R., Rangel, G., Martins, R., Klein, C., Pham, M. (2010). Conceptual modelling and tracer testing at Ribeira Grande, São Miguel, Azores, Portugal. *Proceedings of the World Geothermal Congress,* Bali, Indonesia, pp. 11.

Rangel, M.G. (2014). Temperature model and tracer test analysis for the Ribeira Grande geothermal system, São Miguel Island, Azores. *Report 29 in Geothermal training in Iceland 2014.* UNU-GTP, Iceland, 615-642.

Rangel, G., Ponte, C., Franco, A. (2015). Use of geothermal resources in the Azores islands: a contribution to the energy self-sufficiency of a remote and isolated region. *In* Volcanic Geology of S. Miguel Island (Azores archipelago). Gaspar J.L., Guest J.E., Duncan A.M., Barriga F.J.A.S., Chester D.K. (eds.), *Geological Society of London's Memoirs*, 44, 197-211.

Reyes, A. G. (1990). Petrology of Philippine geothermal systems and the application of alteration mineralogy to their assessment. *Journal of Volcanology and Geothermal Research* 43, 279-309.

Scott S., Driesner, T., and Weis, P. (2016). The thermal structure and temporal evolution of high-enthalpy geothermal systems. *Geothermics* 62, 33-47.

Tómasdóttir, S. & Gunnarsson, G. (ed) 2021: HEATSTORE – Final report on UTES-type/site-specific simulators based on academic/research codes. GEOTHERMICA – ERA NET Cofund Geothermal. 58 pp.

Truesdell, A.H., Nehring, N.L., Janik, C.J. (1984). *Final Report: Geochemical study of thermal fluids from São Miguel Island, Azores,* 16p.

Utami, P., Browne, P.R.L. (1999). Subsurface hydrothermal alteration in the Kamojang geothermal field, West Java, Indonesia. *Proceedings, Twenty-fourth Workshop on Geothermal Reservoir Engineering*, Stanford University, Stanford, California, 25-27, pp.7.

Viveiros, F., Chiodini, G., Cardellini, C., Caliro, S., Zanon, V., Silva, C., Rizzo, A., Hipólito, A., Moreno, L. (2020). Deep CO_2 emitted at Furnas do Enxofre geothermal area (Terceira Island, Azores archipelago). An approach for determining CO_2 sources and total emissions using carbon isotopic data, *Journal of Volcanology and Geothermal Research* 401, 106968.

Viveiros, F., Gaspar, J.L., Ferreira, T., Silva, C., Marcos, M., Hipólito, A. (2015). Mapping of soil CO_2 diffuse degassing at São Miguel Island and its public health implications, Volcanic Geology of São Miguel Island (Azores Archipelago), *Geological Society of London Memoir* 44, 185-195.

Viveiros, F., Silva, C., Matias, D., Moreno, L., Driesner, T., Zanon, V., Uchôa, J., Cruz, J.V., Freire, P., Pereira, M.L., Pacheco, J. (2020+1). Geochemical tools as a contribution to improve geothermal potential on the Azores archipelago. *Proceedings World Geothermal Congress 2020+1*, Reykjavic, Iceland, 8p.

Wallenstein, N., Duncan, A.M., Guest, J.E., Almeida, M.H. (2015). Eruptive history of Fogo Volcano, São Miguel, Azores, Volcanic Geology of São Miguel Island (Azores Archipelago), *Geological Society of London Memoir* 44, 105-123.

Weis, P., Driesner, T., Coumou, D., Geiger, S. (2014). Hydrothermal, multiphase convection of H_2O-NaCl fluids from ambient to magmatic temperatures: a new numerical scheme and benchmarks for code comparison. *Geofluids* 14, 347-371.

Weis, P. (2015). The dynamic interplay between saline fluid flow and rock permeability in magmatic-hydrothermal systems. *Geofluids* 15, 350–371

5.4 Iceland superhigh temperature study

Gunnar Gunnarsson[1], Sigrún Tómasdóttir[1], Thomas Driesner[2], Benoit Lamy-Chappuis[2], Alina Yapparova[2]

[1]Reykjavik Energy, [2]ETH Zürich

5.4.1 Conceptualization

Iceland has vast geothermal resources and harnessing of geothermal resources has played a large role in improving the quality of life in the country. There is a long history of direct use in the country for purposes such as space heating, industry, bathing and even cooking (Gunnlaugsson & Ívarsson, 2010). In recent years and decades, there has been increased interest in electricity production and currently (2019), 30.9% of the electricity production in the country comes from geothermal resources. Nine conventional geothermal power plants are currently operated in Iceland with a combined installed capacity of 755.6 MW$_{el}$ (Orkustofnun, 2020). Production wells in these power plants generally reach depths of 2-3 km and the production temperatures are between approximately 230-330 °C.

In recent years, there have been plans to drill deeper into existing production fields in order to enlargen the resource downwards and to reach formations at higher temperature where conditions might be supercritical. Modeling studies have shown that a well producing from a supercritical geothermal reservoir could produce considerably more energy than a well in conventional high-temperature geothermal reservoirs such as the ones utilized in Iceland (Friðleifsson and Elders, 2017).

The IDDP project is a development and research project aiming to research the interaction of high-temperature (400-600 °C) hydrothermal fluids with basaltic crust in Iceland and the economics of deeper, hotter geothermal exploration. It is a collaboration project between Icelandic power companies, the Icelandic government and international partners. Operators of three high-temperature fields in Iceland; Reykjanes, Hellisheiði and Krafla, agreed to each fund the drilling of a deep well. The IDDP project would then fund the deepest part of the well. So far, 2 wells have been drilled. The first one, IDDP-1 in Krafla, reached magma at a depth of 2.1 km (Elders and Friðleifsson, 2010). The second well, IDDP-2, was drilled in Reykjanes. An existing production well was deepened down to 4659 m. The deepening started in 2016 and was completed in 2017. The highest measured temperature in the IDDP-2 well is 426 °C but is has been suggested that stable bottom hole temperature might reach 535°C (IDDP, 2018). However, damages in the casing have prevented further measurements of the deeper parts of the well. The next well to be drilled in the project will be drilled in the Hengill area, where Reykjavík Energy operates two geothermal power plants. Preparation for that well is the purpose of this study.

Numerical modeling is one tool that can be used to predict and hypothesize on the effect such a deep well could have on the conventional system and to model different utilization strategies. Heat storage or deep production from a deep well in the Hengill area is the second Icelandic case study within the HEATSTORE project.

5.4.1.1 System specifications, scope and aims of the study

The deeper parts of the geothermal system are not well understood. As mentioned above, conventional geothermal wells are drilled down to approximately 2.5 km. There is an interest to develop the systems downwards and thereby enlarge the exploitable resource. In order to do so, better understanding of the deeper parts is required. Experience from the IDDP wells and wells in the Hengill area show that the heat sources in these systems can be found at shallow depths.

The heat sources and their vicinity are more or less unknown territory. We need new methods and technologies to drill into and produce from such conditions. Thus, it is important to do as much research as possible before the drilling of IDDP-3 commences in Hengill. This includes predicting likely conditions and having readymade modeling tools for understanding measurement data that will be collected during drilling. If deep drilling is a feasible way of exploiting the geothermal resource, we need to be able to incorporate the hotter formations at greater depth into the conventional field scale modeling schemes.

The aim with this study is to develop process models of conditions at greater depths and incorporate them into the industrial field scale model of the area. The aim is also to model different production or injection

scenarios for a hypothetical IDDP-3 well. The exact location for the well has not been decided but it will be within the Hengill area (Figure 5.4.1).
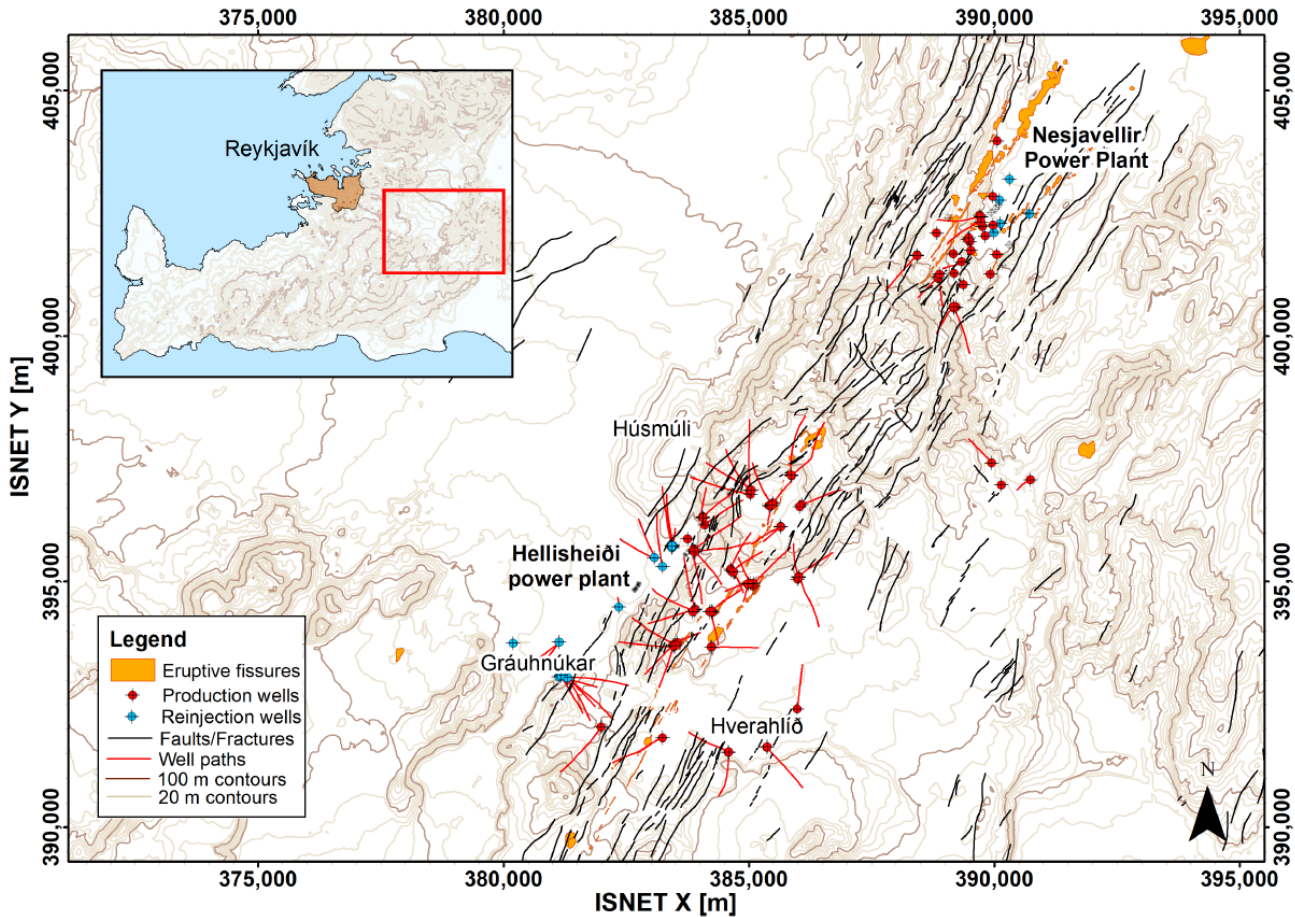

Figure 5.4.1 A map of the Hengill area showing elevation contours, surface fractures, eruptive fissures, production and reinjection wells as well as well paths projected to the surface. 1:90000. The inset shows the location of the area in SW-Iceland (Data Source: Reykjavík Energy and Nation Land Survey of Iceland)

The Hengill area is located in SW-Iceland, about 30 km east of Reykjavík. The area has been studied intensively in connection with geothermal utilization (see e.g. Sinton et al., 2005; Franzson et al., 2005; Franzson et al., 2010; Helgadóttir et al., 2010; Franzson, 1998; Sæmundsson, 1995; Árnason et al., 2010 and references therein). Drilling started in 1965 and today two geothermal power plants are operated in the area: The Nesjavellir Power Plant, commissioned in 1990, in the northern part of the volcanic complex and The Hellisheiði Power Plant, commissioned in 2006, located in the southern part of the volcano. The Hellisheidi and Nesjavellir power plants are both combined heat and power, with total installed capacity of 423 MW$_e$ and 540 MW$_{th}$. The geothermal reservoirs supplying fluid for the power plants are 230-330°C (Figure 5.4.3). In total 88 high temperature production wells, and 26 injection wells, the deepest more than 3000 m, have been drilled into the geothermal systems in the Hengill volcano to supply steam and water for the power plants and receive the spent fluid for reinjection.

The IDDP-3 well will reach greater depths than explored already in the area. Pressure and temperature will surely be higher, the chemical composition different and likely the permeability will be smaller than at shallower depths due to greater lithostatic pressure.
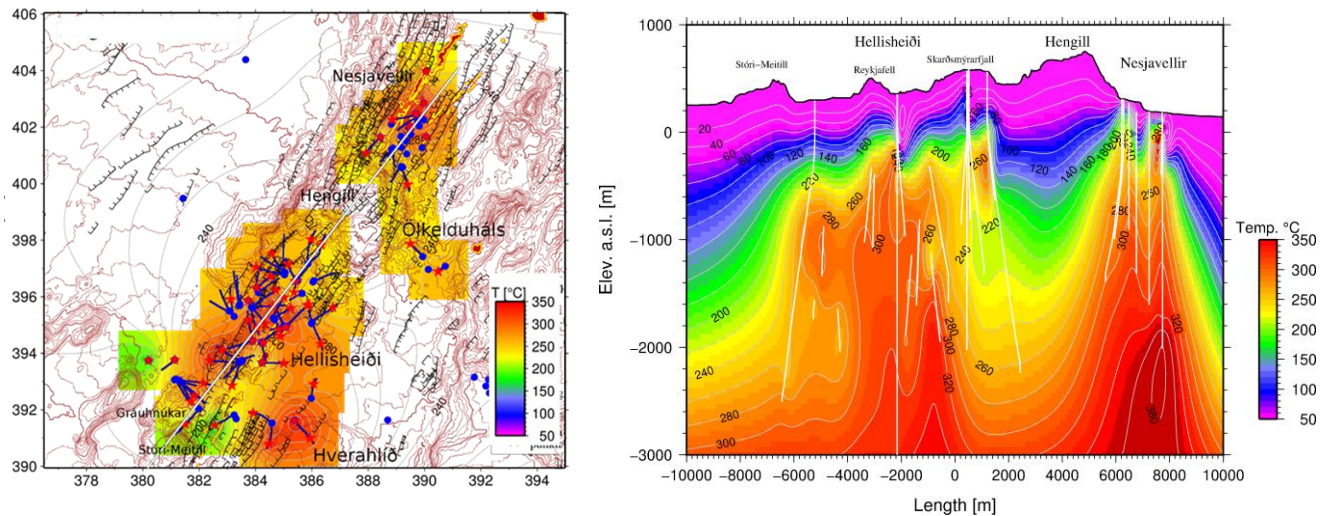
Figure 5.4.3 Left: Formation temperature at 1000 m below sea level in Hengill region (left). Wellheads are shown with blue circles, well trajectories with blue lines and data points for the temperature interpolation with red stars. Right: formation temperature in the cross section shown with a white line on the map. The white traces show well paths.

Different utilization scenarios for the well are possible:

- Using the well for cold water injection only and monitoring the effect on the shallower reservoir (Figure 5.4.2.a)

- Using the well for production (Figure 5.4.2.b)

- Drilling a well doublet, one for production and one for injection (Figure 5.4.2.c)
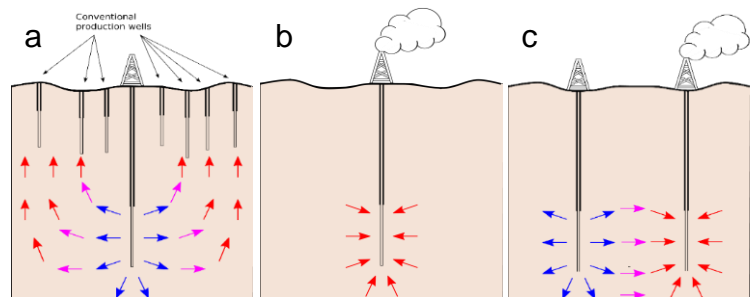
Figure 5.4.2 Different heat mining scenarios with the IPPD-3 well; a) injection b) production c) injection and production well doublet.

5.4.1.2 System Geometry and related Geology

The Hengill volcanic system lies within the western volcanic zone of Iceland, at a location where the rift zone is intersected by the South Iceland Seismic Zone (SISZ), forming a triple junction. The area is very seismically active, with two kinds of tectonic activity prevailing in the area; dilational rifting as evident by a 60-100 km long and 3-5 km wide NE-SW trending fissure swarm with a total throw of more than 300 m, and a transform component related to the SISZ which is concentrated in the eastern part of the area (Franzson et al., 2005, 2010).

The system was formed by several volcanic cycles from various spreading episodes of the rift zone. Postglacial volcanism at Hengill has been confined to three fissure eruptions dated at ~10,300 yrs., ~5,700 yrs. and ~1.800 yrs. (Sinton et al., 2005). These fissure eruptions have been suggested to open up new flow paths and locally intensify the geothermal system (Franzson et al., 2010). An age of about 0.4 million years is proposed for Hengill which puts an upper age limit on the geothermal system (Franzson et al., 2005, 2010). The ages of the fissure eruptions are clearly within the range of the lifetimes of geothermal systems driven by a single stage, small intrusion (Hayba & Ingebritsen, 1997) and, therefore, provide valuable time parameters for developing possible simulation scenarios.

The largest part of the Hengill central volcano is built up of basaltic rocks. These are mainly hyaloclastic (glassy) ridges that erupted sub-glacially during glacial times but hyaloclastic formations dominate the top-

most 1000 m of the Hengill area, but the highest part of the mountain is some 800 m above sea level (Franzson et al., 2010; Helgadóttir et al., 2010; Franzson, 1998). The hyaloclastic formations are very heterogeneous; they can consist of crystalline rocks with minor amounts of volcanic glass, such as pillow basalts, and also almost solely of volcanic glass, or a mixture thereof. In the less mountainous parts of the area the stratigraphy consists of alternating successions of hyaloclastite formations from glacial periods and lava sequences formed during interglacial periods. The most prominent ones originate from large lava shields which have erupted in the highlands and flowed to the surrounding lowlands (Franzson et al., 2010). A simplified lithological model of the Hellisheiði area is shown in Figure 5.4.4. Intrusive rocks dissect the succession below about 800 m depth below sea-level (m b.s.l.) and become dominant part of the strata below 1700 m b.s.l. In addition to being a heat source, intrusive rocks contribute substantially to the permeability in the field, but the fracture networks created by the emplacement of intrusive rocks are a major control on aquifer (feed zone) permeability below 500 m b.s.l., but in the shallower parts of the wells the aquifers are commonly associated with stratigraphic boundaries (Franzson et al., 2005, 2010). With this information in mind, intrusive rocks are assumed to be dominant in the deeper levels of the IDDP-3 well.
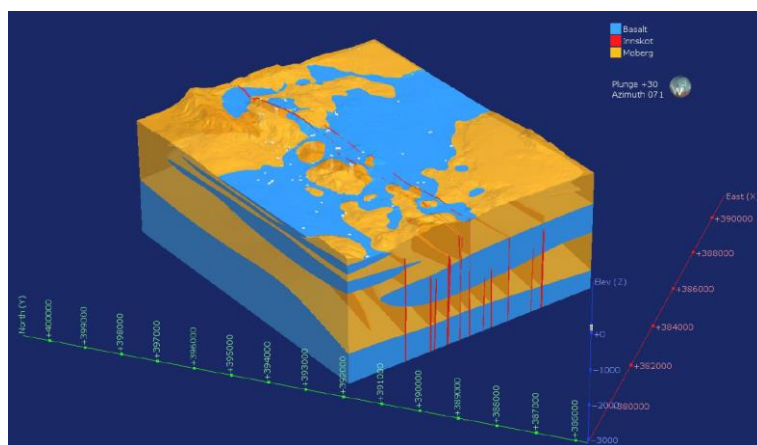
Figure 5.4.4 Lithological model of the Hellisheiði area showing the intrusions in red, the hyaloclastite formations in yellow and the basalt in blue. The view has an azimuth of 71° and a plunge of 30° (Gunnarsdóttir and Poux, 2016).

5.4.1.3 Local geothermal and groundwater conditions

A local groundwater model exists for the capital area, covering the Hengill area as well (Figure 5.4.5). The model is maintained and regularly updated by Vatnaskil Consulting Engineers. The model illustrates the groundwater divides in the area and the directions of major groundwater currents. In general, the groundwater flow in Hengill follows the Þingvellir current. The direction is towards the NE, in alignment with the major NE-SW trending normal faults. The groundwater flow in the Þingvellir current is calculated to be 15 m^3/s (Vatnaskil, 2020). Resistivity surveys, alteration mineralogy and groundwater level measurements in the system have shown that the geothermal system itself is, however, separated from the colder groundwater system above it by a so-called cap rock which has low permeability. The water level in the upper groundwater system is about 30 m below the surface but the water level in wells drilled into the geothermal system is at a depth of about 200 m (see e.g. Gunnarsson, Arnaldsson and Oddsdóttir, 2011; Árnason et al., 2000). The groundwater flow within the geothermal system within the utilized area has been affected by production and injection. Tracer tests have shown that the flow appears to be anisotropic and predominantly in the direction of the major fault lines (Kristjánsson et al., 2016).

In the beginning, the conceptual model of the Hengill area assumed a central upflow zone underneath the central volcano feeding hot fluid to both Hellisheiði and Nesjavellir (Björnsson et al., 2003). More data from wells in Hellisheiði shed new light on the geothermal activity in the area and challenged the idea of a common heat source. This led to a revision of the conceptual model and subsequently updates to the numerical model. The current model assumes that various local heat sources drive the system and that the heat sources are cooling magmatic intrusions and a deeper magma chamber (Gunnarsson, Arnaldsson and Oddsdóttir, 2011).

Figure 5.4.5 Calculated shallow groundwater flow in May 1980 when the groundwater divide reached furthest towards the north. The arrows show the direction of the groundwater flow (Vatnaskil, 2017).

5.4.1.4 Well operation and history

Figure 5.4.6 shows the production/injection mass balance in the Hengill area for 2018. Reinjection of geothermal fluid back into the reservoir takes place in Hellisheiði. Two reinjection zones are operated, Húsmúli and Gráuhnúkar. The figure shows that there is considerable production density in the area, up to 300 kg/s/km^2. Without reinjection, the reservoir pressure in Hellisheiði would drop by more than 10 bar annually, assuming no natural recharge (Kristjánsson et al., 2016). The high production density in Hellisheiði has, despite reinjection, caused a pressure drawdown in the reservoir (Figure 5.4.9). Figure 5.4.7 and Figure 5.4.8 show the production and injection history of Hellisheiði and Nesjavellir, respectively, as well as the evolving of the enthalpy of the produced fluid. The average enthalpy in Hellisheiði has been decreasing and in Nesjavellir it has also started to decrease in recent years.
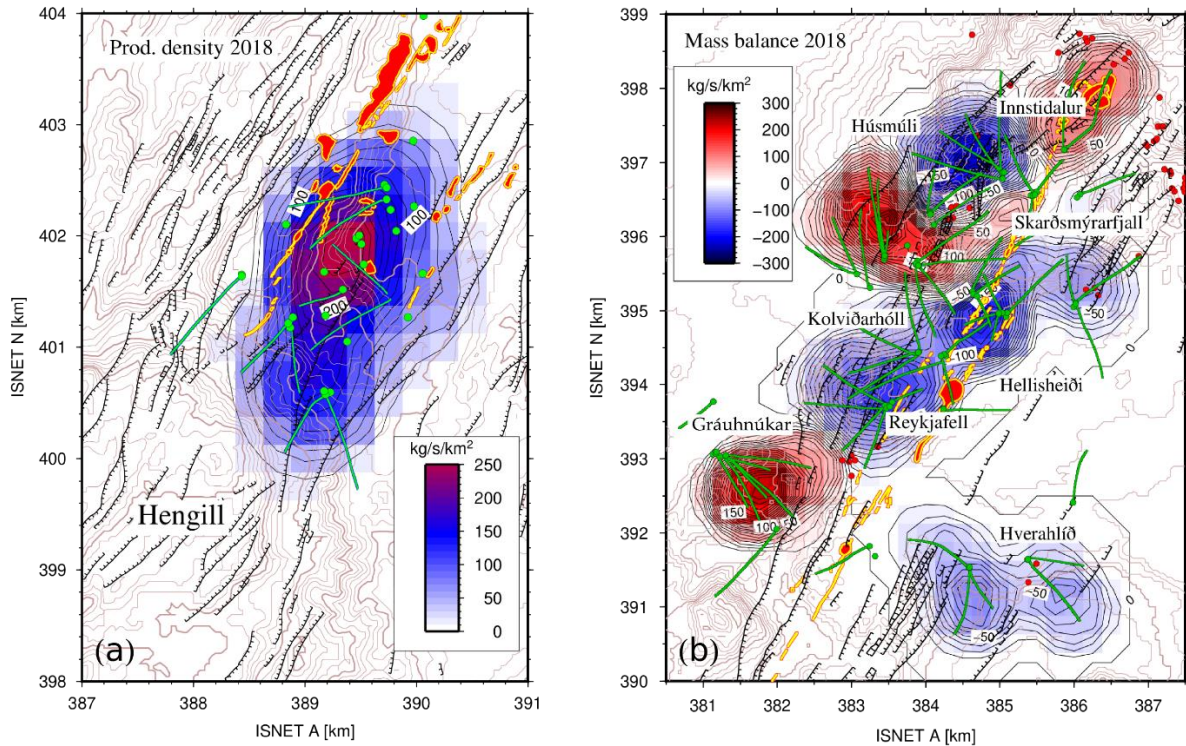
Figure 5.4.6 Production density in the Hengill area in 2018 a) Production density (kg/s/km²) in Nesjavellir. Until recently, water has not been injected into the reservoir itself in Nesjavellir, but fluid is injected into the shallow groundwater system there. Production is positive in the scale, b) Production/injection mass balance (kg/s/km²) in Hellisheiði, injection is positive in the scale and production is negative.
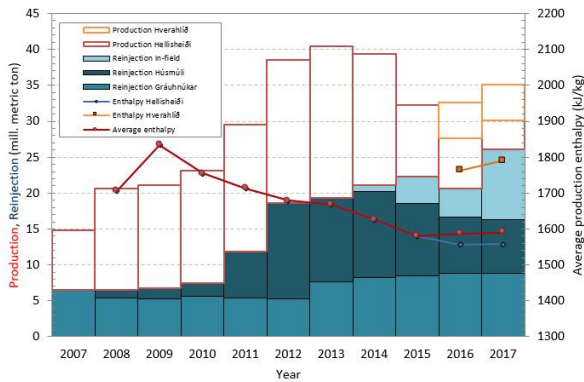
Figure 5.4.7 Production, reinjection and enthalpy development from 2007-2017 in Hellisheiði and from 2016 also in the newly utilized Hverahlíð area.
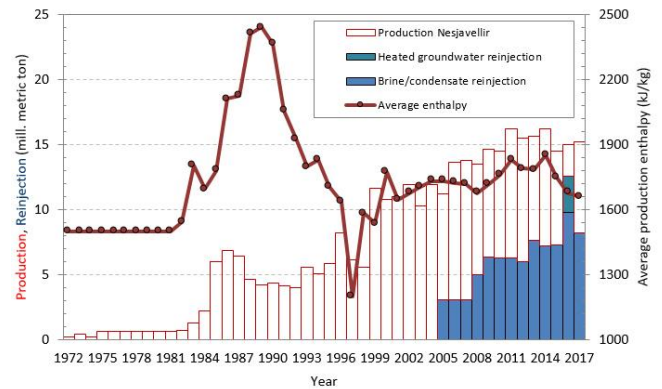
Figure 5.4.8 Production, reinjection and enthalpy development from 1972-2017 in Nesjavellir.
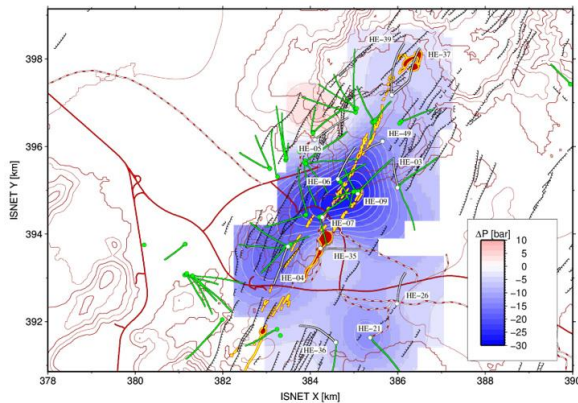
Figure 5.4.9 Pressure drawdown (bars) in Hellisheiði due to production as measured in wells.

5.4.1.5 Defining superhot targets and upflow zones

Scott et al. (2015) modeled how fluid from a supercritical resource will be disseminated in the overlying high-enthalpy system. In essence, the patterns indicate that the thermal structure of the field can be used as a first order "vector to the resource". However, a given heat source may develop several hot plumes; therefore, two hot plumes shown in Figure 5.4.3 could indicate two separate heat sources - one beneath each plume - or a single one located at greater depth between the middle part that is cooler at shallower depth. Scott et al. (2016) explored the effect key geologic controls such as intrusion emplacement depth, host rock permeability and intrusion geometry have on the thermal and hydraulic structures of high enthalpy systems. To show an example from their findings (Scott et al., 2016), Figure 5.4.11 shows the effect varying host rock permeability and different emplacement depth has on the development of thermal plumes. It is apparent that higher permeability (subfigures a.- c.) leads to much faster plume development but also faster cooling of the intrusion. Greater emplacement depth (subfigures g. – i.) then shows even slower plume development. All setups form two distinct plumes that then evolve in a different manner with time. Figure 5.4.10 shows a comparison between two emplacement setups (Scott et al., 2016) and the temperature distribution in Hengill
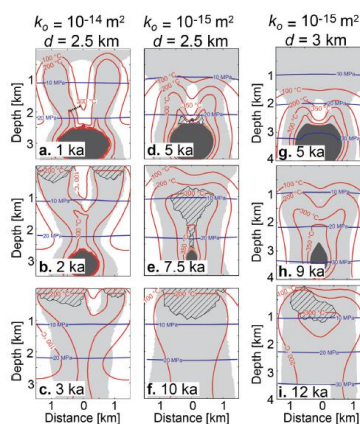
Figure 5.4.11 Effect of intrusion emplacement depth and permeability on the transient development of geothermal systems (Scott et al., 2016, Fig. 5).
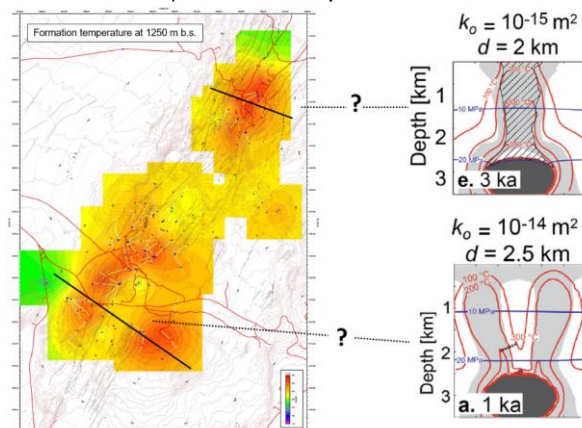
Figure 5.4.10 Temperature distribution at 1250 m below sea level in the Hengill area where the IDDP-3 well will be drilled compared to two simulations from Scott et al. (2016, Fig 4e and 5a) that offer possible interpretations for different parts of the field.

at a depth of 1250 m below sea level (m b.s.l.) to hypothesize on possible heat source setups.

Numerous studies have been carried out to try to shed light on the deeper parts of the Hengill area. Tryggvason et al. (2002) modelled the 3D velocity structure of the field down to 10-15 km. They suggested that supercritical fluids within the volcanic system caused reduced seismic velocities rather than large regions of partial melt and therefore concluded that a magma body several kilometers across does not exist underneath the Hengill area. But their models do not rule out the possibility of smaller pockets of melt. Feigl et al. (2000) studied crustal deformation in Hengill and suggested a magma pocket at 7 ± 1 km beneath the Hrómundartindur peak SE of Nesjavellir. Árnason et al. (2010) conducted an extensive study of the resistivity structure at Hengill using TEM and MT soundings. They found a deep conductor at 3-10 km depth which they interpreted as a group of hot, solidified but still ductile intrusive magmatic bodies. Stefánsson et al. (2019) used boron and chlorine systematics to study signals of superhot fluids in the Hengill area. They found indications of input of superhot fluids for wells both in Nesjavellir and in Hverahlíð where moderate to elevated enthalpy, high B/Cl ratio and high B concentration go together.

The distribution of alteration minerals and temperature in the system can also be used for indication of up-flow zones and proximity to heat sources. The formation of secondary alteration minerals corresponds with the breakdown of primary phases. The alteration minerals form alteration zones which correspond to certain temperatures. Alteration zones in the geothermal system in Hengill go from little too no alteration, to the smectite/zeolite zone, then mixed layer clays, then chlorite/epidote and lastly epidote/actinolite. The last zone forms at temperatures above 280 °C (Snæbjörnsdóttr et al. 2018). Viewing slices of alteration mineralogy along with slices of formation temperature is useful as alteration can also represent older geothermal activity that is not representative of the system at present. Such slices through Nesjavellir, Hellisheiði and Hverahlíð are presented on Figure 5.4.12. These slices show high temperature alteration and upwelling of high temperature underneath the center of Nesjavellir and underneath both the Hellisheiði field and Hverahlíð that could indicate proximity to local heat sources.
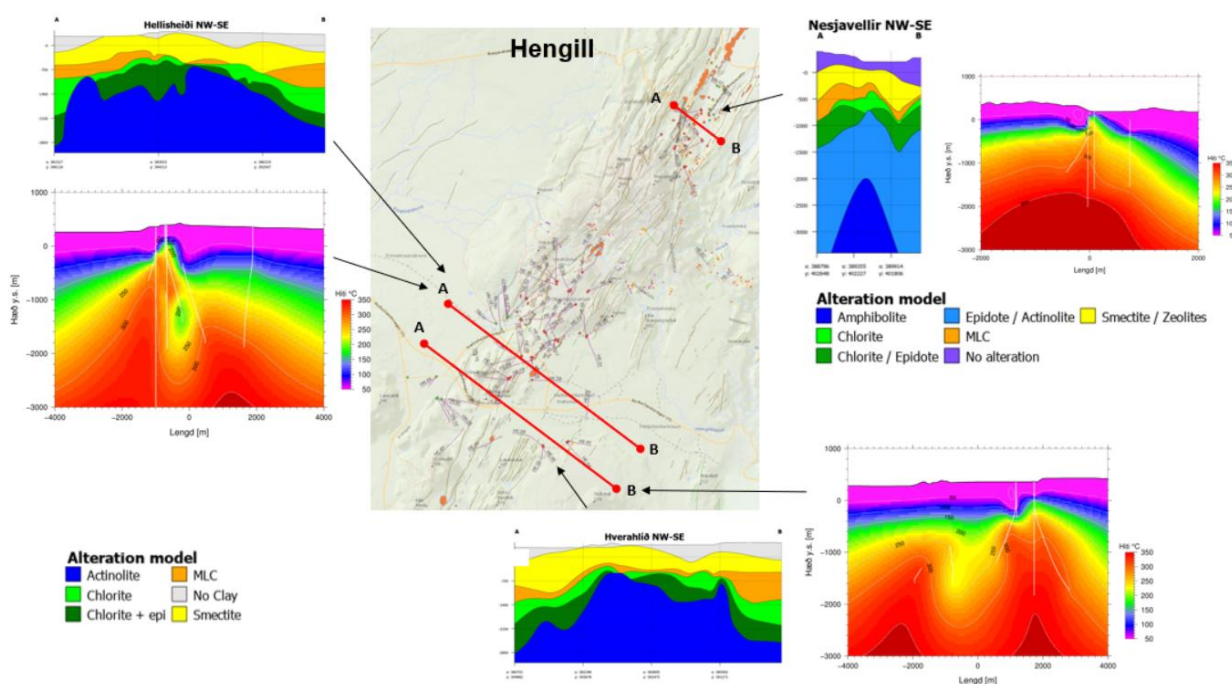

Figure 5.4.12 Slices through the alteration model for the Nesjavellir and Hellisheiði areas as well as slices through an interpolated formation temperature model. The alteration model is constructed using Leapfrog and maintained by ÍSOR for ON Power. The temperature slice for Nesjavellir extends slightly further than then the alteration model.

Temperature profiles from certain wells in Nesjavellir (NJ-11) and Hverahlíð (HE-21) show a step in the well temperature profile near the bottom of the wells. This gives strong indications of proximity to a hot body (Figure 5.4.13).
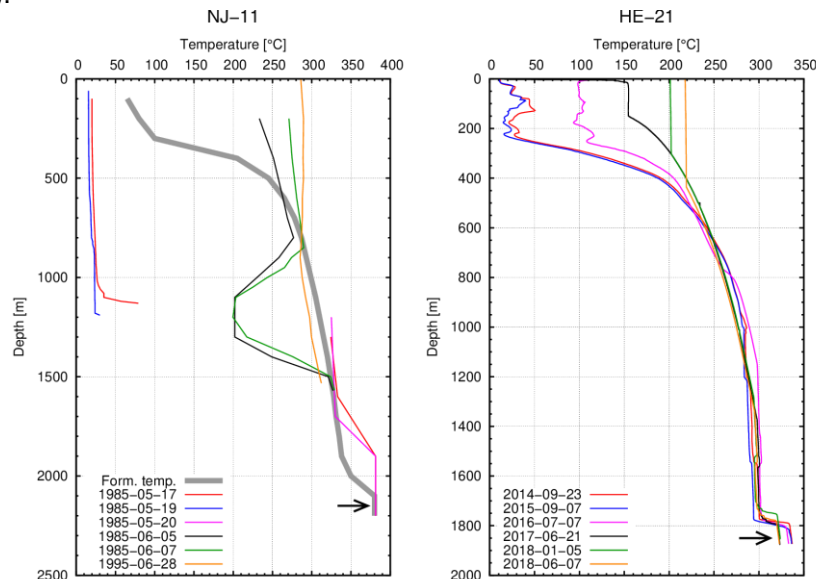

Figure 5.4.13 Temperature profiles of well NJ-11 in Nesjavellir and HE-21 in Hverahlíð. Data from NJ-11 is scarce, however, the formation temperature could roughly be estimated. More data is available in well HE-21 which shows temperature profile of the formation. The step in the temperature near the bottom of the wells might indicate proximity to heat sources.

Kim et al. (2018) did a Reverse Vertical Seismic Profiling (RVSP) study in Krafla in Northern Iceland and they suggest that scattered reflectivity at depth in Krafla could rather be from a distributed network of magmatic intrusions rather than a larger magma chamber as has previously been suggested in Krafla.

The heat sources in Hengill are likely also networks of magmatic intrusions. Holocene fissure eruptions in the area and intrusions analyzed during drilling of production wells are a proof that magma injection into the crust is facilitated. Formation temperature estimates, temperature profiles and alteration minerology indicate upwelling of high temperature underneath Nesjavellir, Hellisheiði and Hverahlíð and boron and chlorine systematics indicate superhot input underneath Nesjavellir and Hverahlíð. But delineating the shape, size and location of smaller intrusive bodies at depth requires very high resolution studies. At this stage, the shape and size of magmatic heat sources in simulation modeling of the Hengill area need to be general.

5.4.2 Modeling approach

5.4.2.1 Conceptual simulation model

Current TOUGH2 reservoir model

A field scale numerical model exists for the whole Hengill area, covering Hellisheiði, Hverahlíð and Nesjavellir. This is a commercial model based on the TOUGH2 simulator, which is calibrated by fitting observed data and production history. It is used to simulate different production scenarios and is used for operational purposes and as a tool for decision making.

The model has a hexagonal grid which is refined around production and injection sites (Figure 5.4.14). It has 11 layers, about 43 thousand elements and 167 thousand connections. Its lateral size is 50x50 km and it reaches from 400 m above sea level (m a.s.l.) down to 2500 m below sea level (m b.s.l.). Porosity in all elements is kept at 10 % which has shown to be a good estimate for the active rock porosity. Rock density is maintained fixed at 2650 kg/m³, heat capacity at 1000 J/kgK and thermal conductivity at 2.1 W/mK (Gunnarsson and Aradóttir, 2015).
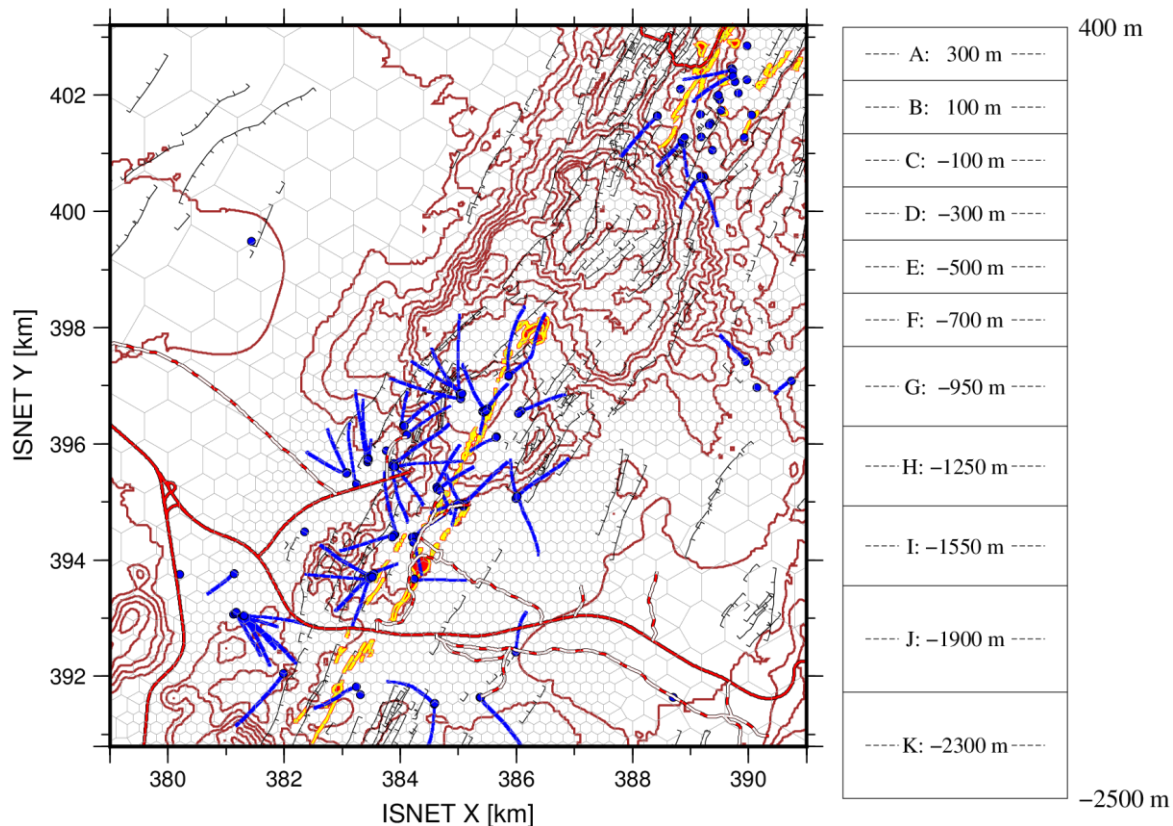
Figure 5.4.14 The grid and layering in the overall Hengill TOUGH2 model.

No mechanics are included in this model which is considered acceptable as the rock is highly permeable. An effective continuum method is used to model the fractured medium so individual fractures are not specifically represented. Permeability barriers are however included in a few places to represent notable anisotropy in the system.

TOUGH2 uses various "equation of state" (EOS) modules which are designed for different applications. The field scale model uses EOS1 which describes water in liquid, vapor and two-phase state. The standard TOUGH2 module that the field scale model uses does not handle supercritical conditions and thus does not allow to explicitly represent the magmatic heat sources in the model structure, which is a limitation as supercritical resources could be expected to be located at the top of such bodies (Scott et al., 2015). This limitation is solved by only simulating the upper part of the system and taking the roots into account by adjusting bottom boundary conditions that emulate flow of heat and hot fluid into the system from greater depths. There does exist a recent extension to the EOS1 equation of state module, EOS1sc, that extends the operational range of conditions to including supercritical conditions (Magnúsdóttir and Finsterle, 2015) but this module had not been used previously for the current Hengill reservoir model.

This field scale model with the above-mentioned simplifications works quite well for operational purposes. However, when we will drill into the deeper parts of the system and into the heat sources, it won´t suffice and new approaches have to be developed. The aim with this project is to combine these functional and flexible field scale simulation methods with the state of the art methods of modeling conditions in the deeper parts.

CSMP++ code for simulating heat sources and their vicinity

The ETH group has developed numerical methods that allow explicitly representing the magmatic heat sources and assigning temperature-, pressure- and stress-dependent material parameters (see e.g. Coumou et al., 2008a, 2008b, 2009; Scott et al., 2015, 2016; Weis et al., 2014). In addition, fracture zones can

explicitly be represented either as volumetrically meshed entities or with lower dimensional representations (i.e., as 1D structures in a 2D computational mesh or with 2D elements in a mesh of 3D elements). The code was used to derive key insights about the geologic factor controlling supercritical sources and is, therefore, considered particularly suited for the problems of interest here.

5.4.2.2 Pre-processing workflow

The workflow for including heat sources in reservoir simulations of the Hengill area can be summarized as;

- Updating and recalibrating the TOUGH2 field scale model of the Hengill area. This includes:

  - Assigning rock types to elements based on geology and system behavior

  - Locating feed zone elements in the model to use for injection/production based on information from drilling and measurements

  - Running simulations using production and injection history

  - Optimizing the model with iTOUGH2 using drawdown, enthalpy and initial pressure and temperature profiles

- Revisiting field data in order to identify interesting targets to drill a deep well into and thus to model

- Identifying possible conditions at depth and constructing a conceptual model of the heat sources

- Performing generic simulations to try to model the anticipated conditions

- Verifying process models using field data

- Including heat sources in a field scale model. For this, three approaches were taken;

  - Implementing the Hengill permeability distribution into a CSMP++ modeling scheme and placing heat sources underneath it

  - Extracting conditions from the CSMP++ model and implementing them as new boundary conditions in the conventional field scale model

  - Updating the equation of state module for the conventional TOUGH2 field scale model to EOS1sc, deepening the model and placing heat sources at greater depths

- Testing production/injection scenarios

For the new models based on the CSMP++ code, the standard workflow involves importing a CAD-constructed geometry into the ICEM meshing module of the ANSYS software package and generating a computational mesh that the simulation software can directly import. Already in the CAD steps, individual model parts (e.g. rock units, fault zones, intrusions) can be defined and given names that are kept during the whole workflow and allow assigning separate material parameters and their dependencies on temperature, pressure etc. for the simulation. Hydraulic and thermal parameters for geologic entities inside the drilled part of the field are imported from the current TOUGH2 model as it represents the best available calibration.

5.4.2.3 Computational approach and software

The field scale model is run using the numerical simulator TOUGH2 (Pruess, Oldenburg and Moridis, 2012) as implemented in forward and inverse mode within the iTOUGH2 code (Finsterle, 2007). TOUGH2 is a multiphase flow and transport simulation program for fractured and porous media. It is widely used in the geothermal industry (Pruess, Oldenburg and Moridis, 2012). The grid is generated using the AMESH program (Haukwa, 1998).

Conceptually, the model simulates the transport of fluid and heat in a geothermal system. It solves governing equations that describe the conservation of mass and energy. The change in mass/energy in a given subdomain V_n across enclosing surface Γ_n is represented as:

$$\frac{d}{dt} \int_{V_n} M^k dV_n = \int_{\Gamma_n} F^k \bullet nd\ \Gamma_n + \int_{V_n} q^k dV_n,$$

where M^k is the mass/energy of the mass/heat component k present in that subdomain. $F^k \bullet n \, d\Gamma_n$ is the flux of component k into domain V_n through the surface Γ_n. Lastly, q^k stands for sinks or sources of component k in domain V_n. Conduction and convection control the heat flow. Thermodynamic conditions are based on local equilibrium of all phases. Advection controls the mass flow and a multiphase version of Darcy's law is used to calculate advective mass fluxes in each phase (Pruess, Oldenburg and Moridis, 2012).

To this end, published studies with ETH's CSMP++ code were restricted to 2D simulations but in this project the capabilities of the code were enhanced to 3D. The code uses a Control Volume Finite Element method to (a) capture realistic geometries and, (b) solve accurately both diffusive- and advective-type equations (Weis et al., 2014). The computational approach for CSMP++ is described in more detail in Deliverable 2.2.

5.4.2.4 Model Development and Analysis

Calibration of current field scale model

The Hengill field scale model covers Hellisheiði, Hverahlíð and Nesjavellir. It is a commercial model which is calibrated by fitting observed data and production history. It is used to simulate different production scenarios and as a tool for decision making.

The top and bottom layers of the model are assumed to have constant conditions, termed "inactive" in the TOUGH2 terminology. The top layer is fixed at 15 °C and 1 bar. The temperature in the bottom layer in the vicinity of wells is estimated from down-hole measurements and else set according to a temperature gradient of 100 °C/km. Specific heat sources are simulated by injecting hot fluid into the system in the second deepest layer. To obtain initial conditions for the system before production started, steady state runs are performed where these heat sources drive the system until it reaches equilibrium. Figure 5.4.15 shows a plan view of the initial bottom temperature of the model and a vertical slice along the center of the model.
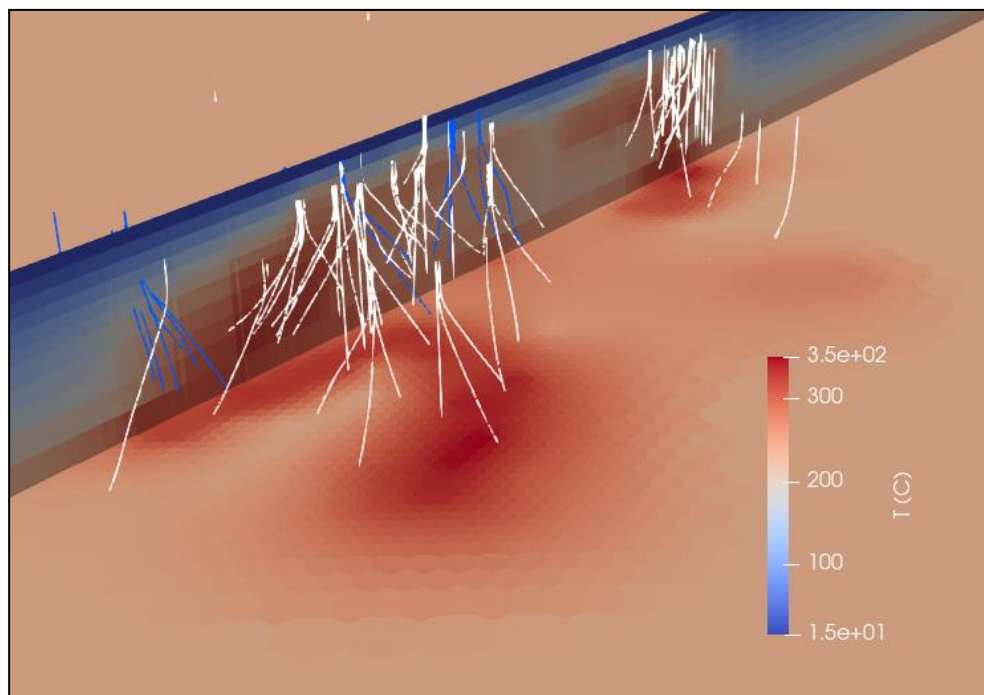
Figure 5.4.15 Initial temperature conditions in the model at 2300 m b.s.l. and in a vertical SW-NE trending slice along the center of the model. Production and monitoring well paths are shown with white traces and reinjection well paths are shown with blue traces. The left cluster of wells is Hellisheiði and Hverahlíð and the right cluster of wells is Nesjavellir.

The model is divided into different rock types based on lithology, alteration, permeability and the behavior of the system in response to utilization. Permeability in these different rock types and the quantity and enthalpy of heat injection are the parameters that are allowed to change during optimization/calibration. Permeability barriers have been introduced to try to improve the model results with regards to drawdown and enthalpy measurements. The horizontal distribution of the different rock types defined within the geothermal system is shown on Figure 5.4.16. The alignment of the rock types is in the direction of the fracture zone that extends through the geothermal system. The rock types within the system are expected to have higher permeability than the surrounding less fractured formation illustrated with gray in Figure 5.4.16.
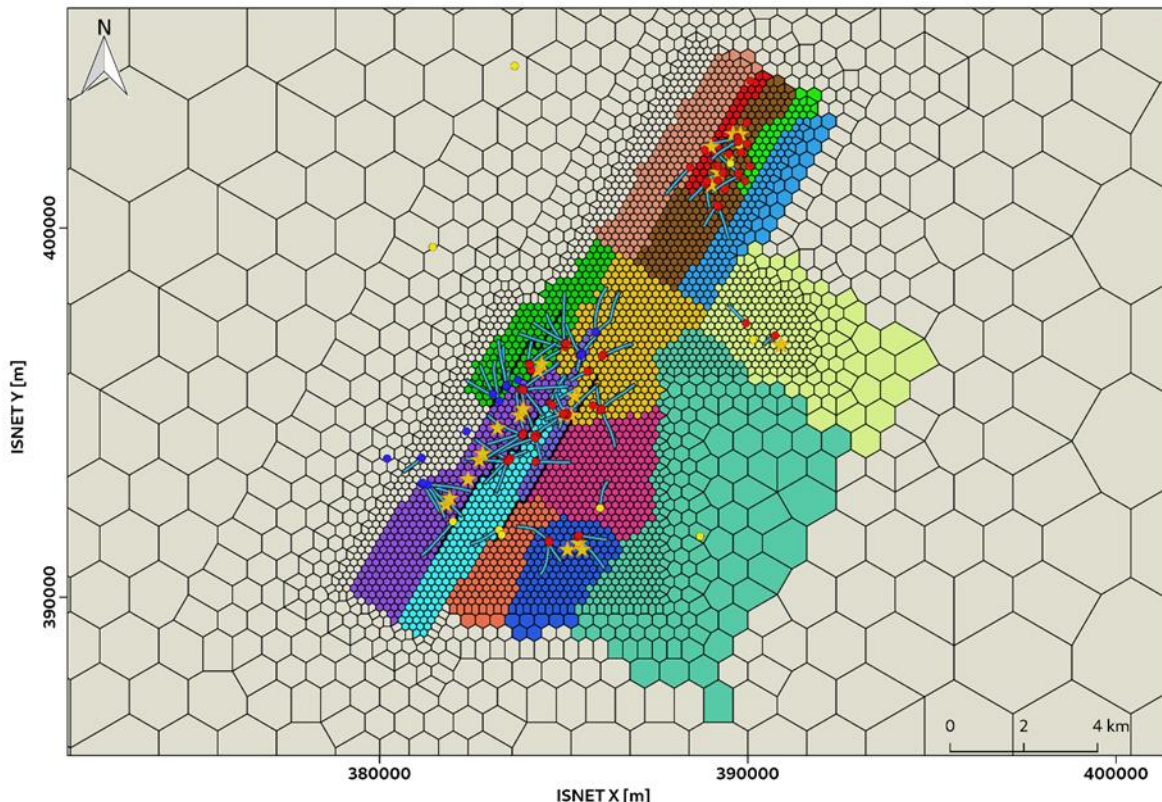
Figure 5.4.16 Model rock type distribution within the geothermal system. Different types are shown with different colors. Production well heads are shown with red circles, injection well heads with blue circles and monitoring wells with yellow circles. The stars indicate locations where hot fluid is injected into the bottom of the system.

Updating and recalibration of the model with new data from 2018, 2019 and 2020 has been conducted. The initial state of the model was calibrated against estimated formation temperature and pressure profiles and the production history was calibrated against drawdown and enthalpy measurements in monitoring wells. Comparisons for estimated and simulated formation temperature for wells HE-42 in Hellisheiði and well NJ-21 in Nesjavellir from a recalibrated model are shown on Figure 5.4.18. A comparison between all simulated and measured formation temperature and pressure values is plotted on Figure 5.4.17 along with a line that would represent a perfect fit. Generally, a good fit is obtained but the fit is better for pressure than temperature. The temperature measurements and simulated values have a correlation coefficient of 0.89 and the pressure measurements and simulated values have a correlation coefficient of 0.98.
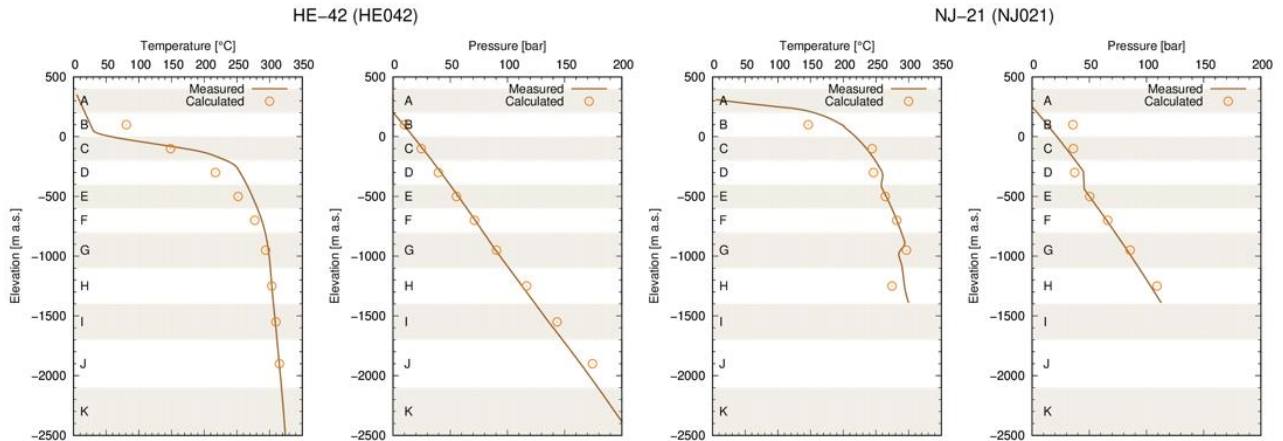
Figure 5.4.18 Examples of initial state comparisons between estimated and simulated formation temperature and pressure for well HE-42 in Hellisheiði and well NJ-21 in Nesjavellir.
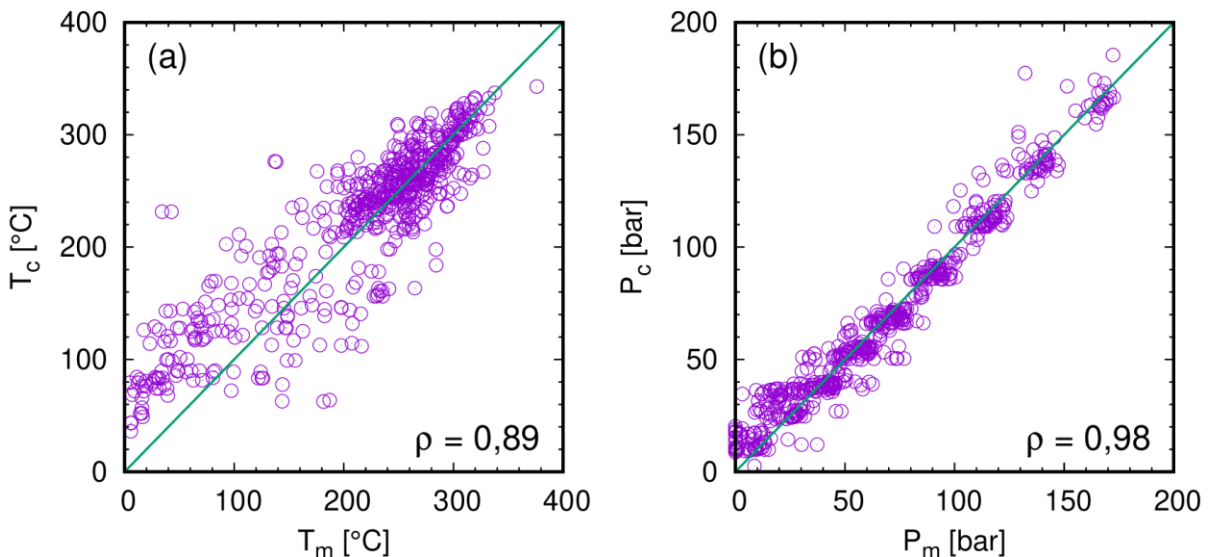

Figure 5.4.17 Comparison between measured (Tm and Pm) and calculated (Tc and Pc) formation temperature (a) and pressure (b) for all wells along with a calculated correlation coefficient (ρ).

Pressure drawdown from geothermal system utilization is highly dependent on system permeability and properties. Matching measured drawdown therefore has a large impact on the calibration results. Measured and calculated pressure drawdown from the recalibrated model is shown for Nesjavellir on Figure 5.4.20 and Hellisheiði on Figure 5.4.20.
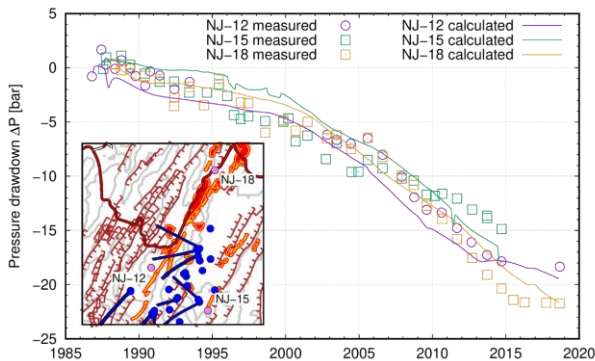
Figure 5.4.20 Comparison between measured and calculated drawdown in monitoring wells in Nesjavellir.
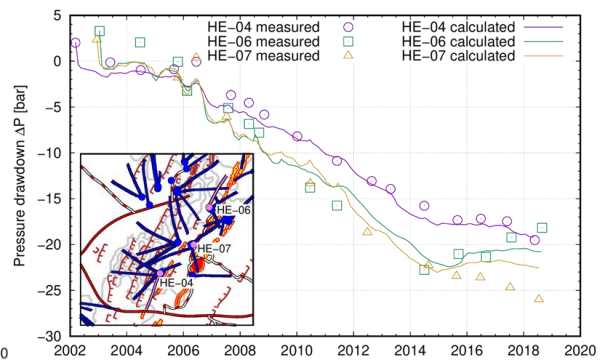
Figure 5.4.20 Comparison between measured and calculated drawdown in monitoring wells in Hellisheiði.

Permeability results from the recalibrated Hengill field scale model are presented on Figure 5.4.21. The values shown are for a depth of -1500 m b.s.l. and represent a geometrical average of the horizontal and vertical permeability. It is apparent that the permeability is the highest in central Nesjavellir and central Hellisheiði.
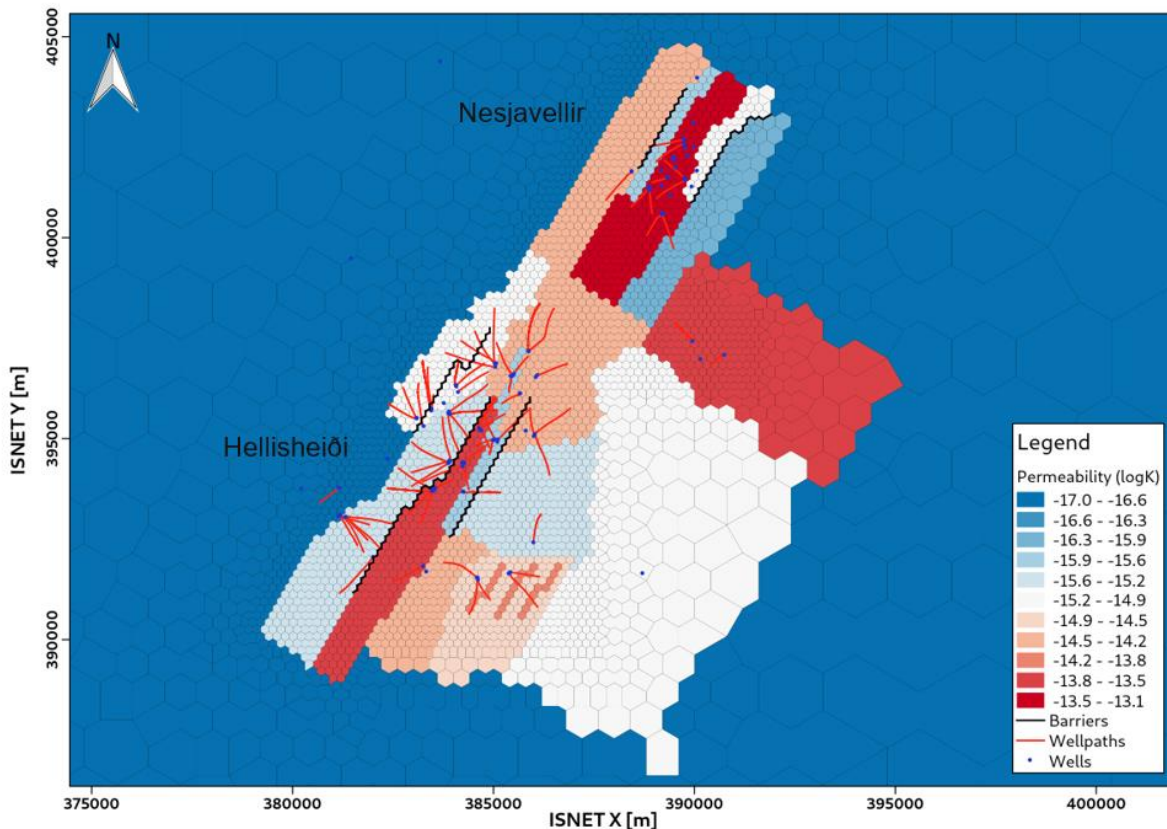
Figure 5.4.21 Geometrical averages for horizontal and vertical permeability at -1500 m b.s.l. from the recalibrated Hengill model.

Heat source modeling using CSMP++ code

In order to explore possible heat source scenarios that could form a temperature pattern similar to the one seen in the Hengill area, which would have very different implications for siting the IDDP-3 well, simplified geometric computational meshes of the system were generated.

The first step was to set up a very generalized preliminary model that could simulate magmatic intrusions. This model was 12 km in diameter and reached 8 km depth. A simplified permeability model was implemented, with only the temperature dependence being accounted for. Two homogeneous matrix permeabilities of $1*10^{-14}$ or $1*10^{-15}$ m^2 were used which would then decrease log-linearly down to $1*10^{-22}$ m^2 at the brittle-ductile transition. The chosen brittle-ductile transition was assumed to take place in the 350 to 500 °C range although a 450-650 °C temperature window might have been more appropriate for the rocks present in Hengill. Initial conditions for this model were a thermal gradient of 90 °C/km (as is common in volcanic areas in Iceland) maintained with basal heat flux of 175 mW/m^2 at the bottom, no flow boundaries at the sides and an inactive 20 °C and 1 bar top layer. A heat source was placed in this simple model in the form of a single magma body initially emplaced at 950°C. The intrusion had an elliptic shape, was 2 km wide and 1 km deep and was located in the 3-4 km depth range.

The flow patterns that formed over 10000 years, as the intrusion progressively exchanged heat with its surroundings, were examined. Simulations without intrusions and in 2D were also performed for comparison. The simulations show vastly different behaviors depending on the permeability, with the high permeability case displaying stronger convective patterns (see Figure 5.4.22). In both cases a hot plume rises and separates itself, leaving a cold downflow zone straight above the intrusion. This plume reaches the surface after 700 years in the high permeability case and 7000 years in the low permeability case. In both cases, as the simulation progresses, this plume merges in a single one. Additional convection cells and hot plumes are formed away from the intrusion, driven almost solely by the very large bottom heat flux. These secondary hot plumes only become significant in the high permeability cases. Similar conclusions were drawn when these simulations were done in 3D, the most distinctive difference being that convection was slightly stronger in 3D than 2D. From this simple study it already appears that using shallow temperature fields to target deeper intrusions might not be straightforward due to the time evolution of the hot plumes generated by these intrusions and the possible presence of secondary hot plumes.

The next step was to make the geometry of the modeling scheme more representative of the Hengill area and to avoid effects of lateral no flow boundaries that had been observed in the previous modeling scheme. The new setup was a 20x20x5 km model containing high permeability ($1*10^{-14}$ m^2) "core" with a horizontal extent of 3x15 km. The whole domain was capped with a low permeability 500 m thick caprock between a depth of -500 and -1000 m. These dimensions roughly represent the Hengill geothermal system. Figure 5.4.23 shows snapshots from simulations after 1000 years with or without a magmatic intrusion being initially
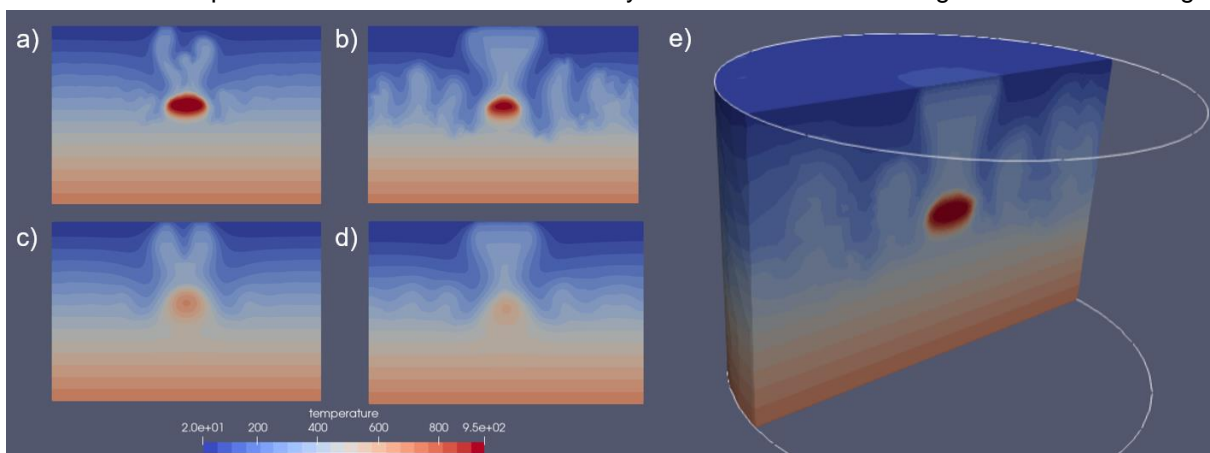

Figure 5.4.22 Simulated temperature pattern over an elliptical intrusion at 3-4 depth in the simple modeling scheme. a), b): $1*10^{-14}$ m^2 permeability case after 700 and 1500 years. c), d): $1*10^{-15}$ m^2 permeability case after 7000 and 10000 years. e): $1*10^{-14}$ m^2 permeability case after 700 years in 3D.

emplaced within the high permeability core. In the case with an intrusion, convection levels off the temperature profile with depth above the intrusion itself and the caprock causes elevated temperatures and the formation of a steam zone. This is in agreement with the behavior observed in the geothermal system in Hengill. The step seen in the temperature profile by the top of the intrusion on Figure 5.4.23 is similar to the step seen in the temperature profiles for well HE-21 presented on Figure 5.4.13. No such steam cap or temperature step are seen in the case without an intrusion. Field observations at Hengill could therefore better be explained by the proximity to a magmatic heat source. Compared to the previous simulations it appears that with this marginally different permeability structure (e.g. with a narrow high permeability core and a low permeability caprock), convection cells generated by an intrusion would be more dominant and shallow expressions of the presence of the intrusion would be more distinguishable.
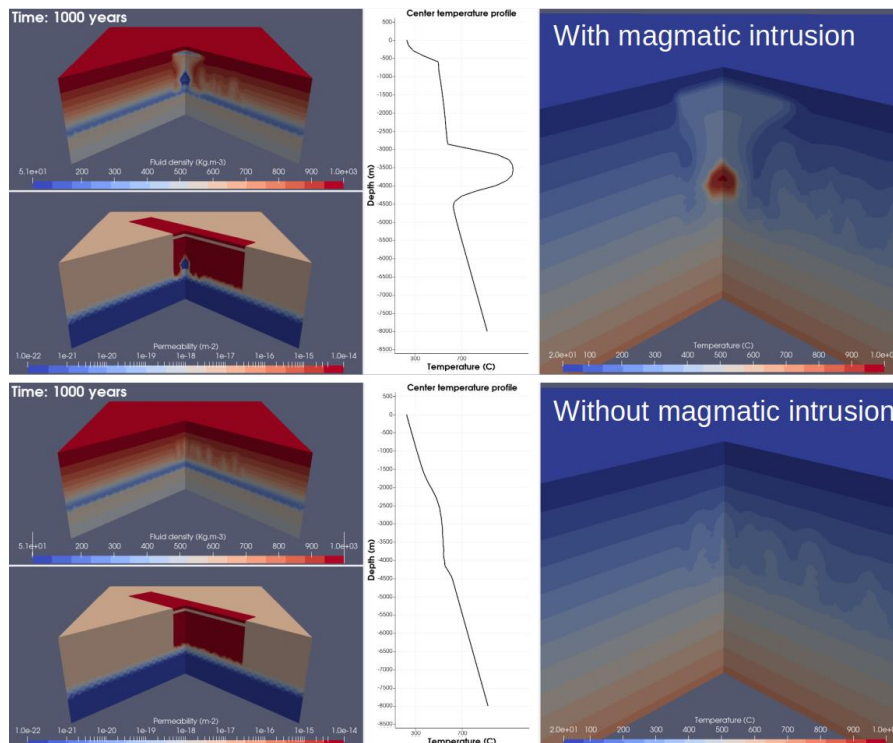
Figure 5.4.23 Reconnaissance simulation of a highly simplified representation of the Hengill area with or without a single magmatic intrusion at 3 km depth at the centre of the field, including a cap-rock.

5.4.3 Scenarios and results - Different approaches for taking the deeper parts of Hengill into account

Following recalibration and updates of the conventional field scale Hengill TOUGH2 model and simplified simulations of flow patterns around heat sources within the CSMP++ modeling scheme, attempts to combine the two could be initiated. Three approaches were taken. Firstly, to import the permeability distribution from the recalibrated field scale TOUGH2 model into a CSMP++ model and introduce heat sources underneath the system in different locations. Secondly to extract conditions from the first approach, the CSMP++ model, and implement them as new boundary conditions in the conventional TOUGH2 model. The third approach was then to deepen the conventional TOUGH2 model, change the equation of state to EOS1sc that can handle higher temperature and pressure and then make new boundary conditions at greater depth. The following chapters describe results from these different approaches.

5.4.3.1 Implementing the Hengill permeability distribution into the CSMP++ modeling scheme

The setup from the first simplified models described in chapter 0 was changed to be able to include the recalibrated permeability structure from the field scale Hengill TOUGH2 model. The aim was to get a more realistic representation of fluid flow in the model and be able to compare the results to field data. This model included the permeability distribution from the Hengill model in the top 2500 m and then a baseline permeability of $1*10^{-17}$ m^2 below that depth along with temperature dependency. Figure 5.4.25 shows how the rock types from the Hengill TOUGH2 model have been re-meshed and incorporated into the CSPM++ model. The figure shows horizontal permeabilities above $1*10^{-17}$ m^2 and therefore only the high permeability system is visible. The extents of the model are shown with a blue box (13x20 km horizontally and 5 km deep). The initial conditions are the same as for the previous models, a 90 °C/km thermal gradient, hydrostatic pressure in the permeable formation and lithostatic pressure in the impermeable parts.

Figure 5.4.25 Horizontal permeabilities above $1*10^{-17}$ m^2 in the deepened Hengill CSMP++ model.

Various intrusion configurations were then modeled in this setup. The first setup was a single cubic intrusion, 2x2x1 km^3 large, underneath the center of the system at depths comprised between 2.7 and 3.7 km. The results from the single cubic intrusion simulations showed that heat flow from a single intrusion underneath the center of the system was not sufficient to create the temperature patterns we observe in Nesjavellir, Hellisheiði and Hverahlíð, more local heat sources would be needed. This is consistent with our understanding of the heat sources in Hengill (see chapter 5.4.1.5). The next setups included two or three separate intrusions underneath the hottest parts of Nesjavellir, Hellisheiði and Hverahlíð. Both cubic and elongated intrusion setups were simulated. In Figure 5.4.24, an approximate horizontal localization for the three elongated intrusions case is shown over a temperature distribution map at 1500 m b.s. These simulations showed much more realistic flow patterns and suggested that three separate magma bodies (or possibly more), emplaced at about 3 km depth, could better explain temperature patterns at shallower depths. The permeability structure in Hengill is complex and some rock units have very high permeability anisotropy. This exerts a strong control

Figure 5.4.24 Approximate location of elongated intrusions for simulation scenarios. They are located underneath the hottest up-flows.

on the ascent and transport of hot fluids. Consequently, temperature maps with the three cubic or elongated intrusions, at -1000 m, and to a lesser measure at -2000 m, are very similar Figure 5.4.26 compares the results with field data at -1000 m.

The shape and localization of the intrusions could be refined to give a better match but this approach already provides realistic temperature distributions when compared to field data and therefore could be a useful tool to target geothermal resources below 3000 m depth. Additional direct or indirect temperature measurements
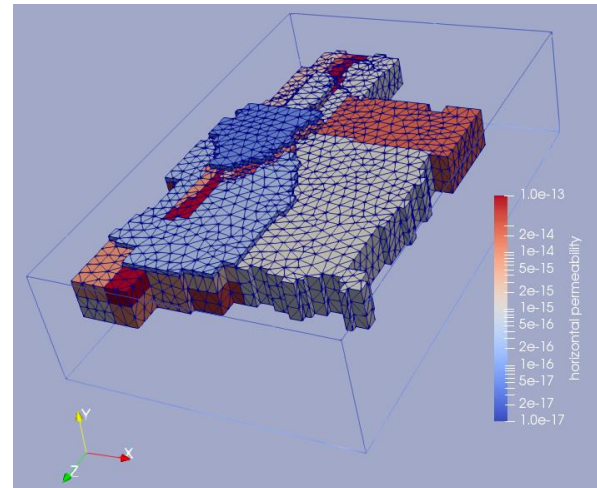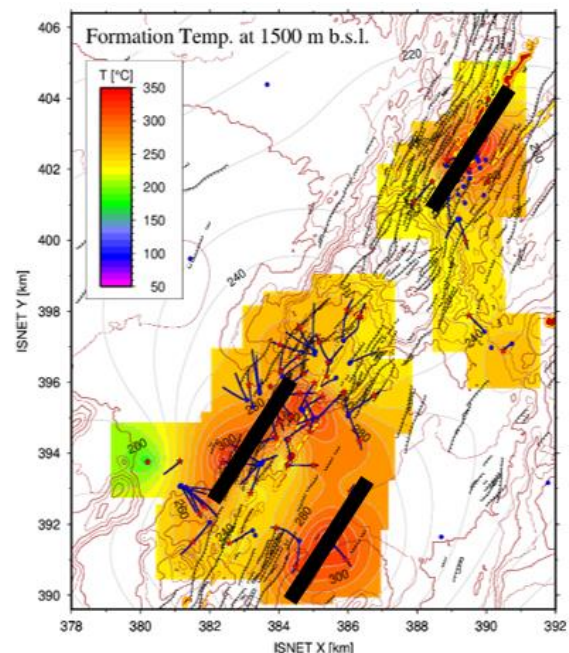
could also help improve the geometrical representation of the intrusions. The principal discrepancy with the field data is that the calculated temperatures seem to be too low, by about 50°C. This could be explained by the fact that the basal heat flux (175 mW/m^2) and the Brittle-Ductile transition temperature (350-500 °C) were too low. Other possible explanations are the fact that we neglected magmatic recharge and that fine, high permeability channels, such as faults, were not included in the the CSMP++ model.

5.4.3.2 Updating boundary conditions for conventional field scale model

The aim with the second approach was to use results from the first approach and incorporate them as updated boundary conditions in the conventional field scale model. That is, to link results from novel academic/research simulations of fluid flow from cooling intrusions with the existing conventional reservoir
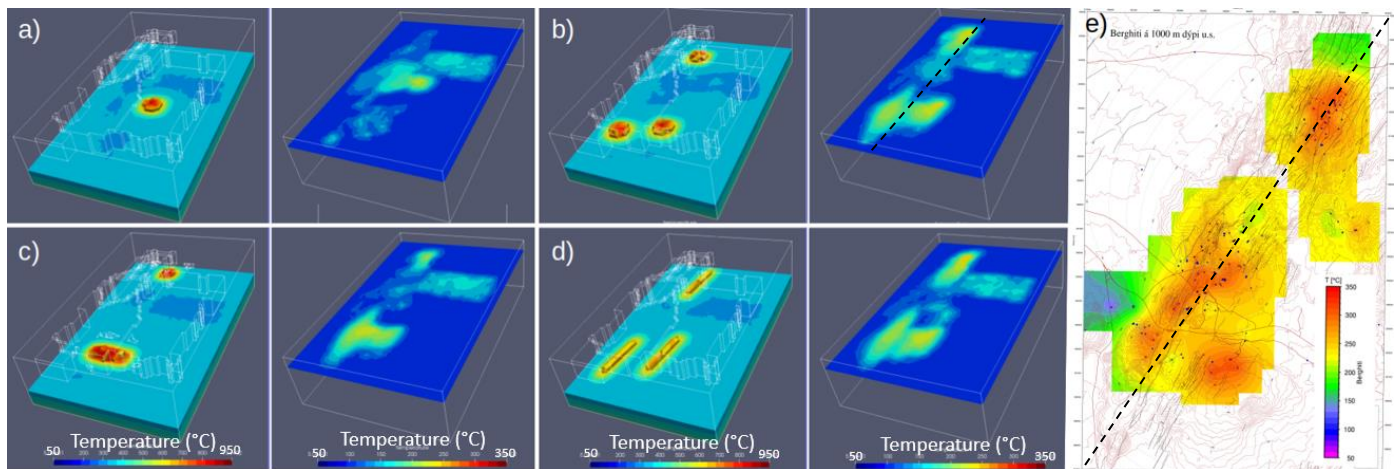
Figure 5.4.26 Vertical slices through the models after 5000 years showing computed temperature maps at -1000 m as well as the localisation of the simulated magmatic intrusions. They can be compared with field data (e).

model and thereby update the current method of injecting hot fluid into the model in the locations shown with stars on Figure 5.4.16. Plots for average values of enthalpy, temperature, vertical component of velocity and fluid density over time were extracted for an 2x2 km^2 area directly above the cubic intrusions at a depth of 2600 m. The values when the velocity was at maximum, after a simulation time of 1000 years, were chosen for exporting. These values were a velocity of $7*10^{-10}$ m/s, density of 400 kg/m^3 and enthalpy of 2500 kJ/kg (see Figure 5.4.28). To be able to introduce this as updated boundary conditions for the TOUGH2 model, average mass flow rates per element were calculated with the following equation:

$$ Q = v \cdot A \cdot \rho = 7 \cdot 10^{-10} \frac{m}{s} \cdot 34360 \, m^2 \cdot 400 \frac{kg}{m^3} = 9.62 \cdot 10^{-3} \, \frac{kg}{s} $$

Where Q is the average mass flow rate per element in kg/s, v is the vertical component of velocity, A is the area of each element in the center of the TOUGH2 model (34,360 m^2) and ρ is the fluid density. These calculations give an average mass flow rate of $9.62*10^{-3}$ kg/s or roughly 0.01 kg/s into each element. This mass flow rate along with an enthalpy of 2500 kJ/kg was introduced as inflow into each element within areas underneath four prominent high temperature anomalies that can be seen in the Hengill area. One in Nesjavellir, one in Hellisheiði, one in Hverahlíð, and one in Bitra, SE of Nesjavellir. These areas can be seen in Figure 5.4.27. The combined number of elements chosen was 400. The inflow was defined as inflow into layer J, the second deepest layer, and therefore represents flux from the bottom layer into the geothermal system.
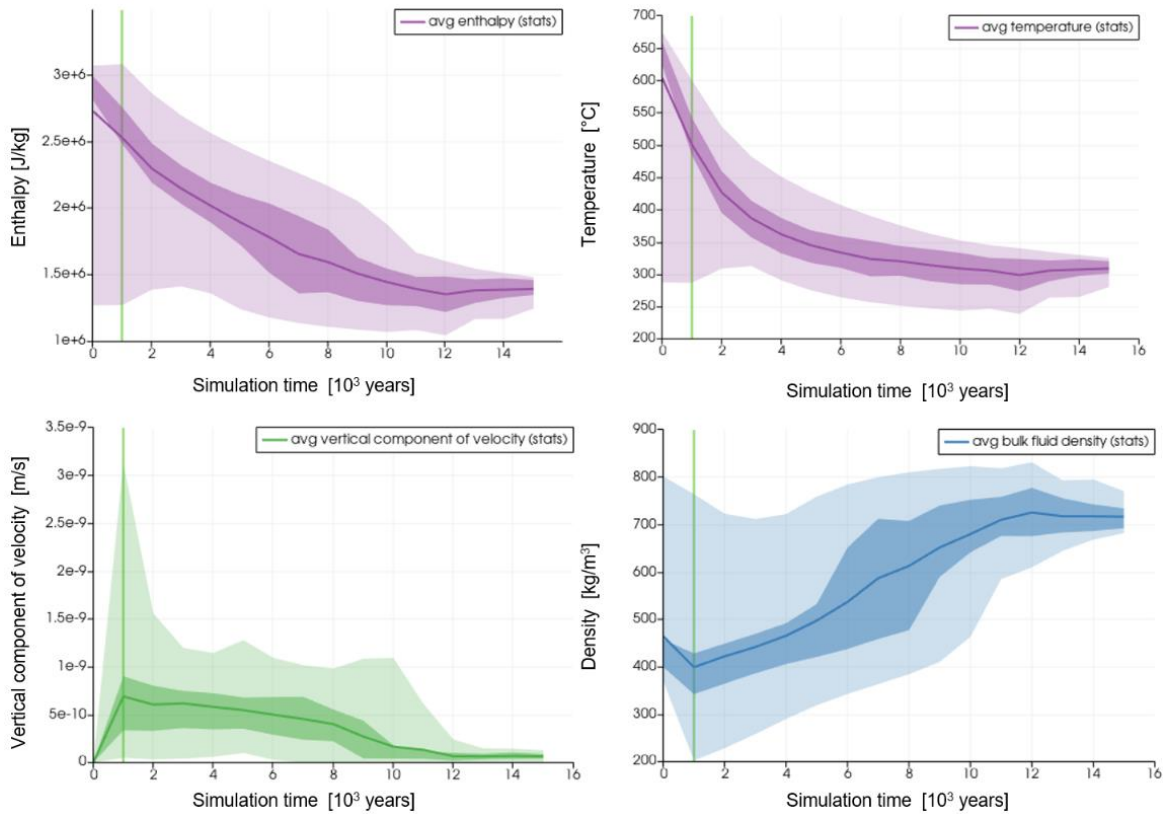
Figure 5.4.28 Plots for average values of enthalpy, temperature, vertical component of velocity and fluid density over time extracted over an 2x2 km² area directly above the cubic intrusions at a depth of 2600 m. The green line indicates a simulation time of 1000 years when the vertical component of velocity was at a maximum.
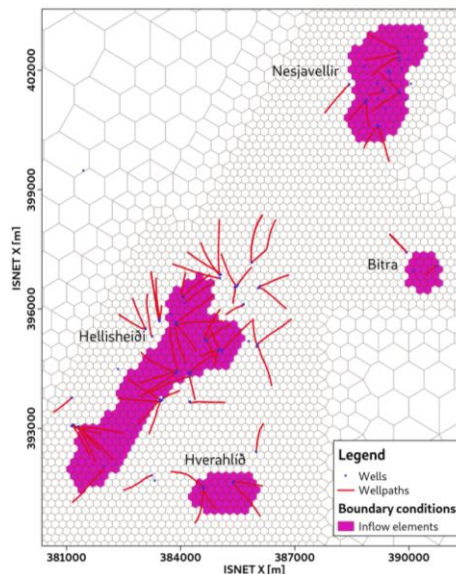

Figure 5.4.27 Location of elements where inflow is defined. The flow into each element is based on results from the CSMP++

In the Hengill TOUGH2 reservoir model the combined inflow of hot fluid into the sources defined in layer J (shown with stars on Figure 5.4.16) is 225 kg/s and the average enthalpy of the fluid is 1,506 kJ/kg. This corresponds to a total injected power of 339 MW. The flow into the second deepest layer when taking the boundary conditions from the CSMP++ model is 3.9 kg/s and the enthalpy is 2,500 kJ/kg. This corresponds to a total injected power of 9.8 MW.

A comparison between all simulated and measured formation temperature and pressure values using the updated boundary conditions from the CSMP++ model is shown on Figure 5.4.30 along with a line that would
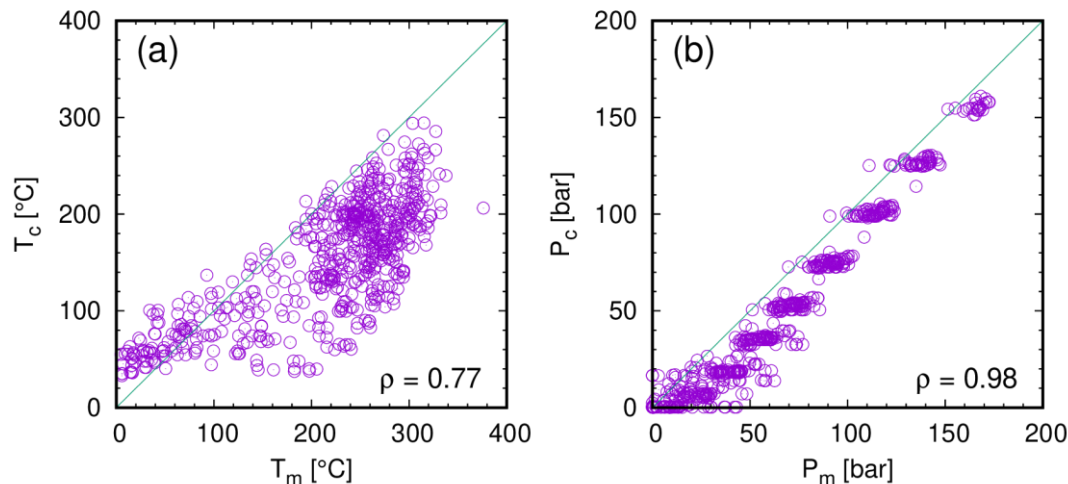
Figure 5.4.30 Comparison between measured (T_m and P_m) and calculated (T_c and P_c) formation temperature (a) and pressure (b) for all wells using the CSMP++ bottom boundary condition along with a calculated correlation coefficient (ρ).
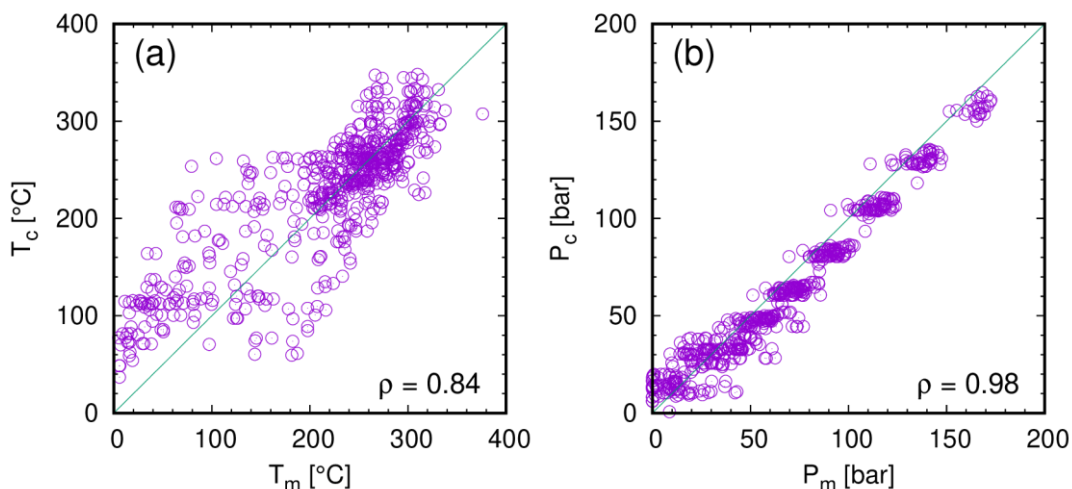

Figure 5.4.29 Comparison between measured (T_m and P_m) and calculated (T_c and P_c) formation temperature (a) and pressure (b) for all wells with the 10x the updated boundary conditions from the CSMP++ model along with a calculated correlation coefficient (ρ).

represent a perfect fit. As can be seen both the temperature and pressure are too low. This figure shows that this inflow did not result in high enough temperatures reaching the shallower system. The calculated drawdown in the monitoring wells was also too high and the simulations did not manage to get through the whole production history. To try to get a better match, the inflow from the CSMP++ model was increased in steps and the results compared to the original model. A reasonable fit was obtained when the inflow was increased by an order of magnitude, injecting a total of 39 kg/s into the system. The enthalpy was maintained at 2,500 kJ/kg. The measured and calculated values of pressure and temperature are compared in Figure 5.4.29.

The pressure values are slightly higher than in the previous simulation and the temperature values look much better. The calculated pressure drawdown in monitoring wells is still slightly higher than in the original model. The simulation, however, managed to get through the whole production history.

At the time of writing we realized that using the upflow properties from the CSMP++ model across a plane located at -2500 m rather than at -2600 m would likely provide a much better fit without requiring a tenfold increase of the mass flow rate. This is because the plane located at -2600 m is in close vicinity of the intrusions and at a temperature of 500°C (after 1000 years) this leads to very low permeability and velocities. At -2500 m, which is closer to the actual lower boundary of the TOUGH2 model, the average upflow velocity in the CSMP++ model is 10^{-8} m/s, the density 700 kg/m^3 and the enthalpy 1500 kJ/kg.

In Figure 5.4.31 the temperature results from the simulations using the CSMP++ boundary condition (both direct and with tenfold flow) are compared to the results from the original TOUGH2 field scale model. The distribution of temperature deviation is plotted. The simulation where the CSMP++ boundary conditions are used directly gives obviously too low temperature values. The temperature values obtained when increasing the inflow by an order of magnitude are very comparable to the results from the original TOUGH2 model. The total inflow is then 39 kg/s of fluid with enthalpy of 2500 kJ/kg, which corresponds to the total injected power of 98 MW. That fluid flow is 17% of the flow injected in the TOUGH2 model (which is 225 kg/s) and the power is 29% of the original TOUGH2 model (which is 339 MW). Despite these large differences the model results with this setup are very comparable to the original model with regards to temperature, pressure, and drawdown.
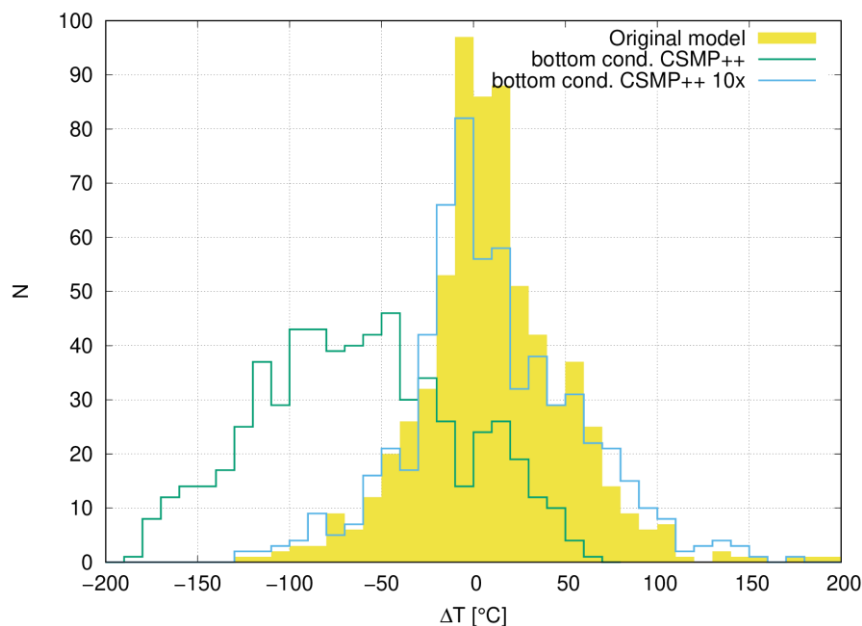

Figure 5.4.31 The distribution of temperature deviation, $\Delta T=T_c-T_m$, where T_c and T_m are calculated and measured temperatures respectively of different modeling approaches compared. The yellow area shows the temperature deviation of the Hengill field scale model, the green line shows the deviation if the boundary conditions are taken from the CSMP++ model and the blue line is for flow 10x that of the CSMP++ model.

5.4.3.3 TOUGH2 EOS1sc and field scale model deepening

The standard EOS1 module in TOUGH2 only handles temperatures up to 350°C. The third approach taken in this project to include heat sources in a simulation model of the Hengill Area revolved around updating the model to a new equation of state, EOS1sc (described by Magnúsdóttir and Finsterle, 2015), deepening the model and placing heat sources at greater depths in stead of injecting heat at shallower depths. As previously mentioned, the EOS1sc module extends the operational range of conditions to including supercritical conditions (Magnúsdóttir and Finsterle, 2015).

Three 500 m thick layers were added to the model, increasing the depth range to -4000 m b.s.l. (Figure 5.4.32). The rock type distribution from the shallower model was maintained for layers A-J but for layers K-N, a new rock type distribution was implemented. As discussed in previous chapters, there is high uncertainty in the location, shape, and size of heat sources in the Hengill area. To form a high temperature geothermal system three things are needed: a heat source, abundant water, and sufficient permeability. Due to the high uncertainty in the characteristics of the greater depths in Hengill, various setups for the combination of heat sources and permeability distribution were tried. Two setups will be presented here; heat sources in the bottom layer and upwelling heat sources that reach shallower depths. The aim with this deepened TOUGH2 model is to be able to use it to simulate the production history and different production scenarios.

Figure 5.4.32 Layering in the current field scale model (left) and in the deepened model (right) where three 500 m thick layers have been added.

Simulations of production history always require the model to be in equilibrium at the start of the production history to be able to see which changes can be attributed to the utilization. Therefore, the aim with the following simulations was also to get a stable system first.
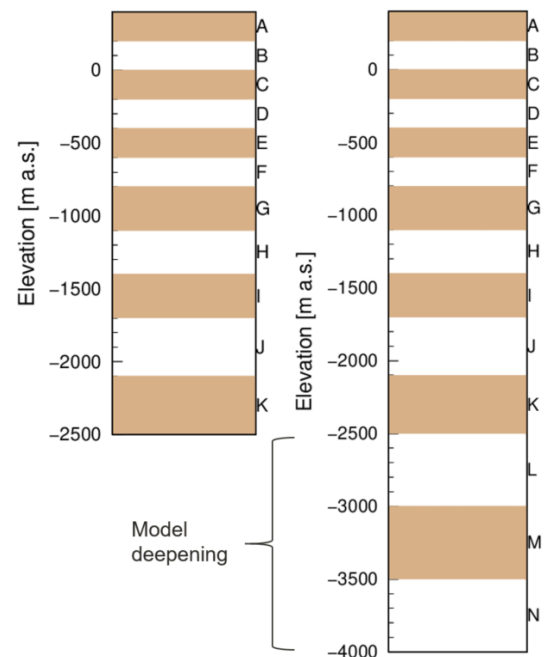
Heat sources in bottom layer and permeable canals

In the first setup we placed four heat sources in the bottom layer (-3500 to -4000 m a.s.l.). We placed them underneath four prominent high temperature anomalies that can be seen in the area. One in Nesjavellir, one in Hellisheiði, one in Hverahlíð and one in Bitra, SE of Nesjavellir. These heat sources can be considered to represent networks of solidified intrusions rather than a large-scale molten body of magma. Above the heat sources we placed canals that could be given higher permeability (magenta colored elements in Figure 5.4.33 represent the heat sources/canals). They are then located within a less permeable rock type that has depth dependent permeability and is located underneath the permeable geothermal system rock types in the shallower system (green colored elements in Figure 5.4.33). The depth dependent permeability for layers K to M was calculated using the formulation from Manning and Ingebritsen (1999):

$$\log k = -14 - 3.2 \log z$$

where k is permeability in m^2 and z is depth in km. The base number for this relationship, -14, was allowed to change during the calibration as local scale permeability in tectonically active crust, such the Icelandic one, can entail permeabilities much higher than suggested by this mean k-z relation. Ingebritsen and Manning (2010) presented a relationship as high as $\log k = -11.5 - 3.2 \log z$.

Figure 5.4.33 Rock type distribution in the deeper layers.

Assuming a brittle/ductile transition (BDT) temperature of 550 °C ± 100 °C (Violay et al. 2010) for Icelandic crust, no temperature dependence was applied for the permeability as the temperatures within these rock types does not exceed the assumed BDT. The bottom layer was given a permeability of $1*10^{-20}$ m^2. The initial conditions in the bottom layer were generally set as 420 °C, based on a 100 °C/km thermal gradient, and a pressure of roughly 300 bars. The exception was the elements within the heat sources. The temperature within these elements was first set to 550 °C but the pressure and temperature were then adjusted in the calibration process as well as the vertical and horizontal permeability in the deep rock types. As in the shallower model, the top layer was fixed at 15 °C and 1 bar. To obtain initial conditions for the whole system before production started, steady state runs were performed where these heat sources drive the system until it reaches pseudo-equilibrium. Reaching equilibrium for this model was not as straight forward as for the shallower system as there is more instability in calculations with higher temperatures and pressures. Generally, the model was run for 12,000 years before production was started. After that time, changes in temperature and pressure were considered minimal. The best results for this setup were obtained with a temperature of 800 °C for the heat sources, a pressure of 310 bars in the bottom layer, a base number of -13 for the depth dependence of the horizontal permeability, a base number of -14 for the vertical permeability and a canal permeability of $4.2*10^{-15}$ m^2 in the horizontal direction and $4.2*10^{-16}$ m^2 in the vertical direction. A snapshot of pseudo-equilibrium temperature conditions at 3600 m b.s.l. and in a vertical slice that extends through the heat sources underneath Hellisheiði and Nesjavellir is shown in Figure 5.4.35. It is apparent how separate convective cells form above the 800°C heat sources and lead hot fluid up and into the permeable geothermal system above them.

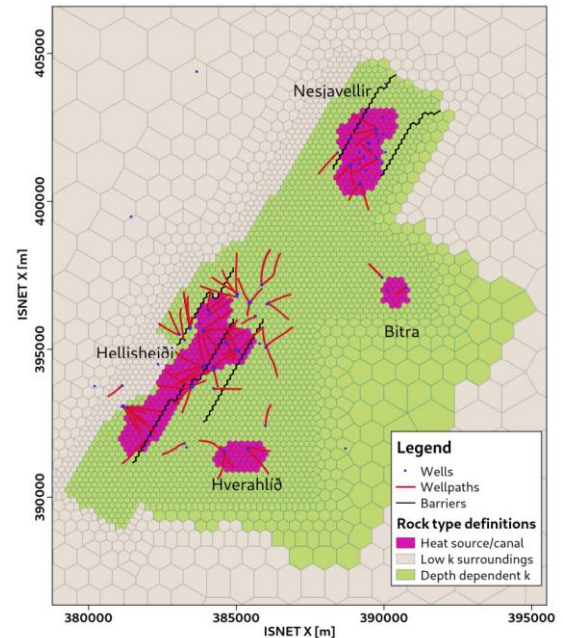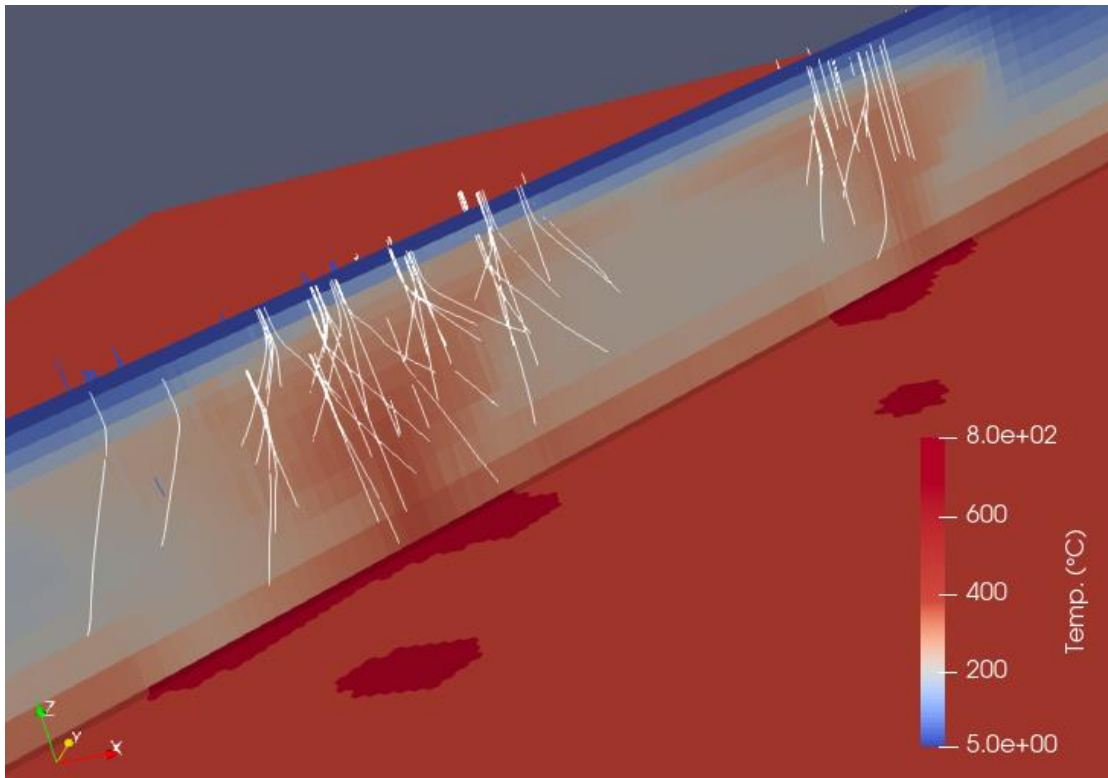**Figure 5.4.35 Snapshot of pseudo-equilibrium temperature conditions at 3600 m b.s.l. and in a vertical slice that extends through the heat sources underneath Hellisheiði and Nesjavellir for a model with heat sources in the bottom layer and permeable canals above them. Production wells are shown with white traces and reinjection wells with blue traces.**

Comparison between measured and calculated initial pressure and temperature conditions in all wells using this setup is shown on Figure 5.4.34. The fit is comparable to the fit for the shallower model (Figure 5.4.17) and the calculated drawdown in monitoring wells is also comparable.
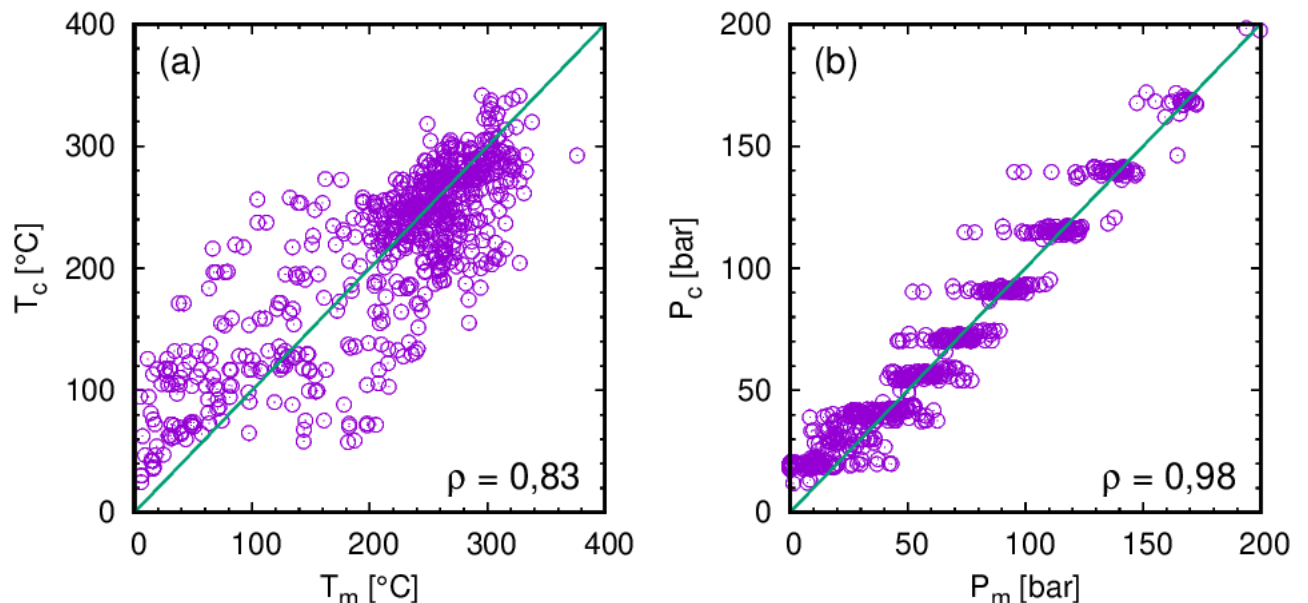

Figure 5.4.34 Comparison between measured (T_m and P_m) and calculated (T_c and P_c) formation temperature (a) and pressure (b) for all wells with heat sources in the bottom layer along with a calculated correlation coefficient (ρ).

This means that the top ~2500 m of the Hengill high temperature geothermal system can also be quite well reproduced with this method. None of the TOUGH2 model methods presented above are, however, able to represent very local high temperature anomalies such as the one in well NJ-11 (Figure 5.4.13). The temperature values at stable conditions in the layer above the heat sources, layer M, in the deep model presented above only reach about 365°C. Shallower heat sources are likely the explanation for such local anomalies.

Upwelling heat sources underneath hottest zones

The previous approach with heat sources in the bottom and permeable canals above them was able to represent the shallower system as we know it quite well but wasn´t able to capture local high temperature anomalies. This third approach attempts to get higher temperatures to shallower depths in areas where local high temperature anomalies are known, such as in Nesjavellir and Hverahlíð. Figure 5.4.36 shows a map of the rock type distribution in the deeper layers with this setup. The heat source underneath Bitra is only in the deepest layer, the heat source underneath Hellisheiði extends up into layer M or to a depth of 3000 m b.s., The heat source underneath Bitra is only in the deepest layer, the heat source underneath Hellisheiði extends up into layer M or to a depth of 3000 m b.s.l., the heat source underneath Hverahlíð extends up into layer L or to a depth of 2500 m b.s.l. and the heat source underneath Nesjavellir reaches all the way up into layer J in the northern side or to a depth of 1700 m b.s.l. The permeability in the bottom layer was maintained at $1*10^{-20}$ m^2. The area surrounding the heat sources, underneath the permeable shallower system, was given depth dependent permeability as in the previous approach. The temperature in the heat source rock types was set at 800°C in layer N, 500°C in layer M, 450°C in layer L, 400°C in layer K and 380 in layer J. The temperature

Figure 5.4.36 Heat source and other rock type distribution in the deeper layers.

within the intrusions was maintained stable by given the rock types high density. Multiple runs were simulated with different values for horizontal and vertical permeability in both the heat source rock types and in the surrounding formation. The values that were able to represent the shallower system in the best way were intrusion permeability of $1*10^{-17}$ m^2 and a base number of -13 for the depth dependance of both the horizontal and vertical permeability in the surrounding formation.
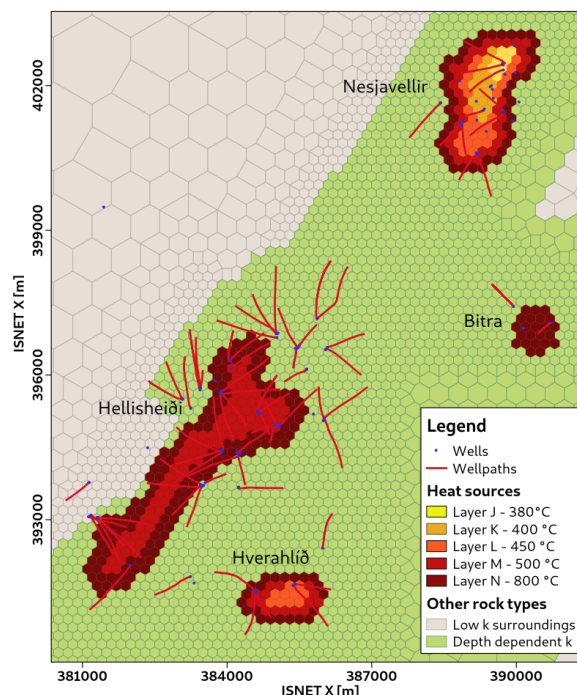
A snapshot of pseudo-equilibrium temperature conditions at 3600 m b.s.l. and in a vertical slice that extends through the heat sources underneath Hellisheiði and Nesjavellir for this approach is shown in Figure 5.4.38. Comparing the temperature pattern seen there with the temperature pattern in Figure 5.4.35 shows that with this setup, higher temperatures are maintained at shallower depths as opposed to the convection within the permeable canal leveling out temperature conditions all the way from the bottom. A comparison between measured and calculated initial pressure and temperature conditions in all wells using this setup is shown on Figure 5.4.37. The fit is slightly better than for the previous approach with heat sources in the bottom layer. The calculated drawdown in monitoring wells from these two approaches is comparable. This means that the top ~2500 m of the Hengill high temperature geothermal system can also be reasonably well reproduced with this method, placing low permeability heat sources in the bottom layer and allowing them to reach shallower depths underneath the hottest areas. This means that the top ~2500 m of the Hengill high temperature geothermal system can also be reasonably well reproduced with this method, placing low permeability heat sources in the bottom layer, and allowing them to reach shallower depths underneath the hottest areas. Because this method brings higher temperature to shallower depths, as we know to be the case in the area, we assume that it represents the system in a more realistic way than only placing heat sources in the bottom layer.
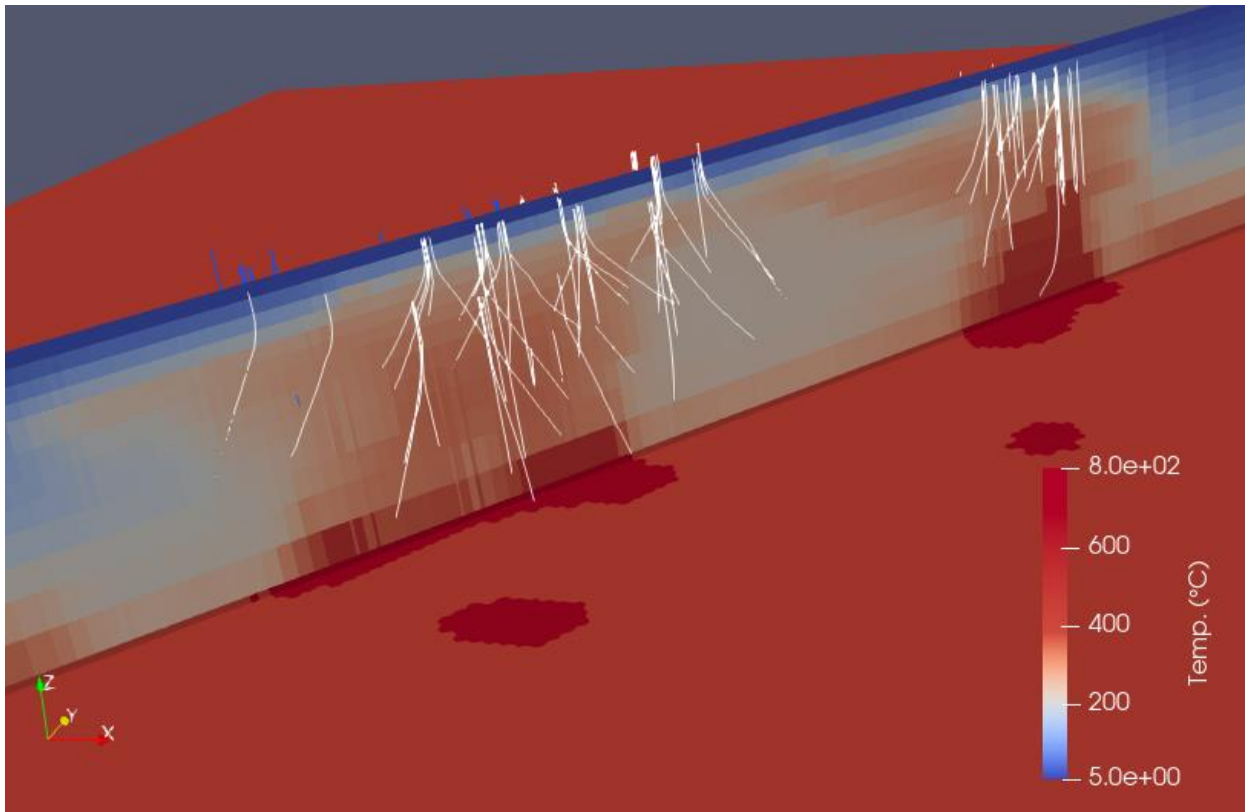
Figure 5.4.38 Snapshot of pseudo-equilibrium temperature conditions at 3600 m b.s.l. and in a vertical slice that extends through the heat sources underneath Hellisheiði and Nesjavellir for a model with upwelling heat sources from the bottom layer and depth dependent permeability around them. Production wells are shown with white traces and reinjection wells with blue traces.
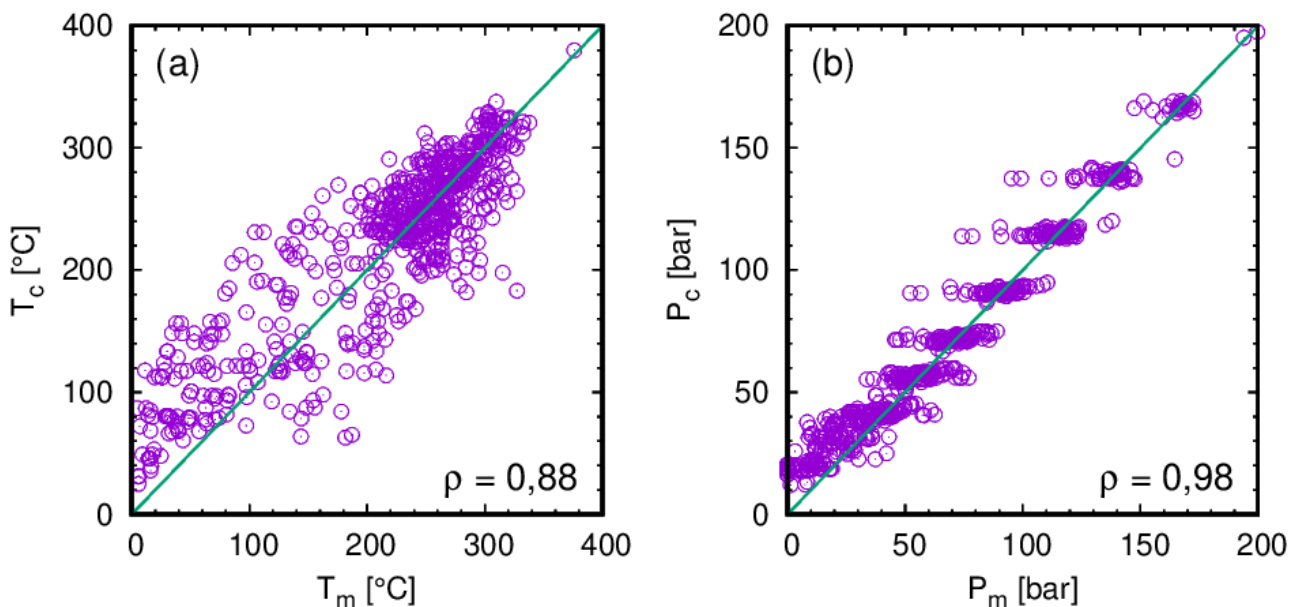

Figure 5.4.37 Comparison between measured (T_m and P_m) and calculated (T_c and P_c) formation temperature (a) and pressure (b) for all wells with the upwelling heat source approach along with a calculated correlation coefficient (ρ).

5.4.3.4 Utilization scenarios

The approach with upwelling intrusions was used to exemplify how the model can be used for utilization scenario simulations.

In these simulations, the pseudo-stable conditions shown in Figure 5.4.38 were used as a starting point. The temperature of the upwelling heat sources had been maintained stable by having those rock types with high density. In these simulations, the density of the heat source rock types was changed to the normal value of 2650 kg/m^3 to allow the temperature to change over the production history simulation time. A hypothetical deep well was chosen a location next to well NJ-11 in Nesjavellir (see location with a red star on Figure 5.4.39). That well has shown the highest temperature seen in the Hengill area. Firstly, the hypothetical well was used for injection of 100 l/s of 80 °C hot fluid. A temperature of 80 °C is representative of temperature of separated water in Nesjavellir. The injection was introduced from the start of the simulation time in 1970 and compared to a case of no injection. The injection itself was modeled in the same way as in the shallower model, by injecting fluid into a chosen element as the wells themselves are not modeled in the standard TOUGH2 modeling scheme. The injection element was placed in layer K, at a depth of -2100 to -2500 m a.s.l. To simulate the well hypothetically intersecting a more permeable fracture zone, connections in the SW-NE direction between the heat source elements in layers J, K and L were given a permeability of $1*10^{-14}$ m^2 instead of the heat source permeability of $1*10^{-17}$ m^2. This approach prevented excessive pressure buildup in the injection element that occurred without increasing the permeability. Figure 5.4.40 shows the simulated development of pressure and temperature in the injection element. The pressure increases from about 187 bars in the beginning of the simulation time to a maximum of 292 bars after about 30 years. The temperature starts decreasing from 400 °C immediately and after 12 years the temperature in the element has stabilized at 80 °C. Figure 5.4.40 shows how the temperature in the surrounding elements evolves with time. A cooling front advances in all directions with time. This injection decreases drawdown in the shallower system and by that also decreases enthalpy from the wells. The pressure is up to 2.5 bars higher in monitoring wells by the end of the simulation using injection than without it.
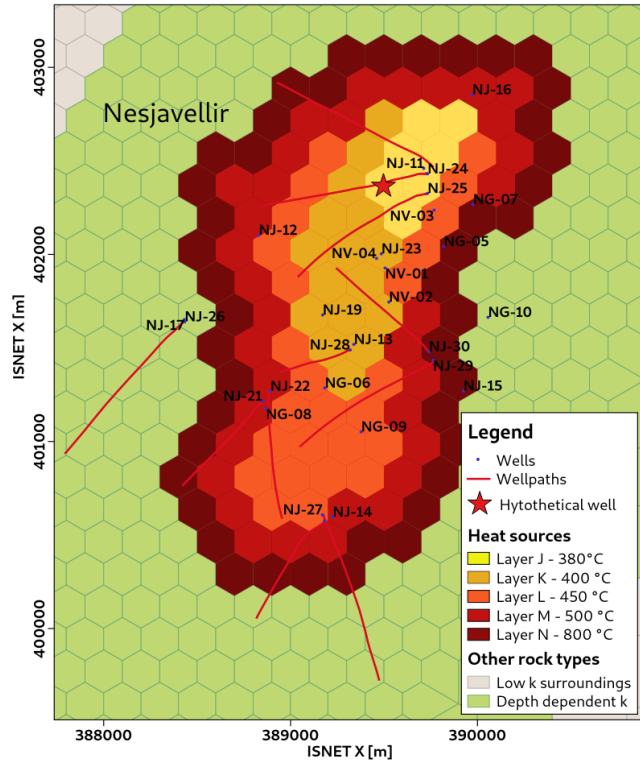

Figure 5.4.39 Heat source and other rock type distribution in the deeper layers in Nesjavellir as well as the location of a hypothetical deep well.
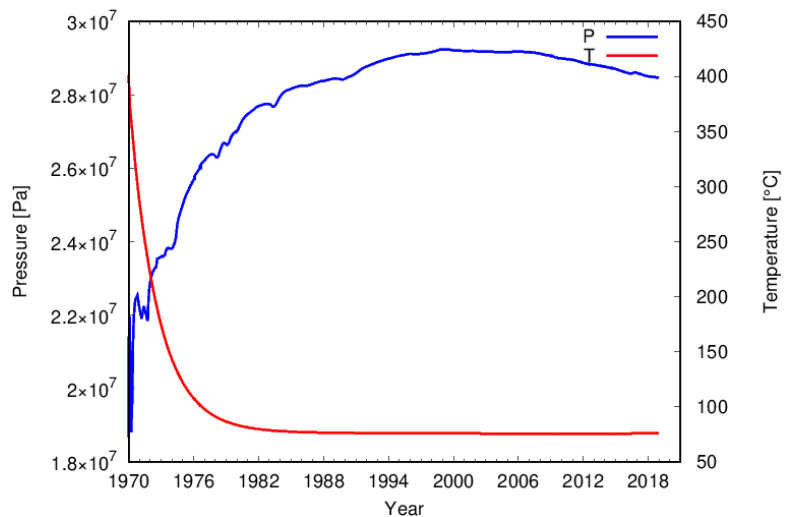

Figure 5.4.40 Pressure and temperature development in the injection element resulting from a 100 l/s injection of 80 °C warm water.
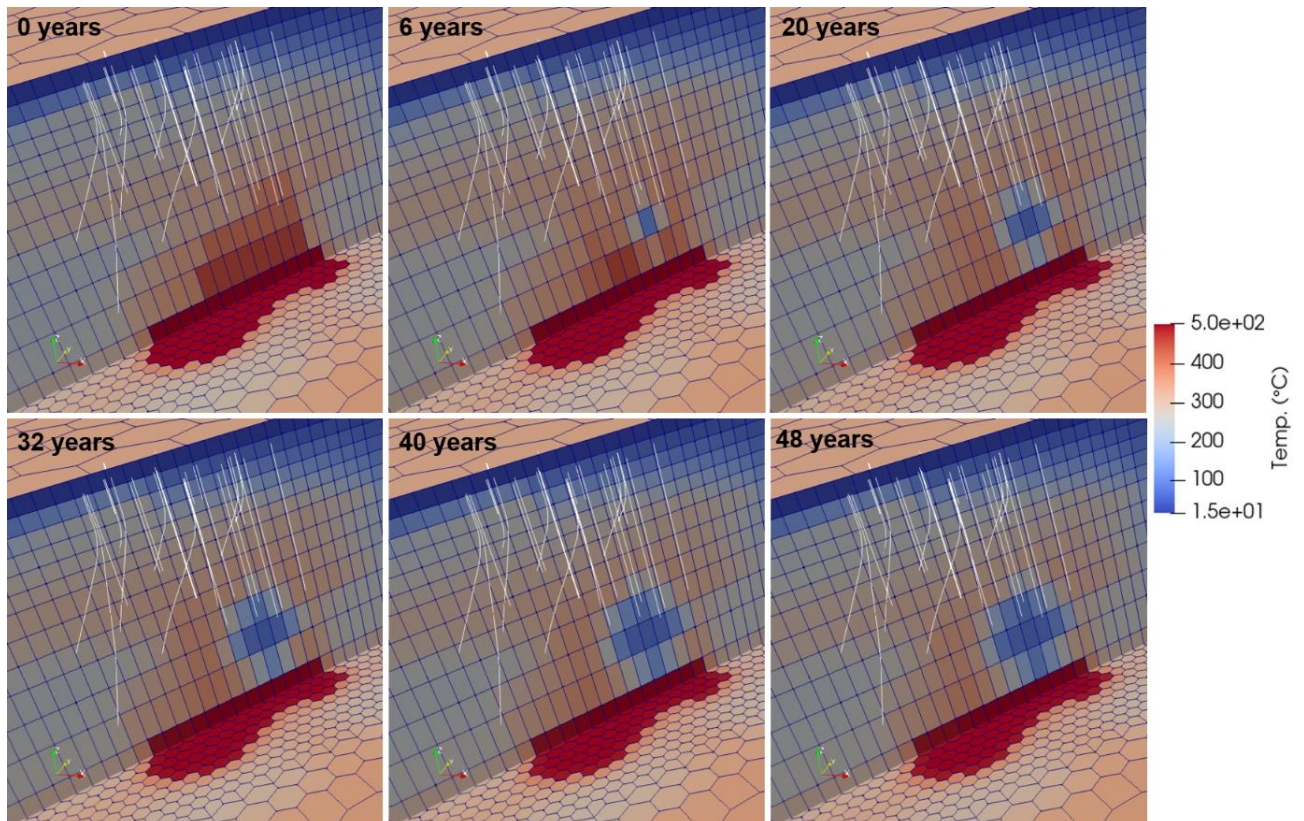
Figure 5.4.41 Evolution of temperature with time in a SW-NE cross section through the injection element and at a depth of 3250 m b.s.l.

Following the injection scenario, production scenarios were simulated. The element used for injection before was now defined as a production element. Two different methods were used to simulate the production. Firstly, a 20 kg/s sink was defined for the element and the pressure and temperature within the element monitored with time. Figure 5.4.42 shows the evolution of pressure and temperature for this method. The temperature drops from 400 °C down to about 355 °C in 8 years. The pressure fluctuates more. It starts with an immediate drop from about 185 bars down to 175 bars. From 1973 the pressure increases but from about 1984 it starts decreasing again with minor fluctuations.

The other method for simulating production from the element was to simulate a well that operates on deliverability against a prescribed flowing bottomhole pressure. The bottomhole pressure value was chosen to be 100 bars. To use this option in TOUGH2, a productivity index needs to be chosen as well. We chose a value of $8*10^{-13}$ m^3 to get an initial flow of about 20 kg/s according to the formulation given in Pruess, Oldenburg and Moridis (2012).
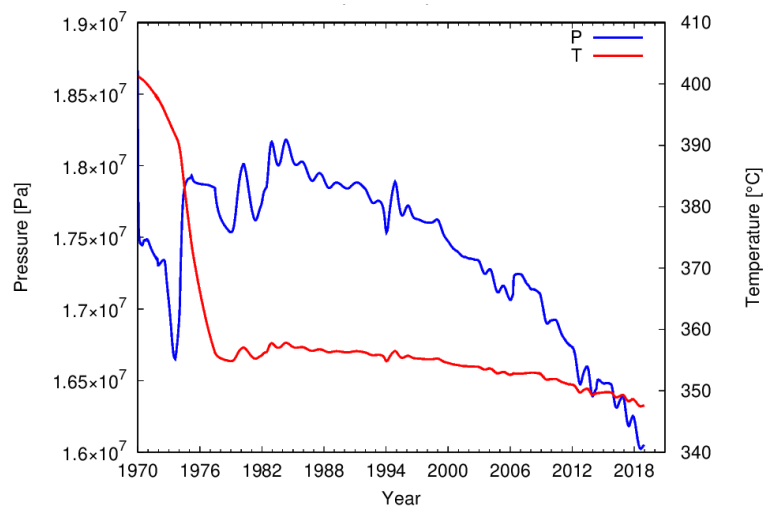

Figure 5.4.42 Pressure and temperature development in the production element resulting from 20 l/s production.

Figure 5.4.43 shows the development of production rate, enthalpy, and electrical power from the well when production occurs against a bottomhole pressure of 100 bars. The initial production rate is about 20 kg/s and the initial enthalpy is 2900 kJ/kg. The enthalpy drops with production and with that the production rate increases as a greater proportion of the flow is in liquid form. The initial electrical power output from the well calculated based on the setup of the Nesjavellir Power Plant is roughly 20 MW. It increases to over 26 MW in the first years. The well maintains an electrical output of over 20 MW for 34 years with this setup. For comparison an average well is about 5.5 MW, so this would be a powerful well.
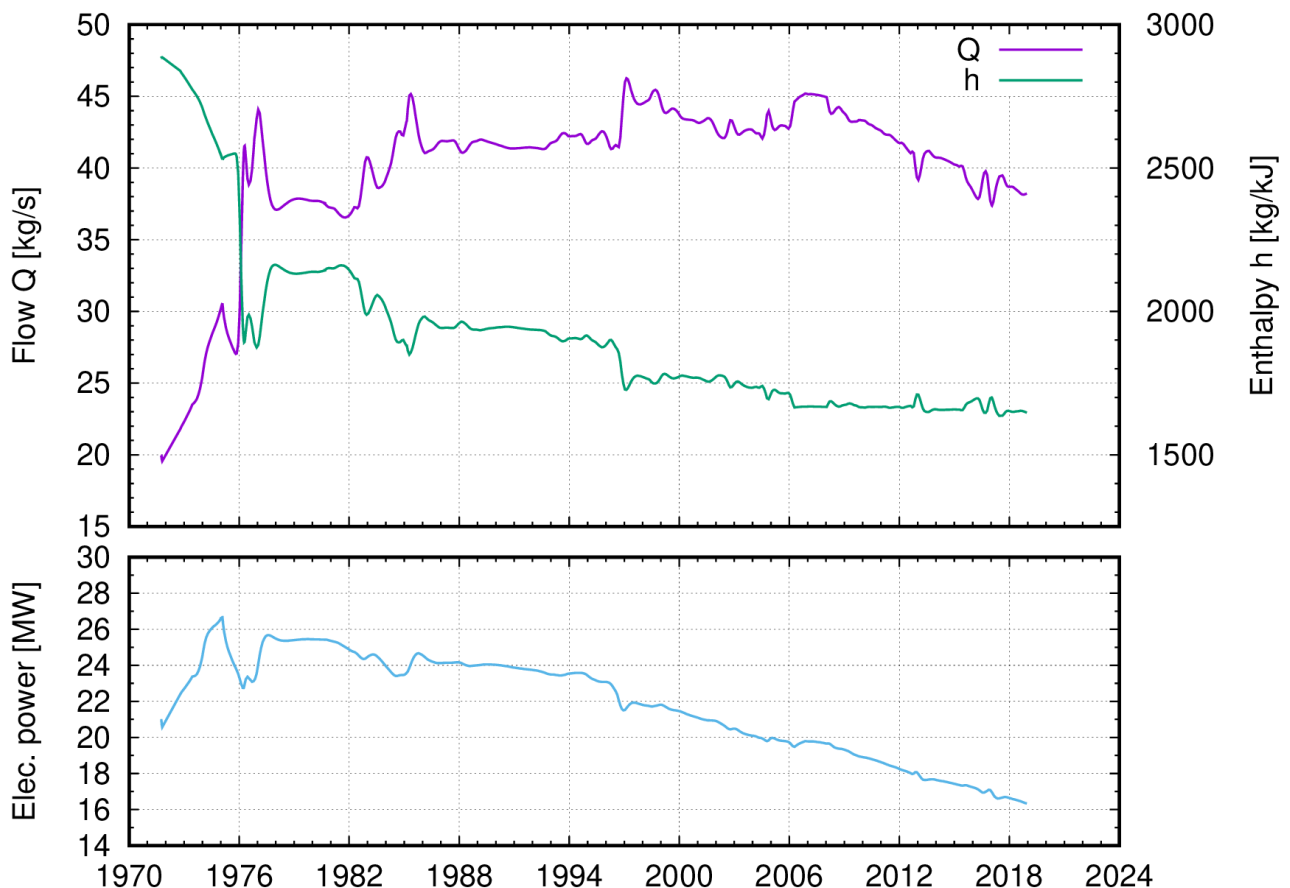

Figure 5.4.43 Production rate (Q), enthalpy (h) and electrical power development resulting from production against a 100 bar bottomhole pressure (top).

5.4.4 Analysis and discussion

The previous chapters have described the general features of the Hengill high temperature geothermal area in Iceland, the industrial TOUGH2 reservoir model of the area and its limitations, heat source modeling with the CSMP++ code and different approaches for combining the two and including heat sources in the field scale model. The aim was to prepare for deeper drilling in the area and have modeling tools that can represent conditions in the greater depths. The overall results show that the shallower geothermal system can be quite well represented with multiple configurations of boundary conditions and the deeper levels. The methods presented were injecting small amounts of hot fluid at -1900 m a.s.l. above a low permeability bottom layer with temperature conditions based on extrapolated temperature profiles, implementing the Hengill permeability distribution into a CSMP++ modeling scheme with heat sources, changing boundary conditions in the TOUGH2 model to an inflow extracted from the CSMP++ model, a deepened TOUGH2 model with four 800°C heat sources at -3500 m b.s.l. and permeable canals that allow fluid transportation above them and a deepened TOUGH2 model with heat sources in the bottom layer that are allowed to reach shallower depths underneath the hottest areas.

The fact that different approaches can give very similar representation of the shallower system is an interesting finding. This emphasizes that there is still a lot unknown about heat sources in the Hengill area or in many other volcanic geothermal systems. The puzzle will likely never be completely solved until a deeper well is drilled.

The field-scale approach presented here does not take mechanical effects into account and fractures are not specifically accounted for. These are fundamental aspects of permeability and by that production properties. This approach also does not include detailed representation of the wells themselves. ETH is developing specific well models for high temperature environments. Those models will be of great importance for understanding near well dynamics.

It is important to have developed a modeling scheme that includes the greater depths and hotter formations and can be used to simulate deeper utilization. This modeling scheme can and will be developed further with increasing knowledge on the deeper parts of the systems and further development in process and well modeling. The modeling scheme presented includes many simplifications. The aim should be to improve those methods, i.e., making them more accurate, without compromising the use of the model for industrial purposes.

This study is an attempt to bridge the gap between "quick-and-dirty" industrial field-scale modeling schemes and state-of-the-art academic simulations tools. We need to have field scale tools that can deliver results in a fast and reliable way. To reach that goal, a lot of bold simplifications are made to represent the detailed processes in the system. However, in order to justify the simplifications and analyse and estimate how accurate they are, more detailed models such as the ETHZ models are necessary. A modeling scheme connecting those approaches is therefore very important for the geothermal industry. Especially when we are aiming for exploring greater depths where the conditions are not well known.

5.4.5 Potential issues related to IP

No issues have been identified.

5.4.6 References

Árnason, K., Karlsdóttir, R., Eysteinsson, H., Flovenz, Ó.G. and Gudlaugsson, S.Th. (2000). The Resistivity Structure of High-Temperature Geothermal Systems in Iceland. In *Proceedings World Geothermal Congress 2000.* Kyushu-Tohoku, Japan. Available at: https://www.geothermal-energy.org/pdf/IGAstandard/WGC/2000/R0416.PDF [2018-11-20]

Árnason, K., Eysteinsson, H., Hersir, P.G. (2010). Joint 1D inversion of TEM and MT data and 3D inversion of MT data in the Hengill area, SW Iceland. *Geothermics,* vol. 39, pp. 13-34.

Björnsson, G., Hjartarson, Á., Bodvarsson, G. and Steingrímsson, B. (2003). Development of a 3-D Geothermal Reservoir Model for the Greater Hengill Volcano in SW-Iceland. In *Proceedings TOUGH Symposium 2003.* Berkley, California.

Coumou D., Matthäi S.K., Geiger S. and Driesner T. (2008a). A parallel FE–FV scheme to solve fluid flow in complex geologic media. *Computers & Geosciences,* vol.34, pp.1697-1707.

Coumou D., Driesner T. and Heinrich C. A. (2008b). The structure and dynamics of mid-ocean ridge hydrothermal systems. *Science,* vol. 321, pp.1825-1828.

Coumou D., Driesner T., Geiger S., Paluszny A., and Heinrich C. A. (2009). High-resolution three-dimensional simulations of mid-ocean ridge hydrothermal systems. *Journal of Geophysical Research – Solid Earth,* vol. 114(B7).

Elders, A. and Friðleifsson, G.Ó. (2010). The Science Program of the Iceland Deep Drilling Project (IDDP): a Study of Supercritical Geothermal Resources. In *Proceedings World Geothermal Congress 2010.* Bali, Indonesia.

Feigl, K.L., Gasperi, J. Sigmundsson, F. and Rigo, A. (2000). Crustal deformation near Hengill volcano, Iceland 1993-1998: Coupling between magmatic activity and faulting inferred from elastic modeling of satellite radar interferograms. *Journal of Geophysical Research,* vol. 105(B11), pp. 25,655-25,670.

Finsterle, S. (2007). *iTOUGH2 User's Guide.* (LBNL-40040). California: Lawrence Berkeley National Laboratory. Available at: https://static1.squarespace.com/static/57b526322994ca46e44b1da6/-t/5aa16391085229dea8c15bd7/1520526232928/iTOUGH2_Users_Guide.pdf [2018-11-21]

Franzson, H. (1998). Reservoir geology of the Nesjavellir hightemperature field in SW-Iceland. In *Proceedings 19th Annual PNOC-EDC Geothermal Conference*, Manila

Franzson, H., Kristjánsson, B.R., Gunnarsson, G., Björnsson, G., Hjartarson, A., Steingrímsson, B., Gunnlaugsson, E., Gíslason G. (2005). The Hengill Hellisheidi geothermal field. Development of a conceptual geothermal model. In *Proceedings World Geothermal Congress 2005*, Antalya, Turkey, CD, 7 pp.

Franzson, H., Gunnlaugsson, E., Árnason, K., Sæmundsson, K., Steingrímsson, B., Harðarson, B.S. (2010). The Hengill Geothermal System, Conceptual Model and Thermal Evolution. In *Proceedings World Geothermal Congress 2010*. Bali, Indonesia.

Friðleifsson, G.Ó. And Elders, W.A. (2017). The Iceland Deep Drilling Project geothermal well at Reykjanes successfully reaches its supercritical target. *GRC Bulletin,* pp. 30-33. Available at: https://geothermal.org/PDFs/Articles/17MarchApril.pdf [2018-11-19]

Gunnarsdóttir, S and Poux, B. (2016). *3D Modelling of Hellisheiði Geothermal Field using Leapfrog: Data, Workflow and Preliminary Models*. Report ÍSOR-2016/039. Reykjavík: ÍSOR.

Gunnarsson, G., Arnaldsson, A. and Oddsdóttir, A.L. (2011). Model Simulations of the Hengill Area, Southwestern Iceland*. Transport in Porous Media*, vol. 90, pp. 3–22. DOI: 10.1007/s11242-010-9629-1

Gunnarsson, G. and Aradóttir E.S.P. (2015). The Deep Roots of Geothermal Systems in Volcanic Areas: Boundary Conditions and Heat Sources in Reservoir Modeling. *Transport in Porous Media*, vol. 108 (1), pp. 43–59. DOI: 10.1007/s11242-014-0328-1

Gunnlaugsson, E. and Ívarsson, G. (2010). Direct Use of Geothermal Water for District heating in Reykjavík and Other Towns and Communities in SW-Iceland. In *Proceedings World Geothermal Congress 2010.* Bali, Indonesia. Available at: https://www.geothermal-energy.org/pdf/IGAstandard/WGC/2010/3418.pdf [2018-02-01]

Hayba D.O. and Ingebritsen S.E. (1997) Multiphase groundwater flow near cooling plutons. *Journal of Geophysical Research,* vol. 102(B6), pp.12235-12252

Haukwa, C.B. (1998*). AMESH—A Mesh Creating Program for the Integral Finite Difference Difference Method.* (LBNL-45284). California: Ernesto Orlando Lawrence Berkeley National Laboratory. Available at: http://esd1.lbl.gov/files/research/projects/tough/documentation/AMESH_Users_Guide.pdf [2018-11-16]

Helgadóttir, H.M., Snæbjörnsdóttir, S.O., Níelsson, S., Gunnarsdóttir, S.H., Matthíasdóttir, T., Harðarson, B.S., Einarsson, G.M., Franzson, H. (2010). Geology and Hydrothermal Alteration in the Reservoir of the Hellisheiði High Temperature System, SW-Iceland. In *Proceedings World Geothermal Congress 2010.* Bali, Indonesia

IDDP (2018). *SAGA REPORT No. 11, IDDP-2 Way Forward Workshop*. Available at: http://iddp.is/wp-content/uploads/2018/04/Way-Forward-Workshop-20-21-March-2018-SAGA-REPORT-No-11.pdf [2018-11-19]

Ingebritsen, S. E., and C. E. Manning (2010), Permeability of the continental crust: Dynamic variations inferred from seismicity and metamorphism, *Geofluids*, vol. 10, pp. 193–205 (Reprinted in Yardley, B., Manning, C., and Garven, G., eds., 2011, Frontiers in Geofluids: Chichester, U. K.,

Wiley-Blackwell, p. 193–205.).

Kim, D., et al. (2018). Magma "bright spots" mapped beneath Krafla, Iceland, using RVSP imaging of reflected waves from microearthquakes, *J. Volcanol. Geotherm. Res*., vol. VOLGEO-06365, DOI: https://doi.org/10.1016/j.jvolgeores.2018.04.022

Kristjánsson, B.R., Axelsson, G., Gunnarsson, G., Gunnarsson, I. and Óskarsson, F. (2016). Comprehensive Tracer Testing in the Hellisheiði Geothermal Field in SW-Iceland. In *Proceedings, 41st Workshop on Geothermal Reservoir Engineering*. Stanford, California. Available at: https://pangea.stanford.edu/ERE-/db/GeoConf/papers/SGW/2016/Kristjansson.pdf [2017-11-06]

Magnúsdóttir, L. and Finsterle, S. (2015). *iTOUGH2-EOS1SC: Multiphase Reservoir Simulator for Water under Sub- and Supercritical Conditions User's Guide*. California: Lawrence Berkeley National

Laboratory. Available at: https://static1.squarespace.com/static/57b526322994ca46e44b1da6/-t/5b64ebe06d2a73ce52d25ad0/1533340641787/iTOUGH2-EOS1sc_Users_Guide.pdf [2019-05-22]

Doc.nr: HEATSTORE-D2.1
Version: Rev. Final 2021.12.21
Classification: Public
Page: 355 of 355

Manning, C.E. and Ingebritsen, S.E (1999). Permeability of the continental crust: Implications of geothermal data and metamorphic systems, *Reviews of Geophysics,* vol. 37(1), pp. 127-150. DOI: https://doi.org/10.1029/1998RG900002

National Land Survey of Iceland (2018). *Niðurhalsþjónusta* [Download service]. Available at: https://www.lmi.is/en/licence-for-national-land-survey-of-iceland-free-data/ [2018-11-18]

Orkustofnun (2020). *Orkutölur 2019.* Reykjavík: Orkustofnun. Available at: https://orkustofnun.is/gogn/os-onnur-rit/Orkutolur-2019-islenska.pdf [2021-04-13]

Pruess, K., Oldenburg, C. and Moridis, G. (2012). *TOUGH2 User's guide, Version 2.* (LBNL-43134). California: Lawrence Berkeley National Laboratory. Available at: http://esd1.lbl.gov/files/research-/projects/tough/documentation/TOUGH2_V2_Users_Guide.pdf [2018-11-21]

Saemundsson, K., 1995: Geological map of the Hengill area 1:50,000. Orkustofnun, Reykjavík.

Scott S., Driesner T., and Weis P. (2015): Geologic controls on supercritical geothermal resources above magmatic intrusions. *Nature Communications,* vol. 6(7837). DOI: 10.1038/ncomms8837

Scott, S., Driesner, T. and Weis, P. (2016). The thermal structure and temporal evolution of high-enthalpy geothermal systems. *Geothermics,* vol. 62, pp. 33-47.Available at: https://www.science-direct.com/science/article/pii/S0375650516300049 [2019-05-22]

Sinton, J., Grönvold, K., Sæmundsson, K. (2005). Postglacial eruptive history of the Western Volcanic Zone, Iceland. *Geochemistry, Geophysics, Geosystems,* vol. 6(12).

Snæbjörnsdóttir, S.Ó. et al. (2018). The geology and hydrology of the CarbFix2 site, SW-Iceland. *Energy Procedia,* vol. 146 (2018), pp. 146-157.

Stefánsson, A., Gunnarsson, J. and Gunnarsson, I. (2019). *Supercritical geothermal reservoir at Nesjavellir and Hellisheiði (Iceland) identified using boron and chlorine systematics.* Unpublished report.

Tryggvason, A., Rögnvaldsson, S.Th. and Flóvenz, Ó.G. (2002). Three-dimensional imaging of the P- and S-wave velocity structure and earthquake locations beneath Southwest Iceland. *Geophys. J. Int.*, vol. 151, pp. 848-866

Vatnaskil (2017). *Höfuðborgarsvæði – Grunnvatns- og rennslislíkan. Árleg endurskoðun fyrir árið 2016.* [Capital area- Groundwater and discharge model. Yearly revision for the year 2016], Report 17.15. Reykjavík: Vatnaskil Consulting Engineers

Vatnaskil (2020). *Höfuðborgarsvæði. Árleg endurskoðun rennslislíkans. Framgangur endurskoðunar 2020.* [Capital area- Yearly revision of Groundwater and discharge model for the year 2020], Report 20.12. Reykjavík: Vatnaskil Consulting Engineers

Violay, M. E. S., B. Gibert, D. Mainprice, B. Evans, J.-M. Dautria, P. Azais, and P. Pézard (2012). An experimental study of the brittle-ductile transition of basalt at oceanic crust pressure and temperature conditions, *J. Geophys. Res.*, vol. 117(B03213). DOI:10.1029/2011JB008884.

Weis, P., Driesner, T., Coumou, D and Geiger, S. (2014). Hydrothermal, multiphase convection of H_2O-NaCl fluids from ambient to magmatic temperatures: a new numerical scheme and benchmarks for code comparison. *Geofluids.* vol. 14(3). Available at: https://onlinelibrary.wiley.com-/doi/full/10.1111/gfl.12080 [2019-05-22]

Weis P. (2015): The dynamic interplay between saline fluid flow and rock permeability in magmatic-hydrothermal systems. *Geofluids*, vol. 15, pp. 350–371

355